ST. PETERSBURG STATE POLYTECHNICAL UNIVERSITY JOURNAL

Physics and Mathematics

VOLUME 18, No.3.1, 2025

ST. PETERSBURG STATE POLYTECHNICAL UNIVERSITY JOURNAL. PHYSICS AND MATHEMATICS

НАУЧНО-ТЕХНИЧЕСКИЕ ВЕДОМОСТИ

САНКТ-ПЕТЕРБУРГСКОГО ГОСУДАРСТВЕННОГО ПОЛИТЕХНИЧЕСКОГО УНИВЕРСИТЕТА

Физико-математические науки

ТОМ 18, №3.1
2025

НАУЧНО-ТЕХНИЧЕСКИЕ ВЕДОМОСТИ САНКТ-ПЕТЕРБУРГСКОГО ГОСУДАРСТВЕННОГО ПОЛИТЕХНИЧЕСКОГО УНИВЕРСИТЕТА. ФИЗИКО-МАТЕМАТИЧЕСКИЕ НАУКИ

Адрес редакции и издательства:

Россия, 195251, Санкт-Петербург, ул. Политехническая, д. 29.
Тел. редакции 8 (812) 552-62-16.
http://ntv.spbstu.ru/physics

PREFACE

12th International School and Conference on Optoelectronics, Photonics, Engineering and Nanostructures (SPb OPEN – 2025) / 12-я Международная школа-конференция по оптоэлектронике, фотонике, инженерии и наноструктурам

The 12th International School and Conference on Optoelectronics, Photonics, Engineering and Nanostructures (SPb OPEN 2025) was held on May 20–25, 2025. It continues the annual schools and seminars for young scientists on physics and technology of nanostructures, organized since 2009, spearheaded by Zhores Alferov, RAS Academician and winner of the 2000 Nobel Prize in Physics.

The School was organized by the St. Petersburg Higher School of Economics, Peter the Great St. Petersburg Polytechnic University, with the support of the HSE Academic Fund Programme, Photonics Russia and Special Systems Photonics LLC.

The Program Committee of the School and Conference selected 250 papers by young scientists, graduate and undergraduate students from 22 cities in Russia and Belarus. The same as last year, the average age of the attendees was under 27 years old, over 70% of the reports were presented by attendees under 30.

Presentations were given in six panels:
- Synthesis and structural properties of semiconductor materials and nanostructures,
- Lasers, solar cells, other optoelectronic devices,
- Nanophotonics, spectroscopy, microresonators, optical properties, plasmonics,
- Biophysics, nanobiotechnology, biophotonics,
- Electrical, magnetic and microwave characteristics and devices,
- Other aspects of nanotechnology.

The highest percentage of reports (23%) were given in the section "Nanophotonics...", closely followed by "Lasers..." with 22% of reports. Twenty of the best reports by young scientists were awarded with diplomas of the conference.

In addition to poster presentations from young scientists, the programme included a series of keynote speeches by prominent researchers, outlining the main advances and challenges in various fields of physics and technology. In total, 99 leading scientists participated in the conference. The keynote speakers included:
- Alexander Alodjants (ITMO University)
- Alexander Mintairov (University of Notre Dame, USA / Ioffe Institute)
- Alexey Toropov (Ioffe Institute)
- Maria Kuznetsova (St. Petersburg State University)
- Ivan Mukhin (Alferov University)
- Ivan Makhov (St. Petersburg Higher School of Economics)
- Georgiy Sapunov (Changchun Institute of Optics, Fine Mechanics and Physics, China)
- Yating Wan (King Abdullah University of Science and Technology, Saudi Arabia)
- Alexey Ustinov (Saint Petersburg Electrotechnical University "LETI")
- Maxim Vinnichenko (Peter the Great St. Petersburg Polytechnic University)

The same as last year, the peer-reviewed reports from the conference are published in St. Petersburg State Polytechnical University Journal: Physics and Mathematics. The Programme Committee of SPbOPEN-2025 hopes that the range of subjects presented at

the conference will be of interest to the journal's audience. We would like to thank the journal for giving us the opportunity to publish the proceedings, and thank the reviewers for useful recommendations and constructive criticism. We of course express our gratitude to all participants of the conference.

We invite young scientists, graduate and undergraduate students to take part in the next Saint Petersburg OPEN School and Conference in 2026! Please visit https://spb.hse.ru/spbopen/ for more details.

Alexey Zhukov
School of Computer Science, Physics and Technology
Higher School of Economics, St. Petersburg

aezhukov@hse.ru

Contents

Condensed matter physics

Simulation of physical processes

Atom physics and physics of clusters and nanostructures

Physical materials technology

Biophysics and medical physics

Radiophysics

Theoretical physics

CONDENSED MATTER PHYSICS

Comparison of the refractive index changes of nanolayers of amidated and carboxylated carbon nanotubes after adsorption of water and ammonia molecules

A.V. Romashkin [1] ✉, R.Yu. Rozanov [2], A.S. Vishnevskiy [3],

A.E. Mitrofanova [2, 4], A.N. Stebelkov [2], V.V. Nepomilueva [1],

D.D. Levin [2], V.V. Svetikov [2, 5], V.K. Nevolin [1]

[1] National Research University of Electronic Technology, Moscow, Russia;

[2] JSC "Zelenograd Nanotechnology Center", Moscow, Russia;

[3] MIREA – Russian Technological University, Moscow, Russia;

[4] Moscow Institute of Physics and Technology, Dolgoprudny, Russia;

[5] Prokhorov General Physics Institute of the RAS, Moscow, Russia

✉ romaleval@gmail.com

Abstract. Spray-deposited layers of amidated carbon nanotubes (ACNTs) were characterized using AFM, Raman scattering, and spectroscopic ellipsometry. The layer thickness, diameters, and band gap of ACNTs, as well as the changes in the refractive index (n) at 1319 nm and 1625 nm after H_2O and NH_3 adsorption in air and H_2O in N_2 were analyzed in comparison with carboxylated CNTs. Modeling the resonance peak shift due to changes in n for the ACNT-coated Si waveguide microring resonator after NH_3 adsorption allows us to propose the use of such a CNT layer set for integrated optical sensors for gas recognition tasks.

Keywords: carbon nanotube, ellipsometry, integrated optics, microring resonator, sensor

Сравнение изменений показателя преломления нанослоев амидированных и карбоксилированных углеродных нанотрубок после адсорбции молекул воды и аммиака

А.В. Ромашкин [1] ✉, Р.Ю. Розанов [2], А.С. Вишневский [3],

А.Е. Митрофанова [2, 4], А.Н. Стебельков [2], В.В. Непомилуева [1],

Д.Д. Левин [2], В.В. Светиков [2, 5], В.К. Неволин [1]

[1] Национальный исследовательский университет «МИЭТ», Москва, Россия;

[2] АО «Зеленоградский нанотехнологический центр», Москва, Россия;

[3] МИРЭА – Российский технологический университет, Москва, Россия;

[4] Московский физико-технический институт (национальный исследовательский университет), г. Долгопрудный, Россия;

[5] Институт общей физики им. А. М. Прохорова РАН, Москва, Россия

✉ romaleval@gmail.com

Аннотация. Аэрозольно нанесенные слои амидированных углеродных нанотрубок (АУНТ) исследовались методами АСМ, комбинационного рассеяния света и спектроскопической эллипсометрии. Изменения показателя преломления (n) при 1319 нм и 1625 нм после адсорбции H_2O и NH_3 сравнивались с карбоксилированными УНТ. Смоделированный сдвиг резонансного пика Si микрокольцевого волноводного резонатора, покрытого АУНТ, при адсорбции NH_3 позволяет предложить использование таких слоев УНТ для интегрально-оптических сенсоров для задач распознавания газов.

Ключевые слова: углеродная нанотрубка, эллипсометрия, интегральная оптика, микрокольцевой резонатор, сенсор

Introduction

For an integrated optical sensor array providing gas recognition, to achieve high sensitivity and form sensors with significantly different responses, it is important to develop thin modifying layers that significantly change the intrinsic refractive index (n) upon adsorption of the analyte [1−4]. Various modified carbon nanomaterials are promising for these tasks and can provide opposite sensor responses to the same analyte by changing only the functional group type [5] or by changing the carrier gas, which can alter their electronic structure [4, 6]. However, identifying the mechanisms of change in the n for CNTs functionalized by different groups at different wavelengths (λ) during the adsorption of various molecules remains a relevant task to develop such a sensor array. Previously, we studied the effect of molecular adsorption on the $n(\lambda)$ dependence only for carboxylated CNTs (CCNT) [4], but amidated CNTs (ACNT) have not been studied enough [5]. Therefore, the aims of this work are to study the change in the n after adsorption of NH_3 and H_2O in both air and oxygen-free (N_2) gas in order to identify the features of the sensor response of ACNT and its differences from CCNTs. Recent results on optical gas sensors based on microring resonators (MRR), which even use metallic layers (high extinction coefficient (k)), also open up new possibilities for the development of such sensor layers [7, 8].

Materials and Methods

We studied sparse and dense networks of ACNTs (P9-SWNT, Carbon Solutions). Layer thicknesses were measured by AFM (NT-MDT). The CNT diameter and band gap (E_g) were

evaluated [9] from the RBM-band Raman map (532 nm laser, Nano Scan Technology). ACNTs were spray deposited from a dispersion [4] onto an oxygen plasma treated Si substrate with 29 nm SiO_2. The residual solvent (ethanolamine, instead of N-methylpyrrolidone used for CCNT [4], due to the higher ACNT dispersion stability) was removed with iterative rinsing in solutions of acetic and then formic acid in butyl acetate. The ACNT layer absorbance was evaluated by the suppression of Raman of Si by the ACNT layer (at $\lambda \approx 550$ nm), and thickness was evaluated by AFM force−distance curves and lithography [4]. Conductivity type in air at a relative humidity (RH) of 40% was determined from the I−V characteristics for the ACNT sparse network on a SiO_2 (300 nm)/Si substrate. The resistive responses were measured by conductivity recovery after exposure for 15 min to ~12500 ppm H_2O (ΔRH ~45%) or 2-propanol (IPA) or ethanol (22% and 17% of saturated vapor at 23 °C, but both ~12500 ppm) or 2000 ppm NH_3 and compared with a denser ACNT network. The latter was also measured by spectroscopic ellipsometry (SENTECH Instruments) using similar analyte concentrations. It was performed at a 75° (70° in N_2) angle of incidence after exposure in a chamber with H_2O or NH_3 and after 25 min of desorption under normal conditions in the same sample area, but different for each analyte. Exposure to H_2O or IPA in N_2 was realized in situ [4]. The values of the n and k of the layer were estimated from the Drude−Lorentz model [4]. Numerical modeling (finite-difference time-domain and beam propagation methods, RSoft CAD) was performed to evaluate phase shift, losses, and resonance peak shift of the ACNT-coated Si waveguide and MRR after NH_3 adsorption at 1625 nm.

Results and Discussion

Dense and sparse ACNT networks (~10 nm and ~1 nm layers, Fig. 1, a) with diameters ranging from 1.3 to 1.7 nm (band gap $E_g \approx 0.63-0.81$ eV) show similar values for both CNT diameters, band gaps, and the dependence of absorbance on layer thickness compared to CCNTs [4] (Fig. 1, b). However, despite the similar (p-type) behavior of channel conductivity under gate field control [10] and similar ACNT resistive responses to H_2O and NH_3 (Fig. 1, c) compared to CCNT [11], the response to IPA (4%) is noticeably lower than to H_2O (40%) or even to ethanol (15%). For CCNT, on the contrary, the response to ethanol can be comparable to NH_3 in N_2 [12]. This can be used to form an array of resistive and optical sensors for gas recognition.
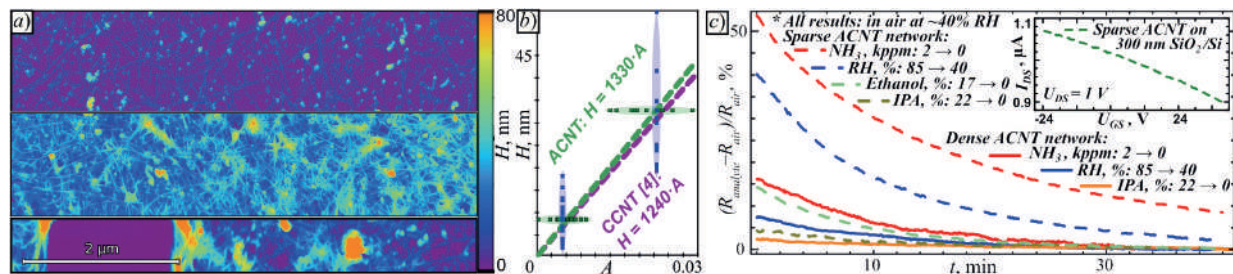
Fig. 1. AFM of sparse (top), dense (below) ACNT networks (a); graph of thickness versus absorbance (b); resistive response versus time after analyte exposure, inset: graph of current (I_{DS}) versus gate voltage (U_{GS}) (c)

When exposed to H_2O in air, the n of ACNT dropped slightly from 1.708 to 1.706 at 1625 nm ($\Delta n \approx -0.002$ as opposed to $\Delta n \approx 0.002$ for CCNT) and was 1.628, but did not change at 1319 nm ($\Delta n < 0.001$ versus $\Delta n \sim 0.012$ for CCNT, Fig. 2, a). The decrease in the n with increasing H_2O concentration occurs only near 1625 and 1410 nm (0.763 and 0.88 eV), which corresponds to the opposite changes in experimental $\Delta(E)$ and $\Psi(E)$ data for ACNT compared to CCNT (Fig. 2, b, c). This is presumably due to specific local changes in the density of states spectrum [13] for ACNTs. Although, when exposed to H_2O, near the main peak of $n(E)$, located at the photon energy close to the CNT band gap energy, an increase in the n is observed in air (but a decrease in N_2) with a slight decrease in the charge carriers concentration (p) for ACNTs in the Drude−Lorentz model: $\Delta p \approx -0.2\%$ in air, but $\Delta p \approx 1\%$ with RH change from 20 to 65% in N_2. This also corresponds to the resistive response in air for CCNT [11] and ACNT (~7% for dense network, Fig. 2, c). This effect is presumably related to a charge carrier type change: from holes in air to electrons in dry N_2, and is observed for both ACNT and CCNT [4, 6]. H_2O and NH_3 are donors for CNTs,

opposed to O_2 and NO_2, both of which are charge acceptors [13]. Thus, in air, H_2O and NH_3 reduce the concentration of CNT carriers [11], but in the absence of O_2, the opposite occurs for both ACNT and CCNT [4]. When exposed to NH_3, the n increased: from 1.697 to 1.710 at 1625 nm, from 1.620 to 1.638 at 1319 nm for ACNTs (Fig. 2, a). It corresponds to an increase in resistivity for both ACNTs (Fig. 1, c) and CCNTs [4, 11]. However, the ratio of responses to NH_3 and H_2O changes for ACNTs from -6.5 at 1625 nm to ~18 at 1319 nm. In contrast, for CCNTs this ratio is ~2 at 1625 nm and close to zero at 1319 nm. These changes in the ratio are apparently due to local but different changes in the band structure (and away from the edges of the CNT band gap) for both ACNT and CCNT and can provide the recognition of NH_3 versus H_2O in air using only CCNTs [4] or ACNTs, in contrast to resistive sensors [11].
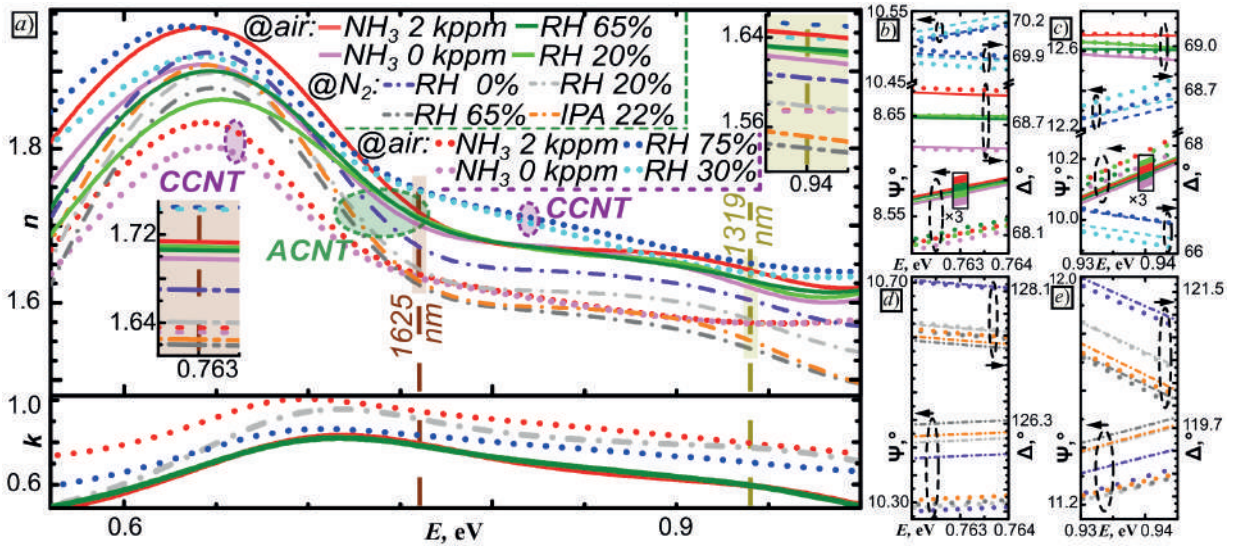
Fig. 2. n and k as a function of photon energy (E) for ACNT and CCNT (a), insets: enlarged $n(E)$ near $\lambda = 1625$ nm and $\lambda = 1319$ nm; Drude−Lorentz model (lines) for fitting to ellipsometry data (dots): $\Delta(E)$ and $\Psi(E)$ near the specified λ for the adsorption of H_2O and NH_3 in air (b, c); H_2O and IPA in N_2 (d, e)

The ACNTs, differing in the Δn direction in air after adsorption of NH_3 ("+" Δn) and H_2O (low, but "−" Δn) at 1625 nm with response (i.e., Δn) only to NH_3 at 1319 nm, also allow recognition of these gases. The response behavior differences for ACNT versus CCNT can only be associated with the different types of functional groups, since the remaining features of CNTs (E_g, the IR absorption peaks) are similar, and for non-functionalized CNTs, both NH_3 and H_2O are donors [4] and should not form the opposite sensor response in air. Although, H_2O in dry N_2 as a carrier gas gives a drop in the n for both ACNT and CCNT. The initial n value at $\lambda = 1319$ nm for ACNT in dry N_2 was 1.602. The n values during exposure to H_2O (subsequent N_2 purging) were at 20% and 65% RH: 1.579 (1.596) and 1.541 (1.565). The incomplete return is due to incomplete desorption during the 20-minute low-flow N_2 purge, which is typical for CNTs [4, 11]. For ACNT, despite the low resistive response to IPA in air and low Δn value at IPA exposure in N_2 near the main peak of $n(E)$ ($\Delta n \approx -0.02$ at $E \approx 0.65$ eV), the Δn was higher in modulus at 1625 nm and 1319 nm ($\Delta n \approx -0.05$), which is higher than for NH_3 in air. This indicates an improvement in the gas recognition capabilities when using several λ.

Modeling showed that the phase shift of 0.2° per 100 μm length is achieved in the Si waveguide coated with a 1 nm ACNT layer with a 50 nm SiO_2 sublayer. Thus, at ~22.5 mm a $\pi/2$ phase shift can be achieved. However, accounting for losses due to the high k of CNT obtained from ellipsometry (Fig. 2, a) does not allow the implementation of such an interferometer arm. The losses are ~0.9 dB per 100 μm (Fig. 3, a). The phase shift to loss ratio is 0.22°/dB.

Further increases in the sublayer do not lead to an improvement in this ratio. However, despite the high losses, the sensor structure can be implemented based on the ACNT-coated Si waveguide MRR structure (Fig. 3, b), similar to known results [7]. Modeling showed that

15
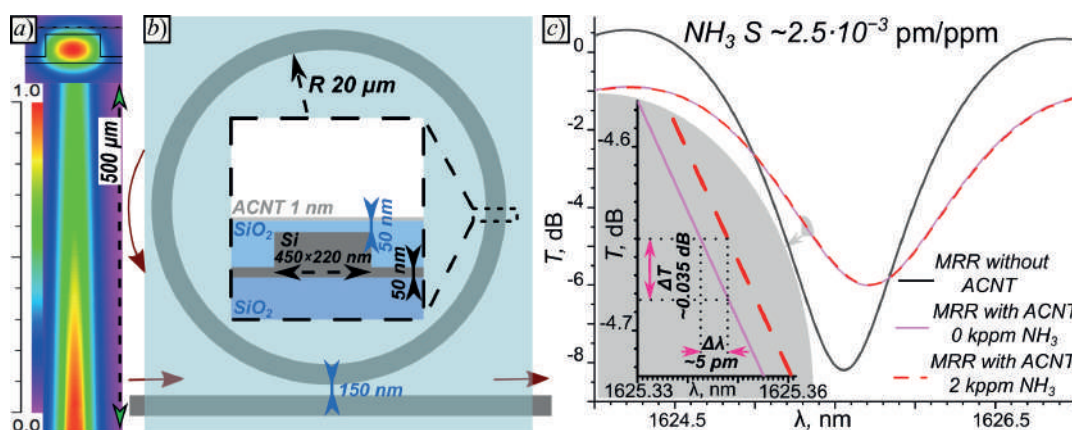
Fig. 3. Simulation results: electric field distribution and losses of ACNT-coated waveguide (*a*); scheme of microring resonator sensor (*b*); transmission spectra with resonance peak shift after NH_3 adsorption (*c*)

the quality factor (*Q*) of the proposed structure is 1900 without the CNT layer and 1200 with it, due to losses in the ACNT layer. Therefore, the MRR radius was chosen to be limited to 20 μm. The free spectral range was 6 nm, slightly higher than known [14] due to the use of a ribbed waveguide (Fig 3, *a*, *b*). Since the implementation of a gap between coupled waveguides less than 150 nm complicates the implementation [7, 8], this distance was chosen, even though critical coupling has not yet been fully realized. Thus, the extinction ratio and *Q* were lower than reported in the experiment [7]. The estimate of the resonance peak shift after NH_3 adsorption was about 5 pm (Fig. 3, *c*, red shift). This, assuming a noise level estimation of ~0.1 pm [7] and a linear response on concentration dependence, yielded an estimate of the sensitivity (*S*) to NH_3 as $2.5 \cdot 10^{-3}$ pm/ppm and a detection limit of ~40 ppm, comparable to the use of a special polymer, with higher changes in its *n* during the analyte adsorption [7]. However, recently a higher *S* value has been achieved for a similar sensor layer by changing only the MRR parameters [8]. Thus, it is presumed that the *S* of the proposed structure can also be improved. Moreover, the proposed structure with ACNT implemented for two λ can allow the recognition of NH_3 versus H_2O due to the difference in their response ratios at 1319 nm and 1625 nm. More reliable recognition can be implemented using ACNTs and CCNTs together, even at the same λ (even at 1625 nm), due to the larger differences in the responses between them. This is important because typically for a single sensor layer, the RH change can also affect the resonance peak shift, interfering with the analysis of target analyte [8]. However, changes in the band structure of CNTs during analyte adsorption can change not only the *n* but also *k*, which distinguishes them from the known polymer [7, 8], and can change the resonance peak width, complicating measurements.

Conclusion

Despite the similar behavior of the resistive response of ACNT and CCNT, ellipsometry showed significant changes in the ratio of responses to NH_3 and H_2O, expressed in the refractive index changes (Δ*n*) at 1625 nm and 1319 nm for both ACNT and CCNT, especially between them, despite their differing only in the functional group types. Therefore, spray-deposited ACNTs or CCNTs can be used to modify the Si waveguide in a microring resonator (MRR) to manufacture the proposed integrated optical sensor, providing acceptable sensitivity, recognition of NH_3 versus H_2O. It can be implemented for two wavelengths using only ACNT or CCNT, or even for one wavelength when using ACNT and CCNT together in a sensor set capable of even better recognition of the gases. Despite the fairly high extinction coefficient of CNTs, the use of the MRR structure allows the use of such thin (~1 nm) CNT layers to implement integral optical sensor structures. The noticeable CNT Δ*n* at photon energies far from the CNT band gap, presumably caused by the density of states changes in the CNT band structure with analyte adsorption, opens up new additional mechanisms for improving the sensors response selectivity. The combined use of such optical and resistive sensors significantly expands the possibilities of developing multisensor systems. This can be used for the development of integrated optical gas sensor array based on functionalized carbon nanomaterials and new principles of gas recognition.

REFERENCES

1. **Laplatine L., Fournier M., Gaignebet N., Hou Y., Mathey R., Herrier C., Liu J., Descloux D., Gautheron B., Livache T.,** Silicon photonic olfactory sensor based on an array of 64 biofunctionalized Mach-Zehnder interferometers, Optics Express. 30 (19) (2022) 33955.

2. **Huang G., Li Y., Chen C., Yue Z., Zhai W., Li M., Yang B.,** Hydrogen sulfide gas sensor based on titanium dioxide/amino-functionalized graphene quantum dots coated photonic crystal fiber, Journal of Physics D: Applied Physics. 53 (32) (2020) 325102.

3. **Huang X., Li X., Yang J., Tao C., Guo X., Bao H., Yin Y., Chen H., Zhu Y.,** An in-line Mach-Zehnder interferometer using thin-core fiber for ammonia gas sensing with high sensitivity, Scientific reports. 7 (1) (2017) 44994.

4. **Romashkin A.V., Rozanov R.Yu., Lashkov A.V., Vishnevskiy A.S., Mitrofanova A.E., Levin D.D., Svetikov V.V.,** Change in the carbon nanotube thin layer refractive index after water and ammonia molecules adsorption, St. Petersburg State Polytechnical University Journal. Physics and Mathematics. 17 (3.1) (2024) 68−74.

5. **Rani S., Kumar M., Garg R., Sharma S., Kumar D.,** Amide functionalized graphene oxide thin films for hydrogen sulfide gas sensing applications, IEEE Sens. J. 16 (9) (2016) 2929.

6. **Avouris P., Martel R., Derycke V.,** Appenzeller J., Carbon nanotube transistors and logic circuits, Physica B: Condensed Matter. 323 (1−4) (2002) 6−14.

7. **Mi G., Horvath C., Van V.,** Silicon photonic dual-gas sensor for H_2 and CO_2 detection, Optics express. 25 (14) (2017) 16250−16259.

8. **Wang J., Zhang H., Chen S., Zhang Z., Wu G., Li X., Ding P., Tan C., Du Y., Geng Y., Li X., Tsang H. K., Cheng Z.,** A Silicon Microring Resonator for Refractive Index Carbon Dioxide Gas Sensing, ACS sensors. 10 (7) (2025) 4938−4944.

9. **Gelao G., Marani R., Perri A. G.,** A formula to determine energy band gap in semiconducting carbon nanotubes, ECS J. Solid State Sci. Technol. 8 (2) (2019) M19.

10. **Struchkov N.S., Romashkin A.V., Rabchinskii M.K., Saveliev S.D., Cherviakova P.D., Chumakov R.G., Nevolin V.K., Varezhnikov A.S., Emelianov A.V.,** Aminated reduced graphene oxide-carbon nanotube composite gas sensors for ammonia recognition, Sensors and Actuators B: Chemical. 417 (2024) 136088.

11. **Romashkin A.V., Lashkov A.V., Sysoev V.V., Struchkov N.S., Alexandrov E.V., Levin D.D.,** Energy-Efficient Chemiresistive Sensor Array Based on SWCNT Networks, WO_3 Nanochannels and SWCNT-Pt Heterojunctions for NH_3 Detection against the Background Humidity, Chemosensors. 10 (11) (2022) 476.

12. **Abdellah A., Abdelhalim A., Horn M., Scarpa G., Lugli P.,** Scalable spray deposition process for high-performance carbon nanotube gas sensors. IEEE Transactions on Nanotechnology. 12 (2) (2013) 174−181.

13. **Zhao J., Buldum A., Han J., Lu J.P.,** Gas molecule adsorption in carbon nanotubes and nanotube bundles, Nanotechnology. 13 (2) (2002) 195−200.

14. **Bogaerts W., De Heyn P., Van Vaerenbergh T., De Vos K., Kumar Selvaraja S., Claes T., Dumon P., Bienstman P., Van Thourhout D.,** Baets R., Silicon microring resonators, Laser & Photonics Reviews. 6 (1) (2012) 47−73.

THE AUTHORS

ROMASHKIN Alexey V.
romaleval@gmail.com
ORCID: 0000-0002-0101-6122

ROZANOV Roman Yu.
roman-roz@yandex.ru
ORCID: 0000-0001-5063-1669

VISHNEVSKIY Alexey S.
alexeysw@mail.ru
ORCID: 0000-0002-4024-5411

MITROFANOVA Anastasia E.
mitrofanova.ae@phystech.edu
ORCID: 0009-0004-5306-278X

STEBELKOV Artem N.
stebelkov@zntc.ru

SVETIKOV Vladimir V.
svetikov@nsc.gpi.ru

NEPOMILUEVA Valeriya V.
valeria.nepomilueva@yandex.ru

NEVOLIN Vladimir K.
vkn@miee.ru

LEVIN Denis D.
skaldd@yandex.ru
ORCID: 0000-0002-8414-6191

Ordered GaAs NW growth on Si(111) substrates modified by two-step FIB treatment

N.A. Shandyba [1] ✉, M.M. Eremenko [1], D.D. Dukhan [1], N.E. Chernenko [1],

D.V. Kirichenko [1], A.D. Kugaevsky [1], I.S. Makhov [2], N.V. Kryzhanovskaya [2],

S.V. Balakirev [1], M.S. Solodovnik [1]

[1] Southern Federal University, Taganrog, Russia;

[2] National Research University Higher School of Economics, St. Petersburg branch,

St. Petersburg, Russia

✉ shandyba.nikita@gmail.com

Abstract. This work demonstrates, for the first time, the selective formation of ordered arrays of vertical GaAs nanowires on Si(111) with a native oxide layer using a two-step pre-treatment of the substrate surface with a focused Ga-ion beam. Based on our previous studies, we show that modifying the substrate through a two-step protocol — first applying a continuous surface treatment with low doses (up to 1×10^{-13} C/μm^2), followed by spot treatment with medium doses (from 1×10^{-13} to 1×10^{-12} C/μm^2) — effectively suppresses parasitic growth and enables nanowire formation at defined surface locations. Furthermore, adjusting the spacing between ion implantation points (from 0.5 to 5 um) allows precise control over the pitch of the nanowire array. By optimizing dose values, we achieve the formation of single, free-standing, vertically oriented nanowires at each ion beam impact site. The study of optical properties of nanowire arrays reveals their high structural quality, as evidenced by intense photoluminescence of GaAs up to room temperatures

Keywords: silicon, focused ion beam, molecular beam epitaxy, nanowires, III-V, nanopatterning, site-controlled

Упорядоченный рост нанопроволок GaAs на Si(111) подложках, модифицированных при помощи двухэтапной обработки поверхности фокусированным ионным пучком

Н.А. Шандыба [1] ✉, М.М. Ерёменко [1], Д.Д. Духан [1], Н.Е. Черненко [1],

Д.В. Кириченко [1], А.Д. Кугаевский [1], И.С. Махов [2], Н.В. Крыжановская [2],

С.В. Балакирев [1], М.С. Солодовник [1]

[1] Южный федеральный университет, г. Таганрог, Россия;
[2] Национальный исследовательский университет «Высшая школа экономики»,
Санкт-Петербургский филиал, Санкт-Петербург, Россия
✉ shandyba.nikita@gmail.com

Аннотация. Впервые продемонстрировано селективное формирование упорядоченных массивов вертикальных нитевидных нанокристаллов GaAs на подложках Si(111) с собственным оксидом, модифицированных путем двухэтапной обработки поверхности ионным пучком Ga⁺. В данном подходе сначала проводится сплошная обработка подложки малыми, а затем точечная большими дозами, что позволяет подавить паразитный рост в области модификации и стимулировать формирование нитевидных нанокристаллов в заданных точках. Оптимизация доз и расстояния между точками воздействия ионного пучка позволяет получать одиночные вертикальные нитевидные нанокристаллы GaAs, демонстрирующие интенсивную фотолюминесценцию при комнатной температуре

Ключевые слова: кремний, фокусированный ионный пучок, молекулярно-лучевая эпитаксия, нитевидные нанокристаллы, полупроводники III-V, нанолитография, позиционно-контролируемый рост

Introduction

III-V nanowires (NWs) open wide possibilities for the fabrication of integrated microscale light sources and detectors on cost-effective Si substrates. NW-based devices require efficient self-organization techniques that ensure precise positioning and control over nanowire properties. A promising approach to this problem involves the pre-treatment of the growth surface by focused ion beam (FIB) and nanowire formation via molecular beam epitaxy (MBE) [1]. However, this method remains poorly understood, especially in the context of creating regular structures and investigating their properties. In this work, we proposed a new approach to obtain regular NWs using a two-step pre-growth FIB treatment of the Si(111) surface with native oxide layer.

Materials and Methods

In our previous research, we have shown that pre-treatment of Si(111) substrate with a low ion dose leads to local suppression of NW growth, a medium dose intensifies NW growth and a high dose results in the formation of polycrystalline GaAs [2]. Understanding the mechanisms and optimizing the modes allows precise control of nanowire characteristics and prediction of surface morphology when using multiple ion beam processing modes simultaneously. In this work, to form ordered NW arrays without parasitic growth, a two-stage treatment of the Si(111) surface by ion beam with growth suppression and intensification modes is proposed. This approach will allow the creation of selective NW arrays without the need for additional masking layers. First, the area of growth suppression was created through low-dose FIB treatment (up to 1×10^{-13} C/μm²) using a uniformly spread pattern. After this modified area was additionally patterned by FIB using a dot-template with different distances between ion beam impact points and a dose optimized for NW growth enhancement, varying in the medium dose range from 1×10^{-13} to 1×10^{-12} C/μm².

The modified substrate was subsequently annealed at 600 °C, followed by MBE synthesis of GaAs NWs at 750 °C. The resulting arrays were analyzed using SEM and PL techniques.

Results and Discussion

Figure clearly illustrates the effect of the proposed FIB treatment on NW growth — an ordered array of vertical GaAs NWs is formed, with nearly complete suppression of parasitic growth between neighboring NWs and within the array itself. A distinct transition zone is observed between the modified region (highlighted in orange) and the unmodified area of the Si surface, where random NW growth occurs. Increasing the spacing between ion beam exposure points results in a corresponding change in the pitch of the NWs. Notably, parasitic growth suppression remains effective even with a tenfold increase in the FIB-treated area size (50×50 µm, pitch 5 µm).

Figure also shows that optimizing the dose allows to limit growth to a single NW at each FIB exposure point (e.g., with 1 µm pitch). However, increasing the dose disrupts array homogeneity, leading to the formation of multiple NWs at a single exposure point and the emergence of extended NW arrays ordered in a line. We attribute this effect to the lateral spread of ions, both during implantation and subsequent annealing. As a result, the growth intensification effect [2] extends over a greater distance at higher doses, promoting the formation of multiple NWs at a single point (e.g., pitch 5 µm). In turn, in arrays with closely spaced exposure points (pitch 0.5−1 µm), this leads to an overlap of the ion spreading areas between neighboring points and their mutual influence, resulting in the formation of NW rows with parasitic growth between exposure sites. The localized dose increases due to overlap likely shifts the process into the high-dose regime, where parasitic growth dominates, leading to the formation of GaAs polycrystals in these regions [2].

The optical characterization of these core-shell NW arrays reveals high structural quality, as evidenced by intense photoluminescence at room temperatures.
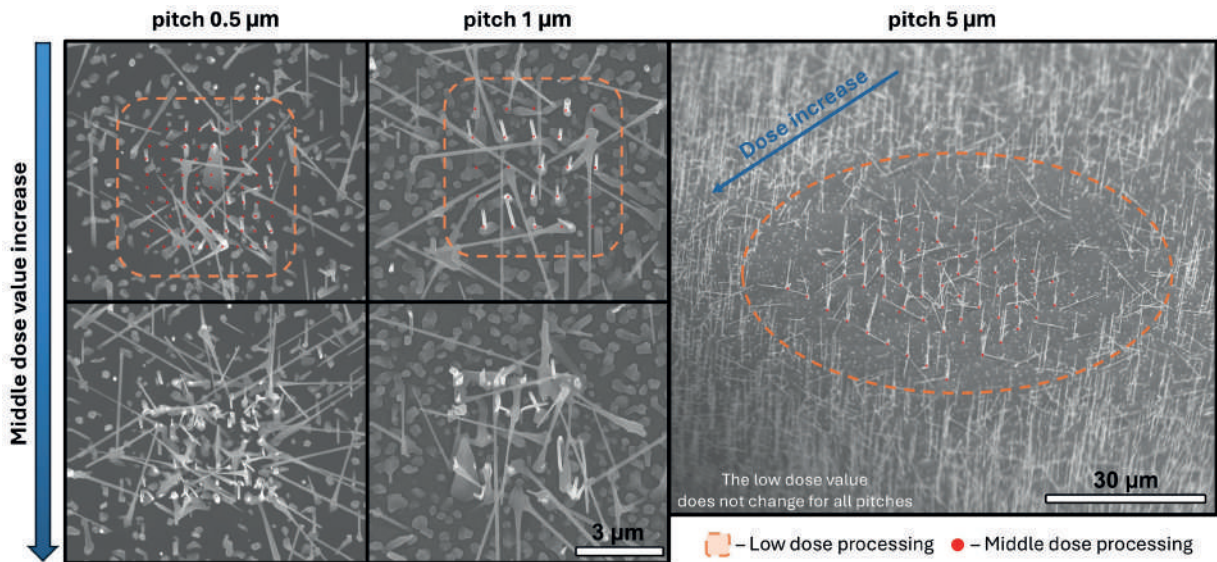
Fig. SEM images of the modified Si(111)/SiO$_x$ surface after GaAs NW growth

Conclusion

Thus, we demonstrated that a two-stage FIB pre-treatment of the Si(111) surface with a native oxide layer enables the selective formation of ordered vertical GaAs NW arrays. The array parameters can be precisely controlled by modifying the FIB treatment template. Additionally, optical characterization revealed that the fabricated arrays exhibit intense photoluminescence, even at room temperatures.

REFERENCES

1. **Shandyba N., Kirichenko D., Sharov V., Chernenko N., Balakirev S., Solodovnik M.,** Modulation of GaAs nanowire growth by pre-treatment of Si substrate using a Ga focused ion beam, Nanotechnology. 34 (46) (2023) 465603.

2. **Shandyba N., Balakirev S., Sharov V., Chernenko N., Kirichenko D., Solodovnik M.,** Effect of Si(111) surface modification by Ga focused ion beam at 30 kV on GaAs nanowire growth, Int. J. Mol. Sci. 24 (1) (2023) 224.

THE AUTHORS

SHANDYBA Nikita A.
shandyba.nikita@gmail.com
ORCID: 0000-0001-8488-9932

EREMENKO Mikhail M.
eryomenko@sfedu.ru
ORCID: 0000-0002-7987-0695

DUKHAN Denis D.
duhan@sfedu.ru
ORCID: 0000-0002-6762-2053

CHERNENKO Natalia E.
nchernenko@sfedu.ru
ORCID: 0000-0001-8468-7425

KIRICHENKO Danil V.
dankir@sfedu.ru
ORCID: 0000-0001-7476-2778

KUGAEVSKY Alexander D.
kugaevskii@sfedu.ru
ORCID: 0009-0001-5183-5396

MAKHOV Ivan S.
imahov@hse.ru
ORCID: 0000-0003-4527-1958

KRYZHANOVSKAYA Natalia V.
nkryzhanovskaya@hse.ru
ORCID: 0000-0002-4945-9803

BALAKIREV Sergey V.
sbalakirev@sfedu.ru
ORCID: 0000-0003-2566-7840

SOLODOVNIK Maxim S.
solodovnikms@sfedu.ru
ORCID: 0000-0002-0557-5909

Thin reduced graphene oxide based films for nanoelectronics and sensors

S.I. Babenko [1], A.S. Bryleva [1], K.V. Kanaev [1], O.A. Kudryavtsev [1],

R.R. Nigmatullina [1], K.A. Rayanova [1], A.D. Sudakova [1],

M.I. Trukhanova [2, 3], I.A. Komarov [1, 4] ✉

[1] Moscow Polytechnic University, Moscow, Russia;

[2] Lomonosov Moscow State University, Moscow, Russia;

[3] Nuclear Safety Institute of the RAS, Moscow, Russia;

[4] Federal Research Center of Problems of Chemical Physics and Medicinal Chemistry RAS,
Chernogolovka, Russia

✉ master_kom@mail.ru

Abstract. Formation of new devices of flexible and organic electronics requires new materials. One of the perspective classes of materials is graphene derivatives. To enhance wettability of polymer substrates we used multicomponent graphene oxide suspension with further reduction of obtained films with laser irradiation. We used UV and IR lasers for local reduction of these films to form transistors and biosensors. Graphene oxide film from 0.93 mg/ml suspension with lacquer thinner was successfully deposited and reduced for BGTE transistor formation. Reduced graphene oxide film acted as an n-type semiconductor with $2-8\times10^{-3}$ cm²/V·s⁻¹ mobility.

Keywords: contact angle, dispersion medium, graphene oxide, reduced graphene oxide, thin films, transistor

Тонкие пленки на основе восстановленного оксида графена для наноэлектроники и сенсоров

С.И. Бабенко [1], А.С. Брылева [1], К.В. Канаев [1], О.А. Кудрявцев [1],

Р.Р. Нигматуллина [1], К.А. Раянова [1], А.Д. Судакова [1],

М.И. Труханова [2, 3], И.А. Комаров [1, 4] ✉

[1] Московский политехнический университет, Москва, Россия;

[2] Московский государственный университет им. М.В. Ломоносова, Москва, Россия;

[3] Институт проблем безопасного развития атомной энергетики РАН, Москва, Россия;

[4] Федеральный исследовательский центр проблем химической физики
и медицинской химии РАН, г. Черноголовка, Россия

✉ master_kom@mail.ru

Аннотация. Создание новых устройств гибкой и органической электроники требует новых материалов. Одним из перспективных классов материалов являются производные графена. Для повышения смачиваемости полимерных подложек использовалась многокомпонентная суспензия оксида графена с последующим восстановлением полученных пленок лазерным облучением. Для локального восстановления этих пленок с целью формирования транзисторов и биосенсоров использовались УФ- и ИК-лазеры. Пленка оксида графена из суспензии 0,93 мг/мл с растворителем для лака была успешно осаждена и восстановлена для формирования транзистора BGTE. Восстановленная пленка оксида графена вела себя как полупроводник n-типа с подвижностью $2-8\times10^{-3}$ см^2/В·с$^{-1}$.

Ключевые слова: угол смачивания, дисперсионная среда, оксид графена, восстановленный оксид графена, тонкие пленки, транзистор

Introduction

Overcoming limitations of classic microelectronic technology has been one of the main points of interest of scientists during last 30 years. Since the beginning of the 2000s, researchers have tried to create or adopt new materials for electronics to obtain flexibility and overcome shape limitations of electronic products.

Among the variety of new materials like fullerenes [1], nanotubes [2], organic semiconductors [3] graphene derivatives seem to be the most perspective [4]. Graphene oxide (GO) is a material that on one hand can be relatively easy deposited on the large area substrates and on the other hand by the management of the presence of functional groups on its surface. The last fact allows reduced graphene oxide (rGO) [5] to be either conducting of semiconducting. Such management can be done by different techniques, including chemical and electrochemical [6, 7], thermal [8] or laser [9], reduction. Presence of functional groups is attractive for other rGO applications, especially for chemical and biosensors [10]. The use of laser for GO reduction may be the most prospect due to the possibility of treatment localization and obtain different additional chemical [11] effects in case of pico- and femtosecond lasers [12].

Wet deposition methods seem to be the most suitable for formation of large area graphene oxide films. And such methods as spin- [13] and spray [14] coating are most perspective due to the possibility of deposition of large-area uniform films. Management of suspension properties can be done by varying its composition. Moreover, the effect of dispersion on the quality of GO structure hasn't been studied properly. According to the literature data [15−17] we found a set of possible additional organic solvents based on its Hildebrand parameter (δT) that should be close or higher than that of graphene oxide ($\delta T = 25.4$ MPa$^{1/2}$).

Based on the multicomponent GO suspension with thinner for lacquer paints as additional component, we made macrosized uniform films for further local laser reduction. We showed the possibility to use the cheap microsecond laser for local reduction of spin-coated GO film with transistor channels formation. We obtained n-type rGO transistor with mobility in the range from 2×10^{-3} cm^2/V·s^{-1} to 8×10^{-3} cm^2/V·s^{-1} that can be used for flexible electronics.

Materials and Methods

For device formation we used 125 μm thick polyethylene terephthalate (PET) film as a substrate with 15×15 mm size. All substrates were mechanically precleaned with isopropanol with further drying in a 4 atm air stream.

For GO film formation we used graphene oxide water suspension with 3.11 mg/ml concentration was synthesized by the modified Hummers method (MIP Graphen LLC, Russian Federation).

As additional component for better wettability we used thinner for lacquer paints (LT, Tamiya Ink., Japan) with concentration 1.24 mg/ml. that is in range of 1−1.5 mg/ml that is suitable for uniform film formation [18]. Also, Hildebrand parameter of the main component of this thinner − ethylene glycol is $\delta T = 33$ MPa$^{1/2}$.

GO deposition was obtained with the EZ4 spin-coater (LEBO Science, PRC) with the following deposition profile: 1000 rpm for 60 sec with a further 30 min heat treatment in the low-vacuum chamber VAC-24 (Stegler, PRC) at 110 °C. Gate (Al), Source and Drain (Ag) electrodes deposited by thermal sputtering on a modified VUP-4 thermal evaporator (USSR). The thickness of all electrodes was ~100 nm, measured by a quartz monitor crystal (INFICON AG, Germany). For Gate passivation, we used anodic oxidation of Al on a self-designed laboratory setup under 30 V voltage. Local laser treatment was carried out by the self-designed system with a 445nm solid-state laser facility with a motorized table. Output laser power was about 200 mW at a 30 MHz frequency. Treatment time in a spot (1.5×10^{-3} mm^2) was constant at 30 ms.

Raman spectra were obtained on an InVia Raman spectrometer (Renishaw, UK). FTIR spectroscopy data for films was collected on the Nicolet iS10 (Thermo Scientific, USA) in attenuated total reflectance mode. I−V curves of reduced graphene oxide transistors were measured on Keithley 4200A (Tektronix, USA). Transfer curve measurements were done with the next parameters: Source-Drain voltage was constant at 5 V in all cases; Gate-Source voltages were measured in a range from −1 V to 10 V depending on the specific transistor. The thickness of the GO film was measured on NTEGRA PRIMA SPM (NT-MDT, Russian Federation) in semicontact mode with an NSG 30 cantilever: 320 kHz resonance frequency, 40 N/m force constant (Tipsnano OÜ, Estonia).

Results and Discussion

Deposition of GO films were done with the use of multicomponent suspension with LT as additional component and 1.24 mg/ml concentration. This suspension allows for better wettability of PET substrate, and its characteristic drying time of about 70 seconds is very close to that of spin coating process. Nevertheless, we observed much better adhesion in case of additional low vacuum thermal treatment at 110 °C for 30 min. After abovementioned operations a thin GO film (thickness about 80−90 nm according to AFM data) that uniformly covers all the substrate was formed.

For investigation of laser modification, we used BGTE transistor configuration (Fig. 1) with GO film (suspension with LT as additional component, 1.24 mg/ml) deposited on the passivated gate electrode with further top source and drain electrode formation by thermal sputtering trough the mask. Local laser treatment was carried out by the own-designed system with a 445nm solid-state laser facility with a motorized table. For GO reduction, we used laser parameters that were equal to ~35−37 mJ/cm^2; the reduction process was made in a camera with nitrogen flow to remove possible impurities arising in the reduction process. Reduced GO areas are shown in Fig. 1 (black regions). Reduction of GO was confirmed by Raman (Fig. 2) and IR spectroscopy (Fig. 3).
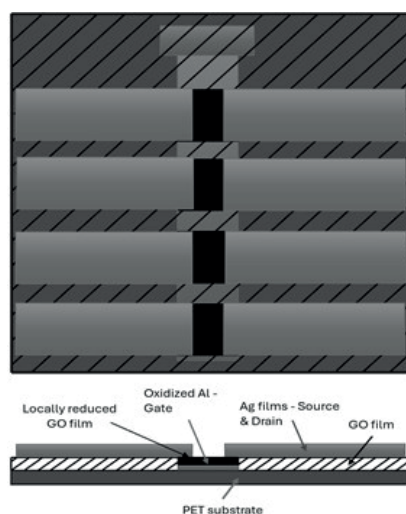
Fig. 1. Scheme of rGO transistor the top view and cross-section

A general view of Raman spectra of rGO correlates with results observed in [19, 20]. From these articles, we can clearly identify high-intensity G, D and 2D bands. We also clearly observe low-intensity D*, G*, D+G, and 2G bands. The relatively sharp and intensive 2D peak in our case tells us that on one hand defects in rGO structure are partially healed, and GO film successfully reduced, on the other the intensity of 2D band is much lower compared to the spectra typical for the fully reduced GO. Thus, we assume that laser irradiation with $35-37$ mJ/cm^2 results in partial reduction of GO film which can be semiconduction due to opening of band gap.
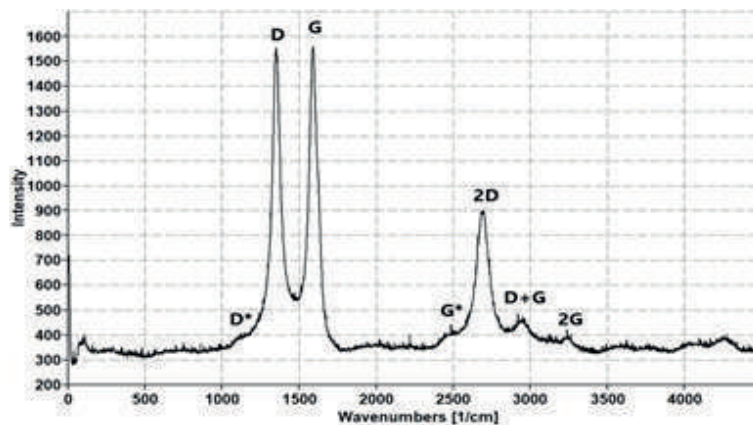
Fig. 2. Raman spectra of locally reduced graphene oxide in transistor channel

In IR spectra (Fig. 3), we clearly observe the presence of different bands, most of which are common for graphene oxide and reduced graphene oxide. This fact is one more confirmation of the partial reduction of the initial graphene oxide film. According to the literature data presented in [21, 22] we can identify the next bands: two small bands at 2927 cm^{-1} and 2849 cm^{-1} are asymmetric and symmetric CH$_2$ stretching of GO. The band at ~1720 cm^{-1} is attributed to the presence of carbonyl and carboxyl groups; the 1582 cm^{-1} band comes from aromatic ring stretching; the 1400 cm^{-1} band comes from $-$OH bending in phenol etc. Thus, we can clearly see the presence of different functional groups that mean partial reduction of graphene oxide. Moreover, partial reduction can be used for the task of transistor formation due to the presence of carbonyl and carboxyl groups (~1720 cm^{-1} band).
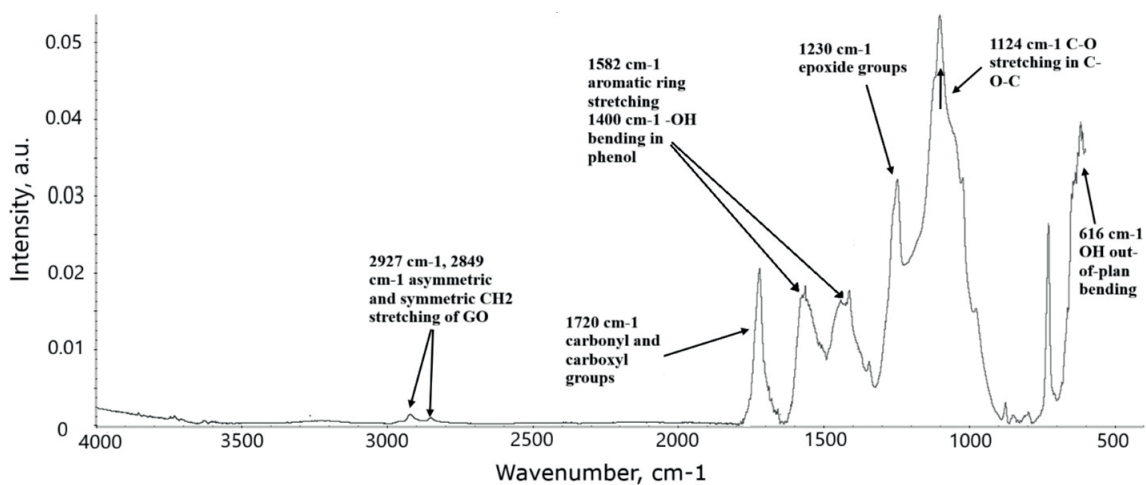
Fig. 3. FTIR spectra of locally reduced graphene oxide in transistor channel

After GO reduction, we made Source and Drain electrodes by thermal evaporation of Ag with a thickness of about 100 nm (measured by a quartz detector in the evaporation camera). The total number of substrates was 5, with four transistors on each substrate, i.e., we made measurements

of 20 individual transistors. Measurement of CV characteristics was made in a nitrogen box with special probes on Keithley 4200A semiconductor measurement station. The typical CV transfer curve of the obtained rGO transistors is shown in Fig. 4.

As can be seen from Fig. 4, the n-type conductivity is observed. This fact correlates with the result of the [23], where the n-type of p-type charge carriers and rGO film depend on reduction temperature. For n-type charge carriers, rGO film should be reduced with temperatures in ranges of 250−450 °C and from 800 to 1000 °C. According to the similarity of FTIR spectra in our article and [23] we can assume the local reduction temperature in the range > 350−450 °C in our case.
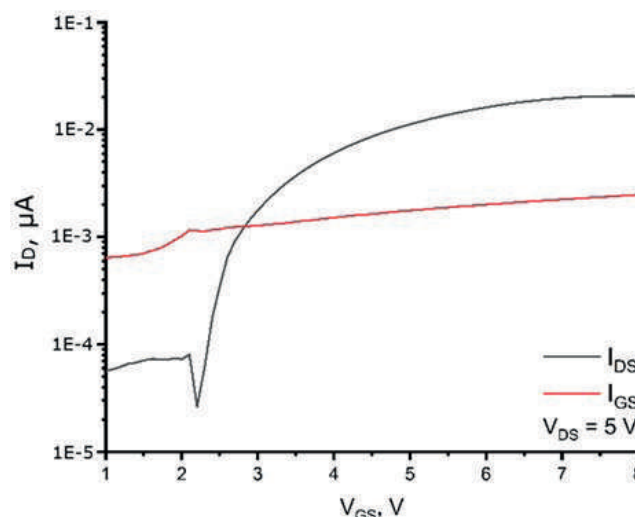
Fig. 4. Transfer CV curve of rGO transistor. IDS − Drain-Source Current, IGS − Gate-Source current, VDS − Drain-Source voltage, VDS − Gate-Source voltage

The mobility of the rGO films was calculated from the CV characteristics of transistors. We found that mobility is in the range from 2×10^{-3} cm^2/V·s^{-1} to 8×10^{-3} cm^2/V·s^{-1}. This result is much lower compared with data from [24, 25] and close to the results obtained in [26]. We attribute relatively low mobility to the not full reduction of GO film. Nevertheless, such transistors can be used in biosensor development due to transistor effect on one hand and presence of carboxyl functional groups that is important sensitive biomolecule immobilization through the coupling with carboxyl groups.

Conclusion

The work successfully demonstrated the possibility of formation of uniform GO films ready for further local laser induced reduction by the use of additional organic component in the deposited GO suspension with concentration in range 1−1.5 mg/ml. By the use of relatively cheap laser, it is possible to obtain local reduction of graphene oxide film with formation of BGTE design transistors, where the rGO film behaved as an n-type semiconductor. Despite the relatively low mobility in range about $2-8\times10^{-3}$ cm^2/V·s^{-1} partially reduced rGO films with the presence of carboxyl functional groups can be used as basis for chemical or biosensor formation due to the possibility of sensitive molecules' immobilization.

REFERENCES

1. **Jebnouni A., Shariq M., Alshehri S. Alshahrani M., Bouzidi M., Aljaloud A.S., AlDheirib A.A., Khan S., Farid A.,** Exploring the structural and electronic properties of fullerenes for advanced photodetectors, diodes, and solar cell applications, Journal of Industrial and Engineering Chemistry. 147 (2025) 125−148.

2. **Novikov I.V., Raginov N.I., Krasnikov D.V., et al.,** Fast liquid-free patterning of SWCNT films for electronic and optical applications, Chemical Engineering Journal. 485 (2024) 149733.

3. **Zhang Q., Hu W., Sirringhaus H., Müllen K.,** Recent Progress in Emerging Organic Semiconductors, Advanced Materials Special Issue: Organic Semiconductors. 34 (2022) 2108701.

4. **Chendake Y., et al.,** Graphene: A Promising Material for Flexible Electronic Devices. In: Patel SK, Taya SA, Das S, Vasu Babu K (eds) Recent Advances in Graphene Nanophotonics, Advanced Structured Materials. Springer, Cham. (2023) 83−118.

5. **Shchegolkov A.V., Parfimovich I.D., Komarov, F.F., et al.,** Optically Adjustable Nanocomposite Electrochromic Film WO_3/rGO to Control Light Transmission and Protect from Electromagnetic Radiation, Inorg. Mater. Appl. Res. 12 (2021) 1547−1553.

6. **Shiyanova K.A., Gudkov M.V., Rabchinskii M.K., et al.,** Graphene Oxide Chemistry Management via the Use of $KMnO_4/K_2Cr_2O_7$ Oxidizing Agents, Nanomaterials. 11 (2021) 915.

7. **Jarić S., Schobesberger S., Velicki L., Milovančev A., Nikolić S., Ertl P., Bobrinetskiy I., Knežević N.Z.,** Direct electrochemical reduction of graphene oxide thin film for aptamer-based selective and highly sensitive detection of matrix metalloproteinase 2, Talanta. 274 (2024) 126079.

8. **Xu X., Huang J., Miao G., Yan B., Chen Y., Zhou Y., Zhang Y., Zhang X., Cai W.,** Visualizing Thermal Reduction in Graphene Oxide. Materials 18 (2025) 2222.

9. **Hwa K-Y., Murugan R., Tseng S-F., Santhan A., Lin J-Y.,** Laser-induced reduced graphene oxide for high-performance electrochemical sensors of antipyretic drug in real samples, Environ. Sci.: Nano. 11 (2024) 951−968.

10. **Dutt S., Singh A., Mahadeva R., Sundramoorthy A.K., Gupta V., Arya S.,** A reduced graphene oxide-based electrochemical sensing and eco-friendly 4-nitrophenol degradation, Diamond and Related Materials. 141 (2024) 110554.

11. **Nekrasov N., Yakunina N., Nevolin V., Bobrinetskiy I., Vasilevsky P., Gerasimenko A.Y.,** Two-Photon Polymerization of Albumin Hydrogel Nanowires Strengthened with Graphene Oxide, Biomimetics. 6 (2021) 66.

12. **Emelianov A.V., Pettersson M., Bobrinetskiy I.I.,** Ultrafast Laser Processing of 2D Materials: Novel Routes to Advanced Devices, Advanced Materials. 36 (2024) 2402907.

13. **Kim S-Y., Gang H-E., Park G-T., Jeon H-B., Jeong Y.G.,** Microstructure and electrothermal characterization of transparent reduced graphene oxide thin films manufactured by spin-coating and thermal reduction, Results in Physics. 24 (2021) 104107.

14. **Sadl M., Repic B., Gorican I., Kuscer D., Ursic H.,** Aerosol-deposition derived graphite thick films for Electrochemical sensors, Journal of Microelectronics, Electronic Components and Materials. 54 (2024) 177−186.

15. **Paredes J.I., Villar-Rodil S., Martınez-Alonso A., Tascon J.M.D.,** Graphene Oxide Dispersions in Organic Solvents, Langmuir 24 (2008) 10560−10564.

16. **Bei-Bei F., Zhao-Hui W., Wen-Hua S., Yi W., Jia-Cheng W., Yu-Fo L., Hong-Li S., Min L., Lin M.,** Performance of graphene dispersion by using mixed surfactants, Materials Research Express. 7 (2020) 095009.

17. **Konios D., Stylianakis M.M., Stratakis E., Kymakis E.,** Dispersion behaviour of graphene oxide and reduced graphene oxide, Journal of Colloid and Interface Science. 430 (2014) 108−112.

18. **Komarov I.A., Danilov E.A.,** On the wetting of polyethylene terephthalate substrates with multicomponent graphene oxide dispersions, St. Petersburg Polytechnic University Journal: Physics and Mathematics. 16 (2023) 177−182.

19. **Kanishka H.K., Pamarti V., Kesava V.R., Suzuki S., Yoshimura M.,** New Insight into the Characterization of Graphene Oxide and Reduced Graphene Oxide Monolayer Flakes on Si-Based Substrates by Optical Microscopy and Raman Spectroscopy, Journal of Physical Chemistry C. 125 (2021) 7791−7798.

20. **Yadava S., Padhib S.K., Srinivasuluc C., Naidu K.L.,** Raman spectroscopy study on the vibration and structural changes of graphene oxide: effect of laser power and time, Journal of Ovonic Research. 20 (2024) 221−232.

21. **Mokhtar M.M., Abo El Enein S.A., Hassaan M.Y., Morsy M.S., Khalil M.H.,** Thermally Reduced Graphene Oxide: Synthesis, Structural and Electrical Properties, International Journal of Nanoparticles and Nanotechnology. 3 (2017) 008.

22. **Hou T.F., Shanmugasundaram A., Nguyen B.Q.H., Lee D.W.,** Fabrication of surface-functionalized PUA composites to achieve superhydrophobicity, Micro and Nano Systems Letters 7 (2019) 12.

23. **Nguyen D.K., Jaeyoo C., Chong R.P., Heesuk K.,** Remarkable Conversion Between n- and p Type Reduced Graphene Oxide on Varying the Thermal Annealing Temperature, Chemistry of Materials 27 (2015) 7362–7369.

24. **Aspermair P., Mishyn V., Bintinger B., et al.,** Reduced graphene oxide−based field effect transistors for the detection of E7 protein of human papillomavirus in saliva, Analytical and Bioanalytical Chemistry. 413 (2021) 779−787.

25. **Vasilijevic S., Mattana G., Anquetin G., Battaglini N., Piro B.,** Electrochemical tuning of reduced graphene oxide in printed electrolyte-gated transistors. Impact on charge transport properties, Electrochimica Acta. 371 (2021) 137819.

26. **Lago N., Buonomo M., Cintra R.H., Sedona F., Sambi M., Casalini M., Cester A.,** Characterization and Modeling of Reduced-Graphene Oxide Ambipolar Thin-Film Transistors, IEEE Transactions on Electron Devices. 69 (2022) 6.

THE AUTHORS

BABENKO Sofiya I.
sofi.bb@yandex.ru

BRYLEVA Anna S.
anniebryleva@yandex.ru

KANAEV Kirill V.
kir-kv2005@mail.ru

KUDRYAVTSEV Oleg A.
oleg6565657@gmail.com

NIGMATULLINA Razalina R.
razalina.n2004@gmail.com

RAYANOVA Kamilla A.
raanovakamilla@gmail.com

SUDAKOVA Alexandra D.
asudakova12@gmail.com

TRUKHANOVA Mariya I.
trukhanova@physics.msu.ru

KOMAROV Ivan A.
master_kom@mail.ru
ORCID: 0000-0002-6397-6671

Hybrid emitters based on two-dimensional WSe$_2$ and ordered plasmonic nanobumps

A.V. Nikolaeva [1, 2] ✉, M.A. Anikina [1, 2], V.M. Kondratev [1, 2],

V.A. Sharov [1, 3], E.Yu. Barulina [4], V.O. Gridchin [5, 1, 6],

A.I. Khrebtov [6], A.A. Kuchmizhak [5], A.D. Bolshakov [1, 2, 6, 7]

[1] Alferov University, St. Petersburg, Russia;
[2] Moscow Institute of Physics and Technology, Moscow, Russia;
[3] Ioffe Institute, St. Petersburg, Russia;
[4] Russian Quantum Center, Moscow, Russia;
[5] Institute for Analytical Instrumentation of the RAS, St. Petersburg, Russia;
[6] St. Petersburg State University, St. Petersburg, Russia;
[7] Far Eastern Federal University, Vladivostok, Russia;
[8] Yerevan State University, Yerevan, Armenia
✉ nikalex2000@bk.ru

Abstract. Two-dimensional transition metal dichalcogenides (TMDs), particularly tungsten diselenide (WSe$_2$), exhibit exceptional optoelectronic properties, including strong light-matter interactions and tunable exciton behavior, making them promising for nanophotonic applications. This work investigates a hybrid system comprising a WSe$_2$ monolayer integrated with a plasmonic metasurface of Au-nanobumps to enhance photoluminescence (PL) through exciton-plasmon coupling and strain-induced bandgap modulation. The WSe$_2$ monolayers were mechanically exfoliated and transferred onto a laser-patterned Au-nanobump array fabricated via femtosecond laser printing, offering a scalable alternative to conventional lithography. Optical characterization showed a threefold enhancement of photoluminescence intensity of WSe$_2$ monolayer lying on a nanobump compared to WSe$_2$ on a flat gold substrate, what attributed to localized plasmon-exciton interactions and strain effects. The study demonstrates a cost-effective, lithography-free approach for tailoring hybrid TMD-plasmonic systems, enabling precise control over optical properties for next-generation optoelectronic devices.

Keywords: WSe$_2$, emitter, nanobump, photoluminescence

Гибридные эмиттеры на основе двумерного WSe$_2$ и упорядоченных плазмонных нанобампов

А.В. Николаева [1, 2] ✉, М.А. Аникина [1, 2], В.М. Кондратьев [1, 2],

В.А. Шаров [1, 3], Е.Ю. Барулина [4], В.О. Гридчин [5, 1, 6],

А.И. Хребтов [6], А.А. Кучмижак [7], А.Д. Большаков [1, 2, 8]

[1] Академический университет им. Ж.И. Алфёрова РАН, Санкт-Петербург, Россия;

[2] Московский физико-технический институт (национальный исследовательский университет), г. Долгопрудный, Россия;

[3] Физико-технический институт им. А.Ф. Иоффе РАН, Санкт-Петербург, Россия;

[4] Российский квантовый центр, Москва, Россия;

[5] Институт аналитического приборостроения РАН, Санкт-Петербург, Россия;

[6] Санкт-Петербургский государственный университет, Санкт-Петербург, Россия;

[7] Дальневосточный федеральный университет, г. Владивосток, Россия;

[8] Ереванский государственный университет, г. Ереван, Армения

✉ nikalex2000@bk.ru

Аннотация. Двумерные дихалькогениды переходных металлов (TMDs) широко известны благодаря своим уникальным оптическим и электрическим свойствам, в особенности двумерный WSe$_2$ обладает выдающимися люминесцентными характеристиками, что делает его перспективным кандидатом для применений в нанофотонике. В данной работе исследуется гибридная система, состоящая из монослоя WSe$_2$, интегрированного с плазмонной поверхностью упорядоченных Au-нанобампов, изготовленных с помощью метода фемтосекундной лазерной печати, предлагающий масштабируемую альтернативу традиционным методам литографии и травления. Оптическая характеристика показала трехкратное усиление интенсивности ФЛ монослоя WSe$_2$ на нанобампе по сравнению с WSe$_2$, лежащим на плоской золотой подложке, что можно объяснить локализованным плазмон-экситонным взаимодействием и деформационными эффектами. Исследование демонстрирует экономически эффективный подход к созданию гибридных TMDs-плазмонных систем, позволяющий точно контролировать оптические свойства двумерного WSe$_2$ для применения в оптоэлектронных устройствах следующего поколения.

Ключевые слова: WSe$_2$, эмиттер, фотолюминесценция

Ссылка при цитировании: Николаева А.В., Аникина М.А., Кондратьев В.М., Шаров В.А., Барулина Е.Ю., Гридчин В.О., Хребтов А.И., Кучмижак А.А., Большаков А.Д. Гибридные эмиттеры на основе двумерного WSe$_2$ и упорядоченных плазмонных нанобампов // Научно-технические ведомости СПбГПУ. Физико-математические науки. 2025. Т. 18. № 3.1. С. 30−35. DOI: https://doi.org/10.18721/JPM.183.104

Introduction

Two-dimensional materials, particularly transition metal dichalcogenides (TMDs) like MoS_2, WS_2, $MoSe_2$, and WSe_2, exhibit exceptional optical and electronic properties, including direct bandgaps in monolayer form, strong light-matter interactions, and tunable exciton behavior [1−3]. Among them, WSe_2 stands out for its superior luminescence, making it promising for optoelectronic applications. This work explores a hybrid system combining WSe_2 with plasmonic nanostructures to enhance optical properties through exciton-plasmon coupling [4]. Additionally, strain induced by transferring WSe_2 onto nanostructured surfaces modifies its bandgap and exciton transitions [5], further boosting photoluminescence efficiency.

Materials and Methods

In our work, WSe_2 monolayers were obtained using a mechanical exfoliation method and transferred to a target substrate with Au-nanobumps using a custom transfer system based on tsc2 hq graphene (HQ Graphene, Netherlands).

Figure 1 shows Au-nanobumps of different heights with periods of 3 μm, 5 μm and 10 μm.
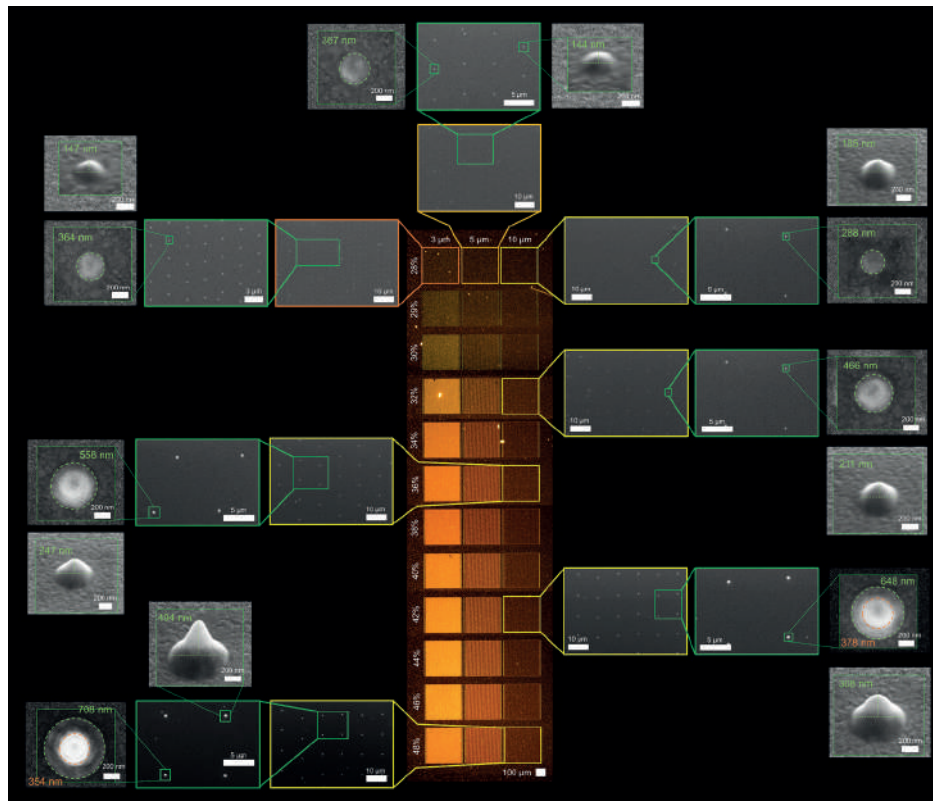
Fig. 1. Au-nanobumps: optical (center) and SEM images of nanobump arrays with periods of 3, 5 and 10 μm obtained using laser pulses of different output, expressed as a percentage, where 100% corresponds to 2 nJ

The Au-nanobumps metasurface was fabricated by combination of an inexpensive and scalable magnetron sputtering of thin Au films with a direct fs-laser printing technique. First, a gold film with a thickness of 50 nm was coated over a glass substrate using magnetron deposition. Then, laser patterning of the glass-supported Au films was carried out using ≈ 200 fs second-harmonic (λ = 515 nm) pulses generated by a regeneratively amplified Yb:KGW laser system (Pharos, Light Conversion) at 50 kHz repetition rate. Output laser radiation with a Gaussian-shaped lateral in tensity profile was focused onto the Au film surface by a microscope objective (50×, Mitutoyo) with a numerical aperture NA = 0.42. A computer-driven nanopositioning platform (ANT130XY, Aerotech) ensured precise (position deviation less than 100 nm) movement of the sample surface with respect to the laser focal spot, allowing each pulse to form isolated nanobumps arranged into a square-shaped lattice with a period (Λ) defined by the sample scanning speed.

Results and Discussion

Optical properties of such a structure were characterized using Raman and photoluminescence (PL) microspectroscopy. The measurements were carried out on a Horiba LabRAM HR 800 spectrometer. The excitation radiation source was a diode-pumped 532 nm solid-state laser.

Figure 2, *a* presents an optical image of a WSe$_2$ layer transferred onto a substrate patterned with an array of Au-nanobumps (147 nm height, 364 nm base diameter), fabricated using a laser pulse output of 28% (0.56 nJ), alongside the corresponding AFM image of the same region. The WSe$_2$ flake exhibits two distinct zones: a monolayer (1L-WSe$_2$) and a bilayer (2L-WSe$_2$). AFM analysis reveals that the flake conforms to the nanobump topography, forming a tensile "tent"-like structure over each bump, while folding between adjacent bumps is a behavior more pronounced in the bilayer regions. Disordered Au particles of varying sizes, residual from fabrication, are also observed on the substrate. PL-mapping along two bump-to-plane directions (Fig. 2, *b*) and their spectra (Fig. 2, *c*, *d*) demonstrate two key strain-dependent effects. First, it is an enhanced PL-intensity as the monolayer approaches the bump region (higher strain), attributed to exciton localization suppressing non-radiative recombination and plasmonic nanoantenna effects from Au-nanobumps amplifying the local electromagnetic field. Second, it is a redshift of the PL-peak (by a few nm) under tensile strain, consistent with bandgap reduction in the deformed WSe$_2$ lattice.
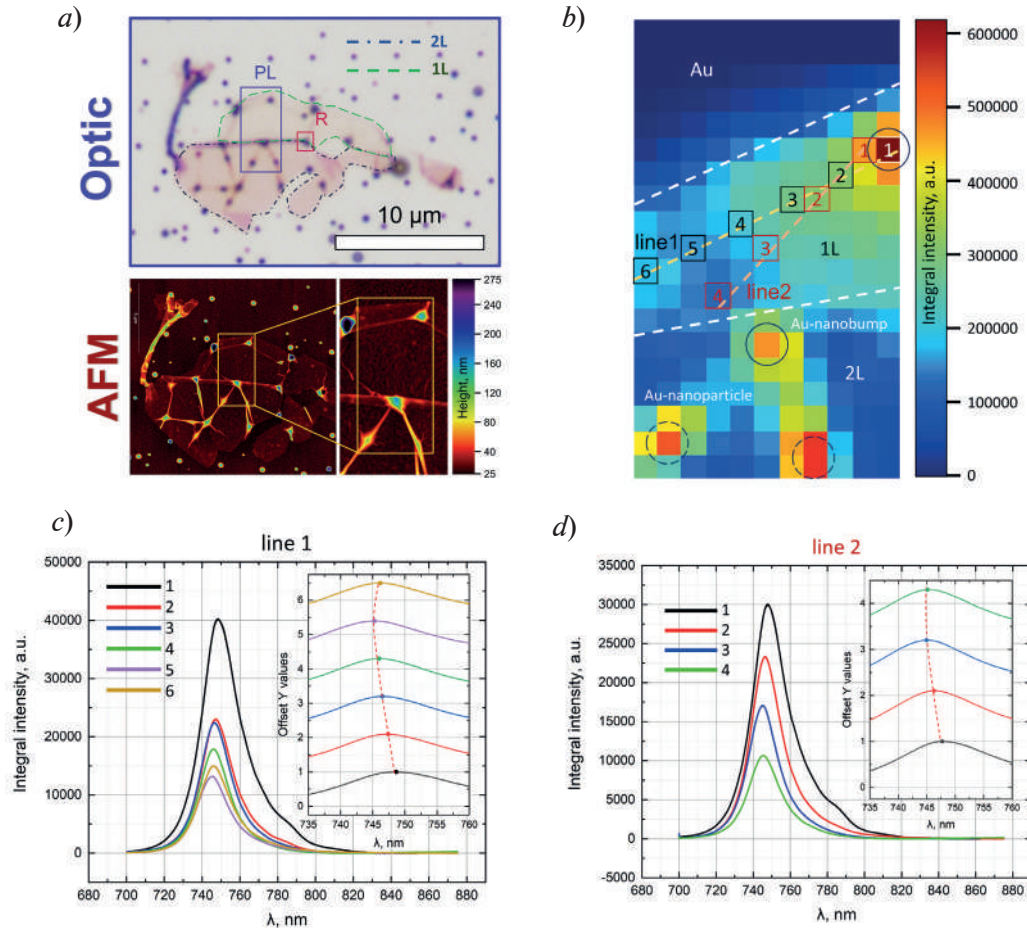
Fig. 2. WSe$_2$ on Au-nanobumps (28%): optical image (above) with the selected areas "*PL*" and "*R*" and AFM-image (below) (*a*); PL-mapping of the selected area "*PL*" representing integral intensity of a PL-spectra (*b*); PL-spectra of line 1 (*c*) and line 2 (*d*) with the addition of waterfall graph showing the shift of the PL-peak respectively (*c*)

To characterize the mono- and bilayer regions of WSe$_2$, Raman mapping was performed in area "*R*" (Fig. 2, *a*). The bilayer region exhibits significantly higher integrated Raman spectra intensity compared to the monolayer (Fig 3, *a*). The spatial boundary between 1L-WSe$_2$ and 2L-WSe$_2$

is further confirmed by the shift in the A_1' peak position (Fig. 3, *b*), with the bilayer showing a distinct cm^{-1}-scale shift. Representative Raman spectra (Fig. 3, *c, d*) reveal key differences: the bilayer not only shows enhanced A_1' and E' modes due to modified electron-phonon coupling but also displays new characteristic modes. The observed modes include a shear mode (ZO') at 138 cm^{-1}, arising from interlayer displacement, a layer breathing mode (LBM) at 311 cm^{-1}, indicative of strong interlayer interactions and also new optical modes at 376 cm^{-1} and 397 cm^{-1}, activated by the reduced crystal symmetry in the bilayer.

Notably, complete photoluminescence quenching was absent at the WSe$_2$/Au interface, suggesting high quantum efficiency in the WSe$_2$ monolayer. The enhanced PL intensity in this system likely stems from two synergistic effects: strain-induced modification of the WSe$_2$ monolayer and plasmonic enhancement from the Au-nanobumps.
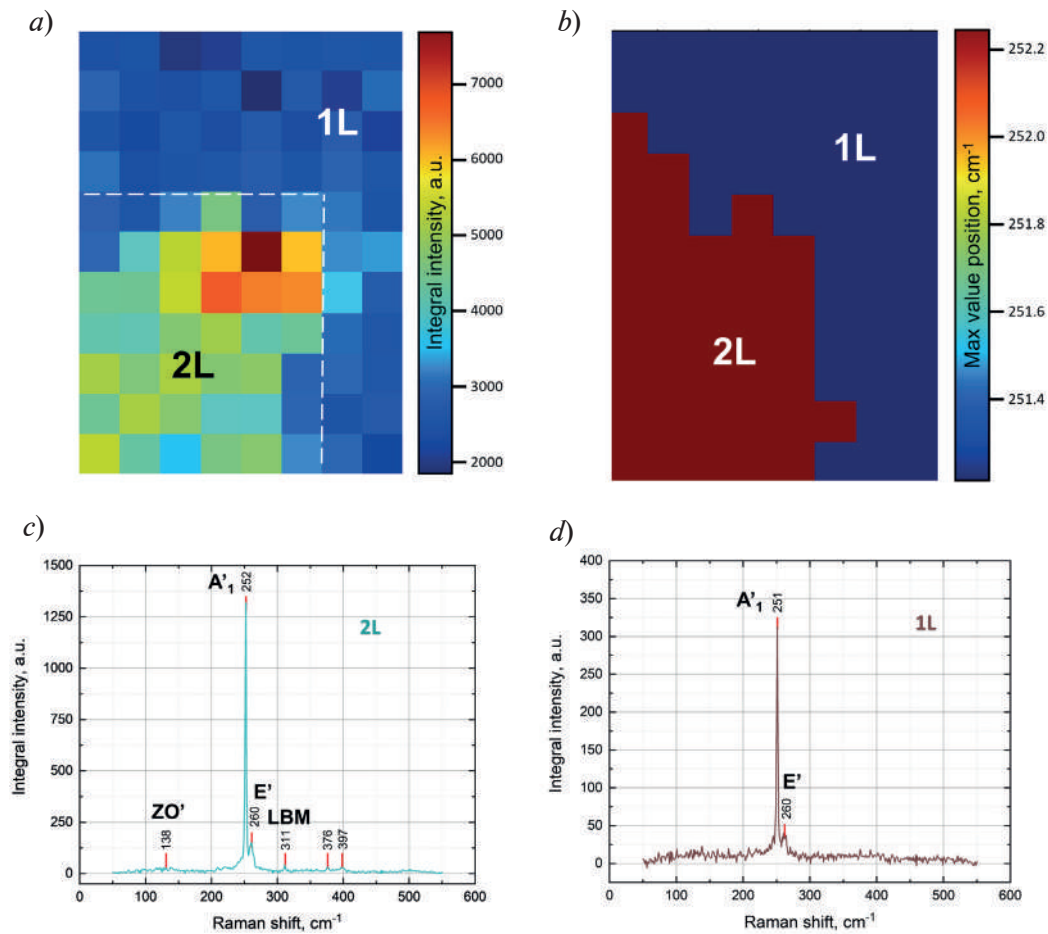
Fig. 3. WSe$_2$ on Au-nanobumps (28%): Raman mapping of the area R representing integral intensity (*a*) and the primary peak position in cm^{-1} (*b*) of Raman spectra; 2L-WSe$_2$ (*c*) and 1L-WSe$_2$ (*d*) Raman spectra with the designation of the main modes of combined light scattering

Conclusion

The innovation and practical significance of the presented work is attributed to the use of Au-nanobumps, the formation of which is carried out by a simple and effective method alternative to the traditional processes of lithography and etching. The laser radiation parameters allow controlling the geometry of the nanobumps and the lattice period, which provides the possibility of precise control over the optical characteristics of the hybrid structure. Furthermore, the ability to transfer two-dimensional WSe$_2$ layers onto such structures with good adhesion provides an avenue for the fabrication of efficient hybrid emitters and heterostructures based on this platform.

Acknowledgments

REFERENCES

1. **Kuznetsov A., Anikina M.A., Toksumakov A.N., Abramov A.N., Dremov V.V., Zavyalova E., Kondratev V.M., Fedorov V.V., Mukhin I.S., Kravtsov V., Novoselov K.S., Arsenin A.V., Volkov V.S., Ghazaryan D.A., Bolshakov A.D.,** In-Plane Directional MoS_2 Emitter Employing Dielectric Nanowire Cavity, Small Struct (2025).

2. **Ermolaev G.A., Stebunov Y.V., Vyshnevyy A.A., Tatarkin D.E., Yakubovsky D.I., Novikov S.M., Baranov D.G., Shegai T., Nikitin A.Y., Arsenin A.V., Volkov V.S.,** Broadband optical properties of monolayer and bulk MoS_2, NPJ 2D Mater Appl. 4 (2020) 21.

3. **Splendiani A., Sun L., Zhang Y., Li T., Kim J., Chim C.-Y., Galli G., Wang F.,** Emerging Photoluminescence in Monolayer MoS_2, Nano Lett. 10 (2010) 1271−1275.

4. **Mueller N.S., Arul R., Kang G., Saunders A.P., Johnson A.C., Sánchez-Iglesias A., Hu S., Jakob L.A., Bar-David J., de Nijs B., Liz-Marzán L.M., Liu F., Baumberg J.J.,** Photoluminescence upconversion in monolayer WSe_2 activated by plasmonic cavities through resonant excitation of dark excitons, Nat Commun. 14 (2023) 5726.

5. **Gong Y., Zhou Q., Huang X., Han B., Fu X., Gao H., Li F., Dr. Tian Cui T.,** Pressure-Induced Photoluminescence Adjustment and Lattice Disorder in Monolayer WSe_2, ChemNanoMat. 3 (2017) 238−244.

THE AUTHORS

NIKOLAEVA Aleksandra V.
nikalex2000@bk.ru
ORCID: 0009-0008-4344-4863

ANIKINA Maria A.
mari.a.nikina@yandex.ru
ORCID: 0000-0002-5522-5026

KONDRATEV Valeriy M.
kvm_96@mail.ru
ORCID: 0000-0002-3469-5897

SHAROV Vladislav A.
vl_sharov@mail.ru
ORCID: 0000-0001-9693-5748

BARULINA Elena Yu.
barulina.eu@mipt.ru
ORCID: 0000-0001-7087-0552

GRIDCHIN Vladislav O.
gridchinvo@gmail.com
ORCID: 0000-0002-6522-3673

KHREBTOV Artem I.
khrebtovart@mail.ru
ORCID:0000-0001-5515-323X

KUCHMIZHAK Aleksandr A.
alex.iacp.dvo@mail.ru
ORCID: 0000-0002-5376-5555

BOLSHAKOV Alexey D.
acr1235@mail.ru
ORCID: 0000-0001-7223-7232

Synthesis of Mg₂Si-based core-shell nanowires

E.Yu. Subbotin [1] ✉, A.G. Kozlov [2], D.V. Pavlov [1], O.E. Lisenkov [1], A.D. Udilov [1],

D.L. Goroshko [1], M.V. Polyakov [3], L.S. Volkova [3], G.A. Prokopeva [1],

I.M. Chernev [1], D.A. Khoroshilov [1], S.A. Sinotova [1], N.G. Galkin [1]

[1] Institute of Automation and Control Processes, FEB RAS, Vladivostok, Russia;
[2] Far Eastern Federal University, Vladivostok, Russia;
[3] Institute of Nanotechnology of Microelectronics of the RAS, Moscow, Russia

✉ subbotineu@iacp.dvo.ru

Abstract. In this work, we proposed the method for synthesis of nanowires with Mg₂Si/Si-based core-shell heterostructure. Silicon nanowires acting as a source of silicon for the silicification reaction were obtained by well-studied metal-stimulated chemical etching of silicon with orientation (100) doped with boron, with a resistivity of $1-10$ Ω×cm. A 30 nm thick gold film with an adhesive titanium sublayer 1.5 nm thick was used as the catalytic metal. The etched nanowires had a height of ~10 microns and a diameter of 1.5 microns. The Mg₂Si shell was formed using the solid-phase epitaxy method under ultrahigh vacuum conditions. The thickness of the silicide shell was $400-600$ nm on the side surfaces of the nanowires.

Keywords: silicon, magnesium silicide, epitaxy, nanowires, core-shell, thermoelectricity, MACE, SEM, EDX, TEM

Синтез нанопроволок типа ядро-оболочка на основе Mg₂Si

Е.Ю. Субботин [1]✉, А.Г. Козлов [2], Д.В. Павлов [1], О.Е. Лисенков [1], А.Д. Удилов [1],

Д.Л. Горошко [1], М. В. Поляков [3], Л.С. Волкова [3], Г.А. Прокопьева [1],

И.М. Чернев [1], Д.А. Хорошилов [1], С.А. Синотова [1], Н.Г. Галкин [1]

[1] Институт автоматики и процессов управления ДВО РАН, г. Владивосток, Россия;
[2] Дальневосточный федеральный университет, г. Владивосток, Россия;
[3] Институт нанотехнологий микроэлектроники РАН, Москва, Россия

✉ subbotineu@iacp.dvo.ru

Аннотация. В данной работе был предложен метод синтеза нанопроволок с гетероструктурой типа ядро-оболочка на основе Mg$_2$Si/Si. Нанопроволоки кремния, выступающие в качестве источника кремния для реакции силицидообразования, были получены хорошо изученным металл-стимулированным химическим травлением кремния с ориентацией (100), легированного бором, с удельным сопротивлением 1−10 Ω×см. В качестве каталитического металла использовалась пленка золота толщиной 30 нм с адгезионным подслоем титана толщиной 1,5 нм. Вытравленные нанопроволоки имели высоту ~10 мкм и диаметр 1,5 мкм. Оболочка Mg$_2$Si была сформирована с помощью метода твердофазной эпитаксии в условиях сверхвысокого вакуума. Толщина силицидной оболочки составляла 400−600 нм на боковых поверхностях нанопроволок.

Ключевые слова: кремний, силицид магния, эпитаксия, нанопроволоки, ядро-оболочка, термоэлектричество, МСХТ, СЭМ, ЭДС, ПЭМ

Introduction

Micrometer-size thermoelectric converters (μ-TEC) [1] are at the cutting edge of science and technology due to their potential of both development and application. These converters could be used as a power source of microelectromechanical systems and micro-watt devices. Surface density of micrometer-size thermocouples (nanowires, for example) arrangement is higher than standard modules for two-three order (10^6 vs 10^3−10^4 cm^{-2}). Such density provides a number of advantages like high cooling response [2] and ability of μ-TECs to work at low temperature gradient [3]. However, traditional production methods (cutting and assembling) are complicated in this size range. So, it is required to find some new approaches. Among them, a reactive ion etching and an anisotropic wet chemical etching combined with a high-resolution lithography or a laser nanofabrication are the most popular. There are many works using these methods of treatment the silicon. Unfortunately, this material has poor thermoelectric properties due to its large thermal conductivity. There is worth considering the Mg$_2$Si as a more perspective Si-based thermoelectric material [4] that could be synthesized directly on etched silicon nanowires as a substrate. We should note that the using of nanowires in thermoelectricity is the promising idea because these objects have both the same power factor and much less thermal conductivity as compared with bulk ones [5].

Materials and methods

Silicon nanowires with controllable size and arrangement were etched by the well-known metal-assisted chemical etching (MACE) of a monocrystalline boron doped silicon wafer with (100) orientation and 1−10 Ω×cm resistivity. A 30 nm thick gold film with an adhesive titanium sublayer 1.5 nm thick was used as the catalytic metal, which was deposited by electron beam evaporation on silicon surface pre-cleaned with isopropanol and Ar$^+$ ion beam. The sample was etched in solution of HF (48%, 5.7M), H$_2$O$_2$ (37%, 1M) and deionized water with 12:4:34 volume ratio, respectively, for one hour at room temperature.

The etched silicon nanowires were cleaned in *aqua regia* for Au film removing, Piranha solution and rinsed in isopropanol and deionized water before loading into ultra-high vacuum (UHV) chamber. After the loading, outgassing was carried out at 600 °C for 12 hours and 850 °C for 20 minutes for SiO_x removing. Mg_2Si was grown by solid phase epitaxy (SPE) in UHV conditions (10^{-9} Torr). Mg amorphous film was deposited onto the cleaned nanowire's surface at room temperature and then there recrystallization annealing was carried out with consequently increasing temperature, at 300, 330 and 360 °C. Size of nanowires was estimated by scanning electron microscope (SEM, Scios 2 DualBeam Thermofisher) combined with X-ray energy dispersive spectroscopy (EDX) to establish chemical element distribution. Structural analysis was carried out by high-resolution transmission electron microscopy (TEM, JEOL JEM-2100 Plus).

Results and discussion

As a result, anisotropic MACE silicon nanowires with 10 μm height and 1.5 μm diameter were etched (Fig. 1, *a*). Mg_2Si shell was grown on the surface of these crystals (core) (Fig. 1, *b, c* and Fig. 2, *a*) with 400−600 nm thickness on sidewalls and ~1 μm on the top (Fig. 1, *c*). The stoichiometric ratio estimated by EDX is 2:1 (Fig. 1, *c*).
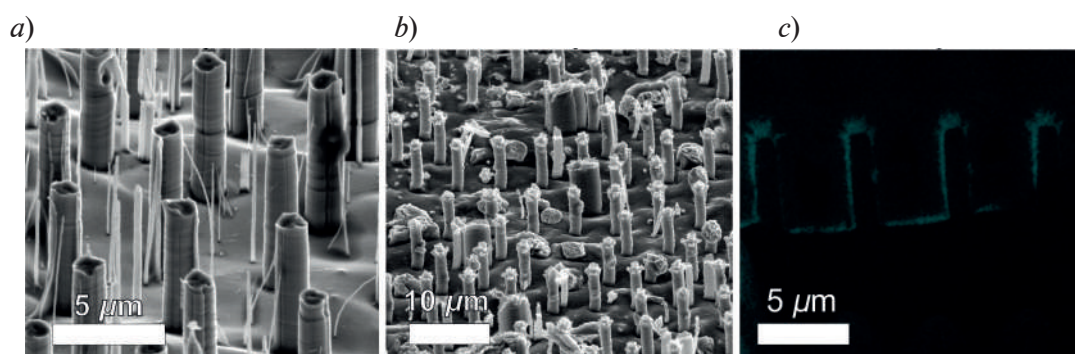
Fig 1. SEM images of etched silicon nanowires (*a*) and synthesized Mg_2Si/Si core-shell nanowires (*b*). Magnesium (blue) distribution on Mg_2Si "shell" (*c*)
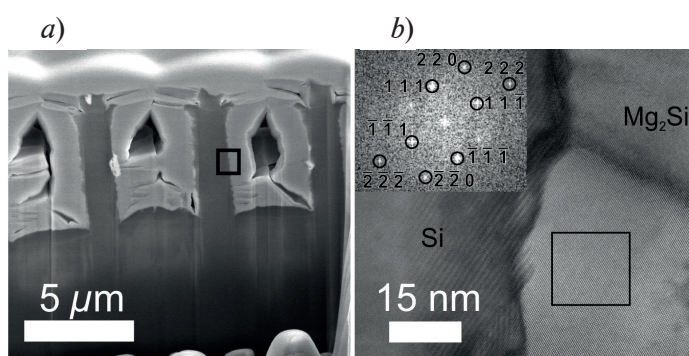
Fig 2. SEM image of Mg_2Si/Si cross-section (*a*) with highlighted section that used for TEM analysis (*b*). On the insert of TEM scan (B) was shown the Fast Fourier Transformation image of selected area with Mg_2Si plane reflexes

The analysis of Mg_2Si/Si structure was carried out by the high-resolution TEM (Fig. 2). Mg_2Si layer has been formed epitaxially with the relation $Mg_2Si(111)\|Si(111)$ (Fig. 2, *b*). According to peak analysis of FFT image (Fig. 2, *b*) Mg_2Si lattice is stretched for 2.7% along [111] and 7.6% along [220].

Conclusion

The Mg_2Si/Si core-shell nanowires were synthesized by the SPE at UHV condition. Silicon nanowires array played the role of a substrate, and a core was etched by MACE. The etched nanowires had a height of ~10 microns and a diameter of 1.5 microns, and the thickness of the

silicide shell was 400−600 nm on the side surfaces of nanowires. Mg_2Si was formed by epitaxy with the epitaxial relationship $Mg_2Si(111)\|Si(111)$. The Mg_2Si lattice is found to be stretched by 2.7% along [111] and 7.6% along [220].

REFERENCES

1. **Ning R., Zeng Y., Rapp V., Zhang B., Yang L., Prasher R., Zheng X.,** Thermoelectric performance of high aspect ratio double-sided silicon nanowire arrays, Journal of Applied Physics. 135 (9) (2024)

2. **Li G., Fernandez J.G., Lara Ramos D.A., Barati V., Pérez N., Soldatov I., Reith H., Schierning G., Nielsch K.,** Integrated microthermoelectric coolers with rapid response time and high device reliability, Nature Electronics. 1 (10) (2018) 555−561.

3. **Hu G., Edwards H., Lee M.,** Silicon integrated circuit thermoelectric generators with a high specific power generation capacity, Nature Electronics. 2 (7) (2019) 300−306.

4. **Cheng X., Farahi N., Kleinke H.,** Mg_2Si-based materials for the thermoelectric energy conversion, Jom. 68 (2016) 2680−2687.

5. **Boukai A.I., Bunimovich Y., Tahir-Kheli J., Yu J.K., Goddard Iii W.A., Heath J.R.** Silicon nanowires as efficient thermoelectric materials, Nature. 451 (7175) 168−171.

THE AUTHORS

SUBBOTIN Evgenii Yu.
jons712@mail.ru
ORCID: 0000-0001-9531-3867

KOZLOV Alexey G.
kozlov.ag@dvfu.ru
ORCID: 0000-0001-8774-0631

PAVLOV Dmitrii V.
pavlov_dim@mail.ru
ORCID: 0000-0001-8726-5615

LISENKOV Oleg E.
oleglis2003@mail.ru
ORCID: 0009-0007-5206-5753

UDILOV Andrei D.
andrey.udilov908@gmail.com
ORCID: 0009-0000-4799-002X

GOROSHKO Dmitry L.
goroshko@iacp.dvo.ru
ORCID: 0000-0002-1250-3372

POLYAKOV Maksim V.
maxsim-polykovv@mail.ru
ORCID: 0000-0001-9304-1490

VOLKOVA Lidiya S.
lidiya.volkova.96@mail.ru
ORCID: 0000-0003-4860-0585

PROKOPEVA Glikeriya A.
glikeriya61@gmail.com
ORCID: 0009-0008-0181-8994

CHERNEV Igor M.
igor_chernev7@mail.ru
ORCID: 0000-0002-8726-9832

KHOROSHILOV Dmitry A.
khoroshilov.20092003@mail.ru
ORCID: 0009-0007-4827-2653

SINOTOVA Sofia A.
sinotovasofia.a@gmail.com
ORCID: 0009-0002-7285-3224

GALKIN Nikolay G.
galkin@iacp.dvo.ru
ORCID: 0000-0003-4127-2988

Influence of the growth regime on the transport properties of doped Mg$_2$Si films

E.Yu. Subbotin [1] ✉, A.D. Udilov [1], G.A. Prokopeva [1], D.L. Goroshko [1],

A.G. Kozlov [2], I.M. Chernev [1], O.E. Lisenkov [1], D.A. Khoroshilov [1],

S.A. Sinotova [1], N.G. Galkin [1]

[1] Institute of Automation and Control Processes FEB RAS, Vladivostok, Russia;
[2] Far Eastern Federal University, Vladivostok, Russia
✉ subbotineu@iacp.dvo.ru

Abstract. In this work, we studied transport properties of the doped Mg$_2$Si film on silicon substrate. The ~1 μm-thickness film was synthesized by the solid phase epitaxy method. Well-proven Ag was chosen as a dopant. At room temperature, the resistivity was 2 $\Omega\times$cm, the mobility was 327 cm^2/(V$\times$s), the density was 9.3$\times10^{15}$ cm^{-3}. We established that using the solid phase epitaxy with the low temperature annealing regime led to mixed electron conductivity of the doped Mg$_2$Si:Ag film due to the substitution of Si-site by Ag. The activation energy of the donor level is 24 meV.

Keywords: silicon, magnesium silicide, solid phase epitaxy, silver, Hall-measurements, SEM, EDX

Влияние режима роста на транспортные свойства легированных плёнок Mg$_2$Si

Е.Ю. Субботин [1] ✉, А.Д. Удилов [1], Г.А. Прокопьева [1], Д.Л. Горошко [1],

А.Г. Козлов [2], И.М. Чернев [1], О.Е. Лисенков [1], Д.А. Хорошилов [1],

С.А. Синотова [1], Н.Г. Галкин [1]

[1] Институт автоматики и процессов управления ДВО РАН, г. Владивосток, Россия;
[2] Дальневосточный федеральный университет, г. Владивосток, Россия
✉ subbotineu@iacp.dvo.ru

Аннотация. В работе исследованы транспортные свойства легированной пленки Mg_2Si на кремниевой подложке. Пленка была сформирована в условиях сверхвысокого вакуума методом твердофазной эпитаксии, ее толщина составляет ~1 мкм. В качестве легирующей примеси было выбрано хорошо зарекомендовавшее себя серебро. Подвижность носителей заряда составила 327 см^2/(В×с), концентрация носителей — 9.3×10^{15} см$^{-3}$.

Ключевые слова: кремний, силицид магния, твердофазная эпитаксия, серебро, холловские измерения, СЭМ, ЭДС

Introduction

Recently, thin-film thermoelectric converters (TEC) have attracted the attention of researchers due to their wide range applications. They could be used as power sources for microwatt devices [1], heat flow sensors [2], and coolers for local thermal management [3]. Also, thin-film TEC could be combined with photovoltaic and thermophotovoltaic cells in hybrid converters [4]. The most popular thermoelectric compounds include expensive and toxic chemical elements that limits their wide commercial distribution. Silicide-based thermoelectric converters are considered as feasible low-cost and eco-friendly alternative. Among them, Mg_2Si-based materials demonstrate competitive properties [5]. The bulk samples are well-researched but there is a lack of works on synthesis and transport measurements of doped films.

Materials and methods

Substrates were cut from floated zone silicon with >1000 Ω×cm resistivity and (111) orientation. First, silicon substrates were washed by isopropanol, and then rinsed in Piranha solution and deionized water. After loading cleaned samples in ultra-high vacuum chamber series of degassing cleaning was conducted at 600 °C and 850 °C for 12 hours and 20 minutes, respectively, for the SiO_x removing. Mg_2Si films were synthesized by solid phase epitaxy (SPE) at ultra-high vacuum condition (~10^{-9} Torr). Amorphous Mg-Ag mixture was deposited on the cleaned Si surface at room temperature. Then, we conducted recrystallization annealing at 300, 330 and 360 °C consequently without interrupting molecular flows. The Mg_2Si forming was proofed by infra-red Fourier spectroscopy. For Hall measurements, metallic pads (Ti-Au) were deposited and annealed in argon atmosphere at 450 °C for 20 minutes to create ohmic contacts. Hall-measurements were carried out in Van der Pauw geometry. The film thickness was estimated by scanning electron microscopy. Stoichiometric ratio was established by X-ray energy dispersive spectroscopy.

Results and discussions

As a result of these growth procedures, a 1 μm-thickness film was synthesized with Mg:Si = 2:1 stoichiometric ratio. Carrier density at room temperature was 9.3×10^{15} cm^{-3}, mobility was 327 cm^2/(V×s) and resistivity was 2 Ω×cm. The characteristic feature of the film synthesized by the described method is electron conductivity with moderate doping level. Previously, in many papers, the Ag impurity was used as an acceptor [6, 7]. This phenomena could be caused by the following. Theoretical works say that Ag impurity can be both donor and acceptor depending
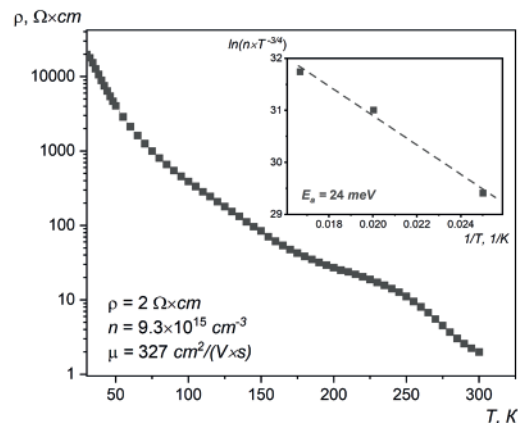
Fig. 1. Temperature dependence of the resistivity from 30 to 300K, main transport coefficients at the room temperature and activation energy of Ag-donor impurities in the insert

on the occupied site [8]. An acceptor level is formed when an Ag atom substitutes a Mg-site. This scenario has the highest probability. A donor level is caused by occupation of a Si-site or a 4b-site by an Ag atom. It should be noted that probability of these scenarios was estimated at 1105 °C that is much more than experimental temperature regime. Also, in reported works, the doping was conducted after the crystallization of Mg_2Si at high temperature (450–500 °C) [6, 7]. This temperature could lead to desorption of Mg atoms that produced vacancy occupied by Ag impurity. In our case, the Mg-Ag mixture was firstly deposited on the Si surface. So, due to the increased diffusion length there is some Si deficit in the Mg_2Si film. The occupation of these Si vacancies by Ag atoms led to the donor level formation [8].

Conclusion

In this work, we reported about the Ag-doped Mg_2Si film growth on the silicon substrate by solid phase epitaxy method under ultra-high vacuum conditions. We measured main Hall parameters. At room temperature, the carrier density was 9.3×10^{15} cm^{-3}, the carrier mobility was 327 cm^2/(V×s), and resistivity was 2 Ω×cm. It was shown that the used growth mechanism leads to donor behavior of the Ag impurity in contrast with thermal diffusion methods described in literature. The phenomena is caused by occupation of Si sites by Ag atoms.

REFERENCES

1. **Jabri M., Masoumi S., Kandukuri T.R., Occhipinti L.G.,** Flexible thin-film thermoelectric generators for human skin-heat harvesting: A numerical study, Nano Energy. 129 (2024) 110001.

2. **Ashok P., Chauhan Y.S., Verma A.,** Low temperature synthesis of VO_2 and hysteresis free VO_x thin films with high temperature coefficient of resistance for bolometer applications, Thin Solid Films. 781 (2023) 139975.

3. **Ihring A., Kessler E., Dillner U., Schinkel U., Kunze M., Billat S.,** A planar thin-film peltier cooler for the thermal management of a dew-point sensor system, Journal of Microelectromechanical Systems. 24 (4) (2014) 990–996.

4. **Chen S., Guo Y., Pan Q., Shuai Y.,** A review on current development of thermophotovoltaic technology in heat recovery, International Journal of Extreme Manufacturing. 6 (2) (2024) 022009.

5. **Ning H., Mastrorillo G.D., Grasso S., Du B., Mori T., Hu C., Xu Y, Simpson K., Maizza G., Reece M.J.,** Enhanced thermoelectric performance of porous magnesium tin silicide prepared using pressure-less spark plasma sintering, J. Mater. Chem. A. 3 (2015) 17426–17432.

6. **Udono H., Tajima H., Uchikoshi M., Itakura M.,** Crystal growth and characterization of Mg_2Si for IR-detectors and thermoelectric applications, Japanese Journal of Applied Physics. 54 (7S2) (2015) 07JB06.

7. **Shimizu T., Miyago D., Shimano K., Sakane S., Udono H.,** Evaluation of Mg_2Si TPV cells fabricated on n-Mg_2Si substrate by thermal diffusion of Ag acceptor, Japanese Journal of Applied Physics. 63 (12) (2024) 12SP17.

8. **Hirayama N., Iida T., Sakamoto M., Nishio K., Hamada N.,** Substitutional and interstitial impurity p-type doping of thermoelectric Mg_2Si: a theoretical study, Science and technology of advanced materials. 20 (1) 160–172.

THE AUTHORS

SUBBOTIN Evgenii Yu.
jons712@mail.ru
ORCID: 0000-0001-9531-3867

UDILOV Andrei D.
andrey.udilov908@gmail.com
ORCID: 0009-0000-4799-002X

PROKOPEVA Glikeriya A.
glikeriya61@gmail.com
ORCID: 0009-0008-0181-8994

GOROSHKO Dmitry L.
goroshko@iacp.dvo.ru
ORCID: 0000-0002-1250-3372

KOZLOV Alexey G.
kozlov.ag@dvfu.ru
ORCID: 0000-0001-8774-0631

CHERNEV Igor M.
igor_chernev7@mail.ru
ORCID: 0000-0002-8726-9832

LISENKOV Oleg E.
oleglis2003@mail.ru
ORCID: 0009-0007-5206-5753

KHOROSHILOV Dmitry A.
khoroshilov.20092003@mail.ru
ORCID: 0009-0007-4827-2653

SINOTOVA Sofia A.
sinotovasofia.a@gmail.com
ORCID: 0009-0002-7285-3224

GALKIN Nikolay G.
galkin@iacp.dvo.ru
ORCID: 0000-0003-4127-2988

Visualization of electric field of e-beam-formed charge patterns in glass

A.N. Terpitskiy [1] ✉, I.V. Reshetov [1,2], S.A. Scherbak [1,2], A.A. Lipovskii [2,1]

[1] Alferov University, St. Petersburg, Russia;

[2] Peter the Great St. Petersburg Polytechnic University, St. Petersburg, Russia

✉ terpiczkij@mail.ru

Abstract. We have formed a given pattern of the second order optical nonlinearity in the subsurface region of a glass by electron irradiation. The nonlinearity was induced by the electric field of the electrons captured by the glass. Formed structure consisted of periodic "strips" and, being irradiated normally to the glass surface with an IR laser, generated the second harmonic (SH) radiation pattern similar to one of a phase diffraction grating. The pattern presented the results of an interference of the SH waves generated by nonlinear strips. Mapping of the SH radiation pattern in orthogonal polarizations of the fundamental laser beam allowed concluding about the distribution of the electric field of electrons captured in the glass.

Keywords: second harmonic generation, glass, e-beam lithography, grating structure

Визуализация электрических полей зарядовых структур, сформированных электронным лучом в стекле

А.Н. Терпицкий [1] ✉, И.В. Решетов [1,2], С.А. Щербак [1,2], А.А. Липовский [2,1]

[1] Академический университет им. Ж.И. Алфёрова РАН, Санкт-Петербург, Россия;

[2] Санкт-Петербургский политехнический университет Петра Великого, Санкт-Петербург, Россия

✉ terpiczkij@mail.ru

Аннотация. Продемонстрирована возможность формирования заданной нелинейной периодической структуры в приповерхностной области стекла электронным облучением. Нелинейность индуцировалась электрическим полем электронов, захваченных стеклом. Сформированная структура при облучении поверхности стекла по нормали ИК лазером генерировала вторую оптическую гармонику с диаграммой направленности, аналогичной диаграммам от фазовых дифракционных решеток. Картирование излучения второй гармоники при ортогональных поляризациях фундаментальной волны позволило сделать вывод о распределении электрического поля захваченных в стекле электронов.

Ключевые слова: генерация второй оптической гармоники, стекло, электронная литография, периодическая структура

Introduction

Currently, nonlinear optical effects are used in various devices, such as optical modulators, optical frequency converters, etc. One of the main fields of research in nonlinear optics relates to the second harmonic generation (SHG). In general, such an effect can only be achieved in materials without the inversion center. However, a lot of optical elements is based on glasses. This is because of their low price, optical transparency in a wide range of wavelengths and a high variability of other characteristics. In glasses, the presence of the inversion center forbids SHG, with the exception of the glass surface. However, SHG in glasses can be provided by the EFISH (electric field induced second harmonic) effect [1] that is nonlinear conversion involving 3rd order electric susceptibility $\chi^{(3)}$ and DC electric field E^{DC} created by a charge "frozen" in the glass. Among such approaches to create a frozen electric charge as thermal poling [2, 3], optical poling [4], etc., the e-beam irradiation stands out primarily due to its high resolution and the opportunity of direct writing of complicated patterns [5].

The visualization of the distribution of electric field is an important problem in the design of various micro- and optoelectronic components. If optically transparent materials are used, SHG can be a convenient tool for this, e.g. mapping of the SHG signal. In this paper we demonstrate the visualization of the electric field distribution in nonlinear periodic structures created by electron irradiation in a glass.

Materials and Methods

We used BF16 glass with the following composition: 27% SiO_2; 6.8% B_2O_3; 2.5% Al_2O_3; 0.6% Sb_2O_3; 0.4% As_2O_3; 10% PbO; 42% BaO; 5.7% ZnO; 5.1% CaO. Electron irradiation was carried out using a Raith EBPG5000 + ES electron beam writer. The electron energy was 100 keV, the beam size was 2 nm, and the charge density of the irradiated pattern was maintained at 8 μC/cm². The written structure is a set of two-dimensional gratings with the periods Λ = 4, 8, 16, and 32 μm. The gaps in the gratings coincided in width with the strips and made up half the period, i.e. $\Lambda/2$. The gratings are about 1 mm wide and 3 mm long. Optical measurements were performed using a 1064 nm pulsed picosecond laser (Nordlase IGUL-PS-205-1064-50-50-10-50). Laser beam width was 90 μm, using a short-focal-length lens allowed to reduce it to 1−2 μm. To map the SH signal, the irradiated glass was mounted on a two-dimensional translation stage. SH signal registration was carried out using a photon counter (Hamamatsu H11890-110).

Results and Discussion

The distribution of E^{DC} in this structure, which was obtained by solving the Poisson equation [6] for the given charge distribution, is characterized by specific SH radiation patterns. These patterns were observed under normal-incidence laser irradiation (see Fig. 1, *a*). Fig. 1, *b* presents the radiation patterns of the SH generated by a 16 μm grating under laser excitation with transverse polarization (relative to the grating stripes). The observed profiles are consistent with the theoretical distributions of diffraction gratings exhibiting π-phase modulation

SHG mapping was performed using a long-focal-length lens (size of the light spot (~90 μm) noticeably exceeds the periods). The obtained maps are presented in Fig. 2. The strongest SH signal is observed at the edges of the gratings − the side faces for the transverse polarizations and the end faces for the longitudinal polarization. Since in this structure SHG occurs via the
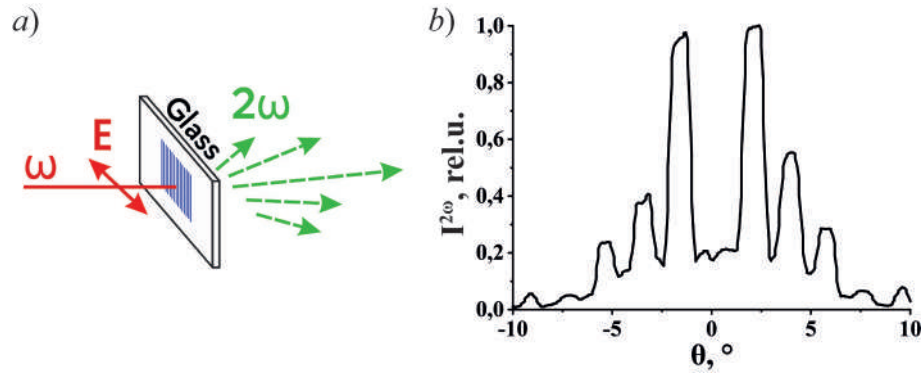
Fig. 1. Optical measurement scheme (*a*); normalized SH signal as a function of the scattering angle for periodically e-beam irradiated area with period $\Lambda = 16$ μm (*b*)
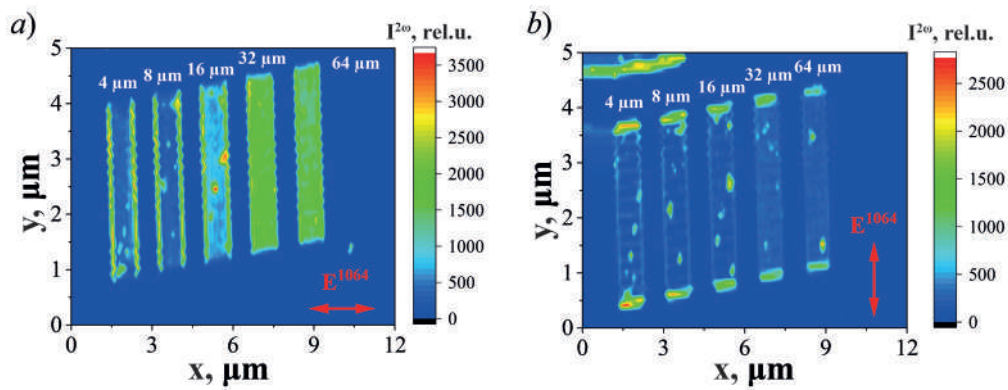
Fig. 2. SHG maps at orthogonal polarizations of the laser beam: across the strips (*a*); along the strips (*b*)

EFISH effect [1], the signal magnitude directly depends on the electric field strength. Thus, Fig. 2 demonstrate visualization of static *E*-field in the structure. Note, since size of the light spot in these measurements (~90 μm) noticeably exceeds the periods, the *E*-field inside the gratings is unresolved.

To visualize *E*-field inside the gratings, we used a short-focal-length lens (the light spot (~2 μm) is smaller than the periods). As described by the model in Ref. [6], the charge distribution expands beyond the boundaries of the fabricated strips due to electron scattering in the glass. This leads to an increase (compared to the grating period) spacing between the E^{DC} maxima in the irradiated region. Fig. 3, *a* presents the SH signal profile for a $\Lambda = 4$ μm grating, measured with the laser polarization oriented transverse to the strips. We observe a significant increase in the SH peaks spacing within the irradiated zone (2.5 μm compared to the original 2 μm), confirming
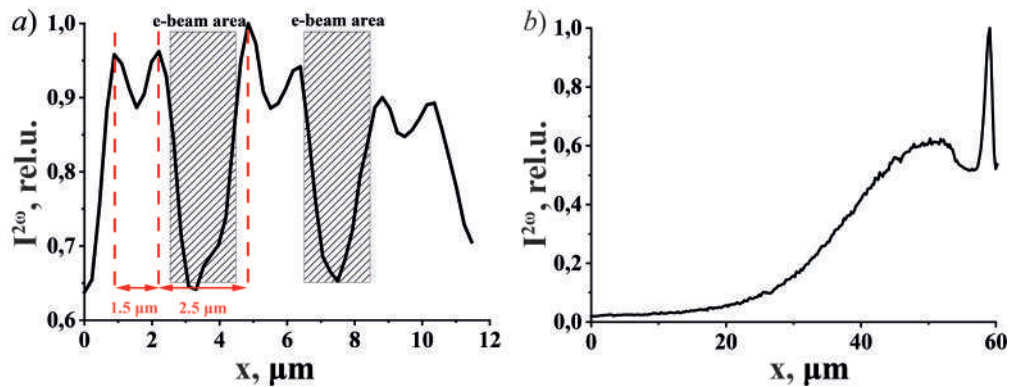
Fig. 3. SH signal profiles under laser irradiation of a $\Lambda = 4$ μm grating: within the grating area (*a*) and at the grating edge (*b*)

the corresponding increase in the E^{DC} maxima separation. Furthermore, at the outermost strip, the implanted charge is no longer confined by neighboring strip, resulting in the predicted decay of the SH signal to zero over extended distances (~40 μm for $\Lambda = 4$ μm), as shown in Fig. 3, *b*.

Conclusion

We demonstrated SHG for visualizing E^{DC} distributions in periodic structures fabricated by electron beam in glass. SHG spatial mapping revealed pronounced electric field localization at grating edges. Moreover, high-resolution SHG profiling with a short-focal-length lens allowed visualizing local electric field inside the grating. Obtained profiles of the local *E*-field are in agreement with the recent simulations [6].

Acknowledgments

REFERENCES

1. **Statman D., Georges III J.A.,** Charge dynamics and poling in glass waveguides, J Appl Phys. 2 (80) (1996) 654−661.

2. **Myers R.A., Mukherjee N., Brueck S.R.J.,** Large second-order nonlinearity in poled fused silica, Opt Lett. 22 (16) (1991) 1732−1734.

3. **Okada A., Ishii K., Mito K., Sasaki K.,** Phase-matched second-harmonic generation in novel corona poled glass waveguides, Appl Phys Lett. 23 (60) (1992) 2853−2855.

4. **Österberg U., Margulis W.,** Dye laser pumped by Nd:YAG laser pulses frequency doubled in a glass optical fiber, Opt Lett. 8 (11) (1986) 516−518.

5. **Kazansky P.G., Kamal A., Russell P.St.J.,** High second-order nonlinearities induced in lead silicate glass by electron-beam irradiation, Opt Lett. 9 (18) (1993) 693−695.

6. **Scherbak S.A., Terpitskiy A.N., Reshetov I.V., Reduto I.V., Kaasik V.P., Zhurikhina V.V., Lipovskii A.A.,** Optically Nonlinear Structures in Glass by Electron Lithography: Direct Writing, ACS Photonics. 4 (12) (2025) 2016−2026.

THE AUTHORS

TERPITSKIY Aleksey N.
terpiczkij@mail.ru
ORCID: 0000-0002-1744-5976

RESHETOV Ilya V.
reshetov_iv@spbstu.ru
ORCID: 0000-0002-8661-3654

SCHERBAK Sergey A.
sergeygtn@yandex.ru
ORCID: 0000-0002-0507-5621

LIPOVSKII Andrey A.
lipovskii@gmail.com
ORCID: 0000-0001-9472-9190

Influence of physical effects on the structure of soot particles of hydrocarbon flames

A.N. Lepaev [1] ✉, S.I. Ksenofontov [2], O.V. Vasilyeva [3], A.A. Kudryavtsev [4]

[1] Cheboksary Institute (branch) of Moscow Polytechnic University, Cheboksary, Russia;

[2] Chuvash State Pedagogical University named after I.Y. Yakovlev, Cheboksary, Russia;

[3] Chuvash State University named after I.N. Ulyanov, Cheboksary, Russia;

[4] INSKAN LLC, St. Petersburg, Russia

✉ it@polytech21.ru

Abstract. The structure of the diffusion flame of TC-1 kerosene has been studied. A film of pyrolytic soot was obtained using the sampling method, and the structural changes of this film under thermal exposure were studied. A new carbon structure — glass carbon was obtained as a result of laser irradiation of highly dispersed carbon black. The mechanism of bubble formation in the glassy carbon structure has been established, and the latent heat of carbon "melting" equal to 2110 J/kg has been determined.

Keywords: flame, soot, carbon, pyrolysis, IR-spectroscopy

Влияние физических воздействий на структуру сажевых частиц углеводородных пламен

А.Н. Лепаев [1] ✉, С.И. Ксенофонтов [2], О.В. Васильева [3], А.А. Кудрявцев [4]

[1] Чебоксарский институт (филиал) Московского Политехнического университета, г. Чебоксары, Россия;

[2] Чувашский государственный педагогический университет им. И.Я. Яковлева, г. Чебоксары, Россия;

[3] Чувашский государственный университет им. И.Н. Ульянова, г. Чебоксары, Россия;

[4] ООО «ИНСКАН», Санкт-Петербург, Россия

✉ it@polytech21.ru

Аннотация. Проведено исследование структуры диффузионного пламени керосина марки ТС-1. Посредством метода пробоотбора получена пленка пиролитической сажи, изучены структурные изменения данной пленки при термическом воздействии. В результате лазерного облучения высокодисперсной сажи получена новая углеродная структура — стеклоуглерод. Установлен механизм формирования пузырьков в структуре стеклоуглерода, определена скрытая теплота «плавления» углерода, равная 2110 Дж/кг.

Ключевые слова: пламя, сажа, углерод, пиролиз, ИК-спектроскопия

Introduction

Soot particles are formed during the combustion of hydrocarbon fuels. Despite numerous studies of the morphology and structure of soot particles, the mechanism of their formation is still not fully understood [1, 2, 3]. According to one hypothesis, soot particles are formed as a result of the hydrogenation of hydrocarbon molecules, followed by their combination into a single particle. Primary soot particles are described as amorphous carbon. In contrast, another hypothesis suggests the formation of more complex molecular structures, in particular polycyclic aromatic hydrocarbons, which serve as nuclei for the formation of carbon black particles.

Materials and Methods

Light fractions of oil (TC−1 fuel) burn to form a diffusive luminous flame. The shape of the flame is determined by the design of the burner device. In the case of a cylindrical burner, the formation of a conical-shaped diffusion flame is observed. At the base of the flare, the mixture formation is such that the hydrocarbon fuel burns almost in a stoichiometric ratio. The position of the combustion front of the flame is close to the side surface of the cone. With increasing altitude, due to the lack of injected oxygen, the completeness of combustion decreases, highly dispersed soot particles are formed from fuel molecules, the glow of which turns the torch yellow-orange. A plume of sooty particles forms at the top of the torch. There is a zone near the top of the flare cone, where the density of the heat flow from the combustion front is high. Volumetric pyrolysis of a combustible substance without ignition is possible in this zone. Pyrolysis products can condense on the surface of soot particles in the plume area at the top of the flare. Pyrolysis products also occur at the boundary adjacent to the combustion zone. They can undergo further oxidation, when pass through the combustion zone.

Results and Discussion

The introduction of the sampler into the volumetric pyrolysis zone creates conditions for pyrolysis products to settle on the surface of the sampler. In the central region of the flame, in the zone of active pyrolysis, carbon was deposited on the surface by a film-island mechanism, on the periphery of the flame − in the form of highly dispersed particles.

Examination of the film surface using an optical microscope shows the absence of pronounced irregularities. However, when the sampler is heated, the film begins to break apart and peel off from the glass (Fig. 1). The lines of discontinuity are characterized by the absence of pronounced symmetry. Eventually, a pile of detached film fragments forms in place of the film.
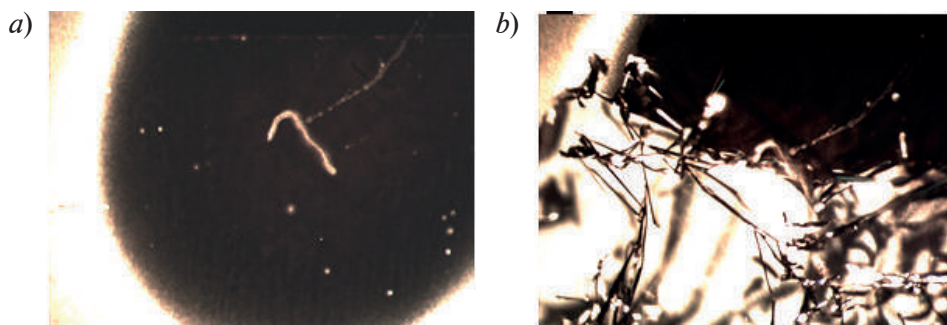
Fig. 1. Pyrolytic carbon film before thermal exposure (*a*); after thermal exposure (*b*)

The use of an atomic force microscope SolverNext made it possible to obtain a micro relief of the film surface (Fig. 2). The film consists of a set of soot particles in contact with each other, having a predominantly rounded shape. The particle sizes range from 200 to 300 nm, but there are also larger formations reaching 1300 nm in diameter. The surface of the particles, as a rule, is not characterized by a spherical shape, but consists of layers.

a)

b)
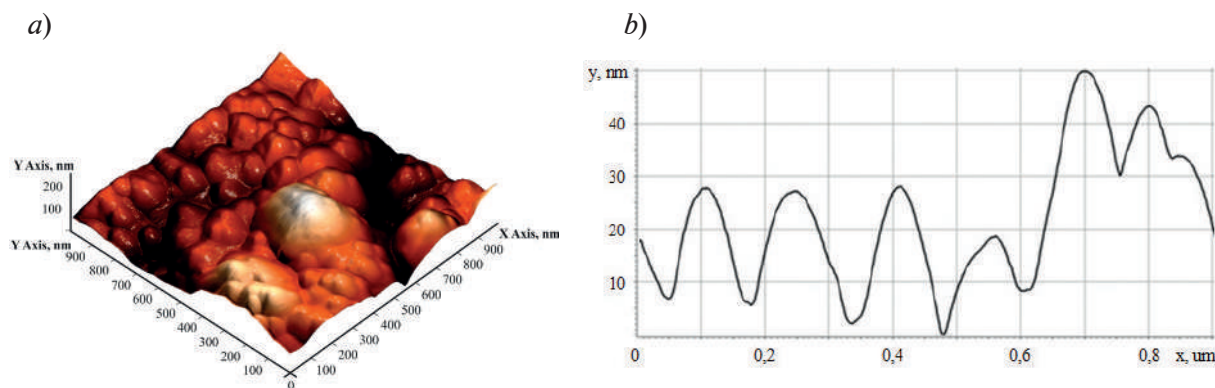
Fig. 2. Surface of pyrolytic film on AFM: 3D−surface (*a*); surface profile at $x = 800$ nm (*b*)

The space between the particles is filled with binder. However, break lines representing structural inhomogeneities (defects) are detected. Thermal influence on the sampler leads to the fact that the film destruction starts in the areas corresponding to these defects.

Spectral analysis of soot samples obtained using the FSM−1201 spectrometer showed continuous absorption of radiation in the entire studied wavelength range [4], from 4000 to 500 cm^{-1}. Similar results were obtained for industrial carbon black samples, in particular, PM-50 and LM-15 grades. During the production process, industrial carbon black undergoes a stabilization stage, during which active centers such as CH-groups and oxygen-containing compounds are removed. Further it provides its long-term storage without significant changes in characteristics.

In the work by Prikhodko N.G., Mansurova Z.A. [2] describes the process of nucleation of carbon nanostructures in the form of C_{60} and C_{70} fullerenes in a hydrocarbon flame at low pressures. At the initial moment, amorphous carbon is formed, from which graphene plates are then formed. Graphene plates, folding, form fullerene molecules. The author emphasizes that the ratio between C_{60} and C_{70} molecules can be controlled. There is no information about the properties of amorphous carbon in the work.

Murga M.S. [3] considers the structure of amorphous carbon as a medium with a short-range order in the arrangement of atoms. It is hypothesized that amorphous carbon in the intergraphine space may exhibit properties characteristic of the liquid phase.

Spherical particles of highly dispersed carbon black consist of a set of individual crystallites [4, 5]. Within each crystallite, the arrangement of carbon atoms is ordered. However, within a spherical particle, the relative arrangement of crystallites is chaotic.

When exposed to laser radiation, the structure of highly dispersed carbon black changes. A semiconductor OCG at a wavelength of 450 nm with a beam power of 4.5 W was used as a laser. When focusing with the output lens, you can get a spot with a diameter of 0.33 mm. Highly dispersed soot within the beam turns into a glassy mass. Some of the carbon is oxidized in the air and forms a gas that inflates the glassy substance into a bubble. Nearby, the bubbles form thin walls between each other, which are easily visualized when viewed with an optical microscope (Fig. 3, *a*). The resulting carbon dioxide diffuses through the pores in the film and leaves the bubble cavity.

Further study of the structure of glass carbon and highly dispersed carbon black was carried out using a scanning electron microscope JQSCAN W−32. Microphotographs of the sampler sections were obtained (Fig. 3, *b*, *c*), the elemental composition of dispersed particles was studied. The film is characterized by a porous structure with pore sizes ranging from 250 to 1250 nm. At a magnification of 50000x, the internal structure of the film itself can be seen. It is a spatial mesh consisting of nanoparticles of 30−60 nm in size and interconnected by thin junctions. Highly dispersed carbon black consists of particles that vary in size over a wide range from 50 to 230 nm. The particles are in contact with each other but do not merge.

a)   *b)*   *c)*
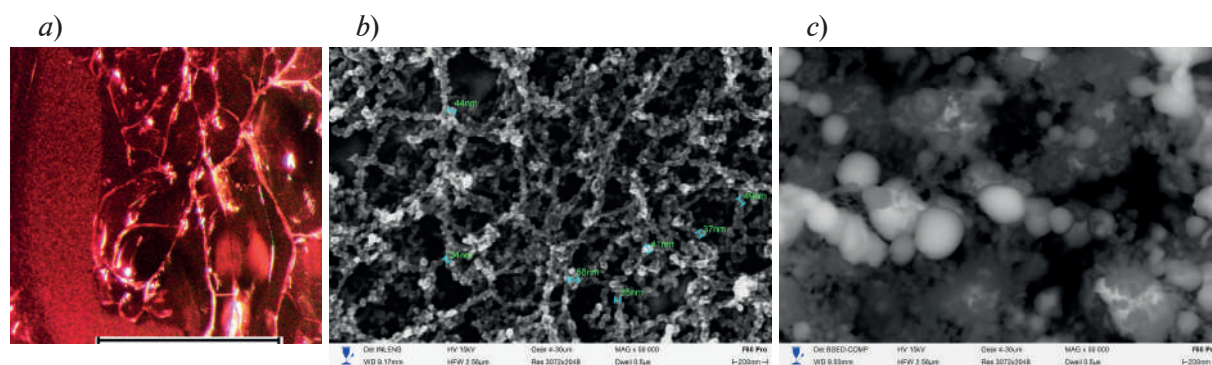
Fig. 3. The surface of the sampler section: the structure of a glass−carbon bubbles − optical microscope (reference line 1 mm) (*a*); scanning electron microscope (50000x) (*b*); the structure of deposited highly dispersed carbon black − scanning electron microscope (50000x) (*c*)

X-ray microanalysis allowed to determine the elemental composition of the studied samples. In particular, the mass fraction of carbon in glass carbon amounted to 23.6%, in highly dispersed carbon black − 25.16%. It was found that under the influence of laser radiation 1.56% of carbon black is burned out with the formation of carbon dioxide, which, expanding, forms a bubble in the glass-carbon matrix.

Thus, the energy of laser radiation is spent on the process of carbon black burnout, as well as on the phase transition of carbon black crystallites into the liquid phase − glass-carbon. The latent heat of carbon "melting" turned out to be equal to 2110 J/kg. The obtained results require further investigation. Literature sources [6] contain data on the heats of phase transitions of graphite and diamond, the values of which are 1000 and 5000 J/kg, respectively.

Glass carbon is produced on an industrial scale by pyrolysis sintering from phenolic resins in vacuum and is subsequently used as a chemically inert structural material capable of withstanding high temperatures [6, 7].

Conclusion

1. A film of pyrolytic soot was obtained by the method of passing a glass plate through a flame, and the structural changes of this film under thermal influence were studied.

2. It has been established that as a result of the effect of optical radiation on highly dispersed carbon black a new carbon structure − vitreous carbon − is formed.

REFERENCES

1. **Tesner P.A.,** Nuclei of soot particles − radicals, Physics of Combustion and Explosion. 3 (28) (1992) 49−52.

2. **Prikhodko N.G.,** Flame synthesis of graphene layers at low pressure, Chemical physics. 9 (34) (2015) 68−73.

3. **Murga M.S.,** Carbon universe: types of carbon particles, mechanisms of their formation and prevalence, Institute of Astronomy: Russian Academy of Sciences. (2023) 88−97.

4. **Vasilyeva O.V., Ksenofontov S.I., Krasnova A.G., Kokshina A.V.,** The structure and properties of soot in the flame of a hydrocarbon fuel, Alternative energy and ecology. 19 (2015) 105−111.

5. **Krishtal M.M., Yasnikov I.S., Polunin V.I.,** Scanning electron microscopy and X-ray microanalysis in examples of practical application: textbook for universities, Technosphere, Moscow. (2009).

6. **Shakhov F.M.,** Experimental investigation of phase transitions in nanocarbon materials at high pressures and temperatures: abstract of the dissertation, PhD in Physics and Mathematics: 01.04.07, Shakhov Fyodor Mikhailovich, St. Petersburg. (2008).

7. **Chekanova V.D., Fialkov A.S.,** Glass carbon. Getting, properties, and application, Successes of Chemistry, 5 (40) (1971) 777−780.

THE AUTHORS

LEPAEV Aleksandr N.
it@polytech21.ru
ORCID: 0000-0003-2498-1192

VASILYEVA Olga V.
dprostokvashino@mail.ru
ORCID: 0000-0001-8432-5635

KSENOFONTOV Sergey I.
ksenofontovsi@mail.ru
ORCID: 0000-0002-9723-5652

KUDRYAVTSEV Andrey A.
aka@tescan.ru
ORCID: 0000-0002-9810-6932

Si-based photodetector with an Mg$_2$Si contact layer for SWIR range

I. M. Chernev [1] ✉, E.Yu. Subbotin [1], A.G. Kozlov [2], S.A. Sinotova [2],

A.V. Prikhodchenko [2], A.O. Lembikov [2], G.A. Prokopeva [2],

D.L. Goroshko [1], N.G. Galkin [1]

[1] Institute of Automation and Control Processes FEB RAS, Vladivostok, Russia;
[2] Far Eastern Federal University, Vladivostok, Russia
✉ chernev@iacp.dvo.ru, igor_chernev7@mail.ru

Abstract. Mg$_2$Si film ~2.3 μm was synthesized by reactive deposition Mg on Si(111) at 340 °C in UHV. The photoresponse of backlighted Al/Si/Mg$_2$Si Schottky structure represents the bell-shaped curve with the peak at 1045 nm and intensity 29 mA/W, 105 mA/W and 195 mA/W under the 0 V, 1 V and 5 V bias respectively with FWHM ~130 nm.

Keywords: magnesium silicide, silicon, films, epitaxy, reactive epitaxy, crystal structure, microscopy, photoresponse

Фотодетектор на основе кремния с контактным слоем Mg$_2$Si для коротковолнового ИК диапазона

И.М. Чернев [1] ✉, Е.Ю. Субботин [1], А.Г. Козлов [2], С.А. Синотова [2],

А.В. Приходченко [2], А.О. Лембиков [2], Г.А. Прокопьева [2],

Д.Л. Горошко [1], Н.Г. Галкин [1]

[1] Институт автоматики и процессов управления ДВО РАН, г. Владивосток, Россия;
[2] Дальневосточный федеральный университет, г. Владивосток, Россия;
✉ chernev@iacp.dvo.ru, igor_chernev7@mail.ru

Аннотация: Пленка Mg$_2$Si толщиной ~2.3 мкм была синтезирована методом реактивного осаждения Mg на Si(111) при температуре 340 °C в сверхвысоком вакууме. Фотоотклик структуры Шоттки Al/Si/Mg$_2$Si представляет собой колоколообразную кривую с пиком при 1047 нм и интенсивностью 29 мА/Вт, 105 мА/Вт и 195 мА/Вт при смещении 0В, 1 В и 5 В, соответственно, с шириной пика ~130 нм.

Introduction

Photodetectors for the 1000−1600 nm range find applications in fields such as medical imaging, health and environmental monitoring, optical communication systems, as well as sorting/identification systems [1, 2] and brain imaging [3]. The narrowband spectral photoresponse with a FWHM of ~100 nm not only reduces the impact of noise-induced illumination but also enables the development of wavelength-division multiplexing devices.

Narrow-band semiconducting Mg_2Si is known as a material for near-infrared *p-n* photodetectors and thermoelectric generators [4−6]. However, beyond these applications, there is evidence that Mg_2Si is perspective as a contact material for silicon as well. It was demonstrated [7, 8] that metal silicides (Yb, Y, Ca, Ba, Sr, Fe) are of particular interest as contact materials for *n*-type silicon because selectively open for the electronic part of the photogenerated carriers. This effect occurs due to the reduction of energy barriers at the silicide/silicon interface caused by Fermi-level pinning, leading to more efficient extraction of photogenerated charge carriers from silicon. This approach avoids overdoping of under-contact regions, thereby further reducing recombination losses.

In this work, we tested an Al/*n*-Si/Mg_2Si Schottky photodetector based on 500 μm thick Si with a Mg_2Si back contact.

Materials and Methods

Growth experiments were conducted in an ultra-high vacuum (UHV) chamber "Varian" with a base pressure of ~10^{-9} Torr. A 500 μm thick Si(111) substrate ($\rho > 1000$ Ω·cm) was first cleaned in a piranha solution and then degassed under UHV conditions at 650 °C for 6 hours. Subsequently, a high-temperature annealing at 850 °C for 10 minutes was performed to remove the native silicon oxide. A high-purity Mg (5N) source was degassed under UHV conditions for several hours as well. The Si substrate temperature of 340 °C was monitored using a PhotriX optical pyrometer. A magnesium portion ≈1.7 μm was deposited onto the preheated up to 340 °C substrate over ≈200 msec. Details of the Mg_2Si film synthesis procedure can be found in our previous works [9−11]. Finally, the Mg_2Si film ≈ 2.3 μm was synthesized.

The X-ray diffraction (XRD) technique was performed on a Kolibri (Burevestnik) X-ray diffractometer equipped with a Cu(29) anode operating at an excitation voltage of U = 8.86 kV, emitting radiation with an average Kα wavelength of λ = 1.54 Å. The thickness of the grown Mg_2Si film was studied with the ThermoFisher Scios 2 DualBeam scanning electron microscope (SEM). For preparing a hole with a smooth flat surface a focused Ga^+ ion beam (FIB) was used. Raman spectroscopy measurements were performed using an NTEGRA Spectra II system (NT-MDT) at room temperature with 473 nm laser excitation.

The spectral photosensitivity was measured in 420−1400 nm spectral range with a setup consisting of: a W halogen lamp, monochromator with a set of optical filters and diffraction gratings, mechanical light modulator (f = 533 Hz) and Lock-In Amplifier for signal enhancement. The current-voltage characteristics were acquired employing high-accuracy multimeters AKIP B7-78/1 and a Keithley instrument.

Results and Discussion

The procedure of sample growth and preparation for photoresponse measurements is schematically illustrated in Fig. 1, *a*. For spectral photosensitivity measurements, the sample was cut to a size of about 2×2 mm and then stacked by Ag glue (to Mg_2Si film side) in a chip with a copper pad − contact "2". The top contact "1" was fabricated with ultrasonic Al wiring to another copper pad (see Fig. 1, *b*).

a)

b)
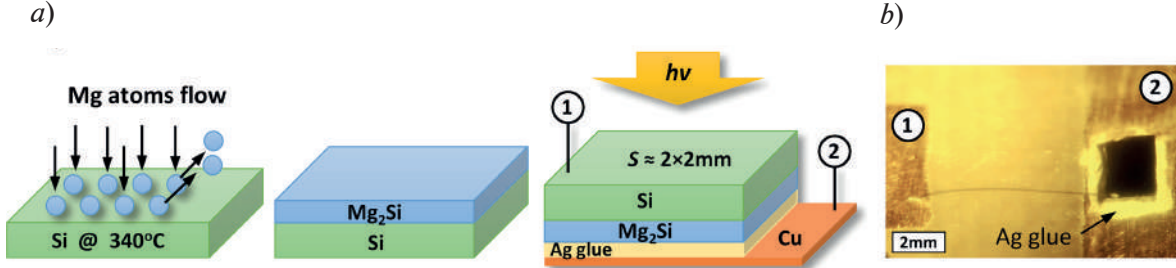
Fig. 1. Schematic growth procedure and sample preparation for photoresponse measurements (*a*), real photo of photodetector prototype. "1" and "2" are copper contact pads (*b*)

The thickness of the fabricated Mg_2Si film is ~2.3 μm, as determined by cross-sectional SEM analysis (see Fig. 2, *a*). The XRD results are presented in Fig. 2, *b*. The spectrum shows peaks associated with diffraction from the Si(111) substrate, as well as Mg_2Si peaks corresponding to diffraction from the (111) and (222) planes at 2θ angles of 24.31° and 49.81°, respectively. The calculated lattice parameter was 6.339 Å, which is 0.2% smaller than the reference value 6.351 Å [13], indicating the compressive strain.

a)　　　　*b*)　　　　*c*)
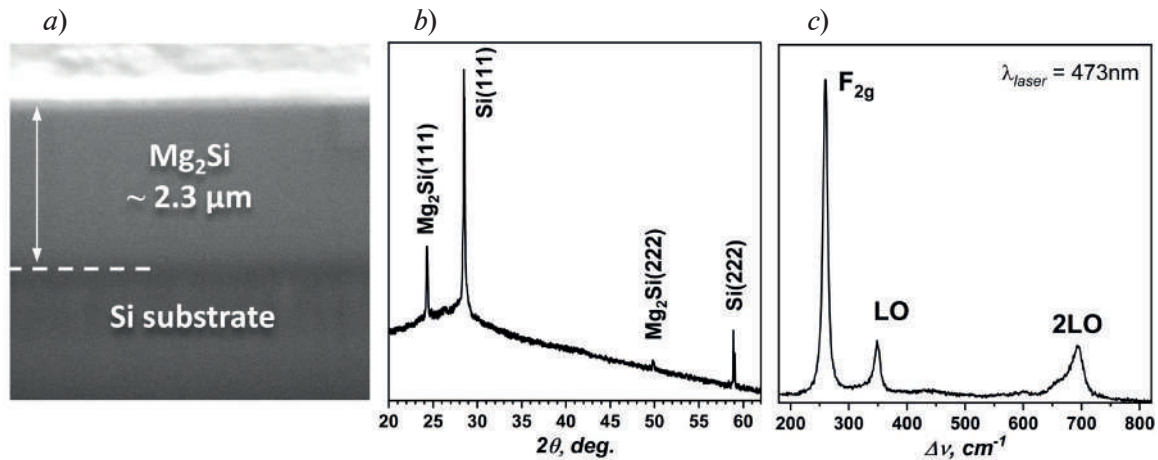
Fig. 2. Mg_2Si film on Si(111) substrate. Cross-sectional SEM image (*a*), XRD pattern (*b*), Raman scattering spectrum (*c*)

Fig. 2, *c* demonstrates Raman spectroscopy data for the grown Mg_2Si film. The intense peak at 259 cm^{-1}, along with peaks at 349 cm^{-1} and 693 cm^{-1}, are characteristic of Mg_2Si [13, 14]. The absence of the 520 cm^{-1} peak, which is typical for crystalline silicon, results from the substantial thickness of the Mg_2Si film that completely absorbs the 473 nm excitation laser radiation.

Fig. 3, *a* shows the spectral photoresponse measurements in the diode mode. The curves exhibit a pronounced peak at a wavelength of 1045 nm. The response behavior is uncommon of conventional Si *p-n* and Schottky photodiodes. For comparison, Fig. 3, *a* presents the spectral photoresponse of a commercially available Hamamatsu Si photodiode (red curve). As the external bias is applied, the signal intensity increases; however, the overall spectral behavior remains the same.

The photoresponse intensity at the peak is 105 mA/W and 195 mA/W under 1 V and 5 V bias, respectively (see Fig. 3, *a*). The Al/Si/Mg_2Si structure also exhibits a photoresponse at zero bias 29 mA/W, indicating the presence of a built-in field at the Si/Mg_2Si junction (see Fig. 3, *b*). The
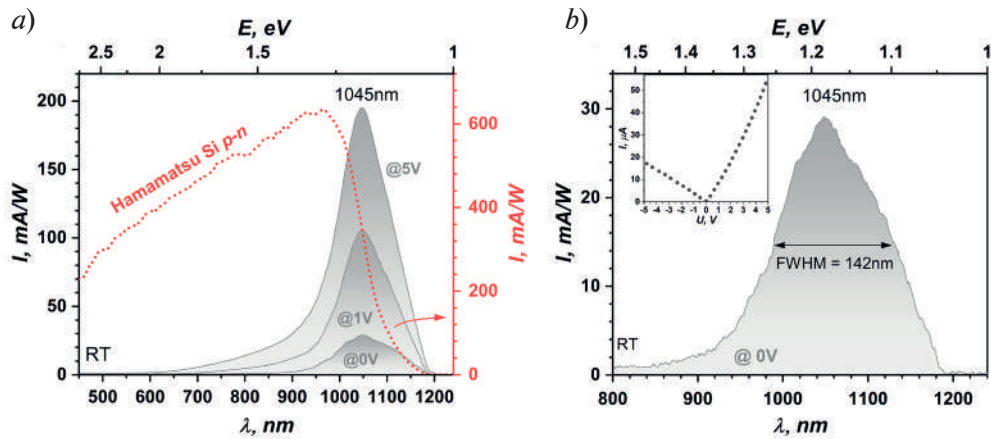
Fig. 3. Spectral photoresponse measured in diode mode, commercially available Hamamatsu Si *p-n* photodiode photoresponse curve is red (*a*), at zero-bias. I-V is in insert (*b*)

rectifying junction is further confirmed by the current-voltage characteristic, which exhibits diode-like behavior (see Fig. 3, *b*, inset). The peak photoresponse wavelength of 1045 nm corresponds to the energy of a number of indirect interband transitions in Si, while the substrate thickness filters out the short-wavelength range of the incident light.

The photoresponse measurements were performed in a configuration where the positive terminal of the external bias source was connected to the top contact "1"(see Fig. 1). The Al/Si/Mg$_2$Si structure forms a double Schottky junction, and the "positive-1" & "negative-2" connection geometry is forward-biasing for the upper Al/Si junction while reverse-biasing the lower Si/Mg$_2$Si junction.
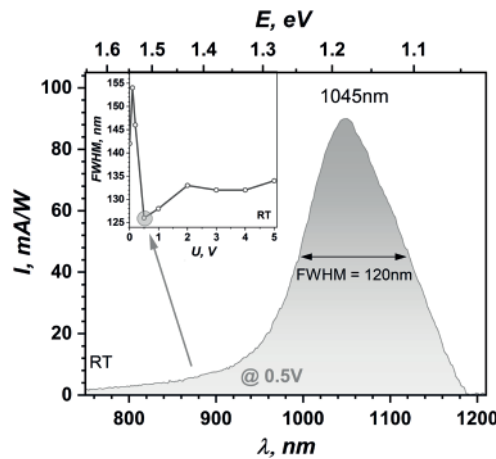
Fig. 4. Spectral photoresponse at 0.5 V bias. FWHM *vs.* bias dependence is in insert

The FWHM exhibited slight variations under different bias, measuring 128 nm and 134 nm at 1 V and 5 V, respectively (see Fig. 4, inset). The minimum FWHM of 120 nm was observed at a bias of 0.5 V (see Fig. 4), with a corresponding photoresponse intensity of 90 mA/W.

Conclusions

High crystal quality ~2.3 µm thick Mg$_2$Si film was fabricated on Si(111). The photosensitive structure Al/Si/Mg$_2$Si was prepared and spectral photoresponse was tested in diode and zero-bias mode. It was demonstrated the narrowband photoresponse with peak at 1045 nm and intensity of 29 mA/W, 105 mA/W and 195 mA/W under the 0 V, 1 V and 5 V respectively. The FWHM varies from 140nm at zero-bias to ~130 nm at 1−5 V. The lowest FWHM = 120 nm observed at 0.5 V bias and 90 mA/W intensity.

Acknowledgments

REFERENCES

1. **Rathnamalala C.S.L., Hernandez S., Lucero M.Y., Swartchick C.B., Shaik A.K., Hammer N.I., East A.K., Gwaltney S.R., Chan J., Scott C.N.,** Xanthene-Based Nitric Oxide-Responsive Nanosensor for Photoacoustic Imaging in the SWIR Window, Angew.Chem. 135 (2023) e202214855.

2. **Wu Z., Zhai Y., Kim H., Azoulay J.D., Nga Ng T.,** Emerging Design and Characterization Guidelines for Polymer-Based Infrared Photodetectors, Acc. Chem. Res. 51(12) (2018) 3144−3153.

3. **Shi L., Sordillo L.A., Rodпguez-Contreras A., Alfano R.,** Transmission in near-infrared optical windows for deep brain imaging, J. Biophotonics. 9 (1-2) (2016) 38−43.

4. **El-Amir A.A.M., Ohsawa T., Nabatame T., Ohi A., Wada Y., Nakamura M., Fu X., Shimamura K., Ohashi N.,** Ecofriendly Mg_2Si-based photodiode for short-wavelength IR sensing, Mater. Sci. Semicond. Process. 91 (2019) 222−229.

5. **Udono H., Tajima H., Uchikoshi M., Itakura M.,** Crystal growth and characterization of Mg_2Si for IR-detectors and thermoelectric applications, Jpn. J. Appl. Phys. 54 (2015) 07JB06.

6. **Zaitsev V.K., Fedorov M.I., Gurieva E.A., Eremin I.S., Konstantinov P.P., Samunin A.Yu., Vedernikov M.V.,** Highly effective $Mg_2Si_{1-x}Sn_x$ thermoelectrics, Phys. Rev. B 74 (2006) 045207.

7. **Lin L., Guo Y., Robertson J.,** Metal silicide Schottky barriers on Si and Ge show weaker Fermi level pinning, Appl Phys Lett. 101(5) (2012) 052110.

8. **Cho J., Sivaramakrishnan Radhakrishnan H., Recaman Payo M., Debucquoy M., Van Der Heide A., Gordon I., Szlufcik J., Poortmans J.,** Low Work Function Ytterbium Silicide Contact for Doping-Free Silicon Solar Cells, ACS Appl Energy Mater. 3 (4) (2020) 3826−3834.

9. **Chernev I.M., Subbotin E.Yu., Kozlov A.G., Gerasimenko A.V., Ustinov A.Yu., Galkin N.G., Poliakov M.V., Volkova L.S., Dudin A.A., and Gouralnik A.S.,** Thick p-type Mg_2Si film on Si: Growth, structure and transport properties, J. Alloys Compd. 964 (2023) 171301.

10. **Gouralnik A.S., Shevlyagin A.V., Chernev I.M., Ustinov A.Yu., Gerasimenko A.V., Gutakovskii A.K.,** Synthesis of crystalline Mg_2Si films by ultrafast deposition of Mg on Si(111) and Si(001) at high temperatures. Mg/Si intermixing and reaction mechanisms, Mater. Chem. Phys. 258 (2021) 123903−123910.

11. **Gouralnik A.S., Maslov A.M., Ustinov A.Yu., Dotsenko S.A., Shevlyagin A.V., Chernev I.M., Il'yashenko V.M., Kitan S.A., Koblova E.A., Galkin K.N., Galkin N.G., Gerasimenko A.V.,** Formation of Mg_2Si at high temperatures by fast deposition of Mg on Si(111) with wedge-shaped temperature distribution, Appl. Surf. Sci. 439 (2018) 282−284.

12. Powder Diffraction File Card No. 30−0080 ($CaSb_2$) and Mg_2Si (65−2988) (CD ROM), International Center for Diffraction Data (ICDD), Newtown Square, PA.

13. **Onari S., Cardona M.,** Resonant Raman scattering in the II-IV semiconductors Mg_2Si, Mg_2Ge, and Mg_2Sn, Phys. Rev. B 14 (1976) 3520−3531.

14. **Buchenauer C.J., Cardona M.,** Raman Scattering in Mg_2Si, Mg_2Ge, and Mg_2Sn, Phys. Rev. B. 3 (1971) 2504−2507.

THE AUTHORS

CHERNEV Igor M.
igor_chernev7@mail.ru
ORCID: 0000-0002-8726-9832

KOZLOV Aleksei G.
kozlov.ag@dvfu.ru
ORCID: 0000-0001-8774-0631

SUBBOTIN Evgeniy Y.
jons712@mail.ru
ORCID: 0000-0001-9531-3867

SINOTOVA Sofia A.
sinotova.sa@dvfu.ru
ORCID: 0009-0002-7285-3224

PRIKHODCHENKO Alena V.
prikhodchenko.av@dvfu.ru
ORCID: 0009-0006-2778-8143

GOROSHKO Dmitrii L.
goroshko@iacp.dvo.ru
ORCID: 0000-0002-1250-3372

LEMBIKOV Aleksei O.
lembikov.ao@dvfu.ru
ORCID: 0000-0003-0436-0612

GALKIN Nikolay G.
ngalk@dvo.ru
ORCID: 0000-0003-4127-2988

PROKOPEVA Glikeriya A.
glikeriya61@gmail.com
ORCID: 0009-0008-0181-8994

Copper deposition onto porous silicon by vacuum thermal evaporation

K.B. Kim [1] ✉, S.S Chernenko [1], S.I. Niftaliev [1], V.E. Frolova [2], M.V. Grechkina [2],

G.S. Grigoryan [2], D.O. Belokopytov [2], A.I. Chukavin [3], A.S. Lenshin [1, 2]

[1] Voronezh State University of Engineering Technology, Voronezh, Russia;
[2] Voronezh State University, Voronezh, Russia;
[3] Udmurt Federal Research Center of the Ural Branch of the RAS, Izhevsk, Russia
✉ kmkseniya@yandex.ru

Abstract. The morphology and composition of porous silicon samples with thermally evaporated copper coatings were studied using atomic-force microscopy (AFM), infrared spectroscopy (IR), and X-ray photoelectron spectroscopy (XPS). Our research demonstrated that nanocomposites obtained with this method involve both metallic copper and copper oxide. The results indicate that vacuum thermal deposition of copper promotes efficient penetration of this element into the porous silicon structure and retards the oxidation process of the porous layer during long-term storage in the atmosphere.

Keywords: porous silicon, composites, thin films, copper, vacuum-thermal sputtering

Осаждение меди на пористом кремнии методом вакуумно-термического напыления

К.Б. Ким [1] ✉, С.С. Черненко [1], С.И. Нифталиев [1], В. Е. Фролова [2], М.В. Гречкина [2],

Г.С. Григорян [2], Д.О. Белокопытов [2], А.И. Чукавин [3], А.С. Леньшин [1, 2]

[1] Воронежский государственный университет инженерных технологий, г. Воронеж, Россия;
[2] Воронежский государственный университет, г. Воронеж, Россия;
[3] Удмуртский федеральный исследовательский центр Уральского Отделения РАН, г. Ижевск, Россия
✉ kmkseniya@yandex.ru

Аннотация. Методами атомно-силовой микроскопии, инфракрасной и рентгеновской фотоэлектронной спектроскопии получены данные о морфологии и составе образцов пористого кремния с вакуумно-термическим напылением меди. Исследования показали, что нанокомпозиты, полученные с использованием данного метода, содержат как металлическую медь, так и оксид меди. Полученные результаты свидетельствуют о том, что вакуумно-термическое осаждение меди способствует эффективному проникновению этого элемента в пористую структуру кремния и замедляет процесс окисления пористого слоя при длительном хранении в атмосферных условиях.

Introduction

The development of technologies in nanoelectronics relies heavily on the use of advanced materials and novel synthesis methods. Among the promising materials for nanoelectronics are porous silicon structures and copper [1, 2]. Porous silicon demonstrates remarkable optical properties, a large specific surface area, and tunable porosity, making it highly attractive for applications in microelectronics, photonics, and sensing [3]. Copper, due to its high electrical conductivity and relatively low cost, is one of the most widely used materials in modern electronics [4].

Copper coatings on porous silicon can be fabricated by various methods, including chemical deposition from solution [2, 5], immersion plating [3], electrodeposition [5, 6], as well as physical and chemical vapour deposition [1, 4, 9]. Many of these approaches require complex technological equipment, strict process control, or the use of aggressive chemical media, which limits their scalability and cost-efficiency. In contrast, thermal deposition of copper offers several advantages: it is a simpler and more technologically feasible method that does not require plasma-based setups or complex chemical precursors [1, 3]. Previous studies have demonstrated that thermal deposition provides good adhesion of copper films to porous silicon substrates, allows precise control of film thickness, and can be integrated into existing microelectronic fabrication schemes [1, 7]. At the international level, research has shown the potential of copper—porous silicon systems in improving sensor sensitivity [4, 5], tailoring surface morphology [2, 8], and filling deep silicon pores uniformly with copper by electrodeposition [5, 6]. Porous silicon/copper nanocomposites have also been explored for enhanced photoluminescence and sensing applications [10]. Nevertheless, systematic studies of thermal deposition mechanisms and features remain limited, which makes this direction scientifically and technologically relevant [1, 3, 7].

The purpose of this work is to study the features of thermal copper deposition into porous silicon.

Materials and Methods

Porous silicon substrates (por-Si) were obtained from single-crystalline silicon (KEF 100; 0.2 Ohm·cm) [7]. Using thermal vacuum deposition technique, copper oxide film was sputtered on por-Si substrate. The process of deposition was employed with VUP-4 facility (P = $0.5 \cdot 10^{-4}$ — 10^{-3} Torr, $\upsilon = 0.9^{-1}$ μm/min), etching time was 10 minutes. Morphology of the samples was studied by atomic-force microscopy (AFM) with Solver P47 PRO microscope. The studies of the chemical bonds and their potential deformations on the surface of porous silicon samples were made with the use of infrared spectroscopy technique (Vertex 70 Bruker). Spectra of X-ray photoelectron spectroscopy (XPS) of the original porous silicon and nanocomposite with the deposited copper were obtained with the use of laboratory spectrometer (SPECS FTI UrO RAS) according to the technique described in [9, 10].

Results and Discussion

AFM images of porous silicon samples before and after copper films deposition are presented in Fig. 1, as well as histograms of distribution of non-uniformities over the surface of samples. AFM images of the original porous silicon demonstrate the presence of non-uniformities with

different sizes (from 50 to 300 nm) on its surface, while the mean roughness of the surface is of ~70 nm. After copper film deposition mean roughness of the surface is reduced up to 6 nm, whereas histogram of distribution shows the presence of non-uniformities on the surface with the size of about 50 nm. Thus, the obtained results demonstrated that copper deposition on the surface of porous silicon in the process of its vacuum-thermal evaporation results in the formation of rather uniform continuous film that considerably smoothened relief of porous silicon.

a)

b)

c)

d)
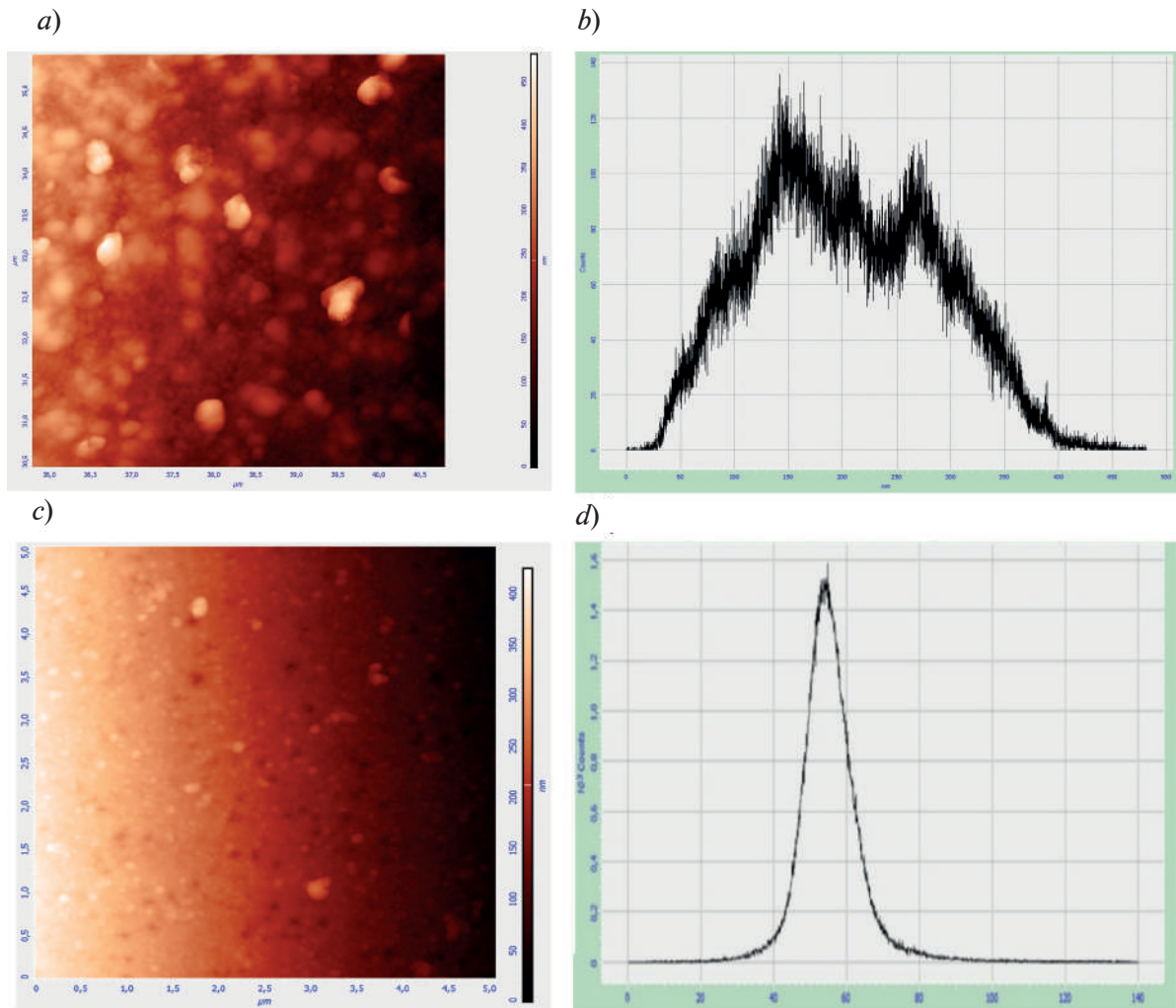
Fig. 1. AFM images of porous silicon samples: (*a*) surface of porous silicon, (*b*) histogram of particle size distribution on porous silicon, (*c*) surface of porous silicon with deposited copper, (*d*) histogram of copper particle sizes on porous silicon

IR transmittance spectra of the porous silicon samples as well as those with the deposited copper obtained by IR-spectroscopy with the use of ATR (Attenuated Total Reflection) attachment are presented in Fig. 2.

Characteristic features of the material are present in IR transmission spectrum (Fig. 2) of porous silicon which correspond to the valence Si-O-Si (1061 cm^{-1}) and non-valence Si-O-Si bonds (432 cm^{-1}), different bonds of Si-H$_x$ type (624, 708 cm^{-1}). The sample also demonstrates adsorbed CO_2 (2355 cm^{-1}), which is present during spectrum survey in the air. One can also see the traces of hydrofluoric acid affect in the form of SiF$_3$ contamination (941 cm^{-1}) and the bonds of O$_x$-SiH$_y$ type (863 cm^{-1}). Within the range of $2400-4000$ cm^{-1} no any distinctions are observed except of the adsorbed water in the band range of 3400 cm^{-1}. From this figure it can be seen that while comparing IR spectra of porous silicon sample with that one where copper was deposited that majority of abrupt absorption jumps in the spectra were leveled. This can be
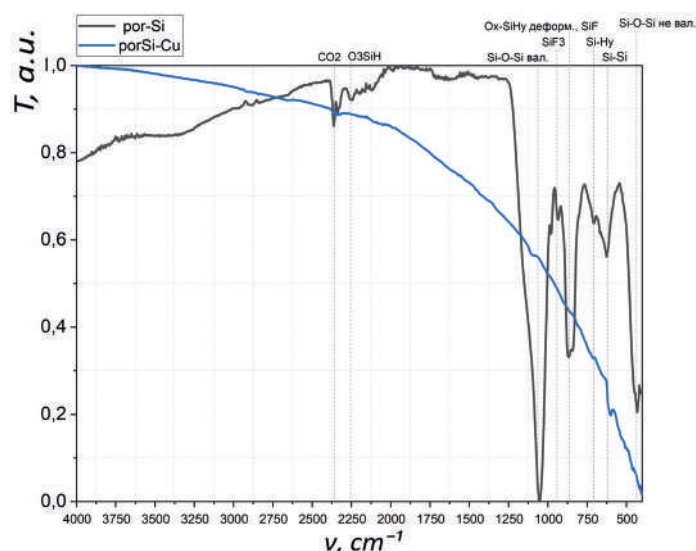
Fig 2. IR-absorption spectrum of por-Si and por-Si/Cu

Table

Absorption bands in IR-spectrum [3]

Wave number, cm^{-1}	Porous silicon
432	Si-O-Si non-valence
616	Si-Si
708	Si-Hy
863	Ox-SiHy deforms., SiF
941	SiF$_3$
1061	Si-O-Si valence.
2253	O$_3$SiH
2355	CO$_2$

explained by the fact that the absorption bands present in the porous silicon bound with oxide and other adsorbing bonds disappear because copper covering the substrate surface restrains its contact with the air and as a result, prevents oxide growth. Hardly observable peak in the range of Si-Si bond (616 cm^{-1}) remains as well. Disappearance of absorption bands can be explained by copper deposition which covers considerable number of silicon nanocrystals/clusters formed in porous silicon. These smallest particles reflect an incident radiation.

Analysis of the survey XPS (X-ray Photoelectron Spectroscopy) spectra allows determining the chemical composition of the material surface. Figure 3, a presents the XPS Si 2p spectrum of the initial porous silicon (por-Si). The obtained data are in good agreement with literature values [7, 9]. The surface layer of porous silicon typically consists of silicon dioxide (Si 2p, $E_b \approx 103.5$ eV), silicon sub-oxides (Si 2p, $E_b \approx 100.5-103$ eV), and non-oxidized silicon in crystalline or amorphous state (Si 2p, $E_b \approx 99.5$ eV). It is also known that with increasing storage time, the amount of oxide phases grows, especially in the near-surface region. For the composite sample por-Si/Cu, the XPS Si 2p spectrum (Fig. 3, b) shows a similar component distribution to that of the initial substrate, with silicon dioxide dominating and a small contribution of sub-oxide at ≈ 101.5 eV, whereas the signal of elemental silicon at ≈ 99.5 eV is absent. The XPS Cu 2p spectrum of the por-Si/Cu sample (Fig. 3, c) indicates that the surface is mainly composed of metallic copper (Cu 2p$_{3/2}$, $E_b \approx 933$ eV) with a minor contribution from copper oxide CuO (Cu 2p$_{3/2}$, $E_b \approx 935$ eV).
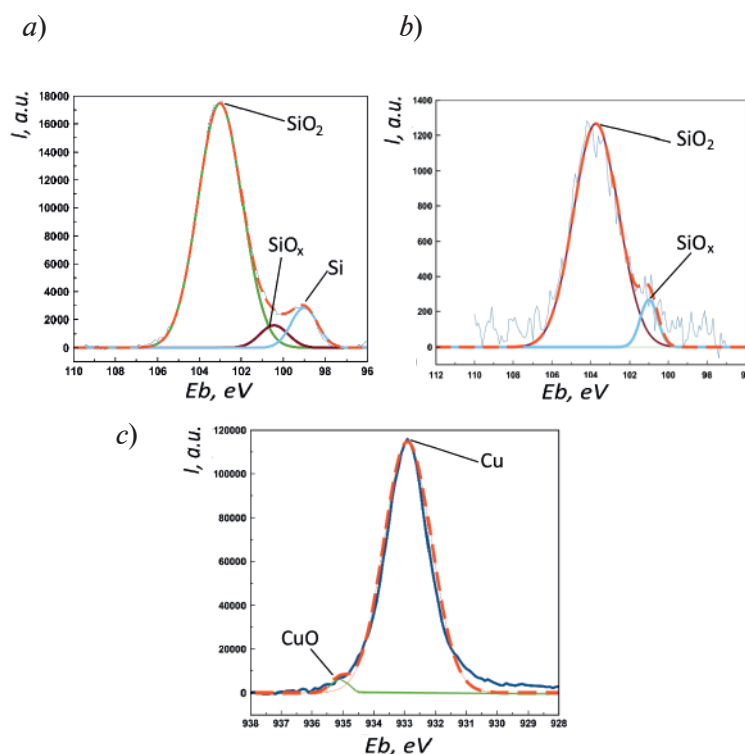
Fig. 3. XPS Si2p spectrum of the original porous silicon (*a*), Si2p spectrum of por-Si/Cu (*b*); Cu2p spectrum of por-Si/Cu (*c*) along with their decomposition into the components

Conclusion

Nanostructures composites of porous silicon with the deposited layer of copper oxide were obtained in the work using vacuum-thermal evaporation technique. The obtained results demonstrated that applying vacuum-thermal evaporation of copper forms steady continuous film repetitive porous silicon relief. Nanocomposites of porous silicon with the deposited copper obtained by vacuum-thermal deposition involve the phases of metallic copper and copper oxide. According to IR-spectroscopy data vacuum-thermal copper deposition retards the oxidation process of porous silicon during its long-term storage in the atmosphere.

REFERENCES

1. **Lenshin A.S., Kim K.B., Agapov B.L., Kashkarov V.M., Lukin A.N., Niftaliyev S.I.,** Structure and composition of a composite of porous silicon with deposited copper, St. Petersburg State Polytechnical University Journal. Physics and Mathematics. 25 (2023) 359–366.

2. **Zhao M.,** Gradient filling of copper in porous silicon using a non-contact electrochemical method, Applied Surface Science. 445 (2018) 115–123.

3. **Darwich W., Garron A., Bockowski P., Santini C., Gaillard F., Haumesser P.-H.,** Impact of surface chemistry on copper deposition in mesoporous silicon, Langmuir. 32 (2016) 7452–7458.

4. **Al-Jumaili B.E.B., Mohammed H.M., Hussein A.H., Al-Janabi A.H.,** Formation and photoluminescence properties of porous silicon/copper oxide nanocomposites fabricated via electrochemical deposition technique for photodetector application, Digest Journal of Nanomaterials and Biostructures. 16 (1) (2021) 297–310.

5. **Halim M.Y.A., Ismail A.F., Zainal Z., Rahman M.A., Othman M.H.D.,** Surface characteristics and catalytic activity of copper deposited on porous silicon, Journal of Nanoscience and Nanotechnology. 14 (1) (2014) 1–6.

6. **Jin L., Zhang J., Li Y., Zhang L., Liu J.,** Copper deposition in microporous silicon using electrochemical method, Journal of Electroanalytical Chemistry. 735 (2014) 1–6.

7. **Lenshin A.S., Seredin P.V., Kashkarov V.M., Minakov D.A.,** Origins of photoluminescence degradation in porous silicon under irradiation and the way of its elimination, Materials Science in Semiconductor Processing. 64 (2017) 71–76.

8. **Sham T.K., Lee P.L.,** Study of copper structures deposited on porous silicon, Journal of Materials Chemistry. 4 (10) (1994) 1579–1583.

9. **Lenshin A.S., Kashkarov V.M., Domashevskaya E.P., Beltyukov A.N., Gilmutdinov F.Z.,** Investigations of the composition of macro-, micro- and nanoporous silicon surface by ultrasoft X-ray spectroscopy and X-ray photoelectron spectroscopy, Applied Surface Science. 359 (2015) 550.

10. **Darwish M., Al-Hadeethi Y., Abdelhamid H.N.,** Copper nanoparticles deposition on porous silicon for enhanced photoluminescence and sensing applications, Journal of Alloys and Compounds. 845 (2020) 156260.

THE AUTHORS

KIM Kseniya B.
kmkseniya@yandex.ru

CHERNENKO Sergey S.
sergey.x173@mail.ru

NIFTALIEV Sabukhi I.
sabukhi@gmail.com

FROLOVA Vera E.
ternovaya@phyc.vsu.ru
ORCID: 0009-0000-2880-8958

GRECHKINA Margarita V.
grechkina_m@mail.ru
ORCID: 0000-0002-7873-8625

GRIGORYAN Gevorg S.
gri7287@yandex.ru
ORCID: 0000-0002-9850-8341

BELOKOPYTOV Dmitry O.
kmkseniya@yandex.ru

CHUKAVIN Andrey I.
andrey_chukawin@mail.ru

LENSHIN Alexander S.
lenshinas@mail.ru
ORCID: 0000-0002-1939-253X

Nonlinear absorption of laser radiation in the carbon nanotubes dispersions in ultraviolet and visible ranges

P.N. Vasilevsky [1] ✉, M.S. Savelyev [1], A.Yu. Gerasimenko [1]

[1] National Research University of Electronic Technology, Zelenograd, Russia

✉ pavelvasilevs@yandex.ru

Abstract. Carbon nanotubes have unique properties and applications in various fields such as nonlinear optics, flexible electronics, biocompatible composites for tissue repair, etc. The properties of carbon nanotubes can be tuned when exposed to laser radiation. The manifestation of nonlinear absorption properties can improve the methods of formation and processing of materials containing carbon nanotubes. In this work, the properties of nonlinear absorption in the ultraviolet (355 nm) and visible (532 nm) ranges depending on the type of carbon nanotubes and the type of solvent are investigated. The study was performed using the Z-scan method with pulsed exposure (pulse duration is 20 ns). It was shown that the homogeneity of the carbon nanotubes distribution in a liquid medium affects the nonlinear absorption of laser radiation. Single-walled carbon nanotubes in dimethylformamide showed the best nonlinear absorption coefficient and the lowest threshold fluence when the interaction of the medium with laser radiation becomes nonlinear. The demonstrated laser stability of nanotubes also makes them a promising material for laser radiation limiters and nonlinear optical switchers.

Keywords: laser radiation, nonlinear absorption, carbon nanotubes, UV range, visible range, nanosecond pulses, Z-scan

Нелинейное поглощение лазерного излучения в дисперсии углеродных нанотрубок в ультрафиолетовом и видимом диапазонах

П.Н. Василевский [1] ✉, М.С. Савельев [1], А.Ю. Герасименко [1]

[1] Национальный исследовательский университет «МИЭТ», г. Зеленоград, Россия

✉ pavelvasilevs@yandex.ru

Аннотация. Углеродные нанотрубки обладают уникальными свойствами и применением в различных областях. Проявление ими свойств нелинейного поглощения позволяет усовершенствовать методы формирования и обработки материалов, содержащих углеродные нанотрубки. В данной работе исследованы свойства нелинейного поглощения в ультрафиолетовом и видимом диапазонах в зависимости от типа углеродных нанотрубок и типа растворителя.

Introduction

Experimental study of nonlinear optical properties of nanodispersed media is an urgent task. It is known that optical parameters of condensed media such as absorption and scattering coefficients, as well as the refractive index are often not constant values. In addition to the linear component, they also have a nonlinear component, which depends on the intensity of the laser radiation incident on the medium [1].

Nonlinear optical properties of media affect the change in the parameters of laser radiation transmitted through the medium, such as the energy and power of laser radiation, the spatial shape of the laser beam, the direction of propagation of radiation, etc. In this regard, media with nonlinear optical properties are important for various applications such as optical limiting and switching, laser formation of three-dimensional materials, its processing, etc [2, 3]. The manifestation of nonlinear optical effects in various media depends on the parameters of laser radiation (continuous exposure or exposure to single pulses, duration of laser pulses, their energy, etc.), as well as the nonlinear optical properties of the medium [4]. One of the most promising objects are carbon nanotubes (CNTs), which have a uniform monotonic spectrum of linear optical transmission in the wavelength range from ultraviolet to near infrared radiation [5].

Laser radiation is a convenient tool for creating or precision modifying the surface of composites and nanosystems based on carbon nanotubes [6]. In turn, the increased absorption of laser radiation due to nonlinear processes such as reverse saturable absorption or multiphoton processes opens up new possibilities for laser 3D formation and patterning of CNT-based systems. In this paper, the nonlinear optical properties of dispersed media with single-walled and multi-walled carbon nanotubes were investigated under the influence of pulsed nanosecond laser radiation in the UV and visible ranges.

Materials and Methods

To study the nonlinear optical characteristics, liquid dispersions with CNTs were prepared. Two types of CNTs were used to create dispersions: single-walled CNTs (SWCNTs) and multi-walled CNTs (MWCNTs). Water and dimethylformamide (DMF) were used as solvents. The mass fraction of the complexes in the dispersion did not exceed 0.004 wt.%. This concentration was chosen so that the linear transmittance was greater than 60%. Ultrasonic treatment with a homogenizer was used to form homogeneous dispersed media. The power of ultrasonic treatment was 300 W and the duration of treatment was 1 h.

The final dispersions were studied by dynamic light scattering (DLS). DLS was performed to determine the hydrodynamic radius of carbon nanotubes, as well as to determine the number of large agglomerates after preparation. The hydrodynamic radius corresponds to the size of the nano-object, based on the assumption of its spherical shape. Since carbon nanoparticles have a shape far from spherical, the values of the hydrodynamic radius for nanotubes only indirectly show the particle size. In this paper, the values of the hydrodynamic radius for nanotubes are used to assess the presence of individual "small" nanoparticles and "large" agglomerates of nanotubes

in the dispersed medium. A large number of large agglomerates may indicate an increased contribution of scattering to the overall attenuation pattern, as well as reduced sedimentation stability of the dispersed medium. The obtained values of the hydrodynamic radii of the particles are presented in Table 1. The graph of the scattering intensity dependence on the hydrodynamic radius of nanoparticles for the carbon nanotubes dispersion has a bimodal distribution. The values of the hydrodynamic radius for peak number 1 correspond to individual separate nanoparticles. The values of the hydrodynamic radius for peak number 2 correspond to large agglomerates of carbon nanotubes. In general, it can be noted that SWCNTs show better sedimentation stability compared to MWCNTs. Nanodispersed media, the solvent of which was DMF, showed the smallest contribution of large agglomerates (less than 10%), which indicates the best stability of such dispersions.

T a b l e 1

DLS results for prepared dispersions

Sample	Peak number	Hydrodynamic radius, nm	Contribution to the total scattering, %
SWCNT/water	1	250 ± 39	69
	2	13000 ± 4300	31
SWCNT/DMF	1	251 ± 43	91
	2	13000 ± 5400	9
MWCNT/water	1	312 ± 69	62
	2	21000 ± 5500	38
MWCNT/DMF	1	311 ± 66	78
	2	19000 ± 4200	22

Optical scheme of experimental setup is shown at Fig. 1. The nonlinear optical properties were evaluated by exposure to pulsed laser radiation with a pulse duration of 20 ns (laser LS-2147N-5, Lotis TII, Belarus). During the experiments using the Z-scanning method, the energy of the laser pulse acting on the nanodispersed medium was ≈ 350 µJ. The experiments were performed at wavelengths of 355 and 532 nm. Lenses with a focal length of 10 cm were used to focus the radiation, the radius of the beam at the lens focus was 35 µm. Optical transmission spectra were obtained using a Genesys 10 UV-Vis spectrophotometer (Thermo Fisher Scientific, US).
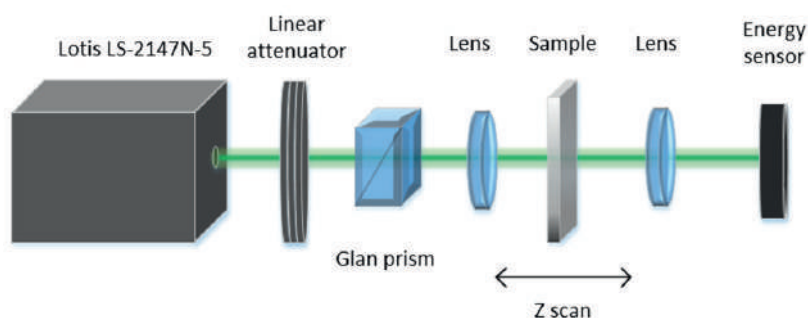
Fig. 1. Optical scheme of experimental setup

Results and Discussion

Experimental dependences of normalized transmittance on the position of the sample relative to the lens focus were obtained as a result of Z-scan experiments. Fig. 2 shows the experimental results for SWCNTs at a wavelength of 532 nm. For each sample studied, a decrease in normalized transmittance (T_{norm}) was obtained when approaching the lens focus. It is worth noting that the decrease in transmittance has a pronounced threshold character. The graphs clearly distinguish the areas of linear (when the normalized transmittance does not change) and nonlinear interaction.

a) *b)*
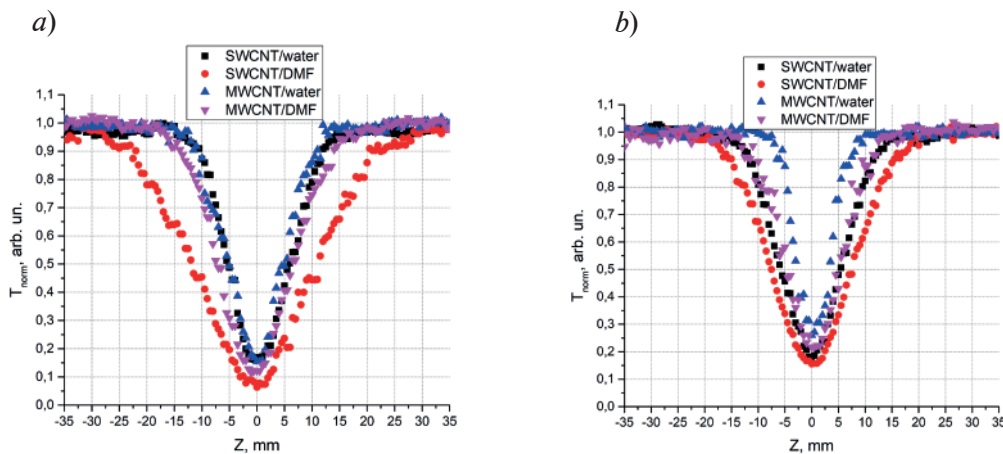
Fig. 2. Dependences of normalized transmittance on Z-axis coordinate for samples at a wavelength of: 532 nm (*a*), 355 nm (*b*)

This phenomenon can be described as follows: the leading edge of the nanosecond pulse acts as an exciter of the medium, itself interacting with the medium linearly. When the medium goes into an excited state, the trailing edge begins to be absorbed much more strongly, which leads to a decrease in the transmittance of the medium.

Based on the experimental dependences obtained, such optical parameters of the studied media as linear absorption, nonlinear absorption, and threshold fluence were calculated. To determine these parameters, the threshold model based on the radiative transfer equation was used [7]. The results are presented in Table 2.

CNTs in DMF showed a larger nonlinear absorption coefficient compared to aqueous dispersions. This is explained by the lower value of surface tension for DMFA. In this way a homogeneous distribution of nanoparticles in the material is achieved, while large agglomerates in aqueous dispersion are slower to enter the excited state.

Table 2

Calculated values of optical coefficients for liquid dispersed media with CNTs

Sample	Wavelength, nm	Linear absorption coefficient, 1/cm	Nonlinear absorption coefficient, cm/GW	Threshold fluence, J/cm^2
SWCNT/water	532	1.54 ± 0.03	70 ± 5	0.2 ± 0.02
	355	1.68 ± 0.03	76 ± 5	0.18 ± 0.02
SWCNT/DMF	532	1.57 ± 0.03	133 ± 7	0.16 ± 0.02
	355	1.68 ± 0.03	108 ± 6	0.15 ± 0.02
MWCNT/water	532	1.57 ± 0.03	68 ± 5	0.21 ± 0.02
	355	1.74 ± 0.03	35 ± 3	0.22 ± 0.03
MWCNT/DMF	532	1.50 ± 0.03	95 ± 5	0.19 ± 0.02
	355	1.72 ± 0.03	40 ± 3	0.1 ± 0.02

The studied media demonstrated high laser stability during the experiments. Optical transmission spectra were obtained before and after the Z-scan experiments (Fig. 3). The graphs show no changes in linear transmission (T_0) after laser exposure, which is especially important for optical applications such as nonlinear optical limiters and switches. This also indirectly indicates the prevalence of nonlinear absorption of light over scattering. Nonlinear scattering of light occurs at scattering centers such as laser-induced solvent bubbles [8] or other inhomogeneities that arise under the action of laser radiation, which lead to a change in the linear absorption of the material [9]. In addition, inhomogeneities can lead to a change in the concentration of CNT in the area of influence, which also negatively affects the nonlinear optical properties of dispersion.

a)

b)
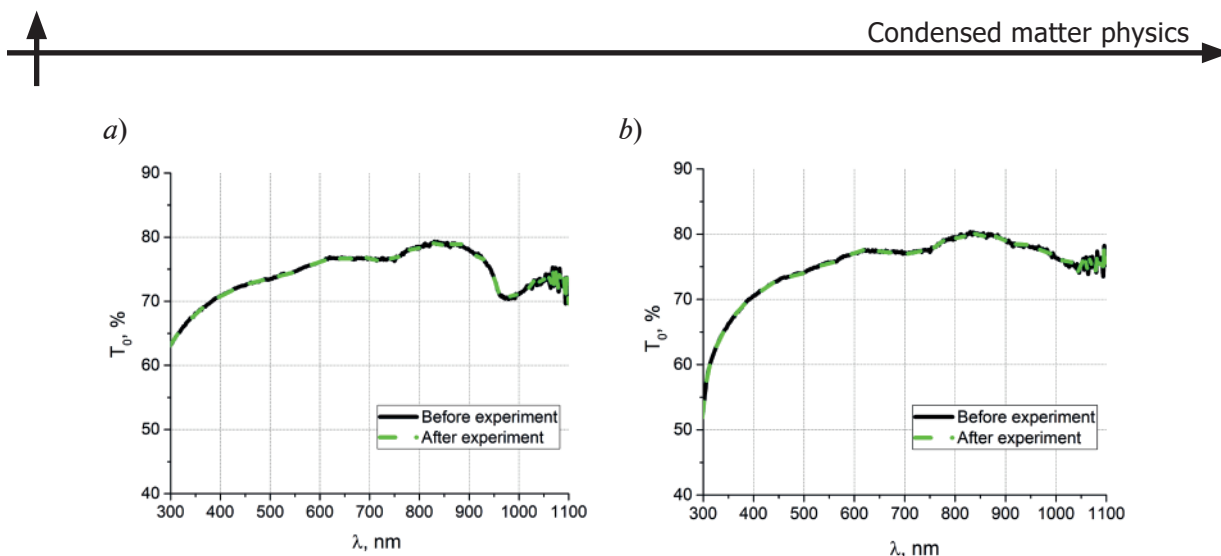
Fig. 3. Optical transmission spectra of dispersed media before and after the experiment: SWCNT/water (*a*), SWCNT/DMF (*b*)

Conclusion

It is shown that SWCNTs in the liquid dispersion medium have better nonlinear absorption properties in comparison with MWCNTs. The choice of solvent is also an important factor that influences the aggregability of nanoparticles in the dispersion. Thus, SWCNTs in solvents with lower surface tension have a greater potential for nonlinear absorption applications. Exposure of the prepared samples to laser radiation does not cause changes in the linear transmission of dispersions.

REFERENCES

1. **Ganeev R.A., Usmanov T.,** Nonlinear-optical parameters of various media, Quantum Electronics. 37 (7) (2007) 605.

2. **Vivien L., Lancon P., Riehl D., Hache F., Anglaret E.,** Carbon nanotubes for optical limiting, Carbon. 10 (40) 2002 1789−1797.

3. **Nair V.S., Pusala A., Hatamimoslehabadi M., Yelleswarapu C.,** Impact of carbon nanotube geometrical volume on nonlinear absorption and scattering properties, Optical Materials. 73 (2017) 306−311.

4. **Sorokina I.T.,** Cr_2^+-doped II−VI materials for lasers and nonlinear optics, Optical Materials. 26 (4) (2004) 395−412.

5. **Kuang Y., Liu J., Sun X.,** Ultrashort single-walled carbon nanotubes: density gradient separation, optical property, and mathematical modeling study, The Journal of Physical Chemistry C. 116 (46) (2012) 24770−24776.

6. **Zhao Y., Han Q., Cheng Z., Jiang L., Qu L.,** Integrated graphene systems by laser irradiation for advanced devices, Nano Today. 12 (2017) 14−30.

7. **Tereshchenko S.A., Savelyev M.S., Podgaetsky V.M., Gerasimenko A.Y., Selishchev S.V.,** Nonlinear threshold effect in the Z-scan method of characterizing limiters for high-intensity laser light, Journal of applied physics. 9 (120) (2016) 093109.

8. **Mansour K., Soileau M.J., Van Stryland E.W.,** Nonlinear optical properties of carbon-black suspensions (ink), Journal of the Optical Society of America B. 9 (7) (1992) 1100−1109.

9. **Côa F., de Souza Delite F., Strauss M., Martinez D.S.T.,** Toxicity mitigation and biodistribution of albumin corona coated graphene oxide and carbon nanotubes in Caenorhabditis elegans, NanoImpact. 27 (2022) 100413.

THE AUTHORS

VASILEVSKY Pavel N.
pavelvasilevs@yandex.ru
ORCID: 0000-0002-5733-8497

GERASIMENKO Alexander Yu.
gerasimenko@bms.zone
ORCID: 0000-0001-6514-2411

SAVELYEV Mikhail S.
nanonlin@yandex.ru
ORCID: 0000-0003-1255-0686

Annealed proton-exchange waveguides in mixed lithium niobate-tantalate solid solutions

A.V. Sosunov [1] ✉, I.V. Petukhov [1], A.R. Kornilicyn [1], A.A. Mololkin [2],

V.E. Umylin [2], R.R. Fakhrtdinov [3], A.G. Kulikov [4]

[1] Perm State University, Perm, Russia;
[2] National University of Science and Technology "MISIS", Moscow, Russia;
[3] Institute of Microelectronics Technology and High-Purity Materials RAS,
Moscow, Russia;
[4] National Research Centre "Kurchatov Institute", Shubnikov Institute of Crystallography of Federal Scientific Research Centre "Crystallography and Photonics" of RAS, Moscow, Russia
✉ alexeisosunov@gmail.com

Abstract. Annealed proton-exchange (APE) waveguides in lithium niobate are widely used in integrated photonics for navigation, telecommunications and electric field sensors. In this paper, we analyze the characteristics of planar APE waveguides in new mixed single crystals of lithium niobate-tantalate solid solution by various methods (prism coupling, XRD and IR spectroscopy). The elemental composition (ratio Nb/Ta) of Z-cut mixed lithium niobate-tantalate samples gives a good uniform distribution over the all-surface area by X-ray fluorescence method. APE waveguides in mixed lithium niobate-tantalate single crystals are characterized by a lower value of refractive index increment due to Ta atoms and higher proton diffusion coefficients due to lattice disordering. High diffusion coefficients provide a deeper APE waveguide layer and rapid recovery of the crystal lattice during post-exchange annealing. These results expand the understanding of the proton exchange process in mixed lithium niobate-tantalate solid solutions for the creation of single-mode APE waveguides.

Keywords: optical materials, lithium niobate-tantalate, APE waveguides

Отожженные протонообменные волноводы в смешанных кристаллах твердого раствора ниобата-танталата лития

А.В. Сосунов [1] ✉, И.В. Петухов [1], А.Р. Корнилицын [1], А.А. Мололкин [2],

В.Е. Умылин [2], Р.Р. Фахртдинов [3], А.Г. Куликов [4]

[1] Пермский государственный национальный исследовательский университет, г. Пермь, Россия;

[2] Национальный Исследовательский Технологический Университет МИСиС, Москва, Россия;

[3] Институт проблем технологии микроэлектроники и особочистых материалов РАН, Москва, Россия;

[4] Национальный исследовательский центр «Курчатовский институт», Институт кристаллографии им. А.В. Шубникова ФНИЦ «Кристаллография и фотоника» РАН, Москва, Россия

✉ alexeisosunov@gmail.com

Аннотация. Отожженные протонообменные волноводы в ниобате лития широко используются в интегральной фотонике для навигации, телекоммуникаций и датчиков электрического поля. В данной работе мы анализируем характеристики планарных волноводов в новых смешанных монокристаллах твердого раствора ниобата-танталата лития с помощью различных методов (призменный элемент связи, рентгеновская дифракция, ИК-спектроскопия, рентгенофлуоресцентный анализ). Элементный состав (соотношение Nb/Ta) исследуемых образцов Z-среза демонстрирует однородное распределение по всей площади поверхности. Оптические волноводы характеризуются более низким значением приращения показателя преломления из-за присутствия атомов Ta (7%) и более высокими коэффициентами диффузии протонов из-за разупорядочения кристаллической решетки по сравнению с ниобатом лития. Высокие коэффициенты диффузии обеспечивают более глубокий волноводный слой и быстрое восстановление кристаллической решетки при постобменном отжиге. Полученные результаты расширяют понимание процесса протонного обмена в смешанных твердых растворах ниобата-танталата лития для создания одномодовых оптических волноводов.

Ключевые слова: оптические материалы, ниобат-танталат лития, волновод, протонный обмен

Introduction

Integrated photonics and nonlinear optics are rapidly growing scientific and practical areas. Integrated optical circuits allow the production of navigation systems [1], telecommunication systems [2] and sensors [3]. The key position of lithium niobate (LN) and lithium tantalate (LT) for optoelectronics is due to their high electrooptical coefficients, excellent piezoelectric and acousto-optic features, strong birefringence and nonlinearity, suitability for industrial manufacturing, etc.

The mixed $LiNb_xTa_{1-x}O_3$ (LNT) crystal attracts the attention since its physical, optical and electrooptical properties can be tuned by varying the crystal composition (changing x from 0 (LT) to 1 (LN)). LNT to combine the best properties of LN (e.g. high electrooptical coefficients and high Tc and thermal stability) and LT (e.g. high photorefractive damage resistance). The possibility of controlling the crystal composition makes it possible to control birefringence and, in the future, to obtain crystals without birefringence at all.

Recently, the production of single-domain LNT crystals with isomorphic substitution of Nb by Ta in the cationic sublattice, with a Curie temperature of 1105 °C, close to the Tc of lithium niobate (1140 °C), was demonstrated [4]. It is shown that the change in the unit cell parameters depends linearly on the composition of the crystals. The LNT solid crystal solutions seem to be promising functional materials for integrated optics.

One of the main passive elements in photonics is an optical waveguide. Diffuse waveguides are obtained either by annealed proton exchange (APE) or by Ti diffusion [5]. APE waveguides are characterized by a complex phase composition, but they are easy to manufacture. Description of structural-phase transformations during proton exchange and annealing in LNT crystals is given in [6, 7].

The aim of this work is to produce a planar APE waveguide in Z-cut LNT single-crystal and study its characteristics in comparison to these of a waveguide in LN produced at the same technological parameters.

Materials and Methods

The crystals of LNT solid solution with composition $LiNb_{0.93}Ta_{0.07}O_3$ were grown by the Czochralski method in NIKA-3M apparatus with induction heating and automatic control of crystal diameter at the Institute of Microelectronics Technology and High Purity Materials, Russian Academy of Sciences. The crystal was drawn along the polar Z axis. The experimental samples had size $10 \times 12 \times 1$ mm and double-side polished. The single-domain state analysis, the phase diagram and the description of the growth effects were also previously reported in [4, 8–9].

X-ray fluorescence (XRF) method was used to analyze the Nb/Ta atomic ratio on the LNT surface (Fig. 1). XRF was performed by ORBIS micro-XRF setup (USA) with a rhodium (Rh) X-ray tube, a probe beam of 30 μm, an accelerating voltage of 40 kV, and a cathode filament current of 400 μA. Two-dimensional maps were obtained. The mapping grid resolution was 256×200 points. The spectral accumulation time at each point was 700 ms in the Live time mode. The "dead time" in the experiment did not exceed 24%. The intensity of the regions of the spectrum corresponding to the NbK (16.6 keV) and TaL (8.1 keV) series lines was analyzed. The percentage ratio of the specified chemical elements was determined by the ratio of the total intensities of all lines included in the specified series.

XRF analysis over the entire LNT sample area shows a fairly uniform distribution of Ta atoms (X and Y axes). We did not observe loci of frontal segregation. This is very important for the stable PE process.
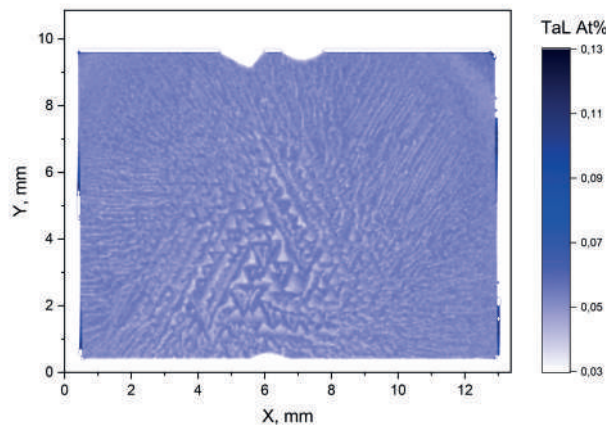
Fig. 1. XRF image of LNT sample

APE waveguides were created in a closed zirconium reactor containing a benzoic acid melt at a temperature of 190 °C for 2 hours and annealed in air at a temperature of 350 °C for 5 hours. APE planar waveguides were obtained in LN and LNT under identical conditions.

The structure of the APE waveguides was studied by X-ray diffraction (XRD) and IR absorption spectroscopy. XRD was carried out using a double-crystal spectrometer. A single crystal of dislocation-free Si was used as a monochromator, set to the reflecting position of the K_β-line of Co-emission ($\lambda = 1.62075$ Å) from the crystallographic plane (111). XRD spectra were obtained from the crystallographic plane (006) for Z-cut samples. The deformations ε_{33} (deformations in the direction normal to the surface of the sample) of the crystal lattice of LNT samples were determined by the shift of lines in the spectrum. Deformations $\varepsilon_{33} = \Delta d/d$ were calculated from the Wulff-Bragg equation:

$$d = \frac{\lambda}{2\sin\theta}, \qquad (1)$$

where λ is the wavelength, d is the interplanar distance, θ is the Bragg reflection angle, $n = 1$ is the order of reflection.

IR spectroscopy was carried out using a Spectrum Two Fourier transform spectrometer (PerkinElmer) in the range valence vibrations of 2800–4000 cm^{-1} with a resolution of 1.0 cm^{-1}. The decomposition of the IR and XRD spectra was done using the Fityk program.

Integrated-optical parameters of APE waveguides were determined by prism coupling method at a wavelength $\lambda_{He-Ne} = 632$ nm. Numerical method for reconstruction of the refractive index profile of diffused APE waveguides was used [10].

Results and Discussion

APE waveguide profile. APE waveguides have a gradient profile (Fig. 2). However, we observe a decrease in the refractive index increment (waveguide contrast) for LNT crystal. The decrease in the refractive index increment Δn_e can be explained by the increase in diffusion coefficients $D_z(T)$, which are caused by a more disordered crystal lattice, which allows protons to penetrate deeper into the LNT crystal faster. The diffusion coefficients were calculated from the root equation, where the waveguide depth X is proportional to the square root of time [11]. This equation allows a comparative assessment of the diffusion coefficient (Table):

$$X = 2\sqrt{D_z \cdot t}, \qquad (2)$$

where t − annealing time. According to equation (2), the proton penetration depth and diffusion coefficient increase for LNT, respectively. The results of the optical properties of the APE waveguides in LNT crystals are well explained by the results of structural studies, which are given in the next section B.
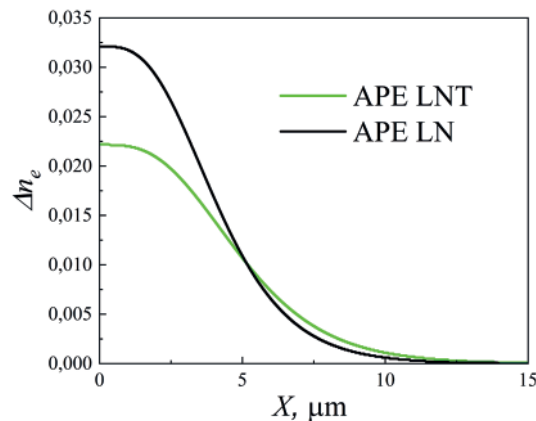
Fig. 2. APE waveguide profile

Table

Optical and diffusion parameters of APE waveguides

Sample	T, °C	t, h	Δn_e	X, µm	$D_z(T)$, µm²/h
APE LN	350	5	0.032	4.8	0.61
APE LNT	350	5	0.022	5.7	0.88

Structure. The phase analysis of the experimental samples is shown in Fig. 3. The IR spectra indicate the formation of the α-phase for APE LNT crystals (Fig. 3, *a*, inset, 3489 cm^{-1} [6]). This is consistent with the contrast of the refractive index, since for the α-phase it is less than ≤ 0.025. At the same time, for APE LN, the phase analysis shows the presence of the κ_1-phase (Fig. 3, *a*, 3494 cm^{-1}).

This means that the annealing time was insufficient for the formation of the α-phase. Also, the integral intensity of the OH-group band in the IR spectrum of APE LNT is lower than for APE LN, which corresponds to a lower proton concentration and faster relaxation of the crystal lattice during post-annealing. This is also confirmed by the XRD results (Fig. 3, *b*). Relative deformations of the crystal lattice show the formation of the κ_1-phase for APE LNT and the α-phase for APE LN. The APE waveguides in LN are characterized by a refractive index increment of ≤ 0.025 and have the so-called stable α-phase [12]. The proton exchange and annealing time allowed us to form such waveguides in mixed LNT solid solutions. However, for LN crystals, an intermediate κ_1-phase is formed, which requires additional annealing time. This means that higher proton diffusion coefficients lead to rapid relaxation of the structure during annealing, which is shown in Section A. Our results show the fundamental possibility of obtaining planar waveguides in new mixed LNT solid solutions.
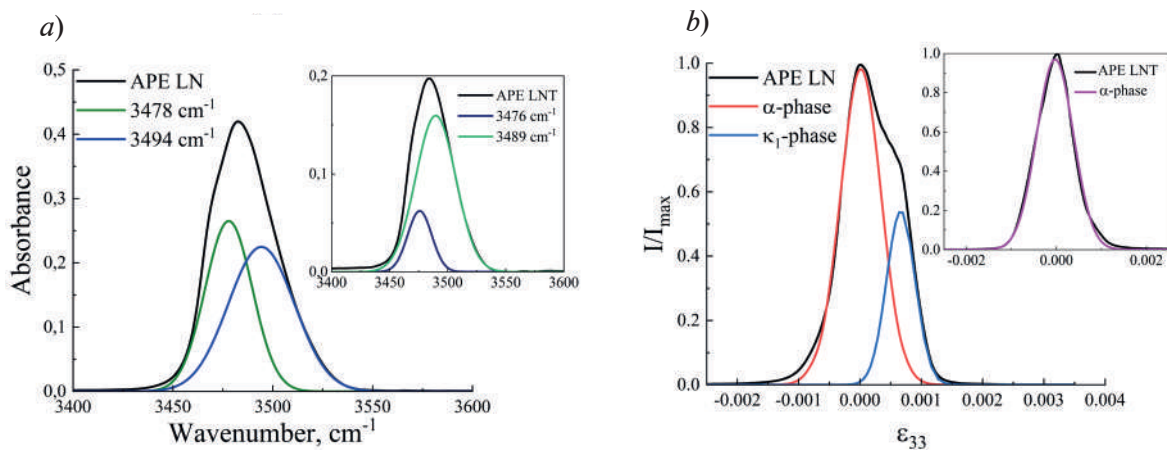
Fig. 3. Structure of APE waveguides: IR spectra of valence vibrations OH groups for APE LN and APE LNT (insert right) (*a*), relative deformations for APE LN and APE LNT (insert right) (*b*)

Conclusion

We have obtained and characterized planar proton-exchange waveguides in mixed crystals of LNT solid solution for the first time. They have higher diffusion coefficients, which lead to rapid relaxation of deformations of the LNT crystal lattice. Our results open up the possibility of using new mixed LNT crystals for the problems of integrated and nonlinear photonics.

Further, it is planned to study the characteristics of channel waveguides and establish the relationship between structure and optical losses.

Acknowledgments

REFERENCES

1. **Karagöz E., Aşık F.Y., Gökkavas M., Akbaş E.E., Yertutanol A., Özbay E., Özcan Ş.,** Reduction in Temperature-Dependent Fiber-Optic Gyroscope Bias Drift by Using Multifunctional Integrated Optical Chip Fabricated on Pre-Annealed $LiNbO_3$, Photonics. 11 (2024) 1057.

2. **Sinatkas G., Christopoulos T., Tsilipakos O., Kriezis E.E.,** Electro-optic modulation in integrated photonics, J. Appl. Phys. 130 (2021) 010901.

3. **Zeng R., Wang B., Yu Z., Niu B., Hua Y.,** Integrated optical E-field sensor based on balanced Mach-Zehnder interferometer, Optical Engineering. 50 (2011) 114404.

4. **Roshchupkin D.V., Emelin E., Plotitcina E. et al.,** Single crystals of ferroelectric lithium niobate-tantalate $LiNb_{1-x}Ta_xO_3$ solid solutions for high-temperature sensor and actuator applications, Acta Crystallographica, Section B: Structural Science. 76 (2020) 1071−1076.

5. **Bazzan M., Sada C.,** Optical waveguides in lithium niobate: Recent developments and applications, Appl. Phys. Rev. 2 (2015) 040603.

6. **Sosunov A.V., Petukhov I.V., Myasnikova E.V., Kornilicyn A.R., Mololkin A.A., Fakhrtdinov R.R., Kulikov A.G., Kuneva M.,** Structural-phase transformations during annealing of proton exchange layers in mixed lithium niobate-tantalate solid solutions, Materials Today Communications. 43 (2025) 111840−6.

7. **Sosunov A.V., Petukhov I.V., Kornilicyn A.R., Mololkin A.A., Komarnitskaya E.A., Tabachkova N.Yu., Kuneva M.,** Structure and properties of proton exchange layers in lithium niobate-tantalate solid solutions, Solid State Ionics. 417 (2024) 116692−6.

8. **Bashir U., Klimm D., Rüsing M., Bickermann M., Ganschow S.,** Evaluation and thermodynamic optimization of phase diagram of lithium niobate tantalate solid solutions, Journal of Materials Science. 59 (2024) 12305−12316.

9. **Bernhardt F., Gharat S., Kapp A., Pfeiffer F., Buschbeck R., Hempel F., Pashkin O., Kehr S.C., Rüsing M., Sanna S. and Eng L.M.,** Lattice Dynamics of $LiNb_{1-x}Ta_x O_3$ Solid Solutions: Theory and Experiment, Phys. Status Solidi A. 222 (2025) 2300968.

10. **Onodera H., Awai I., Ikenoue J.,** Refractive-index measurement of bulk materials: prism coupling method, Appl. Opt. 22 (8) (1983) 1194−1197.

11. **Vohra S.T., Mickelson A.R., Asher S.E.,** Diffusion characteristics and waveguiding properties of proton exchanged and annealed $LiNbO_3$ channel waveguides, J. Appl. Phys. 66 (1989) 5161−5174.

12. **Korkishko Yu.N., Fedorov V.A.,** Relationship between refractive indices and hydrogen concentration in proton exchanged $LiNbO_3$ waveguides, J. Appl. Phys. 82 (1997) 1010−1017.

THE AUTHORS

SOSUNOV Aleksei V.
alexeisosunov@gmail.com
ORCID: 0000-0002-5760-1523

PETUKHOV Igor V.
Petukhov-309@yandex.ru
ORCID: 0000-0002-3110-668X

KORNILICYN Andrey R.
Akornilicyn@gmail.com
ORCID: 0000-0002-8267-0168

MOLOLKIN Anatoliy A.
mololkin@newpiezo.com
ORCID: 0000-0003-3053-1892

UMYLIN Vladislav E.
vu@koncept-lab.ru
ORCID: 0009-0006-1447-3310

FAKHRTDINOV Rashid R.
fakhrtd@gmail.com
ORCID: 0000-0003-1077-7975

KULIKOV Anton G.
ontonic@gmail.com
ORCID: 0000-0002-6040-6403

Thermal poling of photosensitive glasses containing Ag⁺ and Ce³⁺ ions

A.Yu. Moroz [1], I.E. Chistikov [2], V.G. Melehin [3], V.P. Kaasik [1, 4] ✉

[1] Peter the Great St. Petersburg Polytechnic University, St. Petersburg, Russia;

[2] Institute for Problems of Mechanical Engineering RAS, St. Petersburg, Russia;

[3] Ioffe Institute, St. Petersburg, Russia;

[4] Alferov University, St. Petersburg, Russia

✉ vkaasik@yandex.ru

Abstract. We present the results on the crystallization of photo-thermo-refractive glass under thermal poling and ultraviolet (UV) irradiation followed by heat treatment. Poling was carried out at a temperature of 300 °C and a voltage of 400−1000 V. A femtosecond laser with a wavelength of 343 nm was used as UV sources. The studies were carried out using optical microscopy, optical absorption and Raman scattering. It is shown that in the subanode layer of the glass after poling, subsequent UV irradiation and heat treatment, crystallization of glass is completely suppressed. After the poling and the heat treatment cesium ions are also recharged in this layer $Ce^{3+} \rightarrow Ce^{4+}$. The mechanisms of the crystallization suppression and ion recharge in the poled region of the glass are discussed.

Keywords: photosensitive glass, thermal poling, UV irradiation, heat treatment, crystallization

Термическая поляризация фоточувствительных стекол, содержащих ионы Ag⁺ и Ce³⁺

А.Ю. Мороз [1], И.Е. Чистиков [2], В.Г. Мелехин [3], В.П. Каасик [1, 4] ✉

[1] Санкт-Петербургский политехнический университет Петра Великого, Санкт-Петербург, Россия;

[2] Институт проблем машиноведения РАН, Санкт-Петербург, Россия;

[3] Физико-технический институт им. А.Ф. Иоффе РАН, Санкт-Петербург, Россия;

[4] Академический университет им. Ж.И. Алфёрова РАН, Санкт-Петербург, Россия

✉ vkaasik@yandex.ru

Аннотация. Представлены результаты исследования кристаллизации фото-терморефрактивного стекла при термическом полинге и ультрафиолетовом (УФ) облучении с последующей термообработкой. Полинг проводился при температуре 300 °C

и напряжении 400–1000 В. В качестве источников УФ излучения использовалась 3-я гармоника фемтосекундного лазера с длиной волны 343 нм. Исследования проводились методами оптической микроскопии, оптического поглощения и Рамановского рассеяния. Показано, что в прианодном слое стекла после полинга, последующего УФ облучения и термообработки кристаллизация стекла полностью подавляется. После полинга и последующей термообработки в этом слое происходит также перезарядка ионов цезия $Ce^{3+} \to Ce^{4+}$. Обсуждаются механизмы подавления кристаллизации и перезарядки ионов в поляризованной области стекла.

Ключевые слова: фоточувствительные стёкла, термический полинг, УФ облучение, термическая обработка, кристаллизация

Introduction

Photocrystallized glasses [1] are used in various fields of optics, such as holography, photonics, sensors, laser technology (see [2, 3] and references therein). Under the influence of UV radiation in the absorption band of trivalent cerium, its charge exchange occurs, and an electron is captured by a silver ion: $Ce^{3+} + h\nu + Ag^+ \to Ce^{4+} + Ag^0$ [1]. Subsequent heat treatment at 500 °C leads to the formation of silver clusters, which are the crystallization centers of the glass occurring under heat treatment at 600 °C. With local excitation by UV radiation and subsequent heat treatments, local photothermoinduced crystallization of the glass occurs, which is used to create various 2D and 3D structures, such as Bragg gratings for lasers and holographic optical elements [2]. An important factor is also the difference in the rate of chemical etching of the crystalline and amorphous phases in such glasses, which makes it possible to create relief structures at the surface and inside photo-thermo-refractive glasses, e.g. microfluidic chips [3]. A common method of modifying glasses is also thermal poling, the essence of which lies in placing a glass plate between electrodes (flat capacitor configuration) and heating to a temperature at which noticeable ionic conductivity appears (~ 300 °C), with subsequent application of voltage to the electrodes [4]. As a result, the composition and structure of the subsurface layer of glass changes, and the layer itself acquires a set of new properties, e.g. the second-order optical nonlinearity [5]. The aim of this work is to study the effect of thermal poling on photothermally induced crystallization of the glass and the processes of charge recharging of cerium ions.

Experiments and results

In the experiments, we used synthesized alumina-lithium-silicate glass with the following composition (in weight % of oxides): 75.5% of SiO_2; 10.44% of Li_2O; 5.33% of Al_2O_3; 5.74% of K_2O; 1.17% of Na_2O; 1.13% of ZnO; 0.236% of Ag_2O; 0.085% of CeO_2; 0.33% of Sb_2O_3. Transition temperature of this glass is $T_g = 480$ °C. It should be mentioned that in the synthesized glass cerium state is Ce^{3+} [6]. For poling, the glass plate was placed between two electrodes, one (cathode) completely covering the glass surface, and anode only partially. Then the structure was heated to temperature of 300 °C, after which a DC voltage of 400–1000 V (depending on the experiment) was applied to the electrodes. In Fig. 1, *a* we demonstrate differential (minus the spectrum of the initial glass) absorption spectra of the poled glass and the glass poled and subsequently annealed at 500 °C. In the spectra, we observe appearance of an absorption band near 245 nm, which is the charge transfer band of Ce^{4+} [7, 8]. The intensity of this band after poling is weak (see curve 1 in Fig. 1, *a*), but the anneal results in ~ 5-fold increase of the intensity

(see curve 2 in Fig. 1, *a*). This behavior can be apparently associated with a leftward shift in the equilibrium of the following oxidization process: $4Ce^{4+} + 2O^{2-} \leftrightarrow 4Ce^{3+} + O_2$.

Oxidization occurs both during poling due to the recombination of non-bridging oxygens with the formation of O_2 after the alkali ions have gone deep into the glass [9], and evidently during heat treatment in air. With increasing temperature, the rate of oxygen diffusion increases and the process of cerium oxidation activates, as a consequence, the intensity of the 245 nm Ce^{4+} band increases.
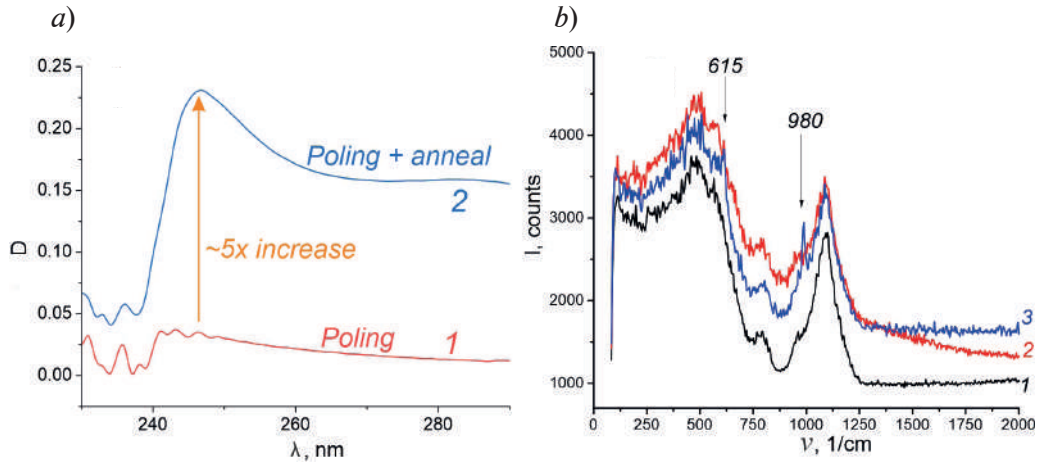
Fig. 1. Differential optical absorption spectra of the glass after poling under 800 V (*1*) and after poling under 500 V followed by anneal at 500 ˚C (*a*); Raman spectra of the initial glass (*1*), glass after poling and subsequent anneals at 500 and 600 ˚C (*2*), glass after poling, UV irradiation and subsequent anneals at 500 and 600 ˚C (*3*) (*b*)

When poled glass is subjected to UV irradiation and conventional crystallization procedure [6], the samples become opaque due to the formation of crystals which scatter the light. Raman spectra (Fig. 1, *b*) clearly demonstrate appearance of the peaks at frequencies of 615 cm^{-1} and 980 cm^{-1}, corresponding to lithium metasilicate, Li_2SiO_3 [8] in the specimen, which was poled, UV-irradiated and annealed. We also performed depth-scan via Raman spectroscopy by varying the distance between the objective lens and the sample surface and studied depth-dependence of intensities of the "glass" peak at ~ 1080 cm^{-1} and the "crystal" peak at ~ 980 cm^{-1}. Using a 530 nm wavelength and a 100x objective lens gave us a depth resolution about one micron. The results are shown in Fig. 2. We see the absence of crystals in a ~ 1 μm-thick subsurface layer. This is due to the fact that during poling lithium ions migrate into the glass under the action of the electric field and the subsurface region is depleted of these ions. Also, depth-scan demonstrated that the crystallites are not uniformly distributed at μm-scale (see "crystal" intensity line in Fig. 2).
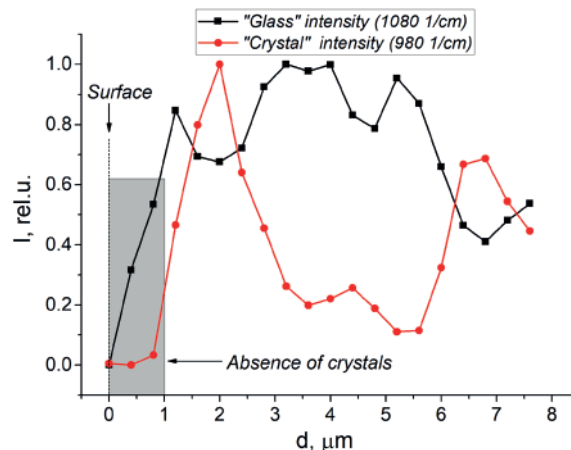
Fig. 2. Depth-dependence of normalized intensities of Raman peaks at ~ 1080 1/cm ("glass" peak) and at ~ 980 1/cm ("crystal" peak)

This nonuniformity, in particular the appearance of a second peak on the 980 1/cm line in parallel with the decline on the 1080 1/cm line may be due to the redistribution of reduced silver atoms during the first thermal treatment (500 °C) of the samples.

We etched the specimen in a 4% hydrofluoric acid solution, which showed that the surface of the poled region of the glass, unlike the regions without polarization, is not sensitive to the etching. This indicates a change in the composition of the near-surface layer of the polarized region, and that it completely lacks lithium metasilicate crystals, which are easily soluble in the etchant used.

Conclusions

We demonstrated that thermal poling of the photo-thermo-refractive glass results in the complete suppression of crystallization in the subsurface ~1 μm-thick layer, but does not affect the crystallization of deeper regions of the glass. Thus, thermal poling provides an additional tool to control crystallization of the photosensitive glass.

REFERENCES

1. **Evans A., Rupp J.L.M., Gauckler L.J.,** Crystallisation of Foturan® glass−ceramics, J. Eur. Ceram. Soc. 32 (2012) 203−210.

2. **Nikonorov N.V., Ivanov S.A., Musikhina E.S.,** Photo-thermo-refractive glass: a promising photonics material, J. Opt. Technol. 90 (2023) 142−160.

3. **He F., Liao Y., Lin J., Song J., Qiao L., Cheng Y., Sugioka K.,** Femtosecond Laser Fabrication of Monolithically Integrated Microfluidic Sensors in Glass, Sensors. 14 (2014) 19402−19440.

4. **Lepienski C.M., Giacometti J.A., Leal Ferreira G.F., Freire F.L., Achete C.A.,** Electric field distribution and near-surface modifications in soda-lime glass submitted to a dc potential, J. Non. Cryst. Solids. 159 (1993) 204−212.

5. **Dussauze M., Kamitsos E.I., Fargin E., Rodriguez V.,** Structural Rearrangements and Second-Order Optical Response in the Space Charge Layer of Thermally Poled Sodium−Niobium Borophosphate Glasses, J. Phys. Chem. C. 111 (2007) 14560−14566.

6. **Moroz A.Y., Babich E.S., Kaasik V.P., Lipovski A.A., Melekhin, V.G., Redkov A.V, Tagantsev D.K.,** Laser-induced optical nonlinearity in a Li-rich glass, J. Phys. Conf. Ser. 2086 (2021) 012024.

7. **Herrmann A., Othman H.A., Assadi A.A., Tiegel M., Kuhn S., Rьssel C.,** Spectroscopic properties of cerium-doped aluminosilicate glasses, Opt. Mater. Express. 5 (2015) 720−732.

8. **Arbuzov V.I., Belyankina N.B.,** Spectroscopic and photochemical properties of cerium, Fiz. Khim. Stekla. 16 (1990) 593−604.

9. **Redkov A.V., Melehin V.G., Lipovskii A.A.,** How Does Thermal Poling Produce Interstitial Molecular Oxygen in Silicate Glasses, J. Phys. Chem. C. 119 (2015) 17298−17307.

THE AUTHORS

MOROZ Alexey Yu.
alex.moroz97@mail.ru
ORCID: 0009-0005-0782-8569

MELEHIN Vladimir G.
melvol@hv.ioffe.ru
ORCID: 0000-0003-3741-3936

CHISTIKOV Ilia E.
chisilia12@gmail.com
ORCID: 0000-0001-9602-9868

KAASIK Vladimir P.
vkaasik@spbstu.ru
ORCID: 0000-0002-9976-6721

Modification of silicon nanowires with silver nanoparticles for gas sensor applications

V.M. Kondratev [1, 2] ✉, E.A. Vyacheslavova [1], T. Shugabaev [1], A.D. Bolshakov [1, 2]

[1] Alferov University, St. Petersburg, Russia;

[2] Moscow Institute of Physics and Technology, Dolgoprudny, Russia

✉ kvm_96@mail.ru

Abstract. This study focuses on methods to modify the adsorption properties of silicon nanowires produced through plasma cryogenic etching. This research demonstrates the potential for synthesizing a nanocomposite composed of silicon nanowires and silver nanoparticles, which can be utilized to develop highly efficient gas sensors.

Keywords: nanowires, selective adsorption sensor, electrical impedance spectroscopy

Модификация нитевидных нанокристаллов кремния наночастицами серебра для решения задач газовой сенсорики

В.М. Кондратьев [1, 2] ✉, Е.А. Вячеславова [1], Т. Шугабаев [1], А.Д. Большаков [1, 2]

[1] Академический университет им. Ж.И. Алфёрова РАН, Санкт-Петербург, Россия;

[2] Московский физико-технический институт (национальный исследовательский университет), г. Долгопрудный, Россия

✉ kvm_96@mail.ru

Аннотация. Работа посвящена разработке высокочувствительных газовых сенсоров на основе нитевидных нанокристаллов кремния (ННК). Сенсоры были использованы для детектирования биологических маркеров здоровья человека на примере аммиака и соляной кислоты.

Ключевые слова: кремний, серебро, ННК, наночастицы, сенсорика

Introduction

The influence of analyte adsorption on the electronic properties of nanostructures has been extensively utilized in sensor technologies, including those based on optical, resistive, capacitive, and current-voltage analyses. Among the earliest materials employed for gas detection were polycrystalline metal oxide films, such as SnO_2 [1, 2] and ZnO [3, 4], which were fabricated in various configurations [5]. The electronic behavior of these sensors is primarily determined by surface depletion effects caused by adsorption processes. Classical materials such as silicon and III-V compounds are also actively used to form sensor devices. The synthesis of these materials can be carried out both by epitaxial methods ("bottom-up") [6] and, for example, by etching methods ("top-down") [7]. As a result, it becomes possible to synthesize nanostructures of complex morphology, which makes it possible to increase the sensitivity of gas sensors [7]. However, such sensors often suffer from significant limitations, including reduced performance in humid conditions and limited selectivity. In this study, we develop gas sensors based on silicon nanowires (Si NWs) and systematically investigate their electronic properties using electrochemical impedance spectroscopy (EIS) [7] when exposed to ammonia (NH_3) and hydrochloric acid (HCl) vapors.

Materials and Methods

Top-down cryogen plasma chemical etching of the [001]-oriented B-doped silicon substrate with resistivity of 12 $\Omega \cdot$cm was used for Si NWs vertical array fabrication by Oxford PlasmaLab System 100 ICP 380 (Oxford instruments, UK) according to the protocol reported previously [7]. These nanowires exhibit a high aspect ratio and offer a significantly large surface area (cylindrical shape, approximately 10 μm in length and 150 nm in diameter). The nanowires were detached from the silicon substrate using ultrasonication in water and transferred onto a sensor platform with pre-patterned gold interdigital electrodes, forming the Si NW-based sensor. The electronic properties of the sensor were characterized using electrochemical impedance spectroscopy (EIS) (with the use of a Z500P impedance meter (Elins, Russia)) under ambient conditions and in the presence of target analytes (ammonia and hydrochloric acid). This study investigated three distinct types of Si NW-based sensors: as-grown Si nanowires, Si nanowires treated with a 10% aqueous hydrofluoric acid (HF) solution for 3 minutes, and Si nanowires decorated with silver nanoparticles (Ag NPs). Spherical silver nanoparticles (~20 nm in diameter) were synthesized via colloidal chemistry, deposited onto the as-grown Si NWs by drop-casting the colloidal solution, and dried under a nitrogen stream to remove residual solvent.

Results and Discussion

The as-grown Si nanowires, Si nanowires treated with HF and Si nanowires decorated with silver nanoparticles (Ag NPs) were studied using scanning electron microscopy (SEM, Zeiss Supra25, Carl Zeiss, Germany) (Fig. 1, *a*) and transmission electron microscopy (TEM, Jeol JEM-2100F, JEOL Ltd, Japan) (Fig. 1, *b–d*). The HRTEM (Fig. 1, *e–g*) and selected area electron diffraction (SAED) patterns demonstrated high crystalline quality of the Si NWs (Fig. 1, *h*) and Ag NPs (Fig. 1, *i*) without amorphization. The Au–NW contacts for all nanowire based sensors are found to be Schottky-type (Fig. 1, *j*). The fabricated sensors were tested upon exposure to HCl and NH_3 vapors. To provide indirect measurement of the fluid chemical composition, aqueous solutions of NH_3 and HCl were poured into 3 ml pools with a diameter of 4 cm and evaporated naturally at ambient conditions. The sensors were located at a distance of 5.0 cm above the pool (Fig. 1, *k*).

To study the sensitivity of the sensors, interdigital electrodes were connected to the impedance meter and EIS spectra were obtained in the presence of air, reference medium – water vapor,
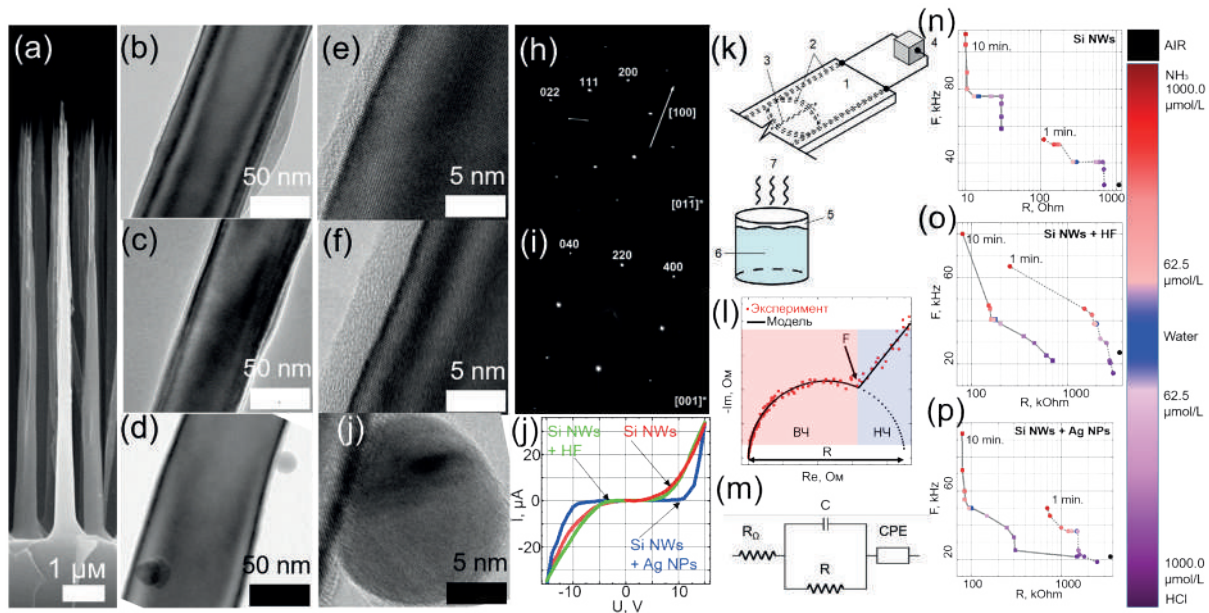
Fig. 1. (*a*) SEM image of the as-fabricated Si NWs. (*b*−*d*) TEM images and (*e*−*g*) HRTEM images of individual as-fabricated Si NW, NW treated with HF and NW decorated with Ag NPs, respectively. (*h*) selective area electron diffraction (SAED) pattern of a Si NW. (*i*) SAED pattern of a Ag NP. (*j*) current−voltage characteristics of the fabricated sensors based on as-fabricated (red), treated with HF (green) and decorated with Ag NPs (blue) Si NWs. (*k*) − Schematic of the measurement setup: 1 − contact platform, 2 − gold electrodes, 3 − NW, 4 − impedance meter, 5 − pool, 6 − solution, 7 − analyzed vapor. (*l*) − typical EIS spectrum of a sensor. (*m*) − equivalent circuit: R_{Ω} − resistance of the electrodes, R − resistance of the sensor, C − capacitance of the sensor and constant phase element (CPE). (*n*−*p*) − $F(R)$ maps for the sensors based on: Si NWs, NWs treated with HF and decorated with Ag NPs, respectively, exposure time 1 min − round dots, 10 min − square dots

and vapors of NH_3 and HCl aqueous solutions in a wide concentration range of 62.5 (1.25 ppm for NH_3 and 1.88 ppm for HCl) to 1000.0 μmol·l^{-1} (20 ppm for NH_3 and 30 ppm for HCl). The impedance spectra were depicted as the Nyquist plots, typical spectrum is presented in Fig. 1, *l*. The obtained curves consist of high-frequency (100 kHz to 500 kHz) and low-frequency (<100 kHz) domains. The high-frequency domain corresponds to the impedance of the NWs and Schottky barrier and represented by a semicircle. The low frequency domain follows nearly linear dependence and is considered as the result of the diffusion processes at the nanowire-gold interface [7]. All the obtained EIS spectra were fitted using the equivalent electrical circuit method. The employed circuit (Fig.e 1, *m*) contains: R_{Ω} − contact resistance corresponding to the resistance of the gold interdigital electrodes, R − resistance related to the Si NWs and Schottky barriers (referred to as the sensor resistance), C − capacitance of the sensor and CPE − constant phase element associated with the linear low frequency part of the spectra. These parameters evolve with adsorption of the analyte species on the NW sidewalls, so their analysis allows us to quantify the sensor response with the change in the resistive and capacitive characteristics. The carried out fitting allows one to obtain two parameters in the presence of various vapors: R and characteristic EIS frequency F (see Fig. 2, *l*−*m*) corresponding to the transition between the predominant action of the contact processes described by CPE at low frequencies, to the major role of the resistance R and capacitance C of the NWs and Schottky barriers at higher frequencies. According to the data analysis results, the R and F parameters are the fingerprint of the atmosphere surrounding the sensor due to the corresponding change in the spectra governed by the analyte species adsorption. So, exposure under NH_3 and HCl vapors of different concentrations can be quantified via $F(R)$ mapping of the sensory response in order to obtain selectivity in sensing (Fig. 1, *n*−*p*).

Conclusion

It is shown that sensors based on silicon nanowires and silver nanoparticles exhibit an enhanced response to hydrochloric acid vapors compared to sensors made from as-grown silicon nanowires.

83

In opposite untreated silicon nanowires demonstrated good sensitivity to ammonia vapors. The results of this study are highly promising for the development of advanced semiconductor devices for portable health monitoring applications.

REFERENCES

1. **Nalimova S.S., Kondrat'ev V.M.,** Study of surface acid-base properties of gas-sensitive metal oxides, IEEE Conference of Russian Young Researchers in Electrical and Electronic Engineering (EIConRus), St. Petersburg and Moscow, Russia. (2020) 987–990.

2. **Levkevich E.A., Maksimov A.I., Kirillova S.A., Nalimova S.S., Kondrat'ev V.M., Semenova A.A.,** Synthesis, Investigation and Gas Sensitivity of Zinc Stannate Layers, IEEE Conference of Russian Young Researchers in Electrical and Electronic Engineering (EIConRus), St. Petersburg and Moscow, Russia. (2020) 984–986.

3. **Nalimova S.S., Bobkov A.A., Kondrat'ev V.M., Ryabko A.A., Moshnikov V.A., Shomakhov Z.V.,** Study of doped zinc oxide nanowires by X-Ray photoelectron spectroscopy, IEEE Conference of Russian Young Researchers in Electrical and Electronic Engineering (EIConRus), St. Petersburg and Moscow, Russia. (2020) 991–993.

4. **Kondratev V.M., Bolshakov A.D., Nalimova S.S.,** Technologically Feasible ZnO Nanostructures for Carbon Monoxide Gas Sensing, IEEE Conference of Russian Young Researchers in Electrical and Electronic Engineering (ElConRus), St. Petersburg, Moscow, Russia. (2021) 1163–1166.

5. **Kadinskaya S.A., Kondratev V.M., Kindyushov I.K., Kuznetsov A., Punegova K.N.,** Hydrothermal ZnO-based Nanostructures: Geometry Control and Narrow Band UV Emission, Conference of Russian Young Researchers in Electrical and Electronic Engineering (ElConRus), Saint Petersburg, Russian Federation. (2022) 958–961.

6. **Kuznetsov A., Roy P., Grudinin D.V., Kondratev V.M., Kadinskaya S.A., Vorobyev A.A., Kotlyar K.P., Ubyivovk E.V., Fedorov V.V., Cirlin G.E., Mukhin I.S., Arsenin A.V., Volkovd V.S., Bolshakov A.D.,** Self-assembled photonic structure: A Ga optical antenna on GaP nanowires, Nanoscale. 15 (5) (2023) 2332–2339.

7. **Kondratev V.M., Vyacheslavova E.A., Shugabaev T., Kirilenko D.A., Kuznetsov A., Kadinskaya S.A., Shomakhov Z.V., Baranov A.I., Nalimova S.S., Moshnikov V.A., Gudovskikh A.S., Bolshakov A.D.,** Si Nanowire-Based Schottky Sensors for Selective Sensing of NH_3 and HCl via Impedance Spectroscopy, ACS Applied Nano Materials. 6 (13) (2023) 11513–11523.

THE AUTHORS

KONDRATEV Valeriy M.
kvm_96@mail.ru
ORCID: 0000-0002-3469-5897

SHUGABAEV Talgat
talgashugabaev@mail.ru
ORCID: 0000-0002-4110-1647

VYACHESLAVOVA Ekaterina A.
cate.viacheslavova@yandex.ru
ORCID: 0000-0001-6869-1213

BOLSHAKOV Alexey D.
acr1235@mail.ru
ORCID: 0000-0001-7223-7232

Aggregation kinetics of silver nanoparticles ensembles in sub-percolating state and its impact on memristive behaviour

Yu.O. Vasilevskaya [1] ✉, J.V. Chumachenko [2]

[1] Scientific-Manufacturing Complex "Technological Centre", Zelenograd, Russia;
[2] Institute of Advanced Materials and Technologies, MIET, Zelenograd, Russia

✉ jo.fedorova@tcen.ru

Abstract. The effect of coalescence and aggregation processes on the memristive properties of silver nanoparticle assemblies has been investigated. Nanoparticles were prepared by vacuum-thermal evaporation on silicon substrates with gold electrodes and quartz glasses for morphological control. The structure of the samples and size distribution of nanoparticles were studied using scanning electron microscopy (SEM) and UV-visible spectroscopy. Memristive properties were estimated using cyclic voltammetry. Due to Ostwald ripening and an increase in average nanoparticle size, the operating voltage required to switch the system into the memristive state decreased, while the conductivity dynamics changed. These findings are useful for ensuring the stability of memristive devices based on silver nanoparticle assemblies.

Keywords: coalescence, silver nanoparticles, surface plasmon resonance, memristive dynamics, surface diffusion

Кинетика агрегации ансамблей наночастиц серебра в субперколяционном состоянии и ее влияние на мемристивное поведение

Ю.О. Василевская [1] ✉, Ю.В. Чумаченко [2]

[1] «Научно-производственный комплекс «Технологический центр», г. Зеленоград, Россия;
[2] Институт перспективных материалов и технологий, НИУ МИЭТ, г. Зеленоград, Россия

✉ jo.fedorova@tcen.ru

Аннотация. Исследуется влияние процессов коалесценции и агрегации на мемристивные свойства ансамблей наночастиц серебра. Системы наночастиц получены методом вакуум-термического испарения на кремниевые подложки с золотыми электродами и на кварцевые стекла для контроля морфологии. Морфологию частиц анализировали методами РЭМ и УФ-видимой спектроскопии, а мемристивные свойства с помощью циклической вольтамперометрии. Вследствие оствальдовского созревания и увеличения среднего размера наночастиц, снижается рабочее напряжение, необходимое для переключения системы в мемристивное состояние, при этом изменяется

динамика проводимости. Приведенные оценки полезны для обеспечения стабильности работы мемристивных устройств на основе ансамблей наночастиц серебра.

Ключевые слова: коалесценция, наночастицы серебра, поверхностный плазмонный резонанс, мемристивная динамика, поверхностная диффузия

Introduction

Silver nanoparticles and nanowires are promising materials for the development of neuromorphic computing devices. Their main advantages include (1) the ability to scale, (2) the technological simplicity of application to various substrates, and (3) the presence of complex nonlinear dynamic characteristics [1−3]. In such systems, a self-organizing network of discrete memristive elements is formed, separated by nanometer gaps, where each nanoobject functions as an independent memristor [4]. The applied electric field induces the formation of atomically thin conductive filaments (filaments) between the nanoparticles, which is clearly detected by the characteristic hysteresis loops on the volt-ampere characteristics [5−7].

Experimental studies [8, 9] confirm the prospects of using nanoscale silver structures for processing time signals and solving predictive tasks. The main advantage of such systems is the implementation of the principle of reservoir computing, where learning affects only the output connections, while the internal network of nanoelements retains the same random configuration of connections. However, the key limitation of this technology is the temporary instability of silver nanostructures caused by the processes of coalescence (gradual particle enlargement) and aggregation (cluster formation), which leads to degradation of the original network architecture and deterioration of its functional characteristics. This work presents the results of a study of the temporal dynamics and the effect of coalescence and aggregation processes in an ensemble of silver nanoparticles on the memristive properties. It has been revealed that, in order to practically apply such systems, it is necessary to address the issue of nanoparticle stabilization, which can be accomplished by either modifying the surface of silver structures or by using additional materials that have increased resistance to structural changes [10].

Materials and Methods

Experimental samples were obtained by vacuum thermal deposition of silver onto a thermally oxidized silicon substrate, with a gap of either 2 or 20 microns (depending on the weight of the sample), between two gold electrodes. Silver weights of 0.62 mg, 1.18 mg, 3.34 mg, 4.71 mg, 6.06 mg, 10.05 mg, 15.06 mg, 17.2 mg, and 20.05 mg were selected for deposition. Simultaneously, deposition also occurred on quartz glass, for further investigation into the temporal dynamics of structural changes using optical spectroscopy (UV-VIS spectrometer, Thermo Fisher Scientific, US). After deposition, all samples underwent vacuum annealing at 230°C for 30 minutes.

The geometric dimensions of the nanoparticles were estimated from the SEM images obtained using the FEI Helios NanoLab 650i DualBeam electron-ion scanning microscope. To calculate the average values of nanoparticle diameters and distances between them, a Python program was developed, which uses the Delaunay method for distance calculation. Voltammograms were obtained for experimental samples using a probe station (Cascade Microtech Summit, US) and a B1500A parametric analyzer (Keysight, US). All samples were stored in a nitrogen-dry storage cabinet at 23 ± 2 °C and $14 \pm 2\%$ humidity.

Results and Discussion

Figure 1 shows the results obtained for the experimental samples in their original form. For samples with an evaporated silver mass above 10 mg, the shape of the nanoparticles became distinct from spherical and represented arbitrarily oriented cluster-like elements. This was confirmed by both SEM images and the position of the surface plasmon resonance peak on optical spectra. The distance between nanoparticles was comparable to their diameter. Over time, coalescence and diffusion led to a characteristic Ostwald ripening process, accompanied by an increase in nanoparticle size due to the system's tendency to minimize surface energy.
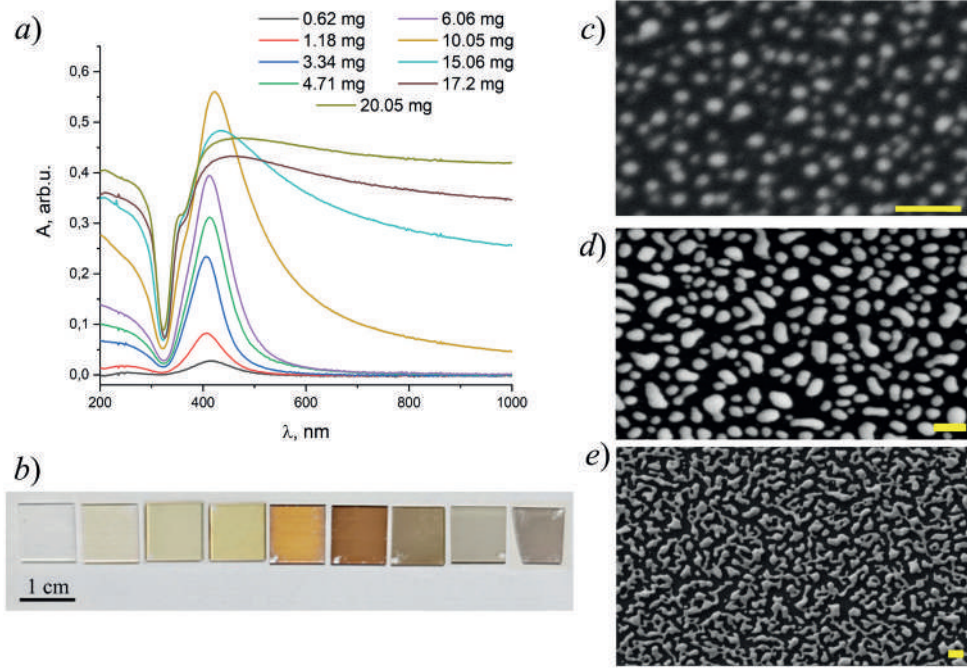
Fig. 1. Optical spectra of annealed experimental samples (*a*) and their photo (*b*) on quartz glass (mass increase from 0.62 mg to 20.05 mg from left to right), (*c*) − (*e*) SEM images for samples 3.34 mg, 10.05 mg and 20.05 mg respectively (from top to bottom). Scale bar for all SEM images is 100 nm

Figure 2 allows to estimate the rate of morphological change in nanoparticle ensembles over time based on the dynamics of the redshift of the absorption peak and its broadening. The results obtained confirm the general trend of nanoparticle enlargement over time. It is worth noting that for large silver sample masses, the rate of change in the geometric dimensions of nanoparticles is lower (for samples weighing 17.2 mg and 20.05 mg, the displacement was in the range of
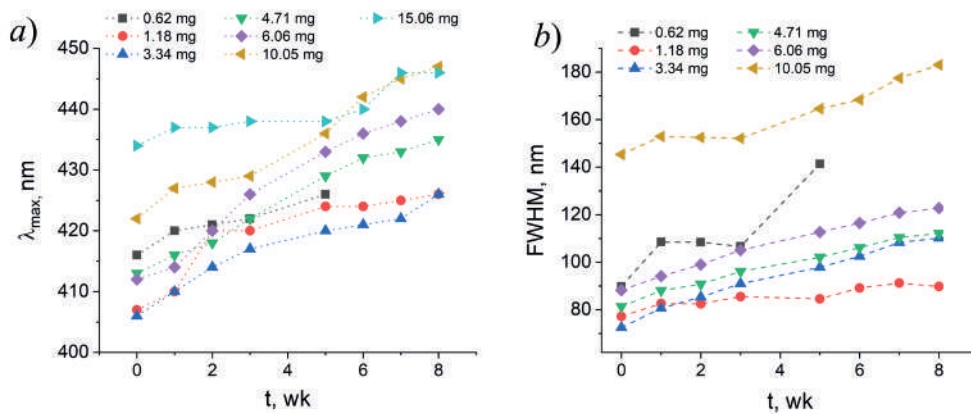
Fig. 2. Shift of the absorption maximum (*a*) and its broadening (*b*) for different masses of silver bulk

up to 5 nm during the presented time), which can be characterized as a more kinetically and thermodynamically stable structure due to a reduction in the surface area to volume ratio, which leads to a decrease in the driving force for minimizing surface energy. A more stable configuration is an important parameter in the development of architecture for practical applications.

Figure 3 also shows the unimodal diameter distribution obtained from analyzing the SEM image in the initial case, and the bimodal distribution after 2 months.

The decrease in the average diameter is explained by the appearance of many small nanoparticles in close proximity to large "nuclei", which is typical of Ostwald ripening. This result was observed in all samples up to a mass of 10 mg, as it reproduced the known mechanism of coalescence, including the stages of formation of a "neck" between adjacent nanoparticles, followed by "spherification" and gradual relaxation towards a thermodynamically stable structure. For elongated silver clusters with larger masses, it will take considerably longer to reach a spherical shape, as they initially have a larger surface area.

After the "molding" process, all experimental samples of silver nanoparticles exhibited characteristic memristive behavior and a hysteresis loop in their voltammograms. The less spherical the nanoparticles were in the ensemble, the lower the value of the switching voltage required to
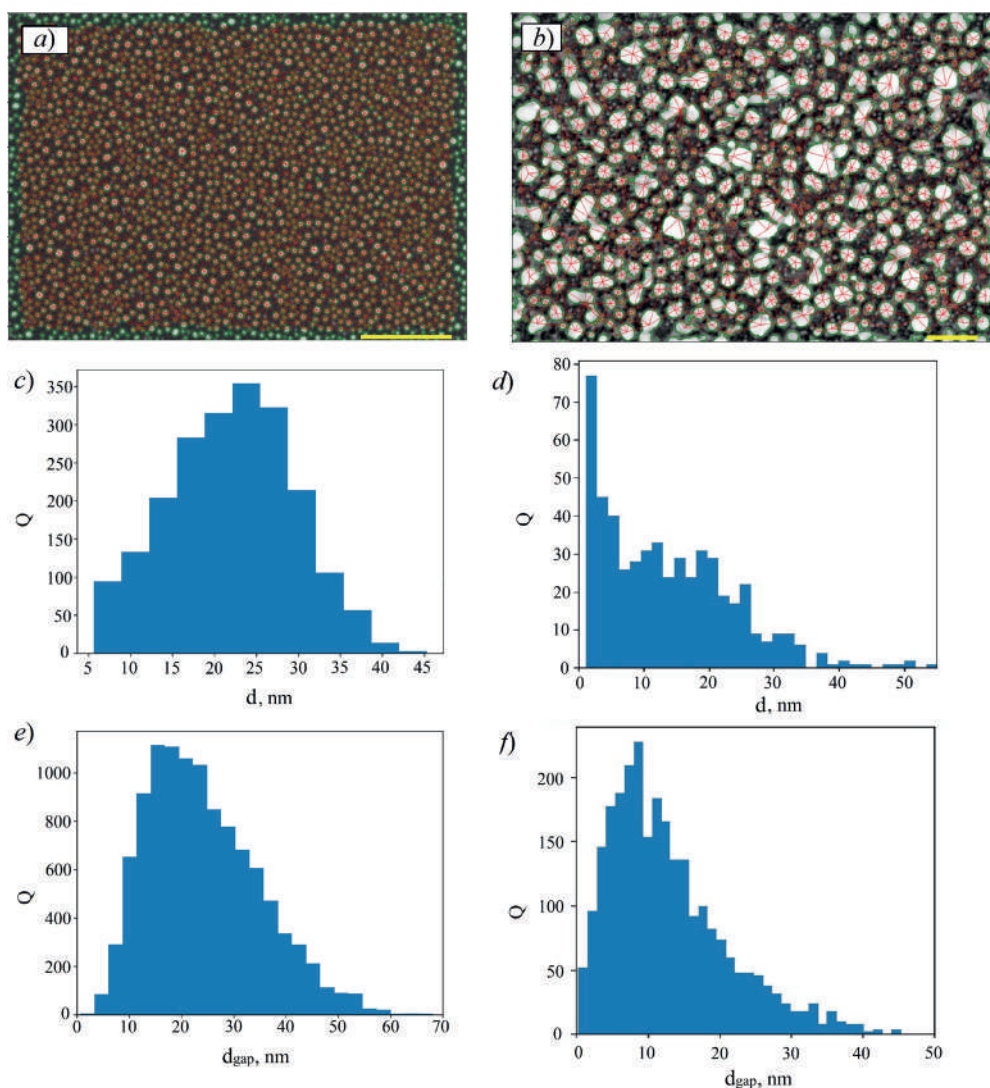
Fig. 3. The result of processing SEM images in the program for a 4.71 mg sample: (*a*) the initial ensemble, (*b*) after 2 months, (*c*) and (*d*) histograms of the diameter (d) size distribution via number of particles (Q), respectively, and (*e*) and (*f*) - a histogram for the gaps sizes (d_{gap}) between nanoparticles. The scale bar on the SEM is 200 nm, the boundaries of the nanoparticles are outlined in green, and the distances taken into account are in red

transition to the conductive state. This behavior can be explained by the presence of areas with higher electric field strength near elongated protrusions on the nanoparticles, which facilitate the formation of conductive pathways (filaments) in a more directed manner.

Over time, a gradual decrease in the "ON" voltage was observed, which is associated with the gradual formation of areas of large clusters, remaining after the incomplete destruction of the percolation cluster by voltages of different polarities. For small spherical nanoparticles, this is also due to their gradual enlargement. There was also an asymmetry of the hysteresis curve for small nanoparticles (Fig. 4) and a decrease in the number of intermediate "memory" states for large ones (a more rectangular loop shape).
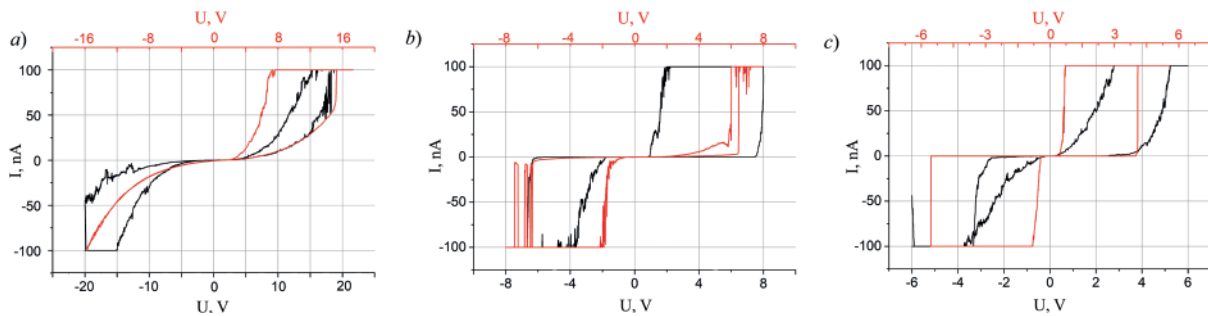
Fig. 4. Voltammograms for samples of 4.71 mg silver (*a*), 10.05 mg (*b*) and 17.2 mg (*c*). The curves for the initial state are highlighted in black, and after 8 weeks − in red

Conclusion

The paper presents the results of a study on the coalescence dynamics of ensembles of silver nanoparticles with various sizes (ranging from 5 nm to 200 nm, for evaporation masses of 0.62 mg and 20.05 mg, respectively), and its impact on the memristive properties. The observed slow relaxation of these systems towards a thermodynamically stable structure leads to changes in the morphology and geometric dimensions of the nanoparticles, which affects the control switching voltage and the operating characteristics. The smaller the nanoparticles are, the greater the ratio of their surface area to their volume, and therefore, the higher the mobility of surface atoms. Therefore, nanoparticles require external conditions for limiting coalescence to stabilize the system and reduce the frequency of tuning output connections.

Acknowledgments

REFERENCES

1. **Yu Y., Xiao M., Fieser D., Zhou W., Hu A.,** Nanoscale memristor devices: materials, fabrication, and artificial intelligence, Journal of Materials Chemistry C. 12 (11) (2024) 3770−3810.

2. **Liu P., Hui F., Aguirre F., Saiz F., Tian L., Han T., Lanza M.,** Nano-Memristors with 4 mV Switching Voltage Based on Surface-Modified Copper Nanoparticles, Advanced Materials. 34 (20) (2022) 2201197.

3. **Vasilevskaya Yu.O., Savitskiy A.I., Sibatov R.T.,** Modeling of molecular dynamics of laments and mesoscopic conductance in a neuromorphic ensemble of nanoparticles, Memoirs of the Faculty of Physics, Lomonosov Moscow State University. 4 (2023) 2341402.

4. **Kim T.H., Jang E.Y., Lee N.J., Choi D.J., Lee K.J., Jang J.T., Cheon J.,** Nanoparticle assemblies as memristors, Nano letters. 9 (6) (2009) 2229−2233.

5. **Sibatov R.T., Savitskiy A.I., L'vov P.E., Vasilevskaya Y.O., Kitsyuk, E.P.,** Self-Organized Memristive Ensembles of Nanoparticles Below the Percolation Threshold: Switching Dynamics and Phase Field Description, Nanomaterials. 13 (14) (2023) 2039.

6. **L'vov P.E., Sibatov R.T., Ryazanov R.M., Novikov D.V.,** Phase-field model of filament formation and growth in percolating memristive systems of nanoparticles, Materials Today Communications. 38 (2024) 108464.

7. **Vahl A., Carstens N., Strunskus T., Faupel F., Hassanien, A.,** Diffusive memristive switching on the nanoscale, from individual nanoparticles towards scalable nanocomposite devices, Scientific reports. 9 (1) (2019) 17367.

8. **Mallinson J.B., Steel J. K., Heywood Z.E., Studholme S.J., Bones P.J., Brown S.A.,** Experimental Demonstration of Reservoir Computing with Self-Assembled Percolating Networks of Nanoparticles, Advanced Materials. (2024) 2402319.

9. **Fan Z., Fan X., Li A., Dong, L.,** In situ forming, characterization, and transduction of nanowire memristors, Nanoscale. 5 (24) (2013) 12310−12315.

10. **Guevara-Chapa E., Mejía-Rosales S.,** Molecular dynamics of coalescence and collisions of silver nanoparticles, Journal of nanoparticle research. 16 (2014) 1−10.

THE AUTHORS

VASILEVSKAYA Yulia O.
fedorovauo@mail.ru
ORCID: 0000-0002-5183-6807

CHUMACHENKO Julia V.
julia.chumachenko@mail.ru
ORCID: 0009-0006-1375-6191

Optical studies of InAs/InAsSb/InAsSbP heterostructures

M.S. Ruzhevich [1] ✉, I.D. Kirilenko [1], I.V. Chumanov [2], D.D. Firsov [2],

O.S. Komkov [2], K.D. Mynbaev [1, 3], V.V. Romanov [3], K.D. Moiseev [3]

[1] ITMO University, St. Petersburg, Russia;
[2] St. Petersburg Electrotechnical University "LETI", St. Petersburg, Russia;
[3] Ioffe Institute, St. Petersburg, Russia
✉ max.ruzhevich@niuitmo.ru

Abstract. Fourier-transform infrared photoluminescence and photoreflectance were used to study the optical properties of InAs/InAsSbP and InAs/InAsSb/InAsSbP heterostructures. A strong dependence of chemical composition and optical quality of the top InAsSbP barrier layers on the composition of the material on which the layer was grown has been established.

Keywords: heterostructures, InAsSbP, photoluminescence, photoreflectance

Оптические исследования гетероструктур InAs/InAsSb/InAsSbP

М.С. Ружевич [1] ✉, Я.Д. Кириленко [1], И.В. Чуманов [2], Д.Д. Фирсов [2],

О.С. Комков [2], К.Д. Мынбаев [1, 3], В.В. Романов [3], К.Д. Моисеев [3]

[1] Университет ИТМО, Санкт-Петербург, Россия;
[2] Санкт-Петербургский государственный электротехнический университет «ЛЭТИ» имени В.И. Ульянова (Ленина), Санкт-Петербург, Россия;
[3] Физико-технический институт им. А.Ф. Иоффе, Санкт-Петербург, Россия
✉ max.ruzhevich@niuitmo.ru

Аннотация. Методами инфракрасной фурье-спектроскопии фотолюминесценции и фотоотражения исследованы оптические свойства гетероструктур InAs/InAsSbP и InAs/InAsSb/InAsSbP. Обнаружена сильная зависимость химического состава и оптического качества верхних барьерных слоев InAsSbP от состава материала, на котором были выращены эти слои.

Ключевые слова: гетероструктуры, InAsSbP, фотолюминесценция, фотоотражение

Introduction

InAsSb is an indispensable material for the fabrication of optoelectronic devices that cover the mid-wavelength infrared (MWIR) spectral range (2−6 μm). MWIR devices are widely used in, e.g., environmental monitoring, defense applications, industry, and medical diagnostics [1]. Using $InAs_{1-y}Sb_y$ in the active layer of a semiconductor heterostructure (HS), one can cover a 3.4−11.0 μm range. Increasing y, which is necessary for extending the working range of the HSs towards longer wavelengths, however, leads to a strong lattice mismatch between the InAsSb epitaxial layer and the substrate (typically made of InAs), as well as in technological challenges in deposition of InAsSbP on InAsSb using metal-organic vapor-phase epitaxy (MOVPE) [2]. These factors can result in a number of competing channels of radiative recombination in the HSs, which, in fact, may be useful in the design of multi-color LEDs [3]. Electroluminescence (EL) and electrical studies used for characterization of HSs do not always give sufficient information on their actual construction and its difference from the original design, inherent to lattice-mismatched systems. This information, however, can be obtained by studying optical properties of HS constituents, with the advantage of optical methods being non-destructive (see, e.g., [4]). In this paper, we present the results of the studies of InAs/(InAsSb)/InAsSbP HSs performed with Fourier-transform infrared (FTIR) photoluminescence (PL) and photoreflectance (PR).

Materials and Methods

The studied HSs were grown by MOVPE on undoped InAs(001) substrates. The deposition of undoped InAsSb active layer and/or zinc-doped InAsSbP layers was performed in a horizontal reactor under atmospheric pressure with the growth details reported elsewhere [2]. The thickness of the $InAs_{0.88}Sb_{0.12}$ layer was ~3 μm, and that of the $InAsSb_{0.22}P_{0.47}$ layers ~1.2 μm.

Optical studies were performed using the setup described in [5] and based on a Bruker Vertex 80 FTIR spectrometer with a cooled InSb or HgCdTe photodetector. PL and PR studies were carried out in a $T = 11-300$ K range under excitation with an 809 nm cw laser diode modulated with 2.5 kHz frequency, and providing power density up to 4.0 W/cm². During the measurements the HSs were placed in a Janis CCS-150 closed-cycle helium cryostat.

Results and Discussion

PL spectra of the InAs/InAsSbP HS (Fig. 1, *a*) contained a strong asymmetrical band with its peak at ~0.52 eV ($T = 11$ K) obviously related to the PL from the InAsSbP layer. The low-energy shoulder of the band could be related to PL from acceptor states in the layer (possibly, arising due to the introduction of Zn) and to the signal coming from the underlying InAs substrate (bandgap $E_g = 0.41$ eV at $T = 11$ K). The intensity of the band was gradually decreasing with T increasing, while the full-width at half-maximum (FWHM ~ 30 meV at $T = 11$ K) of the main peak was increasing.

The PL spectra of InAs/InAsSb/InAsSbP HS (Fig. 1, *b*) contained an almost symmetrical peak from the InAsSbP layer (~0.42 eV at $T = 11$ K) and a peak related to the InAsSb layer (~0.27 eV at $T = 11$ K). The FWHMs of the PL peaks related to InAsSbP layers in the two HSs were similar. The peak from the InAsSb layer had a FWHM of ~25 meV at $T = 11$ K. Its energy differed by ~ 20 meV from that of the EL peak of the HS as presented in [6], which confirmed the interface origin of the EL in these HSs, as was suggested earlier.

Fig. 2, *a* shows PR spectra of the InAs/InAsSbP HS. The spectra had an oscillating shape and, most probably, represented a superimposition of the Fabry-Perot interference and the differential signal from the interband transitions in the InAsSbP layer (marked as 'E_g'). For the InAs/InAsSb/InAsSbP HS, PR signal was not detected, possibly indicating lower structural quality of the InAsSbP layer, which in this case was grown on lattice-mismatched InAsSb. Measured under identical conditions, the PL signal from InAsSbP in the InAs/InAsSb/InAsSbP HS was also weaker than that from the similar layer in the InAs/InAsSbP HS.

The temperature dependences of the energy of the PL and PR peaks are shown in Fig. 2, *b*. For the InAs/InAsSbP HS, the PL peak related to the InAsSbP layer did not change its energy in the $T = 11-120$ K range; at higher T, its energy was decreasing, approaching the Varshni law.

a)

b)
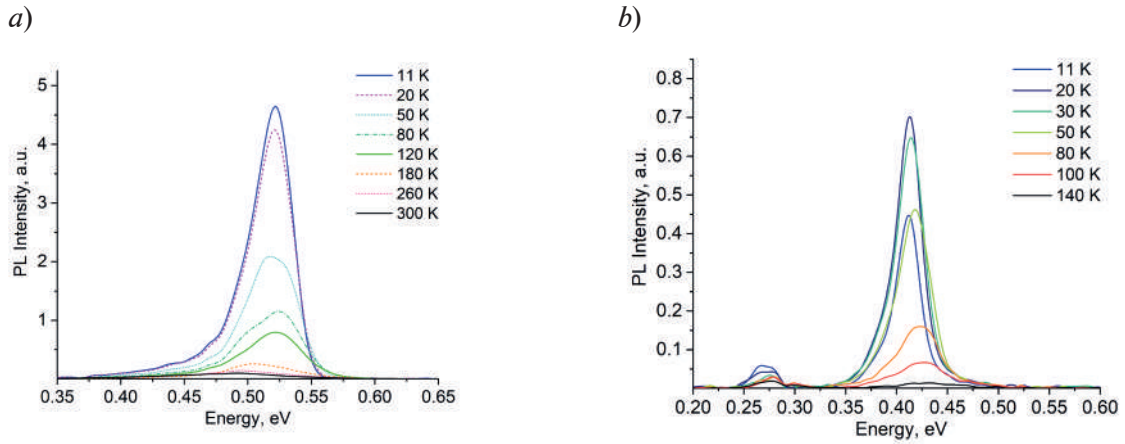
Fig. 1. Variable-temperature PL spectra of InAs/InAsSbP (*a*) and InAs/InAsSb/InAsSbP (*b*) heterostructures

The positions of both the PL and PR peaks within the whole $T = 11-300$ K range did not correspond to the E_g calculated according to the expected composition of the layer. For InAs/InAsSb/InAsSbP HS, the PL peak of the InAsSbP layer in $T = 11-200$ K range showed some blue-shift with temperature increasing, and at higher T also followed the Varshni law. Its position again did not correspond to the calculated E_g, and was indicative of greater InSb content as compared to that in the InAsSbP layer in the InAs/InAsSbP HS.

a)

b)
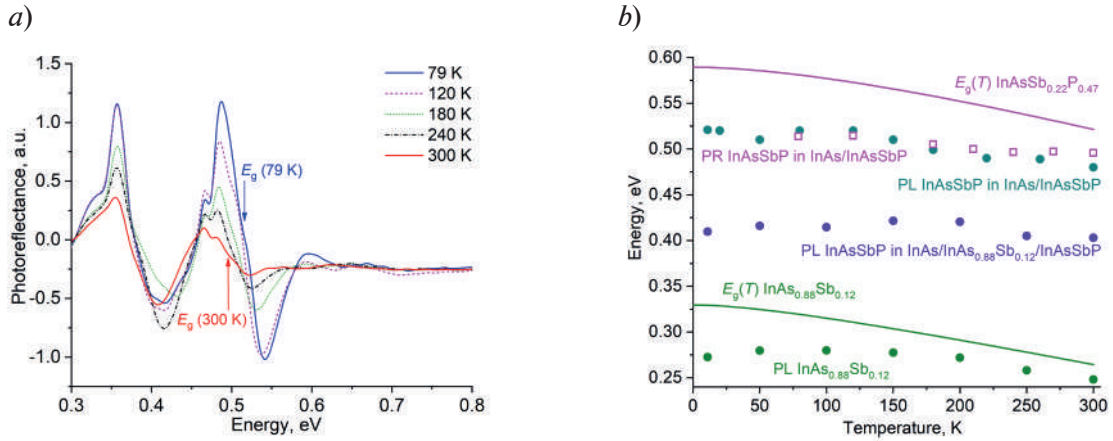
Fig. 2. Variable-temperature PR spectra of InAsSbP/InAs HS (*a*), and temperature dependences of the energy of PL and PR peaks (symbols) with corresponding $E_g(T)$ dependences (lines) calculated according to the Varshni law [7] with parameters $\alpha = 3.3 \cdot 10^{-4}$ eV/K, $\beta = 120$ K for InAsSbP (*b*)

Conclusion

The results of the optical studies of InAs/InAsSbP and InAs/InAsSb/InAsSbP heterostructures performed with FTIR photoluminescence and photoreflectance methods allowed for a non-destructive study of the properties of the layers constituting the structures. For InAs/InAsSb/InAsSbP HS, a weakening of the optical response was detected, indicating lower structural quality of the InAsSbP material. In the PL spectra, a signal was observed from both the InAs(Sb) and InAsSbP, and for the latter, the position of the PL peak depended on the composition of the underlying material. This meant that during the growth of InAsSbP layer, its chemical composition got adjusted to the "substrate", which affected the optical properties of the HS. In the InAs/InAsSbP HS, the presence of defect states was detected, possibly associated with introduction of Zn.

REFERENCES

1. **Tang Y., Zhao Y., Liu H.,** Room-Temperature Semiconductor Gas Sensors: Challenges and Opportunities, ACS Sens. 7 (12) (2022) 3582−3597.

2. **Romanov V.V., Moiseev K.D.,** Features of the Energy Band Structure of the InAsSbP Epilayer Deposited on a Surface of the $InAs_{1-y}Sb_y$ Solid Solution, Phys. Solid State. 65 (10) (2023) 1634−1641.

3. **Grigoryev M.M., Alekseev P.A., Ivanov E.V., Moiseev K.D.,** Two-color luminescence from a single type-II InAsSbP/InAs heterostructure, Semiconductors. 47 (1) (2013) 28−32.

4. **Smołka T., Motyka M., Romanov V.V., Moiseev K.D.,** Photoluminescence Spectroscopy of the InAsSb-Based p-i-n Heterostructure, Materials. 15 (2022) 1419.

5. **Firsov D.D., Komkov O.S., Solov'ev V.A., Kop'ev P.S., Ivanov S.V.,** Temperature-dependent photoluminescence of InSb/InAs nanostructures with InSb thickness in the above-monolayer range, J. Phys. D: Appl. Phys. 49 (28) (2016) 285108.

6. **Ruzhevich M.S., Mynbaev K.D., Bazhenov N.L., Romanov V.V., Moiseev K.D.,** Electroluminescence of narrow-gap $InAs/InAs_{1-y}Sb_y/InAsSbP$ heterostructures with $y = 0.07−0.12$, St. Petersburg. State. Polytech. Univ. J. Phys. Math. 17 (1.1) (2024) 77−82.

7. **Varshni Y.,** Temperature dependence of the energy gap in semiconductors, Physica. 34(1) (1967) 149−154.

THE AUTHORS

RUZHEVICH Maxim S.
max.ruzhevich@niuitmo.ru
ORCID: 0000-0002-4513-6345

KIRILENKO Iaroslav D.
idkirilenko@itmo.ru
ORCID: 0009-0007-1056-5100

CHUMANOV Ivan V.
chumanov2000@yandex.ru
ORCID: 0009-0009-2564-6100

FIRSOV Dmitrii D.
ddfirsov@gmail.com
ORCID: 0000-0001-7608-9580

KOMKOV Oleg S.
oskomkov@yahoo.com
ORCID: 0000-0002-8999-1175

MYNBAEV Karim D.
mynkad@mail.ioffe.ru
ORCID: 0000-0002-9853-8874

ROMANOV Vyacheslav V.
romanovvv@mail.ioffe.ru
ORCID: 0000-0002-9989-3843

MOISEEV Konstantin D.
mkd@iropt2.mail.ioffe.ru
ORCID: 0000-0002-6306-0129

Photoluminescence of InGaAs/InAlAs short-period superlattices grown on InP substrate

V.I. Voitovich [1] ✉, I.S. Makhov [1], V.V. Andryushkin [2], P.E. Kopytov [2]

D.S. Papylev [2], N.V. Kryzhanovskaya [1], A.E. Zhukov [1]

[1] National Research University Higher School of Economics, St. Petersburg branch, St. Petersburg, Russia;

[2] ITMO University, St. Petersburg, Russia

✉ vivoytovich@edu.hse.ru

Abstract. The photoluminescence spectra of short-period InGaAs/InAlAs superlattices emitting in the 1.3 μm spectral range were investigated in the wide range of pumping powers at the temperatures of 5−300 K. The 5 K photoluminescence spectra consisted of luminescence bands associated with radiative electron-hole recombination in superlattices as well as in the InP substrate and buffer layers of heterostructures. Spectral positions of superlattice emission bands are in a good agreement with calculated values obtained with transfer matrix method for all the samples. The temperature evolution of emission spectra was investigated as well.

Keywords: superlattice, photoluminescence, VCSEL, temperature quenching

Фотолюминесценция короткопериодных сверхрешеток InGaAs/InAlAs, выращенных на InP подложке

В.И. Войтович [1] ✉, И.С. Махов [1], В.В. Андрюшкин [2], П.Е. Копытов [2],

Д.С. Папылев [2], Н.В. Крыжановская [1], А.Е. Жуков [1]

[1] Национальный исследовательский университет «Высшая школа экономики», Санкт-Петербургский филиал, Санкт-Петербург, Россия;

[2] Университет ИТМО, Санкт-Петербург, Россия

✉ vivoytovich@edu.hse.ru

Аннотация. Исследованы спектры фотолюминесценции короткопериодных сверхрешеток InGaAs/InAlAs в широком диапазоне мощностей накачки при температурах 5−300 K. Спектры фотолюминесценции при 5 K состояли из полос люминесценции, связанных с излучательной рекомбинацией электронов и дырок в сверхрешетках, а также в подложке и буферных слоях гетероструктур. Спектральные положения полос излучения сверхрешеток хорошо согласуются с расчетными значениями.

Introduction

Nowadays, the development of miniature laser sources for fast data transmission is an important task. One of the them is vertical-cavity surface-emitting laser (VCSEL) [1], which has high temperature stability of the lasing wavelength, small angular divergence and threshold currents. In order to achieve lasing in VCSELs, an active region with high modal gain is necessary, especially for lasers operating near 1.3 μm and 1.55 μm wavelengths. Short-period superlattices (SLs) in this case allow to get a higher modal gain due to increased values of longitudinal optical confinement factor [2] compared to the quantum well or quantum dot active region. Thus, the development of heterostructures with SLs with high optical quality is an actual goal. The present work is devoted to the investigation of photoluminescence (PL) characteristics of InGaAs/InAlAs short-period SLs, which are promising for implementation as an VCSEL active region.

Materials and Methods

Samples under study were molecular beam epitaxy grown on an InP (100) substrate on a 200 nm thick $In_{0.52}Al_{0.48}As$ buffer layer. The active region of each sample consisted of three SLs grown sequentially one after another. First and third SLs were formed by 23 periods of epilayers $In_{0.53}Ga_{0.47}As/In_{0.52}Al_{0.48}As$ with a total period width of 22 Å remaining the same for all the samples in order to provide average mole fractions of Ga and Al in the SLs at the level of 27 and 20% respectively. Middle SL was formed by 25 periods of $In_{0.6}Ga_{0.4}As/In_{0.52}Al_{0.48}As/In_{0.53}Ga_{0.47}As/In_{0.52}Al_{0.48}As$ epilayers with a widths of 6/4.7/12.6/4.7 Å for the sample A, 5/4.9/13.2/4.9 Å for the sample B and 6.5/4.6/12.3/4.6 Å for the sample C. All the studied heterostructures also had a 30 nm thick $In_{0.52}Al_{0.48}As$ and 5 nm thick InP cap layers.

The energy spectrum calculation of SLs under investigation was performed using transfer matrix method. The material parameters used were taken from Ref. [3]. The presence of stresses in lattice-mismatched with substrate $In_{0.6}Ga_{0.4}As$ layers was taken into account by the change in its bandgap value compared to the unstrained one according to Ref. [4].

A continuous-wave Nd:YLF solid state laser ($\lambda = 527$ nm) was used for the optical excitation of the samples, mounted in a low-vibrational closed cycle optical cryostat. Laser radiation was focused on the sample surface using 5× microlense, which was also used to collect the PL of the samples. PL spectra were investigated with a grating monochromator supplemented with a thermoelectrically cooled InGaAs array.

Results and Discussion

The obtained PL spectra of the samples at the temperature $T = 5$ K are presented in Fig. 1, *a*. They look similar and are consisted of one dominant emission band, which is associated with the interband radiative electron-hole recombination in the middle SL since its spectral position is close to the calculated value (it is shown with dashed lines in Fig. 1, *a* for each sample). Temperature increase up to the 300 K leads to the SL emission band shift towards 1.26−1.29 μm (Fig. 1, *a*) due to

the temperature change in bandgap values of heterostructure epilayers. At $T = 300$ K an additional emission band close to the 1.03 eV also appears in the PL spectra of all the samples, attributed to the luminescence from the 1st and 3rd SLs surrounding the central SL of the structures.
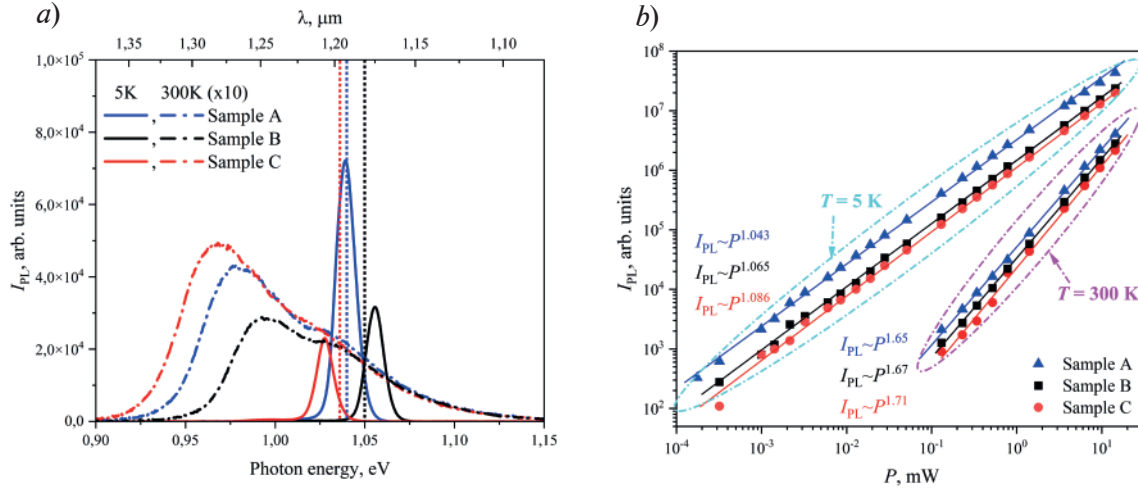
Fig. 1. PL spectra of the samples measured at the pumping power $P = 0.34$ mW and $T = 5$ K (solid curves) and $T = 300$ K (dash-dotted curves) (*a*). Dashed lines show calculated values of optical interband transitions in SLs at the $T = 5$ K. Dependencies of the integrated PL intensity I_{PL} on the pumping power P at the $T = 5$ K and $T = 300$ K and approximating curves P^k (*b*)

Fig. 1, *b* shows the dependencies of the integrated PL intensity on the optical pumping power and their approximation by the power function for all three heterostructures. The exponent of the power function k is close to 1 for all samples at the temperature of 5 K, which indicates the predominance of the radiative recombination processes. At the $T = 300$ K the exponent k varies in the range ~1.6–1.7, which shows that nonradiative recombination via defects also takes place. Temperature increase from 5 K to 300 K also results in decrease in integrated PL intensity for all the samples (Fig. 1, *b*), that we also associate with an increase of nonradiative recombination in SLs at high temperatures. Moreover, increase in the crystal lattice temperature above 75 K leads to a redshift of peak position of the middle SL emission band as it is presented in Fig. 2.

In the temperature range of 75–300 K the experimental data are well approximated within the Varshni model, describing the temperature induced change in bandgap values of epilayers forming SLs. Vertically shifted theoretical dependencies of unstrained $In_{0.6}Ga_{0.4}As$ epilayer energy gap on the temperature are shown in Fig. 2. However, below $T = 75$ K a discrepancy between experimental and theoretical data is obtained and a slight redshift of PL peak position of the SL with the temperature decrease is observed, that can be associated with several reasons.
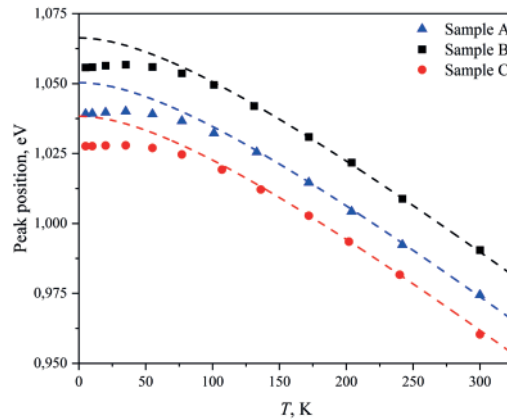
Fig. 2. Temperature dependencies of the photon energies (symbols), corresponded to the peak position of middle SL emission band, measured at the $P = 0.34$ mW. Dashed curves show approximation of the experimental data with the Varshni model with parameters of the unstrained $In_{0.6}Ga_{0.4}As$ epilayer

Firstly, excitonic recombination should dominate at low lattice temperatures over the direct electron-hole recombination. Secondly, such a blueshift of PL peak at low lattice temperatures was also attributed to the exciton population states redistribution due to the potential fluctuations [5].

Conclusion

The PL spectra of short-period SLs are investigated in a wide range of pumping powers and temperatures. The emission bands associated with an optical transitions of charge carriers in SLs and buffer layers of heterostructures are revealed in the spectra. According to the analysis of integrated PL intensity on the pumping power at $T = 5$ K the domination of radiative recombination mechanism is observed. Spectral position of the luminescence peak is controlled in a relatively wide range by changing the SL composition. At room temperature, a required wavelength of about 1.3 μm is achieved.

Acknowledgments

REFERENCES

1. **Rochas S.S., Kovach Y.N., Kopytov P.E., Kremleva A.V., Egorov A.Yu.,** Review on single-mode vertical-cavity surface-emitting lasers for high-speed data transfer, Reviews on Advanced Materials and Technologies. 4 (4) (2022) 1–16.

2. **Karachinsky L.Ya., Novikov I.I., Babichev A.V., Gladyshev A.G., Kolodeznyi E.S., Rochas S.S., Kurochkin A.S., Bobretsova Yu.K., Klimov A.A., Denisov D.V., Voropaev K.O., Ionov A.S.,** Bougrov V.E., Egorov A.Yu., Optical gain in laser heterostructures with an active area based on an InGaAs/InGaAlAs superlattice, Optics and Spectroscopy. 127 (6) (2019) 1053–1056.

3. **Vurgaftman I., Meyer J.R., Ram-Mohan L.R.,** Band parameters for III-V compound semiconductors and their alloys, Journal of Applied Physics. 89 (11) (2001) 5815–5875.

4. **Zhukov A.E., Egorov A.Yu., Ustinov V.M., Tsatsul'nikov A.F., Maksimov M.V., Faleev N.N., Kop'ev P.S.,** Influence of mismatch of the lattice parameters on the structural, optical, and transport properties of InGaAs layers grown by molecular beam epitaxy on InP(100) substrates, Semiconductors. 31 (1) (1997) 15–18.

5. **Lopes E.M., Duarte J.L., Dias I.F.L., Pocas L.C., Laureto E., Harmand J.C.,** Photoluminescence properties of a Si doped InGaAs/InGaAlAs superlattice, Journal of Physics: Condensed Matter. 19 (2007) 086207.

THE AUTHORS

VOITOVICH Veronica I.
vivoytovich@edu.hse.ru
ORCID: 0009-0004-1245-1391

ANDRYUSHKIN Vladislav V.
vvandriushkin@itmo.ru
ORCID: 0000-0002-7471-8627

PAPYLEV Denis S.
dspapylev@itmo.ru
ORCID: 0009-0001-3683-5558

KOPYTOV Pavel E.
kopytovpe@itmo.ru
ORCID: 0009-0008-8345-461X

MAKHOV Ivan S.
makhoviv@gmail.com
ORCID: 0000-0003-4527-1958

ZHUKOV Alexey E.
aezhukov@hse.ru
ORCID: 0000-0002-4579-0718

KRYZHANOVSKAYA Natalia V.
nkryzhanovskaya@hse.ru
ORCID: 0000-0002-4945-9803

Composition and properties of porous silicon nanoparticles with deposited cinnarizine

A.S. Lenshin [1], Yu.A. Polkovnikova [1], O.V. Chernousova [2],

V.E. Frolova [1] ✉, E.P. Domashevskaya [1]

[1] Voronezh State University, Voronezh, Russia;

[2] Voronezh State University of Engineering Technology, Voronezh, Russia

✉ ternovaya@phys.vsu.ru

Abstract. As a result of our work samples of nanopowders of porous silicon with the deposited cinnarizine were obtained and technique of the chemical deposition of cinnarizine into the porous layer was elaborated. The obtained structures of porous silicon can be used for delivery of various therapeutic agents starting from small molecules of the preparations up to the large peptides/protein therapeutic agents while controlling composition of the surface and morphology of the porous layer. Nanopowder of porous silicon was obtained by mechanical and ultrasound grinding of the porous silicon wafers. Using transmission electron microscopy, infrared and ultraviolet spectroscopy morphology and composition of the porous silicon samples were studied. According to the results of transmission electron microscopy (TEM) a presence of both crystalline and amorphous phases was determined. Chemical composition and types of the bonds in the porous silicon layer was studied according to the data of infrared (IR) spectroscopy. The data on ultraviolet (UV) allowed to determine the energy of the possible direct transitions in nanostructures. Adsorption and desorption processes in nanostructures were studied.

Keywords: mesoporous silicon, nanopowders, nanopowders, spectroscopy, cinnarizine, systems of drug delivery

Состав и свойства наночастиц пористого кремния с осажденным циннаризином

А.С. Леньшин [1], Ю.А. Полковникова [1], О.В. Черноусова [2],

В.Е. Фролова [1] ✉, Э.П. Домашевская [1]

[1] Воронежский государственный университет, г. Воронеж, Россия;

[2] Воронежский государственный университет инженерных технологий, г. Воронеж, Россия

✉ ternovaya@phys.vsu.ru

Аннотация. В результате работы были получены образцы нанопорошков пористого кремния с осажденным циннаризином и отработана методика химического осаждения циннаризина в пористый слой. Полученные структуры пористого кремния могут

быть использованы для доставки различных терапевтических средств, от малых молекул препаратов до больших пептидов/белковых терапевтических препаратов при управлении составом поверхности и морфологией его пористого слоя. Нанопорошок пористого кремния был получен механическим и ультразвуковым измельчением пластин пористого кремния. Методами просвечивающей электронной спектроскопии, инфракрасной спектроскопии и ультрафиолетовой спектроскопии исследованы морфология и состав образцов пористого кремния. По результатам исследований просвечивающей электронной микроскопии определили присутствие в образцах как кристаллической, так и аморфной фазы. Химический состав и типы связей в слое пористого кремния был определен по данным инфракрасной спектроскопии. По данным ультрафиолетовой спектроскопии были определены энергии возможных прямых переходов в наноструктурах. Исследованы процессы адсорбции и десорбции на наноструктурах.

Ключевые слова: мезопористый кремний, нанопорошки, наночастицы, спектроскопия, циннаризин, системы доставки лекарств

Introduction

Now one of the most prospective areas for the application of porous silicon proves to be biomedicine. Therefore an interest to porous silicon from the viewpoint of biomedicine problems is due to its good biocompatibility and high specific surface as well to the possibility of modification of the surface chemical properties and controlling of the porous layer morphology. Porous silicon can be well used for the delivery of various therapeutic agents starting from the small molecules of the drugs up to the large peptides/protein preparations while controlling surface composition and morphology of the porous layer. Drug preparations made on the basis of silicon nanostructures show the main properties advanced to systems of directed drug delivery: a slight release of the drug agent after attainment of the predetermined goal, as well a possibility of paranteral dosing, in particular, intravenous injection. Therefore, an experience in the use neuroprotective and neurotrophic preparation of cinnarizine for the patients with neurologic disorders in post-Covid period is of a great interest [1−4]. Goal of the work is a formation of the structures of porous silicon − cinnarizine type and the study of their features, investigations of its composition and sorption-desorption process of cinnarizine from the surface of porous silicon.

Materials and Methods

Samples of porous silicon were obtained by anodic electrochemical etching of single-crystalline silicon with n-type conductivity having specific resistivity of 0.2 Ohm·cm in the alcoholic solution of hydrofluoric acid with an addition of hydrogen peroxide. Nanopowder of porous silicon was obtained first by mechanical separation of the porous layer with its further grinding in the alcohol solution with the use of ultrasound for 10 minutes [4].

Morphology and microstructure of the samples were studied by transmission electron microscopy with the use of transmission electron microscope Libra120 (CarlZeiss, Germany, CKPNO VSU). Chemical composition of the samples was determined with IR-Fourier spectrometer Vertex Bruker 70 with an attachment for the measurement of absorption/transmission in thin-film samples. Optical properties of the samples were investigated by ultraviolet spectroscopy in the range of 190−190 nm with the use of spectrometer LAMBDA 650 produced by Perkin Elmer company.

To study optical properties of the samples in the UV-range specially elaborated approach method was employed applying a technique for surveying of reflection spectra [5]. This technique makes it possible to obtain information concerning the films and layers deposited/formed on the optically denser and bulk substrates. In order to study the features of sorption/desorption of cinnarizine to/from the surface of porous silicon the wafers of silicon with por-Si layers were placed in 0.1 M solution of HCl, containing 0.5 mg/cm^3 of cinnarizine. The volume of the media was 100 cm^3. Tests of dialyzate (5 ml) were sampled every 30 minutes. In order to determine cinnarizine content spectrophotometry technique in the UV-range (254 ± 2 nm) was applied with the use of spectrophotometer SF-2000. Cinnarizine concentration in solutions was determined by the calibrating curve. Release of cinnarizine from the surface was studied by dialysis technique applying semi-permeable cellophane membrane also using spectrophotometer technique.

Results and Discussion

Figure 1 represents TEM-image and electron-diffraction pattern of the obtained porous silicon powder. To make phase analysis with the use of external standard in order to analyze electron-diffraction pattern previously obtained value of the device constant was used.

Results of TEM showed the presence of as crystalline (points at the electron-diffraction pattern) as amorphous phase of silicon (rings at the electron-diffraction pattern) in the powder. Size of the particles according to TEM data was of ~ 5 nm.
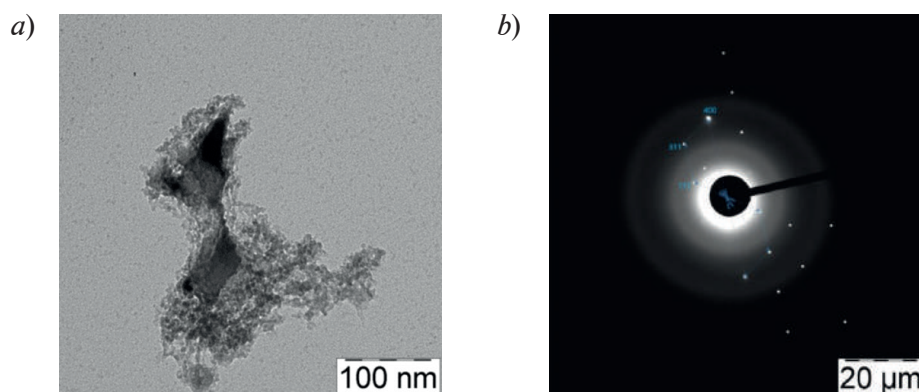
Fig.1. TEM image of the porous silicon powder (*a*) and electron-diffraction pattern of the porous silicon powder (*b*)

IR-spectra of the samples with the deposited cinnarizine are presented in Fig. 2. Comparative analysis of IR-spectra for the samples of original porous silicon and those ones after cinnarizine deposition demonstrated the presence of cinnarizine on the surface of porous silicon. Position of the distinctions in IR-spectra for the deposited drug agents was determined with the use of AIST database: Spectral Database for Organic Compounds, SDBS [6].
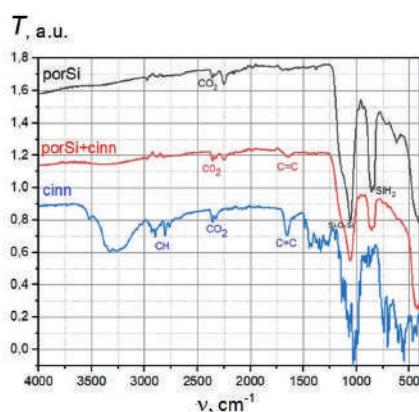
Fig.2. IR transmission spectra of porous silicon with the deposited cinnarizine and reference samples: cinnarizine powder and original porous silicon

While comparing spectrum of the obtained sample with the standard spectrum of cinnarizine it was found that after cinnarizine deposition into porous silicon new peaks appeared in the spectrum, corresponding to those ones of cinnarizine: 2959 cm^{-1} and 2936 cm^{-1}, corresponding to the valence vibrations of C−H bond in alicyclic compounds; 1597 cm^{-1}, corresponding to the valence vibrations of C=C bond in aromatic ring, 1134 cm^{-1}, corresponding to the valence vibrations of C−N bond; 999 cm^{-1} and 962 cm^{-1}, corresponding to the valence vibrations of =CH bond. Note that in the spectra of all the samples one can clearly observe the bands characteristic of porous silicon Si-Si (616 cm^{-1}), Si-O-Si (1060 cm^{-1}), Si-H$_x$ (805 cm^{-1}) [7].

In order to know the mechanism of optical absorption in porous layers formed by electrochemical etching with the use of the software package OPUS Bruker and taking into account Lambert-Bugger formula:

$$T = \exp[-D],$$

where T is transmission, D − optical density, transmission-reflection spectra were reconstructed into absorption spectra. Dependences (D·hν)^2 on the quanta energy for single-crystalline Si are presented in Fig. 3, as well those ones for porous silicon samples; the latter ones were calculated from the spectra of specular reflection with the use of of Kramers-Kronig relations [8]. Graphical analysis allowed to reveal separate parts with linear dependence of (D·hν)^2 on the quanta energy. This can indicate at the presence of the direct allowed transition in this spectral range (Fig. 3). Linear extrapolation of these parts in the spectra to the value makes it possible to determine the energy of direct transitions which are characteristic for these samples.
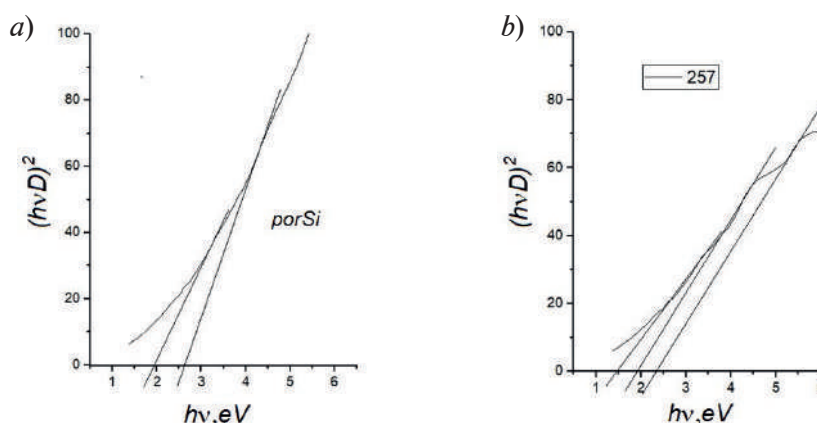
Fig.3. Dependences of (D·hν)^2 on the quanta energy for original porous silicon (*a*) and porous silicon with the deposited cinnarizine (*b*)

Applying tangents concept one can determine the following possible direct transitions in the range of 2.3−2.5 eV for light powders, corresponding to nanocrystals with the size of ~2 nm, according to [9], and to transition of 1.8−2 eV, corresponding to the particles with the size of ~3 nm, for more heavy fractions of mesoporous silicon nanopowders. Basing on the obtained dependences for the samples with the deposited cinnarizine one can also determine direct transition in the range of 1.5 eV, which can be associated with the features of cinnarizine optical absorption, or formation of its bonds with silicon, or either with more large silicon nanocrystals.

During the study of cinnarizine adsorption on the surface of porous silicon (Fig. 4) it was found that for the time of adsorption equal to 30 minutes cinnarizine concentration on the wafers of meso- and macroporous silicon was of 1.1 mg/cm^3 (Fig. 4). While increase of the adsorption time cinnarizine concentration was slightly reduced up to 1.00 mg/cm^3, respectively. Thus, the optimal time for cinnarizine adsorption is of 30 minutes.

While cinnarizine desorption from the surface of silicon wafers with por-Si layer it was determined that for 45 minutes of the experiment cinnarizine concentration in the hydrochloric acid medium of 0.1 M concentration equal to 0.70 mg/cm^3 (Fig. 4, *b*). The obtained results showed the availability of the mesoporous silicon usage for the preparation of the carriers drug agents with a durable action.

a) *b)*
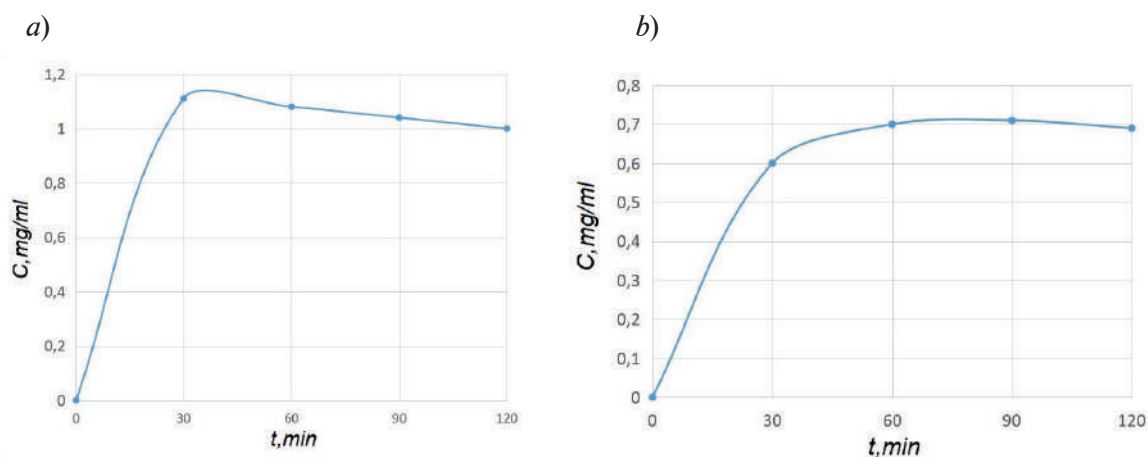
Fig. 4. Dependence of cinnarizine concentration on: (*a*) the time of deposition on the surface of porous silicon and (*b*) on the time of desorption from the surface of porous silicon

Conclusion

As a result of the performed investigations samples of the porous silicon nanopowders with a diameter of less than 5 nm and the deposited cinnarizine were obtained in the work. Data of the transmission electron microscopy helped us to determine a presence of both crystalline and amorphous phase in the sample. Using infrared spectroscopy chemical composition of the porous layer was determined as well as the types of bonds in this layer. It was shown that Si-O, Si-H$_x$, Si-OH and Si-Si bonds are present in the porous layer as well those ones characteristic of cinnarizine. According to UV-spectroscopy possible direct transitions were determined with the energy of 1.8 eV and 2 .3 eV for the original porous silicon and the additional transition at 1.5 eV for the sample with the deposited cinnarizine. It was ascertained that cinnarizine on the surface of porous silicon is most efficiently sorbed and desorbed for the time of 30−45 minutes.

Acknowledgments

REFERENCES

1. **Lenshin A.S., Polkovnikova Yu.A., Seredin P.V.,** Study of the deposition process of vinpocetine on the surface of porous silicon, Results in Physics. 6 (2016) 337−338.

2. **Polkovnikova Yu.A., Lenshin A.S., Seredin P.V., Minakov D.A.,** Nanoparticles with neurotropic drug agents on the basis of porous silicon, Inorganic materials. 53 (5) (2017) 479−485.

3. **Scholtz A.W., Hahn A., Stefflova B., Medzhidieva D., Ryazantsev S.V., Paschinin A., Kunelskaya N., Schumacher K., Weisshaar G.,** Efficacy and safety of a fixed combination of cinnarizine 20 mg and dimenhydrinate 40 mg vs betahistine dihydrochloride 16 mg in pa-tients with peripheral vestibular vertigo: a pro-spective, multinational, multicenter, double-blind, randomized, non-inferiority clinical trial, Clin Drug investing. 39 (11) (2019) 1045–1056.

4. **Lenshin A.S., Kashkarov V.M., Goloshchapov D.L., Seredin P.V., Polumestnaya K.A., Maraeva E.V., Soldatenko S.A., Yurakov Yu.A., Domashevskaya E.P.,** Composition and reactivity of porous silicon nanopowders, Inorganic materials. 48 (10) (2012) 1091.

5. **Lenshin A.S., Seredin P.V., Belorus A.O.,** Investigations of porous silicon layers and nanopowders by X-ray diffraction and ultraviolet spectroscopy, Condensed matter and interphase boundaries. 19 (4) (2017) 529−535.

6. Spectral Database for Organic Compounds SDBS. https://sdbs.db.aist.go.jp/

7. **Tolstoy V.P., Chernyshova I.V., Skryshevsky V.A.,** Handbook of Infrared Spectroscopy of Ultrathin Films. N.Y.:John Wiley & Sons Inc. (2003) 710.

8. **Uhanov Ju.I.,** Optical Properties of Semiconductors, Nauka publ. (1977) 366 (in Russian).
9. **Ledoux G., Guillois O., Porterat D., Reynaud C.,** Phys. Rev. B. 62 (23) (2000) 15943−15951.

THE AUTHORS

LENSHIN Aleksandr S.
lenshinas@mail.ru
ORCID: 0000-0002-1939-253X

FROLOVA Vera E.
ternovaya@phys.vsu.ru
ORCID: 0009-0000-2880-8958

POLKOVNIKOVA Yulia A.
juli-polk@mail.ru
ORCID: 0000-0003-0123-9526

DOMASHEVSKAYA Evelina P.
ftt@phys.vsu.ru
ORCID: 0000-0002-6354-4799

CHERNOUSOVA Olga V.
byolval@mail.ru
ORCID: 0000-0002-8198-574X

Enhanced optical performance of FAPbBr$_3$-MOF composite films

S.V. Pozdniakov [1, 2] ✉, E.D. Matveeva [3], S. Li [2],

M.A. Sandzhieva [1], S.V. Makarov [1, 2]

[1] ITMO University, St. Petersburg, Russia;

[2] Harbin Engineering University, Harbin, China;

[3] Peter the Great St. Petersburg Polytechnic University, St. Petersburg, Russia

✉ stepan.pozdnyakov@metalab.ifmo.ru

Abstract. Metal halide perovskite nanocrystals have emerged as excellent candidate materials for various optoelectronic applications due to their distinguished optoelectronic properties. However, suffering from instability under environmental conditions such as humidity, temperature and ultraviolet radiation restricts its further development and larger-scale application. In this study, we present a one-step method for fabricating composite thin films of formamidinium lead bromide and a lead-based metal-organic framework with enhanced stability. Meanwhile, the obtained composite films exhibited a low amplified spontaneous emission threshold of 12.3 μJ·cm^{-2} enhancing their potential for efficient optoelectronic applications, including light-emitting devices and lasers.

Keywords: perovskite, metal-organic framework, composites, enhanced spontaneous emission

Улучшенные оптические характеристики композитных пленок FAPbBr$_3$-MOF

С.В. Поздняков [1, 2] ✉, Е.Д. Матвеева [3], Ш. Ли [2],

М.А. Санджиева [1], С.В. Макаров [1, 2]

[1] Университет ИТМО, Санкт-Петербург, Россия;

[2] Харбинский инженерный университет, Циндао, Китай;

[3] Санкт-Петербургский политехнический университет Петра Великого,
Санкт-Петербург, Россия

✉ stepan.pozdnyakov@metalab.ifmo.ru

Аннотация. Нанокристаллы металлогалогенидных перовскитов стали отличными материалами-кандидатами для различных применений в оптоэлектронике благодаря своим выдающимся оптоэлектронным свойствам. Однако нестабильность в условиях

окружающей среды, таких как влажность, температура и ультрафиолетовое излучение, ограничивает их дальнейшую разработку и широкомасштабное применение. В этом исследовании мы представляем композитные тонкие пленки перовскита FAPbBr3 и металлоорганического каркаса на основе свинца с повышенной стабильностью, полученные одноэтапным методом. При этом полученные композитные пленки продемонстрировали низкий порог усиленного спонтанного излучения с пороговой плотностью энергии возбуждения 12,3 мкДж·см$^{-2}$, что свидетельствует об их высоком потенциале для эффективного применения в оптоэлектронике, включая светоизлучающие устройства и лазеры.

Ключевые слова: перовскит, металлорганический каркас, композитные материалы, усиленное спонтанное излучение

Introduction

Metal-halide perovskite nanocrystals (MPNCs) based on lead halides exhibit exceptional optoelectronic properties, such as high absorption coefficients, high photoluminescence quantum yields, tunable band gaps, and defect tolerance [1]. These characteristics make them promising candidates for various optoelectronic applications, including light-emitting diodes and lasers. However, due to the ionic structure, halides perovskites are unstable under the influence of external influences such as high temperature, air and ultraviolet radiation.

To address the stability issue, researchers vary the composition of the elements included in the ABX_3 perovskite structure (A is an organic or inorganic cation, B is a divalent metal, X is a halide anion) or use ligands, polymer materials, or metal-organic frameworks [2–4]. Metal-organic frameworks are a class of compounds in which metals and organic ligands form a crystalline structure called a framework [3, 4].

In this work, we focused on the recombination dynamics and amplified spontaneous emission (ASE) characteristics of $FAPbBr_3$ (FA- $CH(NH_2)_2$, formamidinium) by incorporating it into a lead based metal-organic framework constructed with trimesic acid (Pb-MOF). Previous studies have demonstrated improved perovskite stability using Pb-MOF and a two-step method for film fabrication [3, 4]. In contrast, we developed a one-step fabrication approach for $FAPbBr_3$-MOF composite thin films, enabling a simplified and faster preparation process. This approach yielded a record-low ASE threshold for $FAPbBr_3$ (12.3 $\mu J \cdot cm^{-2}$), which we were able to rationalize by examining the underlying recombination mechanisms. A Low ASE threshold is important for photonic applications, as it enables the development of devices with higher efficiency and improved operational stability.

Materials and Methods

Materials. The following materials were used in experiments: Lead Nitrate ($Pb(NO_3)_2$, 99.7%, LenReaktiv), trimesic acid (1,3,5-H_3BTC, 95%, Sigma-Aldrich), Acetic acid (CH_3COOH, 93%, ECOS), dimethyl sulfoxide (DMSO, 99%, ECOS), formamidinium bromide (FABr, >99.99%, Dyesol).

Methods. Pb-MOF was synthesized using a sonochemical method [5]. The obtained Pb-MOF and FABr were dissolved in anhydrous dimethylsulfoxide (DMSO) with the addition of methylammonium acetate (MAAc). The solution was stirred for 5 min (3500 rpm) using vortex MSV-3500 BioSan. The resulting solution was used to fabricate $FAPbBr_3$-MOF composite

thin films via spin-coating: first at 3,000 rpm for 90 seconds, then at 5,000 rpm for 10 seconds, followed by annealing at 80 °C for 10 minutes.

The morphology of the synthesized films was analyzed using a Zeiss LIBRA 200FE transmission electron microscope (TEM) and a scanning probe microscope AIST-NT SPM SmartSPM™−1000.

Optical measurements were performed using an Antaus Ytterbium femtosecond fiber laser operating at a repetition rate of 10 kHz and a wavelength of 343 nm. Time-resolved photoluminescence (TRPL) was measured using a single-photon avalanche diode detector (SPAD PDM, Micro Photon Devices). Photoluminescence spectra were recorded with a QE Pro fiber-optic spectrometer.

The ABC model (equation 1) was used to approximate the decay curves [6].

$$\frac{dn}{dt} = -An - Bn^2 - Cn^3.$$ (1)

The term A is responsible for trap-assisted recombination, B for bimolecular recombination, and C for Auger recombination. At low fluence, Auger recombination does not contribute to charge carrier recombination [6]. Thus, the normalized PL (equation 2) decay curve exhibits bimolecular behavior and can be approximated by the following equation:

$$n(t) = \frac{An \cdot \exp(-At)}{A + Bn(1 - \exp(-At))} + \text{const},$$ (2)

where n is the initial charge carrier density. The initial charge carrier density was calculated using the following equation:

$$n = F \cdot Abs,$$ (3)

where F is the fluence and Abs is the fraction of incident photons that are absorbed. Abs is calculated as:

$$Abs = (1 - R) \cdot \left[1 - \exp(-ad) \right],$$ (4)

d is the thickness of the film and a is the attenuation coefficient.

Results and Discussion

The resulting FAPbBr$_3$-MOF composite film has a low surface roughness of 0.99 nanometers and a thickness of 116 nanometers (Fig. 1, a). The composition of FAPbBr$_3$-MOF composite films was confirmed by X-ray diffraction analysis (XRD). The presence of the cubic Pm−3m phase is indicated by strong peaks at 14.8 degrees (100) and 29.8 (200) (Fig. 1, b), along with weaker peaks at 20.9 (110) and 33.8 (210) [7]. Peaks corresponding to Pb-MOF also confirm the composite nature of the films [5]. Transmission electron microscopy (TEM) revealed encapsulation of perovskite within the Pb-MOF matrix and showed an average FAPbBr$_3$ nanoparticle size of 11.6 nm (Fig. 1, c).
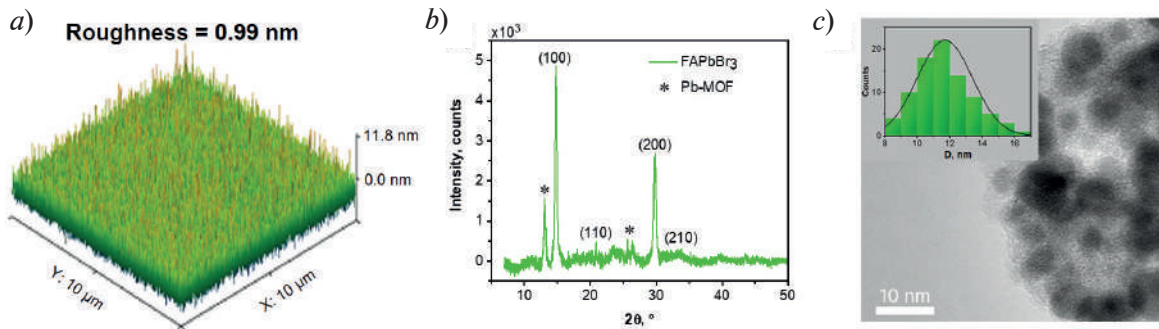
Fig. 1. AFM image of FAPbBr$_3$-MOF film (a), XRD analysis of FAPbBr$_3$-MOF (b), TEM analysis of FAPbBr$_3$-MOF (c). Inset in (c) is a histogram of the NCs size distribution

The photoluminescence (PL) peak of the film is at 530.1 nm with a full width at half maximum (FWHM) is 24.3 nm (Fig. 2, *a*) also a similar peak position was confirmed by studying the absorption spectrum of FAPbBr$_3$-MOF (532.5 nm). For the subsequent analysis of the optical properties of our film, we investigated the dependence of the photoluminescence quantum yield on the increasing power density (Fig. 2, *c*). The best PLQY is 43% at a power density of 993 mW·cm^{-2}, and the growing dependence of PLQY at an increasing power density indicates high film quality, as well as a greater contribution of radiative processes relative to non-radiative [8]. To study the origin of the recombination process in more detail, we performed time-resolved photoluminescence (TRPL) measurements, as shown in Fig. 2, *d*. TRPL measurements showed that the monomolecular (*A*, non-radiative) and bimolecular (*B*, radiative) recombination coefficients increased from $A = 2.4 \cdot 10^6$ s^{-1} and $Bn = 9.4 \cdot 10^6$ s^{-1} at 1.3 μJ·cm^{-2} to $A = 18.7 \cdot 10^6$ s^{-1} and $Bn = 6.5 \cdot 10^8$ s^{-1} at 10.4 μJ·cm^{-2} (Table). This enhancement of radiative recombination and acceleration of carrier dynamics at higher fluence are beneficial for ASE, as these effects support faster population inversion and gain buildup. As a result, PL spectra evolution under increasing pump fluence revealed an ASE threshold of 12.3 μJ·cm^{-2} (Fig. 2, *e*, *f*), which is lower than previously reported [9], demonstrating the suitability of FAPbBr$_3$-MOF films for integration into next-generation low-threshold laser systems and other light-emitting applications.
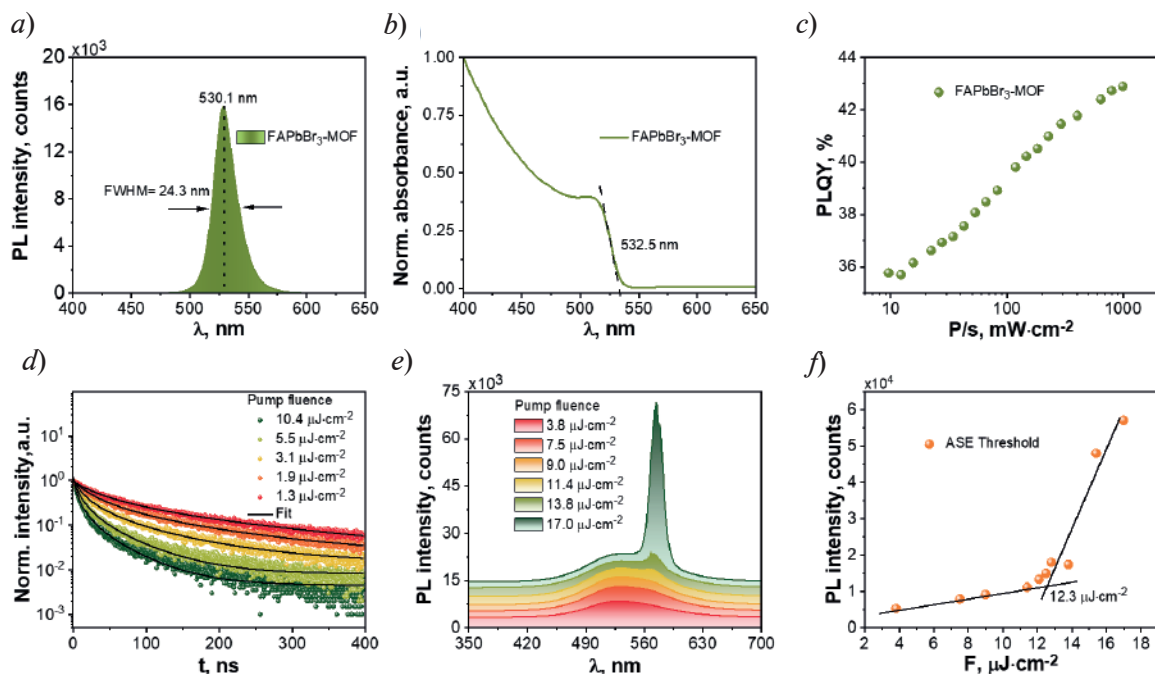
Fig. 2. Photoluminescence spectrum of FAPbBr$_3$-MOF (*a*), Normalized absorbance spectrum of FAPbBr$_3$-MOF (*b*), Dependence of PLQY on the power density (*c*), decay curves of FAPbBr$_3$-MOF under increasing pump fluence (*d*), evolution of the PL spectra of the FAPbBr$_3$-MOF films under increasing pump fluence (*e*), ASE threshold of FAPbBr$_3$-MOF (*f*)

Table

Analysis of decay curves of FAPbBr$_3$-MOF film

Pump fluence, μJ·cm^{-2}	n, cm^{-3}	A, s^{-1}	Bn, s^{-1}
10.4	$3.3 \cdot 10^{18}$	$18.7 \cdot 10^6$	$6.5 \cdot 10^8$
5.5	$1.7 \cdot 10^{18}$	$16.0 \cdot 10^6$	$2.0 \cdot 10^8$
3.1	$9.6 \cdot 10^{17}$	$8.1 \cdot 10^6$	$6.5 \cdot 10^7$
1.9	$5.9 \cdot 10^{17}$	$4.7 \cdot 10^6$	$2.2 \cdot 10^7$
1.3	$4.0 \cdot 10^{17}$	$2.4 \cdot 10^6$	$9.4 \cdot 10^6$

Conclusion

We developed a simple one-step method for fabricating FAPbBr$_3$-MOF composite thin films with improved structural stability and promising optical properties. The encapsulation of Pb-MOF ensured the formation of a stable composite matrix, while the films demonstrated efficient radiative recombination and a low ASE threshold (12.3 μJ·cm^{-2}), making them suitable for photonic applications.

REFERENCES

1. **Manser J.S., Christians J.A., Kamat P.V.,** Intriguing optoelectronic properties of metal halide perovskites, Chemical reviews. 116 (21) (2016) 12956−13008.

2. **Zhou W., Pan T., Ning Z.,** Strategies for enhancing the stability of metal halide perovskite towards robust solar cells, Science China Materials. 65 (12) (2022) 3190−3201.

3. **Tsai H., et al.,** Bright and stable light-emitting diodes made with perovskite nanocrystals stabilized in metal−organic frameworks, Nature photonics. 15 (11) (2021) 843−849.

4. **Zhang C., et al.,** Conversion of invisible metal-organic frameworks to luminescent perovskite nanocrystals for confidential information encryption and decryption, Nature communications. 8 (1) (2017) 1138.

5. **Sadeghzadeh H., Morsali A.,** Sonochemical synthesis and structural characterization of a nano-structure Pb (II) benzentricarboxylate coordination polymer: new precursor to pure phase nanoparticles of Pb (II) oxide, Journal of Coordination Chemistry. 63 (4) (2010) 713−720.

6. **Polushkin A. S., Makarov S.V.,** Recombination of charge carriers in CsPbBr$_3$ films with high quantum photoluminescence efficiency, Zhurnal Tekhnicheskoi Fiziki. 94 (10) (2024) 1633−1638.

7. **Jarmouni N., et al.,** Synthesis of brightly luminescent colloidal formamidinium lead bromide perovskite FAPbBr$_3$ nanoplatelets with tunable emission, MATEC Web of Conferences. EDP Sciences. (348) (2021) 01015.

8. **Li Y. et al.,** Exciton versus free carrier emission: Implications for photoluminescence efficiency and amplified spontaneous emission thresholds in quasi-2D and 3D perovskites, Materials Today. (49) (2021) 35−47.

9. **Chen D., et al.,** Ultralow trap density FAPbBr$_3$ perovskite films for efficient light-emitting diodes and amplified spontaneous emission, Nature Communications. 16 (1) (2025) 2367.

THE AUTHORS

POZDNIAKOV Stepan V.
stepan.pozdnyakov@metalab.ifmo.ru
ORCID: 0000-0002-8319-1492

SANDZHIEVA Maria A.
maria.sandzhieva@metalab.ifmo.ru
ORCID: 0000-0001-9923-3995

MATVEEVA Elizaveta D.
matveeva2.ed@edu.spbstu.ru
ORCID: 0009-0009-5076-6470

MAKAROV Sergei V.
svmakarov@itmo.ru
ORCID: 0000-0002-9257-6183

Li Shixiong
lsx@hrbeu.edu.cn
ORCID: 0009-0009-6600-0592

Analysis of nonlinear susceptibility in ion-exchanged glass

G. Kan [1, 2] ✉, Z. Cui [2], A.N. Terpitskiy [1], S.A. Scherbak [1, 2], V.V. Zhurikhina [2]

[1] Alferov University, St. Petersburg, Russia;

[2] Peter the Great St. Petersburg Polytechnic University, St. Petersburg, Russia

✉ gennadiykang@gmail.com

Abstract. We demonstrate that electric-field-assisted ion-exchange in glass allows one to obtain a structure with close to a step-like concentration and conductivity profiles. Application of DC voltage to the ion-exchanged glass results in charge accumulation. The electric field induces symmetry breaking and provides quadratic optical susceptibility in the glass. Nonlinear optical properties of modified glass are studied using the Maker fringe technique. Particularly, we study the influence of the nonlinear susceptibility tensor components ratio $\chi_{zxx} : \chi_{zzz}$ on resulting characteristics. Comparing modeling and experiments, we deduced the ratio 1:3 which corresponds to Kleinman symmetry of isotropic materials.

Анализ нелинейной восприимчивости в ионообменном стекле

Г. Кан [1, 2] ✉, Ч. Цуй [2], А.Н. Терпицкий [1], С.А. Щербак [1, 2], В.В. Журихина [2]

[1] Академический университет им. Ж.И. Алфёрова РАН, Санкт-Петербург, Россия;

[2] Санкт-Петербургский политехнический университет Петра Великого,

Санкт-Петербург, Россия

✉ gennadiykang@gmail.com

Аннотация. Продемонстрировано, что ионный обмен при помощи электрического поля в стекле позволяет получить структуру с профилями концентрации и проводимости, близкими к ступенчатым. Постоянное напряжение, приложенное к ионообменному стеклу, приводит к накоплению заряда, электрическое поле которого вызывает нарушение симметрии и разрешает квадратичную оптическую нелинейность в стекле. Нелинейно-оптические свойства модифицированного стекла исследованы с использованием метода полос Мейкера. В частности, исследовано влияние соотношения компонент тензора квадратичной оптической восприимчивости $\chi_{zxx} : \chi_{zzz}$ на нелинейно-оптические характеристики. Сравнение экспериментов и моделирования позволило заключить, что это соотношение составляет 1:3, что хорошо соответствует условиям симметрии Клейнмана для изотропных сред.

Introduction

Isotropic nature of glass forbids second order optical nonlinearity, limiting glass functionality in nonlinear optics. Recently, a method was demonstrated [1] that allows for breaking the material's isotropy by applying DC voltage to ion-exchanged (IE) glass at room temperature. During IE, the subsurface layer of glass is enriched with potassium ions, which provides conductivity gradient in the structure. Under applied voltage, nonequilibrium charge can accumulate in the region with conductivity gradient (Maxwell-Wagner effect). Electric field of this charge combined with the third-order nonlinearity induces effective quadratic susceptibility $\hat{\chi}^{(2)}$ due EFISH (Electric-Field Induced Second-Harmonic) phenomenon [2].

Nonlinear optical properties of the material are determined by the $\hat{\chi}^{(2)}$ tensor components, particularly, by their ratio. A powerful tool for evaluating this ratio is the analysis of Maker fringes [3] − dependence of the SH intensity ($I_{2\omega}$) on the angle of incidence of the fundamental wave (θ).

In this study, we analyze the ratio of the tensor components of the second-order nonlinear optical susceptibility of charged field-assisted ion-exchanged (FIE) glass. Advantage of the FIE is that it allows us to obtain a step-like concentration profile, where one can consider known analytical solutions applicable to crystals and thin films. Thus, having determined all parameters except the ratio $\chi_{zxx} : \chi_{zzz}$, we consider a series of Maker fringes with different thicknesses of the nonlinear layer.

Materials and Methods

In our experiments we subjected 1-mm-thick soda-lime glass slide with concentration $C_0 = 6.9 \cdot 10^{27}$ m^{-3} of mobile alkali ions to FIE. On the anodic side of the specimen, we placed a stainless-steel tube with an inner diameter of 16 mm restraining potassium nitrate melt. We use Teflon spacer between the tube and the specimen to prevent any leakage of the melt. Then we placed it in a graphite crucible with glass spacers where cathodic side of the glass contacts with NaNO$_3$ melt. The spacers create a gap filled with the melt, which allows free displacement of sodium ions from the glass by potassium ones. Then, we heated the cell up to 365 °C, applied a DC voltage of $U = 10$ V and registered DC current, which allows to calculate passed charge q_0. After, we cooled down the cell under applied voltage for about 15 min. The charge value allows us to estimate interface depth as $L = q_0/(SeC_0)$ considering full replacement of sodium by potassium, where S is the tube opening and e − electron charge.

For optical measurements we fixed the specimen in motorized rotating platform and irradiated it with a *p*-polarized light beam of a femtosecond laser (wavelength $\lambda = 1.03$ μm). The details of optical setup can be found elsewhere [4].

Results and Discussion

We rewrite analytical expression of Maker fringe [3] as:

$$I_{2\omega} \sim \tilde{\chi}_{\text{eff}}^2 t'^4_\omega T''_{2\omega} \sin^2\left(\frac{1}{2}\Delta kL\right); \tag{1}$$

where $\tilde{\chi}_{\text{eff}}$ − effective nonlinear coefficient (or their combination) corresponding to the geometry of the experiment normalized by χ_{zzz}:

$$\tilde{\chi}_{\mathrm{eff}} = 2\frac{\chi_{zxx}}{\chi_{zzz}}\cos\theta'_{\omega}\sin\theta'_{\omega}\cos\theta'_{2\omega} + \frac{\chi_{zxx}}{\chi_{zzz}}\cos^2\theta'_{\omega}\sin\theta'_{2\omega} + \sin^2\theta'_{\omega}\sin\theta'_{2\omega}; \qquad (2)$$

$t'_{\text{ù}}$ − Fresnel transmission of fundamental p-polarized wave:

$$t'_{\omega} = \frac{2\cos\theta}{n_{\omega}\cos\theta + \cos\theta'_{\omega}}; \qquad (3)$$

$T''_{2\omega}$ − SH transmission determined as [3]:

$$T''_{2\omega} = 2n_{2\omega}\cos\theta'_{2\omega}\frac{\left(n_{\omega}\cos\theta + \cos\theta'_{\omega}\right)\left(n_{2\omega}\cos\theta'_{\omega} + n_{\omega}\cos\theta'_{2\omega}\right)}{\left(n_{2\omega}\cos\theta + \cos\theta'_{2\omega}\right)^3}; \qquad (4)$$

and Δk − wavevector mismatch:

$$\Delta k = \frac{4\pi}{\lambda}\left(n_{2\omega}\cos\theta'_{2\omega} - n_{\omega}\cos\theta'_{\omega}\right), \qquad (5)$$

θ'_{ω}, $\theta'_{2\omega}$ − angle of the propagation of the fundamental and SH waves in glass, defined by Snell's law, refractive index of these waves. For the simulations we use $n_{\omega} = 1.5134$ and $n_{2\omega} = 1.5288$.

Changing $\chi_{zxx} : \chi_{zzz}$ ratio from 1:2 to 1:4 only slightly modifies the shape of the Maker fringe, as illustrated in Fig. 1, a.

Moreover, the influence of $\chi_{zxx} : \chi_{zzz}$ on angular maxima is most noticeable for small thicknesses of the nonlinear layer, becoming negligible when the thickness approaches the coherence length, as shown in Fig. 1, b. Therefore, direct identification of the ratio is challenging, especially
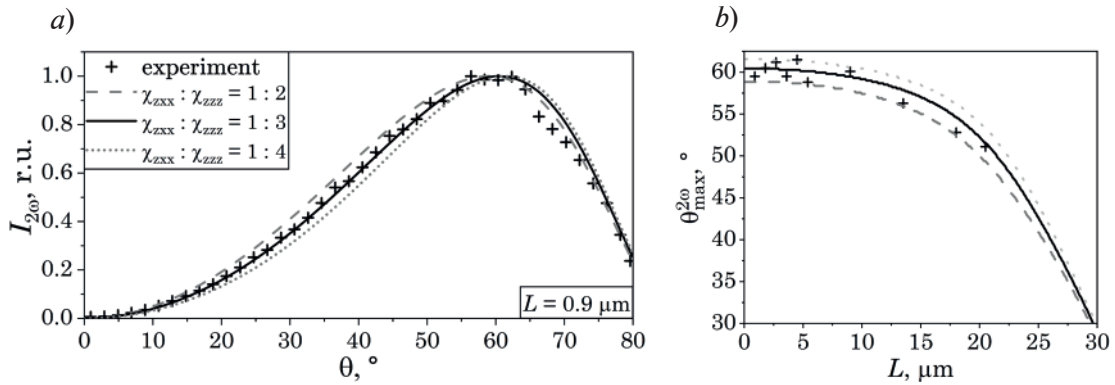
Fig. 1. Simulation of Maker fringe for $L = 0.9$ μm (a) and angle of maximum SH dependence on thickness (b) for different $\chi_{zxx} : \chi_{zzz}$ vs experimental data (crosses)
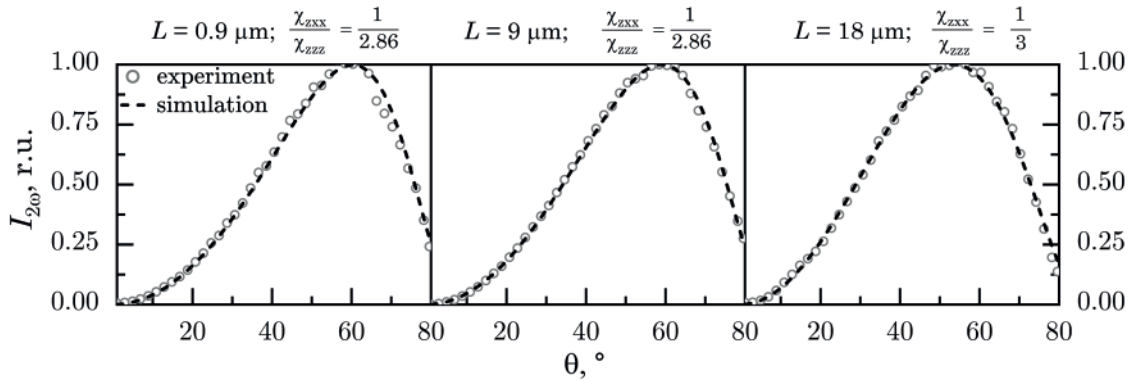
Fig. 2. Experimental data (dots) and simulation with fitted ratio of Maker fringes for $L = 0.9$ μm, 9 μm and 18 μm

for thicknesses close to the coherence length. For more accurate identification of the ratio we consider the ratio $\chi_{zxx} : \chi_{zzz}$ as a fitting parameter and simulate Maker fringes for the specimens different depths of FIE-modified layers. Several results of the fitting are presented in Figure 2.

The average $\chi_{zxx} : \chi_{zzz}$ for 10 specimens with L from 0.9 μm to 20.5 μm was found to be 1:3.1 which is very close to the 1:3 ratio predicted by Kleinman's symmetry condition for isotropic materials [5].

Conclusion

We analyzed the shape of angular dependences of the second harmonic in FIE glass with varying thicknesses of the ion-exchanged layer and ratio $\chi_{zxx} : \chi_{zzz}$. We determined this ratio by fitting, and obtain a value that approximately corresponds to the Kleinman symmetry condition in isotropic media. Thus, we have shown that in polarized ion-exchanged glasses the ratio of nonlinear optical susceptibility components $\chi_{zxx} : \chi_{zzz}$ is confirmed to be 1:3.

Acknowledgments

REFERENCES

1. **Scherbak S., Reshetov I., Zhurikhina V., Lipovskii A.,** Maxwell−Wagner effect and second harmonic generation in gradient structures, Journal of the American Ceramic Society. 107 (2024) 5569−5577.

2. **Kazansky P.G., Kamal A., Russell P.S.J.,** High second-order nonlinearities induced in lead silicate glass by electron-beam irradiation, Optics Letters. 18 (1993) 693−695.

3. **Jerphagnon J., Kurtz S.K.,** Maker Fringes: A Detailed Comparison of Theory and Experiment for Isotropic and Uniaxial Crystals, Journal of Applied Physics. 41 (1970) 1667−1681.

4. **Scherbak S.A., Reshetov I.V., Zhurikhina V.V., Lipovskii A.A.,** Second harmonic generation by surface of poled glasses: modeling and measurement of Maker fringes, St. Petersburg Polytechnical State University Journal. Physics and Mathematics. 14 (3) (2021) 95−113.

5. **Kleinman D.A.,** Theory of Second Harmonic Generation of Light, Physical Review. 128 (1962) 1761−1775.

THE AUTHORS

KAN Gennadiy
gennadiykang@gmail.com
ORCID: 0009-0007-3942-7908

CUI Zhihao
tsuj.ch@edu.spbstu.ru
ORCID: 0009-0009-4341-4346

TERPITSKIY Aleksey N.
terpiczkij@mail.ru
ORCID: 0000-0002-1744-5976

SCHERBAK Sergey A.
sergeygtn@yandex.ru
ORCID: 0000-0002-0507-5621

ZHURIKHINA Valentina V.
zhurihina_vv@spbstu.ru
ORCID: 0000-0003-0685-9409

Capacitive properties of composite electrodes based on polyaniline and nanoporous titanium oxide obtained by plasma-electrolytic oxidation

A.A. Adamovich [1]✉, V.N. Golovanov [1], M.Yu. Makhmud-Akhunov [1],

I.O. Yavtushenko [1], A.A. Solovyev [1], D.S. Bodnarsky [1, 2]

[1] Ulyanovsk State University, Ulyanovsk, Russia;

[2] Joint Stock Company "Ulyanovsk Mechanical Plant", Ulyanovsk, Russia

✉ artem.adamovich@bk.ru

Abstract. The capacitive characteristics of composite electrodes based on nanoporous titanium oxide obtained by plasma electrolytic oxidation are considered. It is shown that the specific capacitance of a multilayer supercapacitor based on formed titanium oxide and polyaniline (PANI) is 10 mF/cm². The resulting oxide layers have a crystalline structure, providing minimal faradaic resistance, which is promising for use in electrochemical double-layer supercapacitors.

Keywords: titanium, electrolyte plasma, nanoporous oxide, polyaniline, supercapacitor

Емкостные свойства композитных электродов на основе полианилина и нанопористого оксида титана, полученного методом плазменно-электролитического оксидирования

А.А. Адамович [1] ✉, В.Н. Голованов [1], М.Ю. Махмуд-Ахунов [1],

И.О. Явтушенко [1], А.А. Соловьёв [1], Д.С. Боднарский [1, 2]

[1] Ульяновский государственный университет, г. Ульяновск, Россия;

[2] АО «Ульяновский механический завод», г. Ульяновск, Россия

✉ artem.adamovich@bk.ru

Аннотация. Рассмотрены емкостные характеристики композитных электродов на основе нанопористого оксида титана, полученного методом плазменно-электролитического оксидирования. Показано, что удельная емкость многослойного суперконденсатора на основе сформированного оксида титана и полианилина (ПАНИ) составляет 10 мФ/см². Полученные оксидные слои имеют кристаллическую структуру, обеспечивая минимальное фарадеевское сопротивление, что является перспективным для использования в электрохимических двухслойных суперконденсаторах.

Introduction

Research and development of high-capacity components and systems are important and rapidly developing areas in modern electronics. To increase the effective area of electrodes of electrochemical capacitors, materials with a highly developed surface are used. Such electrodes are usually formed on the basis of activated carbons [1], carbon nanotubes [2], nanoporous metal oxides [3] and other materials. These materials can significantly increase the specific capacity of devices, improve their energy characteristics and provide a higher charging rate. An important aspect is also ensuring the stability and durability of electrode materials during multiple operating cycles. Modern research is aimed at developing new composite materials, methods for their synthesis and processing, as well as optimizing the structure to achieve maximum efficiency and reliability of high-capacity electrochemical systems. In this paper, the characteristics of supercapacitors based on nanoporous titanium oxide obtained by plasma electrolytic oxidation (PEO) will be considered.

Materials and Methods

Titanium with a purity of 99.7% was used to study the features of plasma electrolytic oxidation (PEO). Porous titanium oxide was obtained by plasma electrolytic treatment in a 1 M aqueous solution of sulfuric acid, the technique is described in [4]. Then, each electrode was chemically coated with a layer of emeraldine form of polyaniline, and a solution of polyvinyl alcohol with 3.4 M orthophosphoric acid served as a layer between the electrodes. The capacitive characteristics of the obtained structures were determined by cyclic voltammetry (potentiostat-galvanostat P-45X) in the range from -0.5 to 0.5 V at potential scan rates from 20 to 100 mV/s. Impedance spectra were recorded in the frequency range from 0.1 Hz to 50 kHz with an amplitude of 50 mV. The EIS Spectrum Analyzer software based on the Levenberg-Marquardt algorithm with amplitude minimization was used for their analysis. The surface morphology of the oxide layers was analyzed using scanning electron microscope (PHENOM PRO-X). A Bruker D2 Phaser diffractometer was used for qualitative and quantitative phase analysis of the samples.

Results and Discussion

The electrolyte used to obtain titanium oxide nanotubes largely determines the characteristics of the structures formed on the metal surface. In this work, an analysis of the structures obtained using an aqueous solution based on sulfuric acid was carried out. A distinctive feature of PEO from conventional oxidation of metals is that when a certain voltage is reached, a breakdown of the screening gas bubbles occurs with the formation of plasma.

The formation of pores (average size ~ 110 nm) in titanium oxide (Fig. 1, *a*) is due to the implementation of extreme conditions during the processing, namely, an increase in the chemical activity of the solution near the anode [4].

The discharges observed visually on the electrode surface move along the surface. Such discharges exist for a rather short time, but this time is sufficient for the polymorphic transformation of the oxide layer from an amorphous state to a crystalline one. This is confirmed by the data of X-ray structural analysis (Fig. 1, *b*).
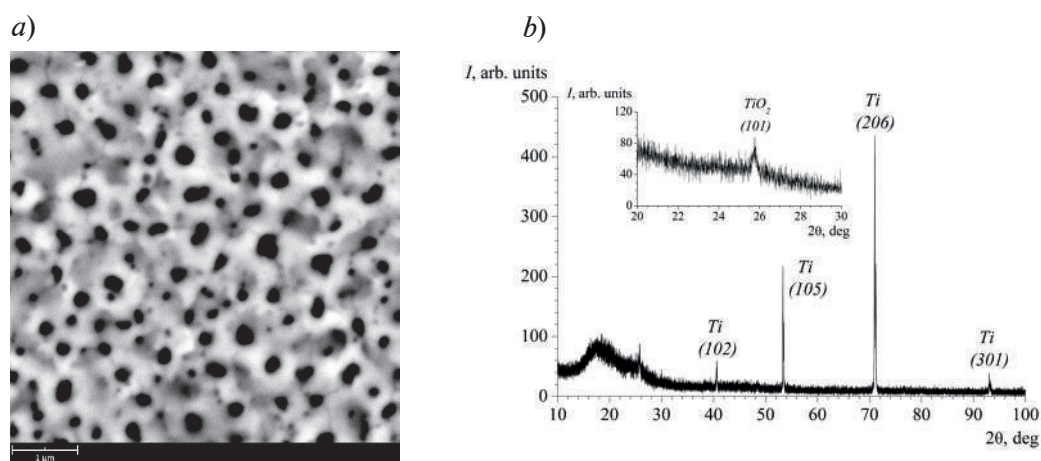
Fig. 1. Characteristics of nanoporous titanium oxide obtained by the PEO method: SEM image of the surface (*a*); diffraction pattern (*b*)

The capacitive properties of the supercapacitor formed on the basis of the obtained electrodes with porous titanium oxide were estimated by cyclic voltammograms, a typical form of which is shown in Fig. 2, *a*. The specific capacitance of the obtained electrodes was ~ 10 mF/cm^2 (at a scanning rate of 20 mV/s). The specific capacitance value of such structures, depending on the degree of modification, can reach ~ 6−7 mF/cm^2 [5].
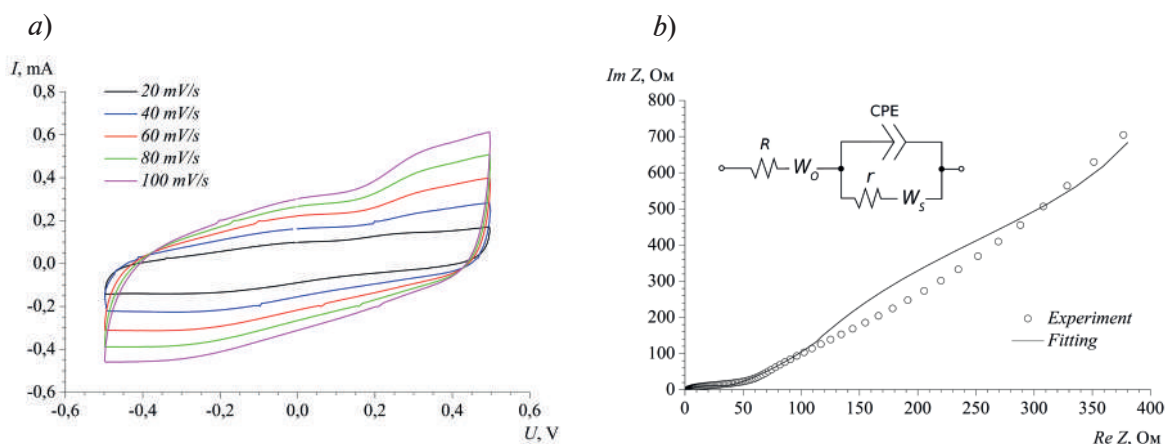
Fig. 2. Capacitive characteristics of the obtained electrodes: cyclic voltammograms (*a*) and electrochemical impedance spectra. The inset shows the equivalent circuit (*b*)

The structural features of the functional layers of the formed multilayer capacitive systems were judged by the impedance spectroscopy data. The Im Z (Re Z) dependencies (Fig. 2, *b*) are typical for capacitors and have sections with a shape close to a semicircle, which characterizes the Faraday resistance value, which is 32 Ohm, which is 6 times less than the electrodes obtained in 0.6 wt. % HF [6]. The end point of the high-frequency region of the obtained impedance spectra is determined by the active resistance R of the systems under consideration, which lies in the range of 1.5 ... 2 Ohm. The nanostructured nature of the electrodes used determines the shape of the impedance in the low-frequency region and is described by a constant-phase element − CPE $(Z_{CPE} = C_\alpha^{-1}(j\omega)^{-\alpha})$. In addition to the surface roughness, diffusion processes occurring in the interelectrode space have a significant effect on the nature of the recorded spectra. To describe these processes, Warburg elements were introduced into the equivalent circuit. Element W_S is characterized by the impedance of finite diffusion with a transmitting boundary, element W_O − is characterized by a reflecting boundary, and $b_{s,o} = \dfrac{d}{\sqrt{D}}$ (d − is the thickness of the Nernst diffusion layer, D − is the ion diffusion coefficient):

$$Z_{W_S} = \frac{W_S}{\sqrt{\omega}}(1-j)\tanh\left(b_S\sqrt{j\omega}\right), \tag{1}$$

$$Z_{W_O} = \frac{W_O}{\sqrt{\omega}}(1-j)\coth\left(b_O\sqrt{j\omega}\right). \tag{2}$$

T a b l e

Equivalent circuit parameters

Parameter	R, Ohm	r, Ohm	C_α, 10^{-5} $s^\alpha\cdot$Ohm^{-1}	α	W_S, Ohm·s$^{-1/2}$	b_s, s$^{-1/2}$	W_O, Ohm·s$^{-1/2}$	b_O, s$^{-1/2}$
Value	1.98	32	6.13	0.65	210	1.43	0.16	0.007

Analysis of the parameters obtained during approximation showed high diffusion permeability (Table) of supercapacitors based on electrodes with nanoporous titanium oxide obtained by the PEO method.

Conclusion

Thus, in this work, nanostructured electrodes based on porous titanium oxide were created by the method of plasma-electrolytic oxidation of titanium. It is shown that the obtained composite electrodes in the supercapacitor structure have a specific capacity of 10 mF/cm^2. The obtained electrodes have a low faradaic resistance (32 Ohm), which is promising for use in electrochemical double-layer supercapacitors.

REFERENCES

1. **Peng Z., Ni J.,** Surface properties and bioactivity of TiO$_2$ nanotube array prepared by two-step anodic oxidation for biomedical applications, Royal Society Open Science. 4 (6) (2019) 181948.

2. **Sibatov R.T., Uchaikin V.V.,** Fractional kinetics of charge carriers in supercapacitors, Handbook of Fractional Calculus with Applications. 8 (2019) 87−118.

3. **Lamberti A., Sacco A., Hidalgo D., Bianco S., Manfredi D., Quaglio M., Pirri C.,** TiO$_2$ Nanotube Array as Efficient Transparent Photoanode in Dye-Sensitized Solar Cell with High Electron Lifetime, Acta Physica Polonica A. 2 (132) (2013) 376−379.

4. **Makhmud-Akhunov M.Y., Adamovich A.A.,** On the Plasma-Electrolytic Formation of Porous Films of Titanium Oxide, Journal of Surface Investigation: X-ray, Synchrotron and Neutron Techniques. 4 (14) (2020) 684−690.

5. **Wu H., Xu C., Xu J., Lu L., Fan Z., Chen X., Li D.,** Enhanced supercapacitance in anodic TiO$_2$ nanotube films by hydrogen plasma treatment, Nanotechnology, 24 (45) (2013) 455401.

6. **Yavtushenko I.O., Makhmud-Akhunov M.Y., Adamovich A.A.,** Nanostructured electrodes for supercapacitors, Journal of Physics: Conference Series. IOP Publishing. 2086 (1) (2021) 012022.

THE AUTHORS

ADAMOVICH Artem A.
artem.adamovich@bk.ru
ORCID: 0000-0002-7829-5326

IYAVTUSHENKO Igor O.
yavigor@mail.ru
ORCID: 0000-0002-8612-6258

MAKHMUD-AKHUNOV Marat Yu.
maratmau@mail.ru
ORCID: 0000-0009-6999-9030

SOLOVYEV Alexander A.
shurken@mail.ru
ORCID: 0000-0001-7317-2813

GOLOVANOV Victor N.
golovanov_vn@mail.ru

BODNARSKY Dmitry S.
bodnarskiy@gmail.com

SIMULATION OF PHYSICAL PROCESSES

The phenomenon of "anomalous electrons" in pulsed high-current vacuum discharges

V.Yu. Kozhevnikov [1] ✉, A.V. Kozyrev [1]

[1] Institute of High Current Electronics, Siberian Branch, RAS, Tomsk, Russia

✉ Vasily.Y.Kozhevnikov@ieee.org

Abstract. This paper presents the first comprehensive theoretical explanation, based on computational physical kinetics, for the phenomenon of electrons attaining energies exceeding the amplitude of the applied voltage (in eV units) in a vacuum diode. The proposed theory thoroughly elucidates the existence of so-called "anomalous electrons", detailing their generation dynamics and underlying mechanisms. Additionally, the work calculates the integral energy spectra of these anomalous electrons in a high-current pulsed vacuum discharge and quantifies their contribution to the total current flow. The main tool used for numerical calculations is the latest meshless method for solving Vlasov-Poisson equation systems, known as the numerical flow iteration method (NuFI). The findings provide critical insights into non-equilibrium electron behaviour under extreme conditions, advancing the understanding of electron transport in vacuum-based high-power devices.

Keywords: vacuum electronics, anomalous electrons, physical kinetics

Явление «аномальных электронов» в импульсных сильноточных вакуумных разрядах

В.Ю. Кожевников [1] ✉, А.В. Козырев [1]

[1] Институт сильноточной электроники Сибирского отделения РАН, г. Томск, Россия

✉ Vasily.Y.Kozhevnikov@ieee.org

Аннотация. В работе впервые представлено теоретическое объяснение явления, при котором электроны в вакуумном диоде приобретают энергии, превышающие амплитуду приложенного напряжения (в единицах эВ). Исследуются динамика формирования «аномальных электронов», их энергетические спектры и их вклад в общий токоперенос в импульсных сильноточных вакуумных разрядах.

Ключевые слова: вакуумная электроника, аномальные электроны, физическая кинетика

Introduction

"Anomalous electrons" is the name given to a group of electrons in a vacuum discharge whose average kinetic energy ε exceeds the maximum value qU_0, where q is the electron charge and U_0 is the voltage amplitude across the vacuum gap. The existence of such electrons has been discussed in some experimental studies, for example in [1], but the reasons for their appearance were considered unclear for a long time. In [1] the electron energy distributions were calculated using Tikhonov regularization for a Fredholm integral equation, minimizing a priori assumptions about the spectral shape. The reconstructed electron spectra, obtained experimentally in a vacuum diode, revealed two distinctive groups in the beam incident on the collector filter: a low-energy component with a monotonic decrease up to 200 keV ($\varepsilon \le qU_0$) and an anomalous high-energy component peaking at 220 keV, followed by an extended tail reaching energies of 320 keV, i.e. $\varepsilon > qU_0$.

For a long time, experiments indicating the existence of electrons with anomalously high energies in vacuum discharges were met with considerable scepticism. Some researchers attributed the observation of such electrons to various experimental artefacts or to inaccuracies in the methods used to reconstruct the energy characteristics of electron beams beyond the anode, given the practical impossibility of performing direct measurements within the interelectrode gap. The first explanation for the emergence of anomalous electrons was provided in [2], where the solution of kinetic equations was studied for a low-current vacuum diode with an unlimited cathode emission capacity. This work presents a more detailed investigation of the fundamental physical mechanisms responsible for the formation of electrons with anomalously high energies in pulsed high-current vacuum diodes.

Materials and Methods

As it is supposed, the phenomenon of anomalous electron generation is a general manifestation in vacuum devices, so the configuration without geometric features was chosen as the starting point of the theory − it is a planar vacuum diode formed by a gap D between two plane-parallel electrodes. The coordinate axis x is located normally to the electrode's surface, where point $x = 0$ corresponds to the cathode position. It is the source of electron emission, which can be specified in terms of corresponding boundary condition for the EDF (electron distribution function) f_e as follow:

$$f_e\left(x=0,v,t\right) = \frac{n_0}{\sqrt{2\pi m_e T_e}} e^{-\frac{m_e v^2}{2T_e}},$$

where x и v − phase coordinates (coordinate and velocity), t − time variable, n_0 − emission number density, T_e − the electron temperature in eV, m_e − electron rest mass. The type of emission in this modeling is not essential, but the value of n_0 is determined by the condition of unlimited electron emission from the cathode − $j_{em} \gg j_{CL}$, where the emission current density and the Child-Langmuir current are determined by the following relationships, respectively

$j_{em} = \frac{qn_0}{4}\sqrt{\frac{8T_e}{\pi m_e}}$, $j_{CL} = \frac{4\varepsilon_0}{9}\sqrt{\frac{2q}{m_e}}\frac{U_0^{3/2}}{D^2}$, where ε_0 − vacuum dielectric permittivity. All variables in this paper are given in SI units.

According to the general methodology of physical kinetics, the dynamics of electron flows in this diode is described in terms of relativistic Vlasov-Poisson equations system

$$\frac{\partial f_e}{\partial t} + \frac{\partial f_e}{\partial x} - \frac{qE_x}{m_e\gamma^3}\frac{\partial f_e}{\partial v} = 0,$$

$$\frac{\partial^2\varphi}{\partial x^2} = -\frac{q}{\varepsilon_0}\int_{-\infty}^{\infty} f_e dx, \quad E_x = -\frac{\partial\varphi}{\partial x},$$

(1)

where E_x − electric field, φ − electrostatic potential, $\gamma = 1/\sqrt{1-v^2/c^2}$ – relativistic gamma factor.

The system of equations (1) forms a closed mathematical model of the proposed theory. The solution of the system is the electron distribution function f_e, knowing which at an arbitrary time point one can find the velocity, current density, and other "moments" of the distribution function. Initially vacuum diode is supposed to be empty, i.e., $f_e(t = 0) = 0$. The emission boundary condition is established at $x = 0$, simulating the injection of the emission current into an empty vacuum diode.

It is necessary to note only one more point, we assume the vacuum diode to be connected to a pulse voltage source $U(t)$ directly without any ballast load. The voltage pulse $U(t)$ has a trapezoidal shape. It is set by three parameters − the duration of the leading (and trailing) edges t_{rise}, the voltage amplitude U_0, and the total pulse duration by its base t_{width}.

Results and Discussion

To analyze the behavior of the solution of system (1) for a pulsed vacuum diode, a numerical solution was constructed. For the numerical solution of the Vlasov−Poisson system of equations, a modern mesh-free method known as NuFI (Numerical Flow Iterations) was employed. This approach provides an effectively infinite spatial resolution in phase space while maintaining second-order accuracy in time. The method has demonstrated particular efficiency in problems requiring a relatively small number of time steps, which is characteristic of the scenario considered in this study. Unlike the widely used grid-based methods or PIC methods [3], which are significantly affected by numerical diffusion or numerical noise, the NuFI method ensures the strict fulfillment of all conservation laws, which is crucial for the accurate simulation of collisionless processes. In the current one-dimensional case (1), the Poisson equation admits a straightforward solution in quadratures.

Thus, for a planar vacuum gap, we can define the so-called "flight time" for electrons $t_f \equiv \sqrt{2m_e D^2/(qU_0)}$. This estimate is obtained directly from solving the equation of motion for a single electron starting with zero velocity at the cathode, i.e. $m_e x'' = qU_0/D$, $x(0) = 0$, $x'(0) = 0$. It determines the characteristic time scale during which electrons from the cathode reach the anode under the action of the accelerating voltage. We consider the numerical solution of (1) for two cases: when a voltage with amplitude U_0 is applied to the diode by a long voltage rise front $t_{rise} \gg t_f$ and a short one $t_{rise} \sim t_f$. In both cases, we plot the time profile of the electron current density through the collector (anode), which is determined by the following moment of the electron distribution function

$$j_{\tilde{n}} = q\int_{-\infty}^{\infty} v \cdot f_e(x = D, v, t)dv.$$

Fig. 1 shows the time profiles j_c for these two cases for $D = 1$ cm, $U_0 = 50$ kV, $j_{em}/j_{CL} = 10$ diode parameters. Short rise time for this configuration corresponds to $t_{rise} = 100$ ps, and the long rise time case here is $t_{rise} = 500$ ps. The most general case of establishing a steady-state current flow in a diode includes three successive stages: a) flight time, b) transition region, and c) region of steady-state current flow. The second stage occurs only if the voltage is applied fast, i.e., $t_{rise} \sim t_f$. Its key feature is the generation of the limiting value of the diode current. Simplified modeling [3] gives an estimate of the limiting current density as $j_{max} = 2.75 \cdot j_{CL}$, and the actual kinetic theory corrects this value downwards.
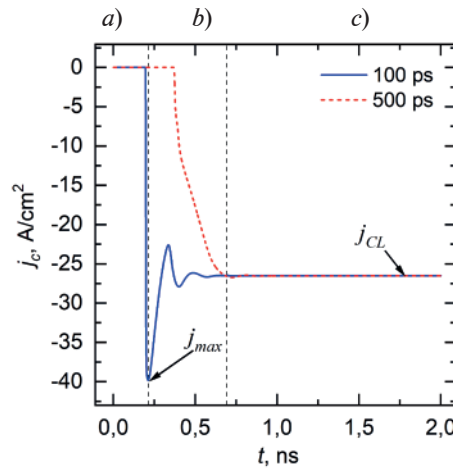
Fig. 1. Collector current density profiles of a planar vacuum diode

The major minimum value of the instant current density is provided by the first electrons that are delivered to the anode in times of the order of t_f, then damped oscillations of the volumetric charge density occur, and the value of the diode current density is established at the level of the stationary value j_{CL}. The key observation of the kinetic theory is the fact that the limiting current j_{max} is delivered to the collector (anode) precisely by anomalous electrons. This was first noted in the work [2] precisely due to the kinetic description.

Figure 2 shows the electron distribution function at two characteristic time points in the case where the voltage rise time is comparable to the pulse duration ($t_{rise} \sim t_f$): (left plot) when the current density reaches its peak value, and (right plot) when it reaches a steady-state level. At $t = 210$ ps, the current density attains its maximum, and the electrons arriving at the anode have an average energy of 57.8 keV, which exceeds the applied voltage amplitude (multiplied by the electron charge) by 16%. Thus, all electrons reaching the anode at this moment are anomalous, with $\varepsilon > qU_0$. When the current density becomes stationary at $t = 2$ ns, the average kinetic energy of the electrons is $\varepsilon = qU_0$.
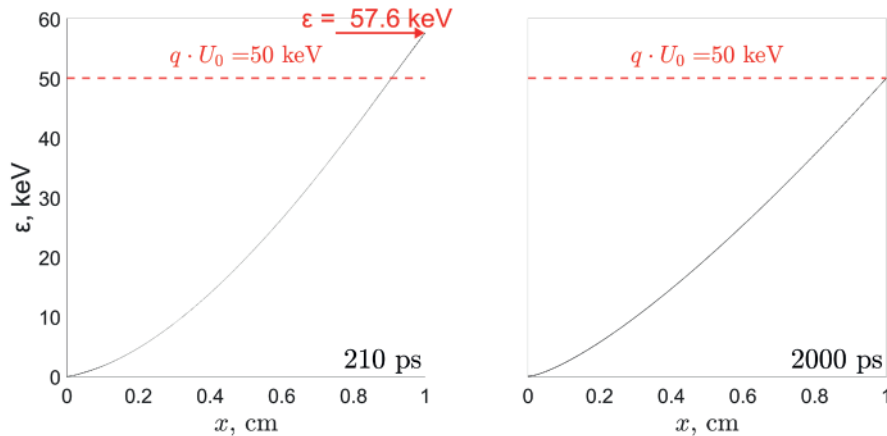
Fig. 2. The collector EDF $f_e (x = D, \varepsilon, t)$ distribution at selected time points corresponding to the peak collector current density ($t = 210$ ps) and the steady-state collector current density ($t = 2$ ns). The red arrow indicates the instantaneous energy of the electrons at the time point when they reach the anode

An extended voltage pulse rise time ($t_{rise} \gg t_f$) leads to the disappearance of the transient region associated with relaxation oscillations and, consequently, to the vanishing of the anomalous energy component in the spectrum of electrons arriving at the collector.

The theory enables the simulation of a pulsed process with short leading (and trailing) edges equal to $t_{rise} = 0.1$ ns of the voltage pulse and a total duration of $t_{width} = 1$ ns, and allows the calculation of the integral spectral energy distribution of electrons at the anode according to the

formula $g(\varepsilon) \sim \int_{0}^{t_{width}} f_e(x = D, \varepsilon(v), t)\,dt$. The resulting energy spectrum is shown in Fig. 3. It can be noted that the spectral distribution contains a principal maximum corresponding to the kinetic energy value $\varepsilon = qU_0$, as well as two additional maxima. One of these characterises the low-energy fraction of the electron beam, $\varepsilon < qU_0$, which corresponds to the peak of the diode current curve at time $t = 333$ ps. The second spectral maximum corresponds to a group of anomalous electrons with $\varepsilon > qU_0$ generated at $t = 210$ ps. This integral spectrum has been obtained for the first time based on the proposed kinetic theory. The spectral energy distribution, including the half-widths of the peaks (at $T_e \ll qU_0$), depends nonlinearly on the pulse front duration and the anode voltage amplitude. This issue requires further research regarding to its use in modern high-current electronic devices with the parameters on demand.
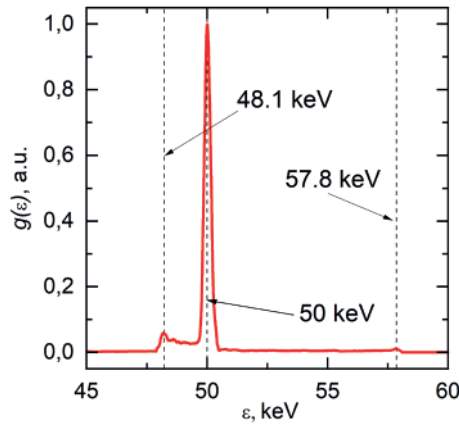
Fig. 3. Integral energy spectrum of the electron beam passing through the anode in a pulsed high-current vacuum discharge of 1 ns duration with a voltage pulse rise time of 0.1 ns

This scenario was simulated for voltage pulses typical of those used in modern nanosecond-scale devices. However, if experimental capabilities allow the generation of subnanosecond pulses with even steeper rise times, it may be possible to achieve conditions under which the electron beam beyond the collector consists exclusively of electrons with anomalously high energies, i.e., with kinetic energies $\varepsilon > qU_0$. This opens up the possibility of using vacuum diodes to generate electron fluxes with energies exceeding the product of the applied voltage and the elementary charge, which is of significant practical interest.

Conclusion

The appearance of anomalous electrons in a vacuum discharge is caused by the imbalance between two physical processes − charged particles entry into the gap (emission current injection) and their absorption at the anode (collector current outflow), which maintains a local space charge oscillations in the gap and the consistent electric field distortion providing the electron acceleration to high kinetic energies $\varepsilon > qU_0$. In this paper, this imbalance is provoked by specific electrophysical conditions (a short front edge of a voltage supply) that are confirmed experimentally [1]. However, in a broader sense, such a space charge imbalance can also be created by other factors inherent in most vacuum electronic devices. For example, the instability of emission current within the "ectonic" mechanism or non-trivial geometrical conditions of the discharge gap can provide short beams of the anomalous electrons, e.g., [4].

Modern vacuum and plasma electronics is an electrophysical technique operating at the nanosecond scales of pulse duration. Further development of high-current electronics is associated with the use of even shorter pulses having subnanosecond durations. For such devices, the influence of anomalous electrons, which inevitably arise in experimental conditions and industrial applications, will become even more significant, since the characteristic voltage rise fronts will be significantly shorter than the flight times of electrons (and ions) in vacuum gaps.

REFERENCES

1. **Kozyrev A.V., Kozhevnikov V.Yu., Baksht E.Kh., Burachenko A.G., Tarasenko V.F.,** Spectrum reconstruction of a nanosecond electron beam from the data on its extinction in thin foils, Russian Physics Journal. 53 (4) (2010) 361−368.

2. **Kozhevnikov V.Yu., Kozyrev A.V.,** On the Physical Nature of 'Anomalous' High Energy Electrons in Vacuum Diodes, Russian Physics Journal. 64 (12) (2022) 2341−2349.

3. **Kozhevnikov V.Yu., Kozyrev A.V., Semeniuk N.S.,** Modeling of Space Charge Effects in Intense Electron Beams: Kinetic Equation Method Versus PIC Method, IEEE Transactions on Plasma Science. 45 (10) (2017) 2762−2766.

4. **Kozhevnikov V.Yu., Kozyrev A.V., Kokovin A.O., Semeniuk N.S.,** The kinetic simulation in vacuum electronics: uncovering the fundamental nature of non-Maxwellian distribution function effects, St. Petersburg State Polytechnical University Journal: Physics and Mathematics. 15 (3.3) (2022) 76−81.

THE AUTHORS

KOZHEVNIKOV Vasily Yu.
Vasily.Y.Kozhevnikov@ieee.org
ORCID: 0000-0001-7499-0578

KOZYREV Andrey V.
kozyrev@to.hcei.tsc.ru
ORCID: 0000-0002-7078-7991

ATOM PHYSICS AND PHYSICS OF CLUSTERS AND NANOSTRUCTURES

Investigation of microdisks lasers with an InGaN/GaN quantum well in the active region at elevated temperatures

D.A. Masyutin [1] ✉, A.A. Rudnev [1], E.I. Moiseev [1], A.G. Vainilovich [2],

E.V. Lutsenko [2], A.F. Tsatsulnikov [3], A.V. Sakharov [3, 4], D.S. Arteev [3, 4],

A.E. Nikolaev [4], A.A. Pivovarova [4], E.E. Zavarin [3, 4], N.D. Il'inskaya [4],

L.K. Markov [4], I.P. Smirnova [4], N.V. Kryzhanovskaya [1], A.E. Zhukov [1]

[1] National Research University Higher School of Economics, St. Petersburg branch,
St. Petersburg, Russia;
[2] Stepanov Institute of Physics of NAS Belarus, Minsk, Belarus;
[3] Submicron Heterostructures for Microelectronics, Research & Engineering Center, RAS,
St. Petersburg, Russia;
[4] Ioffe Institute, St. Petersburg, Russia;
✉ dmasyutin@hse.ru

Abstract. In this work, we present results on high-temperature operation microdisk lasers with an active region based on InGaN/GaN quantum wells. The diameter of the microdisks was 5 μm. The photoluminescence spectra measured in the temperature range from 25 °C to 100 °C. The temperature stability lasing is demonstrated.

Keywords: GaN, InGaN/GaN quantum wells, microdisk resonator, WGM

Исследование микродисковых лазеров с InGaN/GaN квантовой ямой в активной области при повышенных температурах

Д.А. Масютин [1] ✉, А.А. Руднев [1], Э.И. Моисеев [1], А.Г. Войнилович [2],

Е.В. Луценко [2], А.Ф. Цацульников [3], А.В. Сахаров [3, 4], Д.С. Артеев [3, 4],

А.Е. Николаев [4], А.А. Пивоварова [4], Е.Е. Заварин [3, 4], Н.Д. Ильинская [4],

Л.К. Марков [4], И.П. Смирнова [4], Н.В. Крыжановская [1], А.Е. Жуков [1]

[1] Национальный исследовательский университет «Высшая школа экономики»,
Санкт-Петербургский филиал, Санкт-Петербург, Россия;
[2] Институт физики им. Б.И. Степанова НАН Беларуси, г. Минск, Беларусь
[3] НТЦ микроэлектроники РАН, Санкт-Петербург, Россия;
[4] Физико-технический институт им. А.Ф. Иоффе РАН, Санкт-Петербург, Россия
✉ dmasyutin@hse.ru

Аннотация. В работе представлены результаты исследования высокотемпературных характеристик микродисковых лазеров с активной средой на основе квантовых ям InGaN/GaN. Исследовались спектры фотолюминесценции микродисков диаметром 5 мкм в диапазоне температур от 25 °C до 100 °C. Продемонстрирована высокая температурная стабильность лазерной генерации.

Ключевые слова: GaN, InGaN/GaN квантовые ямы, микродиск, МШГ

Introduction

The growing demand for high-speed data transmission in integrated photonic systems has driven the development of compact and efficient on-chip light sources. III-nitride semiconductors have emerged as promising candidates due to their direct bandgap, high thermal and chemical stability, and wide spectral tunability from ultraviolet to near-infrared [1]. GaN microdisk lasers integrated on silicon substrates are of particular interest, as they combine the optical advantages of III-nitrides with the scalability and integration with other silicon devices [2].

This study investigates the impact of microdisk laser heating on lasing threshold power and wavelength shift, which are crucial for ensuring the stability of the laser operation.

Materials and Methods

The studied heterostructure was fabricated by metal-organic chemical vapor deposition (MOCVD) on misoriented (111) Si-substrate. The structure contains a 200 nm thick AlN layer, a composition of AlGaN buffer layers of variable composition with a total thickness of 770 nm, a 200 nm thick GaN waveguide layer, 5x $In_{0.1}Ga_{0.9}N$/GaN quantum wells (QWs) of 2 nm thickness each, separated from each other by 8 nm thick GaN layers, and a 200 nm thick GaN cover layer. Mesas with a diameter of 5 μm were formed by plasma chemical etching method.

Microphotoluminescence (μPL) spectroscopy was used to investigate the optical properties of heterostructures. The sample was placed on heater, the temperature in which varied from 25 °C to 100 °C. Optical pumping was carried out by a pulsed laser ($\lambda = 355$ nm, pulses 9 ns, frequency 10 kHz) with an acousto-optic modulator. The pump laser beam was directed along the normal to the substrate and focused onto a single microlaser using a Thorlabs LMU-5X-NUV objective (NA 0.12). Radiation from the microlaser was collected with a Mitutoyo Plan Apo NUV 50X microobjective (NA 0.42), located at an angle of ~30° relative to the substrate plane. Detection of the microlaser emission spectra was performed using a Thorlabs CCS200/M spectrometer.

Results and Discussion

µPL spectra over a wide temperature range were investigated. The room temperature photoluminescence spectra of the microdisk laser at optical pump powers of 205 uW, 253 uW, and 314 uW ($0.8P_{th}$, P_{th}, $1.25P_{th}$) are shown in Fig. 1, *a*.

At low pumping, the photoluminescence spectrum of microlaser has a form characteristic of spontaneous emission. The emission maximum of the main optical transition was at room temperature at a wavelength of 427 nm. With increasing pumping power, a narrow line appears on the short-wave slope of the emission peak, corresponding to one of the modes of the whispering gallery of the microresonator. For the resonance line (420 nm), the transition to the lasing mode is observed, as evidenced by the threshold dependence of the integral intensity (Fig. 1, *b*). The threshold of lasing is 249 uW for room temperature.
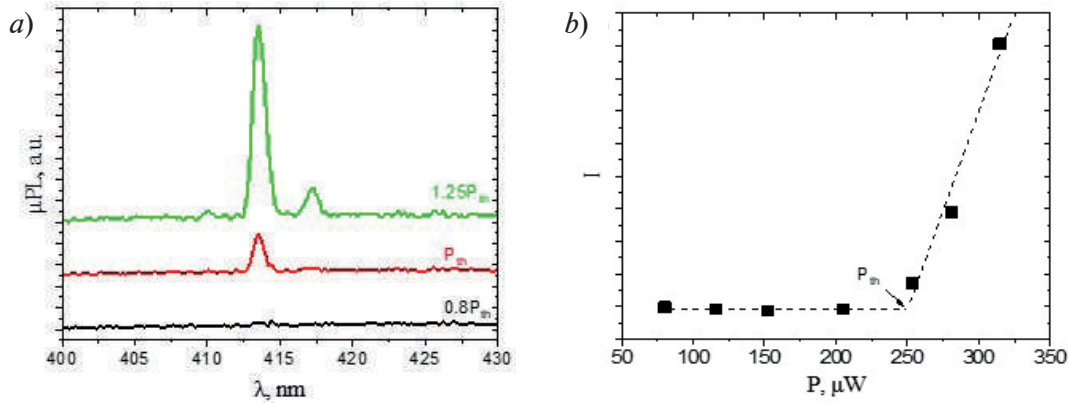
Fig. 1. µPL spectra of microdisk laser at room temperature (*a*) and L-L curves for 5 um microdisk (*b*)

Figure 2, *a* shows the µPL spectra of the laser at 25 °C and 100 °C at an optical pump power of 314 uW. High-temperature lasing is observed, it's confirmed by a defense of mode intensity on pump power (the inset of Fig. 2, *a*). The threshold power is slightly variable between 245 uW and 255 uW (Fig. 2, *b* black) and lasing continued to be observed with a slight long-wavelength shift from 413 nm to 415 nm (Fig. 2, *b* red) in the temperature range from 25 °C to 100 °C. We assume that the additional optical losses at high temperatures are caused by enhanced absorption of free carriers in the waveguide layer of the laser [3].
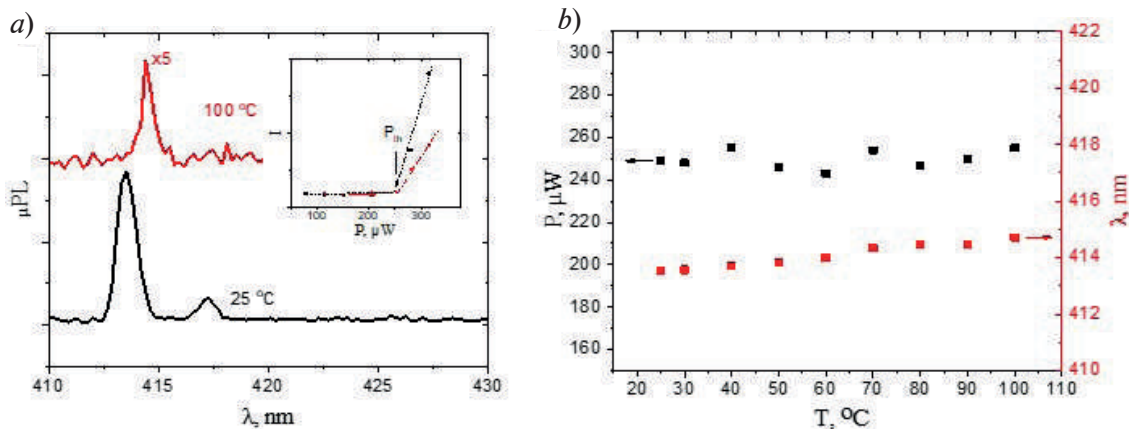
Fig. 2. µPL spectra of microdisk laser and L-L curves (insert) at temperatures 25 °C (black) and 100 °C (red) (*a*), temperature dependence of the threshold power density (black, left axis) and lasing peak position (red, right axis) (*b*)

Conclusion

For the first time, lasing has been demonstrated at elevated temperatures (up to 100 °C) for InGaN/GaN microdisk with QW in the active region. The laser shows line and threshold power stability with a temperature range from 25 °C to 100 °C. The results obtained represent a significant contribution to the progress of technologies integration III-N lasers with Si devices.

REFERENCES

1. **Baten M.Z., Alam S., Sikder B., Aziz A.,** III-Nitride Light-Emitting Devices, Photonics. 8 (2021) 430.

2. **Tabataba-Vakili F., Doyennette L., Brimont C., Guillet T., Rennesson S., Frayssinet E., Damilano B., Duboz J.-Y., Semond F., Roland I., El Kurdi M., Checoury X., Sauvage S., Gayral B., Boucaud P.,** Blue Microlasers Integrated on a Photonic Platform on Silicon, ACS Photonics. 5 (2018) 3643−3648.

3. **Kryzhanovskaya N.V., Moiseev E.I., Polubavkina Y.S., Maximov M.V., Mokhov D.V., Morozov I.A., Kulagina M.M., Zadiranov Y.M., Lipovskii A.A., Tang M., Liao M., Wu J., Chen S., Liu H., Zhukov A.E.,** Elevated temperature lasing from injection microdisk lasers on silicon, Laser Phys. Lett. 15 (2018) 015802.

THE AUTHORS

MASYUTIN Dmitriy A.
dmasyutin@hse.ru
ORCID: 0009-0005-4578-7550

NIKOLAEV Andrey E.
aen@mail.ioffe.ru
ORCID: 0000-0001-6522-4484

RUDNEV Artem A.
aarudnev@edu.hse.ru
ORCID: 0009-0004-6609-9741

PIVOVAROVA Antonina A.
pivovarova.antonina@gmail.com
ORCID: 0000-0002-2313-9051

MOISEEV Eduard I.
emoiseev@hse.ru
ORCID: 0000-0003-3686-935X

ZAVARIN Evgenii E.
EZavarin@mail.ioffe.ru
ORCID: 0000-0001-8380-3172

VAINILOVICH Aliaksei G.
a.vainilovich@ifanbel.bas-net.by
ORCID: 0009-0009-5699-2751

IL'INSKAYA Natalya D.
Natalya.Ilynskaya@mail.ioffe.ru
ORCID: -

LUTSENKO Evgenii V.
e.lutsenko@ifanbel.bas-net.by
ORCID: 0000-0003-2333-7776

MARKOV Lev K.
l.markov@mail.ioffe.ru
ORCID: 0000-0001-7293-1320

TSATSULNIKOV Andrey F.
andrew@beam.ioffe.ru
ORCID: 0000-0002-5078-8946

SMIRNOVA Irina P.
irina@quantum.ioffe.ru
ORCID: 0000-0001-5313-0640

SAKHAROV Alexei V.
val.beam@mail.ioffe.ru
ORCID: 0000-0002-9976-999X

KRYZHANOVSKAYA Natalia V.
nkryzhanovskaya@hse.ru
ORCID: 0000-0002-4945-9803

ARTEEV Dmitri S.
ArteevDS@mail.ioffe.ru
ORCID: 0000-0003-4447-8789

ZHUKOV Alexey E.
zhukale@gmail.com
ORCID: 0000-0002-4579-0718

Surface tension measurement of chitosan aspartate nanoparticle dispersions by a modified Wilhelmy method

X.M. Shipenok [1] ✉, A.M. Mazhikenova [1], E.G. Glukhovskoy [1], A.B. Shipovskaya [1]

[1] Saratov State University, Saratov Russia

✉ kshipenok@gmail.com

Abstract. A modification of the Wilhelmy method is proposed for measuring the surface tension of polymer nanoparticle dispersions, whose key feature is the static nature of the Wilhelmy plate when measuring the surface tension force. Tests on the example of nanostructured chitosan aspartate showed satisfactory accuracy of the modified method in estimating the surface activity of nanodispersions in a wide range of polymer concentrations. The concentration dependence of the surface tension of the dispersion of chitosan aspartate nanoparticles was obtained, and concentration ranges with different surface effects were outlined. The contribution of individual components used in obtaining nanoparticles to the surface activity of the nanodispersion was estimated.

Keywords: chitosan, L- and D-aspartic acid, nanoparticles, surface tension

Измерение поверхностного натяжения дисперсий наночастиц аспарагината хитозана модифицированным методом Вильгельми

К.М. Шипенок [1] ✉, А.М. Мажикенова [1], Е.Г. Глуховской [1], А.Б. Шиповская [1]

[1] Саратовский национальный исследовательский государственный университет им. Н.Г. Чернышевского, г. Саратов, Россия

✉ kshipenok@gmail.com

Аннотация. Предложена модификация метода Вильгельми для определения поверхностного натяжения дисперсий полимерных наночастиц, ключевой особенностью которой является статичность пластины Вильгельми при измерении силы поверхностного натяжения. Тестирование на примере наноструктурированного аспарагината хитозана показало удовлетворительную точность модифицированного метода при определении поверхностной активности нанодисперсий в широком диапазоне концентраций полимерного вещества. Получена концентрационная зависимость поверхностного натяжения дисперсии наночастиц аспарагината хитозана, определены концентрационные диапазоны с различающимися поверхностными эффектами. Оценен вклад индивидуальных компонентов, используемых при получении наночастиц, на поверхностную активность нанодисперсии.

Introduction

Chitosan (CS) nanoparticles with targeted functional action are very promising in nanophotonic biosensors, nanofluidics, nanoelectromechanics, as well as in medical and biological applications and the agro-industrial complex [1, 2]. This is due not only to the biological activity of CS and dimensional features of its nanomaterials (high specific surface area and reactivity of the interacting substance), but also to non-trivial surface properties of nanodispersions [3–5]. E.g., the surface tension of nanosized aggregates of the salt form of CS and aspartic acid (AspA) is determined by the force of electrostatic interaction between positively charged polymer chains and counterions of the acid residue and plays a key role in stabilizing nanoparticles [6]. In the process of forming chitosan-containing nanodispersions, the Coulomb repulsion of charged monomer units is compensated by the dipole–dipole attraction of ionogenic groups of macrochains with condensed counterions, so the nanosized structure is stabilized by hydrogen bonding and hydrophobic interactions [7, 8]. The ability to reduce the surface tension of water was noted for oleoyl chitosan [9]. Chitosan nanoparticles obtained by dispersing salt chitosan in an alkaline medium promote emulsification of edible oil or petroleum in water [3, 4].

The decrease in the surface tension of the main liquid upon introduction of nanoparticles is due to the high adsorption energy and is largely similar to the behavior of surfactant molecules [10]. However, measuring the surface energy of nanodispersions is associated with such methodological difficulties as system metastability, size effects and nanoparticle surface heterogeneity, double electric layer, deformation of the interfacial surface and lateral interactions of particles in the surface layer, the influence of steric effects of stabilizers and artifacts [10–12]. In the case of polymer nanodispersed systems, the problem is also experimental limitations in studying low concentrations of the substance and, accordingly, a limited number of nanoparticles. Minimization of the influence of the above features predetermines modifications of classical methods of experimental evaluation of the surface tension of nanoobjects. In this work, a modification of the Wilhelmy method is proposed to measure the surface energy of dispersions of nanostructured chitosan aspartate.

Materials and Methods

The starting reagents were CS with a viscosity-average molecular mass 200 kDa, a degree of deacetylation 82 mol% (Bioprogress Ltd., RF); L-AspA (JSC Bioamid, RF); D-AspA (Vekton Corp., RF); silicon tetraglycerolate in a 3-molar excess of glycerol $(Si(OGly)_4 \cdot 3\,GlyOH$, Ural Branch of Russian Academy of Sciences, Institute of Organic Synthesis named after I.Ya. Postovsky, RF); distilled water. In obtaining the dispersion of chitosan aspartate nanoparticles (CS·L-(D-)AspA), the concentrations of CS (C_{CS}), L- and D-AspA (C_{AspA}) were varied in a range of 0.05–1.2 g/dL, maintaining the molar ratio [Asp]/[CS] = 1.3 mol·(mol of $NH_2)^{-1}$. To form an aggregation and sedimentation resistant dispersion of nanoparticles, their surface was functionalized with a polysiloxane shell (CS·L-(D-)AspA·Si). A detailed procedure for obtaining shell nanoparticles is described in Ref. [6]. Nanodispersions were obtained by accurately weighing CS and L-(D-)AspA (method A), or by diluting the initial solution with C_{CS} = 1.2 g/dl with distilled water (method B).

Gravimetric measurements were carried out on an analytical balance "OhausDiscovery" (USA), weighing accuracy ± 0.01 mg. Interfacial surface tension (σ, mN/m) was measured by the Wilhelmy plate method at the liquid−gas (air) interface at $24 \pm 2\,°C$ on tensiometers KSV NIMA Langmuir & Langmuir−Blodgett Troug (Biolin Scientific, Sweden), the accuracy being 0.1 mN/m. Three replicate experiments with 10 measurements each were carried out. When calculating σ values, a correction was introduced for the temperature coefficient of the surface tension of water. Ultrasonic treatment was performed on a JY96-IIN ultrasonic homogenizer (Ningbo Scientz Bio-Technology Co., Ltd., China). Exposure time was 15 s, power was 40 W, frequency was 150 kHz, and temperature was $22 \pm 2\,°C$. The probe was immersed into the surface layer of the system under study.

Results and Discussion

The following modification of the Wilhelmy method was proposed to determine the surface tension of aqueous dispersions of polymer nanoparticles. Unlike the classical method, which consists in measuring the force of plate separation from the surface of the tested liquid (International Standard ISO 304), the key feature of the modified approach is the static nature of the Wilhelmy plate during the experiment (Fig. 1). To comply with these conditions, the polymer liquid was placed into a transparent laboratory vessel in the form of a low flat cylinder (e.g., in a Petri dish), which was raised vertically until contact of the studied liquid with the plate fixed on the strain gauge was achieved. The laboratory vessel with the system under study was moved by regulating the distilled water level. This approach allows minimizing the hydrodynamic effects during plate movement which occur in the standard Wilhelmy method and increasing the accuracy of σ measurements due to the directed movement of the test system toward the sensor. A paper deashed filter "Blue Ribbon" was used as the Wilhelmy plate, ensuring rapid complete wettability of the plate with the liquid medium.
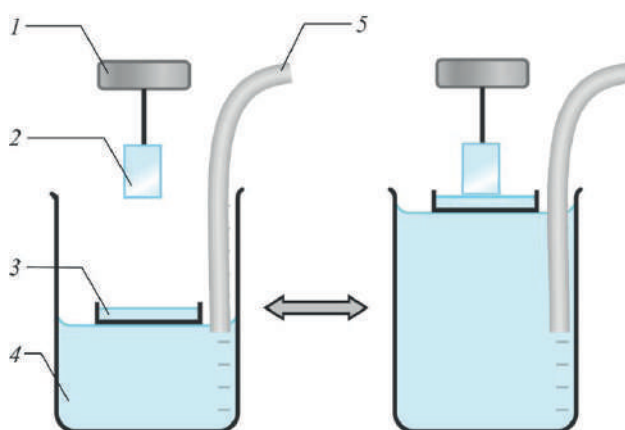
Fig. 1. Scheme of the modified setup for measuring surface tension: *1* − tensiometric sensor, *2* − Wilhelmy plate, *3* − laboratory vessel with the system under study, *4* − laboratory beaker with distilled water, and *5* − liquid level control system

Testing our modified version of the Wilhelmy method on standard liquids showed that the obtained surface tension values were identical to the reference data. The σ values of aqueous solutions of surface-inactive L-(D-) chitosan aspartate and L-(D-) AspA were also reproducible with known literature data. Verification testing also confirmed the manifestation of surface activity by CS·L-(D-)AspA·Si shell nanoparticles, which was more pronounced for CS·L-AspA·Si nanoparticles [6].

The positive approbation of the proposed modification of the Wilhelmy method justified our study of the surface tension of nanostructured CS L-(D-)aspartate in a wide range of polymer concentrations. It was found that the concentration dependence of σ of aqueous CS·L-(D-)AspA·Si nanodispersions had a non-monotonic character and did not depend on the method of obtaining the nanostructured system (Fig. 2, curves *1*, *2* and *4*). In the range of medium concentrations ($C_{CS} = 0.3-1.2$ g/dl) the surface tension decreased with decreasing C_{CS} (region I), which could

be due to weakening of the interactions between the components of the aqueous medium and a decrease in the surface energy at the liquid−gas interface. In the range of low concentrations (C_{CS} = 0.1−0.3 g/dl) an increase in the surface tension of the nanodispersions was observed with a decrease in C_{CS} (region II). When C_{CS} < 0.05−0.1 g/dl the system was surface-inactive and the experimentally determined σ values became comparable with the surface tension of water (region III). This character of σ = $f(C_{CS})$ may be caused by a small number of nanoparticles in the dispersion, which is insufficient to exhibit surface activity and reduce the surface tension at the phase boundary. Since the structure of the nanoparticles contains the salt form of CS, the effect of increasing σ can be also associated with polyelectrolyte swelling of shell macrocoils and, accordingly, an increase in the size of the nanoparticles up to the rupture of their protective polysiloxane shell. In this case, the aqueous medium will be filled with isolated macromolecules of surface-inactive chitosan aspartate. The latter is consistent with the hydrodynamic behavior of the studied nanodispersions, which showed an increase in the viscosity number upon dilution of the system.
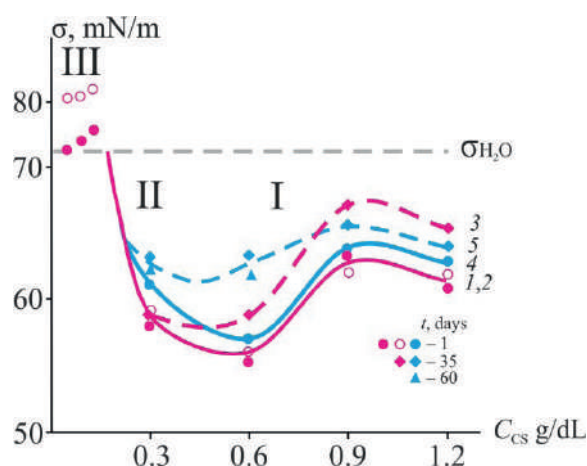
Fig. 2. Concentration dependence of the surface tension of aqueous dispersions of CS·L-AspA·Si (*1–3*) and CS·D-AspA·Si (*4, 5*): freshly prepared (*1, 2,* and *4*) and after aging under room atmosphere conditions for *t* = 35−60 days (*3, 5*), obtained by method A (*1, 3–5*) or method B (*2*); 24 ± 2 °C, The dotted line shows the σ value of distilled water at 25 °C. Roman numerals indicate concentration regions with different surface effects, explanation in the text

When freshly prepared nanodispersions were aged under room atmosphere conditions, an increase in their surface tension was observed (Fig. 2, curves *3* and *5*). This may be a consequence of partial aggregation of particles, but not very significant, since the realized σ values weare lower than the surface tension of the main liquid (water), and the greatest effect was observed in the region with a high concentration of the polymer substance, C_{CS} > 0.4 g/dl (Fig. 2, region I). The greatest tendency for such aggregation over time was shown by the CS·L-AspA·Si nanodispersion when C_{CS} > 0.8 g/dl. It is noteworthy that after a short-term dispersing ultrasonic effect (15 s), the σ values returned to the initial readings, characteristic of a freshly prepared nanostructured system.

The influence of the individual components (GlyOH and $Si(OGly)_4$) of the glycerol solution of silicon tetraglycerolate on the surface activity of aqueous solutions of CS in L-(D-)AspA and L-(D-)AspA (the main ingredients in obtaining the target substance of nanodispersion) was also assessed. The concentration of GlyOH and $Si(OGly)_4$ corresponded to that in forming the shell coating of CS·L-(D-)AspA·Si nanoparticles. It turned out that glycerol incorporation had little effect on the surface tension of aqueous solutions of chitosan and acid (Table). However, silicon tetraglycerolate introduction led to a significant decrease in σ compared to the control solutions. In this case, for chitosan L-(D-)aspartate solutions, the effect of decreasing surface activity upon introduction of $Si(OGly)_4$ was expressed to a greater extent than for L-(D-)aspartic acid solutions. Therefore, the surface energy of the nanodispersion was largely due to the contribution of the shell polysiloxane coating formed as a result of chemical functionalization of silicon tetraglycerolate on the surface of the nanoparticles.

T a b l e

Effect of the individual components of Si(OGly)$_4$·3 GlyOH used in the formation of the shell coating of CS·L-(D-)AspA·Si nanoparticles on the surface tension of aqueous CS solutions in L-(D-)AspA with C_{CS} = 0.3 g/dl, C_{AspA} = 0.3 g/dl and L-(D-)AspA with C_{AspA} = 0.3 g/dl

Aqueous solution	Surface tension σ, mN/m		
	Individual components Si(OGly)$_4$·3 GlyOH		
	–	GlyOH	Si(OGly)$_4$
CS + *L*-AspA	67.4	69.2	58.5
CS + *D*-AspA	70.5	68.7	62.8
L-AspA	74.0	74.1	62.5
D-AspA	72.0	68.5	64.3

Conclusion

The use of filter paper as a contacting test element in the modified capillary-gravimetric Wilhelmy plate method and its static nature when measuring the gravitational tensile force allows measuring the surface tension of chitosan aspartate nanoparticle dispersions with satisfactory accuracy even at low concentrations of the polymer substance. Satisfactory accuracy of σ measurements in the modified Wilhelmy method is manifested up to chitosan aspartate concentrations of ~0.05 g/dl. It was found that the surface tension of nanodispersions depends on the concentration of chitosan aspartate and the isomeric form of aspartic acid and is largely determined by the contribution of silicon tetraglycerolate, which participates in nanoparticle functionalization with a polysiloxane shell coating.

REFERENCES

1. **Mu X.-T., Li Y., Ju X.-J., Yang X.-L., Xie R., Wang W., Liu Z., Chu L.-Y.,** Microfluidic fabrication of structure-controlled chitosan microcapsules via interfacial cross-linking of droplet templates, ACS Applied Materials & Interfaces. 12 (51) (2020) 57514−57525.

2. **Hu B., Guo Y., Li H., Liu X., Fu Y., Ding F.,** Recent advances in chitosan-based layer-by-layer biomaterials and their biomedical applications, Carbohydrate Polymers. 271 (2021) 118427.

3. **Saliu F., Meucci E., Allevi C., Savini A., Imiete I.E., Della Pergola R.,** Evaluation of chitosan aggregates as pickering emulsifier for the remediation of marine sediments, Chemosphere. 273 (2021) 129733.

4. **Ahmed R., Wang M., Qi Z., Hira N.U.A., Jiang J., Zhang H., Iqbal S., Wang J., Stuart M.A.C., Guo X.,** Pickering emulsions based on the pH-responsive assembly of food-grade chitosan, ACS omega. 6 (28) (2021) 17915−17922.

5. **Quicones J.P., Peniche H., Peniche C.,** Chitosan based self-assembled nanoparticles in drug delivery, Polymers. 10 (2018) 235.

6. **Shipenok X.M., Mazhikenova A.M., Glukhovskoy E.G., Shipovskaya A.B.,** Phase separation of L-menthol an aqueous dispersion of biologically active nanoparticles of chitosan L- and D-aspartate, Journal of Biomedical Photonics & Engineering. 10 (4) (2024) 040316.

7. **Pigaleva M.A., Portnov I.V., Rudov A.A., Blagodatskikh I.V., Grigoriev T.E., Gallyamov M.O., Potemkin I.I.,** Stabilization of chitosan aggregates at the nanoscale in solutions in carbonic acid, Macromolecules. 47 (16) (2014) 5749−5758.

8. **Lugovitskaya T.N., Shipovskaya A.B., Shmakov S.L., Shipenok X.M.,** Formation, structure, properties of chitosan aspartate and metastable state of its solutions for obtaining nanoparticles, Carbohydrate Polymers. 277 (2022) 118773.

9. **Li Y.Y., Chen X.G., Liu C.S., Cha D.S., Park H.J., Lee C.M.,** Effect of the molecular mass and degree of substitution of oleoylchitosan on the structure, rheological properties, and formation of nanoparticles, Journal of Agricultural and Food Chemistry. 55 (12) (2007) 4842−4847.

10. **Emelianenko A.M., Boinovich L.B.,** Role of disperger particles in physical-chemical movement of nanofluids, Colloid Journal. 85 (6) (2023) 727−737.

11. **Antonov D., Islamova A.G., Strizhak P.,** Hydrophilic and Hydrophobic Surfaces: Features of Interaction with Liquid Drops, Materials. 16 (17) (2023) 5932.

12. **Traciak J., Żyła G.,** Effect of nanoparticles saturation on the surface tension of nanofluids, Journal of Molecular Liquids. 363 (2022) 119937.

THE AUTHORS

SHIPENOK Xenia M.
kshipenok@gmail.com
ORCID: 0000-0002-9733-751X

GLUKHOVSKOY Evgeny G.
glukhovskoy@gmail.com
ORCID: 0000-0002-8282-3638

MAZHIKENOVA Aliya M.
mazhikenova04@mail.ru
ORCID: 0009-0007-6517-9784

SHIPOVSKAYA Anna B.
Shipovskayaab@yandex.ru
ORCID: 0000-0003-1916-4067

Study of thermal conductivity of polymer materials with carbon nanotubes using laser flash method

S.V. Vasin [1] ✉, N.P. Kuzmin [1], V.A. Sergeev [1], M.V. Buzaeva [2]

[1] Kotel'nikov Institute of Radio Engineering and Electronics of RAS, Ulyanovsk Branch, Ulyanovsk, Russia;
[2] Ulyanovsk State Technical University, Ulyanovsk, Russia

✉ svasin@ulireran.ru

Abstract. The thermal conductivity of nanocomposite polymer materials based on polyvinyl alcohol and epoxy resin with the inclusion of multi-walled carbon nanotubes was studied using the laser flash method. The possibility of using the laser flash method to determine thermal conductivity in thin-film polymer materials is demonstrated and its features are revealed. It has been shown that the presence of carbon nanotubes in polymer matrices leads to an increase in the coefficients of thermal diffusivity and thermal conductivity by several times compared to pure polymer materials.

Keywords: carbon nanotubes, polymers, thermal conductivity, laser flash method

Исследование теплопроводности полимерных материалов с углеродными нанотрубками методом лазерной вспышки

С.В. Васин [1] ✉, Н.П. Кузьмин [1], В.А. Сергеев [1], М.В. Бузаева [2]

[1] Ульяновский филиал института радиотехники и электроники им. В.А. Котельникова РАН, г. Ульяновск, Россия;
[2] Ульяновский государственный технический университет, г. Ульяновск, Россия

✉ svasin@ulireran.ru

Аннотация. Методом лазерной вспышки исследована теплопроводность нанокомпозитных полимерных материалов на основе поливинилового спирта и эпоксидной смолы с включением многостенных углеродный нанотрубок. Продемонстрирована возможность и выявлены особенности использования метода лазерной вспышки для определения теплопроводности в тонкопленочных полимерных материалах. Показано, что наличие в полимерных матрицах углеродных нанотрубок приводит к увеличению коэффициентов температуропроводности и теплопроводности в несколько раз по сравнению с чистыми полимерными материалами.

Introduction

Polymer nanocomposites with carbon nanotubes (CNTs) serve as the basis for creating microelectronic sensors, optical elements, protective coatings and other products [1]. One of the characteristics of polymer nanocomposite materials that determines their functional properties is thermal conductivity [2]. It is expected that the use of CNT additives in polymeric materials can significantly improve their temperature characteristics. The purpose of this work was to study the thermal conductivity of polymer materials with different concentrations of CNTs using a promising non-contact laser flash method (LFM). In LFM, the upper surface of the controlled object is exposed to a short pulse of heating focused laser radiation, and at certain points on the surface on the back side of the object, a thermal imager or IR camera measures the change in temperature over time. It is also of interest to determine the possibilities and features of using LFM for studying polymeric materials, including in the form of thin films.

Materials and Methods

In this study, we used multi-walled carbon nanotubes (MWCNTs) with a diameter of 40-80 nm, synthesized by the MOCVD method at the experimental facility of the Ulyanovsk State Technical University [3]. MWCNTs were subjected to multi-stage liquid-phase treatment to remove metallic impurities and improve the compatibility of MWCNTs with the polymer matrix [4]. Films based on polyvinyl alcohol (PVA) were manufactured using the method described in [5], with different mass concentrations of MWCNTs.

Plates of polymer nanocomposites with a thickness of 2−5 mm and a diameter of 16 cm were obtained on a base of EDP grade epoxy resin, into which, after mixing with a hardener, multi-walled carbon nanotubes (MWCNTs) were introduced, dispersed by ultrasonic treatment [6].

When implementing the LFM using an IR camera as a temperature sensor, a measurement point is selected on the lower surface of the film on the image obtained from the IR camera, located at a distance l from the center of the laser radiation spot on the upper surface of the film (Fig. 1, b). For a point opposite the center of the laser spot on the top surface of the film, this distance is equal to the film thickness d. Based on the measurement results at the selected point, a graph of the dependence of the temperature change $\Delta T(t)$ on time is constructed (Fig. 2). The graph is used to determine the maximum value of the temperature increment ΔT_{max} and the temperature increment ΔT after exposure to a laser radiation pulse (section b in Fig. 2). Next, using formula (1):

$$m_0 = \int\limits_{t_{0.1}}^{t_{0.8}} \frac{\Delta T(t)}{\Delta T_{max}} dt, \quad m_{-1} = \int\limits_{t_{0/1}}^{t_{0.8}} \frac{1}{t} \frac{\Delta T(t)}{\Delta T_{max}} dt, \tag{1}$$

we calculate the partial moments of time m_0 and m_{-1}, and using formula (2):

$$F(m_{-1}) = -0.0819 + 0.305 m_{-1}, \tag{2}$$

we calculate the approximating function $F(m_{-1})$.

And finally, using formula (3):

$$\alpha = \frac{d^2 F(m_{-1})}{m_0},$$ (3)

the thermal diffusivity coefficient α is calculated, and using formula (4):

$$\lambda = \alpha \rho C_p.$$ (4)

the thermal conductivity coefficient λ is calculated, where ρ is the density and C_p is the specific heat capacity of the material.

A laser with a wavelength of 960 nm and a power of 50 mW was used as a source of the heating pulse, and a PI640 Optris IR camera operating in the spectral range of $8-14$ µm with a temperature resolution of 0.04 degrees and a frame refresh rate of 32 Hz was used as a sensor.
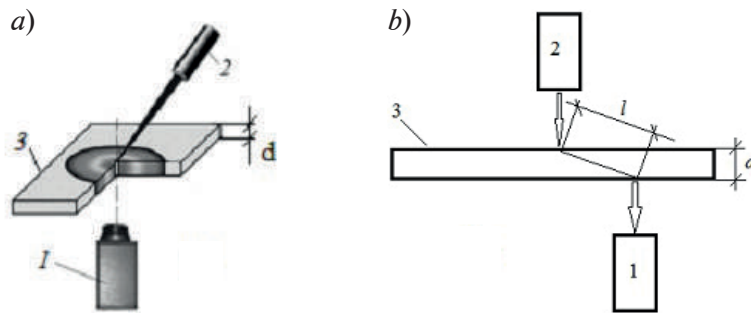
Fig. 1. Scheme (*a*) and geometry (*b*) of the arrangement of the IR camera *1*, laser *2* and object *3* when implementing the LFM
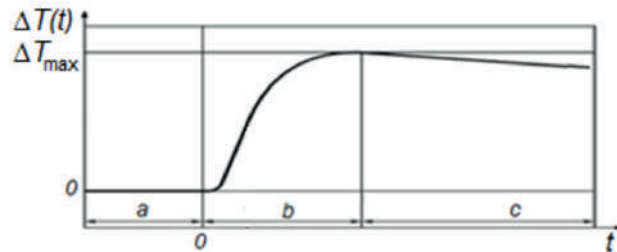
Fig. 2. Temperature change at a given point on the lower surface of the film after exposure to a laser pulse

Results and Discussion

Fig. 3 shows the dependence of the obtained values of the thermal diffusivity coefficient α of PVA films and epoxy resin plates on the concentration of MWCNTs. It can be seen that the addition of MWCNTs to the polymer leads to an increase in the thermal diffusivity and thermal conductivity coefficients several times compared to samples without MWCNTs.

At low concentrations of MWCNTs, the dependence of the thermal diffusivity coefficient α of the polymer nanocomposite on the concentration of MWCNTs C for both polymers is well described within the framework of the partial influence model:

$$\alpha = (1-C)\alpha_{POL} + C \cdot \alpha_{CNT},$$ (5)

where α_{POL} is the thermal diffusivity of the pure polymer, α_{CNT} is the thermal diffusivity of MWCNTs and $\alpha_{CNT} \approx 2.6...3.2$ m²/s. One of the possible explanations for the saturation of the dependence of PVA-based composites at MWCNTs concentrations greater than 2% is the process of MWCNTs clustering in the polymer matrix and an increase in contact resistance at the MWCNTs $-$ polymer interface.
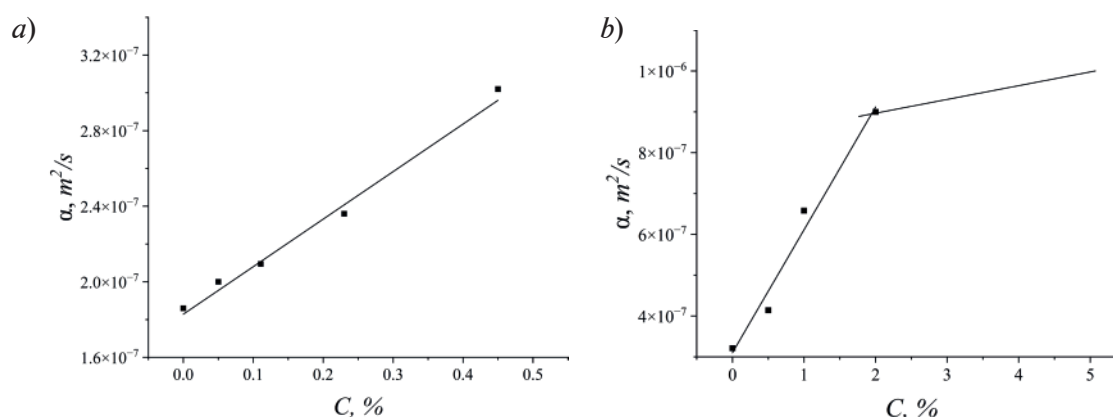
Fig. 3. Dependence of the thermal diffusivity coefficient α of epoxy resin plates (*a*) and PVA films (*b*) on the concentration of MWCNTs

Conclusion

The studies carried out showed a significant effect of the addition of MWCNTs on the thermal conductivity of the resulting polymer composite materials. In our opinion, the LFM for determining the thermal conductivity of polymer nanocomposite materials is a promising method that can be further improved by using, for example, not one, but four measurement points located at the vertices of a square. This orthogonal arrangement of measurement points will make it possible to detect and evaluate the anisotropy of thermal conductivity in composites with ordered nanotubes.

REFERENCES

1. **Zhong H., Haiping H.,** Review on Material Performance of Carbon Nanotube-Modified Polymeric Nanocomposites, Recent Progress in Materials. 5 (3) (2023).

2. **Vorobyeva E.A., Makarenko I.V., Makunin A.V., et al.,** On the synthesis and thermal conductivity of nanocomposites with multiwalled carbon nanotubes. J. Surf. Investig. 9 (2015) 784−788.

3. **Klimov E.S., Buzaeva M.V., Davydova O.A., et al.,** Some aspects of the synthesis of multiwalled carbon nanotubes by chemical vapor deposition and characteristics of the material obtained, Russ. J. Appl. Chem. 87 (2014) 1109−13.

4. **Klimov E.S., Buzaeva M.V., Davydova O.A., et al.,** Change in surface and some technological properties of carbonic nanotubes at their modification, Bashkir Chemical Journal, 21 (3) (2014) 109−113.

5. **Vasin S.V., Nizametdinov A.M., Sergeev V.A., Efimov M.S.,** Structure and electrical conductivity of polyvinyl alcohol films with multi-walled carbon nanotubes cured in a magnetic field, Radioelektronika, Nanosistemy, Informacionnye Tehnologii, 13 (4) (2021) 457–462.

6. **Nezhneva K.G., Hairullova R.M., Gusarova V.S., et al,.** Radioshielding polymer nanocomposite, In Proceedings of the 27th All-Russian Youth Scientific Conference "Actual Problems of Physical and Functional Electronics". Ulyanovsk, (2024) 138–139.

THE AUTHORS

VASIN Sergei V.
svasin@ulireran.ru
ORCID: 0000-0002-6342-8448

SERGEEV Vyacheslav S.
sva@ulstu.ru
ORCID: 0000-0003-4854-2813

KUZMIN Nikolai P.
niko_rus@mail.ru
ORCID: 0009-0007-9634-0745

BUZAEVA Mariya V.
m.buzaeva@mail.ru
ORCID: 0000-0001-6541-2637

Growth of GaN nanowires with InN inserts by PA-MBE

V.O. Gridchin [1, 2, 3] ✉, A.M. Mintairov [4], T. Shugabaev [1, 2], V.Yu. Axenov [4],

A.S. Vlasov [4], V.V. Lendyashova [1, 2], K.P. Kotlyar [1, 2, 3], I.A. Eliseev [4],

A.I. Khrebtov [2], R.R. Reznik [2], V.Yu. Davydov [4], G.E. Cirlin [1, 2, 3]

[1] Alferov University, St. Petersburg, Russia;
[2] St. Petersburg State University, St. Petersburg, Russia;
[3] Institute for Analytical Instrumentation RAS, St. Petersburg, Russia;
[4] Ioffe Institute, St. Petersburg, Russia
✉ gridchinvo@gmail.com

Abstract. For the first time, the growth details and photoluminescence properties of ultra-thin InN insertions embedded in GaN nanowires are presented. The InN insertions embedded in GaN nanowires exhibit photoluminescence in the range of 2.9−3.35 eV, where the most intense emission line at 3.17−3.23 eV is tentatively attributed to monolayer-thick InN insert based on comparative spectral analysis. These findings can be promising for the development of single-photon sources and Wigner quantum dots operating from cryogenic to elevated temperatures.

Keywords: InN, GaN, MBE, quantum dots, nanowires

Рост нитевидных нанокристаллов GaN с вставками InN с помощью МПЭ-ПА

В.О. Гридчин [1, 2, 3] ✉, А.М. Минтаиров [4], Т. Шугабаев [1, 2], В.Ю. Аксенов [4],

А.С. Власов [4], В.В. Лендяшова [1, 2], К.П. Котляр [1, 2, 3], И.А. Елисеев [4],

А.И. Хребтов [2], Р.Р. Резник [2], В.Ю. Давыдов [4], Г.Э. Цырлин [1, 2, 3]

[1] Академический университет им. Ж.И. Алфёрова РАН, Санкт-Петербург, Россия;
[2] Санкт-Петербургский государственный университет, Санкт-Петербург, Россия;
[3] Институт аналитического приборостроения РАН, Санкт-Петербург, Россия;

[4] Физико-технический институт им. А.Ф. Иоффе РАН,
Санкт-Петербург, Россия
✉ gridchinvo@gmail.com

Аннотация. Представлены результаты по росту и фотолюминесцентным свойствам InN вставок в GaN нитевидных нанокристаллах. Установлено, что такие InN вставки демонстрируют фотолюминесценцию в диапазоне 2,9−3,35 эВ, при этом наиболее интенсивная линия излучения при 3,17−3,23 эВ связывается с излучением от монослойных InN вставок на основании сравнительного спектрального анализа. Полученные результаты могут представлять интерес для создания источников одиночных фотонов и вигнеровских квантовых точек, способных работать в диапазоне от гелиевых до более высоких температур.

Ключевые слова: InN, GaN, MBE, квантовые точки, нитевидные нанокристаллы

Introduction

III-N wurtzite materials (AlN, GaN, InN) attract wide attention for fabrication novel two-dimensional optoelectronic structures. Of particular interest is the ultra-thin InN inserts (1 ML thick) embedded in GaN matrices. These structures exhibit photoluminescence at 3.2 eV which is substantially higher than the InN bulk band gap [1]. Theoretical studies predict that thin InN/GaN heterostructures can host topological insulator states [2], potentially enabling new opto-topological electronic applications. Furthermore, combined with the strong piezoelectric fields of III-N wurtzite materials, these structures may exhibit Wigner crystallization when InN is confined as quantum dot (QD) within GaN matric [3].

However, a growth of high-quality InN-based heterostructures remains challenging due to the relatively low growth temperature and the high lattice-mismatch between InN and other III-N materials (GaN, AlN) [4]. To overcome these limitations, we investigate the InN/GaN heterostructures through the nanowire (NW) growth. Due to a very efficient relaxation of elastic stress on strain-free sidewalls, NW heterostructures can be grown in lattice-mismatched system without structural defects or with largely reduced dislocation density compared to epi-layers [5].

In this work, the growth details and photoluminescence properties of ultra-thin InN inserts embedded in GaN NWs are presented. We demonstrate that the InN inserts within GaN nanowires exhibit photoluminescence in the 2.9−3.35 eV with the most intense line at 3.17−3.23 eV which assigns to monolayer-thick InN inserts based on comparative spectral analysis.

Materials and Methods

Growth experiments were carried out on one-side polished *n*-type Si substrates with resistivity of 0.002−0.004 Ohm·cm in a Riber Compact 12 plasma-assisted molecular beam epitaxy (PA-MBE) system. The surface orientation of the substrate was (111) with a 4° miscut toward the [110] direction. The MBE chamber equipped with Addon RF-N 600 plasma source and Knudsen cells of Ga and In. Prior to loading into the growth chamber, the substrate was etched in a 47.5%

hydrofluoric acid solution for 40 seconds, followed by a 60 second washing in deionized water. After that, the substrate was thermally cleaned in the MBE growth chamber at 855 °C for 20 min. Then, the substrate temperature was decreased to 620 °C. Next, the nitrogen plasma was ignited at a source power of 350 W with nitrogen flow of $4.4 \cdot 10^{-6}$ Torr, and the substrate was nitridated for 20 min to form Si_xN_y thin layer. At the next stage, Al was deposited onto the formed layer for 6 seconds in the absence of nitrogen plasma, nominally corresponding to ~2 ML coverage. After that, the substrate temperature was increased to 805 °C, the nitrogen plasma was ignited at the same parameters, and the Ga source was opened to grow of GaN NWs. This procedure allowed one to achieve the N-polar GaN NWs. The beam equivalent pressure of Ga corresponded to $1.5 \cdot 10^{-7}$ Torr. After a 18h of growth, the Ga source was closed, and the substrate temperature was decreased to 425 °C. The In source was opened with beam equivalent pressure of $1 \cdot 10^{-7}$ Torr for 25.9 sec to grow a thin InN insertion. Following the formation of the InN insertion, a 20 nm GaN cupping layer was grown at the same substrate temperature. The beam equivalent pressure of Ga in this case corresponded to $1 \cdot 10^{-7}$ Torr. It should be noted that the substrate temperature was measured using an Optris CT Laser 3MH1 pyrometer calibrated on the 7×7 to 1×1 surface reconstruction of the Si(111) substrate.

Morphological properties were studied using a Carl Zeiss Supra 25 scanning electron microscopy (SEM) system. Micro-PL measurements were carried out using a setup based on Horiba LabRAM HREvo UV-VIS-NIR-Open spectrometer. The spectra were excited by the 325 nm (3.81 eV) line of a He-Cd laser (Kimmon Koha IK5751I-G). To control the sample temperature, it was mounted in a Linkam THMS600 closed-cycle He cryostat (CRYO Industries of America). A long-working-distance objective (Mitutoyo Plan UV 80×, NA = 0.55) was used to focus the laser beam and collect the PL signal from the sample area of ~0.5 μm in diameter. To prevent damage and heating effects on the nanostructures, the incident laser power was limited to 60 μW. The spectra were measured using excitation power density ~0.5 W/cm² and spectral resolution 2–10 meV.

Results and Discussion

The NWs were synthesized through a self-induced mechanism, where NW nucleation occurs due to the lattice mismatch between the epitaxially growing material and the substrate. Figure 1, *a* demonstrates a representative SEM image of the grown InN/GaN NW array. The NW density is only ~10^8 cm^{-2}, which is unusually small for III-N NW growth, and was achieved by exploiting the high substrate growth temperature, where the Ga desorption from the Si surface becomes significant [37]. The NWs have hexagonal shape with a mean lateral sizes D ~ 40 nm and lengths ranging from 100 to 500 nm.

Figure 1, *b* presents integrated PL spectra measured in a region of 30×30 μm region on a squire grid with a step of 1 μm at 5K. The inclusions show PL intensity maps for the ranges 3.34–3.30 eV, 3.23–3.17 eV and 3.15–2.90 eV. We attribute most intense PL (in the range 3.23–3.17 eV) to 1 ML thick InN inserts embedded in GaN nanowires which is in good agreement with previously published data showing the emission from a 1 ML InN quantum well embedded in a GaN layer at ~3.2 eV [6, 7]. Other PL bands may originate from thicker inserts, which will be discussed in detail in subsequent works.

a)   *b*)
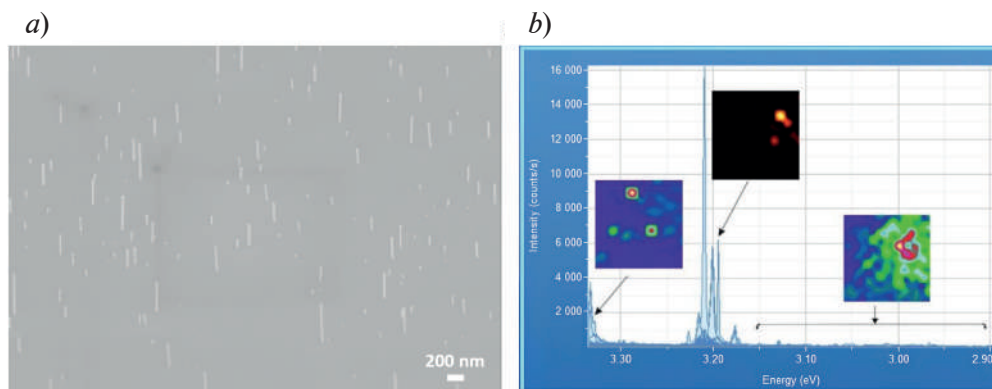
Fig. 1. Representative SEM image of grown InN/GaN nanowires (*a*). Integrated PL spectra measured in a 30×30 μm region on a squire grid having a step 1 μm at 5K (*b*). The inclusions show PL intensity maps for the ranges 3.34–3.30 eV, 3.23–3.17 eV and 3.15–2.90 eV

Conclusion

In summary, our study reveals that InN inserts embedded in GaN nanowires demonstrate distinct photoluminescence at 2.9–3.35 eV and a dominant peak at 3.17–3.23 eV. We attribute the latter dominant peak to monolayer-thick InN inserts based on comparative spectral analysis. Notably, these quantum-confined systems can be promising for single-photon emitters and Wigner quantum dots with operational capabilities ranging from helium temperatures to elevated temperature regimes.

REFERENCES

1. **Pan W., Dimakis E., Wang G.T., Moustakas T. D., Tsui D.C.,** Two-dimensional electron gas in monolayer InN quantum wells, Applied Physics Letters. 105 (21) (2014) 213503.

2. **Barettin D., Auf der Maur M., Pecchia A., Zhang Y., Willatzen Y., Wang Z.L.,** Piezoelectric tunability and topological insulator transition in a GaN/InN/GaN quantum-well device, Journal of Physics: Materials. 4 (3) (2021) 034008.

3. **Mintairov A.M., Axenov V.Yu., Lebedev D.V., Vlasov A.S., Frolov A.S., Ponamarev E.V., Stolyarov V.S.,** Dirac anyons in magnetophotoluminescence spectra of Wigner quantum dots: Molecular versus puddle states, Physical Review B. 111(4) (2025) 045410.

4. **Ivanov S.V., Shubina T.V., Komissarova T.A., Jmerik V.N.,** Metastable nature of InN and In-rich InGaN alloys, Journal of crystal growth. 403 (2014) 83−89.

5. **Dubrovskii V.G., Cirlin G.E., Kirilenko D.A., Kotlyar K.P., Makhov I.S., Reznik R.R., Gridchin V.O.,** Instantaneous growth of single monolayers as the origin of spontaneous core−shell $In_xGa_{1-x}N$ nanowires with bright red photoluminescence, Nanoscale Horizons. 9 (2024) 2360−2367.

6. **Kusakabe K., Imai D., Wang K., Yoshikawa A.,** InN/GaN short-period superlattices as ordered InGaN ternary alloys, physica status solidi (c). 13 (5−6) (2016) 205−208.

7. **Dimakis E., Nikiforov A.Yu., Thomidis C., Zhou L., Smith D.J., Abell J., Kao C.-K., Moustakas T.D.,** Growth and properties of near-UV light emitting diodes based on InN/GaN quantum wells, physica status solidi (a). 205 (5) (2008) 1070−1073.

THE AUTHORS

GRIDCHIN Vladislav O.
gridchinvo@gmail.com
ORCID: 0000-0002-6522-3673

KOTLYAR Konstantin P.
konstantin21kt@gmail.com
ORCID: 0000-0002-0305-0156

MINTAIROV Alexander M.
amintairov@mail.ioffe.ru

ELISEEV Ilya A.
zoid95@yandex.ru

SHUGABAEV Talgat
talgashugabaev@mail.ru
ORCID: 0000-0002-4110-1647

KHREBTOV Artem I.
khrebtovart@mail.ru

AXENOV Valerii Yu.
axenov.v@gmail.com

REZNIK Rodion R.
moment92@mail.ru
ORCID: 0000-0003-1420-7515

VLASOV Alexey S.
vlasov@scell.ioffe.ru

DAVYDOV Valery Yu.
valery.davydov@mail.ioffe.ru

LENDYASHOVA Vera V.
erilerican@gmail.com
ORCID: 0000-0001-8192-7614

CIRLIN George E.
george.cirlin@mail.ru
ORCID: 0000-0003-0476-3630

Optical reflectance spectroscopy for barrier thickness measurement of AlGaN/GaN heterostructures: comparison with X-ray reflectometry

D.S. Arteev [1] ✉, A.V. Sakharov [1, 2], A.E. Nikolaev [1],

E.E. Zavarin [1], A.V. Filimonov [3], A.F. Tsatsulnikov [2]

[1] Ioffe Institute, St. Petersburg, Russia;

[2] Submicron Heterostructures for Microelectronics, Research & Engineering Center, RAS, St. Petersburg, Russia;

[3] Connector Optics LLC, St. Petersburg, Russia

✉ ArteevDS@mail.ioffe.ru

Abstract. This study evaluates optical reflectance (OR) spectroscopy as a rapid, cost-effective alternative to X-ray reflectometry (XRR) for measuring the thickness of the AlGaN barrier layer in AlGaN/GaN heterostructures. OR spectroscopy demonstrated excellent agreement with XRR, with deviations not exceeding 1 nm. The results highlight OR spectroscopy as an efficient and reliable method for routine characterization of GaN-based heterostructures.

Keywords: gallium nitride, AlGaN/GaN, heterostructure, optical reflectance spectroscopy, X-ray reflectance

Измерение толщины барьерного слоя в гетероструктурах AlGaN/GaN методом спектроскопии оптического отражения: сравнение с рентгеновской рефлектометрией.

Д.С. Артеев [1] ✉, А.В. Сахаров [1, 2], А.Е. Николаев [1],

Е.Е. Заварин [1], А.В. Филимонов [3], А.Ф. Цацульников [2]

[1] Физико-технический институт им. А.Ф. Иоффе РАН, Санкт-Петербург, Россия;

[2] НТЦ Микроэлектроники РАН, Санкт-Петербург, Россия;

[3] ООО «Коннектор оптикс», Санкт-Петербург, Россия

✉ ArteevDS@mail.ioffe.ru

Аннотация. В данной работе исследуется возможность применения спектроскопии оптического отражения в качестве быстрой и недорогой альтернативы методу рентгеновской рефлектометрии (XRR) для измерения толщины барьерного слоя AlGaN в AlGaN/GaN гетероструктурах. Результаты, полученные двумя методами, хорошо согласуются друг с другом; отклонения не превышают 1 нм. Полученные данные демонстрируют, что спектроскопия оптического отражения может рассматриваться как практичный и надежный метод для регулярного контроля гетероструктур на основе GaN.

Introduction

Gallium nitride (GaN) is becoming a cornerstone of modern high-power devices due to its wide bandgap (~ 3.4 eV), high electron saturation velocity (~ 2.5×10^7 cm/s) [1] and large breakdown electric fields (> 3 MV/cm) [2]. In Al(Ga)N/GaN heterostructures − key to high-performance transistors — a two-dimensional electron gas (2DEG) with a concentration up to 6×10^{13} cm^{-2} [3] and mobility up to 2500 cm^{2}V^{-1}s^{-1} at room temperature [4] is formed at the heterointerface. Precise control of the barrier layer thickness is crucial, as this parameter affects the 2DEG density, mobility, and overall device performance.

X-ray reflectometry (XRR) is a standard, non-destructive technique capable of measuring layer thickness with sub-nanometer accuracy. However, it is relatively time-consuming, requires expensive complex equipment, and is often impractical for high-throughput measurements. Optical reflectance (OR) spectroscopy offers a simple, rapid, and more accessible alternative, particularly well-suited for routine measurement. Despite its advantages, the accuracy of OR for measuring barrier layers in AlGaN/GaN has yet to be evaluated.

In this work, we compare the performance of OR spectroscopy against XRR for determining the thickness of the barrier layer in AlGaN/GaN heterostructures. We demonstrate that OR spectroscopy provides reliable results with sub-nanometer agreement to XRR, while offering significant benefits in terms of cost, speed, and suitability for full-wafer analysis.

Materials and Methods

The heterostructures were grown on Si(111) substrates via metalorganic vapor phase epitaxy (MOVPE) in a custom Dragon-125 epitaxial system featuring an inductively heated horizontal reactor. Initially, AlN-on-Si templates were prepared in separate growth runs through the deposition of an AlN nucleation layer to prevent unintentional Ga incorporation. The AlN layer prevents Si wafer etching by gallium (referred to as the meltback etching effect [5]). The subsequent structure was grown in a second, main process as follows. First, a six-step compositionally graded AlGaN:Fe buffer layer was deposited on the templates. This design effectively addresses stress arising from the significant lattice mismatch and thermal expansion coefficient differences between GaN and Si, thereby reducing dislocation density and preventing crack formation during growth and cooling [6, 7]. Next, a ~1 μm-thick unintentionally doped GaN channel layer was grown, as we determined this thickness to be optimal for mitigating the detrimental effects of the Fe doping tail on the 2DEG properties, while maintaining good breakdown characteristics [8, 9]. Subsequently, a nominally binary ~1 nm thick AlN interlayer was deposited, followed by an AlGaN barrier layer with a different Al mole fraction and thickness. Finally, the structures were in-situ passivated with a Si_3N_4 layer (0.00 nm, 2.25 nm or 4.50 nm thick). A schematic cross-section of the grown structures is shown in Figure 1. Standard precursors − trimethylgallium (TMGa), trimethylaluminum (TMAl) and ammonia (NH_3), as well as ferrocene (Cp_2Fe) and monosilane (SiH_4), were used. A more detailed description of the growth conditions can be found in [6].

XRR measurements were performed with a PANalytical X'Pert PRO diffractometer (Cu Kα, λ = 1.5406 Å). The measured XRR spectra were analyzed and fit using X-ray Calc 3 software [10]. OR spectra were acquired at quasi-normal incidence using an Avantes AvaSpec 2048 fiber-optic

spectrometer with an AvaLight-DHc light source (deuterium mode only) and a 6-around-1 fiber optic reflection probe. The OR spectra were fit using the general transfer matrix method [11], with a custom Python-based implementation developed in-house. The complex refractive index for GaN were derived from the dielectric function in [12], while for AlGaN, data from [13] were used.
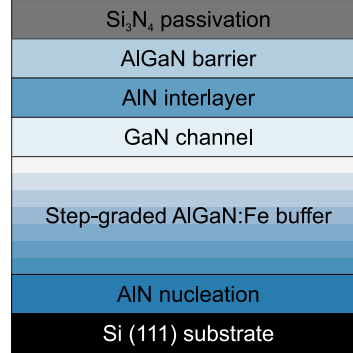
Fig. 1. Schematic cross-section of the epitaxial structures

Results and Discussion

The experimental XRR spectrum of one of the samples, along with the corresponding fitted curve, is shown in Fig. 2, *a*. Only the four topmost layers − namely, the Si_3N_4 passivation, AlGaN barrier, AlN interlayer, and GaN channel − were included in the analysis. The underlying buffer layers and substrate were found to have no impact on the results and were therefore omitted from the model. Consequently, the GaN channel layer was treated as an effective semi-infinite substrate. The obtained thicknesses of the Si_3N_4, AlGaN, and AlN are 4.49 nm, 16.93 nm and 0.71 nm, respectively. However, noted, the determined thickness of such ultra-thin AlN interlayer from XRR measurements may be ambiguous [14]; therefore, only the combined thickness of AlN and AlGaN barrier layers is meaningful.
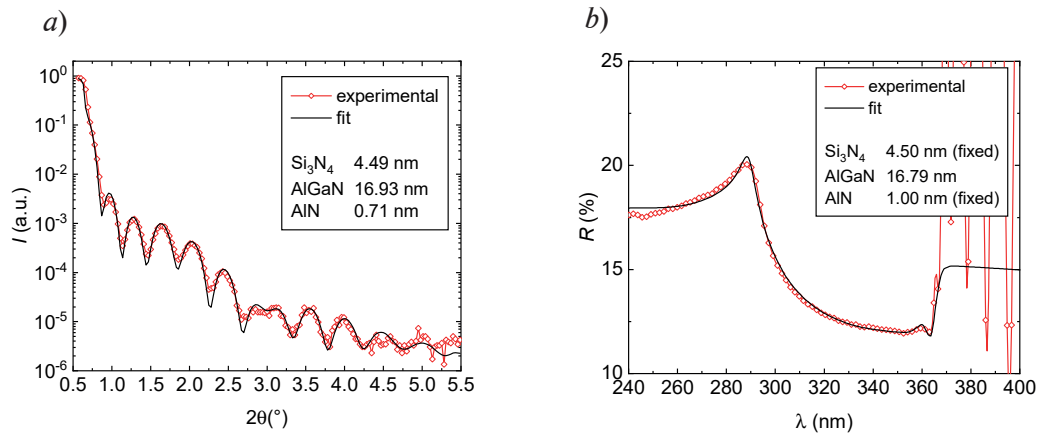
Fig. 2. Examples of the measured (red lines with symbols) XRR spectrum (*a*) and OR spectrum (*b*) along with the corresponding fitted curves (black lines)

Figure 2, *b* shows the measured optical reflectance spectrum of the previously discussed sample. Fabry-Perot oscillations are observed at wavelengths above around 365 nm, while absorption in the GaN layer suppresses these oscillations at shorter wavelengths. A distinct feature at around 290 nm corresponds to the bandgap of the AlGaN barrier layer. Due to the spectral range limitations of the equipment used (~240 nm), distinct spectral features attributable to the Si_3N_4 and AlN layers were not observed. Therefore, their nominal thickness values were fixed during the fitting procedures. Only the four topmost layers were included to the model, as in the XRR analysis. As shown in Fig. 2, *b*, the calculated OR spectrum (thin black line) accurately reproduces the shape and key features of the experimental spectrum. The fitted combined thickness of the barrier layers, 17.79 nm, is in excellent agreement with the XRR-derived value of 17.64 nm.

The fitting procedures described above were repeated for all investigated samples. A comparison of the combined thickness of the AlGaN and AlN barrier layers obtained using the XRR and OR methods is shown in Fig. 3. A good agreement is observed for all samples, with deviations not exceeding 1 nm, which is well within the estimated experimental uncertainty. These small differences may be attributed to spatial non-uniformities across the wafer, uncertainties in the optical constants, or the use of nominal thickness values for the AlN and Si_3N_4 layers in the OR modeling, which may slightly differ from their actual thicknesses.
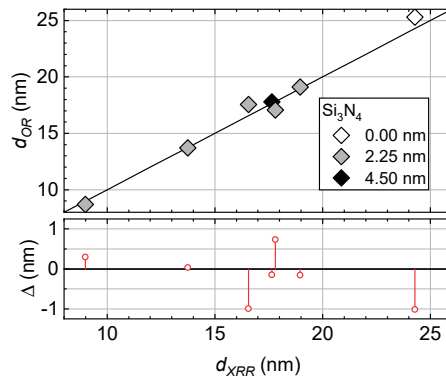
Fig. 3. Comparison of the combined thickness of the AlGaN and AlN barrier layers as determined by the XRR and OR method. The black line represents the ideal 1:1 agreement. Symbol fill denotes Si_3N_4 layer thickness: white for 0 nm, gray for 2.25 nm and black for 4.50 nm. The lower panel shows the difference between the values obtained by the two methods

Beyond the good agreement with XRR, the OR method is fast, non-destructive, and cost-effective. When combined with a CNC router or similar scanning setup, full-wafer mapping at dozens of locations can be completed within several minutes – a significant advantage over XRR, which is time-consuming and less suitable for large-area characterization. Additionally, the equipment required for OR measurements is relatively simple and inexpensive compared to the more complex and costly instrumentation needed for both XRR and spectroscopic ellipsometry, making OR highly accessible for routine use.

Nonetheless, the OR method has some inherent limitations. It requires prior knowledge of the optical constants of the materials involved, and the accuracy of the results strongly depends on the precision of these parameters. Moreover, OR is less sensitive to very thin layers. In contrast, XRR and ellipsometry techniques generally do not require such a priory information, often allowing the extraction of layer thicknesses and optical constants (in the case of ellipsometry) through model fitting. This restricts the flexibility of OR, especially when investigating novel or poorly characterized materials. However, even in the absence of precisely known optical constants, OR can still serve as a valuable tool for comparative "run-to-run" characterization. When a series of nominally identical structures is fabricated, or a previously grown structure is being reproduced, relative variations in OR spectra can be used to monitor process repeatability and detect early signs of drift in growth parameters. Thus, despite its limitations, OR remains a practical and efficient method for routine control in the production of semiconductor heterostructures.

Conclusion

In this work, optical reflectance (OR) spectroscopy was evaluated against X-ray reflectometry (XRR) for measuring the barrier thickness in AlGaN/GaN heterostructure. OR spectroscopy demonstrated excellent agreement with XRR, with deviations not exceeding 1 nm. These results highlight OR as reliable and cost-effective technique for routine, non-destructive analysis of GaN-based heterostructures, particularly in context requiring fast and/or large-area measurements.

REFERENCES

1. **Khurgin J., Ding Y.J., Jena D.,** Hot phonon effect on electron velocity saturation in GaN: A second look, Appl. Phys. Lett. 25 (2007) 252104.

2. **Dmitriev V.A., Irvine K.G., Carter C.H., Kuznetsov N.I., Kalinina E.V.,** Electric breakdown in GaN *p-n* junctions, Appl. Phys. Lett. 2 (1996) 229−231.

3. **Cao Y., Jena D.,** High-mobility window for two-dimensional electron gases at ultrathin AlN/GaN heterojunctions, Appl. Phys. Lett. 18 (2007) 182112.

4. **Yang L., Wang X., Wang T., Wang J., Zhang W., Quach P., Wang P., Liu F., Li D., Chen L., Liu S., Wei J., Yang X., Xu F., Tang N., Tan W., Zhang J., Ge W., Wu X., Zhang C., Shen B.,** Three Subband Occupation of the Two-Dimensional Electron Gas in Ultrathin Barrier AlN/GaN Heterostructures, Adv. Funct. Mater. 46 (2020) 2004450.

5. **Krost A., Dadgar A.,** GaN-Based Devices on Si, Phys. Status Solidi A. 2 (2002) 361−375.

6. **Sakharov A.V., Arteev D.S., Zavarin E.E., Nikolaev A.E., Lundin W.V., Prasolov N.D., Yagovkina M.A., Tsatsulnikov A.F., Fedotov S.D., Sokolov E.M., Statsenko V.N.,** AlGaN HEMT Structures Grown on Miscut Si(111) Wafers, Materials. 12 (2023) 4265.

7. **Arteev D.S., Sakharov A.V., Zavarin E.E., Nikolaev A.E., Yagovkina M.A., Tsatsulnikov A.F.,** Stress Analysis of GaN-Based Heterostructures on Silicon Substrates, Semiconductors. 2 (2024) 99−102.

8. **Arteev D.S., Sakharov A.V., Lundin W.V., Zavarin E.E., Zakheim D.A., Tsatsulnikov A.F., Gindina M.I., Brunkov P.N.,** Influence of doping profile of GaN:Fe buffer layer on the properties of AlGaN/AlN/GaN heterostructures for high-electron mobility transistors, J. Phys. Conf. Ser. 1 (2020) 012206.

9. **Arteev D.S., Sakharov A.V., Lundin W.V., Zavarin E.E., Nikolaev A.E., Tsatsulnikov A.F., Ustinov V.M.,** Scattering Analysis of AlGaN/AlN/GaN Heterostructures with Fe-Doped GaN Buffer, Materials. 24 (2022) 8945.

10. **Penkov O.V., Li M., Mikki S., Devizenko A., Kopylets I.,** X-Ray Calc 3: improved software for simulation and inverse problem solving for X-ray reflectivity, J. Appl. Crystallogr. 2 (2024) 555−566.

11. **Katsidis C.C., Siapkas D.I.,** General transfer-matrix method for optical multilayer systems with coherent, partially coherent, and incoherent interference, Appl. Opt. 19 (2002) 3978.

12. **Kim T.J., Hwang S.Y., Byun J.S., Barange N.S., Park H.G., Dong Kim Y.,** Temperature dependent dielectric function and the *E* critical points of hexagonal GaN from 30 to 690 K, AIP Adv. 2 (2014) 027124.

13. **Liu Y., Li Q.X., Wan L.Y., Kucukgok B., Ghafari E., Ferguson I.T., Zhang X., Wang S., Feng Z.C., Lu N.,** Composition and temperature dependent optical properties of $Al_xGa_{1-x}N$ alloy by spectroscopic ellipsometry, Appl. Surf. Sci. (2017) 389−396.

14. **Lesnik A., Bläsing J., Hennig J., Dadgar A., Krost A.,** Characterization of AlInN/AlN/GaN FET structures using x-ray diffraction, x-ray reflectometry and grazing incidence x-ray fluorescence analysis, J. Phys. Appl. Phys. 35 (2014) 355106.

THE AUTHORS

ARTEEV Dmitri S.
ArteevDS@mail.ioffe.ru
ORCID: 0000-0003-4447-8789

ZAVARIN Evgenii E.
EZavarin@mail.ioffe.ru
ORCID: 0000-0001-8380-3172

SAKHAROV Alexei V.
Val@beam.ioffe.ru
ORCID: 0000-0002-9976-999X

FILIMONOV Arkadii V.
filimonov@connector-optics.com
ORCID:

NIKOLAEV Andrey E.
Aen@mail.ioffe.ru
ORCID: 0000-0001-6522-4484

TSATSULNIKOV Andrey F.
Andrew@beam.ioffe.ru
ORCID: 0000-0002-5078-8946

MBE growth of wurtzite AlGaAs nanowires with zinc-blende insertions

A.S. Andreeva [1] ✉, I.V. Ilkiv [1, 2], K.P. Kotlyar [1, 2, 3], A.I. Khrebtov [1, 2],

V.O. Gridchin [1, 2, 3], G.E. Cirlin [1,2,3], R.R. Reznik [1,2,3]

[1] St. Petersburg State University, St. Petersburg, Russia;

[2] Alferov University, St. Petersburg, Russia;

[3] Institute for Analytical Instrumentation of the RAS, Saint Petersburg, Russia

✉ aa5991696@gmail.com

Abstract. In this work we present the experimental results on the molecular-beam epitaxy growth of wurtzite AlGaAs nanowires with nanoscale zinc-blende insertions on silicon substrate. Structural characterization confirmed the formation of zinc-blende nanoscale segments within the wurtzite nanowire matrix. Autocorrelation function measurements for emission at 710 nm have shown the characteristic dip at zero time delay, which indicates that the synthesized nanostructures are sources of single photons.

Keywords: Nanowires, AlGaAs, quantum dots, wurtzite, molecular-beam epitaxy

Рост методом МПЭ вюрцитных нитевидных нанокристаллов AlGaAs с включениями кубической кристаллографической фазы

А.С. Андреева [1, 2] ✉, И.В. Илькив [2], К.П. Котляр [2], А.И. Хребтов [3, 2],

В.О. Гридчин [2, 1], Г.Э. Цырлин [3, 2], Р.Р. Резник [1]

[1] Санкт-Петербургский государственный университет, Санкт-Петербург, Россия;

[2] Академический университет им. Ж.И. Алфёрова РАН, Санкт-Петербург, Россия;

[3] Институт аналитического приборостроения РАН, Санкт-Петербург, Россия

✉ aa5991696@gmail.com

Аннотация. В работе представлены результаты экспериментальных исследований по росту методом молекулярно-пучковой эпитаксии вюрцитных AlGaAs нитевидных нанокристаллов с наноразмерными вставками кубической кристаллографической

фазы на поверхности кремния. Результаты исследований структурных свойств подтвердили формирование вставок кубической фазы в вюрцитную структуру ННК. Результаты измерений автокорреляционной функции для излучения на длине волны 710 нм продемонстрировали характерный провал при нулевой временной задержке, что характеризует синтезированные наноструктуры как источники одиночных фотонов.

Introduction

Nowadays, III-V semiconductor nanowires (NWs) are promising platform for nanoscale devices due to their unique optoelectronic, electrophysical, transport and other properties [1, 2]. Recent advances in NWs formation enable integration of quantum dots (QDs) in the NWs matrix, allowing precise control over QDs' size and position, which define physical properties of QDs. In turn, III-V QDs are particularly promising as single photon sources, essential components for quantum communication and computing [3]. Moreover, the unique morphology of NWs allows the synthesis of such nanostructures directly on the silicon surface [4, 5]. However, the growth of QDs in NWs based on different material systems may come with a set of challenges, due to the possible reservoir effect during catalytic growth or significant mismatch of lattice constants. It has been shown previously that varying the growth conditions during NWs synthesis, for example III/V flux ratio, enables reversible alternation of the catalyst droplet's contact angle and change the crystallographic phase of the growing NW segment [6]. Furthermore, it was demonstrated that bands offset between the wurtzite (WZ) and zinc-blende (ZB) crystal phases can lead to an indirect electron-hole pair recombination [7] and formation of QDs within the single material system for III-V NWs, including GaAs, InAs and InP NWs, which can be sources of single photons [8]. However, to expand the number of applications, it is necessary to increase the range of compositions for such nanostructures. Previously, we have shown the possibility of Au-catalyzed WZ AlGaAs NWs on silicon for the first time and demonstrated their potential as a promising material system for optoelectronic applications [9, 10]. Formation of crystal phase QDs in such NWs could further increase the range of applications based on this material.

In this work we demonstrate the results of experimental studies on the Au-catalyzed WZ AlGaAs NWs with ZB nanoscale insertions growth by molecular-beam epitaxy (MBE) on Si(111). It was shown for the first time that AlGaAs NWs could be sources of single photons according to autocorrelation function measurements results.

Materials and Methods

Growth experiments were carried out using a Riber Compact 21 MBE setup equipped with Ga and Al effusion cells, As cracker source and additional metallization chamber. The one-side polished *p*-type Si wafers with surface orientation (111) were used as the substrates for

MBE growth. Initially, native oxide layer was removed by wafer etching in aqueous solution of hydrofluoric acid (10:1). Then the substrate was loaded into the metallization chamber where it was annealed at 850 °C for 20 minutes to remove residual oxide layer. Then substrate temperature was decreased to 550 °C and a 1 nm layer of Au was deposited onto the surface. The substrate was kept at the same temperature for one minute to form gold droplets on substrate. On the next stage the substrate was transferred into the growth chamber without breaking ultra-high vacuum conditions. In growth chamber the substrate temperature was increased to 510 °C and As shutter was open. After stabilization of As flux, Al and Ga shutters were opened simultaneously for 20 minutes initiating AlGaAs NWs growth. In order to form ZB segments As flux was periodically decreased from $1 \cdot 10^{-5}$ Torr to $4 \cdot 10^{-6}$ Torr by source aperture modulation from 100% to 45% for 5 seconds. The aperture response time was ~1 second. Although As is not pumped instantly from growth chamber, the growth conditions on the substrate surface change rapidly from group V-stabilized to group III-stabilized and back [8]. The fluxes from the Ga and Al sources corresponded to AlGaAs layer growth rate of 1 monolayer per second at a Ga/Al ratio of 0.5/0.5 according to preliminary calibrations.

Morphological properties of grown samples were studied using a Carl Zeiss Supra 25 scanning electron microscopy (SEM) system. Structural properties of single NWs were studied using Jeol 2100 transmission electron microscopy (TEM) system. Correlation measurements were performed using the optical stand equipped with the cryostat, monochromator, lasers for excitation of nanostructures and single photon detectors.

Results and Discussion

Figure 1, *a* demonstrates the typical SEM image of grown AlGaAs NWs array on Si(111) substrate. As can be seen from the figure, AlGaAs NWs formed strictly in [111] direction which indicates their epitaxial bond with the substrate. The average height of the NWs is 1.4 µm. It should be noted that the NWs have a non-uniform diameter in height − 140 nm at the base and 30 nm at the top of the NWs. The average NWs surface density is ~$2 \cdot 10^7$ cm^{-2} which allows exciting a single NW using the laser with a spot area of 1 µm.
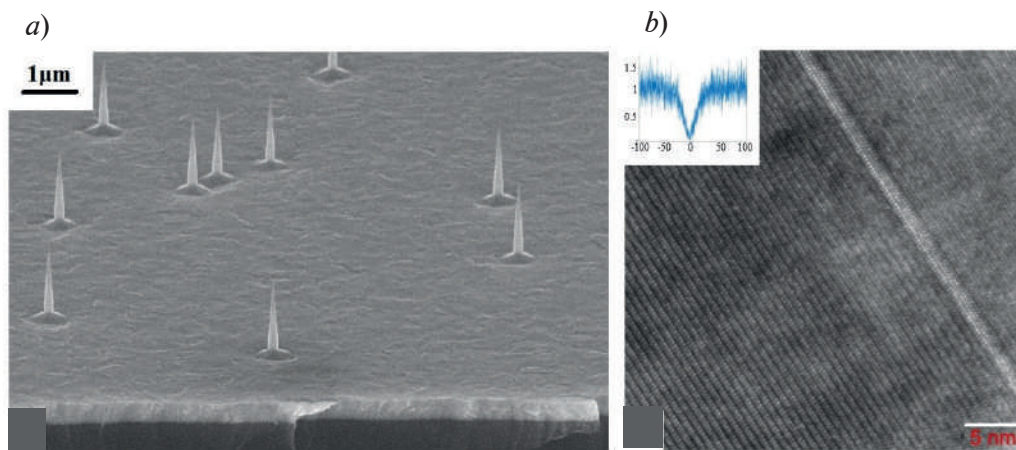
Fig. 1. Typical SEM image of grown AlGaAs NWs array on Si(111) substrate (*a*). Typical TEM image of the AlGaAs NW segment. The insert shows the results of the autocorrelation function measurements for emission at the wavelength of 710 nm (*b*)

Figure 1, *b* shows typical TEM image of the AlGaAs NW segment. It can be seen that NW segment demonstrates predominately WZ crystal structure with a presence of nanoscale ZB insertion. The height of the ZB insertion is ~2 nm. The insert to Fig. 1, *b* shows the results of the autocorrelation function measurements for photoluminescence emission at the wavelength of 715 nm, corresponding to AlGaAs [9]. The characteristic dip of the function at zero time indicates that the synthesized nanostructures are sources of single photons. It should be noted that the high noise level is associated with the short measurement time.

Conclusion

In summary, we demonstrated the MBE growth of WZ AlGaAs NWs with ZB insertions on the silicon surface using Au as a catalyst. The height of the ZB insertion studied using TEM is ~2 nm. The characteristic dip of the autocorrelation function at zero time indicates that the synthesized nanostructures are sources of single photons. These results open up new prospects for creating devices in the field of quantum technologies.

REFERENCES

1. **Agarwal R., Lieber C.M.,** Semiconductor nanowires: optics and optoelectronics, Appl. Phys. A. 3 (85) (2006) 209.

2. **Jia C., et al.,** Nanowire Electronics: From Nanoscale to Macroscale, Chem. Rev. 15 (119) (2019) 9074−9135.

3. **Mäntynen H., et al.,** Single-photon sources with quantum dots in III−V nanowires, Nanophotonics. 5 (8) (2019) 747−769.

4. **Wu Y., et al.,** Synthesis and Properties of InGaN/GaN Multiple Quantum Well Nanowires on Si (111) by Molecular Beam Epitaxy, Phys. Status Solidi A. 7 (217) (2020) 1900729.

5. **Bao X.-Y., et al.,** Heteroepitaxial Growth of Vertical GaAs Nanowires on Si (111) Substrates by Metal−Organic Chemical Vapor Deposition, Nano Lett. 11 (8) (2008) 3755−3760.

6. **Harmand J., et. al.,** Atomic Step Flow on a Nanofacet, Phys. Rev. Lett. 16 (121) (2018) 166101.

7. **Akopian N., et al.,** Crystal Phase Quantum Dots, Nano Lett. 4 (10) (2010) 1198−1201.

8. **Lozano M.S., Gymez V.J.,** Epitaxial growth of crystal phase quantum dots in III−V semiconductor nanowires, Nanoscale Adv. 7(5) (2023) 1890−1909.

9. **Barettin D., et al.,** Direct Band Gap AlGaAs Wurtzite Nanowires, Nano Lett. 3 (23) (2023) 895−901.

10. **Leandro L., et al.,** Wurtzite AlGaAs Nanowires, Sci. Rep. 1(10) (2020) 735.

THE AUTHORS

ANDREEVA Anna S.
aa5991696@gmail.com

ILKIV Igor V.
fiskerr@ymail.com
ORCID: 0000-0001-8968-3626

KOTLYAR Konstantin P.
kopkot95@yandex.ru

KHREBTOV Artem I.
khrebtovart@mail.ru
ORCID: 0000-0001-5515-323X

GRIDCHIN Vladislav O.
gridchinvo@gmail.com
ORCID: 0000-0002-6522-3673

CIRLIN George E.
cirlin.beam@mail.ioffe.ru
ORCID: 0000-0003-0476-3630

REZNIK Rodion R.
moment92@mail.ru
ORCID: 0000-0003-1420-7515

Effect of GaAs buffer layer on the characteristics of GaAs nanowires grown by molecular beam epitaxy on Si(111) substrates

V.V. Lendyashova [1] ✉, K.P. Kotlyar [1, 2, 3], A.I. Khrebtov [2],

G.E. Cirlin [1, 2, 3], I.V. Ilkiv [1, 2, 3]

[1] Alferov University, St. Petersburg, Russia;
[2] St. Petersburg State University, St. Petersburg, Russia;
[3] Institute for Analytical Instrumentation of the RAS, St. Petersburg, Russia
✉ erilerican@gmail.com

Abstract. The possibility of depositing colloidal nanoparticles onto an amorphous GaAs layer grown on Si(111) substrates and the direct molecular beam epitaxy of size-uniform GaAs nanowires with diameters below 20 nm were demonstrated. Examination of the nanowires revealed a nearly pure wurtzite crystal structure with low stacking fault density.

Keywords: nanowire, molecular beam epitaxy, semiconductors

Влияние буферного слоя GaAs на характеристики нитевидных нанокристаллов GaAs, выращенных методом молекулярно-пучковой эпитаксии на подложках Si(111)

В.В. Лендяшова [1] ✉, К.П. Котляр [1, 2, 3], А.И. Хребтов [2],

Г.Э. Цырлин [1, 2, 3], И.В. Илькив [1, 2, 3]

[1] Академический университет им. Ж.И. Алфёрова РАН, Санкт-Петербург, Россия;
[2] Санкт-Петербургский государственный университет, Санкт-Петербург, Россия;
[3] Институт аналитического приборостроения РАН, Санкт-Петербург, Россия
✉ erilerican@gmail.com

Аннотация. Показана возможность осаждения коллоидных наночастиц на аморфный слой GaAs, выращенный на поверхности Si(111) подложек. С использованием полученных подложек методом молекулярно-пучковой эпитаксии продемонстрирован прямой рост однородных по размеру GaAs нитевидных нанокристаллов с диаметром менее 20 нм. Установлено, что формируемые нитевидные кристаллы обладают вюрцитной кристаллической структурой с низким количеством дефектов упаковки.

Introduction

During recent years, semiconductor nanowires (NWs) have attracted great attention due to their unique optical and electronic properties. On the practical side, semiconductor NWs are very attractive for the direct integration of III-V materials on Si, opening up new possibilities for the design and fabrication of various applications, such as light-emitting diodes [1], field-effect transistors [2], etc. For a large number of devices, it is essential to synthesize ensembles with well-defined dimensions, size, shape, and phase purity of NWs because even small variations in size can have a large effect on overall device performance. Up to now, the most common technique for NW synthesis is vapor-liquid-solid growth using Au metal seed particles, which act as catalysts to initiate and guide the growth, directly controlling both diameter and orientation. Recent advances in this area have demonstrated the use of size-selected colloidal particles as seeds for MBE growth of GaAs NWs directly on Si [3−5]. However, there are several key issues concerning the use of colloidal nanoparticles as seed particles for the growth of NWs on Si. Specifically, the formation of GaAs NWs with diameters of about 50−100 nm is typically observed despite the use of nanoparticles 2−20 nm in diameter [4]. Besides that, diameter stabilization at the early growth stages also results in the tapering of NW bases [5]. The observed NW broadening effects are assumed to be due to the presence of Si atoms in the catalyst, which diffuse into the droplet during the high-temperature annealing of Au nanoparticles deposited on Si substrates [5−7].

In this work, we investigate the deposition of gold colloidal nanoparticles on a thin amorphous GaAs layer grown on Si(111) and how the presence of this GaAs layer affects the Au-assisted growth of GaAs NWs.

Materials and Methods

A Compact 21 Riber MBE system was used for the growth experiments. The investigations were carried out using a gold colloid containing 10-nm-diameter nanoparticles and Si(111) wafers. Two approaches for colloid deposition were applied. In the first case, colloid deposition was carried out on Si(111) substrates covered by native oxide with an Ar-plasma-irradiated surface. The plasma treatment was performed to improve the wetting properties of the silicon surface, enabling the direct deposition of Au nanoparticles onto the substrate [7]. In the second case, Si(111) substrates were etched by dipping in an HF solution to remove the native SiO_2 layer. After etching, the substrates were immediately loaded into the MBE chamber to prevent the formation of a new SiO_2 layer. The substrates were then annealed at 800 °C, after which a GaAs layer with a thickness of 50 nm was grown at 330 °C. Finally, the substrates were unloaded for colloidal deposition and loaded back for NW growth.

After the preparation step, NW growth was carried out. Upon loading the substrates, the temperature was ramped up to 520 °C and maintained throughout the process. NW growth was initiated by the simultaneous opening of the Ga and As shutters and lasted for 10 min. The Ga deposition rate was 0.9 ML/s, and the V/III flux ratio was ~20. After growth completion, the samples were cooled to room temperature and unloaded for morphological characterization via scanning electron microscopy (SEM) and transmission electron microscopy (TEM).

Results and Discussion

It is well established that the specific surface states of silicon substrates significantly affect colloidal nanoparticle deposition [8]. The deposition of Au nanoparticles (NPs) from colloidal solutions has been previously demonstrated using short Ar plasma modification [4]. The wettability of the GaAs surface layer grown on Si(111) substrates was significantly improved, resulting in a homogeneous distribution of Au nanoparticles across the substrate.

Bird-view SEM images of the grown samples are shown in Fig. 1. As seen in the figure, GaAs NWs grown on the GaAs/Si(111) substrate exhibited near-vertical alignment, consistent with the {111} crystal orientation family. These NWs maintained a uniform diameter along their entire length. In contrast, most GaAs NWs grown directly on Si(111) were non-directional and exhibited pronounced tapering (Fig. 1, *b*). This non-ideal growth behavior is attributed to suboptimal annealing temperatures for the Au NPs. To address this issue, an additional annealing step at 850 °C was performed to remove the native oxide underneath the Au seed particles. This modification increased the number of vertically aligned GaAs NWs. However, the NW morphology remained inhomogeneous, with noticeable tapering at both the bases and tips. The narrowing of the NW bases suggests the incorporation of Si atoms from the substrate into the Au-Ga catalyst droplet.
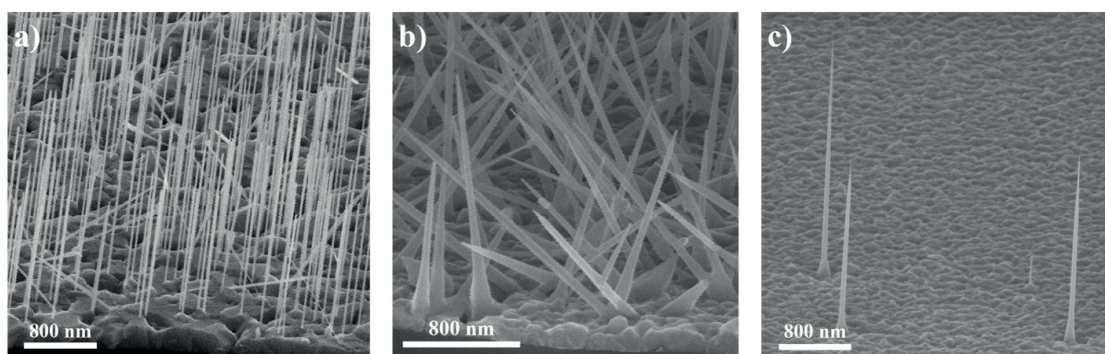
Fig. 1. GaAs NW ensembles grown on GaAs/Si(111) (*a*) and Si(111) surface without (*b*) and with (*c*) high-temperature annealing

Cross-sectional SEM imaging was used to determine the mean nanowire (NW) diameters. For GaAs NWs grown on GaAs/Si(111), the diameters of ten carefully measured nanowires ranged from 13 to 18 nm. In contrast, GaAs NWs grown directly on Si(111) exhibited a mean diameter approximately five times larger, despite the use of identical seed nanoparticles and growth conditions. The average NW length was similar for both samples, measuring approximately 2 μm.

Characterization of thin GaAs NWs by scanning TEM (STEM) was conducted in high angular annular dark field mode. GaAs NW in Fig. 2 exhibited a wurtzite structure. It was uniform along
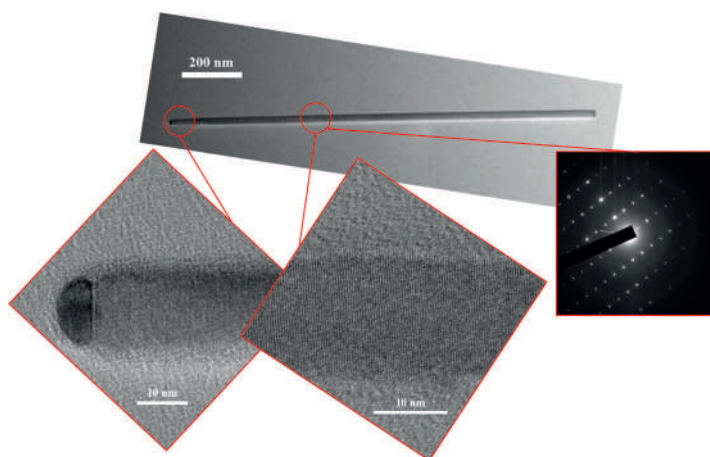
Fig. 2. TEM images of GaAs NW grown on GaAs/Si(111) substrate. Right inset is the diffraction pattern corresponded to wurtzite crustal structure

its length and shows no evidence of zinc-blend structure segmentation. Actually, stacking faults density was found to be around 0.5 μm^{-1}. The diameter of GaAs NW, measured next to NW tops, was found to be consistent with diameter of the 10 nm Au seed nanoparticle used. It indicates the Au-rich growth regime. Meanwhile, the slight increase in diameter towards the NW base was likely due to radial growth during the later growth stage. This result show a possibility of exploiting the bandgap engineering and quantum confinement effects in GaAs.

Conclusion

In summary, the possibility of depositing colloidal nanoparticles onto an amorphous GaAs layer grown on Si(111) substrates and direct molecular beam epitaxy of size-uniform GaAs nanowires with diameters below 20 nm was demonstrated. Examination of nanowires revealed nearly pure wurtzite crystal structure with low stacking fault density.

REFERENCES

1. **Park K., Lee J., Kim D., Seo J., Kim J., Ahn J. P., Park J.,** Synthesis of polytypic gallium phosphide and gallium arsenide nanowires and their application as photodetectors, ACS omega. 4 (2) (2019) 3098−3104.

2. **Patera M., Zieliński M.,** Antibonding ground states in crystal phase quantum dots, Physical Review B. 106 (4) (2022) L041405.

3. **Ilkiv I., Kirilenko D., Kotlyar K., Bouravleuv A.,** Thermal decomposition of GaAs nanowires, Nanotechnology. 31 (5) (2019) 055701.

4. **Bouravleuv A. D., Ilkiv I. V., Reznik R. R., Kotlyar K., Soshnikov I., Cirlin G. E., ... Lipsanen H.,** New method for MBE growth of GaAs nanowires on silicon using colloidal Au nanoparticles, Nanotechnology. 29 (4) (2017) 045602.

5. **Berdnikov Y., Ilkiv I., Sibirev N., Ubyivovk E., Bouravleuv A.,** Comparison of GaAs nanowire growth seeded by Ag and Au colloidal nanoparticles on silicon, Nanotechnology. 31 (37) (2020) 374005.

6. **Hijazi H., Dubrovskii V.G., Monier G., Gil E., Leroux C., Avit G., ... Andre Y.,** Influence of silicon on the nucleation rate of GaAs nanowires on silicon substrates, The Journal of Physical Chemistry C. 122 (33) (2018) 19230−19235.

7. **Andersen C.R.Y., Lehmann S., Tornberg M.U., Maliakkal C.B., Jacobsson D., Mшlhave K., Dick K.A.,** Direct observations of nucleation and early-stage growth of Au-catalyzed GaAs nanowires on Si (111), Nanotechnology. 36 (2025) 13560.

8. **Kolibal M., Konecny M., Ligmajer F., Skoda D., Vystavel T., Zlamal J., ... Sikola T.,** Guided assembly of gold colloidal nanoparticles on silicon substrates prepatterned by charged particle beams, ACS nano. 6 (11) (2012) 10098−10106.

THE AUTHORS

LENDYASHOVA Vera V.
erilerican@gmail.com
ORCID: 0000-0001-8192-7614

CIRLIN George E.
george.cirlin@mail.ru
ORCID: 0000-0003-0476-3630

KOTLYAR Konstantin P.
kopkot95@yandex.ru
ORCID: 0000-0002-0305-0156

ILKIV Igor V.
fiskerr@ymail.com
ORCID: 0000-0001-8968-3626

KHREBTOV Artem I.
khrebtovart@mail.ru
ORCID: 0000-0001-5515-323X

EXPERIMENTAL TECHNIQUE AND DEVICES

Noises in bioelectronic devices: a case study of electromagnetic interference in biolaboratory facilities

N.A. Boitsova [1] ✉, A.A. Abelit [1], N.A. Verlov [2], D.D. Stupin [1]

[1] Alferov University, St. Petersburg, Russia;

[2] Petersburg Nuclear Physics Institute named by B.P. Konstantinov of
NRC "Kurchatov Institute", St. Petersburg, Russia

✉ boitsova_na@spbau.ru

Abstract. Since bioelectrical signals typically have amplitudes below μA and lower than mV, their measurement is significantly susceptible to environmental electromagnetic interference (EMI). In this study, we measured and analyzed the levels of electromagnetic interference in biolaboratory rooms — the birthplace and preliminary test center for any bioelectronic device. We have shown that in an ordinary biolaboratory, which is equipped with typical modern instruments, like digital microscopes, EMI in the sub-250 kHz range can include both periodic and wide-band signals, which can influence the working of impedance sensors and neuroprosthetic implants. The results of our study can be used for the development and testing of noise-suppression systems for bioelectronics applications.

Keywords: electromagnetic interference, noise, impedance devices, spectra analysis, neuroprosthetic care, multielectrode arrays

Шумы в биоэлектронных приборах: исследование электромагнитных помех в биолабораторных помещениях

Н.А. Бойцова [1] ✉, А.А. Абелит [1], Н.А. Верлов [2], Д.Д. Ступин [1]

[1] Академический университет им. Ж.И. Алфёрова РАН, Санкт-Петербург, Россия;

[2] Петербургский институт ядерной физики им. Б.П. Константинова НИЦ
«Курчатовский институт», Санкт-Петербург, Россия

✉ boitsova_na@spbau.ru

Аннотация. Поскольку биоэлектрические сигналы как правило характеризуются низкими значениями своих амплитуд (<мкА и <мВ), на их измерение значительно влияют электромагнитные помехи окружающей среды (ЭМП). В настоящем исследовании мы измерили и проанализировали уровни электромагнитных помех, которые могут возникать в биолабораторных помещениях — в месте создания и первом испытательном центре любого биоэлектронного устройства. Мы показали, что в обычной биолаборатории, которая оснащена типичными современными приборами, такими как цифровые

микроскопы, ЭМП в диапазоне до 250 кГц могут включать как периодические, так и широкополосные составляющие, которые способны влиять на работу импедансных цитосенсоров и нейро-имплантатов. Результаты нашего исследования могут быть использованы для разработки и тестирования систем подавления шума в биоэлектронных приборах.

Ключевые слова: электромагнитные помехи, шумы, спектральный анализ, импеданс, нейропротезы

Introduction

Bioelectronic technologies are rapidly entering our lives today [1−3]. Moreover, the devices most commonly used in this field, such as impedance living cell-based biosensors and living neurons/computer interfaces, show great potential for solving important medical problems, such as lost vision restoration and artificial organ development. At the same time, since any cell-based bioelectronic system requires the usage of low voltage and current levels to prevent cell destruction, one of the central challenges in this field is device protection from external electromagnetic interference (EMI) [4−6]. In addition, in-lab testing of bioelectronic devices also requires the use of EMI mitigation methods.

For the development and application of both in-door and out-door EMI-canceling techniques, it is very useful to have real-life noise profiles, which can be used as an example for modeling and testing of the EMI-combat approaches. For this purpose, we have developed the noise measurement unit and MatLab/GNU Octave data processing scripts for capturing the examples of the EMI signals, which can be found in the ordinary biolaboratory, where bioelectronic devices are tested. The obtained data indicates that in such facilities the EMI signal contains not only 50-Hz powerline interference, but also periodic and wideband parts from other electronic devices, in particular from modern digital microscopes. The results of our study can be used as a methodology for EMI analyzing as well as examples of real noise data samples for noise-suppression digital algorithms approbation. Samples can be found on our GitHub page https://github.com/BioElectronicsLab/Noise-samples or available upon request.

Materials and Methods

EMI signals were measured using the setup, the main scheme of which is presented in Fig.1. It consists of a transimpedance amplifier (TIA) [8], which is commonly used for current measurements in electrophysiological studies [1]. As an operational amplifier, AD8606 (Analog Devices, USA) was used. As input for TIA the 10-cm antenna made of wire was used, which imitates the living-cell interface cable. The TIA output signal was recorded using the L-Card E20-10 ADC (L-Card, Russia). The sampling rate was 500 kHz and the data collection time for one EMI sample was 500 ms (*i.e.* 2 Hz resolution is achieved). The resistance to TIA feedback was 1 MΩ. The EMI spectra were obtained from the analog-to-digital converter time-domain input signal using the fft routine in MatLab and presented in the amplitude spectral density format.

We have measured the EMI noise levels in the five rooms at Saint-Petersburg Academic University: in the special room for cell diagnostics, which contains a lot of switched on devices, including confocal microscope Zeiss Observer.Z1 (Zeiss, Germany); the room for microscopic studies only, which is equipped with Leica DM 4000 B microscope (Leica, Germany); office room, with no switched on devices, which is located near switchgear room; break-room, with
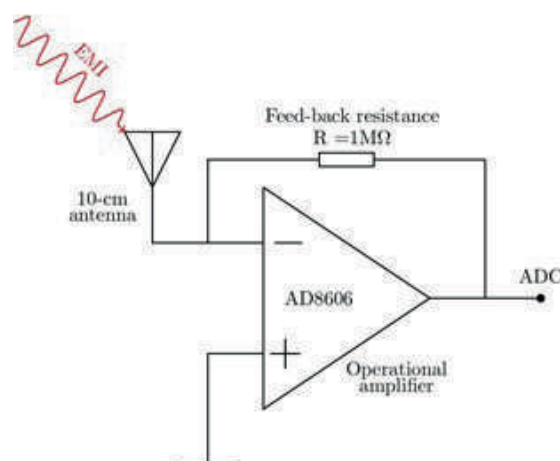
Fig. 1. Experimental setup, used for measuring EMI signals

several switch on PCs; and hall. In addition, since microscopes are widely used in bioelectronics to observe cells, we measured the EMI signals with the microscopes turned on and off to extract the EMI generated by them. For better visual detection of periodic components, the FFT spectra were averaged over 10 EMI samples (i.e. the level of random noise presented in one sample is $\sqrt{10}$ times higher than that shown in the figures).

Results and Discussion

The results obtained are presented in Fig. 2. One can see from Fig. 2, *a* the EMI in the cell diagnostic room contains a wide band spectrum with significant intensity, which increased with frequency. This observation clearly indicates that the noise influence problem can be relevant for bioelectronics devices even in the testing rooms (Table). Moreover, the wide band nature of this noise sample makes the usage of static filtering noise-cancellation methods inapplicable for EMI suppression if the wide band impedance sensors are tested. To overcome this problem, the progressive tools, like artificial intelligence adaptive filtering approach [8], can be used. Contrary to the cell diagnostic room, in the microscopy room we observed only two wide-band noise parts (57−72.5 kHz and 120−135 kHz), and periodic signal at 78 kHz. The presented 78-kHz signal and its overtones are also presented in all other rooms except the cell diagnostic room, where it possibly is lost in the other interferences. The break room also contains band noises in the ranges of 4−10 kHz, 187−194 kHz, and 204−210 kHz. Surprisingly, the clear 50-Hz powerline EMI with odd overtones (Fig. 2, *b*) is observed only in the office room, which is located near the switchgear room. The most noise-free room was a hall, where only 78 kHz interference was observed.

From the panels Fig. 2, *c* and Fig. 2, *d* one can see that microscopes introduce into the EMI new signatures (78−82~kHz for Leica; 24 kHz, 73 kHz $\approx$ 24×3 kHz, and 122 kHz $\approx$ 24×5 kHz for Zeiss); however, their impact is not so high with respect to environment EMI signals. Thus, since the observed EMI spectra demonstrate the variety of noise types, which can be both wide and narrow band, for protecting bioelectronic devices from EMI the common noise canceling techniques are preferable, which may be classified as technological, electronic, and software methods. From a technological point of view, the noise canceling can be achieved not by noise level decreasing, but by increasing the amplitude of the useful signal, which can be done by decreasing the impedance value (increasing current value) of the bioelectrodes via increasing their surface. The last one can be done without affecting the size of bioelectrodes using porous surfaces [1]. The electronic methods for noise canceling include the shielding, which can be utilized in the at-lab conditions; however implementation of such method is complicated in the bioelectronic implantation technologies and with portable biosensor design. The software methods are a more promising tool with respect to shielding for EMI suppression, since these approaches only require the utilization of the computing unit in the bioelectronic device components. For example, the already mentioned above adaptive filtering approach allows to suppress environment noises in the impedance-based biosensors and can be implemented in the real-time regime (see the package NELM for MatLab [9]).
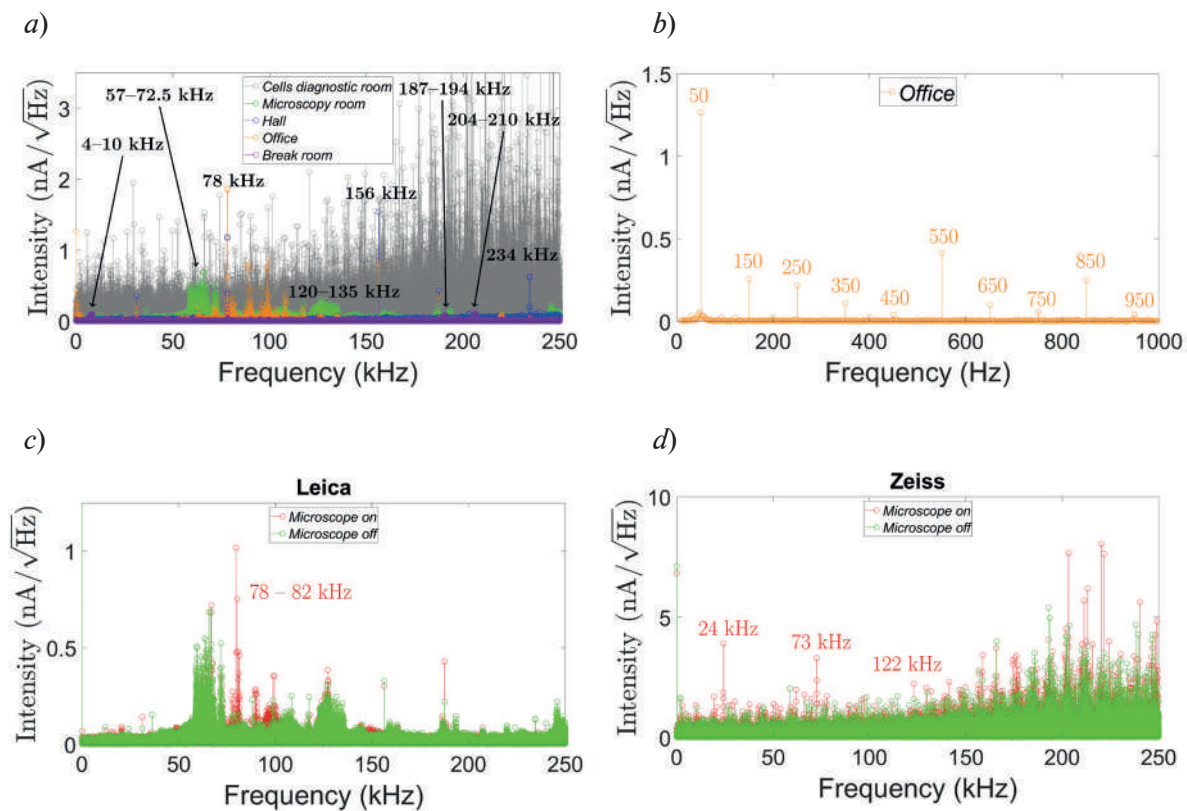
Fig. 2. Comparison of different EMI spectra. For clarity data presented in the amplitude spectral density format. Background (without any microscopes on) noise in a set of rooms (*a*); office room background noise from 1 Hz to 1 kHz that shows 50-Hz powerline and its harmonics (*b*); EMI signals detected while microscopes Leica (*c*) and Zeiss (*d*) were switched on (red) and switched off (green). As one can see, there are clear peaks (78−82 kHz for Leica, and 24 kHz, 73 kHz, and 122 kHz for Zeiss) that correspond with the work of microscopes

Table

Modeled signal-to-noise ratios for multielectrode array (MEA) 60MEA200/30iR-Ti (MultiChannel Systems, Germany)

	Cells diagnostic room	Microscopy room	Hall	Office	Breakroom
Signal-to-noise ratio (dB)	−3.5	14.2	15.0	8.0	16

Notation: The signal-to-noise ratios are calculated in the practically used range 10 Hz − 40 kHz as MEA current power to noise power relation in decibels. The power is calculated using rms MatLab routine. The MEA current excitation was performed by sweep-shaped 15-mV excitation voltage in the 240 kHz range. Both noise and MEA signals were preliminary filtered by 10th-order Butterworth filter with cutting frequency 40 kHz. This is simulation of data processing for wideband MEA experiments. Noises are assumed to be additive.

Conclusion

In this study, we have shown that, in the common case, the influence of EMI on the bioelectronic device functioning cannot be overlooked. Our data shows that even in biolaboratories, where bioelectronic devices are fabricated and tested, the EMI spectra can contain both periodic and wideband noises, which are results of the large number of electronic devices used in the modern world. For fighting with EMI, it is desirable to use low-impedance cell/electronic interfaces

like porous electrodes and short-length cables, as well as software noise suppression techniques. In addition, during our work on this study, we have observed that it is very hard to identify the EMI sources using only standalone EMI spectra because there is a significant lack of information on characteristic EMI peaks for various devices. To our best knowledge, only in a few handbooks [10, 11] about ten EMI sources signatures are presented, including electromotor, cell phones, and marginal EMI from nuclear explosion. The creation of a more informative EMI signature database will be very useful for the development of future EMI combat algorithms and electronic devices design. We believe that the results of our study will help bio-electronic engineers to create robust EMI biosensors and implants, which will solve actual healthcare problems.

Acknowledgments

REFERENCES

1. **Stupin D.D., Kuzina E.A., Abelit A.A., et al.,** Bioimpedance spectroscopy: basics and applications ACS Biomaterials Science & Engineering. 7 (6) (2021) 1962–1986.

2. **Neroev V.V., Astakhov Yu.S., Lobanova M.M., Stupin D.D. et al.,** Artificial vision: advances, topical issues, and prospects, Russian Ophthalmological Journal. 11 (3) (2018) 3–27.

3. **Jiang W. G., et al.,** Electric cell-substrate impedance sensing and cancer metastasis, Springer Science & Business Media. (17) 2012.

4. **Misiri J., Kusumoto F., Goldschlager N.,** Electromagnetic interference and implanted cardiac devices: the nonmedical environment (part I), Clinical cardiology. 35 (5) (2012) 276–280.

5. **Misiri J., Kusumoto F., Goldschlager N.,** Electromagnetic interference and implanted cardiac devices: the medical environment (part II), Clinical cardiology. 35 (6) (2012) 321–328.

6. **Togt R., Lieshout J.E, Hensbroek R. et al.,** Electromagnetic Interference From Radio Frequency Identification Inducing Potentially Hazardous Incidents in Critical Care Medical Equipment, JAMA. 299 (24) (2008) 2884−2890.

7. **Tietze U., Schenk C., Schmid E.,** Electronic circuits, Springer-Verlag. (1991).

8. **Stupin D.D., Koniakhin S.V., Verlov N.A., Dubina M.V.,** Adaptive filtering to enhance noise immunity of impedance and admittance spectroscopy: Comparison with Fourier transformation, Physical Review Applied. 7 (5) (2017) 054024.

9. **Boitsova N.A., Abelit A.A., Stupin D.D.,** NELM: Modern Open-Source Software for Multipurpose Impedance Spectra Analysis, arXiv preprint arXiv. 2506 (2025) 0199.

10. **Ramya K., Gopalakrishnan J., Bharatiraja C., et al.,** A Complete Review of Electromagnetic Interference in Electric Vehicle, IEEE Access. (2025).

11. **Ott H.W.,** Electromagnetic compatibility engineering, John Wiley & Sons. (2011).

THE AUTHORS

BOITSOVA Natalia A.
natab2002@yandex.ru
ORCID: 0009-0006-2524-7618

VERLOV Nikolai A.
verlov_na@pnpi.nrcki.ru
ORCID: 0000-0002-3756-0701

ABELIT Anna A.
anna.abelit@gmail.com
ORCID: 0000-0003-3859-6981

STUPIN Daniil D.
stu87@yandex.ru
ORCID: 0000-0002-5470-9301

PHYSICAL ELECTRONICS

Metamaterials formed on the surface of silicon carbide by plasma treatment

V.S. Klimin [1] ✉, A.V. Demyanenko [1], I.N. Bobkov [1]

[1] Southern Federal University, Taganrog, Russia

✉ kliminvs@sfedu.ru

Abstract. In the presented work, a unit cell of a self-complementary metamaterial was designed, which is alternating patches and holes in a conductive graphene-like layer 7 μm thick on a silicon carbide substrate 250 μm thick. The results of a numerical study of the developed structure are presented. The calculations considered the conductivity of the graphene-like film, as well as the dielectric parameters of the silicon carbide substrate. The developed metamaterial is designed to convert circular polarization into linear; the central operating frequency of the resulting structure is 10 GHz. The dimensions of the unit cell are 2.8 mm × 5.6 mm. The elements obtained can be used in microwave technology and antenna structures. For the manufacture of structures, it is planned to use the method of plasma-chemical etching of silicon carbide in a fluorine-containing gas environment, which destroys the silicon component and leaves a graphene-like conductive layer on the surface. The thickness of the graphene-like layer depends on the power of the inductively coupled plasma source and the processing time; in this work, a thickness of 7 μm was taken, obtained at 800 W and 8.5 minutes of etching SiC in an SF_6/Ar atmosphere.

Keywords: plasma etching, metamaterials, graphene-like film, silicon carbide, microelectronics

Формирование метаматериалов на поверхности карбида кремния методом плазменной обработки

В.С. Климин [1] ✉, А.В. Демьяненко [1], И.Н. Бобков [1]

[1] Южный федеральный университет, г. Таганрог, Россия

✉ kliminvs@sfedu.ru

Аннотация. В представленной работе была спроектирована элементарная ячейка самодополняющего метаматериала, представляющего собой чередующиеся патчи и отверстия в проводящем графеноподобном слое толщиной 7 мкм на подложке из карбида кремния толщиной 250 мкм. Представлены результаты численного

исследования разработанной структуры. При проведении расчетов учитывались проводимость графеноподобной пленки, а также диэлектрические параметры подложки из карбида кремния. Разработанный метаматериал предназначен для конвертации круговой поляризации в линейную, центральная рабочая частота полученной структуры 10 ГГц. Размеры элементарной ячейки 2.8 мм × 5.6 мм. Полученные элементы могут быть использованы в СВЧ-технике и антенных структурах. Для изготовления структур планируется применять метод плазмохимического травления карбида кремния в среде фторсодержащего газа, при котором происходит деструкция кремниевой составляющей и на поверхности остается графеноподобный проводящий слой. Толщина графеноподобного слоя зависит от мощности источника индуктивно-связанной плазмы и времени обработки, так в работе была взята толщина 7 мкм, получаемая при 800 Вт и 8,5 минутах травления SiC в атмосфере SF_6/Ar.

Ключевые слова: плазменное травление, метаматериалы, графеноподобные пленки, карбид кремния, микроэлектроника

Introduction

Modern technologies of micro- and nanoelectronics, operating in extreme conditions such as high temperatures, aggressive environments, strong electric fields, require materials with a unique combination of mechanical strength, thermal stability and controlled electrophysical properties. Silicon carbide (SiC) is a promising basis for such devices due to its wide band gap, high thermal conductivity and chemical inertness. However, to create functional elements such as metamaterials with specified electromagnetic characteristics, it is necessary to form conductive nanostructures on the SiC surface, in particular graphene-like films [1]. One of the most effective methods for their production is plasma etching, which allows for controlled modification of the SiC surface with the formation of conductive carbon layers with atomic precision. The formation of graphene-like films on SiC using plasma etching offers a fundamental new solution that combines the advantages of a semiconductor substrate and a conductive carbon layer [2].

Metamaterials [3] are artificially engineered thin and tightly packed two-dimensional arrays of resonant structures designed to have properties that are not found in naturally occurring materials. They achieve these unusual properties through their carefully structured internal architecture rather than their chemical composition. Metamaterials have been employed to control and manipulate electromagnetic waves.

A specific class of metamaterials exhibits band-pass filtering properties for one linear polarization while simultaneously acting as a band-stop filter for the orthogonal linear polarization [4]. An application of such structures could be the conversion of incident circularly polarized waves to linearly polarized waves. One such metamaterial is a self-complementary patch and hole metasurface [4].

In this paper the feasibility of fabricating self-complementary metasurfaces on a SiC substrates using a two-stage plasma chemical etching method is studied.

Materials and Methods

In this work, we propose obtaining a conductive layer on the surface of silicon carbide by a two-stage plasma-chemical etching method. In this method of obtaining, at the first stage, the near-surface layers are removed in a fluoride and oxygen plasma environment at minimum bias

voltage values and maximum voltage values of the inductively coupled plasma source. This mode allows for the actual plasma polishing of the surface and the removal of several defective surface layers. At the second stage, the bulk of the material was etched in fluoride plasma, which made it possible to remove the silicon component from the surface layers with the formation of a conductive graphene-like layer.

To study the possibility of creating self-complementary metasurfaces on SiC substrates by a two-stage plasma-chemical etching method, a cell of a rectangular patch-hole metasurface was designed and numerically studied using the Ansys HFSS full-wave electromagnetic simulation software.

The designed unit-cell is shown on a Fig. 1. The unit-cell consists of a 250 μm thick SiC substrate (colored light grey) and an etched 7 μm conductive graphene-like layer (colored dark grey on a Fig. 1). The relative permittivity of a SiC substrate in a simulation is equal to 10 and tg(δ) = 1×10^{-6}. Periodic boundary conditions are applied to the A, A', B, B' sides of the unit-cell. Two ports are placed at the sides parallel to the SiC surface. The dimensions of the designed structure are 2.8 mm by 5.6 mm.
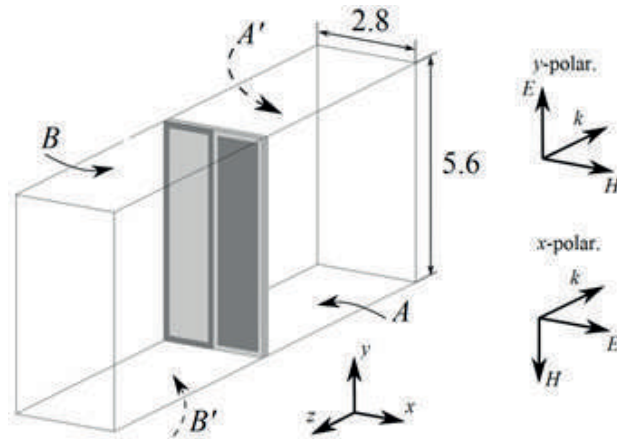
Fig. 1. Unit-cell of the rectangular patch and hole metasurface etched on a SiC substrate. Periodic boundary conditions are applied to the sides A, A', B, B'

Results and Discussion

Simulated transmission and reflection coefficients of the designed unit-cell at normal incidence are shown on a Fig. 2.

The magnitudes of the transmission coefficients for y-polarized and x-polarized waves are shown in Fig. 2, a. The central operating frequency of this metamaterial is 10 GHz. At that frequency, the designed metasurface functions as a band-pass filter for the y-polarized wave, and simultaneously as a band-stop filter for the x-polarized wave. The reflection coefficient for the y-polarized wave in Fig. 2, b approaches zero, confirming the performance of the metasurface.
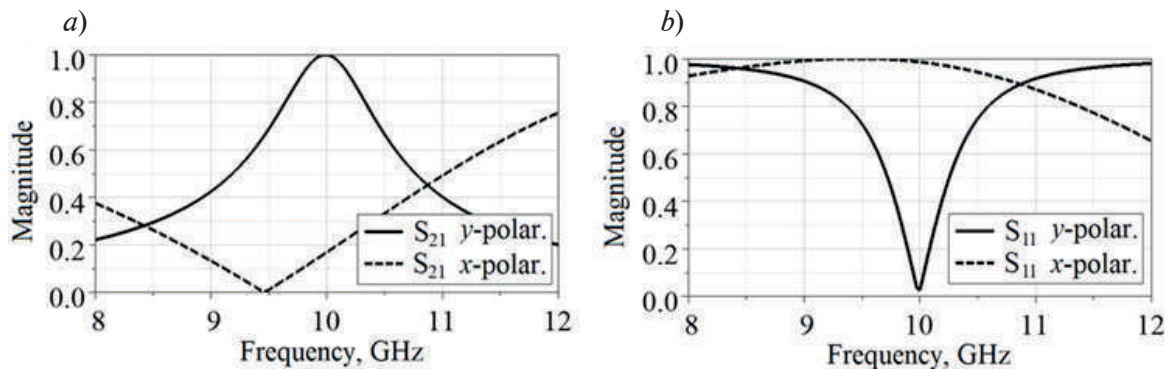
Fig. 2. Simulated magnitude of a transmission (a) and reflection (b) coefficients at normal incidence for rectangular patch and hole metamaterial unit-cell

The numerical study conducted demonstrates the potential for fabricating self-complementary metasurfaces on SiC substrates, for polarization conversion. However, experimental study is planned to validate the proposed hypotheses.

Conclusion

A unit cell of a self-complementary metamaterial for converting circular polarization into linear polarization has been developed and numerically studied. The metamaterial consists of alternating sections and holes in a 7-µm-thick conductive graphene-like layer on a 250-µm-thick silicon carbide substrate. The central operating frequency of the developed metamaterial is 10 GHz. The numerical study demonstrates the possibility of creating self-complementary metasurfaces on SiC substrates for polarization conversion in the X-band.

The developed and numerically studied structure, like most metamaterials, is periodic, which means that it is sufficient to model only one unit cell with periodic boundary conditions on the faces. To manufacture an array of self-complementary metasurface cells, it is planned to use the method of creating a conductive graphene-like film on the SiC surface by plasma destruction of the silicon component.

REFERENCES

1. **Emtsev K.V., Bostwick A., Horn K.,** Towards wafer-size graphene layers by atmospheric pressure graphitization of SiC, Nature Materials. 8 (3) (2009) 203–207.

2. **Klimin V.S., Rezvan A.A., Ageev O.A.,** Study of the effect of carbon-containing gas pressure on the geometric parameters of an array of carbon nanostructures, IOP Conf. Series: Journal of Physics: Conf. Series. 1124 (2) (2018) 022035.

3. **Glybovski S.B., Tretiakov S., Belov P.A., Kivshar Y.S., Simovski C.R.,** Metasurfaces: From microwaves to visible, Physics reports: review section of physics letters. 634 (2016) 1–72.

4. **Ortiz J.D., Baena J.D., Marqures R., Medina F.,** Self-Complementary Metasurface for designing a new kind of Frequency Selective Surface, The Fifth International Congress on Advanced Electromagnetic Materials in Microwaves and Optics, Barcelona, Spain. (2011) 113–115.

THE AUTHORS

KLIMIN Viktor S.
Kliminvs@sfedu.ru
ORCID: 0000-0002-9794-4459

BOBKOV Ivan N.
antennadesign@outlook.com
ORCID: 0000-0002-6923-7917

DEMYANENKO Alexander V.
demalex@inbox.ru
ORCID: 0000-0001-9326-2349

All-silicon elements of terahertz photonics obtained by plasma etching

V.S. Klimin [1] ✉, E.Yu. Gusev [1], V.V. Polyakov [1], P.A. Tarasov [1, 2], M.N. Grigoryev [1],

S. Wang [3], Z. Wang [3], L. Jiang [3], W. Zhang [3], O.A. Ageev [1]

[1] Southern Federal University, Taganrog, Russia;

[2] JSC "TNIIS", Taganrog, Russia;

[3] Qilu University of Technology, Shandong Academy of Sciences, Jinan, China

✉ kliminvs@sfedu.ru

Abstract. In the presented study, nanostructures on a silicon substrate were experimentally formed using the plasma-chemical etching method in a combined discharge plasma. The main objective was to analyze the relationship between the plasma-chemical etching process parameters and the structure geometry, namely: the deviation angle from the vertical, the height of the elements, and deviations from the nominal dimensions. Particular attention was paid to the influence of the active gas concentration, the power of the inductively coupled plasma source (ICP), and the power of the capacitively coupled source (CCP, bias voltage) on the structure geometry. The resulting nanostructures are considered as potential elements of terahertz photonics of metasurfaces. For example, process settings with an ICP power of 400 W, an active gas volume fraction of 7%, and a bias voltage of 101 V made it possible to obtain structures with a height of 136 nm, deviating from the specified dimensions by only 2% (98% compliance).

Исследование формирования элементов терагерцовой фотоники методом плазменного травления

В.С. Климин [1] ✉, Е.Ю. Гусев [1], В.В. Поляков [1], П.А. Тарасов [1, 2], М.Н. Григорьев [1],

Ш. Ван [3], Ж. Ван [3], Л. Янг [3], В. Жан [3], О.А. Агеев [1]

[1] Южный федеральный университет, г. Таганрог, Россия;

[2] АО «Таганрогский научно-исследовательский институт связи», г. Таганрог, Россия;

[3] Технологический университет Цилу, Шаньдунская академия наук, Цзинань, Китай

✉ kliminvs@sfedu.ru

Аннотация. Основная задача представленного исследования заключалась в исследовании связи параметров процесса плазмохимического травления с геометрией структур, а именно: углом отклонения от вертикали, высотой элементов и отклонениями от номинальных размеров. Особое внимание уделялось влиянию концентрации активного газа, мощности индуктивно-связанного плазменного источника (ICP) и мощности емкостно-связанного источника (CCP, напряжение смещения) на геометрию структур. Созданные наноструктуры рассматриваются как потенциальные элементы терагерцовой фотоники метаповерхностей. Например, настройки процесса с мощностью ICP 400 Вт, объемной долей активного газа 7% и напряжением смещения 101 В позволили получить структуры высотой 136 нм, отклоняющиеся от заданных размеров лишь на 2% (соответствие 98%).

Ключевые слова: кремниевая микроэлектроника, терагерцовая фотоника, метаматериалы, плазменное травление, микроэлектроника

Introduction

The development of modern micro- and nanoelectronics technologies dictates the need to create materials with unique properties unattainable in nature. Metamaterials meet these requirements, they open new possibilities for photonics, plasmonic, sensors and stealth technology devices [1]. However, traditional lithography and etching methods are limited in creating the subwavelength structures required for metamaterials [2]. Plasma-chemical etching has several advantages, such as a high degree of control over the geometry of nanostructures, scalability and selectivity of the process [3]. Integration of metamaterials with silicon substrates can expand their functionality and lead to the creation of new optoelectronic devices, including ultra-sensitive sensors and elements of quantum computers. Thus, the study of plasma etching processes for the formation of metamaterials on silicon is of significant scientific and practical interest, opening the way to the development of innovative components for nanophotonic and microelectronics.

Materials and Methods

The samples were silicon wafers coated with a resistive masking aluminum film 500 nm thick, deposited by magnetron sputtering. A group of geometric structures simulating elements of terahertz lenses was formed on part of the surface. The pattern was created using standard photolithography with FP 9120-1 photoresist. Development was carried out in an aqueous NaOH solution (0.6%) until the aluminum areas not protected by the photoresist were completely etched. Complete removal of the photoresist was performed in inductive oxygen plasma for 3 minutes at a plasma source power of 650 W. The composition of the gas mixture during etching was a mixture of oxygen, argon, and dichlorodifluoromethane active gas. The ratio of the gas mixture was changed during the study, the dependence of which is given in the results. The silicon surface was etched using inductive RF plasma (13.56 MHz) with a constant bias generated by a CX-600 generator, the power of which was maintained constant at 100 W during the experiment. Three groups of samples were formed using a CCl_2F_2 gas mixture. In each group, the power of the plasma source and the percentage composition of the gas mixture were varied. The obtained structures were examined on a profilometer, and numerical results were obtained using the SensoVIEW 8.1 software package.

Results and Discussion

As a result of experimental studies, arrays of structures of various configurations were obtained on the silicon surface, some of which are shown in Figure 1.
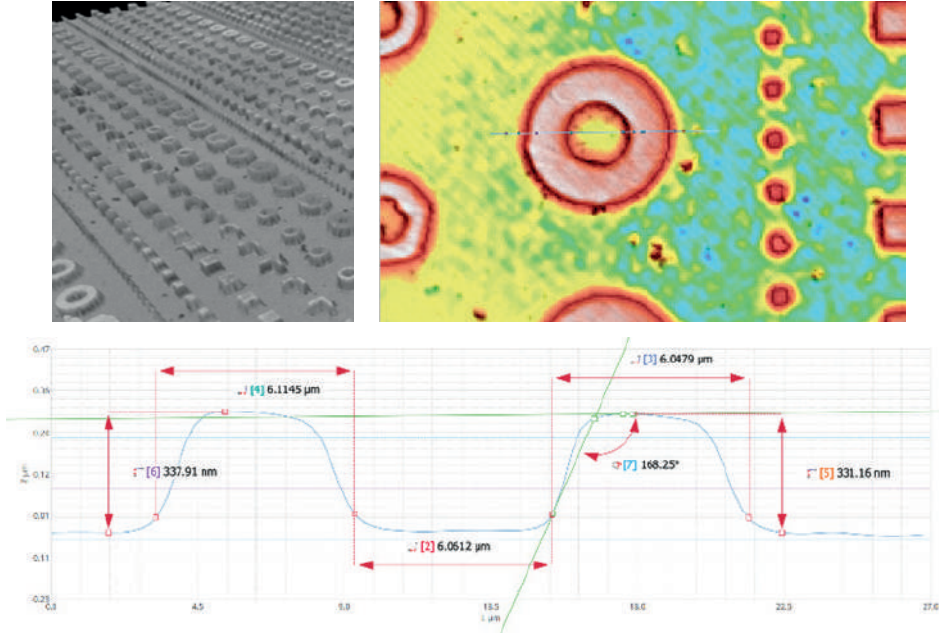
Fig. 1. Images of structures and profiles obtained on the silicon surface by plasma-chemical etching

During the work, the dependence of the height of the formed silicon structures on the power source of capacitive coupled plasma was obtained for different percentages of active gas in the mixture (Fig. 2).
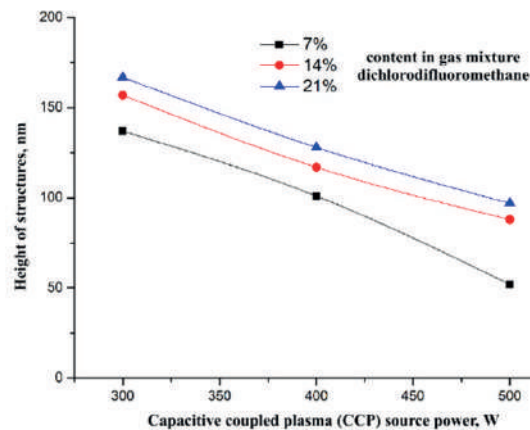
Fig. 2. Dependence of the height of the structures on the power source of capacitive coupled plasma, for different percentages of active gas in the mixture

During the studies, the dependences of the structure parameters on the plasma processing modes were obtained, so with a volume fraction of active gas of 14%, a bias voltage of 157 V, the height of the structures was 256 nm, and the correspondence of the sizes to the initially specified ones was 79%. At the same time, with a volume fraction of active gas of 21% and a bias voltage of 168 V, the height of the structures was 338 nm, and the correspondence of the sizes to the initially specified ones was 99%.

Conclusion

In this paper, we study the dependences of nanostructure parameters on plasma-chemical etching modes. The obtained dependences will allow us to form nanostructures of a given size

and minimize deviations from the given size in terms of deviation angle and lateral dimensions. For example, with an inductively coupled plasma source power of 400 W, an active gas volume fraction of 7%, and a bias voltage of 101 V, we obtained structures measuring 136 nm with 98% compliance with the dimensions specified during design. The obtained structures can be used as metasurface structures for terahertz photonics.

REFERENCES

1. **Bao J., Yu N., Capasso F.,** Plasma-etched silicon metamaterials for visible light applications, Advanced Optical Materials. 8 (12) (2020) 1902089.

2. **Efremov A.A., Kwon K.H., Kim D.P.,** On the relationships between plasma parameters and etching characteristics in $SF_6/O_2/SiCl_4$ plasma, Plasma Chemistry and Plasma Processing. 39 (3) (2019) 643−656.

3. **Klimin V.S., Kessler I.O., Morozova Yu.V., Saenko A.V., Vakulov Z.E., Ageev O.A.,** Study of Silicon Etching Modes in Combined Plasma Discharge for the Formation of Optoelectronic Structures. Bulletin of the Russian Academy of Sciences: Physics. 86 (2022) S96−S99.

THE AUTHORS

KLIMIN Viktor S.
kliminvs@sfedu.ru
ORCID: 0000-0002-9794-4459

GUSEV Eugene. Yu.
eyugusev@sfedu.ru
ORCID: 0000-0001-8635-2573

POLYAKOV Vadim V.
dankir@sfedu.ru
ORCID: 0000-0002-9329-0662

TARASOV Pavel A.
einjpptc@gmail.com
ORCID: 0009-0000-7843-9839

GRIGORYEV Mikhail N.
gregoryevmikhail@gmail.com
ORCID: 0009-0001-1684-1475

WANG Shumeng
smwang@ sdlaser.cn

JIANG Liyuan
jiangliyuan@sdlaser.cn

WANG Zhaowei
zw.wang@qlu.edu.cn

ZHANG Wei
zhang.wei@qlu.edu.cn
ORCID: 0000-0002-3584-8541

AGEEV Oleg A.
ageev@sfedu.ru
ORCID: 0000-0003-1755-5371

Formation of a graphene-like conductive film on the surface of SiC by laser destruction of silicon

V.S. Klimin [1] ✉, P.A. Tarasov [1, 2], M.N. Grigoryev [1, 2],

P.E. Gavrish [1, 2], A.A. Tkachyova [1, 2], V.V. Ptashnic [1, 2]

[1] Southern Federal University, Taganrog, Russia;

[2] JSC "TNIIS", Taganrog, Russia

✉ kliminvs@sfedu.ru

Abstract. This study is devoted to the formation of conductive graphene-like layers on the surface of silicon carbide by laser removal of silicon in local zones. The work demonstrates the effect of the laser system pulse frequency on the thickness and electrical conductivity of the resulting conductive graphene-like layer on a silicon carbide plate. In addition, optimal parameters for obtaining a conductive coating and the required surface roughness suitable for designing antenna devices are determined. At a frequency of 100 kHz, conductive graphene films of the coating with a thickness of 6.5 μm were obtained, while the modified zone was 93% of the total impact area. The thickness of the conductive layer in the local zone processed at a frequency of 40 kHz reached 5 μm, and at a frequency of 120 kHz − 7 μm. The results demonstrate the potential for the development and creation of sensor elements, optoelectronics and photonics devices.

Keywords: graphene, laser destruction, silicon carbide, microelectronics

Формирование графеноподобной проводящей пленки на поверхности карбида кремния методом лазерной деструкции кремния

В.С. Климин [1] ✉, П.А. Тарасов [1, 2], М.Н. Григорьев [1, 2],

П.Е. Гавриш [1, 2], А.А. Ткачева [1, 2], В.В. Пташник [1, 2]

[1] Южный федеральный университет, г. Таганрог, Россия;

[2] АО «Таганрогский научно-исследовательский институт связи», г. Таганрог, Россия

✉ kliminvs@sfedu.ru

Аннотация. Данное исследование посвящено формированию проводящих графеноподобных слоев на поверхности карбида кремния методом лазерного удаления кремния в локальных зонах. В работе продемонстрировано влияние частоты импульсов лазерной системы на толщину и электропроводность образующегося проводящего

графеноподобного слоя на пластине карбида кремния. Кроме того, определены оптимальные параметры для получения проводящего покрытия и требуемой шероховатости поверхности, пригодных для проектирования антенных устройств. В частности, при частоте 100 кГц были получены проводящие пленки графена покрытия толщиной 6,5 мкм, при этом модифицированная зона составила 93% от общей площади воздействия. Толщина проводящего слоя в локальной зоне, обработанной при частоте 40 кГц, достигала 5 мкм, а при частоте 120 кГц − 7 мкм. Полученные результаты демонстрируют потенциал для разработки и создания сенсорных элементов, устройств оптоэлектроники и фотоники.

Ключевые слова: графен, лазерное разрушение, карбид кремния, микроэлектроника

Introduction

In recent decades, graphene and graphene-like materials have gained significant popularity in the scientific community due to their unique electronic, mechanical and thermodynamic properties. These materials offer prospects for the development of more efficient electronic devices and sensors, as well as energy storage systems. Traditional methods of graphene synthesis, such as chemical vapor deposition or mechanical exfoliation, are associated with certain difficulties, including high cost and complexity of the processes [1−2]. One of the promising approaches to the formation of graphene-like coatings is laser ablation of the silicon component from a silicon carbide (SiC) substrate. This technique allows one to obtain graphene-like films directly on the SiC surface and control the process by optimizing the laser exposure parameters. This method provides a high degree of control over the properties of the final material and helps to reduce the time and cost of synthesis [3].

The relevance of this study is due to the growing demand for graphene and graphene-like materials in microelectronics and sensors, which necessitates the creation of new efficient and cost-effective methods for their production. The SiC substrate on which the conductive layer is formed has properties suitable for creating power electronics devices, which makes it a promising basis for working with graphene-like films [4]. In addition, the SiC laser ablation method opens new opportunities for studying the interaction of laser radiation with materials, which can contribute to the creation of innovative technologies for surface treatment and the formation of structures for microelectronics tasks [5−7]. Thus, the study is significant not only for materials science but also has practical value for the creation of new electronic devices, confirming their relevance in modern scientific and technical conditions.

Materials and Methods

The objects of the study were silicon carbide (SiC) substrates of the 6H-SiC polytype, on the surface of which a conductive graphene layer was formed by laser ablation. In this work, we studied the change in the pulse frequency of the laser system at a constant beam scanning speed of 400 mm/s. For the experiments, we used a PL-DFB-1060 laser system − a source of coherent radiation with a central wavelength of 1060 nm. The size of the processed local area was 700×700 μm. The diameter of the laser spot was 20 μm. The resulting graphene-like film samples were laser-cut to measure the thickness.

Results and Discussion

Based on the results of the conducted experimental studies, the dependences of physical and electrophysical parameters on the pulse frequency of laser processing of the local zone were established. Thus, Figure 1, *a* illustrates a local area with a formed graphene-like film at a pulse frequency of 40 kHz, where the thickness of the conductive layer reached 5 μm. Figure 1, *b* demonstrates the result of laser ablation on a section of silicon carbide at a frequency of 120 kHz with a conductive layer thickness of 7 μm.
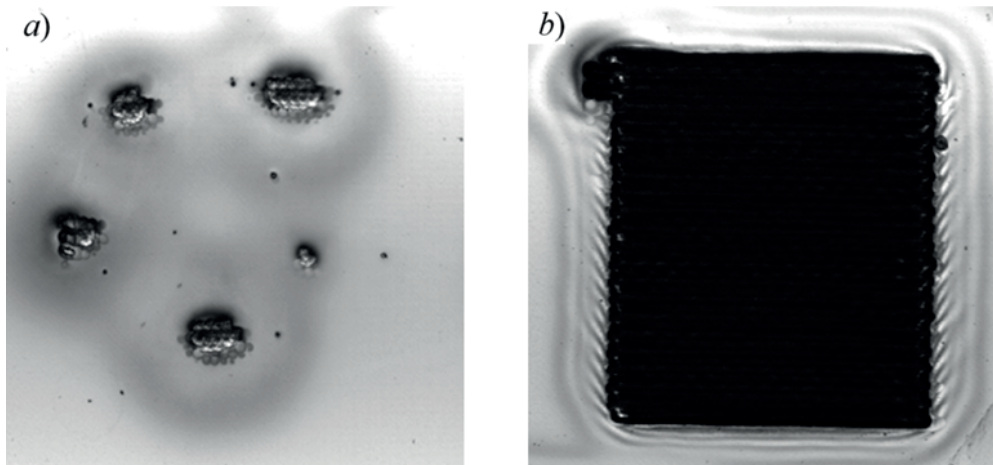
Fig. 1. Images of a local area on the surface of silicon carbide after the formation of a conductive coating using the laser ablation method at a pulse frequency of 40 kHz (*a*) and at a pulse frequency of 120 kHz (*b*)

Despite the color and filling of the area, all local areas starting with a laser pulse frequency of 20 kHz had a conductive surface but had heterogeneity on the surface of the local area, which complicated the calculations of materials or antenna devices for which it was planned to develop this technology. Starting with a pulse frequency of 100 kHz, the surface of the local area changed insignificantly, and the conductivity reached its limit value for the film. The study of samples by Raman spectroscopy showed that it can be stated that graphene was formed on the surface starting with a frequency of 60 kHz. This fact is also indirectly confirmed by the measured specific conductivity of the samples of $5.7 \cdot 10^3$ S/cm.

Conclusion

In the presented work, the effect of the laser system pulse frequency on the thickness and electrical conductivity of the formed conductive graphene-like layer on a silicon carbide plate was established. Additionally, the optimal parameters for the synthesis of the conductive coating and surface roughness suitable for designing antenna devices were determined. At 100 kHz, conductive films of the graphene-like coating with a thickness of 6.5 μm with a proportion of the modified zone of 93% were obtained. The study of the samples by the Raman spectroscopy method directly indicates the formation of graphene on the surface, starting from a frequency of 60 kHz. This fact is indirectly confirmed by the measured specific conductivity of the samples, which was 5.7×10^3 S/cm. The results obtained are applicable in the development of sensor elements, optoelectronics and photonics devices.

REFERENCES

1. **Dmitriev A.N., Cherednichenko D.I.,** Formation of graphene layers by sublimation of silicon carbide in vacuum with a scanning heat source, Bulletin of the Russian Academy of Sciences: Physics. 74 (8) (2010) 1118−1121.

2. **Frolov S.V., Shcherbakov A.V.,** Graphene Synthesis on SiC by Laser Treatment: Structural and Electrical Properties, Materials Science and Engineering. 15 (3) (2023) 789−795.

3. **Ivanov A.V., Petrov A.V.,** Laser-Induced Graphene Formation on Silicon Carbide: Mechanisms and Applications, Journal of Applied Physics. 128 (12) (2023) 123456.

4. **Klimin V.S., Kessler I.O., Morozova Yu.V., Saenko A.V., Vakulov Z.E., Ageev O.A.,** Application of fluoride plasma for the formation of nanoscale structures on the surface of silicon. Applied Physics. 6 (2022) 23−28.

5. **Alekseev N.I., Luchinin V.V.,** Simulation of graphene synthesis on faceted silicon carbide surface for technology of high-crystallinity graphene structures, Nanosystems: Physics, Chemistry, Mathematics. 6 (2) (2015) 135−144.

6. **Osipov A.A. et al.,** Etching of silicon carbide in inductively coupled plasma at low power, Microelectronics. 48 (1) (2019) 31−37.

7. **Kageshima H. et al.,** Graphene growth on silicon carbide, NTT Technical Review. 8 (8) (2010) 17−22.

THE AUTHORS

KLIMIN Viktor S.
kliminvs@sfedu.ru
ORCID: 0000-0002-9794-4459

GAVRISH Polina E.
gavrish@sfedu.ru
ORCID: 0009-0007-7197-9104

TARASOV Pavel A.
einjpptc@gmail.com
ORCID: 0009-0000-7843-9839

TKACHYOVA Anastasia A.
anab@sfedu.ru
ORCID: 0009-0007-2496-9317

GRIGORYEV Mikhail N.
gregoryevmikhail@gmail.com
ORCID: 0009-0001-1684-1475

PTASHNIK Vitaliy V.
vptashnik@sfedu.ru
ORCID: 0009-0005-7668-4079

The operational amplifiers radiation hardness experimental study

S.B. Rybalka [1], D.S. Brundasov [1] ✉, E.A. Kulchenkov [1], A.A. Demidov [1]

[1] Bryansk State Technical University, Bryansk, Russia

✉ kineticx@bk.ru

Abstract. The radiation hardness of the operational amplifiers IS-OU2 and LM358 has been performed experimentally using X-ray research complex. It was found that the measured characteristics of operational amplifiers (input offset voltage, consumption current, voltage gain) for the IS-OU2 and its analogue LM358 are similar and demonstrate radiation hardness. As a result, the designed and produced IS-OU2 operational amplifier can be used for producing of spacecraft equipment electronics that can operate under space radiation conditions.

Keywords: operational amplifiers, X-ray irradiation, ionizing dose effects

Экспериментальное исследование радиационной стойкости операционных усилителей

С.Б. Рыбалка [1], Д.С. Брундасов [1] ✉, Е.А. Кульченков [1], А.А. Демидов [1]

[1] Брянский государственный технический университет, г. Брянск, Россия

✉ kineticx@bk.ru

Аннотация. Радиационная стойкость операционных усилителей IS-OU2 и LM358 была исследована экспериментально с использованием рентгеновского исследовательского комплекса. Установлено, что измеренные характеристики операционных усилителей (входное напряжение смещения, потребляемый ток, коэффициента усиления напряжения) для IS-OU2 и его аналога LM358 схожи и демонстрируют радиационную стойкость. Спроектированный и изготовленный IS-OU2 операционный усилитель может быть использован для производства электроники бортовой аппаратуры космических аппаратов работающих в условиях космического излучения.

Ключевые слова: операционные усилители, рентгеновское излучение, эффекты поглощенной дозы

Introduction

As it is well known, the operational amplifiers are important parts of modern electronics devices that are used widely in many industrial applications such as power engineering, energy systems, electrical engineering etc. [1]. For development of industries (cosmonautics, aircraft, engineering etc) it is necessary to achieve reliable functioning of the electronic components that used under radiation conditions such as space and nuclear radiations [2]. For instance, for similar type of bipolar operational amplifier (LM358) were established earlier its radiation hardness and some radiation-sensitive parameters to the total ionizing dose effects during its irradiation treatment [3]. Therefore, with taking into account, the main goal of this work is to study the radiation behavior features, define radiation-sensitive parameters and estimate radiation hardness to the effects of the total ionizing dose of designed operational amplifier IS-OU2 (analogue of LM358) using the developed X-ray research hardware and software complex (XRC).

Materials and Methods

The objects of the study were operational amplifier IS-OU2 (designed by Bryansk State Technical University) and then manufactured by JSC "GRUPPA KREMNY EL" [4]) and its analogue LM358 in the SO-8 type package. For radiation behavior study was used the developed XRC consisting of the following parts: X-ray equipment RIK-0401, X-ray comparator DRI-0401, a set of measuring equipment (sources-measuring instruments PXIe-4143, PXIe-4139), and the developed software. The developed XRC is described in detail earlier in [5, 6]. For operational amplifier microcircuit, the XRC allows monitoring the main characteristics (input offset voltage, consumption current, voltage gain, input offset current etc.). The radiation behavior study of operational amplifiers IS-OU2 and LM358 was performed the following operating mode of RIK-0401: anode voltage − 70 kV, anode current − 220 µA, the rate of radiation dose accumulation was 250 un./s (un. − units of the DRI-0401 comparator including in XRC), the distance between the X-ray tube window and the sample − 25 mm.

Results and Discussion

The operational amplifiers IS-OU2 and foreign analogue LM358 [7] during irradiation process were in the active electrical mode (at supply voltage ±16 V). During the study, the main radiation-sensitive parameters of the IS-OU2 have been established (V_{OS} − input offset voltage, I_{C} − consumption current, K_{U} − voltage gain). For instance, the dependencies of the input offset voltage V_{OS} at the minimum and maximum supply voltage on the total ionizing radiation dose D for samples of operational amplifier IS-OU2 and analogue LM358 are shown in Fig. 1, *a* and Fig. 1, *b*. As follows from Fig. 1, the input offset voltage at the minimum (Fig. 1, *a*) and maximum (Fig. 1, *b*) supply voltage for the developed operational amplifier IS-OU2 and the analogue LM358 increases very slightly with an increase in the total ionizing dose of radiation up to 600×10^3 un. It should be noted that input offset voltage is the radiation-sensitive parameter as was established earlier for similar operational amplifier LM358 in paper [3] during gamma irradiation treatment. Because of this input offset voltage values for developed amplifier IS-OU2 do not exceed maximum (±3.5 mV [4, 7]) and are comparable with LM358. Also it was found that the consumption current and voltage gain for the samples of the operational amplifiers IS-OU2 and its analogue LM358 are quite close.

a)

b)
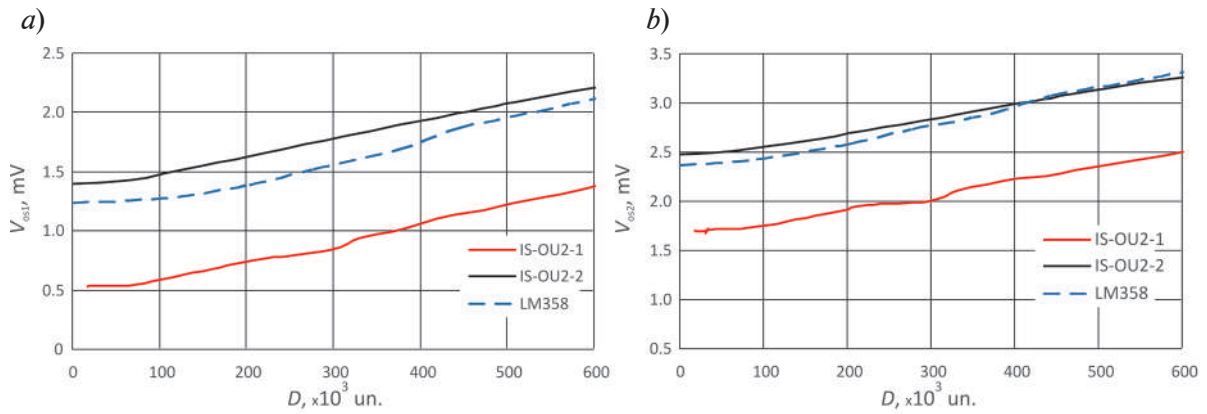
Fig. 1. Dependence of the input offset voltage V_{OS} at the minimum ± 1.5 V (*a*) and maximum ± 16 V (*b*) supply voltage on the total ionizing dose D for operational amplifier LM358 and IS-OU2 (IS-OU2-1 − the first sample and IS-OU2-2 − second sample) and LM358

a)

b)
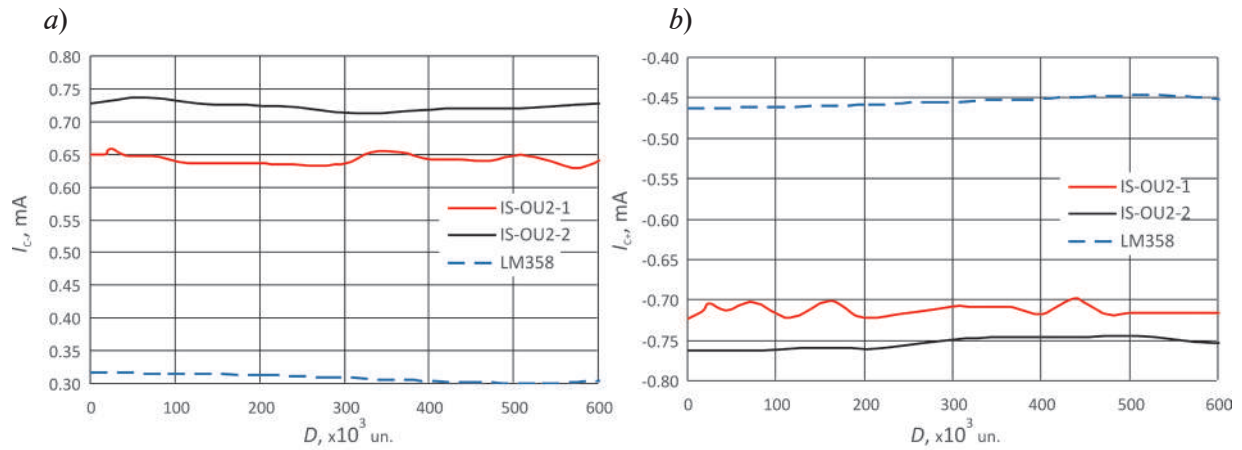
Fig. 2. Dependence consumption current I_C of the negative (*a*) and positive (*b*) polarity on the total ionizing dose D for operational amplifier IS-OU2 (IS-OU2-1 − the first sample and IS-OU2-2 − second sample) and LM358

Figure 2 shows the results of the radiation study of the consumption current I_C of negative (Fig. 2, *a*) and positive (Fig. 2, *b*) polarity of operational amplifiers for 2 samples of IS-OU2 (IS-OU2-1 − the first sample and IS-OU2-2 − second sample) and its analogue − LM358.

The consumption currents for the developed operational amplifier IS-OU2 and the analogue LM321 change very insignificantly with an increase in the total ionizing radiation dose.
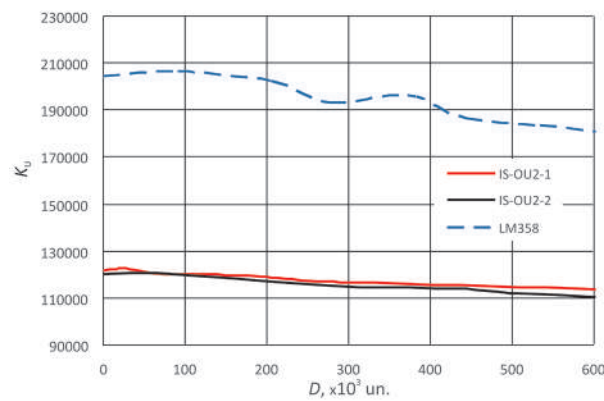
Fig. 3. Dependence of voltage gain K_U on the total ionizing dose D for operational amplifier IS-OU2 (IS-OU2-1 − the first sample and IS-OU2-2 − the second sample) and LM358

At the same time, the values of the consumption currents of negative and positive polarity for the developed operational amplifier IS-OU2 are quite comparable in order of magnitude with the analogue LM358. Figure 3 shows the dependences of the gain K_U on the total ionizing radiation dose D for the operational amplifier IS-OU2 and its foreign analogue LM358. It is evident that the gain does not decrease significantly with increasing total ionizing radiation dose. At the same time, the values of the gain for the developed operational amplifier IS-OU2, although somewhat smaller, are quite comparable in order of magnitude with the analogue LM358. Thus, the operational amplifier IS-OU2 samples and its foreign analogue LM358 in studied radiation exposure interval ($0-600 \times 10^3$ un.) do not undergone a functional failure and demonstrate radiation hardness to the effects of the total ionizing dose by studied parameters (input offset voltage, consumption current, voltage gain) and therefore can operate under radiation conditions such as spice and others [2].

Conclusion

The experimental study of the radiation hardness of the integrated circuit of the operational amplifiers IS-OU2 and analogue LM358 has been performed using X-ray research complex. Based on the results of experimental studies the radiation-sensitive parameters (input offset voltage, consumption current, voltage gain) have been found. It is established that operational amplifier IS-OU2 samples and its foreign analogue LM358 in investigated radiation exposure interval preserves a functional state without functional failure and demonstrate radiation hardness to the effects of the total ionizing dose by studied parameters. Because of this, the measured characteristics for the samples of the designed operational amplifiers IS-OU2 and analogue LM358 are quite close. Therefore, with taking into account, the designed and developed IS-OU2 operational amplifier demonstrates radiation hardness and can operate under radiation conditions and can be used for producing of devices in spacecraft electronics.

Acknowledgments

REFERENCES

1. **Yawale S.,** Operational Amplifier: Theory and Experiments, Springer, Singapore. 2021.

2. **Tapero K.I, Ulimov V.N, Chlenov A.M.,** Radiation effects in silicon integrated circuits for space applications, Laboratoriya Znaniy, Moscow. 2020.

3. **Bakerenkov A., Pershenkov V., Felitsyn V., Rodin A., Telets V., Belyakov V., Zhukov A., Gluhov N.,** Experimental estimation of input offset voltage radiation degradation rate in bipolar operational amplifiers, In: Proceedings of the 31st International Conference on Microelectronics, MIEL, Niš Serbia, 16−18 September, 2019; IEEE. (2019) 251.

4. JSC "GRUPPA KREMNY EL". URL: https://group-kremny.ru. Accessed August. 30, 2025.

5. **Kulchenkov E.A., Rybalka S.B., Demidov A.A.,** Study of radiation hardness of linear voltage regulator, Advances in Applied Physics. 5 (11) (2023) 445−454.

6. **Rybalka S.B., Demidov A.A., Kulchenkov E.A., Pilipenko K.S.,** Radiation behaviour study of linear voltage regulator, St. Petersburg State Polytechnical University Journal: Physics and Mathematics. 3.1 (17) (2024) 195−198.

7. LM158, LM258, LM358, LM158A, LM258A, LM358A Low-power dual operational amplifiers, STMicroelectronics. URL: https://www.st.com/resource/en/datasheet/lm158.pdf. Accessed August. 30, 2025.

THE AUTHORS

RYBALKA Sergey B.
sbrybalka@yandex.ru
ORCID: 0000-0002-7746-3009

KULCHENKOV Eugene A.
ewgeniy2000@mail.ru
ORCID: 0000-0002-7294-7549

BRUNDASOV Daniil S.
kineticx@bk.ru
ORCID: 0009-0001-4724-3734

DEMIDOV Andrey A.
demandr@yandex.ru
ORCID: 0000-0002-8639-3575

MEMS switch with an intermediate electrode for high-speed communication networks

M.O. Morozov [1, 2] ✉, I.V. Uvarov [1]

[1] Valiev Division of Physics and Technology, Yaroslavl Branch, NRC "Kurchatov Institute",
Yaroslavl, Russia;
[2] P.G. Demidov Yaroslavl State University, Yaroslavl, Russia
✉ matvey11212@gmail.com

Abstract. MEMS switches are considered as a promising element base of microwave electronics, but their performance has not reached the required level yet. The ratio of capacitances in the closed and open states does not exceed 10 and has to be increased. A possible method is to apply an intermediate electrode over the dielectric coating of a transmission line. In this work, a MEMS switch with an intermediate electrode is proposed for use in 5G communication networks.

Keywords: MEMS switch, intermediate electrode, capacitance ratio, isolation, insertion loss, finite element method

МЭМС-переключатель с дополнительным электродом для систем высокоскоростной связи

М.О. Морозов [1, 2] ✉, И.В. Уваров [1]

[1] Отдел микротехнологий – Ярославль ОФТИ им. К.А. Валиева НИЦ
«Курчатовский институт», г. Ярославль, Россия;
[2] Ярославский государственный университет им. П.Г. Демидова, г. Ярославль, Россия
✉ matvey11212@gmail.com

Аннотация. МЭМС-переключатели рассматриваются в качестве основы перспективной элементной базы СВЧ-электроники, но к настоящему времени их характеристики не достигли нужного уровня. Отношение емкостей в разомкнутом и замкнутом состояниях не превышает 10 и требует увеличения. Один из способов заключается в нанесении дополнительного электрода на диэлектрическое покрытие линии передач. В настоящей работе представлен МЭМС-переключатель с дополнительным электродом, предназначенный для работы в сетях связи 5G.

Ключевые слова: МЭМС-переключатель, дополнительный электрод, отношение емкостей, изоляция, вносимые потери, метод конечных элементов

Introduction

Development of 5G high-speed communication networks with frequency ranges of 3.4−3.8 and 4.4−4.99 GHz requires advanced electronic components for switching microwave signals. Widely used semiconductor switches are fast and reliable due to the absence of movable mechanical structures, but suffer from high signal loss and power consumption. Alternative switches are fabricated using microelectromechanical systems (MEMS) technology. These are miniature electromechanical relays that operate on an electrostatic principle. MEMS switches provide low insertion loss and high isolation combined with low power consumption and short switching time.

The important parameter of a MEMS switch with a capacitive contact is the ratio of capacitances in the closed and open states. This value usually does not exceed 10 [1−3] and does not provide the required switching effect. The capacitance ratio can be improved by applying an intermediate electrode on top of the dielectric. In this case, the capacitance ratio can be varied widely by changing the size of the intermediate electrode and the dielectric layer material. This work is devoted to the investigation of the working characteristics of a switch with an intermediate electrode designed for the frequency range of 3.4−4.99 GHz.

Materials and Methods

The MEMS switch is schematically shown in Fig. 1, *a*. A movable electrode is an aluminum cantilever with a length of 50 μm attached to a grounded conductor of a coplanar waveguide. A signal conductor with width $w_l = 150$ μm passes under the cantilever at a distance of 1 μm. A 50 nm thick dielectric layer and 100 nm thick intermediate electrode of ruthenium are formed on the signal conductor. When the cantilever is located horizontally (Fig. 1, *b*), the switch is open. The capacitance C_{up} between the signal and the grounded conductor is small, so the signal goes through the transmission line with minimal loss. When a voltage is applied to the driving electrode, the switch is closed. The cantilever bends under the electrostatic force and touches the intermediate electrode. The capacitance between the signal and the grounded conductor increased significantly due to the high capacitance C_{down} between the signal conductor and the intermediate electrode. This capacitance shunts the signal conductor and blocks the signal path. A necessary condition is low contact resistance between the cantilever and the electrode.

The capacitance ratio can be estimated using an expression [4]:

$$\frac{C_{down}}{C_{up}} = \varepsilon \frac{l_e w_l}{S} \frac{g - t_d - t_e}{t_d}, \tag{1}$$

where ε is the dielectric constant of the material between the intermediate electrode and the signal conductor, l_e is the length of the intermediate electrode, $S = 179$ μm^2 is the overlap area between the cantilever and the electrode, $g = 1$ μm is the air gap between the cantilever and the signal conductor, $t_d = 50$ nm and $t_e = 100$ nm are the thicknesses of the dielectric and the electrode, respectively. For $\varepsilon \sim 10$ and $l_e \sim 100$ μm the capacitance ratio is 10^4. This estimate is three orders of magnitude higher than the C_{down}/C_{up} of conventional switches.

The passage of a signal in two states of the switch can be estimated by a single parameter S_{21}:

$$S_{21} = 20 \cdot \log_{10} \left(\left| \frac{2Z}{Z_0 + 2Z} \right| \right), \tag{2}$$

$$Z = R + j \left(\omega L - \frac{1}{\omega C} \right), \tag{3}$$

where $Z_0 = 50$ Ohm is the characteristic impedance, Z is the series impedance, ω is the frequency of the switched signal, R, L, C are the resistance, inductance and capacitance of the switch. In the open state, S_{21} has a minimal value with a capacitance C_{up}, and a maximum value in the closed state with a capacitance C_{down}. However, formulas (1)–(3) use ideal capacitance between cantilever and the signal line. The real switch uses a capacitance between the grounded and the signal conductors, which includes a parasitic component. Parasitic capacitance increases total C, and therefore we have a larger signal loss and lower capacitance ratio. It is impossible to account for all parasitic relationships analytically. Precise calculation is performed by the finite element method. It simulates an actual chip design and takes into account parasitic capacitances.

The model includes a sapphire substrate with an area of 1.7×1.6 mm^2 and a thickness of 460 μm, on which a coplanar waveguide is formed (Fig. 1, c). The conductors consist of ruthenium and an aluminum layers with a thickness of 0.1 and 3 μm, respectively. The cantilever is placed in the central area of the chip, while the driving electrode is connected to a contact pad on the periphery. To reduce the calculation time, the bending of the cantilever under electrostatic force is not considered. The change of the switch state is simulated by varying the height of contact bumps of the cantilever.
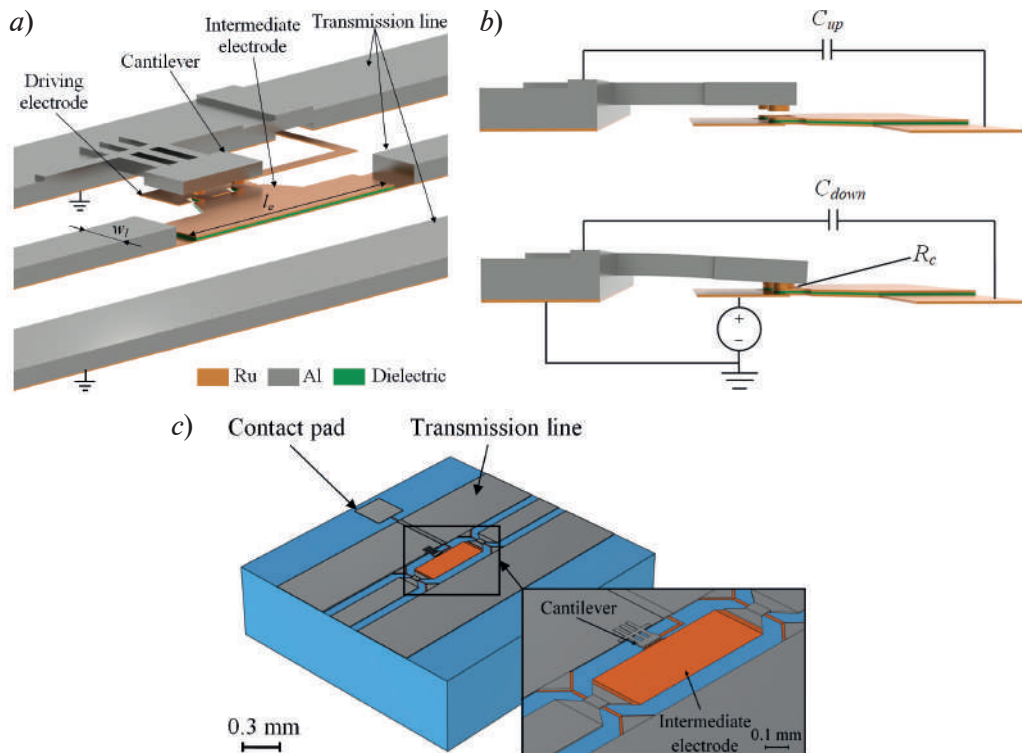
Fig. 1. MEMS switch with an intermediate electrode: general view (a); open and closed states (b); a model of the chip (c)

Results and Discussion

Switch performance is optimized by varying the length of the intermediate electrode and the material of the dielectric layer. The initial parameters are $l_e = 400$ μm and $\varepsilon = 3.9$ (for SiO$_2$). The radio frequency characteristics of a switch with these parameters are shown in Fig. 2, a. Acceptable insertion loss below 0.15 dB and isolation more than 20 dB are provided in the range of 1.3−4.8 GHz, which does not include an upper part of the target range. To shift the operating range upward, one has to increase the resonant frequency f_0, at which the isolation takes the maximum value. An increase of f_0 is achieved by reducing l_e, which reduces the capacitance C_{down}. The performance of the switch with an electrode length of 100 and 200 μm is shown in Fig. 2, a. The optimal value is $l_e = 200$ μm, which provides the working range of 2.1−5.7 GHz. The calculated C_{down} and C_{up} are 20.40 pF and 0.14 pF. The capacitance ratio of 146 is more than an order of magnitude higher than the typical value for switches without an intermediate electrode.

A further growth of the capacitance ratio is possible by use of dielectrics with higher ε. AlN, Si_3N_4, Al_2O_3, Ta_2O_5, HfO_2, TiO_2 and $SrTiO_3$ are considered as an alternative to SiO_2. The highest ratio of 6502 is provided by $SrTiO_3$ (ε = 120) [5]. Increasing ε has negligible effect on insertion loss, but significantly changes isolation, as shown in Fig. 2, *b*. The maximum isolation increases with ε, but the operating range shifts below the target frequencies. For the range of 3.4−4.99 GHz, SiO_2 remains the best material.
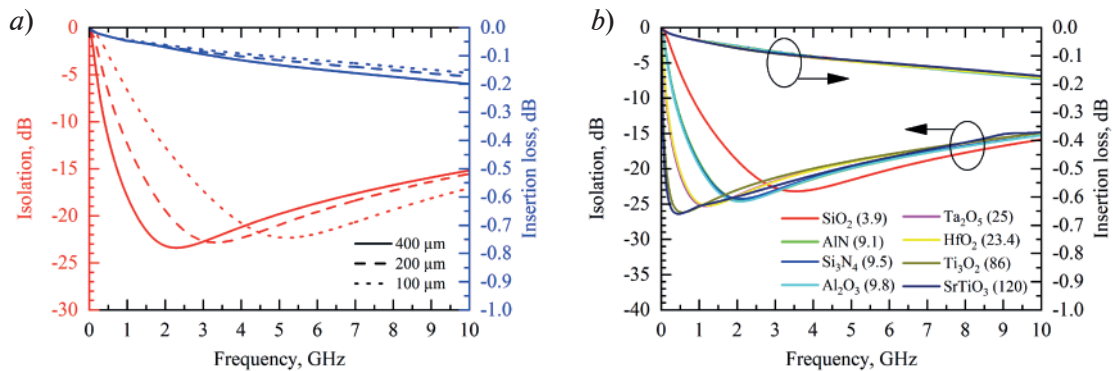
Fig. 2. The dependence of isolation and insertion loss on the signal frequency: for different lengths of the intermediate electrode (*a*); for different dielectrics at l_e = 200 μm (*b*). The values of ε are shown in brackets

Conclusion

The paper describes a MEMS switch with an intermediate electrode designed for 5G communication networks. The finite element method was used to calculate the capacitive characteristics, as well as isolation and insertion loss in the frequency range up to 10 GHz. A switch with an intermediate electrode length of 200 μm and a dielectric layer of SiO_2 provides a capacitance ratio of 146, which is more than an order of magnitude higher than that for switches without an intermediate electrode. Acceptable insertion loss of less than 0.15 dB and isolation higher than 20 dB are achieved in the range of 2.1−5.7 GHz, fully covering the operating frequencies of 5G communication networks.

REFERENCES

1. **Yang H.-H., Zareie H., Rebeiz G.M.,** A high power stress-gradient resilient RF MEMS capacitive switch, J. Microelectromech. 24 (2015) 599−607.

2. **Grichener A., Rebeiz G. M.,** High-reliability RF-MEMS switched capacitors with digital and analog tuning characteristics, IEEE transactions on microwave theory and techniques. 58 (10) (2010) 2692−2701.

3. **Zareie H., Rebeiz G. M.,** High-power RF MEMS switched capacitors using a thick metal process, IEEE transactions on microwave theory and techniques. 61 (1) (2012) 455−463.

4. **Morozov M.O., Uvarov I.V.,** Performance Calculation for a MEMS switch with a Floating Electrode, Russ. Microelectron. 52 (6) (2023) 493−503.

5. **Park J.Y., Kim G.H., Chung K.W., Bu J.U.,** Electroplated RF MEMS capacitive switches, Proceedings IEEE Thirteenth Annual International Conference on Micro Electro Mechanical Systems (Cat. No. 00CH36308). (2000) 639−644.

THE AUTHORS

MOROZOV Matvey O.
matvey11212@gmail.com
ORCID: 0009-0005-3723-5924

UVAROV Ilia V.
i.v.uvarov@bk.ru
ORCID: 0000-0002-6882-0625

Black silicon formation using cryogenic etching and photoresist layer

E.A. Vyacheslavova [1]✉, D.V. Mokhov [1], A.V. Uvarov [1], A.A. Maksimova [1, 2],

O.P. Mikhaylov [1], A.I. Baranov [1], A.S. Gudovskikh [1, 2]

[1] Alferov University, St. Petersburg, Russia;

[2] St. Petersburg Electrotechnical University "LETI", St. Petersburg, Russia

✉ cate.viacheslavova@yandex.ru

Abstract. A series of experiments were conducted to develop the plasma etching of black silicon through a layer of polydimethylglutarimide (PMGI) photoresist. The silicon wafers were previously subjected to wet-chemical treatment. A ~25 nm thick photoresist layer facilitates the process of creating regular black silicon structures on substrates with a diameter of 100 mm. The etching process was varied in terms of the sulfur hexafluoride (SF_6) and oxygen (O_2) gas mixture ratio, RF power applied to the substrate holder (bias power), inductively coupled plasma (ICP) power and chamber pressure. Increasing the bias power from 10 to 30 W under otherwise constant conditions enhances the etching rate. Reducing the pressure in the reactor from 10 to 5 mTorr at a constant gas flow rate leading to a higher etching rate. Increasing the proportion of oxygen in the SF_6/O_2 gas mixture (2:1) enhances passivation, reducing the black silicon structures size.

Keywords: black silicon, PMGI photoresist, cryogenic etching, solar cell

Формирование черного кремния с использованием криогенного травления и слоя фоторезиста

Е.А. Вячеславова [1] ✉, Д.В. Мохов [1], А.В. Уваров [1], А.А. Максимова [1, 2],

О.П. Михайлов [1], А.И. Баранов [1], А.С. Гудовских [1, 2]

[1] Академический университет им. Ж.И. Алфёрова РАН, Санкт-Петербург, Россия;

[2] Санкт-Петербургский государственный электротехнический университет
«ЛЭТИ» им. В.И. Ульянова (Ленина), Санкт-Петербург, Россия

✉ cate.viacheslavova@yandex.ru

Аннотация. Была проведена серия экспериментов по разработке технологии плазменного травления черного кремния через слой фоторезиста полидиметилглутаримида (PMGI). Кремниевые пластины предварительно подвергались жидкой химической обработке. Слой фоторезиста толщиной ~25 нм способствует процессу создания регулярных структур черного кремния на подложках диаметром 100 мм.

Процесс травления проведен с вариаций соотношения газовой смеси гексафторида серы (SF_6) и кислорода (O_2), мощности радиочастотного излучения, подаваемого на держатель подложки (мощность смещения), мощности индуктивно-связанной плазмы (ИСП) и давления в камере. Увеличение мощности смещения с 10 до 30 Вт при прочих равных условиях увеличивает скорость травления. Снижение давления в реакторе с 10 до 5 мТорр при постоянном расходе газа приводит к увеличению скорости травления. Увеличение доли кислорода в газовой смеси SF_6/O_2 (2:1) усиливает пассивацию, уменьшая размер структур черного кремния.

Ключевые слова: черный кремний, резист PMGI, криогенное травление, солнечный элемент

Introduction

Solar photovoltaic power is among the most dynamically advancing fields in renewable energy. Around 95% of the global photovoltaic market consists of silicon solar cells [1]. Nanostructured black silicon (*b*-Si) is a promising solution for reducing optical reflectance in solar cells. This material exhibits excellent optical characteristics across a wide wavelengths range and angles of light incidence [2].

Black silicon can be obtained by various methods, including metal assistant chemical etching (MACE) [3], laser texturing [4] and plasma etching [5]. MACE and laser texturing methods are inferior to plasma etching in terms of precision, structure control, safety and scalability. Thus, plasma etching demonstrates the best balance between structural quality and process flexibility. The cryogenic etching [6] makes it possible to create highly aspect structures on a silicon substrate using plasma etching techniques.

During cryogenic etching of substrates that had wet-chemical treatment, we encountered an issue with the non-uniform formation of areas with *b*-Si structures. Therefore, a series of experiments were conducted to develop and optimize the etching process for nanostructured silicon using a photoresist layer. The influence of key parameters such as bias power, ICP power, gas composition and pressure on the morphology and optical properties of black silicon is investigated.

Experimental section

The etching was carried out using *c*-Si (100) wafers (*n*-type doped, $2-3 \cdot 10^{15}$ cm^{-3}) through a PMGI photoresist layer. The substrates were previously subjected to wet-chemical treatment. It were boiled in carbon tetrachloride and then in isopropyl alcohol for 5 minutes. Then the substrates were dipped in a hydrofluoric acid solution for 1 minute to remove the natural oxide. The substrates were washed with deionized water after each stage.

To obtain a thin and uniform coating, PMGI was diluted with the solvent T-Thinner (by Micro Chem). Before applying PMGI, it was heated to room temperature to ensure optimal adhesion of the photoresist to the substrate surface and to reproduce the layer thickness. The PMGI photoresist was applied via spin coating at 4000 rpm for 4 minutes across the entire surface of silicon substrate with a diameter of 100 mm. Followed by baking on a hotplate of 5 minutes at 180 °C. A thin (~25 nm) photoresist layer acts as the organic layer that initiates the formation of ordered black silicon structures.

Then we used cryogenic etching (−150 °C) in an SF_6/O_2 gas mixture to obtain *b*-Si structures. The etching process time was 10 min. A series of experiments was conducted with variations in SF_6/O_2 process gas flow ratio, RF power, ICP power and pressure. The different technological parameters of cryogenic etching summarized in Table.

Table

Investigation of different cryogenic etching parameters

№	RF power, W	SF_6/O_2	Pressure, mTorr	ICP power, W	h, μm
1.1	10				~4.1
1.2	20				~6.3
1.3	30	3/1			–
1.4	5		5		~1.1
2.2		2/1			~1.4
2.3		5/1		1000	–
3.2			7		~2.8
3.3	10		10		–
4.2		3/1		1200	~6.3
4.3			5	700	–

The *b*-Si morphology was examined by SEM (Carl Zeiss Supra 25). The total reflectance spectra were measured using an integrating sphere and an AvaSpec SensLine spectrometer.

Results and Discussion

The key challenge is to optimize the nanostructure geometry (height, shape, and periodicity) to achieve low reflectivity through surface texturing while maintaining effective passivation properties for recombination suppression.

The etched silicon wafers consist of high density of *b*-Si structures. Figure 1 shows a SEM images of nanostructures at different bias power (*a–c*), pressure (*d*) and ICP power (*e*).
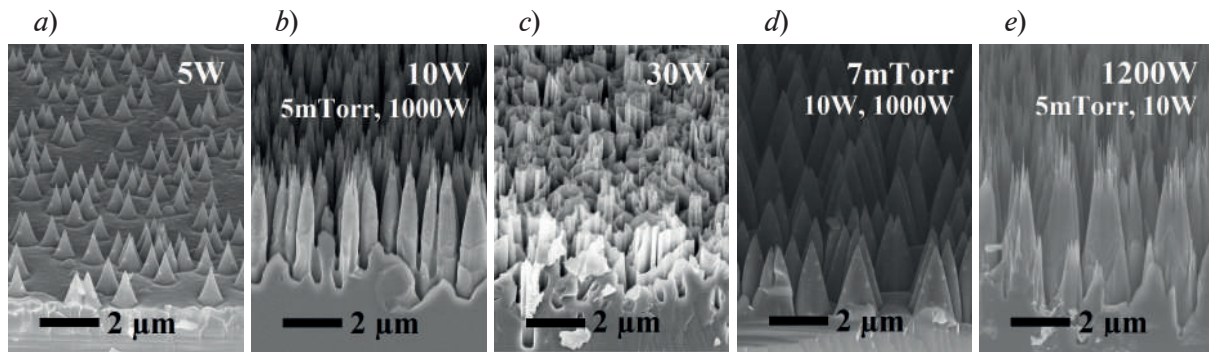
Fig. 1. A SEM image of the *b*-Si at different RF power (*a–c*), pressure (*d*) and ICP power (*e*)

Increasing the RF power from 10 to 30 W under otherwise constant conditions (SF_6/O_2 of 3/1, pressure of 5 mTorr, ICP power of 1000 W) enhances the etching rate due to the growing contribution of the ion-induced (physical) component of the etching process. However, at 30 W, the process becomes destructive to the *b*-Si structure formation.

To investigate the effect of the oxygen ratio in the SF_6/O_2 gas mixture, the gas proportion was varied while keeping the other parameters constant (RF power of 10 W, pressure of 5 mTorr, ICP power of 1000 W). Increasing the proportion of oxygen in the SF_6/O_2 gas mixture (2:1) enhances passivation, reducing the structures size. With an SF_6/O_2 ratio of 5:1, the oxygen proportion may be too low for passivation, and black silicon structures do not form.

Reducing the pressure in the reactor from 10 to 5 mTorr at a constant gas flow rate increases the mean free path and energy of ions, leading to a higher etching rate.

Raising the ICP power to 1200 W causes excessive etching of the nanostructures tips, making subsequent surface passivation more challenging. Constant process parameters include RF power of 10 W, SF_6/O_2 of 3/1, pressure of 5 mTorr.

Figure 2 compares the total reflectance spectra of the non-cryogenically etching c-Si wafer and substrates with black silicon structures.
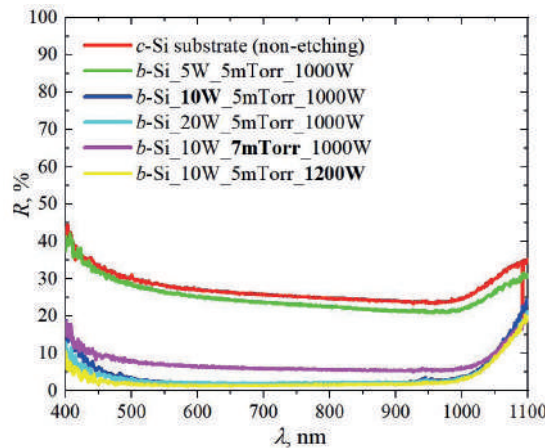
Fig. 2. Total reflectance spectrum of b-Si structures fabricated under different etching parameters

The Si substrate exhibits the total reflectance of more than 24% from 400 to 1000 nm. The nanostructure obtained at a RF power of 5 W consists of sparse cone-shaped formations approximately 1.1 μm in height. Its reflectance is similar to that of an non-etched substrate.

The b-Si structures obtained at a pressure of 7 mTorr exhibit a conical shape with a height of ~2.8 μm. It demonstrate a total reflectance below 10% across a broad spectral range and are likely to achieve even lower reflectivity after the emitter layer deposition.

Conclusion

The technology for plasma etching of black silicon on substrates subjected to wet-chemical treatment has been developed. A ~25 nm thick PMGI resist layer, formed via spin-coating, facilitates the process of creating black silicon structures on substrate with diameter of 100 mm. The etching process was carried out by varying parameters such as the SF_6/O_2 gas mixture ratio, bias power, ICP power and chamber pressure.

Acknowledgments

REFERENCES

1. A report by the International Technology Roadmap for Photovoltaics (ITRPV) Results 2023. 15 Edition (May 2024).

2. **Lv J., Zhang T., Zhang P., et. al.,** Review Application of Nanostructured Black Silicon, Nanoscale Research Letters. 13 (110) (2018).

3. **Arafat M.Y., Islam M.A., Mahmood A.W.B.,** Fabrication of Black Silicon via Metal-Assisted Chemical Etching, A Review, Sustainability. 131 (2021) 766.

4. **Kontermann S., Gimpel T., et al.,** Laser Processed Black Silicon for Photovoltaic Applications, Energy Procedia. 27 (2012) 390−395.

5. **Miakonkikh A., Kuzmenko V.O.,** Formation of Black Silicon in a Process of Plasma Etching with Passivation in a SF_6/O_2 Gas Mixture, Nanomaterials. 14(11):945 (2024).

6. **Vyacheslavova E.A., Morozov I.A., Kudryashov D.A., et. al.,** Study of Cryogenic Unmasked Etching of "Black Silicon" with Ar Gas Additives, ACS Omega. 7 (7) (2022) 6053−6057.

THE AUTHORS

VYACHESLAVOVA Ekaterina A.
cate.viacheslavova@yandex.ru
ORCID: 0000-0001-6869-1213

MOKHOV Dmitriy V.
ORCID: 0000-0002-7201-0713
dm_mokhov@rambler.ru

UVAROV Alexander V.
lumenlight@mail.ru
ORCID: 0000-0002-0061-6687

MAKSIMOVA Alina A.
deer.blackgreen@yandex.ru
ORCID: 0000-0002-3503-7458

MIKHAYLOV Oleg P.
oleg.mikhaylov.00@gmail.com
ORCID: 0009-0005-6836-4091

BARANOV Artem I.
itiomchik@yandex.ru
ORCID: 0000-0002-4894-6503

GUDOVSKIKH Alexander S.
gudovskikh@spbau.ru
ORCID: 0000-0002-7632-3194

Technological process of manufacturing a gas-sensitive multisensor chip based on a passivating coating of zinc oxide nanorods obtained by thin-film technology

A.E. Shepeleva [1] ✉, S.A. Gurin [1], M.D. Novichkov [2],

D.V. Agafonov [1], E.A. Pecherskaya [2], V.D. Zuev [1]

[1] Joint Stock Company "Research Institute of Electronic and Mechanical Devices",
Penza, Russia;

[2] Penza State University, Penza, Russia

✉ anastasiya.shepeleva.01@mail.ru

Abstract. A method for manufacturing a gas-analytical multisensor chip is presented. The technological process of manufacturing with an additional SiO_2 layer is described. It was found that the design of the experimental sample of the multisensor chip and the technology of synthesis of low-dimensional gas-sensitive layers provide sensitivity to detected gases up to 1 ppm and allow to increase the speed and temporal stability.

Keywords: gas-sensitive layer, dopant, response time, recovery time, technological process

Технологический процесс изготовления газочувствительного мультисенсорного чипа на основе пассивирующего покрытия наностержней оксида цинка, полученных по тонкопленочной технологии

А.Э. Шепелева [1] ✉, С.А. Гурин [1], М.Д. Новичков [2],

Д.В. Агафонов [1], Е.А. Печерская [2], В.Д. Зуев [1]

[1] АО «Научно-исследовательский институт электронно-механических приборов»,
г. Пенза, Россия;

[2] Пензенский государственный университет, г. Пенза, Россия

✉ anastasiya.shepeleva.01@mail.ru

Аннотация. Представлен способ изготовления газоаналитического мультисенсорного чипа. Описан технологический процесс изготовления с дополнительным слоем SiO_2. Установлено, что конструкция экспериментального образца мультисенсорного чипа и технология синтеза низкоразмерных газочувствительных слоев обеспечивают чувствительность к детектируемым газам до 1 ppm и позволяют повысить быстродействие и временную стабильность.

Introduction

Despite their high gas sensitivity and long-term stability, existing methods for manufacturing a gas multisensor based on zinc oxide have obvious drawbacks. In one method, a zinc oxide layer is obtained by electrochemical deposition on a dielectric substrate with strip electrodes, to which a constant electric potential is applied. The disadvantage is that it is impossible to completely control the filling of the zinc oxide structures of the gaps between the strip electrodes, which demonstrates the lag of the electrochemical deposition method compared to the hydrothermal method of zinc oxide deposition. In another method, the heaters are placed on the opposite side from the gas-sensitive layer, which leads to a longer heating due to the heat flow to the heater through the substrate [1].

Thus, there is a problem of creating a gas-analytical multisensor chip, the chemoresistive elements of which are made on the basis of zinc oxide nanostructures, the synthesis of which is carried out by the hydrothermal method with high temporal stability and increased speed. Such a multisensor chip should be distinguished by an increased service life at a low cost and is capable of detecting organic vapors with different concentrations.

Experimental technique

During the implementation of the technology for obtaining a gas-sensitive multisensor based on zinc oxide nanorods, sitall St 50−1−1, which has low thermal conductivity, was taken as the material of the dielectric substrate [2]. At the first stage, the substrate is cleaned and the surface is prepared. At the second stage, a set of meander heaters is formed from Pt using the thermal vacuum deposition method. At the third stage, a dielectric heat-transfer layer is deposited from polycrystalline SiC with a thickness of 1.5−2 μm, which has low oxide formation energy with high thermal conductivity. This allows increasing the heating rate of the gas -analytical layer. At the fourth stage, a set of coplanar interdigital electrodes is formed. At the fifth stage, zinc oxide nanorods obtained by hydrothermal synthesis are deposited. The technological process is shown in Figure 1.

The nanorods are synthesized as follows. The first seed layer of zinc oxide is applied by magnetron sputtering methods with a thickness of about 20−50 nm. To form the embryonic layer, a solution was prepared by mixing 50 ml of isopropyl alcohol and 0.05 g of dihydrate zinc acetate. This solution was first applied in a single layer (10 μl), then subjected to centrifugation at 3000 rpm for 60 seconds, followed by annealing at 350 °C for 2 minutes. This layer application process was repeated three times. Accordingly, the embryonic layer consists of a base of three layers of 10 μl each, applied using the described technology. To grow the second structured functional layer of ZnO nanostructures, zinc acetate (175.6 mg), water (80 ml), hexamethylenetetramine (112.1 mg) and centrimonium bromide (27.6 mg) are mixed. Substrates with the seed layer are dipped into the resulting solution. Synthesis is carried out in a thermostat at a temperature of 85 °C for 1 hour. Then the substrates are washed with distilled water and dried at room temperature. Then, annealing is performed and ZnO nanorods with a SiO_2 film, followed by etching to the level of colloidal quantum dots are passivated. The SiO_2 film, which provides protection from oxidation, is obtained by RF magnetron sputtering [3].
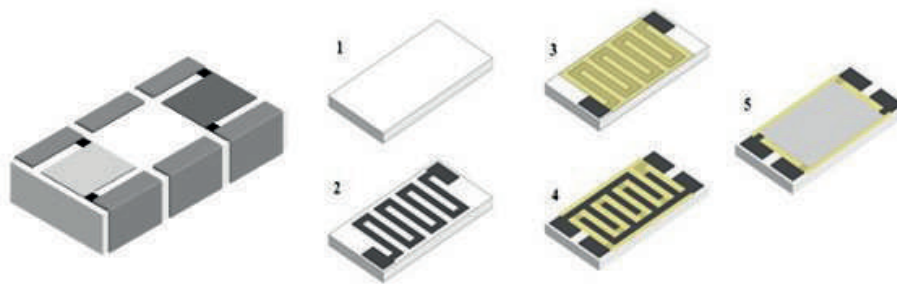
Fig. 1. Scheme of the sensor layer structure synthesis

Results and Discussion

The analysis of the obtained gas-sensitive multisensor chip was conducted using scanning microscopy on an atomic force microscope (AFM) platform NTEGRA, which allows contact and semi-contact modes. However, it was more appropriate to measure the samples using the more complex semi-contact mode, due to the inevitable damage to fragile nanorods in contact mode.

Analysis showed that the growth pattern of nanorods on the metal and on the embryonic layer differs [4]. Nanorods grow not only on the embryonic layer (the substrate itself) but also throughout the volume of the solution. However, nanorods growing within the solution volume eventually fall onto the surface of the substrate [5]. Such rods do not participate in electrical conductivity (they are not anchored) and, therefore, do not affect gas sensitivity.

Nanorods were studied under the influence of isopropanol vapors of concentrations equal to 1150 ppm and 5370 ppm (Fig. 2).
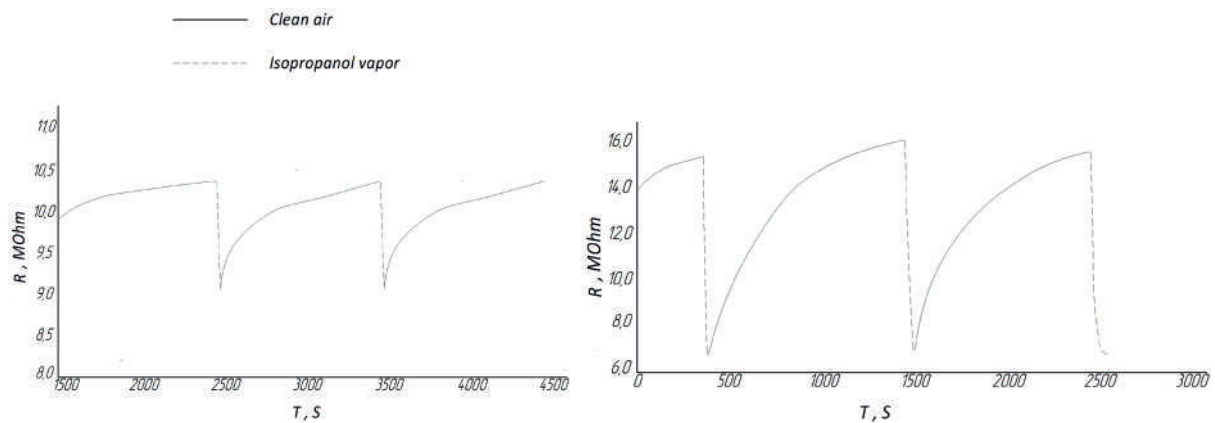
Fig. 2. A graph of resistance dependence upon exposure to isopropanol vapors of concentrations equal to 1150 ppm and 5370 ppm

The results are presented in Table. It was found that the gas-sensitive chip meets the specified parameters and provides sensitivity to detected gases up to 1 ppm.

Table

Chip characteristics

Isopropanol concentration	Sensitivity, ppm	Detection rate, s	
n	S	t	T heater
1150	1.01	219	
1150	0.99	287	210 ˚C
5370	1.18	340	
5370	0.96	417	

Thus, due to the location of the heaters on the front side of the substrate and the high thermal conductivity of SiC, the gas-sensitive chip reaches the mode faster. Evaluation of the effect of an additional protective layer of SiO_2 demonstrated the absence of an effect of this film on gas sensitivity. For this purpose, samples with and without SiO_2 film were placed in an environment with detectable gas (isopropanol) at a temperature for 10 days and it was found that the deviations in resistance were insignificant.

Conclusion

Thus, the use of the proposed method for manufacturing a gas-sensitive multisensor chip allows to increase performance with higher temporal stability. It has been established that the protective SiO_2 layer does not impair the sensitivity of the gases being detected.

REFERENCES

1. **Bobkov A., Moshnikov V., Varezhnikov A. et al.,** The multisensor array based on grown-on-chip zinc oxide nanorod network for selective discrimination of alcohol vapors at sub-ppm range, Sensors. 19 (19) (2019) 4265.

2. **Obvintseva L.A.,** Metal oxide semiconductor sensors for determination of reactive gas impurities in air, Russian Journal of General Chemistry. 78 (12) (2008) 2545–2555.

3. **Singh R.C., Singh O., Singh M.P., Chandic P.S.,** Synthesis of zinc oxide nanorods and nanoparticles by chemical route and their comparative study as ethanol sensors, Sensors and Actuators B: Chemical. 135 (1) (2008) 352–357.

4. **Meng F. et al.,** Detection of four alcohol homologue gases by ZnO gas sensor in dynamic interval temperature modulation mode, Sensors and Actuators B: Chemical. 350 (2022) 130867.

5. **Theerthagiri J., Salla S., Senthil R.A., Nithyadharseni P., Madankumar A., Arunachalam P., Maiyalagan T., Kim H.S.,** A review on ZnO nanostructured materials: Energy, environmental and biological applications, Nanotechnology. 30 (2019) 392001.

THE AUTHORS

SHEPELEVA Anastasiya E.
anastasiya.shepeleva.01@mail.ru
ORCID: 0000-0002-8600-084X

AGAFONOV Dmitriy V.
dmitryagafonov@list.ru
ORCID: 0009-0009-4548-3724

GURIN Sergey A.
teslananoel@rambler.ru
ORCID: 0000-0001-9602-7221

PECHERSKAYA Ekaterina A.
pea1@list.ru
ORCID: 0000-0001-5657-9128

NOVICHKOV Maksim D.
novichkov1998maks@gmail.com
ORCID: 0000-0001-9319-2475

ZUEV Vyacheslav D.
vdzuev@yandex.ru
ORCID: 0009-0005-5656-4918

PHYSICAL OPTICS

Investigation of second harmonic generation in spherical mesoporous Si/SiO$_2$ nanoparticles on gold

A.S. Funtikova [1] ✉, A.M. Mozharov [1, 2], V.A. Sharov [3],

K.N. Novikova [1, 2], L.N. Dvoretckaia [2]

[1] Peter the Great St. Petersburg Polytechnic University, St. Petersburg, Russia;

[2] Alferov University, St. Petersburg, Russia;

[3] Ioffe Institute, St. Petersburg, Russia

✉ n.fn@mail.ru

Abstract. In this work, experimental and numerical investigation of second harmonic generation (SHG) in mesoporous Si/SiO$_2$ nanoparticles has been performed. Experimental results are well-described by simulations. Spectral analysis reveals that SHG efficiency maxima correlate with Mie resonances of Si/SiO$_2$ nanoparticles. Tuning the diameter of the structures the maximum SHG efficiency for required wavelength can be achieved. The nonlinear optical susceptibility of the studied nanoparticles attains values on the order of 1.59×10^{-14} m^2/V, which exceeds that of bulk silicon. Spherical mesoporous Si/SiO$_2$ nanoparticles demonstrate effective second harmonic generation with simple, low-cost fabrication, making them promising candidates as tunable frequency converters for integrated nanophotonic circuits.

Keywords: second harmonic generation, silicon, spherical nanoparticles, Mie resonances, gold, mesoporous

Исследование генерации второй гармоники в сферических мезопористых наночастицах Si/SiO$_2$ на золоте

А.С. Фунтикова [1] ✉, А.М. Можаров [1, 2], В.А. Шаров [3],

К.Н. Новикова [1, 2], Л.Н. Дворецкая [2]

[1] Санкт-Петербургский политехнический университет Петра Великого, Санкт-Петербург, Россия;

[2] Академический университет им. Ж.И. Алфёрова РАН, Санкт-Петербург, Россия;

[3] Физико-технический институт им. А.Ф. Иоффе РАН, Санкт-Петербург, Россия

✉ n.fn@mail.ru

Аннотация. В данной работе проведено экспериментальное и численное исследование генерации второй гармоники (ГВГ) в мезопористых наночастицах Si/SiO$_2$. Спектральный анализ показывает, что максимумы эффективности ГВГ коррелируют

с резонансами Ми наночастиц Si/SiO$_2$. Путем настройки диаметра структур можно достичь максимальной эффективности ГВГ для требуемой длины волны. Нелинейная оптическая восприимчивость исследуемых наночастиц достигает значений порядка $1{,}59 \times 10^{-14}$ м^2/В, что превышает значения для объемного кремния. Сферические мезопористые наночастицы Si/SiO$_2$ демонстрируют эффективную генерацию второй гармоники при простом и недорогом изготовлении, что делает их перспективной альтернативой в качестве перестраиваемых преобразователей частоты для интегральных нанофотонных схем.

Ключевые слова: генерация второй гармоники, кремний, сферические наночастицы, Ми резонансы, золото, мезопористый

Introduction

Second-order nonlinear optical effects are essential for coherent light sources, optical amplifiers, and nanophotonic devices, particularly for converting infrared to visible light via second harmonic generation (SHG). While nonlinear crystals like KDP and LiNbO$_3$ [1, 2] and III-V semiconductors [3] offer efficient frequency conversion, their high cost and limited silicon compatibility restrict integration into modern optical systems.

Silicon platforms provide cost-effective fabrication of diverse structures but suffer from poor second-order nonlinear efficiency due to silicon's symmetry of the crystal lattice, which eliminates bulk SHG. However, SHG can be allowed through symmetry breaking at crystal boundaries [4] and higher-order interactions. Since SHG depends on morphology and surface properties, approaches include porous silicon and silicon nanoparticles/nanowires with favorable second-order characteristics [5]. Additional enhancement approaches include optical cavities for electromagnetic field enhancement, which are formed by dielectric or plasmonic materials.

Previous work, devoted to the study of the mesoporous Si/SiO$_2$ nanoparticles [6], represents experimental results for the array of the nanoparticles. In this work, investigation of the second harmonic generation in single mesoporous nanoparticles of different diameters was held numerically and experimentally. Nanoparticles are a framework of silicon oxide (SiO$_2$) filled with nanocrystalline silicon.

Materials and Methods

The mesoporous Si/SiO$_2$ nanoparticles have complex structure that is challenging to construct and calculate numerically. However, when material crystallites are much smaller than the incident wavelength, the Bruggeman effective medium approximation can describe the optical properties of these composite materials. Numerical calculations were performed using COMSOL Multiphysics for spherical mesoporous Si/SiO$_2$ nanoparticles of different diameters. The model used Si/SiO$_2$ particles laying on gold substrate and surrounded by air shell, with incident wavelengths of 840−1000 nm. Refractive indices and extinction coefficients for silicon and silicon oxide taken from references [7] and [8], respectively.

Nonlinear polarization, which determines the SHG in the studied Si/SiO$_2$ nanoparticles on gold is considered as follows:

$$\vec{P}^{NL} = \vec{P}^{surf} + \vec{P}^{cryst},$$

$$\vec{P}^{surf} = \varepsilon_0 \delta(z) \left[\hat{n} \left(\chi^{(2)}_{\perp\perp\perp} \left(E_n^{(\omega)} \right)^2 + \chi^{(2)}_{\perp\parallel\parallel} \left(E_\tau^{(\omega)} \right)^2 \right) + 2\hat{\tau} \chi^{(2)}_{\parallel\perp\parallel} E_n^{(\omega)} E_\tau^{(\omega)} \right],$$

$$\vec{P}^{cryst} = \frac{1}{V_{cryst}} \int\limits_{V_{cryst}} \varepsilon_0 \delta(z) \chi^{surf} \left(\vec{E}_0 + \hat{D}\vec{E} \cdot \vec{r} \right) \left(\vec{E}_0 + \hat{D}\vec{E} \cdot \vec{r} \right) d^3\vec{r}.$$

There are 2 possible mechanisms of SHG: surface SHG $\vec{P}^{surf}$, determined by violations of translational symmetry of the crystal lattice and crystallites SHG $\vec{P}^{cryst}$. $\chi^{(2)}_{\perp\perp\perp}$, $\chi^{(2)}_{\perp\parallel\parallel}$, $\chi^{(2)}_{\parallel\perp\parallel}$ — components of the surface tensor of nonlinear optical susceptibility.

Second harmonic measurements were performed using a Zeiss LSM-980 confocal scanning laser microscope with a Coherent Discovery-NX acousto-optic modulator. The sample was excited by 150 fs femtosecond pulses at 80 MHz repetition rate with maximum power of ~25 MW (0.3 nJ per pulse). Signals were detected in reflection geometry.

Results and Discussion

Experimental and numerical results of the investigation are represented on Fig. 1.
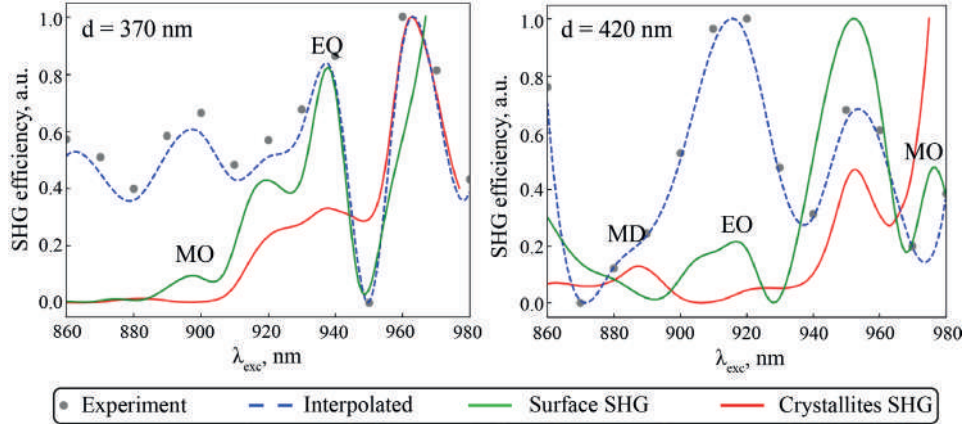
Fig. 1. SHG efficiency spectra (λ_{exc} — excitation wavelength) for mesoporous Si/SiO$_2$ nanoparticles with diameters d = 370 nm and 420 nm

Experimental spectra has different maxima, representing enhancement in nonlinear response. However, the nature of these peaks can be figured out using numerical calculations. Thus, the results of the numerical calculations, related to different SHG mechanisms, were plotted in the experimental graphs. In Fig. 1, one can see two main contributions to SHG from mesoporous Si/SiO$_2$ nanoparticles: external surface contribution and nonlinear response from the crystallites edges. Both this mechanisms shows some maxima that can be related to different Mie and hybrid resonances formed by nanoparticle and gold substrate. The calculated nonlinear optical susceptibility of the considered nanoparticles under resonance conditions can reach values on the order of 1.59×10^{-14} m^2/V, which exceeds that of bulk silicon [9].

Comparing experimental and numerical results one can talk about the relationship of the maxima of the spectra with the resonances at different wavelengths. Both mechanisms of SHG in nanoparticles under investigation contribute to experimental nonlinear response. All peaks obtained experimentally are described by calculated curves adjusted for their intensity. This correction may be related to the inaccuracy of modeling in relation to experimental conditions. Nevertheless, we can talk about a good agreement between experiment and theory.

Conclusion

In this work, the results of a numerical and experimental study of the second harmonic response from single mesoporous Si/SiO$_2$ nanoparticles are considered. SHG in such strictures is mainly described by two mechanisms: external surface SHG and crystallites edges SHG.

193

It was found that both SHG mechanisms contribute to nonlinear response in the nanoparticles, which manifests itself as an increased efficiency of second harmonic generation at resonant wavelengths.

Thus, the possibility of effective generation of the second harmonic in spherical mesoporous Si/SiO$_2$ nanoparticles is shown. The simplicity, as well as the low cost of their manufacture, makes it possible to propose these structures as efficient tunable frequency converters for nanophotonic circuits.

Acknowledgments

REFERENCES

1. **Phan V.T., Do T.T.P., Ho T.M., Nguyen D.T., Le B. van, Le A.T.Q., Duong P.A., Huynh D.T.,** Fabrication of KDP crystal prisms for second harmonic generation, Optik. 171 (2018) 230–236.

2. **Luo R., He Y., Liang H., Li M., Lin Q.,** Highly tunable efficient second-harmonic generation in a lithium niobate nanophotonic waveguide, Optica. 5 (2018) 1006−1011.

3. **Anthur A.P., Zhang H., Akimov Y., Rong Ong J., Kalashnikov D., Kuznetsov A.I., Krivitsky L.,** Second harmonic generation in gallium phosphide nano-waveguides, Optics Express. 20 (7) (2021) 10307−10320.

4. **Aktsipetrov O.A., Bessonov V.O., Dolgova T.Y.V., Maidykovskii A.I.,** Second harmonic generation induced by mechanical stresses in silicon, JETP letters. 90 (2010) 718−722.

5. **Makarov S.V., Petrov M.I., Zywietz U., Milichko V., Zuev D., Lopanitsyna N., Kuksin A., Mukhin I., Zograf G., Ubyivovk E., Smirnova D.A., Starikov S., Chichkov B.N., Kivshar Y.S.,** Efficient second-harmonic generation in nanocrystalline silicon nanoparticles, Nano letters. 17 (5) (2017) 3047−3053.

6. **Mastalieva V., Neplokh V., Aybush A., Stovpiaga E., Eurov D., Vinnichenko M., Karaulov D., Kirillenko D., Mozharov A., Sharov V., Kolchanov D., Machnev A., Golubev V., Smirnov A., Ginzburg P., Makarov S., Kurdyukov D., Mukhin I.,** Second harmonic generation and broad-band photoluminescence in mesoporous Si/SiO$_2$ nanoparticles, Nanophotonics. 13 (18) (2024) 3299–3309.

7. **Green M.A.,** Solar Energy Materials and Solar Cells, Solar Energy Materials and Solar Cells. 92 (11) (2008) 1305−1310.

8. **Radhakrishnan T.,** Further studies on the temperature variation of the refractive index of crystals, Proceedings of the Indian Academy of Sciences. 31 (1951) 22−34.

9. **Falasconi M., Andreani L.C., Malvezzi A.M., Patrini M., Mulloni V., Pavesi L.,** Bulk and surface contributions to second-order susceptibility in crystalline and porous silicon by second-harmonic generation, Surface Science. 481 (2001) 105−112.

THE AUTHORS

FUNTIKOVA Anastasiia S.
n.fn@mail.ru
ORCID: 0009-0000-3147-6974

NOVIKOVA Kristina N.
novikova_k@spbau.ru
ORCID: 0000-0001-8440-494X

MOZHAROV Alexey M.
mozharov@spbau.ru
ORCID: 0000-0002-8661-4083

DVORETCKAIA Liliia N.
liliyabutler@gmail.com
ORCID: 0000-0002-4172-940X

SHAROV Vladislav A.
vl_sharov@mail.ru
ORCID: 0000-0001-9693-5748

Laser polishing of steel surface for microfluidic applications

V.V. Lavrinenko [1] ✉, A.V. Vasilieva [1], V.A. Parfenov [1]

[1] St. Petersburg Electrotechnical University "LETI", St. Petersburg, Russia

✉ Lavrinenko_valerav@inbox.ru

Abstract. The paper examines various modes of laser polishing of stainless steel surface to decrease a surface roughness for creating model micro-grooves corresponding to the elements of the microfluidic topology. The effect of the formation of an oxide film and its effect on the roughness of the treated area is considered as well. The data obtained is confirmed by measurements using a profilometer.

Keywords: microfluidics, laser processing, laser polishing, steel

Лазерная полировка стальной поверхности для микрофлюидных применений

В.В. Лавриненко [1] ✉, А.В. Васильева [1], В.А. Парфенов [1]

[1] Санкт-Петербургский государственный электротехнический университет «ЛЭТИ» им. В.И. Ульянова (Ленина), Санкт-Петербург, Россия

✉ Lavrinenko_valerav@inbox.ru

Аннотация. В статье рассмотрены различные режимы лазерной полировки поверхности нержавеющей стали с целью снижения шероховатости поверхности для создания модельных микроканавок, соответствующих элементам микрофлюидной топологии. Рассмотрен эффект образования оксидной пленки и ее влияние на шероховатость обработанной области. Полученные данные подтверждены измерениями с помощью профилометра.

Ключевые слова: микрофлюидика, лазерная обработка, лазерная полировка, сталь

Introduction

Microfluidics is one of the fastest growing fields in the modern world. Microfluidic technologies are used in such areas as medicine, pharmacology, microelectronics, mechanical engineering and the aerospace industry [1]. Therefore, the search for new materials and methods of their processing determines the economic, environmental and technological needs of microfluidic chip production.

The main difficulty is to create microchannels with low roughness and surface morphology without microcracks and nanopoils. Previously, in our work [2], using multi-stage laser processing of a stainless steel plate, where parameters such as repetition rate, power and pulse duration were changed between iterations, model microchannels were obtained on its surface (Fig. 1), which are elements of a microfluidic system.
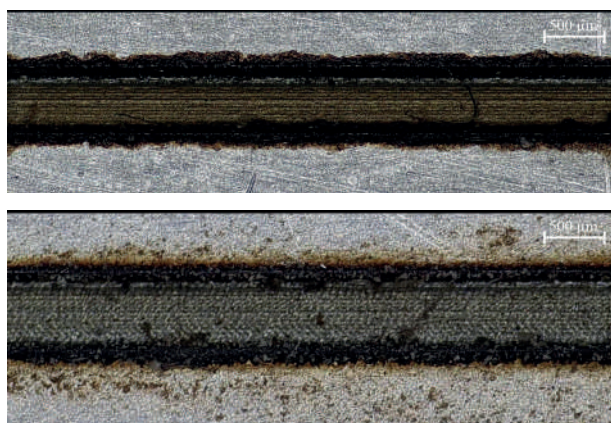
Fig. 1. Photos of experimental grooves

Obtained results showed that the stripes corresponding to the scanning paths of the laser beam are clearly visible on the walls of the obtained topologies, which indicate the high roughness of this surface of the microchannels. In particular, these parameters are important for controlling the technological process, since a high roughness value can noticeably change the properties of fluid movement due to the transformation of the influence of capillary and gravitational forces inside the microfluidic chip, up to the impossibility of stable functioning of the entire system [3, 4]. Therefore, the development and improvement of the polishing process when creating a microfluidic topology is very important. Moreover, AFM research indicated micro cracks on the surface after laser treatment with such energy parameters, which meant that laser processing iterations must be transform and include some steps, which allow decreasing the surface roughness. To reduce this surface parameter, it was decided to develop softer, polishing laser treatment modes.

There are 3 main processes of laser polishing: ablation of large areas of the surface, ablation of local (small) areas of the surface and polishing by remelting the surface layer of the material [5]. When polishing large areas by ablation, the material evaporates over the entire surface, while local areas ablation leads to removing the material from the peaks of the surface (a complex and expensive measurement system is needed to find the peak positions). When polishing by remelting, a thin surface layer melts and the surface tension leads to the alignment of the material [6, 7]. In this paper, the results of the development of laser treatment modes based on the 3rd method of polishing metal surfaces described above are presented.

Materials and Methods

The studies were carried out on a 2 mm thick stainless steel plate. The percentage of chemical elements of metal is shown in Table 1 (the data were obtained by X-ray fluorescence analysis). The sample was processed with a precision laser marker "MiniMarker2" (Laser Center LLC, Russia) based on ytterbium fiber laser with a wavelength of 1.064 microns.

Percentage content of chemical Elements

Elements	Content, %	Elements	Content, %
Iron (Fe)	71.738 ± 0.348	Silicon (Si)	0.424 ± 0.115
Chromium (Cr)	18.233 ± 0.147	Cobalt (Co)	0.259 ± 0.020
Nickel (Ni)	8.076 ± 0.138	Vanadium (V)	0.077 ± 0.011
Manganese (Mn)	1.165 ± 0.040	Titanium (Ti)	0.021 ± 0.006

The roughness of the treated surface was assessed using an Industrial NSRT-100 profilometer (NORGAU, Russia). Before evaluating the roughness parameter of the treated zones, the profilometer was calibrated on a reference sample with known roughness. The measurement error of the parameter R_a was about 5%. Measurements of 1 sample occurred 5 times, after which the average roughness was calculated.

Results and Discussion

During a multi-stage exposure to a metal plate with an IR laser, it was possible to identify processing modes to create a polished surface. The initial roughness of the plate (R_a) is 0.754 microns. Such parameters as power, frequency, pulse duration, and fill angle were changed between the stages of exposure. Examples of some modes are shown in Figure 2.
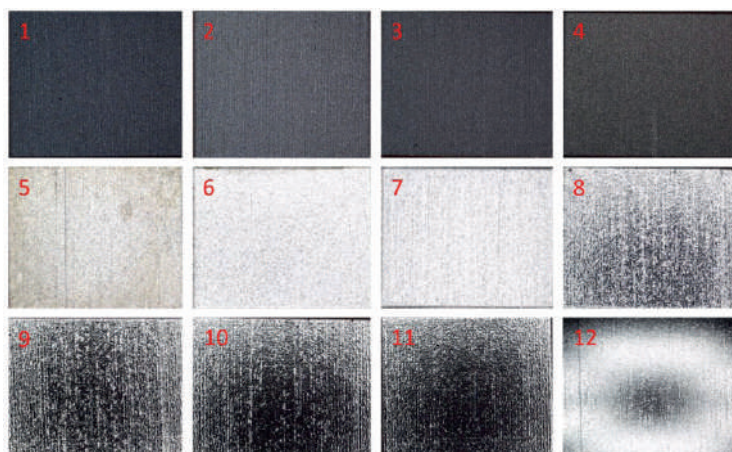
Fig. 2. Photos of polishing treatment modes

In the first 4 treatment modes, one can notice a change in the color of the treated area as a result of the appearance of an oxide film. This effect is observed due to the fact that heated ambient gases react with the heated plate material, forming iron oxides and other impurities on its surface.

Roughness parameters of polishing modes

№	R_a, μm	№	R_a, μm
1	0.775	7	0.447
2	0.690	8	0.270
3	0.615	9	0.232
4	0.704	10	0.188
5	0.420	11	0.180
6	0.370	12	0.173

According to our previous study [2] the effect of oxide film formation is negative, as it increases the roughness of a larger area, as can be seen from the table above. It proves our previous measurements and conclusions.

At the same time, the presence of a metallic sheen indicates a lower surface roughness value. In this case, the most effective laser treatment modes are from 10 to 12 from the table above. These modes were obtained by a laser beam with a diameter of 50 microns and a pulse duration of 350 ns with four-stage processing, between which the power (from 5.4 to 2.1 W), pulse repetition rate (from 40 to 60 kHz), scanning speed (from 500 to 1000 mm per second), as well as the fill density varied (from 100 to 200 lines per mm) and the fill angle (from 45 to 315 degrees).

However, it is necessary to take into account the corrosion resistance of the material both with and without the presence of an oxide film to the effects of chemical liquids, therefore, one of the next stages of the work will be experiments to identify the corrosion resistance of the metal under different polishing conditions.

Conclusion

Using laser treatment with IR radiation, it was possible to reduce the roughness from 0.754 microns to 0.173 microns, that is, this parameter improved by 77.1%. The most effective laser polishing modes demonstrated in this work will be used in further studies as part of iterations in obtaining model grooves with subsequent AFM examination for the presence of microcracks.

REFERENCES

1. **Sahu A.K., Jha S.,** Microchannel fabrication and metallurgical character ization on titanium by nanosecond fiber laser micromilling, Materials and Manufacturing Processes. 35 (2020) 279−290.

2. **Lavrinenko V.V., Vasilieva A.V., Parfenov V.A., Novikov I.A.,** Investigation of microfluidic topology formation with the use of IR pulse laser, St. Petersburg State Polytechnical University Journal. Physics and Mathematics. 17 (3.2) (2024) 173−176.

3. **Aniskin V.M., Adamenko K.V., Maslov A.A.,** Changing the power of microchannels of various directions, Nanosystems: physics, chemistry, mathematics. 3 (2) (2012) 37−46.

4. **Platonov I.A., Platonov V.I., Kolesnichenko I.N., Gorynov M.G.,** Microfluidic systems in gas analysis (review), Sorption and chromatographic processes. 15 (6) (2015) 754−768 (in Russian).

5. **Chesnokov D.V., Shapran E.V.,** Scientific and technical aspects of the development of laser glass polishing methods, Interexpo Geo-Siberia. (2016) 76−81 (in Russian).

6. **Nusser C., Kumstel J., Kiedrowski T., Diatlov A., Willenborg E.,** Process- and Material Induced Surface Structures During Laser Polishing, Advanced Engineering Materials. 17 (3) (2015) 268−277.

7. **Temmler A., Liu D., Preußner J., Oeser S.,** Influence of laser polishing on surface roughness and microstructural properties of the remelted surface boundary layer of tool steel H11, Materials and Design. 192 (2020) 1−25.

THE AUTHORS

LAVRINENKO Valeriy V.
Lavrinenko_valerav@inbox.ru
ORCID: 0009-0001-8930-5438

PARFENOV Vadim A.
vadim_parfenov@mail.ru
ORCID: 0000-0002-2048-4677

VASILIEVA Anastasia V.
anastasiastru@mail.ru
ORCID: 0000-0002-5317-3322

Perovskite-GST hybrid platform for optical memristors with complex optical response

G.A. Verkhogliadov [1, 2] ✉, A.A. Marunchenko [2, 3], E.V. Sapozhnikova [1, 2],

O.M. Kushchenko [2], A.D. Sinelnik [2], A.P. Pushkarev [1, 2]

[1] Skolkovo Institute of Science and Technology, Moscow, Russia;
[2] ITMO University, St. Petersburg, Russia;
[3] Lund University, Lund, Sweden
✉ g.verkhogliadov@skoltech.ru

Abstract. This study explores the optical properties of a perovskite-GST hybrid platform, revealing a remarkable, up to twofold, increasing of photoluminescence intensity of halide perovskite thin film by switching the phase of GST substrate from amorphous to crystalline. The underlying mechanisms responsible for this strong modulation in photoluminescence intensity are related to interaction between the halide perovskite and the GST substrate, which we are investigating through comprehensive morphological and optical characterization techniques, highlighting the different reflectance properties of the crystalline and amorphous phases of GST. We consider this hybrid platform as a promising architecture for a neuromorphic system, leveraging the volatile properties of halide perovskites with the non-volatile characteristics of GST. This architecture aims to mimic the functionalities of the human brain, including the behavior of neurons and synapses, thus opening new avenues for the development of energy-efficient and highly adaptive computing systems. Our findings contribute to a deeper understanding of hybrid perovskite-GST platform and its potential in future technological applications in neuromorphic systems.

Keywords: halide perovskite, phase-change materials, volatile memory, nonvolatile memory

Гибридная платформа перовскит-GST для оптических мемристоров со сложным оптическим откликом

Г.А. Верхоглядов [1, 2] ✉, А.А. Марунченко [2, 3], Е.В. Сапожникова [1, 2],

О.М. Кущенко [2], А.Д. Синельник [2], А.П. Пушкарев [1, 2]

[1] Сколковский институт науки и технологий, Москва, Россия;
[2] Университет ИТМО, Санкт-Петербург, Россия;
[3] Университет Лунда, г. Лунд, Швеция
✉ g.verkhogliadov@skoltech.ru

Аннотация. Данное исследование изучает оптические свойства гибридной платформы на основе перовскита и GST, демонстрируя увеличение интенсивности фотолюминесценции тонких пленок галогенидного перовскита до двух раз при переключении фазы GST с аморфной на кристаллическую. В этой работе мы фокусируемся на исследовании возможных механизмов такой модуляции и ее потенциальных применений для нейроморфных систем.

Ключевые слова: галогенидный перовскит, материалы с фазовым переходом, волатильная память, неволатильная память

Ссылка при цитировании: Верхоглядов Г.А., Марунченко А.А., Сапожникова Е.В., Кущенко О.М., Синельник А.Д., Пушкарев А.П. Гибридная платформа перовскит-GST для оптических мемристоров со сложным оптическим откликом // Научно-технические ведомости СПбГПУ. Физико-математические науки. 2025. Т. 18. № 3.1. С. 199−203. DOI: https://doi.org/10.18721/JPM.183.140

Introduction

Nowadays, artificial intelligence (AI) and machine learning are making significant progress as they can be applied to various aspects of our lives. While AI software continuously improves through machine learning techniques, it is also important to develop the technical basis of AI. Commonly, advanced AI systems use bio-inspired neuromorphic architectures that operate based on the principles of the human brain, utilizing volatile neurons and non-volatile synapses [1]. To increase the operational speed and energy efficiency of such systems, the scientific community is actively exploring novel architectures and materials suitable for this application. Hybrid platforms with halide perovskite, such as silicon-perovskite, already demonstrate high potential in optoelectronic applications, including Si-perovskite tandem solar cells and photodetectors [2, 3]. Here, we study the properties of halide perovskite in combination with germanium-antimony-tellurium (GST) phase-change alloy as it is a promising platform for neuromorphic applications. This combination possesses the energy-independent (non-volatile) properties of GST [4] and the energy-dependent (volatile) characteristic of halide perovskite [5], effectively imitating the functionality of the human brain.

Materials and Methods

$CsPbBr_3$ solution was synthesized using stoichiometric mixtures of 0.3 mmol CsBr (>99.999%) and 0.3 mmol $PbBr_2$ (> 99.9%) in dimethyl sulfoxide. The solution was prepared and stored in an inert atmosphere of nitrogen-filled glove box. Halide perovskite thin films were deposited via spin-coating method using a one-step spin-cycle with 3000 rpm to obtain a film with thickness of 80−100 nm. Amorphous GST (a-GST) films were deposited on the glass substrate by a magnetron sputtering. Switching from a-GST to crystalline GST (c-GST) phase was made by local heating of one half of the substrate on the hotplate at 200°C, which allows us to obtain substrate with a-GST and c-GST areas. Reflectance (R) and photoluminescence (PL) spectra were measured using a QE pro Ocean optic spectrometer connected to the Axio Imager.A2m (Carl Zeiss SMT) optical microscope with optical fiber. For PL measurements, optical pumping was performed using a 350 nm wavelength UV lamp. Optical pumping for time-resolved photoluminescence (TRPL) measurements was achieved using a TEMA femtosecond pulse laser with a wavelength of 350 nm, frequency of 10 kHz, and a laser fluence of 10 nJ/cm^2. Atomic force microscopy (AFM) was made on AIST-NT SmartSPM 1000.

Results and Discussion

In this work we studied the optical properties of perovskite-GST platform by comparing the R and PL spectra of $CsPbBr_3$ halide perovskite deposited on a-GST and c-GST thin film.

Fig. 1, *a* presents a photo of a 100 nm GST thin film deposited on a glass substrate. The different crystal structures of the a-GST and c-GST phases result in different optical properties. In the transmission mode, where the light source is positioned behind the sample, c-GST appears as a darker region compared to the lighter a-GST. The morphology of the thin film of $CsPbBr_3$ perovskite deposited on top of both the a-GST and c-GST phases was analyzed using AFM. The results, shown in Fig. 1, *b*, indicate no significant differences, suggesting that the GST phase does not affect the formation of the perovskite thin film. Fig.1, *c* presents an optical microscope image in reflection mode of the perovskite thin film on the GST layer, clearly divided into two regions: lighter area associated with c-GST and darker area with a-GST.
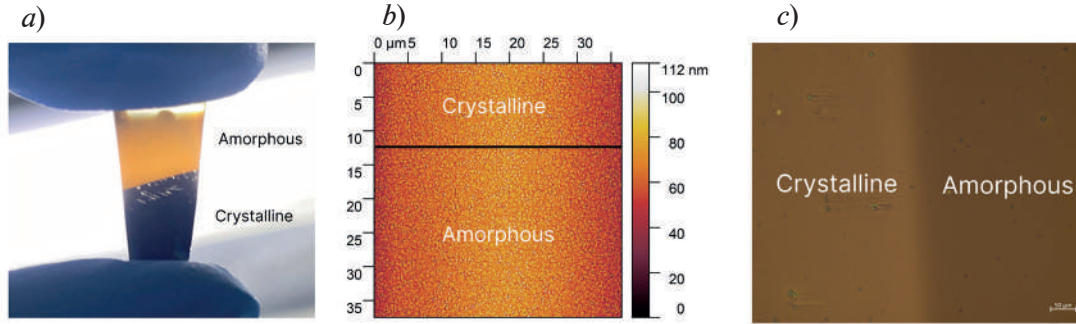
Fig. 1. Photo of 100 nm GST thin film in both phases of the glass substrate (*a*). AFM image of $CsPbBr_3$ film on top of the a-GST and c-GST (*b*). Image made by optical microscope of $CsPbBr_3$ thin film on the border of a-GST and c-GST (*c*)

In addition to morphology study and optical imaging, we measured the R spectra for both GST phases. The c-GST, with a higher refractive index due to highly ordered crystal structure, demonstrated increased reflection, as illustrated in Fig. 2, *a*. This trend remains consistent even after the deposition of the $CsPbBr_3$ thin film on top of the GST layer, as shown in Fig. 2, *b*. Notably, the reflection peak observed near 525 nm in Fig. 2, *b* corresponds to the bandgap energy of the perovskite layer, which is supported by absorption spectra measurements also presented in Fig. 2, *b*. Furthermore, the photoluminescence (PL) peak of the $CsPbBr_3$ thin film, depicted in Fig. 2, *c*, is located at the same wavelength of 525 nm, indicating that it represents band-edge photoluminescence.

Furthermore, the reflection difference of the two GST phases can influence the PL intensity of $CsPbBr_3$ thin film, as demonstrated in Fig. 2, *c*. The PL intensity of perovskite film deposited on top of the c-GST is twice higher compared to the same film deposited on a-GST. The strong PL modulation can be attributed to several factors. The primary factor is the difference in reflectance, which likely has the most significant impact. Additionally, two other important factors influence the PL intensity of halide perovskite. The first factor is Purcell effect which involves a modification of the local density of photonic states due to the GST impact. The second factor is the difference in defect density at the perovskite-GST interface between the crystalline and amorphous phases. Carriers can migrate to and localize at the defects present at this interface. Regarding the last two factors, the crystalline state is more favorable for emission enhancement [6].

To demonstrate the influence of different defect densities in the two phases, we conducted TRPL measurements on $CsPbBr_3$ perovskite film deposited on both a-GST and c-GST, as illustrated in Fig. 2, *d*. To extract the non-radiative lifetime (τ_{nr}) from the decay data plot, the ABC-model fitting was employed [7]. In this analysis, the C coefficient, which corresponds to Auger recombination, was set to zero due to the low pump fluence of 10 nJ/cm². The equation (1) governing the dependence of charge carrier density (*n*) on time (*t*) is presented below:

$$\frac{n(t)}{n_0} = \frac{\exp\left(-\dfrac{t}{\tau_{nr}}\right)}{\left(1 + \tau_{nr}\left(\dfrac{n_0}{\tau_r}\right)\left(1 - \exp\left(-\dfrac{t}{\tau_{nr}}\right)\right)\right)} + D, \tag{1}$$

Here, n represents the charge carrier density, t is a time, τ_{nr} denotes the trap-assisted lifetime, τ_r is a radiative lifetime, n_0 is the initial charge carrier density, and D is a constant. Based on the fitting results τ_{nr} for $CsPbBr_3$ film on c-GST was found to be 14.58 ± 0.2 ns, while for the film on a-GST, it was 13.95 ± 0.16 ns. This small difference (approximately 4-5%) in τ_{nr} indicates a minor variation in defect density. Consequently, the possible impact of defect density at the perovskite-GST interface – between the crystalline and amorphous phases – on photoluminescence modulation is several times lower than that of the Purcell effect [8] and an order of magnitude lower compared to the reflectance factor. Therefore, this influence can be considered negligible.

The PL enhancement attributed to the Purcell effect is approximately 15−20% [6, 8]. However, when we account for the reflectance factor, we observe an enhancement of around 100%. This demonstrates that reflectance is a primary factor in PL modulation.
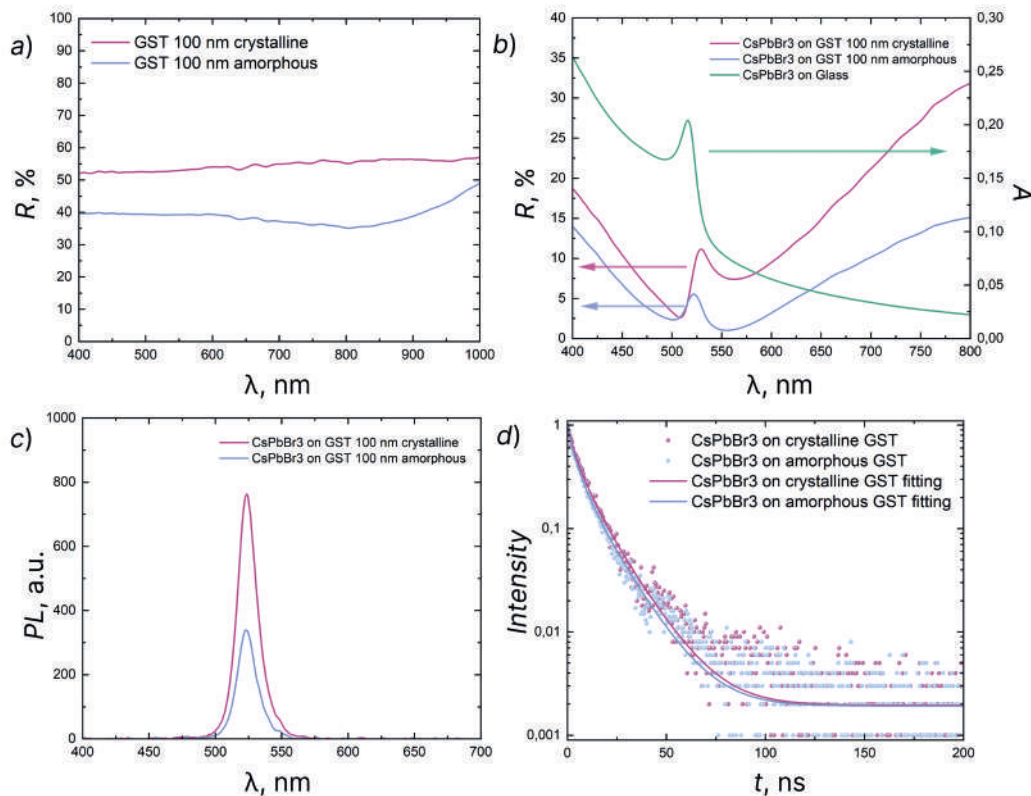
Fig. 2. R spectra of a-GST and c-GST thin film on the glass substrate (*a*). R spectra of $CsPbBr_3$ thin film on top of the a-GST and c-GST alongside with absorption spectra of $CsPbBr_3$ thin film (*b*). PL spectra of $CsPbBr_3$ thin film on top of the a-GST and c-GST layer. (*d*) TRPL measurement of $CsPbBr_3$ thin film on crystalline and amorphous GST and fitting with ABC-model (*c*)

Conclusion

Our research highlights the potential of tuning the PL signal of perovskite thin film through the phase switching of GST substrate for possible application in photoluminescence computing. Our findings indicate that the difference in reflectance between a-GST and c-GST is the primary factor influencing the modulation of the PL signal. This platform could significantly enhance the development of all-optical memristors, utilizing direct laser writing for GST phase switching, resulting in a distinct PL response from halide perovskite thin films. Furthermore, we propose that optoelectronic devices employing electrical field-induced GST phase transitions (or hybrid optical-electrical) might also be a promising direction for future research.

Acknowledgments

REFERENCES

1. **Kim K., et al.,** A comprehensive review of advanced trends: From artificial synapses to neuromorphic systems with consideration of non-ideal effects, Frontiers in Neuroscience. (18) (2024) 1279708.

2. **Kan C., et al.,** Efficient and stable perovskite-silicon tandem solar cells with copper thiocyanate-embedded perovskite on textured silicon, Nature Photonics. 1 (19) (2025) 63–70.

3. **Liu J., et al.,** Ultrasensitive Perovskite Photodetector Achieved When Configured with a Si Metal Oxide Semiconductor Field-Effect Transistor, Advanced Photonics Research. 1 (4) (2023) 2200034.

4. **Zhang S., et al.,** On-Chip Non-Volatile Reconfigurable Phase Change Topological Photonics, Advanced Materials. (2025) 2418510.

5. **Marunchenko A., et al.,** Memlumor: A Luminescent Memory Device for Energy-Efficient Photonic Neuromorphic Computing, ACS Energy Letters. 5 (9) (2024) 2075–2082.

6. **Kushchenko O.M., et al.,** All optically switchable active photonics based on the halide perovskite GST platform, Laser & Photonics Reviews. 8 (17) (2023) 2200836.

7. **Shen Y.C., et al.,** Auger recombination in InGaN measured by photoluminescence, Applied Physics Letters. 14 (91) (2007).

8. **Litvinov D.A. et al.,** Enhancement of perovskite spontaneous emission by phase change materials, Journal of Physics D: Applied Physics. 15 (57) (2024) 155103.

THE AUTHORS

VERKHOGLIADOV Grigorii A.
g.verkhogliadov@skoltech.ru
ORCID: 0000-0002-6222-5526

KUSHCHENKO Olga M.
olga.kushchenko@metalab.ifmo.ru
ORCID: 0000-0003-2283-3495

MARUNCHENKO Alexandr A.
a.marunchenko@metalab.ifmo.ru
ORCID: 0000-0002-0616-2524

SINELNIK Artem D.
artem.sinelnik@metalab.ifmo.ru
ORCID: 0000-0003-2423-7945

SAPOZHNIKOVA Elizaveta V.
e.sapozhnikova@metalab.ifmo.ru

PUSHKAREV Anatoly P.
An.Pushkarev@skoltech.ru
ORCID: 0000-0002-1793-6812

Mechanical scanning probe lithography of van der Waals antiferromagnetic CrSBr for fabrication of high-index waveguides and resonators

I.E. Kalantaevskii [1] ✉, T.D. Gorelkina [1], K.A. Gasnikova [2], N.V. Glebov [1],

A.I. Chernov [3, 4], P.A. Alekseev [2], V.A. Kravtsov [1]

[1] ITMO University, St. Petersburg, Russia;

[2] Ioffe Institute, St. Petersburg, Russia;

[3] Moscow Institute of Physics and Technology (National Research University),
Dolgoprudny, Russia;

[4] Russian Quantum Center, Skolkovo, Moscow, Russia

✉ i.kalantaevskii@metalab.ifmo

Abstract. Recently emerged van der Waals antiferromagnetic CrSBr provides new opportunities for developing compact integrated photonic and optoelectronic devices since it exhibits high refractive index, strong excitonic response, and magnetic ordering. However, experimental methods for nanostructuring CrSBr to tailor its photonic properties are not yet well developed. Here we demonstrate photonic dispersion engineering in subwavelength-thick CrSBr slabs through patterning and creating slab photonic crystal structures. Using mechanical scanning probe lithography – a non-destructive technique benefiting from piezostage precision – we fabricate nanostructured CrSBr flakes of controlled geometry. Back-focal-plane reflectance spectroscopy measurements reveal modified photonic dispersion characteristics, with the photonic crystal dispersion tuned close to the CrSBr exciton resonance. The demonstrated engineering of the photonic dispersion in CrSBr, with tunable alignment between the photonic crystal resonance and the exciton energy, provides a base for further studies of exciton-photon interaction in 2D magnetic materials.

Keywords: scanning probe lithography, van der Waals magnetics, photonic crystal slab

Механическая сканирующая зондовая литография Ван-дер-Ваальсова антиферромагнетика CrSBr для изготовления высокоиндексных волноводов и резонаторов

И.Э. Калантаевский [1] ✉, Т.Д. Горелкина [1], К.А. Гасникова [2], Н.В. Глебов [1],

А.И. Чернов [3, 4], П.А. Алексеев [2], В.А. Кравцов [1]

¹ Университет ИТМО, Санкт-Петербург, Россия;
² Физико-технический институт им. А.Ф. Иоффе РАН, Санкт-Петербург, Россия;
³ Московский физико-технический институт (национальный исследовательский университет), г. Долгопрудный, Россия;
⁴ Российский квантовый центр, Сколково, Москва, Россия
✉ i.kalantaevskii@metalab.ifmo

Аннотация. Новый Ван-дер-Ваальсов антиферромагнетик CrSBr открывает перспективы для компактных фотонных и оптоэлектронных устройств благодаря сочетанию высокого показателя преломления, сильного экситонного отклика и магнитного упорядочения. Однако методы наноструктурирования CrSBr для управления его фотонными свойствами пока недостаточно развиты. В данной работе мы демонстрируем управление фотонной дисперсией в CrSBr путем создания фотонно-кристаллических структур. Используя механическую зондовую литографию – неразрушающую методику с прецизионным пьезопозиционированием – мы создаем наноструктурированные фотонные кристаллы в CrSBr с контролируемой геометрией.

Ключевые слова: сканирующая зондовая литография, Ван-дер-Ваальсовы антиферромагнетики, фотонные кристаллы

Introduction

In recent years, enhanced light-matter interaction in novel van der Waals materials has attracted significant attention as a promising approach for developing nonlinear optical and optoelectronic devices. In the regime of strong light-matter coupling, exciton-polariton quasiparticles can be formed, which are manifested in the energy spectrum as Rabi splitting between material and optical dispersions. A promising platform for realizing exciton-polaritons with additional degrees of freedom is the two-dimensional van der Waals magnetic semiconductor CrSBr. Its optical response is dominated by an excitonic resonance, with excitons exhibiting high oscillator strength, stability under ambient conditions, and strong anisotropy – making CrSBr a promising candidate for room-temperature polaritonic devices with enhanced functionality [1]. Typically, strong light-matter interaction is achieved by coupling excitonic resonances in thin-layer materials to resonant optical modes supported by external cavities, such as distributed Bragg reflectors [2] and subwavelength gratings [3]. CrSBr is also a high-refractive-index semiconductor (refractive index of ~5), enabling its use as a waveguide for self-hybridized polaritons [4].

Additionally, since CrSBr excitons are sensitive to magnetic order [5], this provides a new degree of freedom for tuning the optical response. However, nanostructuring this material for creating waveguides and photonic crystal slabs remains largely unexplored. In this work, we investigate photon dispersion engineering in CrSBr to align the photonic crystal resonance with the exciton energy via scanning probe lithography.

Materials and Methods

To fabricate photonic crystals in CrSBr, we employed mechanical probe lithography, a technique chosen for its non-degradative impact on the material, simplicity, and dynamic tunability via high-precision piezostages. To enhance contrast and photonic crystal quality factor (Q), we

selected samples with 50–100 nm thicknesses supporting only a single transverse electric (TE) mode. The required thickness was achieved via iterative mechanical exfoliation from bulk crystals with low-residue Nitto tape monitored via optical microscopy. Atomic force microscopy (AFM) was used to precisely determine sample thickness after dry transfer onto SiO_2/Si substrates with oxide thickness of 1000 nm.

Results and Discussion

Crystal orientation was determined via polarization-resolved photoluminescence revealing the excitonic easy axis (b-axis), which is critical for dispersion control. Photonic crystals were fabricated via mechanical probe lithography. The method is schematically illustrated in Fig. 1, *a*. Designs for 4 photonic crystals were calculated via Fourier modal method (FMM) and implemented via scanning probe. Fig. 1, *b* and Fig. 1, *c* show the AFM maps and profiles of the resulting photonic crystals. Atomic force microscopy measurements confirmed that the spatial parameters of the fabricated photonic crystals closely match the designed values.
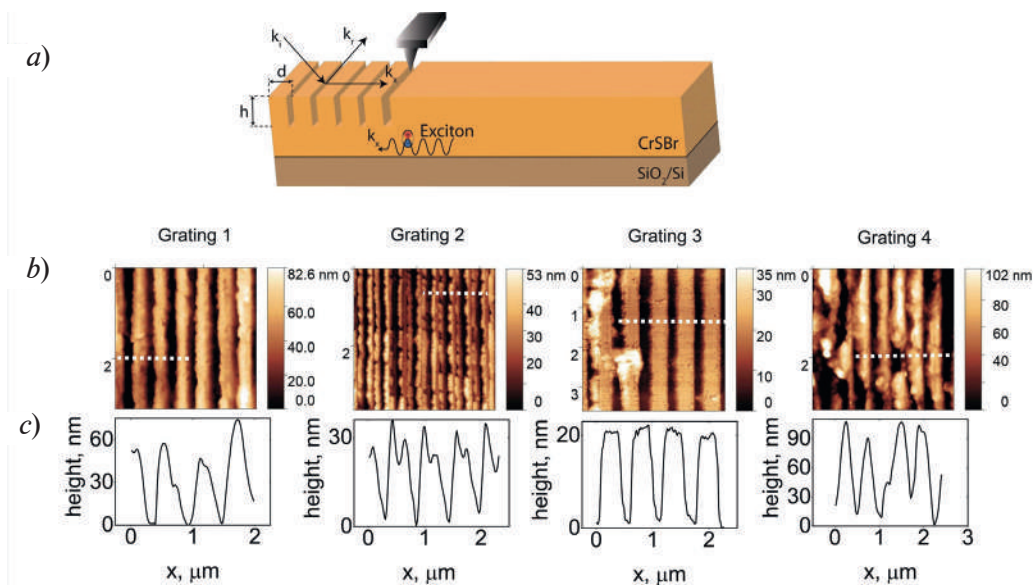
Fig. 1. Schematic illustration of the scanning mechanical probe lithography method (*a*), AFM images of fabricated photonic crystals (*b*), AFM profiles of the obtained photonic crystals (*c*)

Using the FMM method, the dispersion relations of the fabricated photonic crystals were calculated as angle-resolved reflectivity spectra. Fig. 2, *a* shows the simulation results for the 4 structures with thickness of 105 nm, duty cycle of, 0.3, and different grating periods indicated above each plot. The optical dispersions of the fabricated nanostructured CrSBr films were experimentally investigated through back-focal-plane (BFP) photoluminescence measurements with angular resolution in the polarization channel corresponding to TE modes. The experimental dispersion characteristics are shown in Fig. 2, *b* and exhibit good agreement with the results of FMM simulations.

In Fig. 2, *b*, the red line indicates the exciton resonance position, while the orange dashed line shows the lower polariton branches calculated using the coupled oscillator model. From the plots, we observe increasing bending of the dispersion curve away from the exciton resonance as they approach each other for gratings with smaller periods. This is due to increase of the exciton-photon interaction, which can be described by a coupled oscillator model with parameters including the coupling strength and excitonic/photonic relaxation rates. The exciton-photon coupling strength *g* values were derived from curve fitting for all gratings. It was found to be in a range of 35−45 meV, indicating a sizeable interaction between the photonic and excitonic modes. The results showed that the photonic-crystal dispersion can be sensitively controlled via the pitch and duty cycle of the grating fabricated in the CrSBr flake and thus can be brought into resonance with CrSBr exciton at 1.34 eV. The demonstrated coupling strength ($g = 35−40$ meV) significantly exceeds the polariton linewidth ($\gamma \approx 20$ meV), which suggests that the system operates in the strong light-
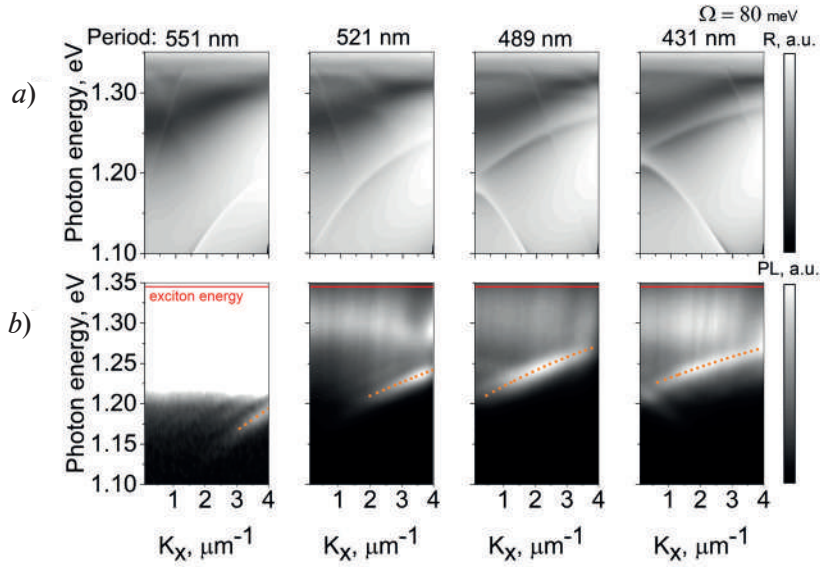
Fig. 2. Simulated grating dispersions using FMM (*a*) and experimentally measured photoluminescence spectra in the back focal plane from fabricated CrSBr gratings (*b*)

matter coupling regime. Future studies should characterize temperature-dependent linewidth narrowing to fully exploit the light-matter hybridization for polaritonic devices.

In Fig. 3, *a*, the expected energy of the original photonic mode without coupling to the exciton resonance is shown as extracted from fitting the experimental data with the coupled oscillator model. In Fig. 3, *b*, the actual experimentally observed energy is shown, when coupling to the exciton resonance is present. The overall energy is lower in the coupled case (Fig. 3, *b*) due to anticrossing, while the photonic mode (Fig. 3, *a*) can actually reach the exciton energy at 1.34 eV and cross it. The difference in energy for 2 selected wavevectors (empty and filled symbols, corresponding to 0.5 μm^{-1} and 3.5 μm^{-1}) is smaller in the coupled case (*b*), which is due to the increased fraction of excitons in the polaritons at higher *k*.
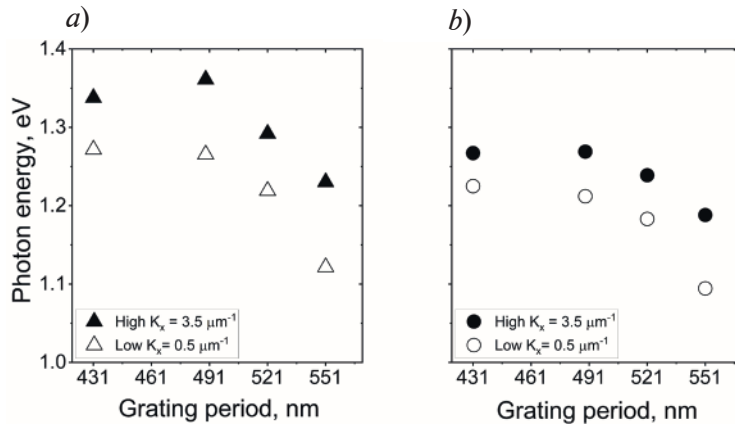
Fig. 3. Photonic dispersion energy in (*a*) in the absence of exciton-photon coupling.
Polaritonic dispersion energy in (*b*) in the presence of exciton-photon coupling

Conclusion

Using mechanical scanning probe lithography, we successfully patterned subwavelength thick flakes of van der Waals antiferromagnetic CrSBr and engineered its photonic dispersion, achieving tunable alignment between the photonic crystal resonance and the excitonic transition energy. The coupling strength between the excitonic and photonic modes was evaluated and determined to lie in the range of 35–40 meV. These results create further opportunities for achieving enhanced light-matter coupling in nanopatterned CrSBr for developing novel compact photonic and optoelectronic devices.

REFERENCES

1. **Li C., et al.,** 2D CrSBr Enables Magnetically Controllable Exciton-Polaritons in an Open Cavity, Advanced Functional Materials. 34 (51) (2024) 2411589.

2. **Wang T., et al.,** Magnetically-dressed CrSBr exciton-polaritons in ultrastrong coupling regime, Nature Communications. 14 (1) (2023) 5966.

3. **Li Q., et al.,** Two-dimensional magnetic exciton polariton with strongly coupled atomic and photonic anisotropies, Physical Review Letters. 26 (133) (2024) 266901.

4. **Dirnberger F., et al.,** Magneto-optics in a van der Waals magnet tuned by self-hybridized polaritons, Nature. 7974 (620) (2023) 533–537.

5. **Komar R., et al.,** Colossal magneto-excitonic effects in 2D van der Waals magnetic semiconductor CrSBr, arXiv preprint arXiv:2409.00187. (2024).

THE AUTHORS

KALANTAEVSKII Ivan E.
royal37lol@gmail.com

GORELKINA Tatiana D.
tatiana.gorelkina@metalab.ifmo.ru

GASNIKOVA Ksenia A.
k.gasnikova@metalab.ifmo.ru

GLEBOV Nikita V.
nikita.glebov@metalab.ifmo.ru
ORCID: 0000-0002-9026-6106

CHERNOV Alexander I.
a.chernov@rqc.ru
ORCID: 0000-0002-6492-9068

ALEKSEEV Prokhor A.
npoxep@gmail.com
ORCID: 0000-0002-8143-4606

KRAVTSOV Vasily A.
vasily.kravtsov@metalab.ifmo.ru
ORCID: 0000-0002-3555-1027

Optical properties of disk microresonators based on wide-bandgap III-N materials

S.D. Komarov [1] ✉, A.G. Vainilovich [2], G.A. Feigin [1], A.V. Sakharov [3], A.E. Nikolaev [3],

K.A. Ivanov [1], E.I. Moiseev [1], N.V. Kryzhanovskaya [1], E.V. Nikitina [4],

A.F. Tsatsulnikov [3], E.V. Lutsenko [2], A.E. Zhukov [1]

[1] National Research University Higher School of Economics, St. Petersburg branch,
St. Petersburg, Russia;

[2] Institute of Physics of the NAS of Belarus, Minsk, Belarus;

[3] Ioffe Institute, St. Petersburg, Russia;

[4] Alferov University, St. Petersburg, Russia

✉ skomarov@hse.ru

Abstract. Fabrication, optical study, and mode modeling of III-N microdisk resonators with InGaN/GaN quantum wells on Al_2O_3 are presented. It is shown that the created epitaxial structures have high optical quality, and the microresonators support high-Q whispering gallery modes.

Keywords: III-N, WGM microresonators, InGaN/GaN quantum wells, microdisk lasers

Оптические свойства дисковых микрорезонаторов на основе широкозонных III-N материалов

С.Д. Комаров [1] ✉, А.Г. Войнилович [2], Г.А. Фейгин [1], А.В. Сахаров [3], А.Е. Николаев [3],

К.А. Иванов [1], Э.И. Моисеев [1], Н.В. Крыжановская [1], Е.В. Никитина [4],

А.Ф. Цацульников [3], Е.В. Луценко [2], А.Е. Жуков [1]

[1] Национальный исследовательский университет «Высшая школа экономики»,
Санкт-Петербургский филиал, Санкт-Петербург, Россия;

[2] Институт физики им. Б.И. Степанова НАН Беларуси, г. Минск, Беларусь;

[3] Физико-технический институт им. А.Ф. Иоффе РАН, Санкт-Петербург, Россия;

[4] Академический университет им. Ж.И. Алфёрова РАН, Санкт-Петербург, Россия

✉ skomarov@hse.ru

Аннотация. Проведено исследование оптических свойств и моделирование мод III-N микродисковых резонаторов с квантовыми ямами InGaN/GaN на подложке Al_2O_3. Показано, что созданные эпитаксиальные структуры обладают высоким оптическим качеством, а микрорезонаторы поддерживают высокодобротные моды шепчущей галереи.

Ключевые слова: III-N, МШГ, квантовые ямы InGaN/GaN, микродисковые лазеры

Ссылка при цитировании: Комаров С.Д., Войнилович А.Г., Фейгин Г.А., Сахаров А.В., Николаев А.Е., Иванов К.А., Моисеев Э.И., Крыжановская Н.В., Никитина Е.В., Цацульников А.Ф., Луценко Е.В., Жуков А.Е. Оптические свойства дисковых микрорезонаторов на основе широкозонных III-N материалов // Научно-технические ведомости СПбГПУ. Физико-математические науки. 2025. Т. 18. № 3.1. С. 209−213. DOI: https://doi.org/10.18721/JPM.183.142

Introduction

Microdisk lasers based on III-N semiconductor materials are promising candidates for use as compact and efficient radiation sources in optoelectronic and photonic integrated circuits due to a combination of their unique characteristics [1]. III-N materials feature a wide direct bandgap, high thermal stability of their characteristics, and significant chemical and mechanical durability, enabling the development of light-emitting devices operating across a broad wavelength range and capable of functioning in harsh environmental conditions [2−4]. Resonators of disk shape support the propagation of high-quality whispering gallery modes (WGMs), allowing lasers with such resonators to achieve ultralow lasing thresholds [5]. Moreover, these lasers have a small footprint, low power consumption, and offer high modulation frequencies [1]. In this study, the design and fabrication of epitaxial structures with InGaN/GaN quantum wells on an Al_2O_3 substrate were carried out. Microscale disk resonators were formed from these structures, and their optical properties were investigated using photoluminescence (PL) spectroscopy.

Materials and Methods

A heterostructure with an active region in the form of $In_{0.1}Ga_{0.9}N$/GaN quantum wells (QWs) was grown on an Al_2O_3 (0001) substrate using metalorganic vapour-phase epitaxy (MOVPE). The growth process started with a low-temperature GaN nucleation layer, followed by the deposition of a 3 μm thick GaN buffer layer ensuring full surface planarization. The active region was then formed, consisting of three 5 nm thick $In_{0.1}Ga_{0.9}N$ QWs separated by 100 nm thick GaN barriers. A 30 nm thick GaN capping layer was then grown as the final step. Disk microresonators with diameters ranging from 1 to 12 μm were fabricated via plasma chemical etching through a Ni mask. Figure 1 shows scanning electron microscopy (SEM) images of the formed microresonators. The spatial distribution of mode intensity in the fabricated disk resonators was simulated using the finite element method (FEM).

The photoluminescence study was performed under optical pumping in continuous wave excitation mode at room temperature using a He Cd laser ($\lambda = 325$ nm). Laser beam was focused on the sample surface into an 8 μm spot with a 5× UV objective. The PL signal was collected by the same objective and recorded using a SOL Instruments MS 5004i monochromator and a Sol Instruments HS 101H CCD camera.

Results and Discussion

The PL spectra obtained from different regions of the samples with grown epitaxial heterostructure exhibit negligible variation, which indicates a high degree of their homogeneity. These spectra
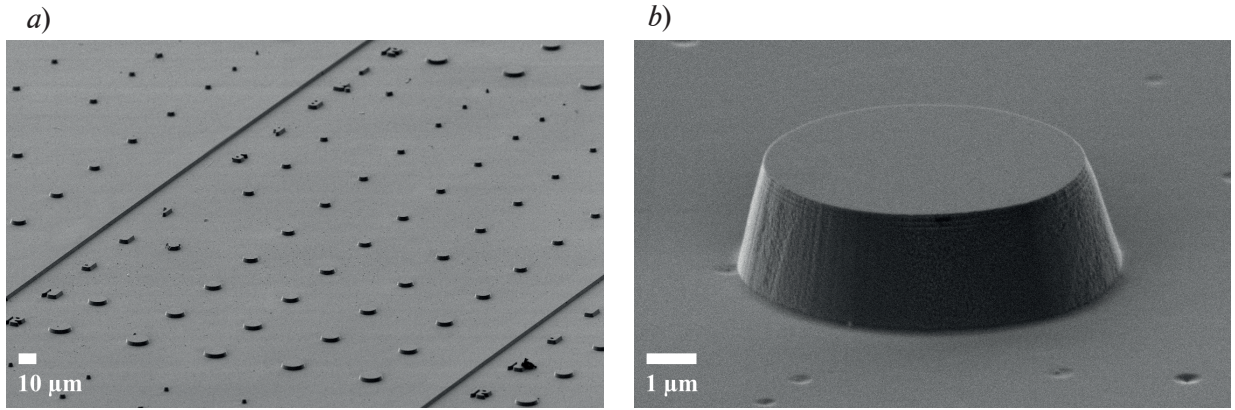
Fig. 1. SEM images of an array of formed disk resonators (*a*) and a single 6 μm diameter resonator (*b*)

feature two PL bands at wavelengths of 365 nm and 415 nm, corresponding to emission from GaN layers and $In_{0.1}Ga_{0.9}N$ quantum wells, respectively (Fig. 2, *a*). In the PL spectra of the microresonators, multiple intensity maxima are observed within the QW emission band, spaced by a few nanometers. Specifically, in the PL spectrum of the 6 μm-diameter resonator, shown in Fig. 2, *b,* these maxima are ~3 nm apart.
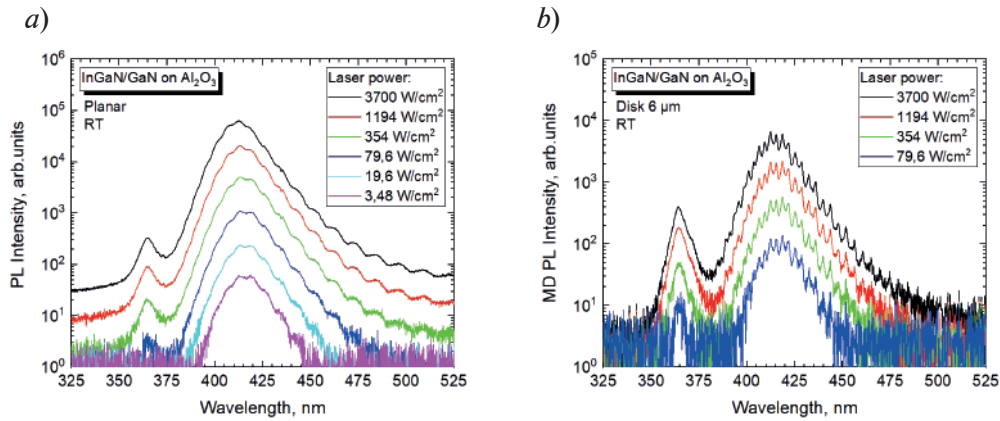
Fig. 2. PL spectra of the planar epitaxial heterostructure (*a*) and a single 6 μm diameter resonator (*b*)

For microdisks of all diameters, the distance between the maxima closely matches the WGM free spectral range, corresponding to the respective resonator sizes. The integrated PL intensity of the quantum wells exhibits a linear dependence on the optical pump power over a wide range for both planar heterostructures and fabricated disk microresonators of all diameters (Fig. 3, *a*).
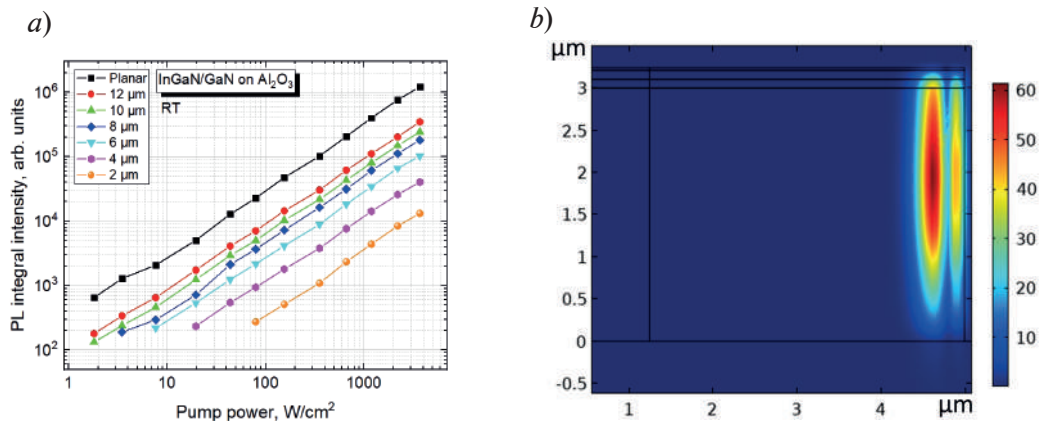
Fig. 3. Dependences of integrated PL intensity of the QWs on pump power (*a*) and a spatial distribution of WGM in 10 μm diameter resonator (*b*)

This indicates the predominance of the radiative recombination mechanism and, as a consequence, the high quality of the obtained structures [6]. However, laser emission was not achieved in the fabricated resonators. The calculated spatial distribution of WGM in the formed microresonators is presented on Fig. 3, *b*. The obtained modeling results indicate strong mode leakage into the buffer layer, with a calculated Γ factor of only 0.2%. This is attributed to insufficient optical confinement in the structure, which is likely the reason for the absence of lasing.

Conclusion

This study demonstrates that the fabricated heterostructure on Al_2O_3 substrate have high quality and uniformity, while the disk microresonators created from this structure support the propagation of high-quality whispering gallery modes. Additionally, spatial intensity distribution modeling of the modes in the investigated resonators was performed to further optimize the heterostructures for laser applications. The obtained results are an important step in the advancement of technologies for the development of nitride-based microdisk lasers. Subsequently, taking into account the significant leakage of modes into the buffer layer, the vertical confinement in the epitaxial structure will be improved by introducing additional buffer layers with a low refractive index. This change is expected to enable laser generation under optical pumping.

Acknowledgments

REFERENCES

1. **Mei Y., Xie M., Long H., Ying L., Zhang B.,** Low threshold GaN-based microdisk lasers on silicon with high Q factor, Journal of Lightwave Technology. 40 (9) (2022) 2952–2958.

2. **Butté R., Grandjean N.,** III-nitride photonic cavities, Nanophotonics. 9 (3) (2020) 569–598.

3. **Baten M.Z., Alam S., Sikder B., Aziz A.,** III-nitride light-emitting devices, Photonics. 8 (10) (2021) 430.

4. **Li X., Liu X.,** Group III nitride nanomaterials for biosensing, Nanoscale. 9 (22) (2017) 7320–7341.

5. **Tamboli A.C., Haberer E.D., Sharma R., Lee K.H., Nakamura S., Hu E.L.,** Room-temperature continuous-wave lasing in GaN/InGaN microdisks, Nature photonics. 1 (1) (2007) 61–64.

6. **Karpov S.Yu.,** ABC-model for interpretation of internal quantum efficiency and its droop in III-nitride LEDs: a review, Optical and Quantum Electronics. 47 (6) (2015) 1293–1303.

THE AUTHORS

KOMAROV Sergey D.
skomarov@hse.ru
ORCID: 0000-0002-7025-3527

FEIGIN Grigorii A.
gafeygin@edu.hse.ru
ORCID: 0009-0007-9304-6401

NIKOLAEV Andrey E.
aen@mail.ioffe.ru
ORCID: 0000-0001-6522-4484

MOISEEV Eduard I.
emoiseev@hse.ru
ORCID: 0000-0003-3686-935X

NIKITINA Ekaterina V.
mail.nikitina@mail.ru
ORCID: 0000-0002-6800-9218

LUTSENKO Evgenii V.
e.lutsenko@ifanbel.bas-net.by
ORCID: 0000-0003-2333-7776

VAINILOVICH Aliaksei G.
a.vainilovich@ifanbel.bas-net.by
ORCID: 0009-0009-5699-2751

SAKHAROV Alexei V.
val.beam@mail.ioffe.ru
ORCID: 0000-0002-9976-999X

IVANOV Konstantin A.
kivanov@hse.ru
ORCID: 0000-0003-2165-1067

KRYZHANOVSKAYA Natalia V.
nkryzhanovskaya@hse.ru
ORCID: 0000-0002-4945-9803

TSATSULNIKOV Andrey F.
andrew@beam.ioffe.ru
ORCID: 0000-0002-5078-8946

ZHUKOV Alexey E.
zhukale@gmail.com
ORCID: 0000-0002-4579-0718

Profile construction and determination of geometric parameters of the rolling surface of a railway wheel using a laser profilometer

K.G. Arinushkina [1, 2] ✉, I.Yu. Savelev [2], V.V. Davydov [3],

A.S. Adadurov [4], P.I. Tsomaev [2]

[1] Bonch-Bruevich Saint-Petersburg State University of Telecommunications,
St. Petersburg, Russia;

[2] JSC "Scientific Research and Design Institute of Informatization, Automation and Communication in Railway Transport" (JSC "NIIAS"), Moscow, Russia;

[3] Peter the Great St. Petersburg Polytechnic University, St. Petersburg, Russia;

[4] Petersburg State Transport University, St. Petersburg, Russia

✉ k-arinushkina@mail.ru

Abstract. The problems arising in the processing of optical images formed from laser signals reflected from the surface of a railway wheel are considered. A design has been developed for the placement of laser emitters and photodetector devices for examining railway wheels in motion. A new algorithm has been developed aimed at improving the accuracy of constructing the profile of the rolling surface of the wheel. To process the recorded optical images in the laser radiation reflected from the surface of the wheel, a new technique based on the use of data filtering has been proposed, which uses a new algorithm that allows removing glare (a cloud of points with false data), outliers (single false points) and leaving only the necessary profile points. The new algorithm is based on the HDBSCAN (Hierarchical Density-Based Spatial Clustering of Applications with Noise) clustering algorithm. The algorithm makes it possible to exclude points forming errors during the construction of the profile of the rolling surface of the wheel. The use of a new design for the placement of optical elements and an algorithm made it possible to increase the accuracy of measurements of key wheel parameters, such as thickness, height and steepness of the ridge, and uniform rolling.

Keywords: laser radiation, reflected signal, optical image, matrix photodetector, wheel pair profile, surface, defects

Построение профиля и определение геометрических параметров поверхности катания железнодорожного колеса с помощью лазерного профилометра

К.Г. Аринушкина [1, 2] ✉, И.Ю. Савельев [2], В.В. Давыдов [3],

А.С. Ададуров [4], П.И. Цомаев [2]

[1] Санкт-Петербургский государственный университет телекоммуникаций
им. проф. М.А. Бонч-Бруевича, Санкт-Петербург, Россия;

[2] АО «Научно-исследовательский и проектно-конструкторский институт информатизации,
автоматизации и связи на железнодорожном транспорте» (АО «НИИАС»),
Москва, Россия;

[3] Санкт-Петербургский политехнический университет Петра Великого,
Санкт-Петербург, Россия;

[4] Петербургский государственный университет путей сообщения
Императора Александра I, Санкт-Петербург, Россия

✉ k-arinushkina@mail.ru

Аннотация. Рассмотрены проблемы, возникающие при обработке оптических изображений, сформированных из отраженных от поверхности колеса железнодорожного транспорта лазерных сигналов. Разработана конструкция размещения лазерных излучателей и фотоприемных устройств для обследования колес в движении. Разработан новый алгоритм, направленный на повышение точности построения профиля поверхности катания колеса. Для обработки регистрируемых оптических изображений в отраженном от поверхности колеса лазерном излучении предложена новая методика, основанная на использовании фильтрация данных, в которой применен новый алгоритм, позволяющий удалить засветку (облако точек с ложными данными), выбросы (одиночные ложные точки) и оставить только нужные точки профиля. Новый алгоритм разработан на основе плотностного алгоритма кластеризации HDBSCAN (Hierarchical Density-Based Spatial Clustering of Applications with Noise). Алгоритм позволяет исключить точки формирующие ошибки при построении профиля поверхности катания колеса. Использование новой конструкции размещения оптических элементов и алгоритма позволило повысить точность измерений ключевых параметров колеса, таких как толщина, высота и крутизна гребня, и равномерный прокат.

Ключевые слова: лазерное излучение, отраженный сигнал, оптическое изображение, матричный фотоприемник, профиль колесной пары, поверхность, дефекты

Introduction

Traditional methods of monitoring the condition of rolling stock wheels based on manual measurements during routine maintenance demonstrate significant limitations: high labor intensity, significant time costs and insufficient accuracy [1]. These disadvantages make them ineffective for modern conditions of intensive railway operation. The use of other methods for monitoring the condition of wheels, which are successfully used in the subway [2] or in trams [3] on mainline railways, is not effective.

Modern research in the field of surface control of both rail condition and wheel design focuses on the development of optoelectronic measurement methods [4]. The use of laser systems has been recognized as the most effective approach [4−7]. This technique includes capturing images of wheelsets using matrix receivers, processing the received data with special algorithms, and automatically determining geometric parameters.

Experimental data confirm that laser measuring systems, which are used in many devices, provide the necessary accuracy with minimal processing time [8−10]. The use of optical systems on railways makes it possible to effectively solve the problems of operational control of the condition of wheelsets in real-world operating conditions, meeting modern requirements for transportation safety.

In this paper, we consider a wheel parameter monitoring system that provides automated non-contact measurement of the geometric characteristics of wheelsets for a wide range of railway rolling stock. The key feature of solving the problem considered in this paper is the ability to take measurements during the movement of the train without having to stop it, which significantly increases the effectiveness of diagnostic procedures. This required the development of a new optical image processing algorithm, as well as the modernization of the design for placing optical elements below the rail level on various sections of the railway, mainly at stations and stages.

Materials and Methods

The developed monitoring system is based on the principle of laser triangulation and includes three key components: a high-precision laser profilometer, a multi-channel photodetector and specialized software for digital signal processing [11, 12].

The measuring complex is based on a pulsed semiconductor laser source ($\lambda = 638$ nm) with an integrated thermal stabilization system [12]. A special feature of the design is the use of Peltier elements with a digital control controller and a precision temperature sensor mounted on a Common heat-dissipating substrate with an emitter. To form the measuring field, an optical scheme for converting a laser beam into a line is used, including a collimating module for forming a parallel light flux and a spherical prism that rotates the beam into a $1.0-1.3$ m long line.

The formed light plane is projected onto the controlled surface of the wheel at a given angle. The reflected radiation is recorded by a highly sensitive CMOS sensor, while the spatial distribution of the light line on the matrix carries information about the geometric parameters of the profile. The distance to the object, which complements the information about the spot's coordinate, is calculated using the formula (1).

$$L = \frac{D \cdot \sin(\alpha)}{\sin(\theta + \alpha)}. \tag{1}$$

The angle θ is determined by changing the image on the matrix for each highlighted pixel with coordinates (u, v). D and α are set during calibration.

The optical matrix receiver is made in the format of a highly sensitive CMOS matrix with a dimension of n×m pixels, it provides the transformation of the spatial distribution of the light line into a digital profile image in the coordinate system (u, v). The information processing device is implemented on the basis of an industrial programmable controller, it performs data processing in real time, followed by recalculation from the pixel coordinate system to the matrix (u, v), into the real coordinate system of the measuring object.

Built-in protection and self-diagnosis mechanisms guarantee safe operation in conditions of heavy railway traffic, and special signal processing algorithms compensate for the effects of external interference, ensuring the reliability of results in real-world operating conditions.

The method of irradiating the wheel is shown in Figure 1.
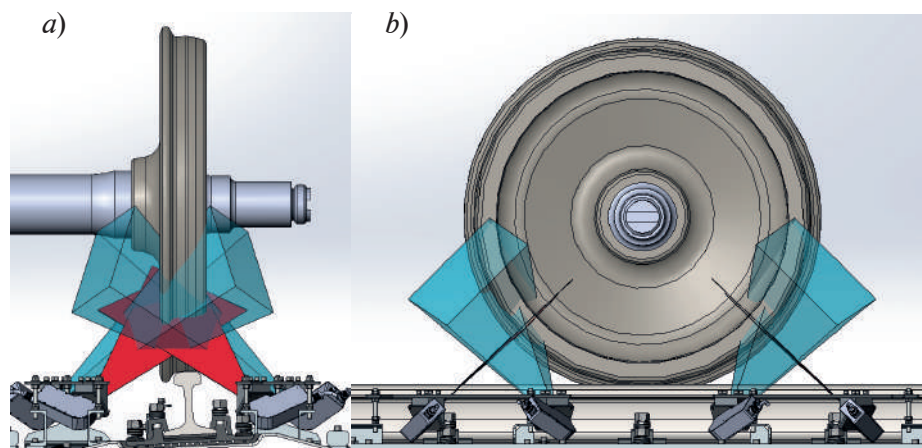
Fig. 1. The process of irradiating the wheel with profilometers side view (*a*), front view (*b*)

The outer (rolling surface) and inner sides (wheel crest) of the wheel profile are scanned separately with two profilometers pre-calibrated into one coordinate system.

The main task of the system is to measure the parameters and highlight the defects of the skating surface against the background of noise and other interference. To solve this problem, an algorithm for mathematical data processing based on the analysis of surface geometry was tested. This method analyzes the geometric parameters of the surface, such as the thickness, height and steepness of the ridge, rolling along the rolling circle and the width of the wheel rim, using laser scanning data. The known defect data is used for the analysis.

The algorithm for filtering profile data

When processing data obtained from laser profilometers in the form of a cloud of points $\{(x_k, y_k)\}$ (where $k = 1 \dots N$), various spurious reflections can have a significant impact on the measurement accuracy, forming separate clusters of points that do not correspond to the real profile of the wheelset, and random emissions that distort the measurement results. Spurious reflections mainly occur due to the reflection of sunlight from a controlled surface, droplets of moisture or other reflective elements, creating false light signals on the receiver. Optical noise (emissions) they appear under the influence of external factors: vibration loads, electromagnetic interference, mutual influence of signals and other operational influences.

To remove outliers and spurious reflections, filtering using the density clustering algorithm HDBSCAN (Hierarchical Density-Based Spatial Clustering of Applications with Noise) is used [13, 14].

For HDBSCAN to work, two parameters need to be set: the neighborhood ε is the maximum distance between data points so that they can be considered part of the same cluster, and m is the minimum number of points required to form a cluster. Two stages of clustering are performed. In the first stage, the values $\varepsilon = 5$ and $m = 20$ are selected so as to discard outliers located at a distance greater than $\varepsilon = 5$ mm from the main point cloud. For the second stage, the values $\varepsilon = 0.5$ and $m = 2$ are chosen so as to divide the entire point cloud into a set of clusters A and subsequently discard those clusters that do not characterize the profile. For further filtering of clusters that do not characterize the profile, the distance d between the last point of cluster A_i and the first point of cluster A_j is estimated, where $j = i + 1$.

$$d = \sqrt{\left(x_{Ai_{end}} - x_{Aj_{end}}\right)^2 + \left(y_{Ai_1} - y_{Aj_1}\right)^2}. \tag{2}$$

According to the value of the RMS error (RMSE) of the linear approximation, clusters are obtained. If d is less than 1 mm, then the points A_j of the cluster are added to A_i, the value of 1 was selected empirically. If d is greater than 1, then the standard deviation of the linear approximation of the N boundary points of the two clusters A_i and A_j is estimated. 5 points are taken from each, where the value of 5 is selected empirically. If the RMSE is less than 0.25, then the clusters are combined into one. At the end of the algorithm, there should be one, the largest cluster characterizing the profile of the railway wheel.

The values were selected based on the representation of the data and the resulting shape of the wheel profile. The threshold distance $d = 1$ mm is close to the average Euclidean distance between neighboring points in the main cloud characterizing the rail profile. If you choose $d \ll 1$, the algorithm will become unnecessarily strict. Neighboring clusters that are parts of the same profile but are separated due to small noise or profilometer errors will not be combined.

If you select $d \gg 1$ mm (for example, 3 mm), the algorithm will begin to combine the real profile and sufficiently distant parasitic reflections into one cluster, which is an error.

The value 5 is selected for the number of boundary points. If you select fewer points (1–3), the approximating line will be extremely sensitive to noise and outliers. Any "bad" point will greatly distort the tilt angle and RMSE.

If you select a large number of points (10–15), the algorithm will lose its ability to respond to local curvature. On the rounded edges of the profile (for example, the crest of the wheel), the local geometry is nonlinear.

The threshold of the deviation RMSE $= 0.25$ was chosen based on the analysis of the approximation error of obviously continuous sections of the profile.

217

The algorithm for restoring the profile and calculating its basic geometric parameters

The filtered data set is divided into i number of segments, with 10 points in each segment, and a 5−point shift between segments. A linear approximation and calculation of the average current is performed for each segment. This part of the algorithm was called piecewise linear approximation. In the end, the external and internal profiles are combined into one, taking into account the potential for rupture, that is, if necessary, a quadratic approximation of the rupture site on the wheel crest is performed.

The point cloud profile reconstruction algorithm uses a piecewise linear approximation for a set of filtered point data $\{(x_k, y_k)\}_{k=1}^{N_f}$, the outer and inner profiles separately, with their subsequent combination.

Each segment is approximated by a first-degree polynomial using the least squares method. The problem is reduced to solving a system of linear equations:

$$\begin{bmatrix} 1 & x_1 \\ 1 & x_2 \\ \vdots & \vdots \\ 1 & x_n \end{bmatrix} \begin{bmatrix} a_0 \\ a_1 \end{bmatrix} = \begin{bmatrix} y_1 \\ y_2 \\ \vdots \\ y_n \end{bmatrix}. \tag{3}$$

Also, the key step of the algorithm is to connect the two parts of the profile − the outside of the wheel and the inside. When data breaks in the ridge area, approximation by a second-degree polynomial is provided for a data set of the outermost 5 points from each part of the profile. If there is no gap, then the data on the ridge overlaps, since at this point the right and left halves of the profile obtained from the two profilometers are stitched.

In the end, all the coordinates are combined into the resulting matrix P:

$$P = \begin{cases} \left(x_i^{(outer)}, y_i^{(outer)}\right) \\ \begin{cases} (x_m, \hat{y}_m), \text{when breaking up} \\ \hat{x}_{\min}, \hat{y}_{\min}, \text{if there is no gap} \end{cases} \\ \left(x_i^{(inner)}, y_i^{(inner)}\right) \end{cases}. \tag{4}$$

The basic geometric parameters shown in Table are calculated using the reconstructed profile.

Results and Discussion

The graph of the gap approximation in the ridge area and the reconstructed wheel profile along with the dimensions are shown in Fig. 2. In this profile, there are a total of 1635 points, 359 filtered points (points from the ridge approximation are added here), 350 segments and 29 clusters.
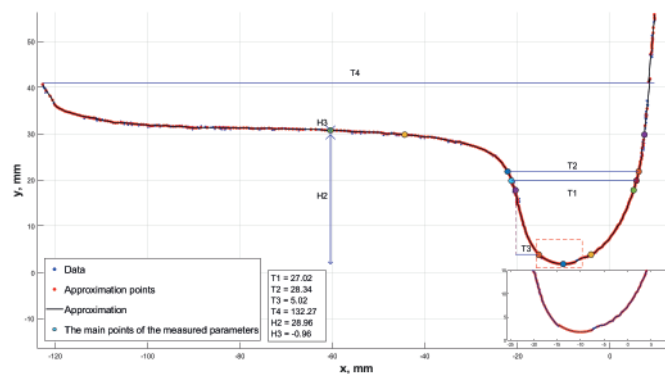
Fig. 2. Restored wheel profile: H2 − is the height of the ridge; H3 − is the rolling circle; T1 − is the thickness of the ridge at a distance of 18 mm from the top; T2 − is the thickness of the ridge at a distance of 20 mm from the top; T3 − the steepness of the ridge; T4 − the width of the rim or band.

The root−mean−square error of each segment, where t is the index of a point in the segment, $\hat{y}_i$ is the approximated segment value, calculated using the formula:

$$\text{RMSE}_i = \sqrt{\frac{1}{n}\sum_1^n (y_t - \hat{y}_i)^2}. \tag{5}$$

In the result after averaging: $\text{RMSE}_{\text{average}} = 0.0818$ mm (Fig. 3).
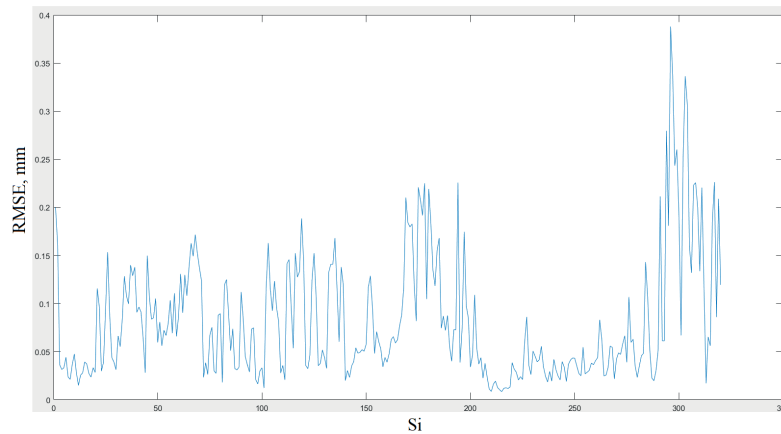
Fig. 3. Approximation error by internal profile segments

The test was carried out on a laboratory stand, the parameters were controlled using templates for monitoring and measuring the parameters of wheelsets of T−series wagons - an absolute template, universal and thickness gauge.

The laboratory wheel was measured 60 times, and based on this, the COE and confidence interval for each size were calculated using the formula:

$$\delta = \frac{t(n, p) \cdot \sigma}{\sqrt{n}}, \tag{6}$$

where, the number $t(n, p)$ is determined by special tables of critical values of the Student's distribution points;

σ is the mean square deviation. $t(60, 95\,\%) = 2$; $n = 60$.

The results are listed in Table 1.

Table

Geometric parameters of the wheel

Name of the parameter	The value of the parameters in mm			
	Algorithm	RMSE	Template measurement	Acceptable range
Parameter ridge thickness at a distance of 18 mm from the top – T1	27.02 ± 0.07	0.23	27.0 ± 0.3	from 24 to 33
Parameter ridge thickness at a distance of 20 mm from the top – T2	28.34 ± 0.06	0.19	28.5 ± 0.5	–
Parameter ridge steepness – T3	5.02 ± 0.02	0.07	5 ± 0.1	–
The thickness of the bandage – T4	132.27 ± 0.03	0.13	132 ± 0.5	–
Ridge height parameter – H2	28.96 ± 0.09	0.27	29.0 ± 0.1	–
Rolling circle parameter – H3	0.96 ± 0.01	0.03	1.0 ± 0.1	less than 2

Analysis of the data obtained shows that the values of the wheel parameters do not exceed the permissible limits, therefore, this wheelset can be operated further.

The system demonstrates reliability in monitoring critical parameters of wheelsets, such as ridge height, rim thickness and rolling size, ensuring stable measurement quality at rolling stock speeds up to 120 km/h.

Conclusion

In the course of the research, an optoelectronic monitoring system for the geometric parameters of wheelsets and track was developed and improved, adapted to work in difficult operating conditions of railway transport. Optimized operation in real conditions due to adaptability to vibrations, temperature fluctuations and precipitation. Data recovery capabilities with partial signal loss have optimized the system's performance in harsh environments.

It was possible to increase the accuracy and reliability of measurements due to the pulse mode of operation of the thermally stabilized laser, which provides resistance to external illumination, improved filtration algorithms that effectively suppress spurious reflections and noise, and an optical circuit that forms a uniform light line with high spatial resolution.

Early detection of defects (cracks, potholes, wear) with an accuracy of 0.2 mm, reduction of maintenance costs due to the transition to repairs according to the actual condition will improve the safety of rolling stock.

The prospects for further research are related to the integration of machine learning methods for automatic defect classification and prediction of the remaining life of undercarriage elements. The developed technical solutions can be scaled for use in other areas of non-destructive testing.

REFERENCES

1. **Wang N., Jia L., Zhang H., Wang Z., Zhao X.,** Manifold-Contrastive Broad Learning System for Wheelset Bearing Fault Diagnosis, IEEE Transactions on Intelligent Transportation Systems. 24 (9) (2023) 9886−9900.

2. **Yan Z., Zhang H., Liu B., Zhu H., Wan H.,** Abnormal noise monitoring of subway vehicles based on combined acoustic features, Applied Acoustics. 197 (2022) 108951.

3. **Jelila Y.D., Pamuła W.,** Detection of Tram Wheel Faults Using MEMS-Based Sensors, Sensors. 22 (17) (2022) 6373.

4. **Emoto T., Ravankar A.A., Ravankar A., Emaru T., Kobayashi Y.,** Wheel Surface Defect Detection Method Using Laser Sensor and Machine Vision. In proceeding 62-nd Annual Conference of the Society of Instrument and Control Engineers SICE, (2023) 1194−1199.

5. **Arinushkina K.G.,** Overview of Fiber Optic Communications in Railway Transport: Challenges and Impact of Processing Time, In proceedings of the 2024 Conference of Young Researchers in Electrical and Electronic Engineering Elcon. (2024) 870−874.

6. **Zheng F., Zhang B., Gao R., Feng Q.,** A high-precision method for dynamically measuring train wheel diameter using three laser displacement transducers, Sensors. 19 (2019) 4148.

7. **Dubnishchev Y.N., Belousov P.Y., Sotnikov V.V., Belousova O.P.,** Optical control of the radius of a wheel rolling on a rail, Optoelectronics, Instrumentation and Data Processing. 48 (1) (2012) 75−80.

8. **Boronenko Y., Rahimov R., Tretyakov A., Zimakova M., Petrov A.,** Method of Continuous Registration of Dynamic Processes of Interaction Between Rolling Stock and Railway Track, Lecture Notes in Mechanical Engineering. 2 (2022) 450−460.

9. **Zheng Z., Song D., Xu X., Lei L.,** A fault diagnosis method of bogie axle box bearing based on spectrum whitening demodulation, Sensors Switzerland. 20 (24) (2020) 1−19.

10. **Davydov V.V., Smirnov K.J.,** An Optical Method of Monitoring the State of Flowing Media with Low Transparency That Contain Large Inclusions, Measurement Techniques. 62 (6) (2019) 519−526.

11. **Wang X., Lu Z., Wen J., Wei J., Wang Z.,** Kinematics modelling and numerical investigation on the hunting oscillation of wheel−rail nonlinear geometric contact system, Nonlinear Dynamics. 107 (3) (2022) 2075−2097.

12. **Arinushkina K.G., Adadurov A.S., Davydov V.V.,** Features of the operation of a laser profilometer in an automated rolling stock control system, St Petersburg State Polytechnical University Journal Physics and Mathematics. 16 (3.2) (2023) 56−62.

13. **Stewart G., Al-khassaweneh M.,** An Implementation of the HDBSCAN* Clustering Algorithm. Applied Sciences. 12 (2022) 2405.

14. **Bhandary P., Joyce R.J., Nicholas C.** Ransomware Evolution: Unveiling Patterns Using HDBSCAN, Ceur Workshop Proceedings. 3920 (2024) 174−189.

THE AUTHORS

ARINUSHKINA Kseniya G.
k-arinushkina@mail.ru
ORCID: 0000-0002-1156-2071

SAVELEV Igor Yu.
savelev.igor@mail.ru
ORCID: 0009-0002-7511-7740

DAVYDOV Vadim V.
davydov_vadim66@mail.ru
ORCID: 0000-0001-9530-4805

ADADUROV Aleksandr S.
vorudada@mail.ru
ORCID: 0000-0002-9520-4596

TSOMAEV Pavel I.
pav.tsomaev@mail.ru
ORCID: 0009-0002-4609-1692

The investigation of Laguerre–Gaussian (0,1) mode focusing in the near-field diffraction by subwavelength variable-height ring gratings

D.A. Savelyev [1] ✉

[1] Samara National Research University, Samara, Russia

✉ savelev.da.2@ssau.ru

Abstract. The parameters of the height of individual zones of subwave ring gratings were established in this paper for which the formation of a long light needle (7.85 wavelengths) is observed in the near diffraction zone with azimuthal polarization of laser radiation. The possibility of reducing the focal spot size to 0.31 wavelengths with circular polarization of the Laguerre–Gauss mode (0,1) was also shown.

Keywords: Laguerre–Gaussian mode, optical needle, FDTD, subwavelength ring gratings, polarization

Citation: Savelyev D.A., The investigation of Laguerre–Gaussian (0,1) mode focusing in the near-field diffraction by subwavelength variable-height ring gratings, St. Petersburg State Polytechnical University Journal. Physics and Mathematics. 18 (3.1) (2025) 222–225. DOI: https://doi.org/10.18721/JPM.183.144

Исследование фокусировки мод Лагерра–Гаусса (0,1) в ближней зоне дифракции субволновыми кольцевыми решетками переменной высоты

Д.А. Савельев [1] ✉

[1] Самарский национальный исследовательский университет имени академика С.П. Королёва, г. Самара, Россия

✉ savelev.da.2@ssau.ru

Аннотация. В работе установлены параметры высоты отдельных зон субволновых кольцевых решеток, для которых в ближней зоне дифракции наблюдается формирование длинной световой иглы (7,85 длин волн) при азимутальной поляризации лазерного излучения. Также показана возможность уменьшения размера фокального пятна до 0,31 длин волн при круговой поляризации моды Лагерра–Гаусса (0,1).

Ключевые слова: мода Лагерра–Гаусса (0,1), оптическая игла, FDTD, субволновая кольцевая решетка, поляризация

Introduction

It should be noted that with the development of optical technologies, it has become necessary to form structured optical fields with certain characteristics of phase, amplitude, and polarization [1–3]. Such structured laser beams find application in such areas as data processing [4], creation of three-dimensional images [5], optical manipulation [6], tight focusing [7], formation of optical needles [8] and others. It should be noted that laser beams with phase and polarization singularities [9] have become widely used to solve problems of modern photonics. Their formation is possible using various optical structures, among which are metasurfaces [5, 10], diffractive optical elements [11] and ring gratings [12].

In this paper, the finite difference time domain (*FDTD*) method is used to study the optimization of the height of individual zones of subwavelength ring gratings to form a long light needle. The numerical calculations of the Laguerre–Gaussian (0,1) modes propagation in the near diffraction zone (3*D*) are carried out using high-performance computer systems.

Materials and Methods

The numerical simulation by the *FDTD* method was carried out with the following parameters: the size of the 3*D* region surrounded on all sides by the absorbing *PML* layer was 18λ, the *PML* thickness was 1.1λ, $\lambda = 0.532$ μm. The following simulation steps were considered: the time step was $\lambda/(100c)$, where c is the speed of light, and the spatial step was $\lambda/50$.

The ring gratings with a period of 1.05λ were used, in this elements the relief height varied in accordance with the phase of π radians. The refractive index of the relief n was chosen to be 2.46, and the refractive index of the substrate was 1.46. Then, the relief height is:

$$h = \frac{\pi}{k(n-1)} = 0,34\lambda, \tag{1}$$

where $k = 2\pi/\lambda$ is the wave number. The height of individual zones of the grating relief changed in multiples of this value.

The Laguerre–Gaussian mode (0,1) with circular and azimuthal polarizations was considered as the input beam. The sign of the circular polarization was chosen to be opposite to the sign of the vortex phase singularity in order to maximize the intensity value on the optical axis.

The assessment of the formed light segment on the optical axis in the transverse region was determined by the full width at half maximum (*FWHM*) intensity value on the optical axis, and similarly in the longitudinal region (depth of focus – *DOF*).

Results and Discussion

A diffraction axicon with a height of $h = 0.34\lambda$ was used as a standard element for comparison (Fig. 1, *a*, *e*). Also a diffraction patterns in the case of a simultaneous increase in the height of all relief zones are shown in Fig. 1, which led to a reduction in the size of the light needle for azimuthal polarization and its slight increase for circular polarization. Also it should be noted that the focal spot broadened for circular polarization.

Let us move on to changing the size h_i of individual zones of the ring gratings relief. The following cases of changing the height of the relief rings were considered (Fig. 2): with a step of 0.34λ (π), from the minimum height in the center ($h_1 = 0.34\lambda$) to the maximum height at the edge of the element ($h_8 = 2.72\lambda$); a similar change in height, but with the height of even elements $h_2 = h_4 = h_6 = h_8 = 0$ ($h_1 = 0.34\lambda$, $h_3 = 1.02\lambda$, $h_5 = 1.7\lambda$, $h_7 = 2.38\lambda$); the case when the height of
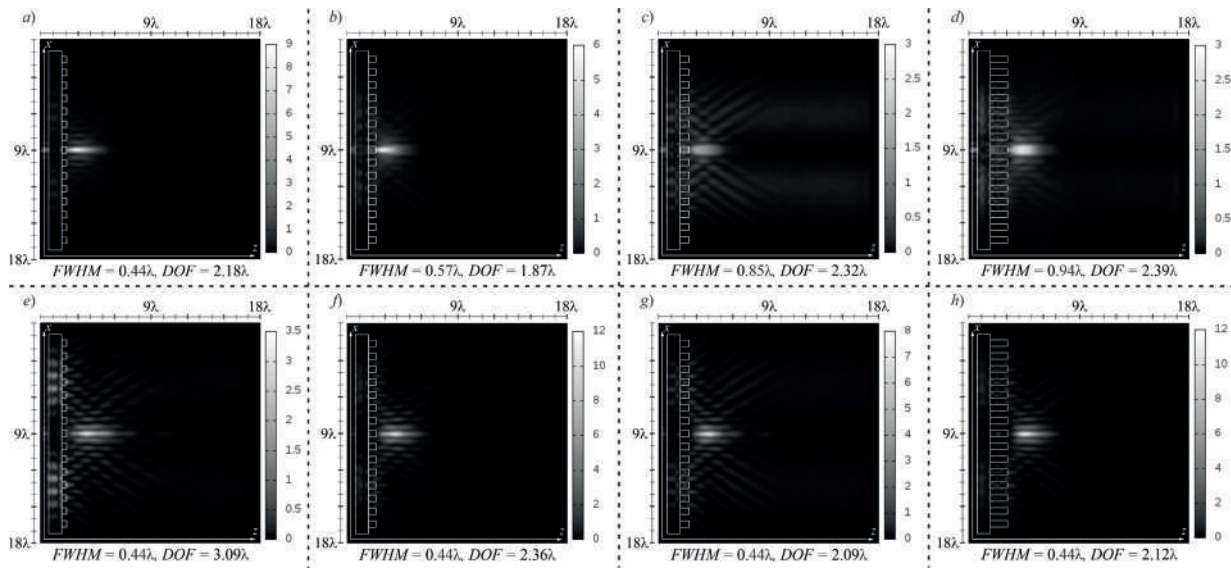
Fig. 1. Laguerre−Gaussian mode (0,1) diffraction, intensity, (*a–d*) circular polarization and (*e–h*) azimuthal polarization: (*a, e*) $h = 0.34\lambda$, (*b, f*) $h = 0.51\lambda$, (*c, g*) $h = 0.68\lambda$, (*d, h*) $h = 1.36\lambda$
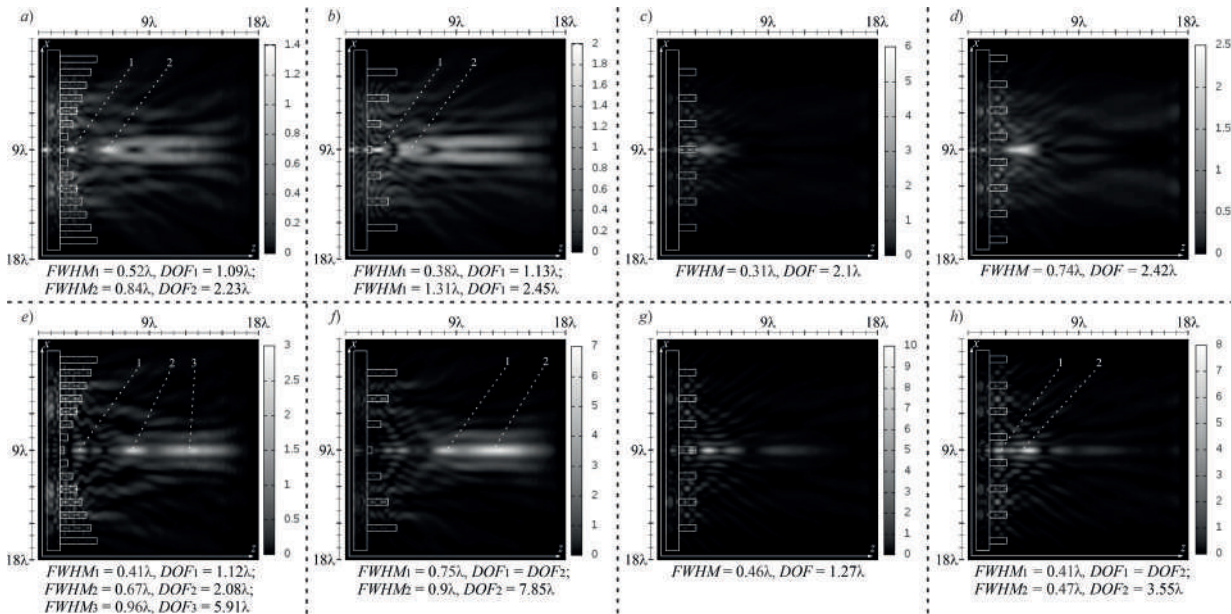
Fig. 2. Laguerre−Gaussian mode (0,1) diffraction, intensity, (*a–d*) circular polarization and (*e–h*) azimuthal polarization: (*a, e*) $h_1 = 0.34\lambda$, $h_2 = 0.68\lambda$, $h_3 = 1.02\lambda$, $h_4 = 1.36\lambda$, $h_5 = 1.7\lambda$, $h_6 = 2.04\lambda$, $h_7 = 2.38\lambda$, $h_8 = 2.72\lambda$; (*b, f*) $h_1 = 0.34\lambda$, $h_3 = 1.02\lambda$, $h_5 = 1.7\lambda$, $h_7 = 2.38\lambda$, $h_2 = h_4 = h_6 = h_8 = 0$; (*c, g*) $h_1 = h_3 = h_5 = h_7 = 1.36\lambda$, $h_2 = h_4 = h_6 = h_8 = 0$; (*d, h*) $h_1 = h_3 = h_5 = h_7 = 0$, $h_2 = h_4 = h_6 = h_8 = 1.36\lambda$

the odd zones was the same ($h_1 = h_3 = h_5 = h_7 = 1.36\lambda$), and the height of the even zones was 0, and also the opposite case ($h_2 = h_4 = h_6 = h_8 = 1.36\lambda$, and the height of odd zones is 0).

The required distribution on the optical axis can be formed by selecting the heights of individual relief zones. The formation of a long light needle, a set of optical bottles, and a sharply focused beam are shown in Fig. 2.

It should be noted that the reduction in the number of ring gratings relief zones made it possible to increase the size of the light needle in the case of azimuthal polarization (Fig. 2, *e, f*), and a significant reduction in the size of the focal spot is observed for circular polarization: from $FWHM = 0.52\lambda$ to $FWHM = 0.38\lambda$ (Fig. 2, *a, b*) in the case of changing all relief zones, as well as from $FWHM = 0.94\lambda$ to $FWHM = 0.31\lambda$ in the case of the same height of the remaining non-zero relief zones (Fig. 1, *d*; Fig. 2, *c*).

The smallest focal spot size was $FWHM = 0.31\lambda$, and the longest light needle was $DOF = 7.85\lambda$, which was 2.54 times larger than the light needle formed by a standard diffractive axicon with $h = 0.34\lambda$. Experiments have shown that using electron-beam lithography it is possible to produce similar elements (with different heights of individual relief rings).

Conclusion

The numerical simulation using the $FDTD$ method showed that it is possible to optimize the height of individual zones of ring gratings to obtain the required distribution on the optical axis in the near diffraction zone.

The parameters have been established at which the size of the formed light segment is maximum ($DOF = 7.85\lambda$): the height of even zones is zero, and the height of odd zones of the element increases from the center to the edges ($h_1 = 0.34\lambda$, $h_3 = 1.02\lambda$, $h_5 = 1.7\lambda$, $h_7 = 2.38\lambda$) with azimuthal polarization of the Laguerre−Gaussian mode (0,1). The minimum size of the focal spot ($FWHM = 0.31\lambda$) was also obtained at zero height of even zones and $h_1 = h_3 = h_5 = h_7 = 1.36\lambda$ with circular polarization of the laser radiation.

REFERENCES

1. **Shen Y., Nape I., Yang X., Fu X., Gong M., Naidoo D., Forbes A.,** Creation and control of high-dimensional multi-partite classically entangled light, Light: Science & Applications. 10 (1) (2021) 50.

2. **Dorrah A.H., Capasso F.,** Tunable structured light with flat optics, Science. 376 (6591) (2022) 6860.

3. **Rosales-Guzmán C., Ndagano B., Forbes A.,** A review of complex vector light fields and their applications, Journal of Optics. 20 (12) (2018) 123001.

4. **Angelsky O.V., Bekshaev A.Y., Hanson S.G., Zenkova C.Y., Mokhun I.I., Zheng, J.,** Structured light: ideas and concepts, Frontiers in Physics. 8 (2020) 114.

5. **Choi E., Kim G., Yun J., Jeon Y., Rho J., Baek S.H.,** 360 structured light with learned metasurfaces, Nature Photonics. 18 (8) (2024) 848−855.

6. **Yang Y., Ren Y.X., Chen M., Arita Y., Rosales-Guzmán C.,** Optical trapping with structured light: a review, Advanced Photonics. 3 (3) (2021) 034001.

7. **Ke L., Yang Y., Zhu M., Zhou H., Chen Y., Tian Y., Li C., Fang B., Hong Z., Jing X.,** Tight focusing of fractional-order topological charge vector beams by cascading metamaterials and metalens, Microsystems & Nanoengineering. 10 (1) (2024) 146.

8. **Savelyev D.A.,** The optical needles formation by ring gratings of variable height with quantized substrate [in Russian], Opticheskii Zhurnal. 92 (5) (2025) 12−25.

9. **Porfirev A.P., Kuchmizhak A.A., Gurbatov S.O., Juodkazis S., Khonina S.N., Kulchin Y.N.,** Phase singularities and optical vortices in photonics, Phys. Usp. 192 (8) (2022) 841−866.

10. **Ahmed H., Kim H., Zhang Y., Intaravanne Y., Jang J., Rho J., Chen S., Chen X.,** Optical metasurfaces for generating and manipulating optical vortex beams, Nanophotonics. 11 (5) (2022) 941−956.

11. **Khonina S.N., Kazanskiy N.L., Skidanov R.V., Butt M.A.,** Advancements and applications of diffractive optical elements in contemporary optics: A comprehensive overview, Advanced Materials Technologies. 10 (4) (2025) 2401028.

12. **Savelyev D.A.,** Peculiarities of focusing circularly and radially polarized super-Gaussian beams using ring gratings with varying relief height, Computer Optics. 46 (4) (2022) 537−546.

THE AUTHORS

SAVELYEV Dmitry A.
dmitrey.savelyev@yandex.ru
ORCID: 0000-0003-2282-3895

Laser cleaning of organic pigments on paper

A.D. Neelova [1, 2] ✉, V.A. Parfenov [1, 3]

[1] St. Petersburg Electrotechnical University "LETI", St. Petersburg, Russia;
[2] Russian National Library, St. Petersburg, Russia;
[3] Saint-Petersburg Institute of History of the RAS, St. Petersburg, Russia

✉ angelina.neelova@gmail.com

Abstract. This paper is devoted to the investigation of laser cleaning of organic pigments on paper. In recent years, laser technologies have been widely used in the preservation of Cultural Heritage (CH). One of the main fields of laser application in this area is the cleaning of CH objects from various contaminations of natural or anthropogenic origin. Experimental results of laser cleaning with the Ytterbium pulsed fibre laser (1064 nm wavelength) of model samples of modern organic pigments on paper as well as Raman spectroscopy analysis of the obtained results are presented.

Keywords: cultural heritage, laser cleaning, pigments, contaminations, fibre laser

Лазерная очистка органических пигментов на бумаге

А.Д. Неелова [1, 2] ✉, В.А. Парфенов [1, 3]

[1] Санкт-Петербургский государственный электротехнический университет «ЛЭТИ» им. В.И. Ульянова (Ленина), Санкт-Петербург, Россия;
[2] Российская национальная библиотека, Санкт-Петербург, Россия;
[3] Санкт-Петербургский Институт истории РАН, Санкт-Петербург, Россия

✉ angelina.neelova@gmail.com

Аннотация. Статья посвящена исследованию лазерной очистки органических пигментов на бумаге. В последнее время лазерные технологии все чаще распространяются в сфере сохранение культурно-исторического наследия. Одним из основных направлений применения лазерных технологий в реставрации является очистка объектов культурно- исторического наследия от различных загрязнений естественного и антропогенного происхождений. В данной работе представлены экспериментальные результаты лазерной очистки модельных образцов современных органических пигментов на бумаге при помощи иттербиевого импульсного лазера на длине волны 1064 нм, а также анализ полученных результатов методом спектроскопии комбинационного рассеяния.

Introduction

Recent studies have shown that laser cleaning is a safe and efficient instrument for restoration of cultural heritage (CH) objects [1−2]. Laser cleaning of artefacts made out of inorganic materials such as stone and metal is well developed, whereas cleaning CH objects based on organic ones is still in the process of experimental studies. Organic materials in cultural heritage include paper, leather, parchment, textiles and also organic paints and colourants.

Based on scientific literature on the topic and authors' experience laser could be applied for removing various deteriorations such as dust, soot, fungi, foxings, oil and wax from the surface of the paper without causing it any damage [3−5]. CH artefacts on paper base such as books, documents, manuscripts and painting are complex objects and include not only paper but ink, pencil, paint, colourant, etc.

In the given research we will consider laser treatment of organic pigments on paper. Organic pigments for paints and colourants production were used since the dawn of time. A lot of historical paints and colourants are known to be of organic origin, for example, plant derivative ones, such as indigo or madder. These pigments could be found in paintings, books, documents, historical textiles, taxidermy objects, etc. Nowadays organic pigments are even more widely spread in the manufacturing of paints and colourants, apart from their predecessors modern pigments are nearly all synthesised. Therefore, using organic synthetic pigments is a well established practice by contemporary artists. Thus, investigating novel restoration and conservation technics for the future CH objects is an actual scientific task.

Experiment

The authors of this work have already reported about laser cleaning of CH objects on paper base using Ytterbium fibre laser with the wavelength of 1064 nm [3−5]. Given wavelength was chosen based on the reflectance of the paper. Preliminary to the experiment on leaser cleaning reflectance spectra of pigments on paper samples were obtained as well. Reflectance spectra show that up from 800 to 1100 nm about 80−90 % of laser irradiation is reflected from the paint surface (Fig. 1). Therefore, it was proven that laser with the wavelength of 1064 nm is suitable for carrying out the given task.

Investigated pigments are modern organic synthetic pigments most widely used in paint production. These pigments are pigment blue 15 (PB15), pigment green 7 (PG7), pigment violet 19 (PV19), pigment violet 23 (PV23) and pigment yellow 3 (PY3). Pigments were present in different paints such as watercolour, gouache and acrylic. The selection of listed pigments was based on the fact that they make an average palette of a contemporary artist.

Samples were prepared by applying paint on the surface of the paper. To imitate contamination graphite dust was used. During the experiment samples were cleaned from the contamination by laser and then studied by optical microscopy and Raman spectroscopy.

Laser cleaning from contaminations was achieved by laser irradiation with following parameters: wavelength of 1064 nm, pulse duration of 100 ns, pulse repetition frequency of 20 kHz, peak power density about $3 \cdot 10^5$ W/cm^2, beam scanning speed of 800 mm/s. Cleaned area was 10 by 10 mm.
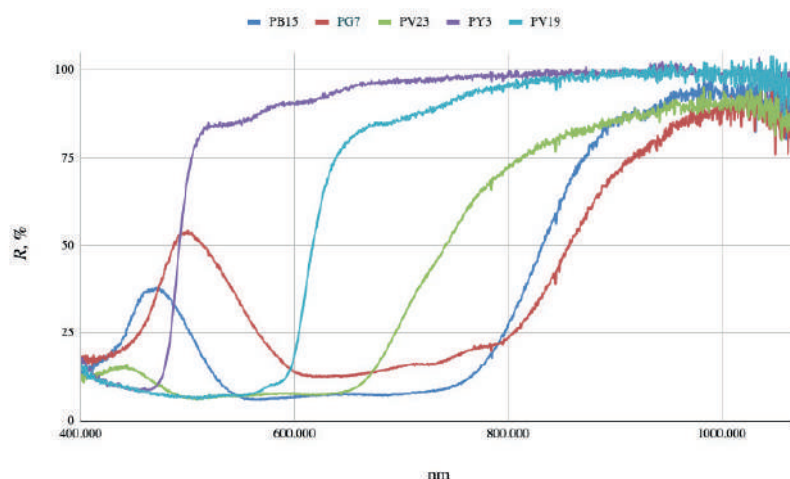
Fig.1. Reflectance spectra of pigments on paper

Results and Discussion

Samples of pigments on paper were successfully cleaned by laser irradiation from contamination without any visual damage. The results of laser cleaning are shown in Fig. 2. Images obtained by the means of optical microscope additionally proved that the laser irradiation caused no damage to the paint layer or any colour degradation in it.

Raman spectroscopy was performed to detect any changes in the chemical composition of pigments caused by laser irradiation and to control the efficacy of laser cleaning. Raman microscope by SOL Instruments (Belarus) was utilised during the experiment with the solid laser irradiation source with the wavelength of 785 nm. Spectra were registered with the diffraction grating of 600 lines per mm, measurement range ran from 100 to 1800 cm^{-1}, integration time for a spectrum was set at 20 seconds. Spectral resolution of a microscope 0.07 nm. Spectra were obtained in two points of a sample: in the untreated area and in the area undergone laser cleaning. In Fig. 2 untreated area labeled by number (1) and cleaned area is within the white square.
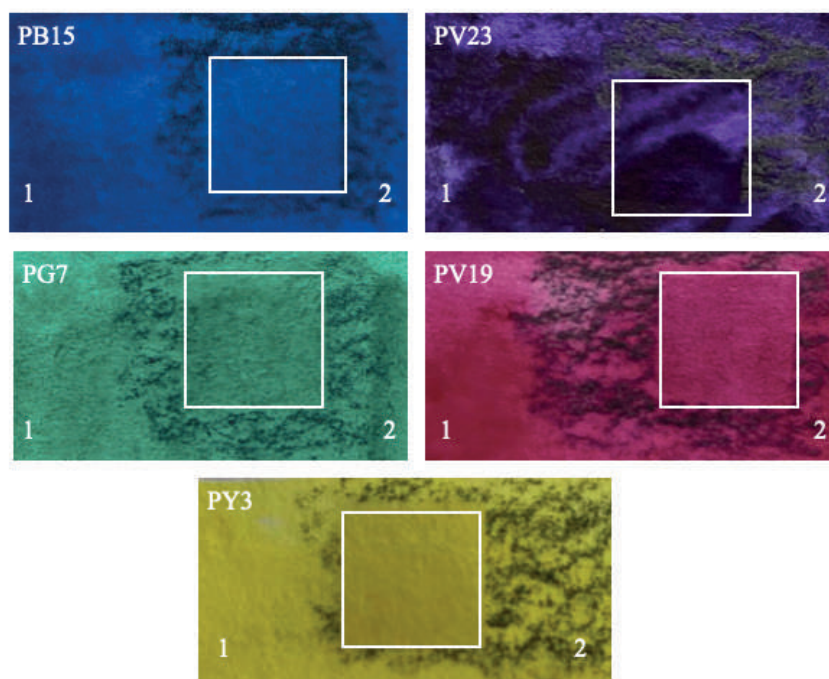
Fig.2. Images of samples after laser cleaning. Cleaned areas are marked with white (10×10 mm). Untreated area of a sample is marked (1) and contaminated area (2)

Summary results of laser cleaning and Raman analysis are presented in Table. It can be seen that cleaning results and spectra analysis correlate. There are no visible changes in the treated areas and there are no changes in a pigment spectrum.

Table

Summary table of laser cleaning results and Raman spectroscopy analysis

Pigment	Class of the chemical substance of a pigment	Laser cleaning result	Raman spectroscopy result	
			Raman wavenumbers (cm^{-1}) before cleaning	Raman wavenumbers (cm^{-1}) after cleaning
PY 3	Azomethine	No damages	Intense peaks at 1619, 1500, 1390, 1338, 1314, 1141; medium peaks at 1678, 1250 and 1198; weak peaks at 1572, 1449, 1282, 1040, 960, 826, 748, 650, 622, 410, 393, 201, 181, 133, 108	Intense peaks at 1618, 1498, 1390, 1341, 1314, 1141; medium peaks at 1685, 1250 and 1198; weak peaks at 1575, 1446, 1295, 1039, 990, 960, 824, 748, 650, 621, 411, 393, 201, 185, 135 and 103
PV 19	Quinacridone	No damages	Intense peaks at 1612 and 1366; medium peaks at 1552, 1519, 1491, 1289, 1250, 1169, 1247, 731; weak peaks at 1433, 1390, 1336, 1117, 1017, 968, 804, 610, 575, 522, 502, 425, 333, 260, 210	Intense peaks at 1613 and 1366; medium peaks at 1553, 1517, 1491, 1287, 1249, 1169, 733; weak peaks at 1428, 1391, 1334, 1121, 1014, 966, 804, 611, 577, 522, 501, 426, 331, 261, 210
PV 23	Dioxazine	No damages	Intense peaks at 1435, 1396, 1349, 1209; medium peaks at 1595, 1260, 1168; weak peaks at 1655, 1533, 1113, 999, 925, 674, 622, 592, 528, 485, 418, 315	Intense peaks at 1435, 1393, 1349, 1209; medium peaks at 1595, 1260, 1168; weak peaks at 1655, 1533, 1113, 999, 925, 674, 622, 592, 528, 485, 418, 315
PB 15	Phthalocyanine	No damages	Intense peaks at 1525, 1338, 746; medium peaks at 1452, 1144, 678; weak peaks at 1637-1578, 1214, 1190, 1010, 953, 879-820, 775, 596, 485, 256, 171	Intense peaks at 1525, 1338, 746; medium peaks at 1452, 1144, 678; weak peaks at 1633-1576, 1216, 1199, 1111, 953, 879-820, 777, 596, 481, 255, 171
PG 7	Phthalocyanine	No damages	Intense peak at 1538, peaks of medium intensity at 1335, 1280, 1206, 772, 741, 685, weak peaks are at 1384, 1077 and 980	Intense peak at 1538, peaks of medium intensity at 1335, 1280, 1206, 772, 741, 685, weak peaks are at 1384, 1077 and 980

Obtained Raman spectra of samples are shown in Fig. 3. The difference in intensity of the spectra before and after cleaning is likely to be due to the unequal distribution of the pigment layer on paper since there is no evidence of any damage done to it during laser treatment.
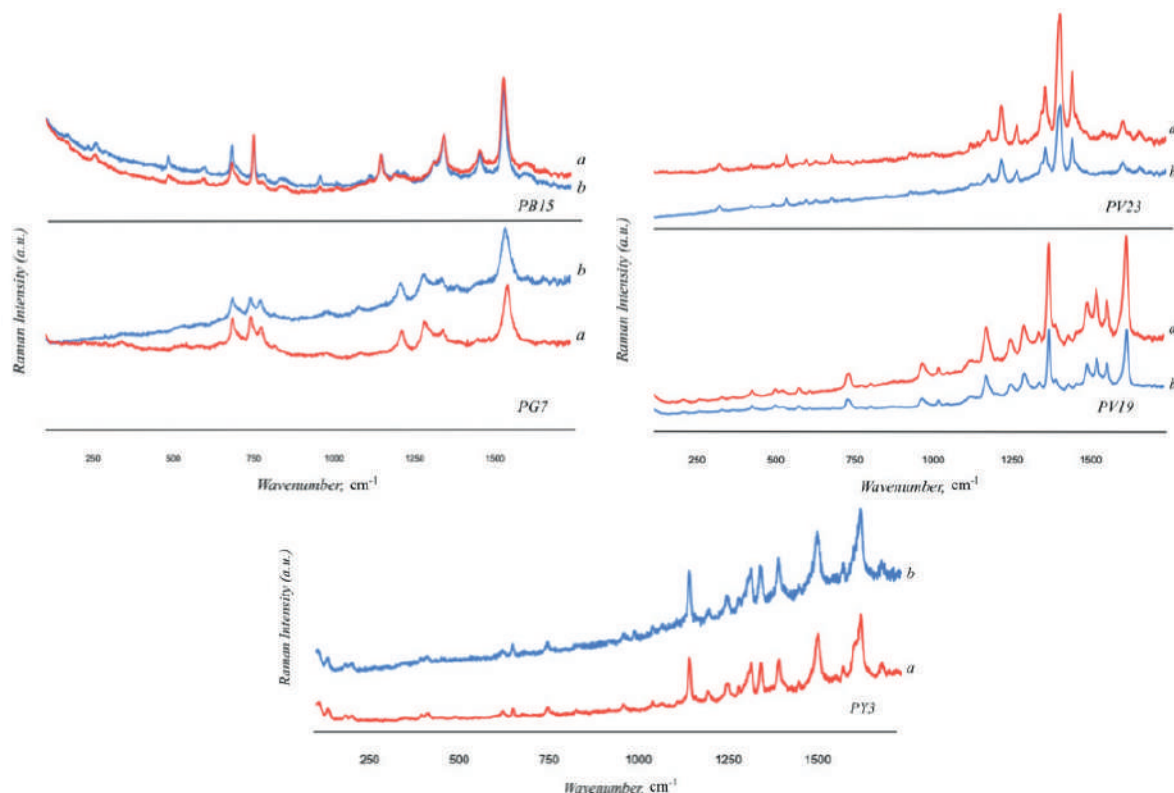
Fig.3. Raman spectra of pigment samples in the untreated area (*a*) and in the laser cleaned area (*b*)

It can be seen that for all of the samples Raman spectra in the untreated area and in the cleaned area do not differ. Main peaks are listed in Table, it can be noted that there is an insignificant shift in the wavenumbers of the corresponding peaks of a sample. Nevertheless, it can be concluded that laser irradiation impact does not lead to any dangerous changes in the pigment layer after removing contaminations.

Conclusion

Samples of organic pigments on paper were successfully cleaned from contaminations by the laser irradiation with the wavelength of 1.06 μm. Investigation of laser treatment results by means of optical microscopy showed no damage to the pigment layer after laser cleaning. A study of the issue using the method of Raman spectroscopy further proved that laser cleaning does not cause damage to the pigment layer as well as chemical transformation in it.

To conclude, it could be presumed that laser cleaning can be safely applied to the restoration of cultural heritage objects containing organic synthetic pigments of paper, such as paintings, book miniatures, documents, etc. Nevertheless, authors will proceed with further investigation on the matter.

REFERENCES

1. **Cooper M.,** Laser Cleaning in Conservation: An Introduction, Oxford: Butterworth-Heinemann. (1998).

2. **Fotakis C., Anglos D., Zafiropulos V., Georgiou S., Tornari V.,** Lasers in the preservation of cultural heritage: principles and applications, CRC Press. (2006).

3. **Arif S., Kautek W.,** Laser cleaning of paper: Cleaning efficiency and irradiation dose, Stud. Conserv. 60 (2015) 97–105.

4. **Parfenov V., Galushkin A., Tkachenko T., Aseev V.,** Laser Cleaning as Novel Approach to Preservation of Historical Books and Documents on a Paper Basis, Quantum Beam Science. 3 (6) (2022) 23.

5. **Neelova A.D., Shepilova E.M., Nosova E.I., Rongonen S.L., Parfenov V.A.,** A Study of Chemical and Mechanical Properties of Paper Under Its Laser Cleaning, St. Petersburg Polytechnic University Journal: Physics and Mathematics. 3.2 (69) (2023) 114–119.

THE AUTHORS

NEELOVA Angelina D.
angelina.neelova@gmail.com
ORCID: 0009-0004-8098-2055

PARFENOV Vadim A.
vadim_parfenov@mail.ru
ORCID: 0000-0002-2048-4677

Optical properties of aluminum nanostructures modified by polymer coatings

D.E. Kostina [1] ✉, D. Malo [1, 2], A.A. Lizunova [1], E.I. Kameneva [1]

[1] Moscow Institute of Physics and Technology (National Research University),
Dolgoprudny, Russia;

[2] Damascus University, Damascus, Syria

✉ frolova.de@mipt.ru

Abstract. In this research, optical properties of Al films based on Al nanoparticles (Al NPs) with a particle size of 55 nm were studied by analyzing the absorption spectra before and after deposition of polymer coatings. Plasmonic Al nanostructures films were fabricated using spin-coating on quartz substrates, followed by sequential deposition of polymer using poly-L-lysine (PLL) and dextran. The obtained results showed that dextran coating did not induce significant spectral changes, whereas PLL provided a shift in the absorption resonance peak of Al films from 230 nm to 300 nm. Additionally, at an excitation wavelength of 325 nm, the photoluminescence enhancement of ZnO nanocrystals with 27 nm in particle size was investigated in the presence of Al nanostructures with and without PLL film as intermediate film. The results demonstrated that the increase in photoluminescence enhancement factor at an emission wavelength of 377 nm in the presence of PLL film between ZnO and Al films up to 68%. These findings proved that polymer coatings have a significant impact on the optical response of aluminum nanostructures. The obtained results provide a promising methodology for tuning their optical properties and plasmon-enhanced photoluminescence factor for many plasmonic and biosensing applications in the ultraviolet region.

Keywords: aluminum nanoparticles, poly-L-lysine, dextran, zinc oxide nanoparticles, plasmon resonance, plasmon-enhanced photoluminescence, ultraviolet, spin-coating

Аннотация. Проведено исследование влияния полимерных покрытий, нанесенных методом спинкоатинга, на оптические свойства алюминиевых наноструктур. Показано, что использование поли-L-лизина (PLL) приводит к сдвигу пика поглощения с 230 до 300 нм, тогда как декстран не вызывает значимых спектральных изменений. Аналогичный эффект смещения пика поглощения наблюдается и в спектрах поглощения для тонкой пленки из платиновой наноструктуры, что подтверждает универсальность метода. Установлено, что внедрение PLL в структуру ZnO/Al для получения ZnO/PLL/Al структуры обеспечивает увеличение интенсивности фотолюминесценции на длине волны 377 нм до 68% по сравнению с двухслойной системой ZnO/Al без полимерной прослойки при длине волны возбуждения 325 нм. Результаты демонстрируют потенциал полимерной модификации для управления оптическим откликом наноструктур в задачах создания ультрафиолетовых биосенсоров и металл-усиленной фотолюминесценции.

Ключевые слова: наночастицы алюминия, поли-L-лизин (PLL), декстран, наночастицы оксида цинка, плазмонный резонанс, плазмон-усиленная фотолюминесценция, ультрафиолет (UV), спин-коатинг

Introduction

In recent decades, there has been an increasing interest in Al NPs and the methods of their synthesis, as well as film creation and characterization due to their promising properties in the UV region of spectrum especially their role in plasmon-enhanced photoluminescence for several applications in biosensing [1−3]. One of the approaches to altering the optical response of nanostructures is surface modification with polymer coatings [4]. Polymers such as poly-L-lysine (PLL) and dextran can interact with metal nanoparticles differently, affecting their spectral characteristics. PLL, a positively charged polymer, is known to induce electronic and dielectric modifications at the nanoparticle interface, while neutral polymers like dextran primarily act as passive stabilizers. These interactions are crucial for understanding the plasmonic nanomaterials and optimizing their behaviors [5]. For instance, polymeric coatings on thin films of gold nanoparticles (Au NPs) have been shown to induce a redshift in the localized surface plasmon resonance (LSPR) peak due to changes in the surrounding dielectric permittivity [6]. Moreover, the localized surface plasmon resonance of silver nanoparticles (Ag NPs) had shown to red-shift in response to increasing polymer such as PS-b-PBD-b-PS, PS-co-PMMA and PS-b-PI-b-PS layer thickness and refractive index, as both experimental data and numerical simulations revealed a strong dependence of the plasmonic behavior on the dielectric properties of the surrounding polymer matrix [7]. These results confirm that surface polymer modification enables precise control over the plasmonic response of metal nanostructures. In this work, we investigated the influence of PLL and dextran coatings on the optical properties of Al NPs films by analyzing changes in the absorption in the UV region and the plasmon-enhanced photoluminescence of ZnO NPs in the presence of Al NPs, providing insights into potential applications in plasmonic sensing and material design.

Materials and Methods

Poly-L-lysine (PLL) (Sigma-Aldrich, USA; 0.1% w/v in H_2O) and Dextran (Sigma-Aldrich, USA; 1 g/L in deionized water) were used as film-forming polymers. Both polymer solutions were pre-diluted by the ratio of 1:3 (v:v) with 2-propanol for HPLC (Hipersolv Chromanorm, VWR BDH Chemicals, Allemagne). Aluminum NPs colloid of 0.18 g/L (54.6 $\pm$ 25.1 nm in particle size, synthesized by an electrical wire explosion method) was prepared in chromatographically

pure isopropanol containing citric acid (0.05 g/L) as a stabilizer, following the procedure described in [1]. Zinc oxide NPs colloid of 1.1 g/L with an average particle size of 26.6 ± 7.4 nm was prepared from a dispersion of ZnO particles (Sigma-Aldrich, Switzerland; 40 wt.%) by the steps described in [1]. Suspensions were spin-coated onto quartz substrates (1.2×4) cm^2 using a spin coater (EZ4, Schwan technology) with the following coating parameters: 15 µL of suspension, 1000 rpm for 30 s, and acceleration 500 rpm/s (Fig. 1).

The changes of absorption spectra were analyzed for two Al films with different optical densities, resulting in 12 and 27 layers of Al NPs (AlI and AlII), coated with 5 sequential polymer layers, separately.
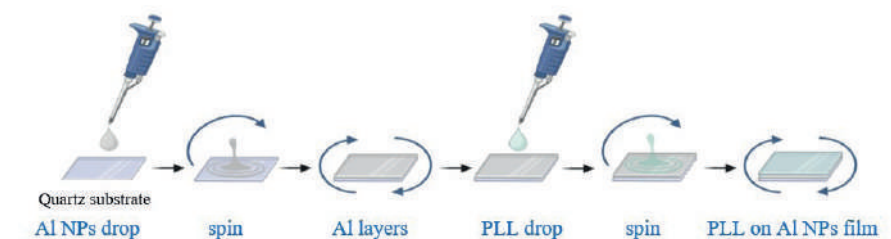
Fig. 1. Spin-coating process for Al NPs with sequential PLL layering

For photoluminescence enhancement investigation, three layers of ZnO NPs were spin-coated and studied in presence of PLL film (5 layers of PLL) and Al NPs film (12 layers of Al). Where seven samples were prepared with various structures: pure film of PLL (PLL), pure film of Al NPs (Al), pure film of ZnO NPs (ZnO), ZnO film applied on PLL film (ZnO/PLL), ZnO film on Al film (ZnO/Al), PLL film on Al film (PLL/Al), and PLL film deposited between ZnO and Al films (ZnO/PLL/Al).

The size and crystal structure of primary NPs were received by transmission electron microscopy (TEM) JEOL JEM 2100 (200 kV). UV-vis-NIR spectra and luminescence emission were obtained using JASCO V-770 and JASCO FP-8300 spectrometers, correspondingly. Surface morphology of the obtained nanostructures films was analyzed by scanning electron microscopy (SEM) JEOL JSM 7001F.

Results and Discussion

TEM analysis showed spherical shape and core-shell structure for Al nanoparticles with metal crystal core and oxide shell (Fig. 2, *a*). The average primary particle size of Al NPs, which formed large agglomerates, was 54.6 ± 25.1 nm including the shell thickness of 3 nm.

According to the obtained spectra of Al NPs films (AlI and AlII) with different initial optical densities before and after coating with PLL layers (Fig. 2, *b*), the absorption peak of Al NPs films, initially observed at approximately 230 nm, shifts towards longer wavelengths after the deposition of PLL layers, reaching approximately 300 nm.
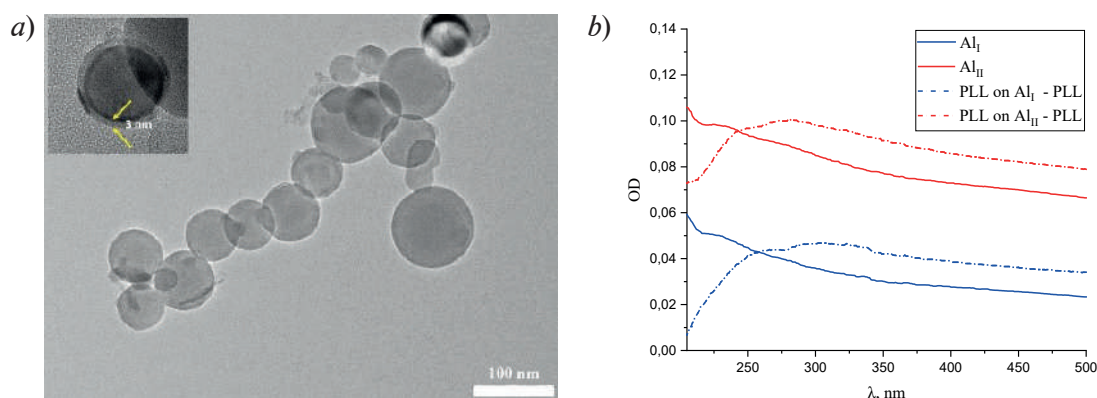
Fig. 2. TEM analysis of aluminum nanoparticles, synthesized by an electrical wire explosion method (*a*); Optical density spectra of Al NPs films before (solid lines) and after PLL modification (dashed lines) (*b*)

In contrast, no significant peak shift was observed when dextran was used as the polymer coating. This shift is attributed to the changes in the local refractive index and potential electronic interactions at the nanoparticle-polymer interface. Another group [8] presented that the absorption peak of oleate-modified iron oxide magnetite nanoparticles shifted from 255 nm to 267 nm after PLL adsorption onto OL-MNPs. This confirms that PLL coating significantly influences the UV plasmonic behavior of different metal nanoparticles that can be utilized for tuning their optical properties in UV region.

SEM images of the surface morphology for various nanostructures films of pure Al, pure ZnO, and ZnO applied on PLL deposited on Al films (ZnO/PLL/Al), presented in (Fig. 3, *a*). The Al film consists of aggregated nanoparticles forming uneven coverage on the substrate. The ZnO film exhibits large, poorly distributed clusters with weak surface adhesion. In contrast, the ZnO/PLL/Al nanostructure demonstrates a more uniform and continuous layer, indicating improved adhesion and surface compatibility using polymer PLL between ZnO and Al films.
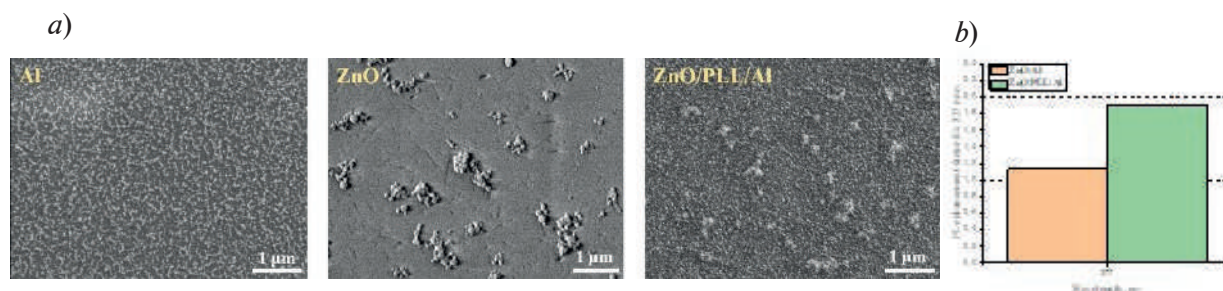
Fig. 3. SEM images of nanostructures films: pure Al, pure ZnO, and ZnO/PLL/Al (*a*); Photoluminescence enhancement factor of ZnO film in the presence of Al nanostructure with and without PLL film between them at an excitation wavelength of 325 nm (*b*)

The optical properties of various structures, including (PLL, Al, ZnO, ZnO/PLL, ZnO/Al, PLL/Al, and ZnO/PLL/Al), were examined to determine the effect of PLL film on PL enhancement of ZnO NPs emission in the presence of Al NPs. As shown in (Fig. 3, *b*), the ZnO film deposited on Al film (ZnO/Al) has provided PL enhancement factor of 1.13-fold at an emission wavelength of 377 nm, whereas applying PLL film between ZnO and Al films (ZnO/PLL/Al) increased the PL enhancement factor up to 1.9-fold. In another study [9], the researchers used PLL coating to achieve yield percentage of Au nanoplates up to 59%.

In summary, the obtained results indicate a positive role of polymer not only to modify the optical behaviors of metal nanoparticles but also to enhance the fluorescence and the electromagnetic interaction between fluorophore and metal nanoparticles to reach higher amplification of PL emission.

Conclusion

The influence of polymer coatings on the optical properties of Al nanostructures films in UV region was investigated. The obtained results showed that while dextran did not induce any noticeable spectral shifts, PLL caused a significant shift in the absorption peak of Al NPs films from 230 nm to 300 nm. Moreover, the ZnO/PLL/Al nanostructure demonstrated PL enhancement amplification up to 68% at an emission wavelength of 377 nm compared to ZnO/Al sample without PLL, at an excitation wavelength of 325 nm. These outcomes confirm the promising potential of polymer-modified aluminum nanostructures for plasmon-enhanced photoluminescence. Thus, polymer modification on plasmonic behavior of Al NPs will be a promising field to tune and achieve new properties of Al nanostructures for many metal-enhanced fluorescence applications and biosensing in the UV region.

REFERENCES

1. **Lizunova A.A., Malo D., Guzatov D.V., Vlasov I.S., Kameneva E.I., Shuklov I.A., Urazov M.N., Ramanenka A.A., Ivanov V.V.,** Plasmon-enhanced ultraviolet luminescence in colloid solutions and nanostructures based on aluminum and ZnO nanoparticles, Nanomaterials. 12 (22) (2022) 4051.

2. **Malo D., Lizunova A.A., Vershinina O.V., Filalova E.M., Ivanov V.V.,** Ultraviolet photoluminescence enhancement of zinc oxide nanocrystals in colloidal mixtures with spark discharge aluminum nanoparticles, St. Petersburg State Polytechnical University Journal: Physics and Mathematics. 16 (3.2) (2023) 261–266.

3. **Kameneva E.I., Lizunova A.A., Filalova E.M., Malo D., Kornyushin D.V., Ivanov V.V.,** Technology of manufacturing thin-film aluminum nanostructures by dry aerosol printing, St. Petersburg State Polytechnical University Journal: Physics and Mathematics. 16 (3.2) (2023) 282–287.

4. **Diez-Pascual A.M.,** Surface engineering of nanomaterials with polymers, biomolecules, and small ligands for nanomedicine, Materials. 15 (9) (2022) 3251.

5. **Petrila L.M., Bucatariu F., Mihai M., Teodosiu C.,** Polyelectrolyte multilayers: An overview on fabrication, properties, and biomedical and environmental applications, Materials. 14 (15) (2021) 4152.

6. **Stamatelatos A., Tsarmpopoulou M., Geralis D., Chronis A.G., Karoutsos V., Ntemogiannis D., Maratos D.M., Grammatikopoulos S., Sigalas M., Poulopoulos P.,** Interpretation of localized surface plasmonic resonances of gold nanoparticles covered by polymeric coatings, Photonics. 10 (4) (2023) 408.

7. **Tsarmpopoulou M., Ntemogiannis D., Stamatelatos A., Geralis D., Karoutsos V., Sigalas M., Poulopoulos P., Grammatikopoulos S.,** Silver nanoparticles' localized surface plasmon resonances emerged in polymeric environments: theory and experiment, Micro. 4 (2) (2024) 318–333.

8. **Antal I., Strbak O., Zavisova V., Vojtova J., Kubovcikova M., Jurikova A., Khmara I., Girman V., Džunda R., Kovaľ K., Konercka M.,** Development of positively charged poly-L-Lysine magnetic nanoparticles as potential MRI contrast agent, Nanomaterials. 13 (12) (2023) 1831.

9. **Morsin M., Nafisah S., Sanudin R., Razali N.L., Mahmud F., Soon C.F.,** The role of positively charge poly-L-lysine in the formation of high yield gold nanoplates on the surface for plasmonic sensing application, Plos one. 16 (11) (2021) e0259730.

THE AUTHORS

KOSTINA Dina E.
frolova.de@mipt.ru
ORCID: 0009-0000-7489-4391

MALO Dana
malo.d@mipt.ru
ORCID: 0000-0001-6310-9183

LIZUNOVA Anna A.
lizunova.aa@mipt.ru

KAMENEVA Ekaterina I.
katerinakamenev@yandex.ru
ORCID: 0009-0001-7234-8730

Optical studies of InGaAs/GaAs quantum well mesa structures passivated with sol-gel SiO$_2$

I.A. Melnichenko [1] ✉, T. Shugabaev [2, 3], V.O. Gridchin [3, 2], N.V. Kryzhanovskaya [1],

S.V. Balakirev [4], M.S. Solodovnik [4], A.E. Zhukov [1]

[1] National Research University Higher School of Economics, St. Petersburg branch, St. Petersburg, Russia;
[2] Institute for Analytical Instrumentation of the RAS, St. Petersburg, Russia;
[3] Alferov University, St. Petersburg, Russia;
[4] Southern Federal University, Taganrog, Russia

✉ imelnichenko@hse.ru

Abstract. A remarkable increase in photoluminescence intensity for passivated mesa structures with InGaAs/GaAs quantum wells were demonstrated using the method of sol-gel SiO$_2$ passivation. The photoluminescence signal enhancement up to 50 times for 1.25 μm diameter mesas after passivation was observed. The obtained results are promising for use in microlasers with active region based on InGaAs quantum wells.

Keywords: sol-gel passivation, InGaAs quantum well, photoluminescence

Оптические исследования меза-структур на основе квантовых ям InGaAs/GaAs с золь-гель пассивацией SiO$_2$

И.А. Мельниченко [1] ✉, Т. Шугабаев [2, 3], В.О. Гридчин [3, 2], Н.В. Крыжановская [1],

С.В. Балакирев [4], М.С. Солодовник [4], А.Е. Жуков [1]

[1] Национальный исследовательский университет «Высшая школа экономики», Санкт-Петербургский филиал, Санкт-Петербург, Россия;
[2] Институт аналитического приборостроения РАН, Санкт-Петербург, Россия;
[3] Академический университет им. Ж.И. Алфёрова РАН, Санкт-Петербург, Россия;
[4] Южный федеральный университет, г. Таганрог, Россия

✉ imelnichenko@hse.ru

Аннотация. Продемонстрировано значительное увеличение интенсивности фотолюминесценции для пассивированных SiO$_2$ методом золь-гель меза-структур с квантовой ямой InGaAs/GaAs. Наблюдалось усиление сигнала фотолюминесценции до 50 раз для мез диаметром 1,25 мкм после пассивации. Полученные результаты

перспективны для использования в микролазерах с активной областью на основе квантовых ям InGaAs.

Ключевые слова: золь-гель пассивация, квантовая яма InGaAs, фотолюминесценция

Introduction

Semiconductor materials based on GaAs are widely used in modern optoelectronic devices, solar cells, and communication due to their high electron mobility and direct bandgap structure. However, one of the critical challenges limiting the efficiency of GaAs-based devices is the high density of surface states, which leads to an increased surface recombination velocity on the order of 10^5-10^6 cm/s [1]. To minimize negative factors affecting the surface of devices, various approaches have been developed for passivating the surface of radiating devices, including thin film deposition using atomic layer deposition (ALD), plasma treatment, and surface nitridation, which significantly improve the optical characteristics of GaAs structures [2].

A new promising technique for passivating microstructures is the sol-gel SiO$_2$ passivation method, which is attractive due to its low-temperature deposition process and high efficiency [3, 4]. Notably, sol-gel-derived SiO$_2$ coatings provide uniform coverage with controllable thickness (10−100 nm), leading to a substantial enhancement in the photoluminescence intensity and carrier lifetime of InGaN nanostructures [4]. In this study, we investigate the impact of sol-gel SiO$_2$ passivation on the photoluminescence emission properties of InGaAs/GaAs quantum well (QW) structures, demonstrating its potential for enhancing the performance of semiconductor lasers.

Materials and Methods

The epitaxial structures were grown on a GaAs (001) substrate using molecular beam epitaxy. Sample №1 consists of a 250 nm-thick GaAs buffer layer. Followed by a 500 nm-thick Al$_{0.33}$Ga$_{0.67}$As barrier layer to confine carriers within the active region. The active region was grown in a 100 nm-thick GaAs layer and consisted of a single 10 nm-thick In$_{0.2}$Ga$_{0.8}$As QW. Finally, the structure was capped with a 100 nm-thick Al$_{0.33}$Ga$_{0.67}$As upper barrier and a 10 nm-thick GaAs layer to prevent oxidation.

In sample №2 a GaAs buffer layer was deposited, then a 50 nm thick Al$_{0.25}$Ga$_{0.75}$As layer was formed to prevent the leakage of charge carriers into the substrate. Then, a 200 nm thick GaAs layer was grown with a 10 nm-thick In$_{0.2}$Ga$_{0.8}$As QW layer placed in the middle, followed by 10 periods of superlattice (SL) consisting of GaAs/AlAs layers with thicknesses of 10 nm/10 nm. The structure was covered up with a 10 nm thick GaAs layer.

Microdisk mesas of various diameters from 1 to 20 μm were fabricated using photolithography and plasma etching for both structures. Samples №1 and №2 also differed in the density of the etched mesas: sample №1 had single mesostructure etched, while sample №2 had arrays of mesas etched in an area with a diameter of 20 μm.

The SiO$_2$ passivation shell was synthesized using the Stöber's method, which involves the hydrolysis and condensation of tetraethoxysilane in an ethanol-water-ammonia solution as follows. 2.1 mL of ethanol and 2.9 mL of deionized water were added to the sample, after which 0.012 g of the surfactant cetyltrimethylammonium bromide (CTAB) was introduced, which acts as growth centers for the SiO$_2$ gel structure and ensures the formation of SiO$_2$ gel on the entire microlaser surface. The resulting mixture was incubated for 5 min at room temperature. Then 25 μl of 20%

aqueous ammonia solution and 13 μl of TEOS were added. Then reaction mixture was maintained under stirring for 60 minutes. The thickness of the resulting SiO_2 layer strongly depends both on the reaction time and on the concentrations of reagents and estimated to be around 10 nm thick.

Photoluminescence (PL) spectra were measured using an Integra Spectra NT-MDT confocal microscope at room temperature. The excitation laser radiation (YAG:Nd 527 nm) was focused using a 20x objective (Mitutoyo, M Plan APO NIR) with numerical aperture NA = 0.4 into a spot up to approximately 5 μm in diameter with pump power density of 1 kW/cm². Detection was performed using a Sol Instruments MS5204i monochromator and a cooled CCD Si camera (Andor iVac).

Results and Discussion

The PL spectra of disk mesas in sample №1 were studied at room temperature before and after SiO_2 sol-gel passivation. Fig. 1, *a* shows PL spectra for mesa with 2 μm diameter. In the inset to Fig. 1, *a* there is a scanning electron microscope image of a single mesa with a diameter of 2 μm. The PL maximum in the range of 950−1000 nm characterizes the transition in a single $In_{0.2}Ga_{0.8}As/GaAs$ QW. The Fig. 1, *a* shows that the PL signal intensity for both GaAs and the $In_{0.2}Ga_{0.8}As/GaAs$ QW demonstrates strong enhancement after passivation. The maximum change in PL intensity for the ground-state transition of the $In_{0.2}Ga_{0.8}As/GaAs$ QW in a 2 and 3 μm mesa was approximately 8-fold (Fig. 1, *b*) after passivation. To compile comprehensive statistics, five mesas were examined for each diameter. An increase in PL intensity after passivation is observed across the entire range of studied mesas diameters. The significant spread of PL intensities for the 1 μm diameter mesa is due to etching defects in the mesa structures.

a)   *b)*
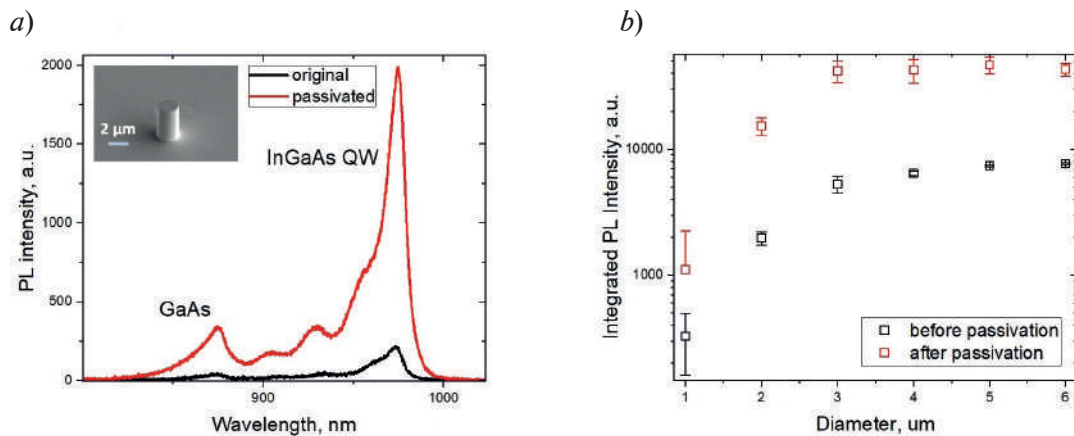
Fig. 1. PL spectra of 2 μm diameter mesa from sample №1 before and after passivation with sol-gel SiO_2 layer (*a*) integrated PL intensity for mesas of different diameter in 890−1000 nm wavelength range for structure №1 (*b*)

To verify the passivation effect and to investigate the influence of the mesa alignment further, sample №2 with a denser arrangement of mesa structures was also investigated. For sample №2, the pump laser illuminated the entire array of mesas with same diameter simultaneously. On insert to Fig. 2, *b* one can observe a scanning electron microscope image of an array of mesas with a diameter of 2 μm.

Fig. 2, *a* shows the PL spectra for an array of 1.25 μm diameter mesa structures before passivation and after passivation immediately and after 1 min of pump laser exposure. The spectra show an emission maximum associated with the GaAs/AlAs superlattice at 845 nm, GaAs at 870 nm, as well as line at 950−1000 nm characterizing the emission of $In_{0.2}Ga_{0.8}As/GaAs$ QW. Prolonged exposure to optical pumping on the surface of mesas leads to a gradual decrease in the PL signal of $In_{0.2}Ga_{0.8}As/GaAs$ QW. The observed photoluminescence decline within one minute (green spectra on Fig. 2, *a* can be related to the photopolymerization within the SiO_2 passivation layer structure under the action of optical pumping by the laser.

The PL intensity of the GaAs/AlAs superlattice also increases after SiO_2 passivation, but not as much as the QW signal (demonstrating a maximum signal amplification of 5 times for mesas with

a)

b)
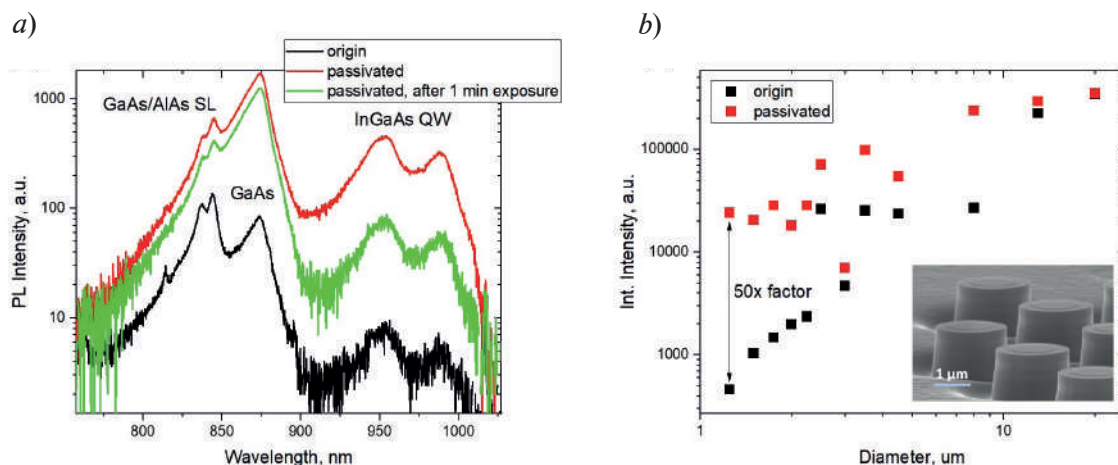
Fig. 2. PL spectra before and after passivation for sample №2 with 1.25 μm diameter mesas (*a*). Integrated PL intensity for different mesas diameter of sample №2 (*b*)

a diameter of 1.25 μm). The reason for much lower PL enhancement of SL signal may be that AlAs is much more sensitive to moisture and oxidation and can degrade or form unstable oxides that are not eliminated by passivation.

Fig. 2, *b* shows the integral PL intensity of the studied arrays of mesa structures of different diameters for sample №2. The greatest enhancement of the integral PL intensity is observed for mesostructures with a diameter of 1.25 μm. As the mesa's diameter increases, the contribution of nonradiative recombination to the PL signal decreases, leading to the most significant passivation effect being observed for small mesas with diameters of 1.25−3 μm in diameter. Thus, further mesas's diameter increment does not lead to enhancement of PL signal. This dependence also can be attributed to the diffusion length of charge carriers in InGaAs/GaAs quantum wells, which is on the order of 2−3 μm [5].

Conclusion

For the first time the effect of surface passivation of GaAs mesa structures with active region on the basis of InGaAs/GaAs QW using SiO_2 layer obtained by sol-gel method was investigated. Investigated PL intensity from the InGaAs/GaAs QW was significantly enhanced after SiO_2 passivation by sol-gel method. For sample №1 a maximum increase in the integrated intensity of 8 times was observed for the 2 and 3 μm diameter mesa structures. For sample №2 the maximum PL signal enhancement was 50 times for the diameter of 1.25 μm structures. The obtained results are promising for usage in microlasers with active region based on InGaAs/GaAs quantum wells.

REFERENCES

1. **Boroditsky M., Gontijo I., Jackson M., Vrijen R., Yablonovitch E., Krauss T., Cheng C.-C., Scherer A., Bhat R., Krames M.,** Surface recombination measurements on III−V candidate materials for nanostructure light-emitting diodes, Journal of Applied Physics. 87 (2000) 3497−3504.

2. **Theeuwes R.J., Kessels W.M.M., Macco B.,** Surface passivation approaches for silicon, germanium, and III−V semiconductors, Journal of Vacuum Science & Technology A. 42 (2024) 060801.

3. **Shen J., Chen H., He J., Li Y., Yang X., Zhu M., Yuan X.,** Enhanced surface passivation of GaAs nanostructures via an optimized SiO2 sol-gel shell growth, Applied Physics Letters. 124 (2024).

4. **Sheen M., Ko Y., Kim D., Kim J., Byun J., Choi Y., Ha J., Yeon K.Y., Kim D., Jung J.,** Highly efficient blue InGaN nanoscale light-emitting diodes, Nature. 608 (2022) 56−61

5. **Fiore A., Rossetti M., Alloing B., Paranthoen C., Chen J.X., Geelhaar L., Riechert H.,** Carrier diffusion in low-dimensional semiconductors: A comparison of quantum wells, disordered quantum wells, and quantum dots, Phys. Rev. B. 70 (2004) 205311.

THE AUTHORS

MELNICHENKO Ivan A.
imelnichenko@hse.ru
ORCID: 0000-0003-3542-6776

SHUGABAEV Talgat
talgashugabaev@mail.ru
ORCID: 0000-0002-4110-1647

GRIDCHIN Vladislav O.
gridchinvo@gmail.com
ORCID: 0000-0002-6522-3673

KRYZHANOVSKAYA Natalia V.
nkryzhanovskaya@hse.ru
ORCID: 0000-0002-4945-9803

BALAKIREV Sergey V.
sbalakirev@sfedu.ru
ORCID: 0000-0003-2566-7840

SOLODOVNIK Maxim S.
solodovnikms@mail.ru
ORCID: 0000-0002-0557-5909

ZHUKOV Alexey E.
zhukale@gmail.com
ORCID: 0000-0002-4579-0718

PHYSICAL MATERIALS TECHNOLOGY

Development of heterogeneous bioinks with microgels for creating 3D tissue engineering models for drug screening

A.A. Tiushkevich [1] ✉, P.S. Pleshakov [1], N.A. Filatov [1], A.S. Bukatin [1]

[1] Alferov University, St. Petersburg, Russia

✉ ternet121@gmail.com

Abstract. To achieve clinical relevance, tissue-engineered constructs should replicate the metabolic activity and vasculature of native tissues and organs. Currently, conventional bioinks struggle to mimic the structural complexity of human tissues. Adding microgels with living cells into bioinks enables precise control over structural and functional complexity, offering a scalable platform for regenerative therapies and drug testing. The study introduces a heterogeneous bioink with microgels designed to bioprint tissue engineering constructs with complex architecture. To do this, we optimized the 1.5 % wt. alginate bioink composition adding Pluronic F-127 10 % wt. together with 3.75 % wt. gelatin microgels, fabricated via droplet microfluidics. An extrusion bioprinter was used to print test structures using this compound. As a result, it was possible to outline the first steps toward an effective protocol for creating tissue-engineered constructs from the multicomponent hydrogel solution with CT-26 eGFP cell viability up to 95% for the 10th cultivation day.

Keywords: tissue engineering, hydrogel microparticles, microgels, droplet microfluidics, 3D bioprinting

Разработка гетерогенных биочернил с микрогелями для создания тканевых моделей методом 3D печати для тестирования лекарственных препаратов

А.А. Тюшкевич [1] ✉, П.С. Плешаков [1], Н.А. Филатов [1], А.С. Букатин [1]

[1] Академический университет им. Ж.И. Алфёрова РАН, Санкт-Петербург, Россия

✉ ternet121@gmail.com

Аннотация. В настоящее время технология тканевой инженерии не позволяет воссоздавать сложную структуру тканей и органов человека. Добавление микрогелей, представляющих собой гидрогелевые микрочастицы диаметром от 10 до 500 мкм с клетками, в раствор биочернил позволяет задавать расположение клеток в получаемых тканеинженерных конструкциях. Такие структуры в дальнейшем могут использоваться в качестве масштабируемых моделей для регенеративной терапии и тестирования лекарств. Состав гетерогенных биочернил представлял собой 1,5% wt. раствора

альгината с добавлением 10% wt. PluronicTM F-127 и желатиновых микрогелей диаметром 120 мкм, изготовленных методом капельной микрофлюидики. Для печати тестовых структур использовался экструзионный биопринтер. В результате удалось получить тканеинженерные конструкции из двухкомпонентного гидрогелевого раствора с жизнеспособностью клеток CT26 eGFP до 95% на 10-й день культивирования.

Ключевые слова: тканевая инженерия, гидрогелевые микрочастицы, микрогели, капельная микрофлюидика, 3D биопечать

Introduction

To be used in clinical practice, tissue engineering constructs must replicate cellular metabolic activity and have a vascular system that mimics human tissues and organs. Currently, bioprinting methods that use conventional homogeneous bioink solutions challenge imitating the structural complexity of natural tissues [1]. Adding microgels with living cells to such solutions allows precise control of the structural and functional features of the selected tissue while offering a scalable model for the course of diseases and drug testing for cytotoxicity [2]. The aim of this study is to develop tissue engineering models made of composite bioinks based on hydrogel solution with hydrogel microparticles and encapsulated living cells, synthesised by droplet microfluidics, for drug testing applications.

Materials and Methods

Microfluidic Device Fabrication. A soft lithography approach was employed to fabricate microfluidic devices from polydimethylsiloxane (PDMS, Sylgard 184, Dow Silicones, Midland, MI, USA) [3−4]. The mold was produced using a two-step contact photolithography process through a chromium mask on a silicon wafer coated with SU-8 2025 photoresist layers (Kayaku Advanced Materials, Westborough, MA, USA). The PDMS mixture, comprising prepolymer and curing agent in a 10:1 weight ratio, was thoroughly mixed, degassed, and subsequently put onto the mold. Following a 4-hour curing process in an oven at 65 °C, the PDMS replica was detached from the mold and sectioned into individual devices. Inlet and outlet interfaces were made via a 2 mm biopsy puncher. Oxygen plasma treatment was used to bond the PDMS replica with a standard glass slide. A rain-repellent treatment (Aquapel, USA) was used to create a hydrophobic coating on the inner walls of the microchannels achieving a contact angle of ~ 100°.

Microgel Synthesis. To prepare hydrogel microparticles (microgels) with living cells we used a microfluidic device with a flow-focusing "water-in-oil" droplet generator. A dispersed and continuous phase of liquids were injected into the microfluidic device under constant pressures using a custom microfluidic pressure controller [5]. As a dispersed phase we used 0.8 ml of 5 % wt. gelatin solution (Bovine gelatin, Sigma-Aldrich, CAS Number 9000-70-8) and mixed it with a 0.2 ml mice colon adenocarcinoma with enhanced green fluorescent protein (CT26 eGFP) cell solution with final cell concentration from 4 to 5 million cells per 1 ml. Roswell Park Memorial Institute (RPMI) 1640 growth cell medium with 10% vol of fetal bovine serum (FBS) was used for cell cultivation, which facilitated cell proliferation and tissue model development. As a continuous phase for microgel generation we used fluorinated oil (HFE-7500, CAS Number 297730-93-9) with 1 % wt. nonionic surfactant (FluoSurf-C™, Emulseo, France).

Bioink Preparation. A detailed scheme of heterogeneous bioink fabrication is shown in Figure 1. The whole process can be divided into four stages: microgel synthesis, microgel

selection, solutions mixing and extrusion bioprinting. Initially we synthesized the monodispersed microgels with diameter from 120 ± 5 um in the microfluidic device. Subsequently, the acquired microparticles were transferred from oil to cell media and concentrated via centrifugation to achieve a dense suspension of microgels. After that, we mechanically mixed this suspension with the homogeneous bulk bioink solution in a ratio of 1:1 in a 5 ml tube placed in an icebox. The bulk solution consisted of alginate 3% w/v, Pluronic™ F-127 20% w/v, D-mannitol 4.65 w/v and FBS 3% vol and was prepared by so-called "cold method", presented elsewhere [6]. The resulting heterogeneous solution was loaded into 1 ml syringe and inserted into the customized 3D bioprinter.

3D bioprinting. Direct-write deposition of the bioink solution was performed using a custom extrusion 3D bioprinter. The bioink mixture was loaded into a 1 ml syringe with 0.41 ID blunt end dispensing tip. The syringe was inserted into the printing head and connected to a E-axed motorized stage for the extrusion to the sterile 12-well cell plate (Fig. 1, *c*) with a relative speed between the nozzle and X-Y table of 1.3 mm. s⁻¹.

To prepare computer-aided designed (CAD) models for bioprinting we used custom scripts written in Python and the Slic3r program. Printing commands were transmitted to the printer as a G-code through the Repetier-Host program. A test model was a 10 mm long and 0.3 mm high square lattice (Fig. 1, *d*). The distance between the neighboring extruding fibers was in the range from 1 to 1.7 mm. After bioprinting, the lattice was exposed to 0.2 % wt. $CaCl_2$ within 2 minutes for alginate cross-linking. Thereafter, the cross-linked structures were filled with cell culture medium and placed in a CO_2 incubator for further cell development. The cell structures were analyzed using a Zeiss Axio Observer Z1 spinning disk confocal microscope. Dead and damaged cells were stained with 1 mM propidium iodide (red). Live CT26 eGFP cells expressed green fluorescent protein (green).
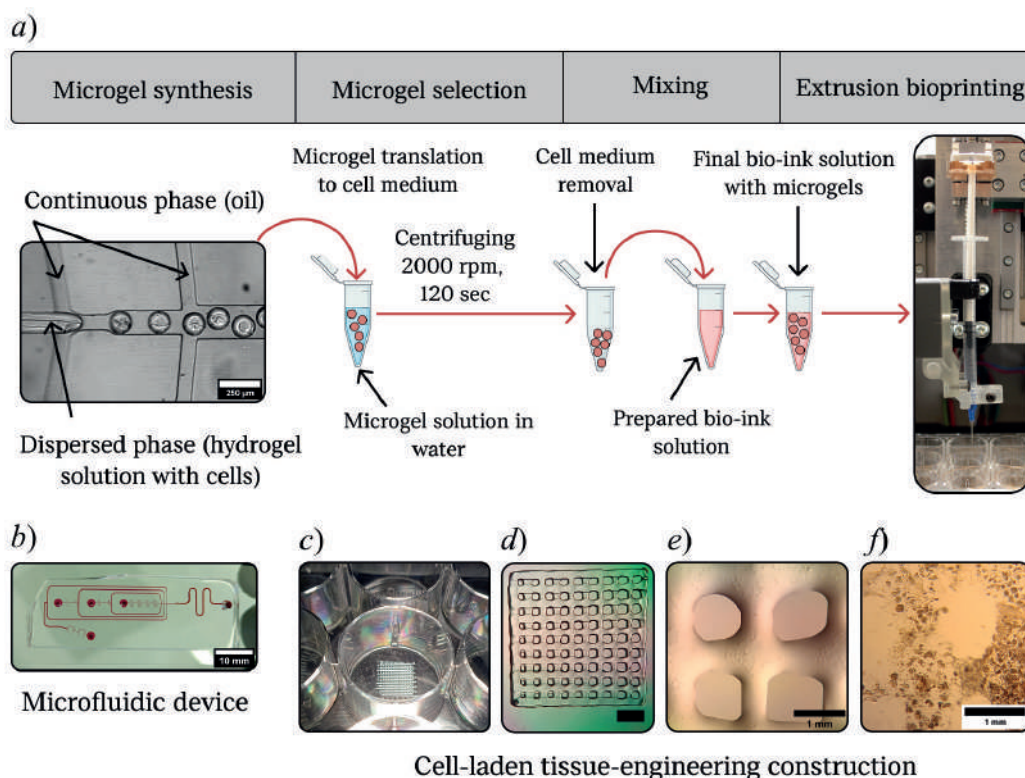
Fig. 1. Bioprinting using a heterogeneous bioink solution. Preparation scheme of heterogeneous bioink solution with microgels incorporation (*a*); top view of a microfluidic PDMS device used for generation microgels with living cells (*b*); a well of 12-well cell plate with a 3D printed model (*c*); an optical image of the 3D printed model (the scale bar is 2 mm) (*d*); an enlarged image of the 3D printed model with gelatin microgels and living cells directly after fabrication (*e*); an optical image of the 3D printed model after 10 days of cultivation (*f*)

Results and Discussion

Initially, we printed the test models using a homogeneous bioink solution of alginate/Pluronic™ F-127 with CT26 eGFP cells, which are shown in Fig. 2, *a*. In the obtained structures the cells evolved separately, increasing in size and forming spheroids during cultivation. The viability of the cells in the first 7 days of cultivation was below 85% increasing above 95% by day 12 (Fig. 2, *b*), which showed that a significant amount of cells was damaged during the bioprinting. After that, we printed the 3D lattice structure using a heterogeneous bioink solution where CT26-eGFP cells were encapsulated in gelatin microgels (Fig. 2, *c*). The presence of gelatin microgels reduces the viscosity of the final solution and thus affects the spatial resolution of the final structure. Therefore, we set a distance of 1.6 mm between the nearest parallel lines in the test lattice model. As a result, the width of each filament line in the printed model was 0.6 ± 1 mm. In this case the cell's viability exceeded 90% after printing and increased up to 95% by day 10 (Fig. 2, *d*). Moreover, on the 5th day of cultivation, the number of cells increased, and they were spread along the inner microgel surface (Fig 2, *c*(ii)). On the 10th day of cultivation, the cells were intended to fill the entire volume of microgels (Fig 2, *c*(iii)). In both cases the cells kept growing inside the lattice and did not transfer to the surface of the microwell plate. Such behavior indicates that the cells have high adhesion to the alginate surface.
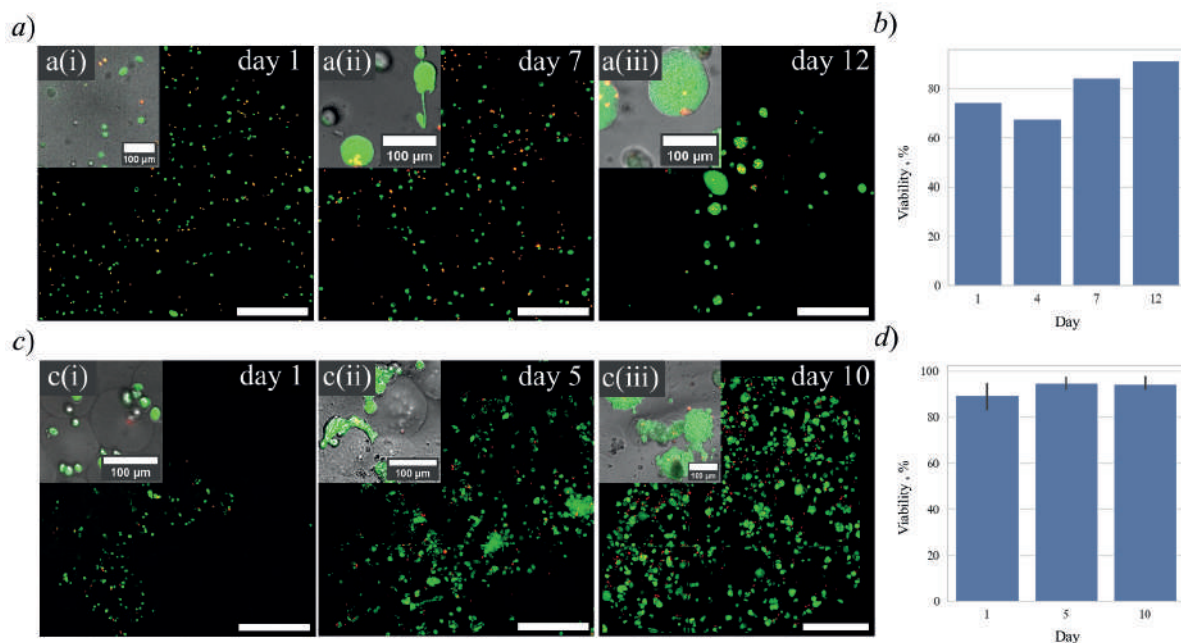
Fig. 2. Viability of CT26-eGFP cells inside 3D printed test lattices: confocal fluorescent images of a test lattice printed from the homogeneous solution of alginate/Pluronic F-127 with CT26 eGFP cells during in vitro cultivation (the scale bar is 500 um) (*a*); the CT26 eGFP cells viability in the lattice made from homogeneous bioink (*b*); confocal fluorescent images of a test lattice printed with heterogeneous solution of alginate/Pluronic™ F-127 with CT26 eGFP cell-laden gelatin microgels during in vitro cultivation (the scale bar is 500 um) (*c*); the CT26 eGFP cells viability in the lattice made from heterogeneous bioink with gelatin microgels (n = 3 experiments). The inserts show representative enlarged merged bright field and confocal images of test structures (the scale bar is 100 μm) (*d*)

Conclusion

Here we presented 3D printed tissue engineering models consisting of a heterogeneous bioink solution with monodisperse gelatin microgels that contain CT26 eGFP cells. The microgels were synthesized in a microfluidic flow-focusing "water-in-oil" droplet generator. Their diameter was 120 μm, which showed to be enough for encapsulation of several cells and their development inside. Careful mixing of dense suspension of microgels with the bulk hydrogel solution allowed to obtain a heterogeneous bioink with uniform distribution of microgels. Extrusion of the obtained bioink via a custom 3D bioprinter allowed us to achieve a test lattice with an average extruding

fiber width of 0.6 ± 0.1 mm. According to the optical images, the distribution of microgels in the printed lattice was uniform along the whole structure. The cells inside gelatine microgels in printed lattices had the total viability up to 95% by the fifth day of incubation, whereas the cells inside a lattice printed from homogeneous bioink solution demonstrated a viability rate below 80% by the seventh day of incubation. This shows that encapsulation of cells into gelatin microgels can protect them from the large shear rate in the nozzle during the bioprinting process. Moreover, in the lattice with microgels the cells have better proliferation activity and form a 3D construct with higher cell density during 10 days of incubation. We believe that the obtained 3D cell structures are promising to be used as models for drug cytotoxicity testing.

REFERENCES

1. **Fang Y., Guo Y., Liu T., Xu R., Mao S., Mo X., ... & Sun W.,** Advances in 3D bioprinting, Chinese Journal of Mechanical Engineering: Additive Manufacturing Frontiers. 1 (1) (2022) 100011.

2. **Daly A.C., Riley L., Segura T., Burdick J.A.,** Hydrogel microparticles for biomedical applications, Nature Reviews Materials. 5 (1) (2020) 20–43.

3. **Bukatin A.S., Mukhin I.S., Malyshev E.I., Kukhtevich I.V., Evstrapov A.A., Dubina M.V.,** Fabrication of high-aspect-ratio microstructures in polymer microfluid chips for in vitro single-cell analysis, Technical Physics. 61 (2016) 1566–1571.

4. **Qin D., Xia Y., Whitesides G.M.,** Soft lithography for micro-and nanoscale patterning, Nature protocols. 5 (3) (2010) 491.

5. **Filatov N.A., Denisov I.A., Evstrapov A.A., Bukatin A.S.,** Open-source pressure controller based on compact electro-pneumatic regulators for droplet microfluidics applications, IEEE Transactions on Instrumentation and Measurement. 71 (2022) 1–10.

6. **Gori M., Giannitelli S.M., Torre M., Mozetic P., Abbruzzese F., Trombetta M., ... & Rainer A.,** Biofabrication of hepatic constructs by 3D bioprinting of a cell-laden thermogel: An effective tool to assess drug-induced hepatotoxic response, Advanced Healthcare Materials. 9 (21) (2020) 2001163.

THE AUTHORS

TIUSHKEVICH Andrei A.
ternet121@gmail.com

PLESHAKOV Pavel S.
avekipp@gmail.com
ORCID: 0009-0005-9354-4297

FILATOV Nilita A.
nikita.filatov@inbox.ru
ORCID: 0000-0003-0111-6542

BUKATIN Anton S.
antbuk.fiztek@gmail.com
ORCID: 0000-0002-5459-1438

Structural and optical properties of InP layers obtained by plasma-enhanced atomic layer deposition at different temperatures

A.V. Uvarov [1] ✉, A.I. Baranov [1], A.A. Maksimova [1], E.A. Vyacheslavova [1],

V.A. Pozdeev [1], O.P. Mikhaylov [2], E.V. Nikitina [1], A.S. Gudovskikh [1]

[1] Alferov University, St. Petersburg, Russia;

[2] St. Petersburg Electrotechnical University "LETI", St. Petersburg, Russia

✉ lumenlight@mail.ru

Abstract. Plasma-enhanced atomic layer deposition (PE-ALD) was employed to deposit indium phosphide (InP) thin films on silicon substrates at temperatures ranging from 250 °C to 380 °C. Using trimethylindium and phosphine as precursors, the influence of deposition temperature on film growth rate, structural, and optical properties was investigated. A stable growth per cycle (GPC) was observed within the 250−350 °C range, indicating self-limiting ALD behavior, while an increase in GPC at 380 °C suggested onset of non-ideal growth mechanisms. Raman spectroscopy revealed improved crystallinity with increasing temperature, demonstrated by intensified longitudinal optical phonon peaks. Photoluminescence measurements showed near-band-edge emission around 1.36−1.39 eV, with a blue shift and narrowing of the emission peak at higher temperatures, indicating enhanced optical quality and reduced defect density.

Keywords: indium phosphide, atomic layer deposition, plasma, silicon, raman spectroscopy, photoluminescence

Citation: Uvarov A.V., Baranov A.I., Maksimova A.A., Vyacheslavova E.A., Pozdeev V.A., Mikhaylov O.P., Nikitina E.V., Gudovskikh A.S., Structural and optical properties of InP layers obtained by plasma-enhanced atomic layer deposition at different temperatures, St. Petersburg State Polytechnical University Journal. Physics and Mathematics. 18 (3.1) (2025) 247−251. DOI: https://doi.org/10.18721/JPM.183.149

Структурные и оптические свойства слоев InP, полученных методом плазмохимического атомно-слоевого осаждения при различных температурах

А.В. Уваров [1] ✉, А.И. Баранов [1], А.А. Максимова [1], Е.А. Вячеславова [1],

В.А. Поздеев [1], О.П. Михайлов [2], Е.В. Никитина [1], А.С. Гудовских [1]

[1] Академический университет им. Ж.И. Алфёрова РАН, Санкт-Петербург, Россия;

[2] Санкт-Петербургский государственный электротехнический университет «ЛЭТИ» им. В.И. Ульянова (Ленина), Санкт-Петербург, Россия

✉ lumenlight@mail.ru

Аннотация. Метод плазмохимического атомно-слоевого осаждения, (PE-ALD), использован для осаждения фосфида индия (InP) на кремниевые подложки при

температурах от 250 до 380 ˚C. Изучено влияние температуры осаждения на скорость роста, структуру и оптические свойства пленок. Повышение температуры приводит к улучшению кристалличности и качеству фотолюминесценции, что указывает на снижение плотности дефектов.

Ключевые слова: фосфид индия, атомно-слоевое осаждение, плазма, кремний, спектроскопия комбинационного рассеяния, фотолюминесценция

Introduction

Deposition of functional materials by the method of plasma-enhanced atomic layer deposition (PE-ALD) has gained increasing popularity in recent years. The number of different precursors, as well as the number of materials available for this method, continues to grow [1]. One such material is indium phosphide (InP), an AIII-BV semiconductor with a direct band gap of 1.34 eV, making it highly useful for optoelectronic devices such as laser diodes and photonic integrated circuits in the optical telecommunications industry. Atomic layer deposition (ALD) is a critical technique for achieving precise, conformal, and uniform thin-film growth at the atomic scale. PE-ALD further enhances this capability by enabling low-temperature processing and improved film quality, which is essential for temperature-sensitive substrates and advanced semiconductor applications. PE-ALD of InP presents a potential solution by enabling low-temperature, conformal growth, which could facilitate the monolithic integration of InP-based optoelectronics with silicon platforms, opening new possibilities for advanced photonic and electronic systems [2]. This work investigates the PE-ALD of InP using trimethylindium and phosphine as precursors, focusing on the influence of deposition temperature on the structural and optical properties of the resulting films. The findings are aimed at advancing the integration of III−V/Si heterostructures for future photonic and electronic applications.

Materials and Methods

Indium phosphide thin films were deposited on (100)-oriented n-type silicon wafers (double-side polished, 5−10 Ω·cm) using a plasma-enhanced atomic layer deposition (PE-ALD) process. Prior to deposition, the substrates were cleaned in a 10% aqueous hydrofluoric acid (HF) solution to remove the native oxide layer. The deposition process were carried out in an Oxford Instruments Plasmalab 100 PECVD system equipped with a 13.56 MHz capacitive-coupled RF direct plasma source. Trimethylindium (TMI) and phosphine (PH_3), both diluted in hydrogen, were used as the indium and phosphorus precursors, respectively, while high-purity argon served as the purge gas. The plasma was ignited during the PH_3 pulse only, with an RF power of 200 W (power density 440 mW/cm^2). The precursor pulse and purge times were optimized to ensure self-limiting surface reactions and avoid parasitic CVD effects. The deposition sequence are summarized in Table.

In all experiments, the number of ALD cycles was fixed at 400. The substrate temperature was varied between 250 ˚C and 380 ˚C to study its effect on the film's growth rate and structural quality. Film thicknesses were measured using a Zeiss Supra 25 scanning electron microscope (SEM). Raman spectroscopy was performed using an Enspectr R532 system equipped with a 532 nm excitation laser to assess the crystallinity of the deposited layers. Photoluminescence (PL) measurements were carried out at room temperature using an Accent RPM Sigma system with an excitation wavelength of 798 nm to evaluate the optical quality of the InP films.

Process parameters

Step	Indium deposition	Purge	Phosphorus deposition	Purge
Precursor	TMI/H$_2$	Ar	PH$_3$/H$_2$	Ar
Pulse time, s	5	10	3	10
Dose, nmol/cm^2	50		2	
Pressure, mTorr	350	0	350	0
RF power, W	0	0	200	0

Results and Discussion

The structural and optical properties of InP thin films deposited by PE-ALD were investigated across a substrate temperature range from 250 °C to 380 °C. In all experiments, the number of ALD cycles was fixed at 400, resulting in film thicknesses ranging from 26.0 to 43.7 nm depending on the growth per cycle (GPC) at each temperature.
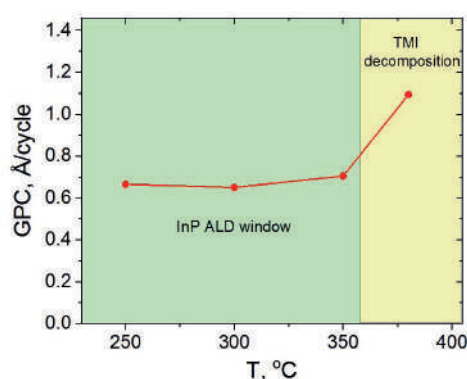
Fig. 1. GPC of InP at PE-ALD process as a function of deposition temperature

These results indicate a relatively stable growth rate in the 250−350 °C range, suggesting operation within the ALD saturation window. The pronounced increase in GPC at 380 °C is likely due to enhanced surface reactivity or partial onset of non-self-limiting reactions at elevated temperature. At these temperatures, partial decomposition of TMI may also occur, leading to an increased growth rate due to monolayer densification and reduced steric hindrance. Figure 2, *a* presents Raman spectra of the InP films deposited at different temperatures. A pronounced longitudinal optical (LO) phonon peak near 345 cm^{-1} is observed for all samples, with increasing intensity at higher temperatures, indicating improved crystallinity. In contrast, broader spectral features and reduced LO intensity at lower temperatures suggest higher structural disorder [3].

Room-temperature photoluminescence (PL) spectra (Fig. 2, *b*), measured using an Accent RPM Sigma system with 798 nm excitation, revealed a strong near-band-edge (NBE) emission in the range of 893−890 nm (corresponding to 1.388−1.393 eV), which is close to the fundamental bandgap of bulk InP. A slight blue shift of the emission peak with increasing deposition temperature − from 893 nm at 250−300 °C to 890 nm at 380 °C − may be attributed to quantum confinement effects in nanocrystalline grains or internal strain in the film [4, 5]. In addition to peak position, the full width at half maximum (FWHM) of the PL signal exhibited a strong temperature dependence, decreasing from 35 nm at 250 °C to 23.2 nm at 350 °C. The narrowing of the emission band indicates an improvement in structural and electronic uniformity, with a reduction in defect-related localized states and nonradiative recombination centers [6, 7]. A slight broadening at 380 °C (FWHM = 24.5 nm) may result from increased surface roughness or grain coalescence at elevated temperatures. These PL results are in good agreement with the Raman data and confirm the superior optical quality of films grown at higher temperatures.
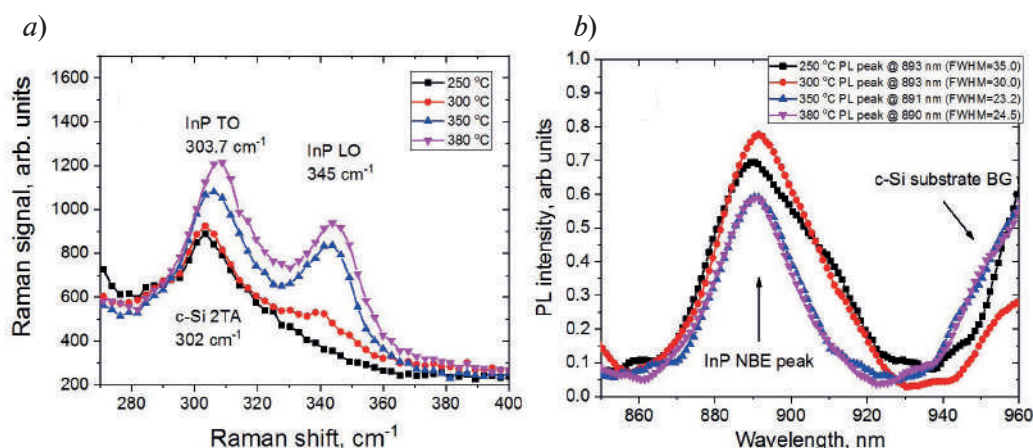
Fig. 2. Raman spectra of PE-ALD InP films deposited at 250 °C − 380 °C (*a*). Room-temperature photoluminescence spectra of InP films (*b*)

Conclusion

Indium phosphide thin films were successfully deposited on silicon substrates using plasma-enhanced atomic layer deposition (PE-ALD) at temperatures ranging from 250 °C to 380 °C. A consistent ALD growth regime was observed at lower temperatures (250−350 °C), with a significant increase in GPC at 380 °C, reaching 1.09 Å/cycle. Structural characterization via Raman spectroscopy confirmed that higher deposition temperatures resulted in improved crystallinity, as evidenced by the intensified LO phonon peak. Photoluminescence analysis revealed near-band-edge emission centered around 1.36−1.39 eV, with a slight blue shift and pronounced narrowing of the emission peak at higher growth temperatures. This behavior suggests enhanced optical quality due to reduced defect density and improved electronic uniformity. These findings demonstrate that PE-ALD enables the low-temperature growth of high-quality InP thin films on silicon, making it a promising method for the monolithic integration of III−V optoelectronic components with Si-based platforms.

Acknowledgments

REFERENCES

1. **Hagen D.J., Pemble M.E., Karppinen M.,** Plasma-enhanced atomic layer deposition of functional materials: progress and prospects, Applied Physics Reviews. 6 (4) (2019) 041309.

2. **Maksimova A.A., Uvarov A.V., Kirilenko D.A., Baranov A.I., Vyacheslavova E.A., Gudovskikh A.S.,** Low-temperature PEALD growth of InP films on silicon substrates, St. Petersburg State Polytechnical University Journal: Physics and Mathematics. 15 (3.3) (2022) 123−127.

3. **Cuscó R., Ibáñez J., Blanco N., González-Díaz G., Artús L.,** Raman scattering in ion-implanted InP, Nuclear Instruments and Methods in Physics Research Section B: Beam Interactions with Materials and Atoms. 132 (4) (1997) 627−632.

4. **Gudiksen M.S., Wang J., Lieber C.M.,** Synthetic control of the diameter and length of single crystal semiconductor nanowires, Journal of Physical Chemistry B. 106 (16) (2002) 4036−4039.

5. **Fryauf D.M., Zhang J., Norris K.J., Diaz Leon J.J., Oye M.M., Wei M., Kobayashi N.P.,** Enhancement of photoluminescence in indium phosphide nanocrystals grown by atomic layer deposition, Physica Status Solidi (RRL) − Rapid Research Letters. 8 (7) (2014) 663−667.

6. **Ubbink M., Reiss P.,** Near-unity photoluminescence quantum yield of core-only InP quantum dots via InF_3 passivation, ACS Nano. 14 (10) (2020) 13409−13417.

7. **Wang Z., Zhang Y., Zhang X., Wang Y., Li X.,** Green InP quantum dots with high brightness and narrow emission through layer-by-layer modification with aluminum, ACS Applied Nano Materials. 6 (9) (2023) 6421−6429.

THE AUTHORS

UVAROV Alexander V.
lumenlight@mail.ru
ORCID: 0000-0002-0061-6687

BARANOV Artem I.
itiomchik@yandex.ru
ORCID:0000-0002-4894-6503

MAKSIMOVA Alina A.
deer.blackgreen@yandex.ru
ORCID: 0000-0002-3503-7458

VYACHESLAVOVA Ekaterina A.
cate.viacheslavova@yandex.ru
ORCID:0000-0001-6869-1213

MIKHAYLOV Oleg P.
oleg.mikhaylov.00@gmail.com
ORCID: 0009-0005-6836-4091

POZDEEV Vyacheslav A.
pozdeev99va@gmail.com
ORCID: 0009-0009-4023-6185

NIKITINA Ekaterina V.
mail.nikitina@mail.ru
ORCID: 0000-0002-6800-9218

GUDOVSKIKH Alexander S.
gudovskikh@spbau.ru
ORCID: 0000-0002-7632-3194

Morphological features of CVD-grown Si nanostructures in meso- and macroporous silicas

D.A. Eurov [1] ✉, V.G. Golubev [1], S.A. Grudinkin [1], D.A. Kurdyukov [1],

D.A. Kirilenko [1], A.A. Yakovleva [1], E.Yu. Stovpiaga [1]

[1] Ioffe Institute, St. Petersburg, Russia

✉ post@mail.ioffe.ru

Abstract. Morphology of silicon nanostructures obtained by thermal chemical vapour deposition (CVD) method in mesoporous silica particles (mSiO$_2$) and macroporous synthetic opal were studied. The proposed method allows obtaining a uniform Si layer on the surface of non-porous spherical silica particles forming macropores in opal, in contrary, to complete filling of 3-nm pores inside mesoporous particles with amorphous silicon. The thermal CVD provides for gradual change of pore filling which, in turn, leads to step-to-step variation of porosity characteristics in the case of mSiO$_2$/Si and the modification of photonic crystal properties in the case of opal-Si.

Keywords: spherical particles, silicon, nanostructures, silica, mesopores, opal

Особенности морфологии Si наноструктур, выращенных в мезо- и макропористых кремнеземах методом CVD

Д.А. Еуров [1] ✉, В.Г. Голубев [1], С.А. Грудинкин [1], Д.А. Курдюков [1],

Д.А. Кириленко [1], А.А. Яковлева [1], Е.Ю. Стовпяга [1]

[1] Физико-технический институт им. А.Ф. Иоффе РАН, Санкт-Петербург, Россия

✉ post@mail.ioffe.ru

Аннотация. Изучена морфология кремниевых наноструктур, получаемых методом термического газофазного осаждения, внутри частиц мезопористого кремнезема (mSiO$_2$) и коллоидного кристалла − макропористого синтетического опала. Предложенный метод позволяет получить однородный слой Si на поверхности непористых сферических частиц кремнезема, образующих макропоры в опале, тогда как 3-нм поры внутри мезопористых частиц полностью заполняются аморфным кремнием. Применяемый технологический подход обеспечивает постепенное изменение степени заполнения пор, в свою очередь, определяющее ступенчатое изменение характеристик пористости mSiO$_2$/Si и модификацию фотонно-кристаллических свойств композита опал-Si.

Introduction

There has been rapidly increasing interest in design and synthesis of silicon-based nanostructured materials for photonics, photovoltaics and bioapplications [1, 2]. Silicon nanocrystals, nanowires and photonic crystals are key examples of functional nanostructures with properties determined by their morphology [1, 2]. One of the ways to tailor the morphology of nanostructures is the use of porous template approach [3, 4]. The pore size and shape of the template are the main characteristics which determine the morphological features and thus the structural parameters of the silicon nanostructures formed. The goal of this work was to study the difference in morphology of silicon nanostructures grown by thermal chemical vapor deposition (CVD) method in two kind of silica templates: mesoporous particles and macroporous synthetic opals. The variation of porosity characteristics and the modification of opal-Si photonic crystal properties were demonstrated.

Materials and Methods

Materials. We used the following reagents: cetyltrimethylammonium bromide (CTAB, $C_{16}H_{33}N(CH_3)_3Br$), 99.99% (Acros Organics); aqueous ammonia (NH_3), 24 wt%; ethanol (C_2H_5OH), 95.7 vol%; deionized water (H_2O) with a resistance of 10 MΩ; tetraethoxysilane (TEOS, $Si(OC_2H_5)_4$), 99.9% (Acros Organics); monosilane (SiH_4), electronic grade (Sigma-Aldrich); argon (Ar), 99.998% (Sigma-Aldrich). All the chemicals were of analytical purity grade commercially available. There was no need to additionally purify the reagents.

Methods. The silica particles, opals and SiO_2/Si composites were obtained based on our previously developed methods. In particular, the procedure for the synthesis of non-porous spherical silica particles ($nSiO_2$) with a diameter of 740 ± 30 was similar to that employed in [5, 6] via hydrolysis of TEOS in a mixture $NH_3-H_2O-C_2H_5OH$. Spherical mesoporous silica particles ($mSiO_2$) with a diameter of 385 ± 20 nm and a pore diameter of 3.1 ± 0.15 nm were synthesized according to the method developed by us via basic hydrolysis of TEOS in $NH_3-H_2O-C_2H_5OH-$ CTAB mixture [7, 8]. The opal films were grown from close-packed $nSiO_2$ particles on substrates made from optically polished microscope glass by using the vertical deposition technique as described in [9, 10]. The volume available for filling was up to 26% of the total opal volume, and the interparticle macropore size was 100–300 nm. For the synthesis of silicon within the pores of opal and $mSiO_2$ particles we used the modified method of monosilane thermal decomposition at 450 °C during 0–60 h [11, 12].

Transmission electron microscopic (TEM) measurements were performed using a Jeol JEM-2100F microscope (accelerating voltage 200 kV, point-to-point resolution 0.19 nm) equipped with Bruker XFlash 6T-30 energy dispersive X-ray (EDX) spectrometer. The nitrogen adsorption was performed using a Micromeritics 3FLEX at a temperature of 77 K. The specific surface area was calculated by the Brunauer – Emmett – Teller (BET) method, and the pore size distribution was found using the nonlocal density functional theory (NLDFT). The optical transmission spectra were measured by a Bruker IFS 113v Fourier spectrometer in the near infrared region. The spectra were registered by using a cooled InSb detector and a halogen lamp as a light source. The spectral resolution was 4 cm^{-1}. The incident light was focused onto the sample within the solid angle of 10°.

Results and Discussion

We used different porous silicas, namely, spherical $mSiO_2$ particles with 3-nm cylindrical mesopores and silica colloidal crystals (synthetic opals) with interparticle macropore size of $100-300$ nm. The thermal destruction of SiH_4 occurs uniformly within the whole pore volume of the templates because in the thermal CVD method we developed, the limiting stage of the process in which pores are filled with silicon is the reaction in which monosilane is decomposed, rather than its diffusion within template pores [11, 12]. According to X-ray diffraction and Raman measurements, silicon formed in the macro- and mesopores is amorphous.

Fig. 1, a shows the isotherms for the $mSiO_2$ particles as the mesopores are filled with silicon due to thermal decomposition of SiH_4. It can be seen, that for particles that were filled with Si for up to 45 hours, the shape of the isotherms does not change. The NLDFT pore size distribution (Fig. 1, b) indicates the presence of only one pronounced peak at 3.1 nm, which corresponds to the size of CTAB micelles. Apparently, inside the $mSiO_2$ particles, there is a complete filling of the mesopores with silicon (Fig. 1, c, inset). Probably, the near-surface pores are filled first, then, gradually, as the duration of the process increases, the boundary between the regions of filled and unfilled pores shifts deeper inside the particles. Access of SiH_4 into the volume of particles preserves since they possess the branched interconnected structure of pores. When the pore
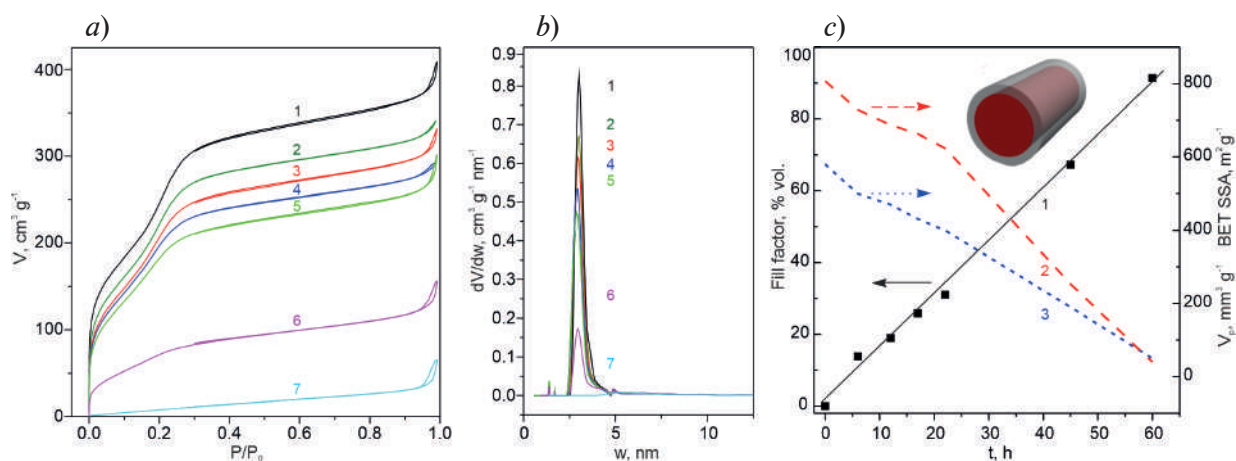
Fig. 1. N_2 adsorption and desorption isotherms measured at 77 K (a) and NLDFT pore size distributions (b) for the mesoporous silica particles filled with silicon. Filling duration (h): $1 - 0$, $2 - 6$, $3 - 12$, $4 - 17$, $5 - 22$, $6 - 45$, $7 - 60$. (c) Dependence of pore fill factor (1), specific surface area (2) and free pore volume (3) of $mSiO_2$/Si particles on filling duration. Inset shows a schematic of filled pore
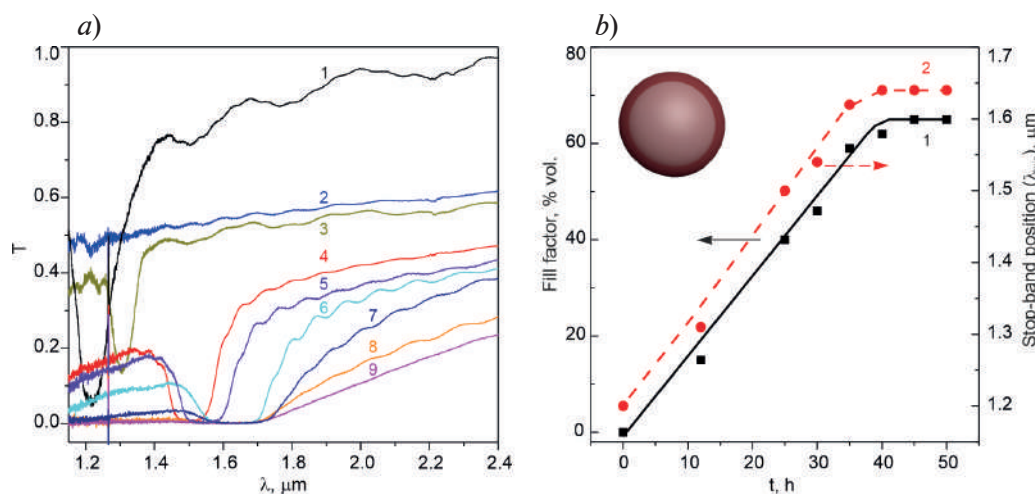
Fig. 2. (a) Transmission spectra of the opal/Si composite on a glass substrate. Filling duration (h): $1 - 0$, $2 - 6$, $3 - 12$, $4 - 25$, $5 - 30$, $6 - 35$, $7 - 40$, $8 - 45$, $9 - 50$. (b) Dependence of pore fill factor (1), and photonic stop-band position (2) of opal/Si on filling duration. Inset shows a schematic of a non-porous particle covered with Si layer

filling is close to complete (Fig. 1, *a*, *b*, curve *7*), the 3-nm pores disappear and larger pores are recorded, which are apparently interparticle pores. The SSA values calculated by BET method (BET SSA) and pore volumes decrease monotonically as filling time increases (Fig. 1, *c*). The pore filling degree was calculated based on the change in free pore volume. The TEM images of mSiO$_2$/Si composite particles (Fig. 3, *a*) show that the particle contrast is uniform, indicating uniform filling of the particles with silicon without any unfilled regions. Note, that there is no silicon layer on the outer surface of the particles, thus the developed technique allows selective filling of mesopores.

a)

b)
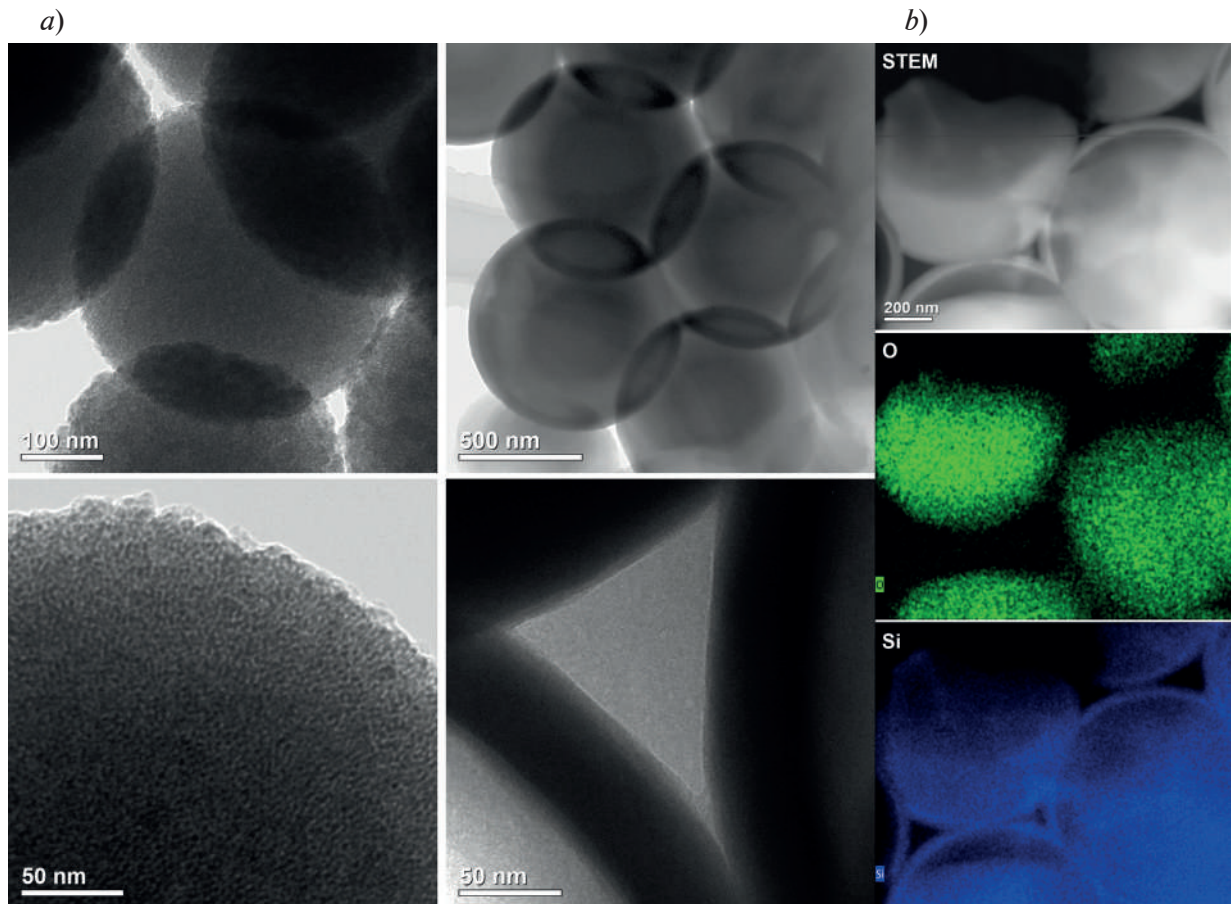
Fig. 3. TEM and STEM images for the mSiO$_2$/Si (*a*) and opal/Si (*b*) and EDX elemental maps for opal/Si (*b*)

An essential feature of the opal/Si composite obtained is the manifestation of typical properties of photonic crystals [10, 13]. We could control and estimate the filling degree from the stop-band (dip) position in the transmission spectra caused by Bragg diffraction from the (111) planes of the f.c.c. lattice of the composite (Fig. 2, *a*). The position of the extremum of the diffraction line λ_{111} at normal incidence can be described by Bragg's formula $\lambda_{111} = 2d_{(111)}\sqrt{\langle\varepsilon\rangle}$, where $d_{(111)}$ is the interplane distance, $\langle\varepsilon\rangle$ is the average dielectric constant of the composite, and $\langle\varepsilon\rangle = \sum \varepsilon_i f_i$ (ε_i and f_i are the dielectric constant and the volume fraction of the *i*-th constituent, respectively [10]). The dielectric constant of the SiO$_2$ spheres and a-Si were taken to be 1.96 [10], and 13.7, correspondingly. There is no stop-band in curve 2 in Fig. 2, *a* due to the absence of optical contrast when the alignment of the average dielectric constants of spherical particles and the pore space occurs. In addition to the Bragg diffraction line, the transmission spectra contained interference fringes due to light reflection from two plane-parallel film surfaces.

Fig. 2, *b* shows that in the opal film, which was filled with Si for up to 40 hours, the position of the stop-band and the corresponding value of the pore fill factor change linearly with the change in the duration of the filling process. Then, the dependencies reach saturation, probably due to

the fact that the narrowest areas of the pores are completely filled with silicon. Unlike mesoporous particles, in opal the complete filling of the pores is not achieved, the maximum degree of filling is ~65%.

Fig. 3, *b* shows TEM images and EDX elemental maps for the obtained opal/Si composite. The boundaries of the nSiO$_2$ particles forming opal structure and silicon shell are clearly distinguishable. It can be seen that, unlike the mesoporous template, in opal the process of layer-by-layer coating of the surface of silica particles with silicon is realized (Fig. 2, *b*, inset) and the thickness of the layer can be controllably varied, which follows from the smooth change in the photonic crystal properties of the composite (Fig. 2).

Conclusion

An approach for the gradual variation of fill factor of both meso- and macroporous silicas with amorphous silicon by use of thermal CVD technique is proposed. The synthesis of a-Si is carried out by thermal decomposition of monosilane within the pores of the templates. It is shown that the fill factor changes lead to step-to-step variation of porosity characteristics and the modification of opal-Si photonic crystal properties. It is found that in the opal template the formation of uniform layer of the same thickness on each SiO$_2$ particle occurs, in contrast, the complete filling of 3-nm pores inside mesoporous particles with amorphous silicon takes place. The developed technique is a promising tool for obtaining functional particles for biomedical applications and active optical media on the base of synthetic opals.

Acknowledgments

REFERENCES

1. **He Y., Fan C., Lee S.-T.,** Silicon nanostructures for bioapplications, Nanotoday. 5 (2010) 282−295.

2. **Priolo F., Gregorkiewicz T., Galli M., Krauss T.F.,** Silicon nanostructures for photonics and photovoltaics. Nature Nanotechnology. 9 (2014) 19−32.

3. **Martin C.R.,** Nanomaterials: a membrane-based synthetic approach, Science. 266 (1994) 1961−1966.

4. **Colilla M., González B., Vallet-Regi M.,** Mesoporous silica nanoparticles for the design of smart delivery nanodevices. Biomaterial Science. 1 (2013) 114−134.

5. **Stöber W., Fink A., Bohn E.,** Controlled growth of monodisperse silica spheres in the micron size range, Journal of Colloid and Interface Science. 26 (1) (1968) 62−69.

6. **Trofimova E.Yu., Aleksenskii, A.E., Grudinkin S.A., Korkin I.V., Kurdyukov D.A., Golubev V.G.,** Effect of tetraethoxysilane pretreatment on synthesis of colloidal particles of amorphous silicon dioxide, Colloid Journal. 73 (2011) 546−550.

7. **Trofimova E.Yu., Kurdyukov D.A., Yakovlev S.A., Kirilenko D.A., Kukushkina Yu.A., Nashchekin A.V., Sitnikova A.A., Yagovkina M.A., Golubev V.G.,** Monodisperse spherical mesoporous silica particles: fast synthesis procedure and fabrication of photonic crystal films, Nanotechnology. 24 (2013) 155601.

8. **Eurov D.A., Kurdyukov D.A., Medvedev A.V., Kirilenko D.A., Tomkovich M.V., Golubev V.G.,** Micro-mesoporous submicron silica particles with pore size tunable in a wide range: synthesis, properties and prospects for LED manufacturing, Nanotechnology. 32 (2021) 215604.

9. **Jiang P., Bertone J.F., Hwang K.S.,** Colvin V.L., Single-crystal colloidal multilayers of controlled thickness, Chemistry of Materials. 11 (1999) 2132−2140.

10. **Grudinkin S.A., Kaplan S.F., Kartenko N.F., Kurdyukov D.A., Golubev V.G.,** Opal-hematite and opal-magnetite films: lateral infiltration, thermodynamically driven synthesis, photonic crystal properties. Journal of Physical Chemistry C. 112 (2008) 17855−17861.

11. **Bogomolov V.N., Golubev V.G., Kartenko N.F., Kurdyukov D.A., Pevtsov A.B., Prokof'ev A.V., Ratnikov V.V., Feoktistov N.A., Sharenkova N.V.,** Fabrication of regular three-dimensional lattices of submicron silicon clusters in an SiO$_2$ opal matrix. Technical Physics Letters. 24 (2017) 326−327.

12. **Kurdyukov D.A., Eurov D.A., Shmakov S.V., Kirilenko D.A., Kukushkina J.A., Smirnov A.N., Yagovkina M.A., Klimenko V.V., Koniakhin S.V., Golubev V.G.,** Fabrication of doxorubicin-loaded monodisperse spherical micro-mesoporous silicon particles for enhanced inhibition of cancer cell proliferation, Microporous Mesoporous Mater. 281 (2019) 1–8.

13. **López C.,** Materials aspects of photonic crystals, Advanced Materials. 15 (2003) 1679−1704.

THE AUTHORS

EUROV Daniil A.
edan@mail.ru
ORCID: 000-0002-7471-4028

GOLUBEV Valery G.
golubev@gvg.ioffe.ru
ORCID: 0000-0003-2956-6561

GRUDINKIN Sergey A.
grudink@gvg.ioffe.ru
ORCID: 0000-0003-1344-9483

KURDYUKOV Dmitry A.
kurd@gvg.ioffe.ru
ORCID: 0000-0002-3041-9609

KIRILENKO Demid A.
zumsisai@gmail.com
ORCID: 0000-0002-1571-209X

YAKOVLEVA Anastasiia A.
nastama@mail.ru
ORCID: 0000-0003-0651-6860

STOVPIAGA Ekaterina Yu.
kattrof@gvg.ioffe.ru
ORCID: 0000-0003-0434-5252

Capacitance characterization of GaN/InP multilayer structures

O.P. Mikhaylov [1] ✉, A.I. Baranov [2], V.A. Pozdeev [2], A.V. Uvarov [2],

A.A. Maksimova [1], E.A. Vyacheslavova [2], A.S. Gudovskikh [2]

[1] St. Petersburg Electrotechnical University "LETI", St. Petersburg, Russia;

[2] Alferov University, St. Petersburg, Russia

✉ oleg.mikhaylov.00@gmail.com

Abstract. This study investigates defect states in GaN/InP multilayer structures fabricated using plasma-enhanced atomic layer deposition (PEALD) for potential applications in high-efficiency multijunction solar cells. Deep-level transient spectroscopy (DLTS) and admittance spectroscopy were employed to characterize defects in the heterostructures. The DLTS spectra revealed a distinct peak in the temperature range of 230–300 K, corresponding to defect states with activation energies of 0.46–0.58 eV under various bias voltages (from 0 to +2 V and from −1 to 0 V). Admittance spectroscopy confirmed the presence of similar defects, demonstrating voltage-dependent activation energies in the range of 0.36–0.57 eV, which is likely associated with interface states at the GaN/InP interface.

Keywords: multilayer structures, defects, admittance spectroscopy, DLTS

Исследование емкостных характеристик многослойных структур GaN/InP

О.П. Михайлов [1] ✉, А.И. Баранов [2], В.А. Поздеев [2], А.В. Уваров [2],

А.А. Максимова [1], Е.А. Вячеславова [2], А.С. Гудовских [2]

[1] Санкт-Петербургский государственный электротехнический университет «ЛЭТИ» им. В.И. Ульянова (Ленина), Санкт-Петербург, Россия;

[2] Академический университет им. Ж.И. Алфёрова РАН, Санкт-Петербург, Россия

✉ oleg.mikhaylov.00@gmail.com

Аннотация. В данной работе изучены дефектные состояния в многослойных структурах GaN/InP, выращенных методами плазмохимического атомно-слоевого осаждения (PEALD), для потенциального применения в высокоэффективных многопереходных солнечных элементах. Для характеризации дефектов в гетероструктурах использовались методы нестационарной спектроскопии глубоких уровней (DLTS) и спектроскопии полной проводимости. Спектры DLTS показали четко выраженный пик в температурном диапазоне 230−300 K, соответствующий дефектным состояниям с энергиями активации

0,46–0,58 эВ при различных напряжениях смещения (от 0 до +2 В и от −1 до 0 В). Спектроскопия полной проводимости подтвердила наличие аналогичных дефектов, продемонстрировав зависимость энергии активации от приложенного напряжения в диапазоне 0,36–0,57 эВ, вероятно, связанных с поверхностными состояниями на границе раздела GaN/InP.

Introduction

In the modern world, there is a shift toward renewable energy sources, which has been particularly active since 2020, after which the cost of electricity has significantly increased. Today, single-junction solar cells (SCs) based on an anisotype heterojunction of hydrogenated amorphous and crystalline silicon (a-Si:H/c-Si) demonstrate the most popular in terms of efficiency and economic benefits. However, such structures have practically reached its maximum theoretical efficiency due to fundamental reasons [1]. The most significant limitation on the maximum achievable efficiency of single-junction solar cells is the thermalization loss of charge carriers, where the excess photon energy transferred to the generated charge carriers is dissipated as lattice vibrations. Consequently, researchers have recently been exploring alternative approaches to enhance efficiency, with multi-junction solar cells with active layers of III-V semiconductors in top subcells emerging as a promising solution [2−3]. However, the selection of top-junction materials must satisfy energy balance requirements, where the optimal bandgap should fall within the 1.7−1.8 eV range [4]. Therefore, selecting appropriate materials presents a significant challenge. Additionally, lattice constant mismatch must be considered as it can significantly degrade the quality of the top-junction material [5]. Layers of short-period superlattices of GaN/InP is promising candidate for these challenges since its bandgap can be precise tuned, and strain-induced elastic deformations can be compensated by lattice mismatch. Most studies in this field is devoted to exploration of III-V alloys grown by molecular beam epitaxy (MBE) [6]. For mass production, however, this approach is prohibitively expensive and complex. Therefore, we fabricate these structures using plasma-enhanced chemical deposition (PECVD) as for amorphous silicon. The resulting samples were then characterized for defects using deep-level transient spectroscopy (DLTS) and admittance spectroscopy.

Materials and Methods

InP and GaN layers were deposited using plasma-enhanced atomic layer deposition (PEALD) on n-type monocrystalline Si (100) substrates. Prior to deposition, the Si substrates were treated with a 10% HF/H_2O solution to remove the native oxide. The growth program consisted of 5 repetitions of 60-cycle InP (6 nm) and 20-cycle GaN (3 nm) depositions. The deposition process was carried out in an Oxford Plasmalab System 100 PECVD reactor at a pressure of 350 mTorr, temperature of 380 °C, and P = 200 W. Further, DLTS measurements were performed for the obtained structures. DLTS is a capacitance-based method for investigating defect properties in semiconductors, which relies on analyzing capacitance relaxation in response to changes in applied bias voltage. Measurements of capacitance DLTS were performed using an automated installation based on a Boonton-7200B capacitance bridge in the temperature

range of 80−360 K in a Janis VPF-100 nitrogen vacuum cryostat. Admittance spectroscopy measurements were also performed. This technique involves temperature scanning of the sample while continuously measuring its capacitance and conductance at multiple frequencies.

Results and Discussion

In the DLTS spectra in Figure 1, obtained under positive (0 to +2 V) and negative (−1 to 0 V) biases, a characteristic peak is observed in the temperature range of 230−300 K, corresponding to a defect with an activation energy of 0.46−0.58 eV.
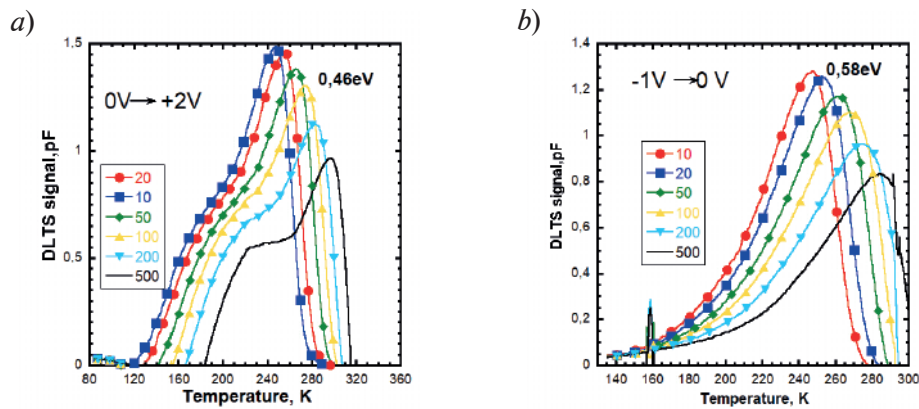
Fig. 1. DLTS signal graphs for the studied samples at (*a*) Vinit = 0 V, Vpulse = +2 V and (*b*) Vinit = −1 V, Vpulse = +1 V for emission rate of 10−500 s^{-1}
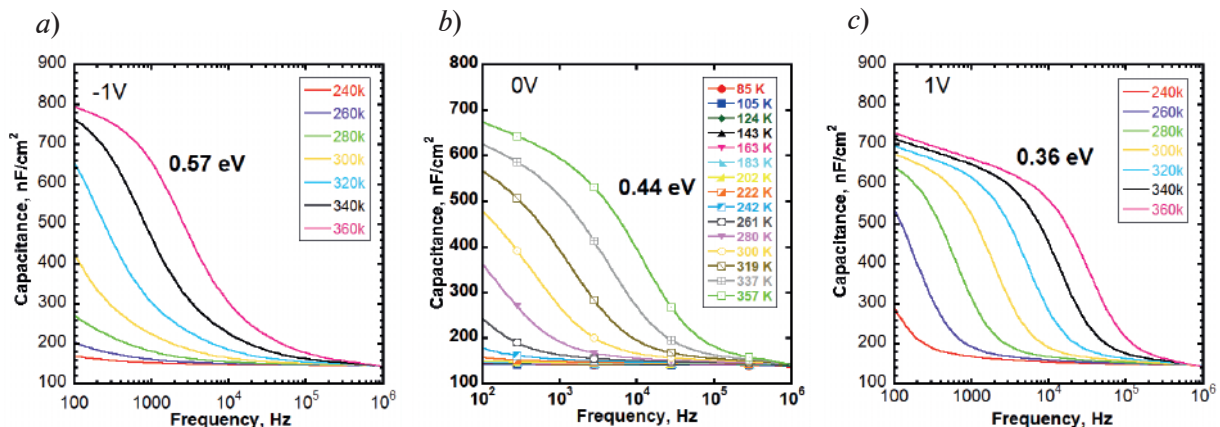
Fig. 2. The C-t plot for the studied sample under different bias voltages

The observed dependence of activation energy on bias voltage in GaN/InP superlattices clearly indicates the presence of interface states at the GaN/InP heterointerface, where the applied bias voltage modifies the potential barrier at the heterojunction through band bending.

Figure 3 shows the band diagram of the studied structure under different applied voltages, obtained using the A-force software. The data used is specified in Table. In Fig. 3, *a*, the applied voltage is 0 V, while Fig. 3, *b* displays the band diagram at −1 V. It is clearly visible that the applied bias voltage leads to band bending and an increase in the activation energy (the distance from the Fermi level to the conduction band, indicated by the arrow on the graph).

T a b l e

Parameters used for obtaining the band diagrams

	InP	GaN	Si
Eg, eV	1.34	3.39	1.12
χ, eV	4.4	4.1	4.05
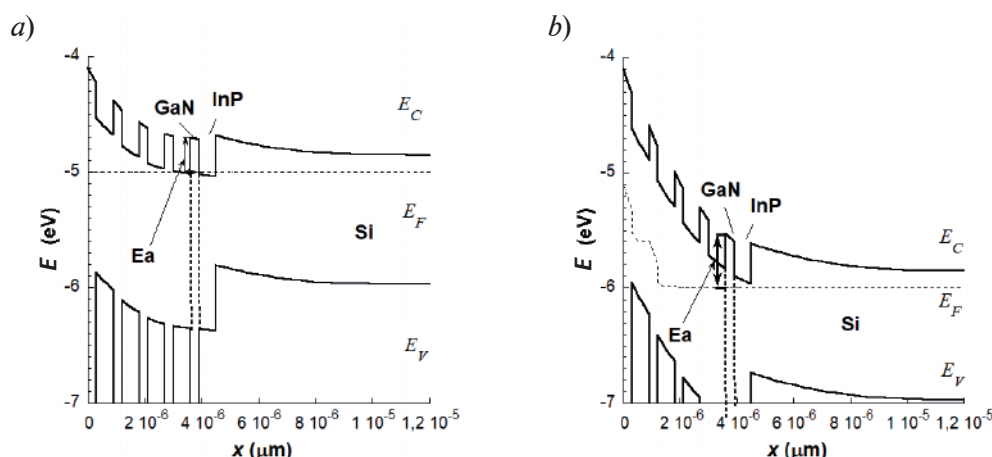
Fig. 3. Schematic view of the simulated band diagram for the GaN/InP superlattice structure at voltages of: 0 V (*a*) and −1 V(*b*)

Conclusion

The observed dependence of defect activation energies (0.36–0.58 eV) on applied bias voltage in GaN/InP heterostructures unequivocally indicates that the primary defect states are localized at the interface, where the activation energy is modulated by external voltage through band bending effects. These results highlight the critical importance of interface engineering, including optimization of growth conditions.

Acknowledgments

REFERENCES

1. **King R.R., Law D.C., Edmondson K.M., Fetzer C.M., Kinsey G.S., Yoon H., Sherif R.A., Karam N.H.,** Applied Physics Letters. 90 (18) (2007) 183516.

2. **Zou Y., Zhang C., Honsberg C., Vasileska D., King R., Goodnick S.,** IEEE 7th World Conference on Photovoltaic Energy Conversion, (IEEE). (2018) 0279−0282.

3. **Dushaq G., Siddiqui A., Jumaa K., Nayfeh A., Rasras M.,** IEEE 7th World Conf. Photovolt, Energy Conversion, WCPEC, A Jt. Conf. 45th IEEE PVSC. (2018) 3857−3860.

4. **Zeitouny J., Katz E.A., Dollet A., Vossier A.,** Band Gap Engineering of MultiJunction Solar Cells: Effects of Series Resistances and Solar Concentration, Scientific Reports. 7 (1) (2017).

5. **Orzali T., Vert A., O'Brien B., Herman J.L., Vivekanand S., Hill R.J.W., Karim Z., Papa Rao S.S.,** GaAs on Si epitaxy by aspect ratio trapping: Analysis and reduction of defects propagating along the trench direction, J. Appl. Phys. 118 (10) (2015) 105307.

6. **André J.P., Hallais J., Schiller,** Heteroepitaxial growth of GaP on silicon. Journal of Crystal Growth. 31 (1975) 147−157.

THE AUTHORS

MIKHAYLOV Oleg P.
oleg.mikhaylov.00@gmail.com
ORCID: 0009-0005-6836-4091

BARANOV Artem I.
itiomchik@yandex.ru

POZDEEV Vyacheslav A.
pozdeev99va@gmail.com
ORCID: 0009-0009-4023-6185

UVAROV Alexander V.
lumenlight@mail.ru
ORCID: 0000-0002-0061-6687

MAKSIMOVA Alina A.
deer.blackgreen@yandex.ru
ORCID: 0000-0002-3503-7458

VYACHESLAVOVA Ekaterina A.
cate.viacheslavova@yandex.ru
ORCID: 0000-0001-6869-1213

GUDOVSKIKH Alexander S.
gudovskikh@gmail.com

Phase control of quasi-2D halide perovskite by post-treatment and antisolvent treatment techniques

G.A. Verkhogliadov [1, 2], A.A. Ekgardt [2] ✉, D.A. Semyonov [2], S.S. Anoshkin [2],

I.A. Andreev [3], N.K. Ratmanova [3], A.P. Pushkarev [1]

[1] Skolkovo Institute of Science and Technology, Moscow, Russia;
[2] ITMO University, St. Petersburg, Russia;
[3] Patrice Lumumba Peoples' Friendship University of Russia, Moscow, Russia
✉ aleksei.ekgardt@metalab.ifmo.ru

Abstract. The fabrication of efficient and stable deep blue halide perovskite light-emitting diodes has attracted significant interest nowadays due to their potential applications in next-generation display technologies. Quasi-2D halide perovskite seems to be perfect material for this application, owing to their unique optoelectronic properties and tunability. However, during the deposition from stoichiometrically clear phase solution mixture of phases is forming in the thin film leading to redshift of luminescence peak. This shift occurs due to energy transfer between different phases, affecting the performance and stability of the light-emitting diode. In this study, we explore various approaches for phase control in multiple quantum well structures to achieve stable and efficient emission in the blue region. Additionally, we conduct a comparative analysis of two distinct quasi-2D ligands used in the synthesis of these materials, evaluating their influence on the optical and electronic properties. We study possible ways for synthesis of pure phase quasi-2D perovskite thin films for their implementation in light-emitting diodes.

Keywords: quasi-2D halide perovskite, phase control, photoluminescence, absorption spectroscopy

Контроль фаз в квазидвумерном галогенидном перовските с помощью методов постобработки и обработки антирастворителем

Г.А. Верхоглядов [1, 2], А.А. Экгардт [2] ✉, Д.А. Семёнов [2], С.С. Аношкин [2],

И.А. Андреев [3], Н.К. Ратманова [3], А.П. Пушкарев [1]

[1] Сколковский институт науки и технологий, Москва, Россия;
[2] Университет ИТМО, Санкт-Петербург, Россия;

³ Российский университет дружбы народов имени Патриса Лумумбы,
Москва, Россия
✉ aleksei.ekgardt@metalab.ifmo.ru

Аннотация. Данное исследование изучает различные подходы для контроля фаз в квази-двумерных перовскитных тонких пленках для получения стабильного излучения в синей области видимого спектра. Мы сравниваем различные подходы, а также квазидвумерные лиганды для их дальнейшего применения в изготовлении светодиодов.

Ключевые слова: квазидвумерный галогенидный перовскит, фазовый контроль, фотолюминесценция, абсорбционная спектроскопия

Introduction

Quasi-2D halide perovskites are currently attracting significant interest due to their remarkable properties and diverse applications in photonics and optoelectronics. One of the most promising areas is in perovskite light-emitting diodes (PeLEDs), where the incorporation of quasi-2D perovskites has enabled the achievement of brightness exceeding 10^5 cd/m^2 and external quantum efficiency (EQE) over 30% [1]. Moreover, these materials are valuable for the development of efficient and stable deep blue PeLEDs [2]. For instance, the excitonic peak of the widely used phenethylammonium (PEA)-based quasi-2D perovskite phase $PEA_2MA_{n-1}Pb_nBr_{3n+1}$, where $n = 2$, exhibits a deep blue luminescence wavelength around 450 nm [3]. Another unstudied but promising ligand for stable PeLED applications is methyl-phenethylammonium (MePEA) [4]. However, even a stoichiometric $n = 2$ solution can result in a mixture of phases during deposition, leading to a redshift in the luminescence peak due to energy transfer between these phases. Consequently, effective phase control in quasi-2D halide perovskites is crucial for the development of stable blue PeLEDs.

Materials and Methods

$PEA_2FAPb_2Br_7$ and $MePEA_2FAPb_2Br_7$ quasi-2D perovskite were prepared using stoichiometric mixtures of 0.3 mmol PbBr2 (>99.9%), 0.15 mmol FABr (>99.9%) and 0.3 mmol MePEABr or PEABr (>98%) in dimethyl sulfoxide. The solution was deposited and stored in a glove box filled with nitrogen atmosphere. Halide perovskite thin films were deposited via spin-coating method using a one-step spin-cycle with 2000 rpm to obtain a film with thickness of 60−80 nm. For antisolvent treatment 0.3 ml of toluene was dripped during the spin-coating deposition. For post-treatment techniques diluted polar solvent with toluene was deposited on formed perovskite thin film [5]. Absorption spectra were measured using a UV-Vis-NIR spectrophotometer UV-3600 Plus (Shimadzu). The instrument is equipped with a grating−grating dual-monochromator system, which minimizes stray light and allows for high-accuracy spectral measurements. A deuterium lamp was employed as the radiation source for the ultraviolet region, while a tungsten−halogen lamp provided illumination for the visible and near-infrared regions. Spectral detection across the range of 185−3300 nm was achieved using three detectors: a photomultiplier tube for the ultraviolet−visible region, and InGaAs and cooled PbS detectors for the near-infrared region. Photoluminescence (PL) spectra were obtained using a QE pro Ocean optic spectrometer

connected to the Axio Imager.A2m (Carl Zeiss SMT) optical microscope via fiber optic, with optical pumping provided by a UV lamp emitting at a wavelength of 350 nm. Atomic force microscopy (AFM) was made on AIST-NT SmartSPM 1000.

Results and Discussion

In this work, we study approaches for phase control in quasi-2D perovskite, using two treatment techniques. The first technique involves antisolvent treatment. We examined two types of quasi-2D ligands, PEA and a novel MePEA, and demonstrated that this antisolvent method is effective for both ligands.

Although we employ a stoichiometric solution for quasi-2D perovskite with $n = 2$, the thin film deposited via the spin-coating technique consists of a mixture of different phases, as illustrated in Fig. 1, a and 1, b (green curves). In addition to the $n = 2$ phase, we clearly observe an excitonic peak corresponding to $n = 1$ and another peak associated with the bandgap of bulk $FAPbBr_3$ perovskite. Due to energy transfer between these quasi-2D phases, peak shifts closer to the wavelength of bulk $FAPbBr_3$, as shown in Fig. 1, c and 1, d (green curves).
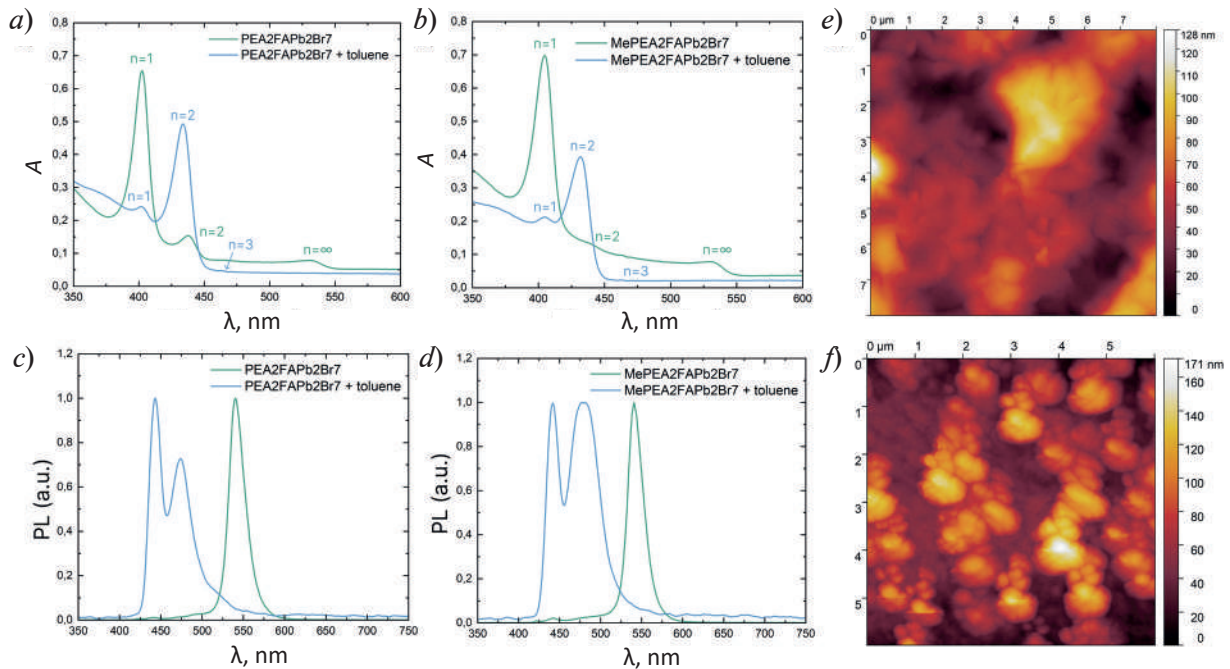
Fig. 1. Antisolvent treatment technique. Absorption spectra for $PEA_2FAPb_2Br_7$ with and without toluene treatment (a). Absorption spectra for $MePEA_2FAPb_2Br_7$ with and without toluene treatment (b). Normalized PL spectra for $PEA_2FAPb_2Br_7$ with and without toluene treatment (c). Normalized PL spectra for $MePEA_2FAPb_2Br_7$ with and without toluene treatment (d). AFM image of $PEA_2FAPb_2Br_7$ thin film without toluene treatment (e). AFM image of $PEA_2FAPb_2Br_7$ thin film with toluene treatment (f)

There are several methods to control the phase formation in quasi-2D perovskite thin films. By dripping toluene at a specific time during the spin-coating process, we can promote the formation of the quasi-2D phase with $n = 2$, as illustrated in Fig. 1, a and 1, b (blue curves), while reducing or even washing away unwanted phases. This approach enables us to achieve blue photoluminescence with two distinct peaks at 450 nm ($n = 2$ phase) and 470 nm ($n = 3$ phase), as shown in Fig. 1, c and 1, d (blue curves). Furthermore, while removing higher n phases, this method also reduces the amount of the $n = 1$ phase (peak near 400 nm in the absorption spectra), which contains many dielectric quasi-2D ligands that can decrease the electrical conductivity of the thin films. The full width at half maximum (FWHM) values of the absorption spectra were analyzed to evaluate the effect of toluene treatment on the optical properties of the films. For the $PEA_2FAPb_2Br_7$ samples (Fig. 1, a), the untreated film exhibited FWHM values of 12.76 nm

for the $n = 1$ peak and 11.73 nm for the $n = 2$ peak. After toluene treatment, the corresponding values were 8.48 nm ($n = 1$) and 14.45 nm ($n = 2$). For $MePEA_2FAPb_2Br_7$ (Fig. 1, b), the untreated sample displayed a FWHM of 15.15 nm for the $n = 1$ peak, while the $n = 2$ peak was barely distinguishable. Following toluene treatment, in general, the MePEA-based films exhibited slightly larger FWHM values than the PEA-based films, although the differences were relatively small.

Similar trends were observed in the photoluminescence (PL) spectra (Fig. 1, c and 1, d). For $PEA_2FAPb_2Br_7$, the untreated sample showed a single emission peak with a FWHM of 22.93 nm. In contrast, the toluene-treated film exhibited two emission peaks: one at 443 nm (FWHM = 14.17 nm) and another at 473 nm (FWHM = 30.10 nm). For $MePEA_2FAPb_2Br_7$ PL spectra on Fig. 1, d FWHM is 22.29 nm, and for $MePEA_2FAPb_2Br_7$, the untreated film displayed an emission peak with a FWHM of 22.29 nm. Upon toluene treatment, two peaks emerged at 442 nm (FWHM = 22.61 nm) and 481 nm (FWHM = 45.96 nm). Notably, the toluene-treated MePEA-based films exhibited broader PL emission compared to the PEA-based counterparts.

Additionally, atomic force microscopy (AFM) was employed to compare the morphology of thin films before and after toluene treatment. Fig. 1, e and 1f display images of $PEA_2FAPb_2Br_7$ thin films: one without toluene treatment (Fig. 1, e) and the other with treatment (Fig. 1, f). Both films exhibit relatively similar morphological characteristics; however, small difference is observed in the average grain sizes. The average grain size in the perovskite film after toluene treatment is smaller compared to the thin film without treatment. This reduction in grain size may influence the material's properties and performance in potential device applications.

The second method involves post-treatment, originally described in work [5]. This approach also reduces the intensity of unwanted excitonic peaks in the absorption spectrum; however, it decreases the intensity of all peaks, albeit at different ratios. In this technique a polar solvent (DMF) is mixed with antisolvents (toluene) to make a 15% DMF solution in our case. This mixture is deposited on the surface of the fully-formed perovskite film for a few seconds. After that, the substrate rotates at high speed. This brief exposure helps to reduce certain unwanted quasi-2D phases, especially the low-n phases, without damaging the thin film itself. A 15% DMF solution in toluene can significantly reduce the $n = 1$ phase in PEA-based perovskite, while the $n = 2$ phase remains largely unchanged, as illustrated in Fig. 2, a.
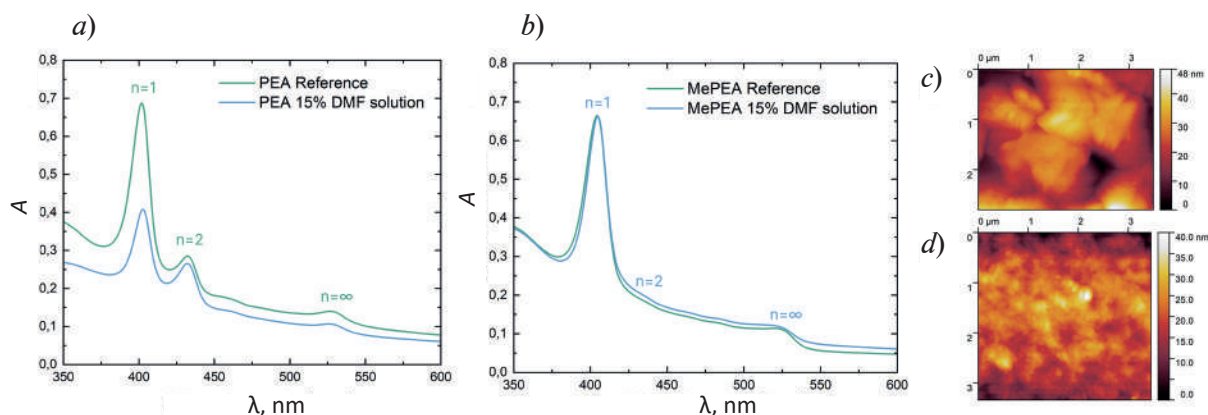
Fig. 2. Post-treatment technique: $PEA_2FAPb_2Br_7$ post-treatment with 15% DMF solution (a). $MePEA_2FAPb_2Br_7$ post-treatment with 15% DMF solution (b). AFM image of AFM image of $PEA_2FAPb_2Br_7$ thin film before solvent post-treatment (c). AFM image of AFM image of $PEA_2FAPb_2Br_7$ thin film after solvent post-treatment (d)

Quasi-2D perovskites that use a methyl-substituted PEA derivative, known as MePEA, show improved stability against moisture and polar solvents compared to traditional PEA-based quasi-2D perovskites. When exposed to a 15% DMF solution, which can greatly decrease the $n = 1$ phase of the PEA-based thin film, the MePEA-based perovskite thin film remains mostly unaffected, as illustrated in Fig. 2, b. This demonstrates that MePEA-based perovskite films have enhanced structural stability compared to PEA-based quasi-2D halide perovskites.

Furthermore, the AFM images of PEA-based thin films (Fig. 2, *c* and 2, *d*) reveal an improved morphology following solvent post-treatment. This technique effectively dissolves and removes some of the thin film's surface. Such uniformity is crucial for future device applications, as it can significantly influence charge transport, reduce defects, and improve overall device performance. The observed morphological enhancements suggest that solvent post-treatment could be a promising strategy for optimizing PEA-based materials in various optoelectronic applications.

Conclusion

Our research demonstrates effective methods for controlling the formation of quasi-2D phases in halide perovskites. This approach enables us to achieve clearer quasi-2D perovskites, shifting the luminescence peak to a deep blue region, in contrast to the initial green luminescence, while also reducing the presence of the highly dielectric $n = 1$ phase in the thin film. Furthermore, we compared two different quasi-2D ligands and discovered a new property of MePEA-based perovskite films, which exhibit greater structural stability against solvent influence. These findings represent significant progress toward the development of efficient and stable deep blue PeLEDs.

Acknowledgments

REFERENCES

1. **Bai W., et al.,** Perovskite light-emitting diodes with an external quantum efficiency exceeding 30%, Adv. Mater. 35 (39) (2023) 2302283.

2. **Zhou N., et al.,** Co-Interlayer Engineering for Homogenous Phase Quasi-2-D Perovskite and High-Performance Deep-Blue Light-Emitting Diodes, Adv. Optical Mater. 12 (18) (2024) 2302273.

3. **Kim J., et al.,** Spectrally Stable Deep-Blue Light-Emitting Diodes Based on Layer-Transferred Single-Crystalline Ruddlesden−Popper Halide Perovskites, ACS Applied Materials & Interfaces. 16 (5) (2024) 6274−6283.

4. **Alahbakhshi M., et al.,** Highly efficient quasi 2D blue perovskite electroluminescence leveraging a dual ligand composition, Adv. Funct. Mater. 33 (28) (2023) 2214315.

5. **Ding S., et al.,** Phase dimensions resolving of efficient and stable perovskite light-emitting diodes at high brightness, Nature Photonics. 18 (4) (2024) 363−370.

THE AUTHORS

VERKHOGLIADOV Grigorii A.
g.verkhogliadov@skoltech.ru
ORCID: 0000-0002-6222-5526

ANDREEV Ivan A.
ivan.andreev@dgoi.ru
ORCID: 0000-0002-7195-0535

EKGARDT Alexey A.
aleksei.ekgardt@metalab.ifmo.ru

RATMANOVA Nina K.
nina.ratmanova@fccho-moscow.ru

SEMYONOV Dmitrii A.
dmitrii.semenov@metalab.ifmo.ru

PUSHKAREV Anatoly P.
An.Pushkarev@skoltech.ru
ORCID: 0000-0002-1793-6812

ANOSHKIN Sergey S.
sergey.anoshkin@metalab.ifmo.ru
ORCID: 0000-0003-4552-3991

Optical and radio-frequency properties of silver mesh transparent conductor with irregular structure

A.S. Voronin [1, 2], M.O. Makeev [2], B.A. Parshin [2] ✉, S.V. Khartov [1]

[1] Federal Research Center "Krasnoyarsk Science Center of the Siberian Branch of the RAS", Krasnoyarsk, Russia;

[2] Bauman Moscow State Technical University, Moscow, Russia

✉ parshbgal@bmstu.ru

Abstract. The article presents the results of studying the optical and radio-frequency properties of silver irregular mesh transparent conductors obtained using an original self-organized template. It is shown that variation in the thickness of the deposited silver allows easy control of the surface resistance, which is the determining factor affecting the transmission in the radio-frequency range. In particular, we have obtained an irregular silver mesh, which has a surface resistance of 1.44 Ω/sq with an optical transparency in the visible range of about ~81%. This combination of optoelectric parameters made it possible to achieve an extremely low transmittance in the range of 0.7–14 GHz, an average of −37.34 dB over the range, which means that this mesh blocks 99.9815% of radiowave.

Keywords: cracked template, transparent conductor, irregular mesh, shielding efficiency

Оптические и радиочастотные свойства серебряных микросеток с нерегулярной структурой

А.С. Воронин [1, 2], М.О. Макеев [2], Б.А. Паршин [2] ✉, С.В. Хартов [1]

[1] Федеральный исследовательский центр «Красноярский научный центр Сибирского отделения РАН», г. Красноярск, Россия;

[2] Московский государственный технический университет им. Н.Э. Баумана, Москва, Россия

✉ parshbgal@bmstu.ru

Аннотация. Представлены результаты исследования оптических и радиочастотных свойств серебряных нерегулярных микросетчатых прозрачных проводников, полученных при помощи оригинального самоорганизованного шаблона. Показано, что вариация толщины напыляемого серебра позволяет легко управлять поверхностным сопротивлением, что является определяющим фактором, влияющим на пропускание в радиочастотном диапазоне. В частности, нами получена нерегулярная серебряная микросетка, которая имеет поверхностное сопротивление 1,44 Ом/кв при оптической

прозрачности в видимом диапазоне, порядка ~81 %. Такое сочетание оптоэлектрических параметров, позволило достичь крайне малого коэффициента пропускания в диапазоне 0,7–14 ГГц в среднем по диапазону равно −37,34 дБ, что означает, что данное покрытие блокирует 99,9815 % излучения радиочастотного диапазона.

Ссылка при цитировании: Воронин А.С., Макеев М.О., Паршин Б.А., Хартов С.В. Оптические и радиочастотные свойства серебряных микросеток с нерегулярной структурой // Научно-технические ведомости СПбГПУ. Физико-математические науки. 2025. Т. 18. № 3.1. С. 268−272. DOI: https://doi.org/10.18721/JPM.183.153

Introduction

Optically transparent conductors are an important class of materials for optoelectronics, automotive, aerospace, and buildings industries. Studying the radio-frequency (RF) characteristics of these materials is crucial for designing optically transparent screens, antennas and metamaterials. Metallic meshes are among the most promising types of transparent conductors, particularly for RF applications [1], due to their combination of high optical transparency and low surface resistance. Typically, metallic micro- and nanomeshes are fabricated using standard methods such as: photolithography [2], imprinting [3], Electrohydrodynamic jet printing [4]. These methods for producing micro- and nanomeshes offer advantages related to excellent performance parameters but also have drawbacks, such as difficulties in scaling or high production costs. In terms of balancing optoelectronic properties, shielding performance, and production costs, some of the most notable examples include cracked template lithography [5] and nanosphere lithography [6]. In this work, we investigate the broadband shielding properties of irregular Ag meshes fabricated using the cracked template method.

Materials and Methods

The method of forming cracked template, based egg white and irregular Ag meshes based him is described in detail in our previous work [5]. The morphology of cracked tenplate and irregular silver meshes was studied by the method of scanning electron microscopy (SEM) using Hitachi TM-4000 Plus (Hitachi, Japan).

Optical Transmittance spectra of irregular Ag meshes were obtained in the range of 400−800 nm on a UV-3600i Plus spectrophotometer (Shimadzu, Japan).

The sheet resistance was measured by the four-probe method using a JG ST2258 four-point probe station (Suzhou Jingge Electronics Co., China) and a JG ST2558-F01 four-probe head (Suzhou Jingge Electronics Co., China).

The transmission (S_{21}) and reflection (S_{11}) coefficients were measured in the range of 0.7−14 GHz. The measurement technique is described in our previous work [7].

Results and Discussion

Fig. 1, *a* shows an SEM image of the cracked template. Statistical analysis of the SEM image revealed an average cell size of 78.9 ± 39.4 μm and an average crack width of 6.5 ± 3.3 μm. Fig. 1, *b* presents an SEM image of the irregular Ag mesh with a deposited silver thickness of 600 nm. According to statistical analysis, the average cell size is 75.3 ± 37.7 μm, and the average track width is 7.2 ± 3.6 μm. The Ag mesh closely replicates the geometry of the original cracked template, demonstrating high fidelity in structural transfer.
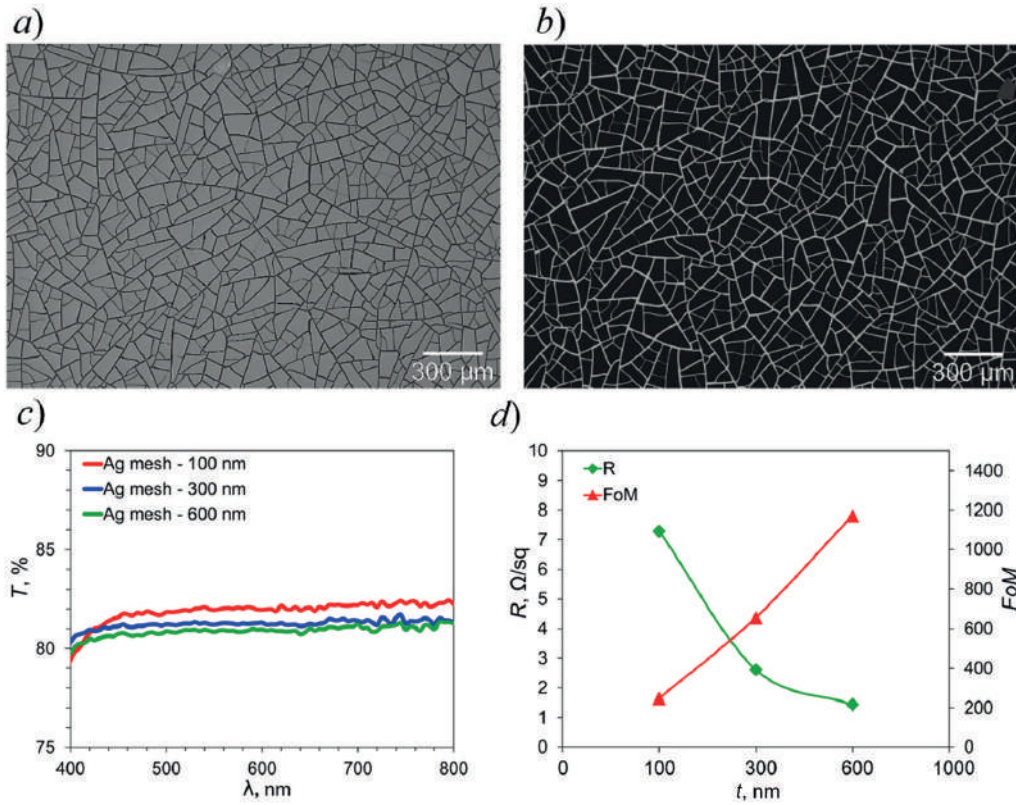
Fig. 1. SEM image cracked template (*a*) and irregular mesh with 600 nm Ag thickness (*b*) Optical transmittance irregular Ag meshes (*c*) and sheet resistance with FoM parameter (*d*)

Visible-range transmittance of irregular Ag meshes with varying thicknesses is presented in Fig. 1, *c*. The data show that increasing the silver thickness leads to only a minor reduction in transmittance. At a wavelength of 550 nm, the transmittance values are 81.94%, 81.25%, and 80.84%, respectively. On the other hand, the sheet resistance decreases significantly with increasing deposited silver thickness (Fig. 1, *d*). The relationship between these two values is characterized by the Figure of Merit (*FoM*) parameter, calculated using the formula:

$$FoM = \frac{Z_0}{2R_\square\left(\frac{1}{\sqrt{T}} - 1\right)}. \tag{1}$$

Here, T is the optical transmittance at a wavelength of 550 nm; $R_\square$ is the sheet resistance; $Z_0 = 377\ \Omega$ is the impedance of free space. Increasing the thickness of the deposited silver leads to a significant decrease in sheer resistance, with a slight decrease in transmission in the visible range, which ultimately leads to an increase in the *FoM* parameter (Fig. 1, *d*).

The spectral transmission (S_{21}) and reflection (S_{11}) coefficients for all fabricated irregular Ag meshes are presented in Fig. 2, *a* and Fig. 2, *b*. The transmission coefficient decreases proportionally with increasing mesh thickness due to the corresponding reduction in sheet resistance. The average transmission coefficients measure −28.15 dB, −34.91 dB, and −37.34 dB, respectively. The frequency dependence of transmission coefficients in the 0.7−14 GHz range results from wave diffraction through the mesh perforated structure. This dependence is well described by the Kontorovich model [8]. Notably, the frequency dependence of S_{21} becomes more pronounced with decreasing sheet resistance of the Ag mesh.

The reflection coefficient (S11) is also quite uniform throughout the studied range; there is a tendency for the reflection coefficient to increase with decreasing sheet resistance of the irregular mesh (Fig. 2, *b*).
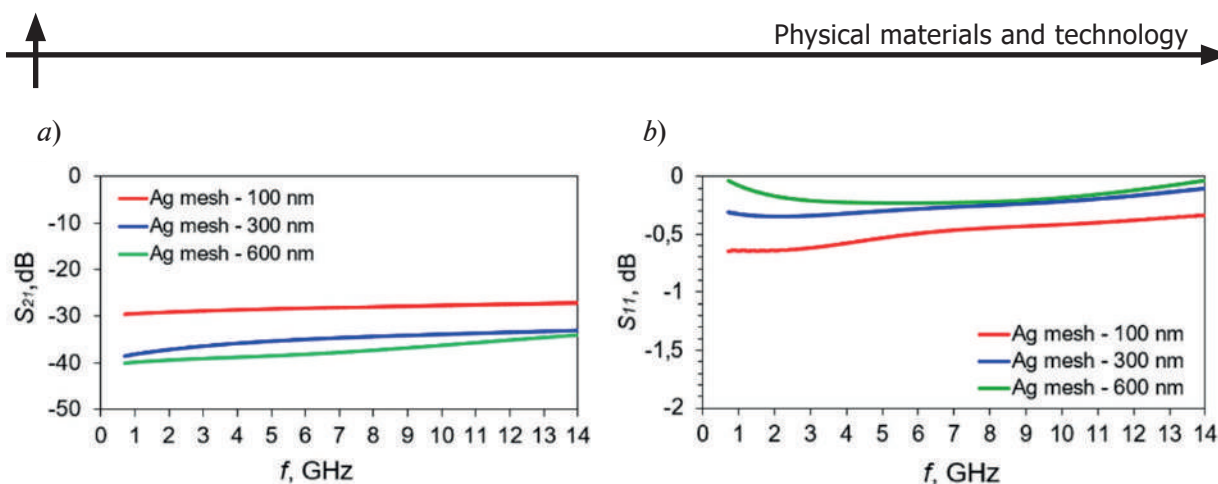
Fig. 2. Transmittance (*a*) and reflectance (*b*) spectra of irregular Ag meshes

Conclusion

We have demonstrated how template structures can be obtained using a self-organized cracking process of egg white. Based on their crack patterns, irregular Ag grids were created with a unique combination of optoelectric and shielding parameters. The properties of the coatings can be easily tuned by varying the thickness of the sputtered metal.

Acknowledgments

REFERENCES

1. **Li Q., Bi S., Wang X., et al.,** Development and current situation of flexible and transparent EM shielding materials, Journal of Materials Science Materials in Electronics. 32 (2021) 25603−25630.

2. **Osipkov A., Makeev M., Konopleva E., et al.,** Optically Transparent and Highly Conductive Electrodes for Acousto-Optical Devices, Materials. 14 (23) (2021) 7178.

3. **Chung S.-I., Kim P. K., Ha T.-G., et al.,** High-performance flexible transparent nanomesh electrodes, Nanotechnology. 30 (2019) 125301.

4. **Vishwanath S.K., Kim D.G., Kim J.,** Electromagnetic interference shielding effectiveness of invisible metal-mesh prepared by electrohydrodynamic jet printing, Japanese Journal of Applied Physics. 53 (2014) 05HB11.

5. **Voronin A.S., Fadeev Y.V., Ivanchenko F.S., et al.,** Waste-free self-organized process manufacturing transparent sonductive mesh and micro flakes in closed cycle for broadband electromagnetic shielding and heater application, Journal of Materials Science Materials in Electronics. (36) 62 (2025).

6. **Zarei M., Mohammadi K., Mahmood A.A., et al.,** Flexible Embedded Metal Meshes by Nanosphere Lithography for Very Low Sheet Resistance Transparent Electrodes, Joule Heating, and Electromagnetic Interference Shielding, ACS Applied Electronic Materials. 7 (9) (2025) 4266−4278.

7. **Voronin A.S., Makeev M.O., Damaratsky I.A.,** Aluminium Mesh Transparent Conductor with Irregular Structure as Effective EMI Shielding Material. IEEEXplore. International Ural Conference on Electrical Power Engineering (UralCon). (2024) 663−667.

8. **Khodzitsky M.K., Bassarab V.V., Shakhmin A.A., et al.,** The Electromagnetic Shielding of Optoelectronic Devices by Mesh Structures, Applied Science. 11 (2021) 9841.

THE AUTHORS

VORONIN Anton S.
a.voronin1988@mail.ru
ORCID: 0000-0001-6908-9945

MAKEEV Mstislav O.
m.makeev@bmstu.ru
ORCID: 0000-0001-8945-3919

PARSHIN Bogdan A.
parshbgal@bmstu.ru
ORCID: 0009-0000-9787-6831

KHARTOV Stanislav V.
khartov.sv@ksc.krasn.ru

ITO films as a functional material for THz radiation modulation

B.A. Parshin [1] ✉, A.S. Voronin [2, 1], K.T. Makarova [1], M.O. Makeev [1],

M.V. Butina [1], Yu.V. Fadeev [1], P.A. Mikhalev [1], S.Yu. Hydyrova [1], K.M. Moiseev [1]

[1] Bauman Moscow State Technical University, Moscow, Russia;

[2] Federal Research Center "Krasnoyarsk Science Center of the Siberian Branch of the RAS",
Krasnoyarsk, Russia

✉ parshbgal@bmstu.ru

Abstract. In this paper, we investigate the terahertz (THz) transmittance and band gap (BG) properties of magnetron sputtered indium tin oxide (ITO) thin films. The THz transmittance was measured using THz time domain spectroscopy, which provides insight into the interaction of terahertz radiation and free carriers inside the films. The band gap was determined from spectrophotometric data using Tauc diagrams, which allowed the analysis of both direct and indirect electron transitions. The results showed that the THz transmittance decreases with increasing film thickness, primarily due to the increase in free carrier absorption associated with higher conductivity and carrier concentration in thicker films. The observed optical band gap values depend on the Burstein−Moss effect caused by the filling of low-energy states in the conduction band with free electrons. The obtained results demonstrate a close relationship between the electronic structure and terahertz response in ITO films, confirming their potential for efficient control of terahertz radiation and application in optoelectronic devices.

Keywords: indium tin oxide, Terahertz transmittance, band gap, THz time-domain spectroscopy, spectrophotometry, Tauc plots

Citation: Parshin B.A., Voronin A.S., Makarova K.T., Makeev M.O., Butina M.V., Fadeev Yu.V., Mikhalev P.A., Hydyrova S.Yu., Moiseev K.M., ITO films as a functional material for THz radiation modulation, St. Petersburg State Polytechnical University Journal. Physics and Mathematics. 18 (3.1) (2025) 273−277. DOI: https://doi.org/10.18721/JPM.183.154

ITO-пленки как функциональный материал для управления ТГц излучением

Б.А. Паршин [1] ✉, А.С. Воронин [2, 1], К.Т. Макарова [1], М.О. Макеев [1],

М.В. Бутина [1], Ю.В. Фадеев [1], П.А. Михалев [1], С.Ю. Хыдырова [1], К.М. Моисеев [1]

[1] Московский государственный технический университет им. Н.Э. Баумана,
Москва, Россия;

[2] Федеральный исследовательский центр «Красноярский научный центр
Сибирского отделения РАН», г. Красноярск, Россия

✉ parshbgal@bmstu.ru

Аннотация. В данной работе мы исследуем пропускание в терагерцовом (ТГц) диапазоне и ширину запрещенной зоны (ЗЗ) тонких пленок оксида индия-олова (ITO), полученных магнетронным распылением. Пропускание в ТГц диапазоне измерялось с помощью терагерцовой спектроскопии во временной области, что позволило изучить взаимодействие терагерцового излучения со свободными носителями заряда в пленках. Ширина запрещенной зоны определялась по спектрофотометрическим данным с использованием диаграмм Таука, что позволило проанализировать как прямые, так и непрямые электронные переходы. Результаты показали, что пропускание в ТГц диапазоне уменьшается с увеличением толщины пленки, в первую очередь из-за увеличения поглощения свободными носителями заряда, связанного с более высокой проводимостью и концентрацией носителей заряда в более толстых пленках. Наблюдаемые значения оптической ширины запрещенной зоны зависят от эффекта Бурштейна–Мосса, вызванного заполнением низкоэнергетических состояний в зоне проводимости свободными электронами. Полученные результаты демонстрируют тесную взаимосвязь между электронной структурой и терагерцовым откликом пленок ITO, подтверждая их потенциал для эффективного управления терагерцовым излучением и применения в оптоэлектронных устройствах.

Ключевые слова: оксид индия-олова, ТГц пропускание, запрещенная зона, ТГц спектроскопия временного разрешения, спектрофотометрия, диаграммы Таука

Introduction

The terahertz (THz) range is regarded as one of the most promising and has seen significant development in recent years [1] for a wide range of applications, including wireless communications [2], spectroscopy [3], and biomedical diagnostics [4]. However, the effective shielding of THz radiation remains a challenge, especially in the development of functional coatings that are transparent in the visible range.

One of the most promising materials for THz radiation shielding is indium tin oxide (ITO) thin films. Thanks to their combination of high transparency in the visible range and excellent electrical conductivity [5], ITO films are widely used in display technologies [6], sensors [7], and solar cells [8]. Importantly, the optoelectronic performance of ITO can be significantly improved through post-deposition annealing, which enhances crystallinity, increases carrier mobility, and reduces the concentration of lattice defects, thereby simultaneously improving both conductivity and transparency.

In recent years, numerous studies have focused on the electrical and optical properties of ITO films across a broad spectral range, including the visible and THz regions. These investigations have addressed both as-deposited and annealed samples. However, most studies have focused on films thicker than 100 nm. For example, Sahoo et al. [9] examined the effect of annealing in a nitrogen atmosphere at 400–800 °C on the THz optical properties and their correlation with electrical characteristics of ITO films with a thickness of approximately 275 nm.

At the same time, ultrathin coatings with thicknesses below 100 nm remain largely unexplored. In this thickness range, carrier concentration, structural defects, and annealing conditions play a particularly significant role, directly affecting terahertz transmittance and the optical band gap.

In the present work, we investigate annealed ultrathin ITO films with thicknesses of 20–100 nm

and demonstrate how thickness influences their terahertz transmittance and optical band gap. This approach allows us to establish the correlation between carrier concentration and the spectral properties of ITO.

Materials and Methods

ITO films of various thicknesses (20, 40, 60, and 100 nm) were deposited on glass substrates (25×25 mm) by magnetron sputtering using a VUP-11M vacuum system. The deposition was carried out in an argon atmosphere at a working pressure of 0.2 Pa and a DC power of 85 W. Prior to deposition, the substrates underwent ultrasonic cleaning.

To improve the structural and optoelectronic properties of ITO films, such as crystallinity, conductivity and transparency, post deposition annealing was performed. Thermal treatment helps to eliminate lattice defects, increase the mobility of charge carriers and reduce the resistance of the film, which is especially important for its use as a transparent conductive coating.

Annealing of ITO coated glass samples was performed in a nitrogen atmosphere at 200 °C for 1 hour using a CVDomna setup. The heating rate was 10 °C/min, and the nitrogen pressure was maintained at 20 kPa throughout the thermal cycle.

The THz transmittance of ITO thin films was characterized using terahertz time-domain spectroscopy (THz-TDS), which allows direct measurement of both the amplitude and phase of THz pulses passing through samples in the frequency range of 0.1−1.0 THz. The optical band gap (BG) of the films was determined using UV-visible spectrophotometric measurements. Transmission spectra were analyzed by the Tauc plot method, which involves plotting $(\alpha h\nu)^{1/n}$ versus photon energy where α is the absorption coefficient and n depends on the type of electronic transition.

Results and Discussion

The results of the transmittance coefficient study in the THz range for ITO films of different thicknesses are presented in Fig. 1. The decrease in transmittance with increasing thickness in the THz range is primarily due to the increase in the absorption of terahertz radiation in thicker ITO layers. This effect is associated with the high concentration of free charge carriers in ITO. The behavior can be described by the Drude model, which takes into account the dynamics of these free carriers. According to this model, the terahertz electromagnetic field causes oscillations of free electrons, which leads to a loss of field energy due to scattering and absorption processes.
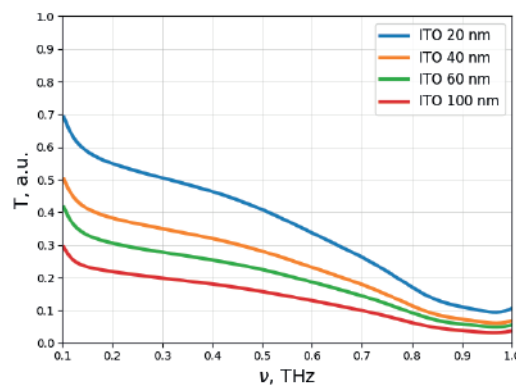
Fig. 1. Transmission spectra of ITO films with different thicknesses in the THz range

To gain a deeper understanding of the electronic properties of the ITO films, the optical band gap energy was investigated. The band gap was determined using the Tauc plot method, which is a widely used approach to extract optical band gap values from absorption spectra. Since ITO is an indirect bandgap semiconductor, Tauc plots were constructed for both direct and indirect electronic transitions. The parameter n in the Tauc equation determines the type of electronic transition, with $n = 1/2$ used for direct allowed transitions which are generally more probable, and $n = 2$ for indirect allowed transitions, which typically have lower probability due to the involvement of phonons. The corresponding Tauc diagrams for the films are shown in Fig. 2.

In ITO films, the optical band gap determined from direct transitions is approximately 3.86 eV for all film thicknesses. This wide band gap is attributed to the Burstein-Moss effect, where a

Fig. 2. Tauc plots used to determine the optical bandgap of the ITO films
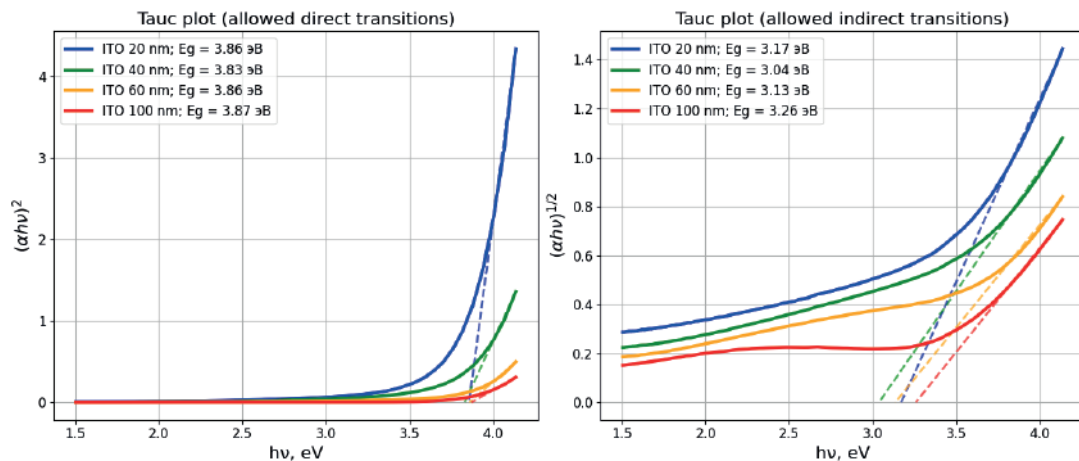
high concentration of free carriers fills the low-energy states in the conduction band. As a result, electrons require higher energy to transition from the valence band to the conduction band, which shifts the absorption edge to higher energies, resulting in increased transmission in the visible range and higher electrical conductivity. Meanwhile, the lower-energy indirect band gap is due to defect states or localized structural disorder inside the films, which introduce absorption channels in the ultraviolet region due to below-bandgap transitions.

Conclusion

In this work, we investigated the spectral characteristics of annealed ultrathin ITO films deposited by magnetron sputtering in the terahertz range. It was shown that films with thicknesses below 100 nm can provide effective shielding, reducing the transmittance down to 0.1 at 1 THz. This behavior is attributed to the high concentration of free charge carriers, which also affects the optical band gap via the Burstein−Moss effect and ensures high transparency in the visible range. The interplay between carrier concentration, band structure, and scattering processes governs both THz absorption and the optical properties of the films.

However, a more precise correlation between the optical band gap and THz transmittance requires further investigation. In particular, additional measurements, including the determination of carrier mobility and concentration via the Hall effect, as well as the study of structural features of ultrathin films, will be essential for a comprehensive quantitative understanding of the relationship between free carrier dynamics, optical absorption, and electrical conductivity.

The present study provides a foundation for further research and the optimization of ultrathin ITO films for applications in transparent and flexible optoelectronic and terahertz devices.

REFERENCES

1. **Bharadwaj A.N., Kashyap A.M., N G.B., et al.,** A Survey on Terahertz Devices-A cutting edge Technology, 2023 International Conference on Recent Trends in Electronics and Communication (ICRTEC), Mysore, India. (2023) 1−6.

2. **Liu K., Feng Y., Han C., et al.,** High-speed 0.22 THz communication system with 84 Gbps for real-time uncompressed 8K video transmission of live events, Nat. Commun. 15 (2024) 8037.

3. **Koch M., Mittleman D.M., Ornik J., et al.,** Terahertz time-domain spectroscopy, Nat. Rev. Methods Primers. 3 (2023) 48.

4. **Gong A., Qiu Y., Chen X., et al.,** Biomedical applications of terahertz technology, Appl. Spectrosc. Rev. 55 (2019) 418−438.

5. **Mikhalev P.A., Parshin B.A., Hydyrova S.Y., et al.,** Study of the Influence of Substrate Material and Thickness of Indium Tin Oxide Coatings on Their Optoelectronic Characteristics, 2024 Intelligent Technologies and Electronic Devices in Vehicle and Road Transport Complex (TIRVED), Moscow, Russian Federation. (2024) 1−4.

6. **Sun J., Chang Y., Liao J., et al.,** Integrated, self-powered, and omni-transparent flexible electroluminescent display system, Nano Energy. 99 (2022) 107392.

7. **Mokrushin A.S., Fisenko N.A., Gorobtsov P.Y., et al.,** Pen plotter printing of ITO thin film as a highly CO sensitive component of a resistive gas sensor, Talanta. 221 (2021) 121455.

8. **Girtan M., Negulescu B.,** A review on oxide/metal/oxide thin films on flexible substrates as electrodes for organic and perovskite solar cells, Opt. Mater. X. 13 (2022) 100122.

THE AUTHORS

PARSHIN Bogdan A.
parshbgal@bmstu.ru
ORCID: 0009-0000-9787-6831

VORONIN Anton S.
a.voronin1988@mail.ru
ORCID: 0000-0001-6908-9945

MAKAROVA Kamila T.
mkt@bmstu.ru
ORCID: 0000-0003-2808-5600

MAKEEV Mstislav O.
m.makeev@bmstu.ru
ORCID: 0000-0001-8945-3919

BUTINA Maria V.
masha.butina.54@mail.ru
ORCID: 0009-0003-1526-4607

FADEEV Yuriy V.
daf.hf@list.ru
ORCID: 0000-0002-2967-9075

MIKHALEV Pavel A.
pamikhalev@bmstu.ru
ORCID: 0000-0003-0672-4627

HYDYROVA Selbi Yu.
hydyrova.selbi@ya.ru
ORCID: 0000-0002-5510-0899

MOISEEV Konstantin M.
k.moiseev@bmstu.ru
ORCID: 0000-0002-8753-7737

277

Optical characterization and surface plasmon polariton mode simulation of GaN/InGaN nanowires on Ag/AlO$_x$ film for plasmonic nanolasers

T. Shugabaev [1, 2] ✉, A.A. Kharchenko [2], A.M. Dautov [1, 2],

A.K. Kuznetsov [3], V.V. Lendyashova [1, 2], N.V. Kryzhanovskaya [4],

R.R. Reznik [1, 2, 5], V.O. Gridchin [1, 2, 5], G.E. Cirlin [1, 2, 5]

[1] St. Petersburg State University, St. Petersburg, Russia;

[2] Alferov University, St. Petersburg, Russia;

[3] Moscow Institute of Physics and Technology (National Research University),
Dolgoprudny, Russia;

[4] National Research University Higher School of Economics, St. Petersburg branch,
St. Petersburg, Russia;

[5] Institute for Analytical Instrumentation RAS, St. Petersburg, Russia;

✉ talgashugabaev@mail.ru

Abstract. Plasmonic nanolasers based on semiconductor nanowires are presently attracting wide interest due to the breaking in the light diffraction limit and the deep subwavelength mode operation. In this work, we synthesize and investigate the optical properties of GaN nanowires with InGaN quantum wells as the core element of plasmonic nanolasers. The results of modeling the electric field intensity distribution for propagating modes and dispersion curve of surface plasmon polaritons in the studied nanowires placed on the AlO$_x$-coated atomically flat Ag film confirm the formation of hybrid plasmonic modes and the viability of these structures for subwavelength light confinement and nanolaser applications.

Keywords: InGaN, GaN, nanowires, nanoplasmonics, nanolasers, molecular beam epitaxy, photoluminescence, numerical simulations

Оптические свойства и моделирование поверхностных плазмон поляритонов GaN/InGaN нитевидных нанокристаллов на пленках Ag/AlO$_x$ для создания плазмонных нанолазеров

Т. Шугабаев [1, 2] ✉, А.А. Харченко [2], А.М. Даутов [1, 2],

А.К. Кузнецов [3], В.В. Лендяшова [1, 2], Н.В. Крыжановская [4],

Р.Р. Резник [1, 2], В.О. Гридчин [1, 2, 5], Г.Э. Цырлин [1, 2, 5]

[1] Санкт-Петербургский государственный университет, Санкт-Петербург, Россия;

[2] Академический университет им. Ж.И. Алфёрова РАН, Санкт-Петербург, Россия;

[3] Московский физико-технический институт (национальный исследовательский университет), г. Долгопрудный, Россия;

[4] Национальный исследовательский университет «Высшая школа экономики», Санкт-Петербургский филиал, Санкт-Петербург, Россия;

[5] Институт аналитического приборостроения РАН, Санкт-Петербург, Россия

✉ talgashugabaev@mail.ru

Аннотация. Данная работа посвящена синтезу и исследованию оптических свойств гетероструктурных нитевидных нанокристаллов InGaN/GaN как потенциально ключевых элементов плазмонных нанолазеров. Представлены результаты моделирования распределения электрического поля и дисперсионных кривых поверхностных плазмон-поляритонов в исследуемых нитевидных нанокристаллах, размещенных на атомарно гладкой серебряной подложке с покрытием из оксида алюминия. Полученные результаты открывают возможность для создания экстремально малых по своим размерам источников когерентного излучения.

Ключевые слова: InGaN, GaN, нитевидные нанокристаллы, наноплазмоника, нанолазеры, молекулярно-пучковая эпитаксия, фотолюминесценция, численное моделирование

Introduction

Semiconductor nanowires (NWs) are promising structures for creating micro- and nanolasers due to their inherent high crystal quality and large aspect ratio. However, the size of semiconductor lasers is limited by the diffraction limit, which obstruct them to use in many optoelectronic applications. A promising route to overcome this limitation is the integration of NWs with a metal-dielectric system. Such hybrid structures enable the realization of plasmonic nanolasers operating at the deep subwavelength scale [1]. Among them, NWs based on ternary InGaN compounds occupy a special niche, capable of emitting in the entire visible range and having a gain of about 10^4 cm^{-1} [2].

In this work, we synthesize and study the optical properties of GaN NWs with embedded InGaN quantum wells (QWs) which demonstrated room temperature photoluminescence at 545 nm. Numerical simulations were conducted to analyze the dispersion curve and propagation modes of surface plasmon polaritons (SPPs) in the NW/AlO$_x$/Ag heterostructure. The results demonstrate that these NWs placed on an AlO$_x$-coated ultra-smooth Ag film are well-suited for nanolaser fabrication.

Materials and Methods

The GaN NWs with InGaN QWs were grown directly on p-type Si(111) substrates using Riber Compact 12 molecular beam epitaxy setup, equipped with Ga, In, Al effusion cells, and a nitrogen plasma source. Prior to growth, the substrates were heated up to a temperature of 920 °C and annealed for 20 min to remove the native oxide. The substrate temperature was then lowered to 600 °C, after which nitrogen plasma was activated and applied for 20 minutes to form a thin Si$_x$N$_y$ layer. At the next stage, Al was deposited onto the formed layer in the absence of nitrogen. Next, the substrate temperature was increased to 865 °C, the nitrogen plasma was ignited, and the Ga source was opened to grow of GaN NWs. After the 17h of growth, the Ga source was closed, and the substrate temperature was decreased to 580 °C. Then the In, Ga, Al sources were opened and closed in the required order to form 15 periods of InGaN QWs/(Al,Ga)N barriers.

Photoluminescence (PL) was excited by a He-Cd laser operating at a wavelength of 325 nm. The diameter of the focused laser spot on the sample was 125 μm. The total optical power incident on the sample was amounted to 11.3 mW. Detection was performed using a single-channel silicon photodetector in combination with synchronous amplification. Measurements were carried out on an array of NWs, with the excitation area encompassing a large number of individual nanostructures. Therefore, the recorded PL spectra represent ensemble-averaged optical properties of the sample. The measurements were performed at room temperature. The structural properties of the samples were examined by scanning electron microscopy (SEM) on a Supra 25 microscope.

Modeling the dispersion curve of SPP for the Ag/AlO$_x$/InGaN was performed via finite elements method in COMSOL Multiphysics software. The hybrid system was simulated using a 2D layered model with the following sequence: a 300-nm-thick Ag layer, a 5-nm-thick AlO$_x$ layer, an InGaN layer (thickness equal to the NW diameter), and a top air cladding. The in-plane length of the structure was 1 μm. The optical constants of InGaN and AlO$_x$ were adopted from Refs. [3, 4]. Distribution of the electric field intensity in the Ag/AlO$_x$/NW cross section for the propagating SPP mode was calculated using the finite-difference method in the frequency domain using the Ansys Lumerical software.

Results and Discussion

Figure 1, *a* shows typical SEM images of the grown InGaN/GaN NW array. Measurements revealed an average NW diameter of 58 nm and a height of 1.3 μm. Structurally, 15 periods of axial InGaN QWs and (Al,Ga)N barriers were formed on the top of the NW (see Fig. 1, *b*).

Figure 1, *c* demonstrates room temperature PL spectrum of the NW array. The sample has a bright PL with two maxima corresponding to a short wavelength peak (361 nm) and a long wavelength peak (545 nm). We attribute the short wavelength peak of PL with bulk GaN area of NW and long wavelength peak with InGaN QWs, respectively.

For the fabrication of the InGaN NW-based plasmonic nanolaser, the NW should be transferred to a plasmonic substrate (see Fig. 2, *a*) featuring an atomically flat Ag surface coated with a
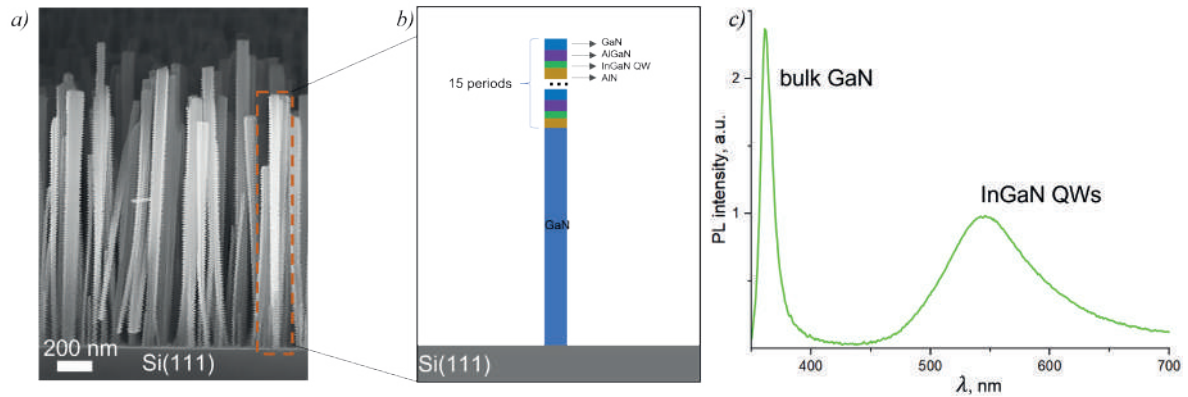
Fig. 1. Typical cross-section SEM image of synthesized NW array (*a*); schematic image of the single NW (*b*); room-temperature PL spectra of the NW array (*c*)

5 nm thick low-refractive-index layer (AlO$_x$ or SiO$_x$) [2, 5]. Furthermore, strong exciton-plasmon interaction requires spectral overlap between the nanowire emission and the SPP dispersion in the semiconductor/dielectric/metal system [6]. To verify this, the modeling the dispersion curve of SPP were performed. A clear overlap was observed between the calculated Ag/AlO$_x$/InGaN SPP dispersion and the PL spectrum of the InGaN QWs in the energy range of 2.0−2.5 eV, indicating efficient energy transfer from the synthesized heterostructured NWs to surface plasmon modes (see Fig. 2, *b*).
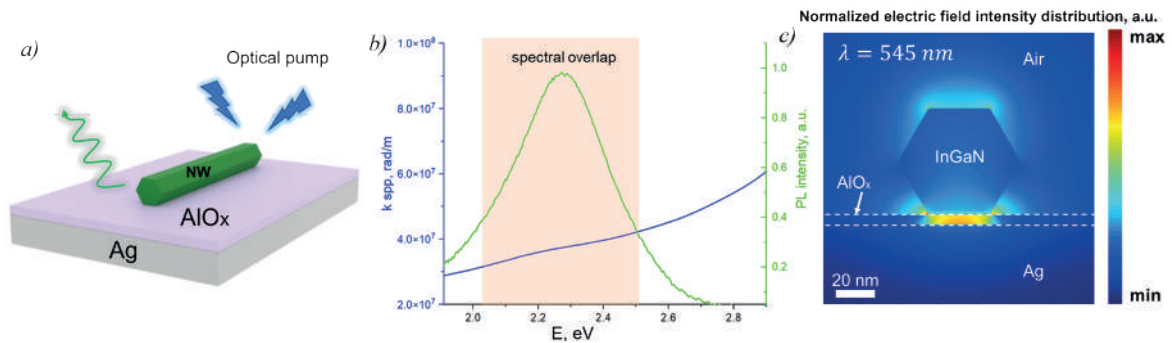
Fig. 2. Schematic illustration of the plasmonic nanolaser design (*a*); calculated dispersion relation of Ag/AlO$_x$/InGaN SPP and spectral overlap with InGaN QWs emission (*b*); distribution of the electric field intensity in the cross section view for the propagating SPP mode (*c*)

As a result, the excitation of the SPPs in such hybrid structures manifests itself the localization of the electric field in a thin dielectric layer [2, 7]. Figure 2, *c* shows the distribution of the electric field intensity in the cross section view for the propagating SPP mode. As expected, a significant part of the intensity is concentrated in the 5 nm thick AlO$_x$ layer, which is unattainable in the case of a fully dielectric waveguide for the above PL of InGaN QWs.

Conclusion

In summary, we synthesized heterostructured GaN NWs with InGaN QWs by molecular beam epitaxy. The observed photoluminescence of these structures and the results of numerical simulation showed that these NWs can be used as an element of plasmonic nanolasers. Thus, the demonstrated capabilities may be of interest for the creation of components of photonic integrated circuits and other applications related to the localization of light on the nanometer scale.

REFERENCES

1. **Ellis T.C., Eslami S., Palomba S.,** Nanolasers: More than a decade of progress, developments and challenges, Nanophotonics. (2024).

2. **Lu Y.-J., Wang C.-Y., Kim J., Chen H.-Y., Lu M.-Y., Chen Y.-C., Chang W.-H., Chen L.-J., Stockman M.I., Shih C.-K.,** All-color plasmonic nanolasers with ultralow thresholds: autotuning mechanism for single-mode lasing, Nano Letters. 14 (2014) 4381−4388.

3. **Kazazis S., Papadomanolaki E., Androulidaki M., Kayambaki M., Iliopoulos E.,** Optical properties of InGaN thin films in the entire composition range, Journal of Applied Physics. 123 (2018).

4. **Franta D., Nečas D., Ohlídal I., Giglia A.,** Dispersion model for optical thin films applicable in wide spectral range, in: SPIE. (2015) 342−353.

5. **Jiang D., Li P., Liu B., Huang K., Tao T., Zhi T., Yan Y., Xie Z., Kang J., Zheng Y.,** InGaN/GaN Nanorod Arrays for a Hybrid Nanolaser, ACS Applied Nano Materials. 5 (2022) 16971−16977.

6. **Stockman M.I.,** Brief history of spaser from conception to the future, Advanced Photonics. 2 (2020) 054002−054002.

7. **Zhang Q., Li G., Liu X., Qian F., Li Y., Sum T.C., Lieber C.M., Xiong Q.,** A room temperature low-threshold ultraviolet plasmonic nanolaser, Nature Communications. 5 (2014) 4953.

THE AUTHORS

SHUGABAEV Talgat
talgashugabaev@mail.ru
ORCID: 0000-0002-4110-1647

KHARCHENKO Anton A.
antoshkerrr@gmail.com
ORCID: 0000-0001-9686-2649

DAUTOV Albert M.
amdautov24@gmail.com
ORCID: 0000-0002-0374-7033

KUZNETSOV Alexey K.
alkuznetsov1998@gmail.com
ORCID: 0000-0001-7143-6686

LENDYASHOVA Vera V.
erilerican@gmail.com
ORCID: 0000-0001-8192-7614

KRYZHANOVSKAYA Natalia V.
nkryzhanovskaya@hse.ru
ORCID: 0000-0002-4945-9803

REZNIK Rodion R.
moment92@mail.ru
ORCID: 0000-0003-1420-7515

GRIDCHIN Vladislav O.
gridchinvo@gmail.com
ORCID: 0000-0002-6522-3673

CIRLIN George E.
george.cirlin@mail.ru
ORCID: 0000-0003-0476-3630

Effect of short-term heating on the morphology of AlF$_3$ microstructures

A.M. Dautov [1, 2] ✉, V.V. Fedorov [3, 2], K.P. Kotlyar [2], V.V. Lendyashova [2],

T. Shugabaev [1, 2], V.O. Gridchin [2, 4], I.V. Shtrom [4, 1], N.V. Sibirev [1]

[1] St. Petersburg State University, St. Petersburg, Russia;

[2] Alferov University, St. Petersburg, Russia;

[3] Peter the Great St. Petersburg Polytechnic University, St. Petersburg, Russia;

[4] Institute for Analytical Instrumentation RAS, St. Petersburg, Russia

✉ amdautov24@gmail.com

Abstract. This work explores thermally modified AlF$_3$ microstructures synthesized via aluminum-zinc reaction in hydrofluoric acid. Brief heating produces cushion-like morphologies, while room-temperature growths results in cracked crystals. The thermally treated samples exhibit anisotropic brittleness and easy delamination, suggesting weak interlayer bonding. SEM-EDS and XRD analyses reveal structure-property relationships, offering insights for tailored AlF$_3$ microstructures in electronics and nanomaterials.

Keywords: aluminum fluoride, rosenbergit, XRD analyze, microstructures

Влияние кратковременного нагрева на морфологию микроструктур AlF$_3$

А.М. Даутов [1, 2] ✉, В.В. Федоров [3, 2], К.П. Котляр [2], В.В. Лендяшова [2],

Т. Шугабаев [1, 2], В.О. Гридчин [2, 4], И.В. Штром [4, 1], Н.В. Сибирев [1]

[1] Санкт-Петербургский государственный университет, Санкт-Петербург, Россия;

[2] Академический университет им. Ж.И. Алфёрова РАН, Санкт-Петербург, Россия;

[3] Санкт-Петербургский политехнический университет Петра Великого,
Санкт-Петербург, Россия;

[4] Институт аналитического приборостроения РАН, Санкт-Петербург, Россия

✉ amdautov24@gmail.com

Аннотация. В данной работе приводятся результаты исследования влияния кратковременного нагрева раствора HF:H$_2$O-Al-Zn на морфологию и фазовый состав микроструктур AlF$_3$. Исследование показало, что кратковременный нагрев раствора

HF-Al-Zn способствует формированию подушкообразной микроструктуры AlF_3. Для получившихся структур приведены результаты исследований методами растровой электронной микроскопии и рентгенодифракционного анализа. Полученные результаты расширяют возможности управления формой наноструктур на основе AlF_3.

Ключевые слова: фторид алюминия, розенбергит, рентгенодифракционный анализ, микроструктуры

Introduction

The attention of many research groups is increasingly drawn to materials based on group III-VII elements of the periodic table, among which aluminum fluoride (AlF_3) stands out prominently [1]. This material serves as an active emitting component in ultraviolet devices, independent catalyst, functions as an inorganic photolithographic resist [2]. The physicochemical properties of AlF_3 present particular interest for applications in advanced micro- and nanostructures.

Despite existing theoretical and experimental investigations [3], the full potential for creating functional microstructures remains unexplored. To explain the fundamental mechanisms governing the formation of distinct AlF_3 microstructures and fully explore their synthesis opportunities, comprehensive experimental investigations are required to systematically evaluate synthesis parameter effects. One of the most fundamental key factors for controlling material synthesis processes is temperature. Building upon previous findings [4], in this work we investigated the influence of short-term heating on the morphological and phase characteristics of AlF_3-based structures.

Materials and Methods

The experiments were conducted in polypropylene bath. The dissolution reaction of aluminum (Al) was carried out in an aqueous hydrofluoric acid solution (HF:H_2O~x:y) using zinc (Zn) as a catalyst. The solution volume was 15 mL. Al and Zn were immersed simultaneously in the HF solution and allowed to react until complete dissolution of Al was achieved. Following complete dissolution, the solution was mixed up using an ultrasonic bath to ensure uniformity. Subsequently, 1 mL aliquots were extracted from each reaction mixture and transferred to polypropylene Petri dishes. In the first experiment, the solution was maintained at ambient temperature (25 °C) until precipitation was complete, which took approximately 20 hours. Under the second condition, the solution was heated under controlled conditions at 60°C. Precipitation occurred within 9 seconds. Table 1 summarizes the initial precursor data.

Table 1

Synthesis parameters

HF_{init},%	x	y	Al, g	Zn, mg	Al, mol	C_m,%	C_M, mol/L	ν_{HF}, mol	ν_{HF}/ν_{Al}
3.63	1	10	0.257	5	0.01	0.043	2.161	0.032	3.4

In all experiments, high-purity (5N) Al and Zn (Saying, China) were used for analysis. The hydrofluoric acid solution complied with Russian GOST standards (GOST 10484-78) and had a concentration of 47.5%. Sample microstructures were characterized using a SUPRA 25 scanning electron microscope (SEM) (Carl Zeiss, Germany) equipped with an Ultima 100 energy-dispersive X-ray spectrometer (EDS; Oxford Instruments). To characterize the phase composition of the synthesized structures, X-ray diffraction (XRD) analysis was performed using a Bruker Kappa APEX II DUO system equipped with a microfocus source and a two-dimensional CCD detector.

Results and Discussion

Figure 1 demonstrates SEM images of the obtained sample morphologies. When the solution was dried without heating, scanning revealed that the resulting aluminum fluoride structure was characterized by numerous cracks (Fig. 1, *a*). Notably, upon closer examination, the crystals located between cracks exhibited a visually smooth surface morphology.

a) *b)*
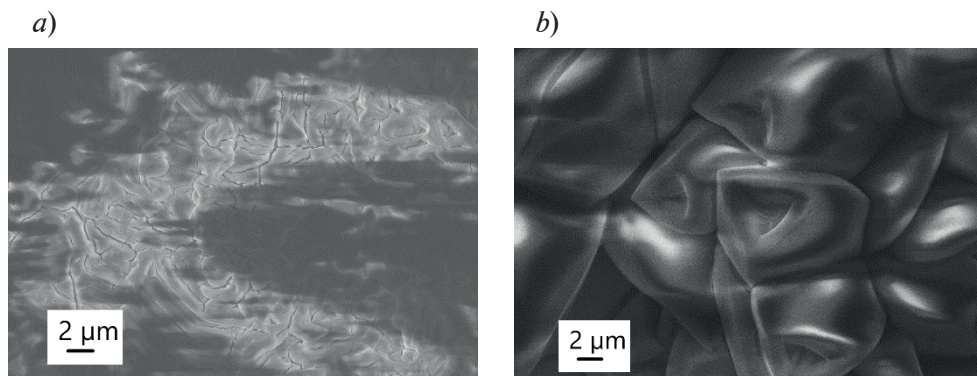
Fig. 1. SEM images show the obtained samples in isometric view: without heating (*a*), with heating (*b*)

In contrast, the solution subjected to short-term heating exhibited a distinct cushion-like morphology (Fig. 2, *a*). At higher magnification, this pillow-like structure was observed across the entire sample. Furthermore, the heat-treated sample was exceptionally brittle and exhibited a strong tendency to delaminate, readily fragmenting into thin flakes upon minimal disturbance.

The formation of cracks is typically caused by stresses in the structure resulting from non-uniform crystallization and solvent evaporation [5]. Short-term heating significantly accelerates synthesis, creating conditions for rapid nucleation and growth of fine-grained structures. Figure 2, *a* shows the XRD patterns of the obtained structures. According to the results, the spectrum of the sample synthesized without heating corresponds to rosenbergite ($AlF_3 \cdot 3H_2O$) [6]. This observation can be explained by the fact that the synthesis solution was highly diluted. Due to prolonged synthesis in a highly aqueous environment, the hydrated form of AlF_3 was obtained.

a) *b)*
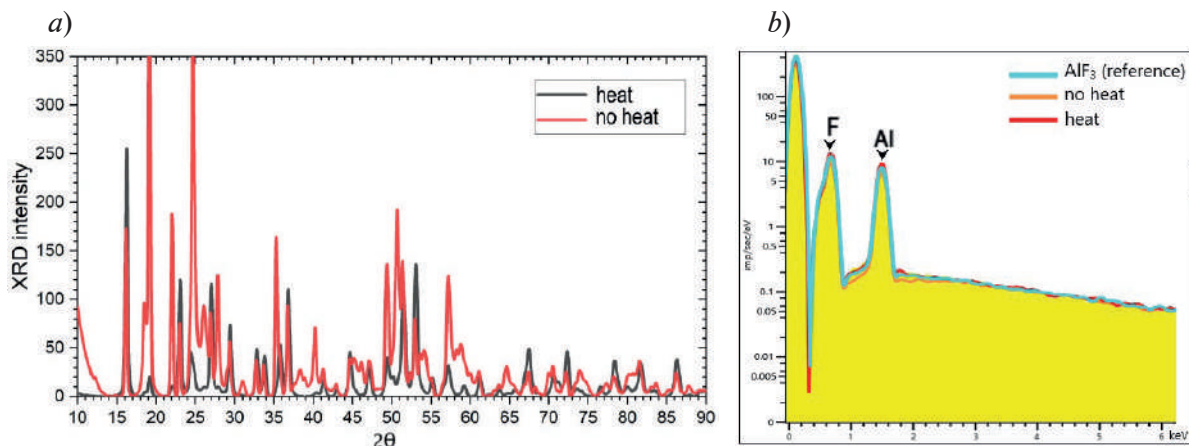
Fig. 2. XRD pattern of the synthesized samples (*a*). X-ray diffraction analysis data comparison for the synthesized samples (*b*)

However, the spectrum of the sample obtained under short-term heating requires further study. The peaks in the region of $20-30°$ (2θ) correspond to the crystalline phases of AlF_3. Rapid precipitation could have led to amorphous phases, which is reflected in the peak broadening. It is also noteworthy that no significant differences in the Al:F ratio of the obtained samples were detected by X-ray spectroscopy (Fig. 2, *b*).

Conclusion

This work demonstrates that short-term heating during synthesis significantly alters the morphology and crystallinity of AlF_3 microstructures, producing cushion-like formations. The rapid thermal treatment promotes crystalline AlF_3 formation, while room-temperature conditions yield hydrated rosenbergite, as confirmed by XRD analysis. The observed structural differences highlight the crucial role of temperature in controlling nucleation kinetics and material properties. Obtained results provide valuable insights for engineering AlF_3 microstructures with tailored characteristics for advanced applications in electronics and nanotechnology.

REFERENCES

1. **Pandharkar R., Becker C., Budau J.H., Kaawar Z.,** Paulus B., A Computational Study of AlF_3 and ACF Surfaces, Inorganics 6.4 (2018) 124.

2. **Vergara L.I., Vidal R., Ferron J.,** Electron induced reduction on AlF_3 thin film. Appl. Surf. Sci. 229 (2004) 301.

3. **Daniel P., Bulou A., Rousseau M., Nouet J., Fourquet J.L., Leblanc M., Burriel R.,** A study of the structural phase transitions in AlF_3: X-ray powder diffraction, differential scanning calorimetry (DSC) and Raman scattering investigations of the lattice dynamics and phonon spectrum, Journal of physics: Condensed matter. 2 (26) (1990) 5663.

4. **Dautov A.M., Lendyashova V., Shugabaev T., Khafizova A.M., Kotlyar K.P.,** Growth and properties of microstructures based on aluminum fluoride, In 2024 International Conference Laser Optics (ICLO) IEEE. (2024) 352–352.

5. **Soshnikov I.P., Kotlyar K.P., Reznik R.R., Gridchin V.O., Lendyashova V.V., Vershinin A.V., Lysak V.V., Kirilenko D.A., Bert N.A., Cirlin G.E.,** Specific features of structural stresses in InGaN/GaN nanowires, Semiconductors. 55 (10) (2021) 795–798.

6. **Clos D.P., Nekse P., Johnsen S.G., Aune R.E.,** Investigation on scale formation in aluminium industry by means of a cold-finger, Light Metals, Springer International Publishing. (2019).

THE AUTHORS

DAUTOV Albert M.
amdautov24@gmail.com
ORCID: 0000-0002-0374-7033

FEDOROV Vladimir V.
fedorov_vv@spbstu.ru
ORCID: 0000-0001-5547-9387

KOTLYAR Konstantin P.
kopkot95@yandex.ru

LENDYASHOVA Vera V.
erilerican@gmail.com
ORCID: 0000-0001-8192-7614

SHUGABAEV Talgat
talgashugabaev@mail.ru
ORCID: 0000-0002-4110-1647

GRIDCHIN Vladislav O.
gridchinvo@gmail.com
ORCID: 0000-0002-6522-3673

SHTROM Igor V.
igorstrohm@mail.ru
ORCID: 0000-0001-8912-2570

SIBIREV Nikolai V.
nicksibirev@yandex.ru
ORCID: 0000-0002-7566-2522

Control over the Stöber silica particles size within two orders of magnitude by tailoring the nucleation

D.V. Volodina [1] ✉, Z.S. Balysh [1], D.A. Eurov [1], D.A. Kurdyukov [1], E.Yu. Stovpiaga [1]

[1] Ioffe Institute, St. Petersburg, Russia

✉ dasha13129@gmail.com

Abstract. A panoscopic approach for governing the size of Stöber silica particles over a wide length scale, from tens of nanometers to several microns has been suggested. Low-size particles (10−400 nm) are obtained by changing the silica precursor, mid-size particles (0.4−0.7 mm) are synthesized with variation of ammonia concentration, large particles (up to 4 mm) are made by successive growth method.

Синтез по методу Штобера частиц кремнезема контролируемого размера, варьируемого в пределах двух порядков

Д.В. Володина [1] ✉, З.С. Балыш [1], Д.А. Еуров [1], Д.А. Курдюков [1], Е.Ю. Стовпяга [1]

[1] Физико-технический институт им. А.Ф. Иоффе РАН, Санкт-Петербург, Россия

✉ dasha13129@gmail.com

Аннотация. Предложен универсальный подход для управления размером частиц кремнезема, синтезируемых по методу Штобера, в широком диапазоне размеров − от десятков нанометров до нескольких микрон. Частицы малого размера (10−400 нм) получены путем замены кремниевого прекурсора, частицы среднего размера (0.4−0.7 мкм) синтезированы за счет варьирования концентрации аммиака, крупные частицы (до 4 мкм) получены методом послойного доращивания.

Introduction

Spherical silica particles (SSPs) are one of the most important and widely used materials in many advanced applications, such as catalysis, chromatography, sensor technology, photonics, and biomedicine [1−5]. Monodisperse SSPs are used, in particular, for the fabrication of opal-like photonic crystals [6], whose pores are filled with various semiconductor materials for optical contrast enhancement [6, 7]. Traditionally SSPs are synthesized by hydrolysis of orthosilicic acid ethers, such as tetraethoxysilane (TEOS), in the C_2H_5OH-H_2O-NH_3 media (the Stöber−Fink−Bohn (SFB) method [8]). The diameter of spherical particles prepared by the SFB method depends on together with temperature, the concentrations of TEOS [9, 10], H_2O [8] and NH_3 [8] in a reaction mixture. A doubling in the concentration of each reagent leads to an approximately twofold enlargement of the SSP diameter [8, 10, 11]. To obtain the particles with the sizes over 1 μm the successive growth method is applied [12]. To vary the size of SSP in a wide range (up to an order of magnitude), it is often necessary to substantially modify the synthesis procedure. As a result, the conditions for obtaining the particles with the sizes of tens and hundreds of nanometers vary significantly, which raises technological problems [10, 11]. The goal of this work was to develop an approach to the synthesis of SSPs that would allow varying their sizes in a wide range (from tens of nanometers to several microns) through minimal changes of the synthesis parameters.

Materials and Methods

Materials. TEOS, $Si(OC_2H_5)_4$, 99+% (Acros), 3-methacryloxypropyltrimethoxysilane (MPTMOS), $C_{10}H_{20}O_5Si$, 98+% (Aldrich); aqueous ammonia (NH_3), 24% wt., ≥ 99.99%; ethanol (C_2H_5OH), 95% wt.; deionized water (H_2O) 10 MΩ. TEOS was subjected to fractional distillation collecting a fraction with boiling temperature $T_b = 166−168$ °C.

Methods. SSPs were synthesized via basic hydrolysis of TEOS (or TEOS+MPTMOS) in a H_2O-NH_3-C_2H_5OH mixture (1 L) at 30 °C. We performed three sets of syntheses. The ratio of the reagent concentrations (TEOS:NH_3:H_2O) in the first set was 0.18 : 1.8 : 9 mol L^{-1}, respectively. A part (0−12.5 % mol.) of the silica precursor TEOS was replaced by MPTMOS. In the second set only ammonia concentration was varied in the range 1.8−3.5 mol L^{-1}. A successive growth method was used to obtain the particles with the sizes over 700 nm. For this purpose, 5-g portions of TEOS were added every 10 min to 1 L of NH_3 : H_2O : C_2H_5OH (3.4 : 9 : 14 mol L^{-1}, respectively) mixture containing 1 g of 720 nm SSPs. The obtained particles were centrifuged, dried, and annealed in air for 2 h at 500 °C.

Particle size distribution (PSD) of synthesized SSPs was determined by dynamic light scattering (DLS) at 25 °C with the use of a Malvern Zetasizer Nano analyzer. The PSD was calculated using the built-in analyzer software. Transmission electron microscopic measurements (TEM) were performed using a Jeol JEM-2100F microscope (accelerating voltage 200 kV, point-to-point resolution 0.19 nm). Large particles were additionally studied using an optical microscope.

Results and Discussion

The mechanism of SSPs formation is based on the aggregative model of the particle growth and lies in the fact that TEOS hydrolysis is occurred in the reaction mixture of H_2O-NH_3-C_2H_5OH under intensive stirring with the formation of the initial SiO_2 particles of several nanometers in size, which then coagulate into submicron spherical aggregates. The formation, growth rate and the final size of SSPs directly depends on the conditions chosen. Fig. 1 shows the values of the synthesized particles diameters depending on the synthesis parameters. The size of the particles was determined by TEM, DLS (for D < 1.5 μm) and optical microscopy (for D > 2 μm).
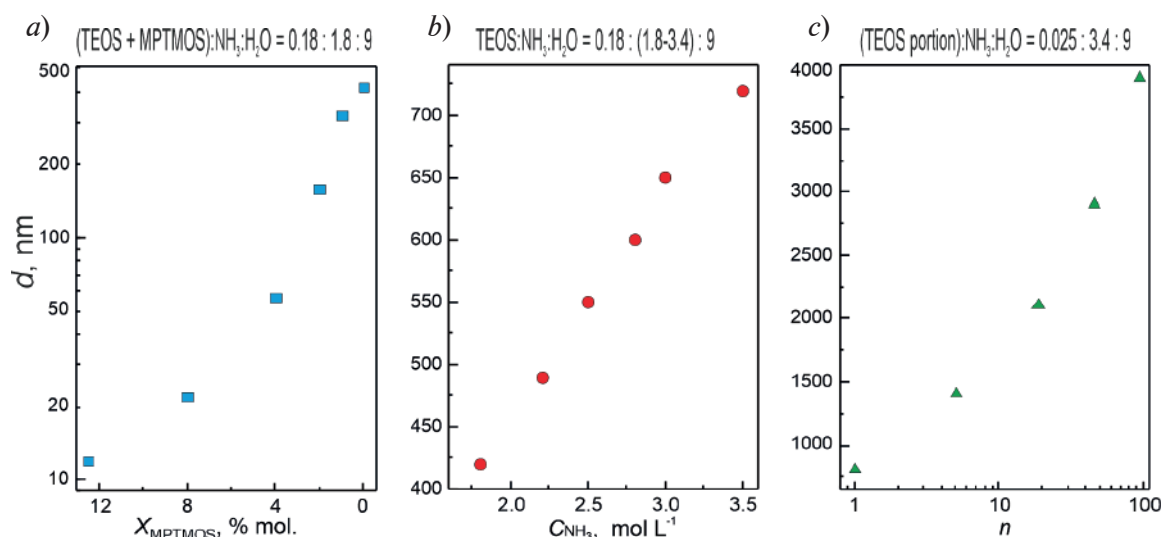
Fig.1 Dependence of particle diameter on: MPTMOS content in organosilane precursor (*a*); ammonia content in the reaction mixture (*b*); number of successive growth runs (*c*). The main synthesis parameters are shown above the panels

It can be seen (Fig.1, *a*) that an increase of the final size of the particles obtained by at least an order of magnitude can be achieved by reducing MPTMOS content (X_{MPTMOS}) in the mixture of organosilanes. In Ref. [11], the mechanism by which MPTMOS affects the particle nucleation process was considered. The MPTMOS molecule has, compared with TEOS one, only three, rather than four, alkoxy groups subject to hydrolysis, the methacryloyloxypropyl group is not hydrolyzed. In the TEOS molecule, the electron density is uniformly distributed among the silicon atom and oxygen atoms. In turn, silicon is bonded in the MPTMOS molecule to a carbon atom, instead of the fourth oxygen atom, which leads to a shift of the electron density (the electronegativities of C and O are 5.2 and 8.1, respectively) and to a larger effective negative charge on three oxygen atoms of methoxy groups. This increased charge on oxygen atoms hinders the deprotonation of hydrolyzed monomers. As a result, the joint hydrolysis of TEOS + MPTMOS leads to a larger content of electroneutral (with respect to those ionized) orthosilicic acid monomers that can form siloxane bonds and, accordingly, nucleate as compared with a reagent mixture containing only TEOS. As X_{MPTMOS} is reduced from 12.5 to 0 % mol., the number of nucleation centers becomes
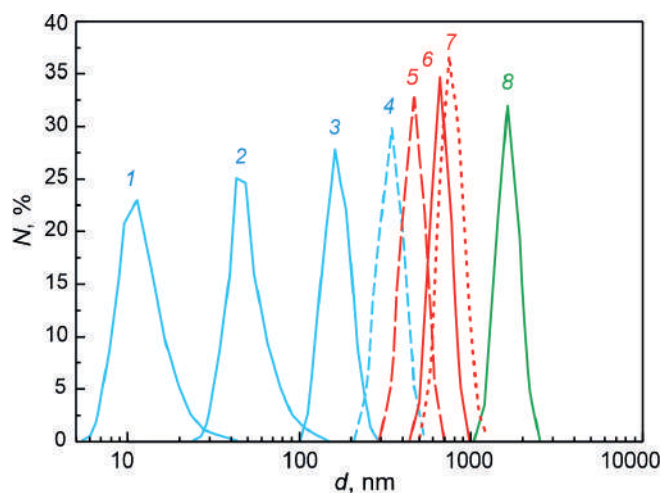
Fig.2 Particle size distribution (by number) measured by DLS method. (*1−4*) SSPs synthesized at NH_3 concentration of 1.8M and variable MPTMOS content in organosilane precursor: (*1*) − 12.5 % mol., (*2*) 4 % mol., (*3*) 2% mol., (*4*) 1% mol.; (*5−7*) SSPs synthesized using TEOS as silica precursor and variable NH_3 concentration: (*5*) 1.8M, (*6*) 2.5M, (*7*) 3.4M. (*8*) SSPs obtained by successive growth of 720 nm nuclei at NH_3 concentration of 3.4M (5 TEOS portions were added)

four to five orders of magnitude lower [11], which leads, at a constant precursor concentration, to a larger particle size. As a result, at the same total content of precursor and as amount of MPTMOS in the TEOS + MPTMOS mixture is reduced from 12.5 % to 0 mol., the final size of the resulting SiO_2 particles increases from ~10 nm to ~400 nm (Fig. 1, 2). SSPs, synthesized at low MPTMOS content, have low size deviation (Fig. 2 curves *3−4*) and remain spherical (Fig. 3, *b*, *c*). The results of DLS measurements (Fig. 2) correlate with TEM data (Fig. 3).
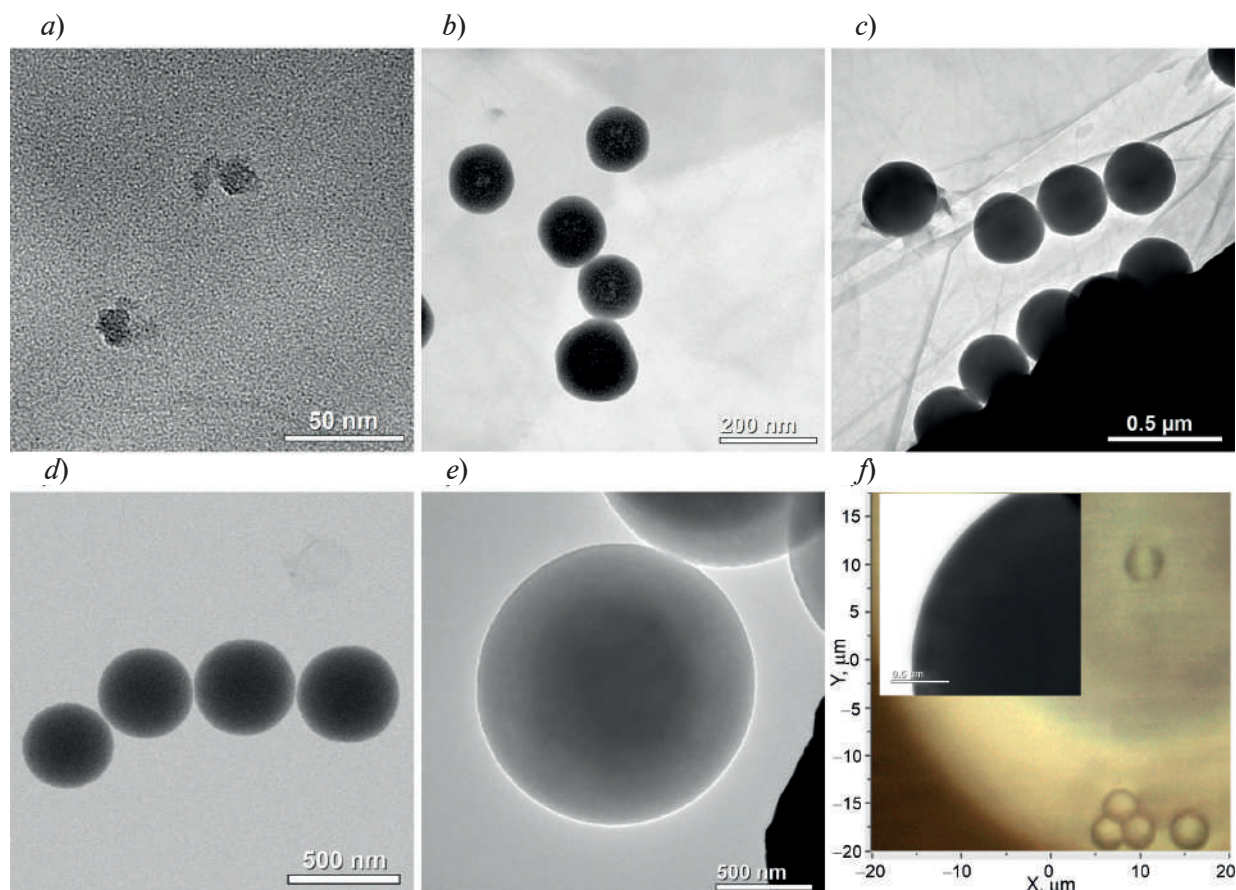
Fig.3 TEM (*a−e*, *f* (*inset*)) and optical microscopy (*f*) images of the particles obtained. (*a−d*) SSPs synthesized at NH_3 concentration of 1.8M and variable MPTMOS content in organosilane precursor: (*a*) − 12.5 % mol., (*b*) 2 % mol., (*c*) 1% mol., (*d*) 0 % mol. (*e–f*) SSPs obtained by successive growth of 720 nm nuclei at NH_3 concentration of 3.4M: (*e*) 5 growth runs; (*f*) 95 growth runs were done

Ammonia in the reaction mixture act as a catalyst of the TEOS hydrolysis reaction. As the ammonia concentration increases the rate of TEOS hydrolysis and condensation of its products increase as well, which leads to a fast formation and growth of SSP. In this case new nucleation centers are not formed − they appear and dissolve [13]. When the ammonia concentration is increased in our reaction mixture from 1.8 to 3.5 mol L^{-1} the diameter of particles increases from ~400 to ~700 nm (Fig. 1, *b*, Fig. 2, Fig. 3). Note, at higher ammonia concentration the particles obtained possess the lowest root-mean-square deviation of the sizes (< 4 %), spherical shape and low surface roughness of a few nanometers (Fig. 3, *d*).

We used a successive growth method to obtain particles with the sizes over 700 nm. Portions of TEOS (5 g) were added every 10 min to 1 L of ammonia-water-alcoholic mixture containing 1 g of 720 nm SSPs. TEOS hydrolysis products were concentrated in the vicinity of the submicron particle surface and coated the particles with a layer of hydrated a-SiO_2 and, hence, providing their further growth. Ammonia concentration was 3.4 mol L^{-1} in the reaction mixture in order, first, to reduce the duration of the TEOS hydrolysis process to 10 min and, second, to prevent the formation of new nucleation centers [9, 12]. It can be seen (Fig. 1, *c*), that after addition of 5 TEOS portions the particle diameter doubled, 20 portions − tripled, and after addition of

95 portions the diameter increases up to ~4 µm. Fig. 3, *e*, *f* demonstrates that the particles are covered with a uniform SiO$_2$ layer as a result of TEOS portions addition, they have smooth surface and the root-mean-square deviation of the sizes does not exceed 10%.

Conclusion

An approach has been developed to one-pot synthesis of spherical silica particles which allows controlling over the size of the particles in the wide range 10–4000 nm. The proposed approach is based on the governing the nucleation process within the reaction mixture by either varying the number of nuclei within five orders of magnitude by changing the concentrations of MPTMOS and ammonia or its forced suppression in the case of successive growth of the artificially added nucleation centers. It has been shown that by sequentially varying just one parameter of the reaction mixture − the composition of the silicon precursor, the concentration of ammonia or the number of additional portions of TEOS, it is possible to controllably change the final size of the resulting particles within two orders of magnitude in a single technological cycle.

Acknowledgments

REFERENCES

1. **Ghimire P.P., Jaroniec M.,** Renaissance of Stöber method for synthesis of colloidal particles: New developments and opportunities, Journal of Colloid and Interface Science. 584 (2021) 838−865.

2. **Gao W., Rigout M., Owens H.,** Facile control of silica nanoparticles using a novel solvent varying method for the fabrication of artificial opal photonic crystals, Journal of nanoparticles Research. 18 (2016) 387.

3. **Huang Y., Li P., Zhao R., Zhao L., Liu J., Peng S., Fu X., Wang X., Luo R., Wang R., Zhang Z.,** Silica particles: Biomedical applications and toxicity, Biomedicine and Pharmacotherapy. 151 (2022) 112053.

4. **Walcarius A.,** Silica-based electrochemical sensors and biosensors: Recent trends, Current Opinion in Electrochemistry. 10 (2018) 88−97.

5. **Ren X., Cao E., Lin W., Song Y., Liang W., Wang J.,** Recent advances in surface plasmon-driven catalytic reactions, RSC Advanced. 7 (50) (2017) 31189−31203.

6. **Galisteo-Lypez J.F., Ibisate M., Sapienza R., Froufe-Pérez L.S., Blanco Б., Lypez C.,** Self-assembled photonic structures, Advanced Materials. 23 (2011) 30−69.

7. **Bogomolov V.N., Golubev V.G., Kartenko N.F., Kurdyukov D.A., Pevtsov A.B., Prokof'ev A.V., Ratnikov V.V., Feoktistov N.A., Sharenkova N.V.,** Fabrication of regular three-dimensional lattices of submicron silicon clusters in an SiO$_2$ opal matrix, Technical Physics Letters. 24 (4) (2017) 326−327.

8. **Stöber W., Fink A., Bohn E.,** Controlled growth of monodisperse silica spheres in the micron size range, Journal of Colloid and Interface Science. 26 (1) (1968) 62−69.

9. **Masalov V.M., Aldushin K.A., Dolganov P.V., Emel'chenko G.A.,** SiO$_2$-microspheres ordering in 2D structure, Physics of Low − Dimensional Structures. 5−6 (2001) 45−54.

10. **Santamaria Razo D.A., Pallavidino L., Garrone E., Geobaldo F., Descrovi E., Chiodoni A., Giorgis F.,** A version of Stöber synthesis enabling the facile prediction of silica nanospheres size for the fabrication of opal photonic crystals, Journal of Nanoparticle Research. 10 (2008) 1225–1229.

11. **Eurov D.A., Kirilenko D.A., Kurdyukov D.A.,** Nucleation of silica Stöber particles in the presence of methacryloxypropyltrimethoxysilane, Colloid Journal. 79 (2017) 56−60.

12. **Grudinkin S.A., Feoktistov N.A., Trofimova E.Yu., Kurdyukov D.A., Bogdanov K.V., Baranov A.V., Fedorov A.V., Golubev V.G.,** Spherical microresonators with luminescent a-Si:C:H coating, Technical Physics Letters. 39 (4) (2013) 341−343.

13. **Matsoukas T., Gulari E.,** Dynamics of growth of silica particles from ammonia-catalyzed hydrolysis of tetra-ethyl-orthosilicate, Journal of Colloid and Interface Science. 124 (1) (1988) 252−261.

THE AUTHORS

VOLODINA Daria V.
dasha13129@gmail.com
ORCID: 0009-0009-4336-0712

BALYSH Zoya S.
balyshzoe@gmail.com
ORCID: 0009-0001-1698-9162

EUROV Daniil A.
edan@mail.ru
ORCID: 0000-0002-7471-4028

KURDYUKOV Dmitry A.
kurd@gvg.ioffe.ru
ORCID: 0000-0002-3041-9609

STOVPIAGA Ekaterina Yu.
kattrof@gvg.ioffe.ru
ORCID: 0000-0003-0434-5252

Effect of synthesis modes on the properties of microarc oxide coatings

M.D. Novichkov [1] ✉, S.A. Gurin [2], A.E. Shepeleva [2], E.A. Pecherskaya [1],

P.E. Golubkov [1], A.A. Maksov [1], D.V. Agafonov [2]

[1] Penza State University, Penza, Russia;

[2] Joint Stock Company "Research Institute of Electronic and Mechanical Devices",
Penza, Russia

✉ novichkov1998maks@gmail.com

Abstract. The article presents studies of the physical patterns of formation of oxide coatings on aluminum substrates by microarc oxidation. Correlation dependences of the influence of technological modes, such as current density and time, on the properties of microarc oxidation coatings have been established. A method for monitoring the quality parameters of formed oxide coatings in real time is proposed, based on the analysis of the deviation of the voltage−time curves from the traditional piecewise linear form. The results of the study can be used in the development of intelligent algorithms for creating a digital twin of the microarc oxidation process.

Keywords: microarc oxidation, oxide coating, coating parameters, controlled synthesis, technological modes

Исследование влияния режимов синтеза на свойства микродуговых оксидных покрытий

М.Д. Новичков [1] ✉, С.А. Гурин [2], А.Э. Шепелева [2], Е.А. Печерская [1],

П.Е. Голубков [1], А.А. Максов [1], Д.В. Агафонов [2]

[1] Пензенский государственный университет, г. Пенза, Россия;

[2] АО «Научно-исследовательский институт электронно-механических приборов»,
г. Пенза, Россия

✉ novichkov1998maks@gmail.com

Аннотация. В статье представлены исследования физических закономерностей формирования оксидных покрытий на алюминиевых подложках методом микродугового оксидирования. Установлены корреляционные зависимости влияния технологических режимов, таких как плотность тока и время, на свойства покрытий, полученных

микродуговым оксидированием. Предложен метод контроля параметров качества формируемых оксидных покрытий в режиме реального времени, основанный на анализе отклонения формовочной кривой от традиционного кусочно-линейного вида. Результаты исследования могут быть использованы при разработке интеллектуальных алгоритмов для создания цифрового двойника процесса микродугового оксидирования.

Ключевые слова: микродуговое оксидирование, оксидное покрытие, параметры покрытия, контролируемый синтез, технологические режимы

Introduction

Microarc oxidation (MAO) is a plasma−chemical method of hardening valve metals, which synthesizes coatings with high microhardness (up to 25 GPa), wear resistance, corrosion resistance, electrical strength and heat resistance, and at the same time has good adhesion to the substrate, which contributes to the widespread use of the method in various industries [1, 2]. However, the spread of microarc oxidation technology Production is still limited due to insufficient fundamental study of the coating forming process. There is no single systematic assessment of the effect of technological conditions on the properties of coatings made of valve metals and their alloys [3, 4]. This leads to difficulties in choosing optimal technological modes that take into account many different factors, which reduces the quality of coatings and complicates the management of the technological process [5].

Materials and Methods

To form the MAO coatings, a galvanic cell with an anode (aluminum billet AD31T1 measuring 23×15×1.5 mm) and a stainless steel cathode was used, to which a process current source was connected via a current line made of aluminum wire insulated with a polyolefin heat shrink tube. For the purity of the experiment, the surface of the samples was preliminarily adjusted to a roughness of Ra ≈ 0.1...0.2 microns. The oxidation was performed in the anode-cathode mode with the ratio of anode and cathode current equal to 1. Studies of the patterns of the MAO process, the development and debugging of new technological modes were carried out by registering the voltage−time curves. The parameters of the microarc oxidation process are shown in Table.

T a b l e

Parameters of the MAO process

#	Na_2SiO_3, g/l	NaOH, g/l	current density, A/dm^2
1	50	0.5	10
2	25	0.5	50
3	25	0.5	25
4	25	0.5	10
5	40	0.5	5
6	30	0.5	5

Results and Discussion

The voltage−time curves of the samples obtained under different modes of the microarc oxidation process are shown in Fig. 1.
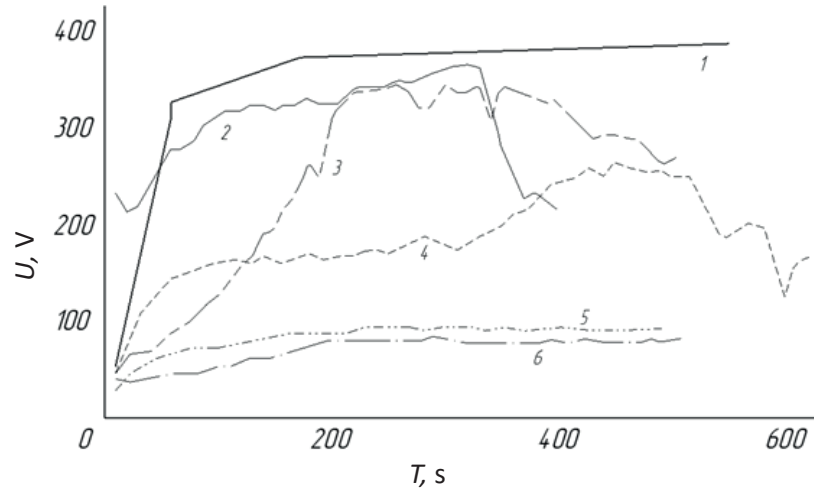
Fig. 1. The voltage−time curves

Analyzing the forming curves, the following factors can be established that affect the quality of the coating being formed:

− destruction of the coating by powerful arc discharges (curve *2*) due to too high current density;

− low rate of increase in forming voltage at the beginning of the process and a rapid transition to the stage of arc discharges (curve *3*);

− low forming voltage (curves *4−6*). At the same time, for curves *4−6*, the process did not enter the stage of spark discharges and was only electrochemical in nature.

High-quality MAO coverage was obtained according to the modes corresponding to curve *1*.

Thus, it can be concluded that a piecewise linear curve can serve as a reliable sign of the formation of a high-quality coating. The structure of the coatings was studied on a VEGA 3 scanning electron microscope using SBH surface topography. The results of the analysis are shown in Fig. 2.
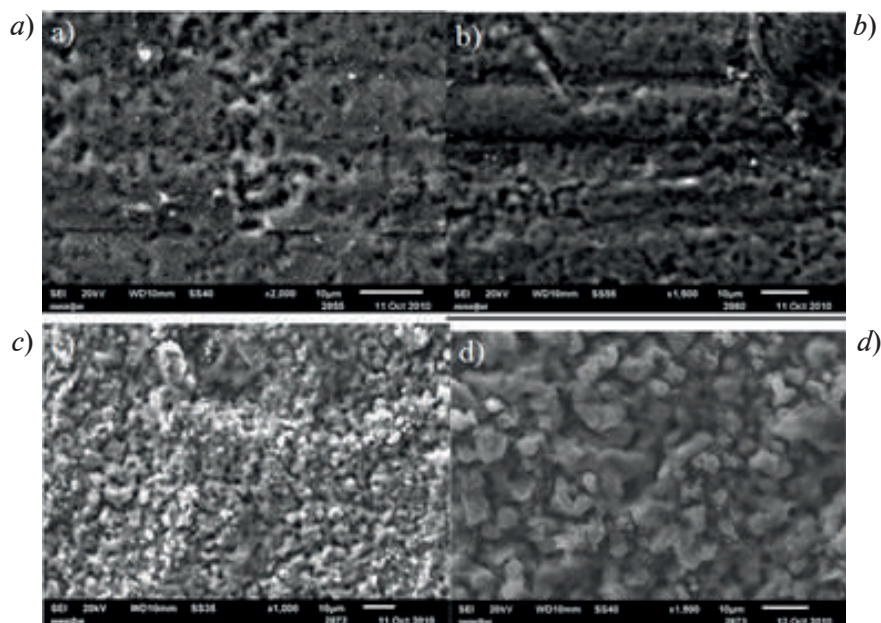
Fig. 2. MAO coating in various stages of oxidation: 60 s (*a*); 120 s (*b*); 240 s (*c*); 480 s (*d*)

From those shown in Fig. 2 images of the surface of MAO coatings, it can be seen that with an increase in the processing time of aluminum plates, the surface development increases, the size and number of pores increase. Thus, we can talk about the layering of the resulting ceramic coating. Also, the image taken after the minimum processing time shows that the coating is not porous and repeats the structure of the substrate. Such a coating can be attributed to the basic adhesive sublayer. Further exposure time leads to the appearance of small pores, the coating structure gradually develops. Such layers have a well-developed structure. At the last stage, the fourth sample has a highly porous structure.

The study of surface roughness was carried out on a Mitaka FS150 3d laser conturograph profilometer. Examining the values of the arithmetic mean of the absolute values of the profile deviations within the base length Ra, it turns out that after the minimum processing time, before the start of the spark discharge stage, they are within 0.1 ...0.3 microns. This indicates that the coating at the initial stages of growth repeats the structures of the substrates, since the surface roughness of the samples was adjusted to the same values. As the time of the MAO process increases, the roughness gradually increases due to an increase in porosity and the development of relief. The data shows values in the range of 0.4...0.7 microns.

To assess the effect of current density, a sample was made in the same electrolyte, but at a current density of 15 A/dm^2. Micrographs of the sample taken at various processing stages are shown in Fig. 3.
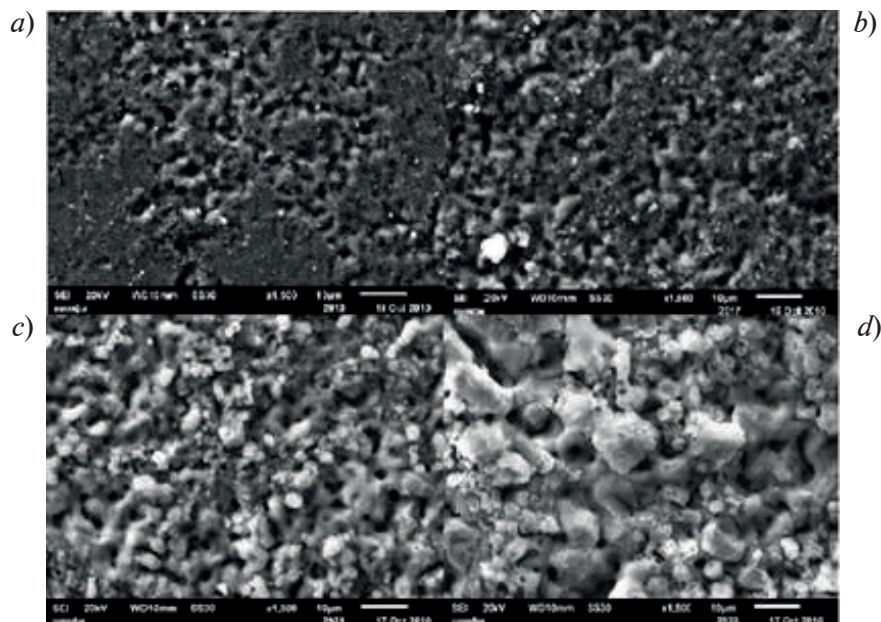
Fig. 3. MAO coating at a current density of 15 A/dm^2 at various stages of oxidation: 60 s (*a*); 120 s (*b*); 240 s (*c*); 480 s (*d*)

Based on the image obtained, it can be concluded that an increase in current density to 15 A/dm^2 leads to an even more complex surface development and an increase in porosity, which is associated with a higher power of microarc discharges and increased dissolution processes in the cathode half-life. This is also confirmed by roughness measurements, according to which the arithmetic mean is Ra = 1 micron.

Conclusion

The forming curves of all the samples are shown on the slide and they all have a piecewise linear appearance. The above makes it possible to establish a quality criterion for MAO coatings, which can be used for an express assessment of the suitability of the technological regime in production conditions: the coating will be of inadequate quality if the voltage−time curves has a distorted shape.

The formed MAO coatings obtained according to these methods can be characterized as multilayer, consisting of a base adhesive layer, an intermediate porous layer and a highly porous layer with a developed surface microstructure.

REFERENCES

1. **Shirani A., Joy T., Aouadi S.M.,** PEO-Chameleon as a potential protective coating on cast aluminum alloys for high-temperature applications, Surface and Coatings Technology. (397) (2020) 126016.

2. **Sivkov A., Shanenkova Y., Vympina Y.,** Deposition of copper coatings on internal aluminum contact surfaces by high-energy plasma spraying, Surface and Coatings Technology. (440) (2022) 128484.

3. **Pecherskaya E.A., Konovalov S.V., Semenov A.D.,** Simulation of the Electrical Parameters of Microarc Oxide Coatings Using the Matrix-Operator Method, J. Surf. Investig. (18) (2024) 551−556.

4. **Rui Yao, Yang Li, Zhongping Yao,** Peng Zhang, Songtao Lu, Xiaohong Wu, Black PEO coating with enhanced thermal stability on titanium alloy and its thermal control properties, Surface and Coatings Technology. (429) (2022) 127934.

5. **Clyne T.W., Troughton S.C.,** A review of recent work on discharge characteristics during plasma electrolytic oxidation of various metals, International Materials Reviews. 64 (2019) 127–162.

THE AUTHORS

NOVICHKOV Maksim D.
novichkov1998maks@gmail.com
ORCID: 0000-0001-9319-2475

GOLUBKOV Pavel E.
golpavpnz@yandex.ru
ORCID: 0000-0002-4387-3181

GURIN Sergey A.
teslananoel@rambler.ru
ORCID: 0000-0001-9602-7221

MAKSOV Andrey A.
maksov.01@mail.ru
ORCID: 0009-0001-4255-1383

SHEPELEVA Anastasiya E.
anastasiya.shepeleva.01@mail.ru
ORCID: 0000-0002-8600-084X

AGAFONOV Dmitry V.
dmitryagafonov@list.ru
ORCID: 0009-0009-4548-3724

PECHERSKAYA Ekaterina A.
pea1@list.ru
ORCID: 0000-0001-5657-9128

BIOPHYSICS AND MEDICAL PHYSICS

The effect of femtosecond laser on DNA destruction assisted with SYTO fluorescent dye

A.D. Zalessky [1] ✉, A.A. Osychenko [1]

[1] N.N. Semenov Federal Research Center for Chemical Physics RAS, Moscow, Russia

✉ aleksandr.zalesskij@phystech.edu

Abstract. Tightly-focused femtosecond laser radiation is widely used as a convenient tool for manipulating biological objects. The method of femtosecond laser surgery proved to be useful for the multiple applications, from eye correction to the subcellular structures destruction. Among other things, femtosecond laser surgery shown to be used as a tool for DNA destruction, which could be beneficial for assisted reproductive technologies in humans. In the context of the development of this method, the study of the DNA laser assisted destruction efficiency is of significant importance. In this work, DNA laser assisted destruction efficiency in presence of SYTO fluorescent dye was studied.

Исследование разрушения ДНК при помощи фемтосекундного лазерного излучения в присутствии флуоресцентного красителя SYTO

А.Д. Залесский [1] ✉, А.А. Осыченко [1]

[1] Федеральный исследовательский центр химической физики им. Н.Н. Семенова РАН, Москва, Россия

✉ aleksandr.zalesskij@phystech.edu

Аннотация. Узконаправленное, сфокусированное фемтосекундное лазерное излучение широко используется как удобный инструмент для манипуляции биологическими объектами. Метод фемтосекундной лазерной хирургии оказался полезным для множества приложений, от коррекции зрения до разрушения субклеточных структур. Среди прочего, фемтосекундная лазерная хирургия продемонстрирована в качестве инструмента для разрушения ДНК, что может быть полезным для вспомогательных репродуктивных технологий. В контексте разработки этого метода изучение эффективности разрушения ДНК лазером является необходимым этапом. В данной работе была исследована эффективность разрушения ДНК лазером в присутствии флуоресцентного красителя SYTO.

Introduction

Near-infrared femtosecond laser radiation has recently proved to be a low-invasive and high-precision tool for manipulating biological objects. Through the focusing of femtosecond laser pulses with the microscope objectives of a high numerical aperture, highly localized biomaterial destruction on a submicron resolution level could be achieved (so called nanosurgery technique). Nanosurgery can be applied to perform operations inside living cells without damaging their integrity − in particular, to destroy DNA, that is, to perform enucleation. This approach has specific practical applications, for example, the preparation of recipient cytoplast for assisted reproductive technologies in humans and animal cloning. We have previously shown that using a femtosecond laser, mouse and human oocytes can be successfully enucleated [1, 2]. We have previously shown that femtosecond laser enucleation of mouse oocytes can be effectively performed using the fluorescent dye Hoechst 33342. The fluorescence spectrum of this dye is in the blue region of the spectrum (max. 454 nm), and ultraviolet light (max. 342 nm) is required for its excitation. In this work, possibility of using another dye with visible excitation was considered.

Materials and Methods

Animals and oocyte collection. The study was carried out on C57BL6/CBA female mice aged 6−8 weeks (Mus musculus). The mice were induced to superovulate by the standard method of intraperitoneal (i.p.) injection of 10 IU pregnant mare's serum gonadotropin (A036A02, Intervet) followed by an i.p. injection of 10 IU human chorionic gonadotropin (hCG) (A038A01, Intervet) 48 h later. The mice were sacrificed by cervical dislocation 17 h after hCG injection. The oviducts were placed onto a Petri dish in a drop of M2 medium (M7167, Sigma-Aldrich) supplemented with 0.1% hyaluronidase (H4272, Sigma-Aldrich). The ampulla of the oviduct was disrupted with a pair of thin tweezers. The oocytes purified from cumulus were placed in M2 in four-well dishes (179830, Nunc). We used metaphase II oocytes in the experiments.

Fluorescence measurement. The oocytes were stained in M2 medium at a dye concentration of 1 μM for 30 minutes, then washed twice in a clean medium. The fluorescence of SYTO 9 was excited at wavelengths of 430−490 nm. The oocytes were stained with 5 μg/ml Hoechst 33342 dye (B2261, Sigma-Aldrich) for 15 minutes in M2 and then washed twice. Single-photon excitation of Hoechst was performed with the 405 nm laser wavelength. The fluorescence intensity of oocytes DNA was measured on a confocal microscope Zeiss LSM 980 (Carl Zeiss Microscopy, Jena, Germany), 20x Plan-Apochromat objective (NA = 0.8).

Femtosecond laser treatment. Enucleation was performed at a wavelength of 900 nm, femtosecond laser pulse duration was 100 fs, pulse energy 3 nJ, and bursts of 50 ns with a pulse repetition frequency of 3 MHz were selected from the initial pulse sequence of 80 MHz using a modulator built into the laser. The selected wavelength of femtosecond laser radiation is due to the fact that it corresponds to 450 nm during a two-photon absorption process, which in turn falls into the absorption spectrum of the fluorescent dye SYTO 9 (Fig. 1).

In the experiment, a metaphase plate was first visualized, then it was irradiated with femtosecond laser pulses until the fluorescence stopped. After that, a control staining with a spectrum-contrasting dye (Hoechst 33342) was performed and the samples were visualized on a confocal microscope in order to identify the remnants of the metaphase plate after enucleation.
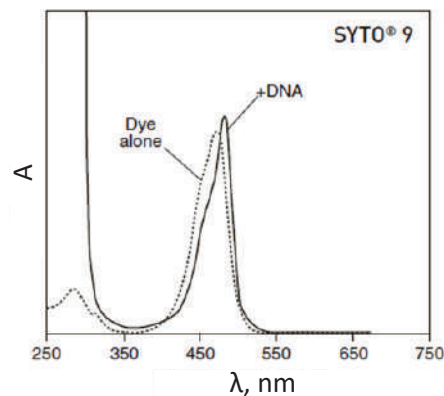
Fig. 1. The excitation and absorption spectrum of the dye SYTO 9 (S34854, Molecular probes)

Results and Discussion

As an alternative to the previous studies were we used Hoechst 33342 fluorescent dye, the vital fluorescent dye SYTO 9 (S34854, Molecular probes) was chosen, the absorption spectrum of which is shown in Fig. 1. Light with a wavelength of 400–500 is less phototoxic than UV, therefore, the use of this dye for enucleation may be less traumatic for the sample. We observed visible fluorescence from SYTO 9 dye during femtosecond laser treatment, which proves two-photon excitation of dye. Similar results were reported by Kwok et al on successful two-photon excitation of cyanine-based dyes [3].

When the metaphase plate of an oocyte stained with the vital fluorescent dye SYTO 9 is exposed to femtosecond laser radiation with a wavelength of 900 nm, two-photon processes occur, leading to the luminescence of the dye at the time of irradiation, as in the case of Hoechst. The femtosecond laser treatment was performed until this visible fluorescence stops − this could be due to photobleaching. Moreover, in case of SYTO 9 usage, DNA destruction practically does not occur − upon repeated staining, the metaphase plate is revealed almost unchanged, and the area of its detection after irradiation does not significantly differ from the area of detection before exposure (Fig. 2, *b*).
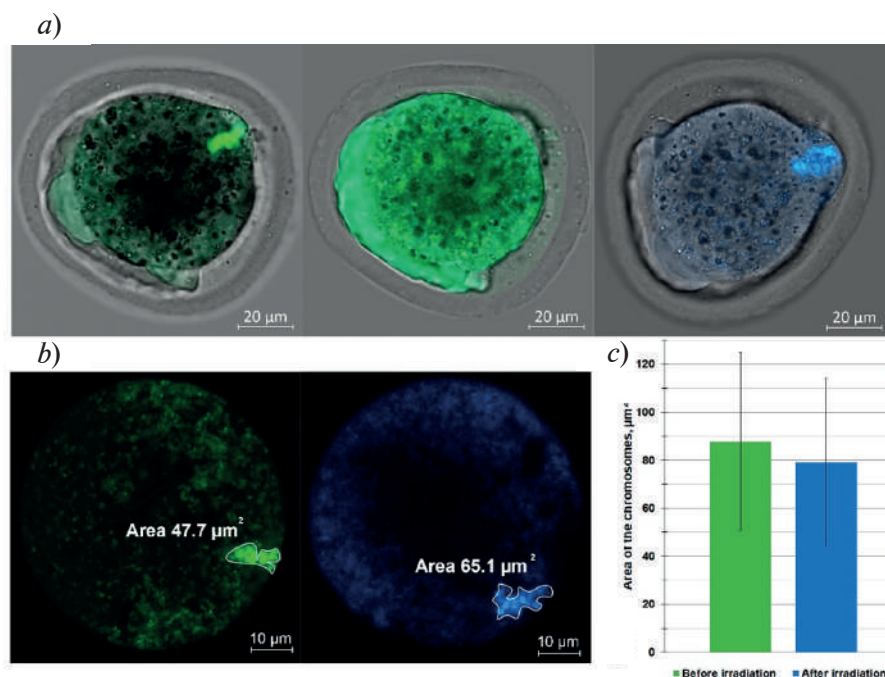
Fig. 2. In a row from left to right: oocyte before laser treatment, immediately after treatment, contrast staining with Hoechst 33342 (*a*); fluorescent image of oocyte SYTO before treatment, Hoechst 33342 after treatment (*b*); area of metaphase plate before and after treatment comparison (*c*)

The mechanism of DNA destruction mediated via fluorescent dye under femtosecond laser irradiation is not fully revealed yet. Mechanisms of DNA destruction by itself (without any additional reagents) under femtosecond laser irradiation are traditionally described through low-density plasma formation and resonant electron-molecule scattering [4, 5]. Additionally, reactive species produced upon the laser-induced lysis of water could be involved in DNA destruction and modification processes [6]. In our previous studies, we have shown that usage of fluorescent dye could decries amount of laser power density, required for DNA destruction [7] and for this reason we assume that fluorescent dye could be involved in processes of DNA destruction. In case of SYTO 9 usage, we think that the laser-induced lysis of water became less effective than in case of Hoechst 33342 dye usage, and so the production of reactive species declines. However, this hypothesis needs further investigation.

Conclusion

In this work, possibility of SYTO vital fluorescent dye usage for performing femtosecond laser-assisted metaphase plate enucleation of mouse oocyte was studied. We have shown that under femtosecond laser treatment photo bleaching of dye take place without significant DNA destruction. This result is quite interesting, considering that under similar laser parameters with only difference in wavelength (800 nm and 1033 nm) usage of Hoechst 33342 was efficient for DNA destruction. These results introduce new material for the model of femtosecond laser and biomaterial interaction.

Acknowledgments

REFERENCES

1. **Osychenko A.A., Zalessky A.D., Tochilo U.A., Martirosyan D.Yu., Silaeva Yu.Yu., Nadtochenko V.A.,** Femtosecond laser oocyte enucleation as a low-invasive and effective method of recipient cytoplast preparation, Biomedical Optics Express. 13 (3) (2022) 1447–1456.

2. **Osychenko A.A., Zalessky A.D., Bachurin A.V., Martirosyan D.Yu., Egorova M.S., Nadtochenko V.A.,** Stain-free enucleation of mouse and human oocytes with a 1033 nm femtosecond laser, Journal of Biomedical Optics. 29 (6) (2024) 065002.

3. **Kwok S.J., Choi M., Bhayana B., Zhang X., Ran C., Yun S.H.,** Two-photon excited photoconversion of cyanine-based dyes, Sci Rep. Mar 31. (6) (2016) 23866.

4. **Vogel A., Noack J., Hüttman G., Paltauf G.,** Mechanisms of femtosecond laser nanosurgery of cells and tissues, Applied Physics B. (81) (2005) 1015–1047.

5. **Zalessky A., Fedotov Y., Yashkina E., Nadtochenko V., Osipov A.N.,** Immunocytochemical Localization of XRCC1 and γH2AX Foci Induced by Tightly Focused Femtosecond Laser Radiation in Cultured Human Cells, Molecules. 26 (13) (2021) 4027.

6. **Belmouaddine H., Madugundu G.S., Wagner J.R., Couairon A., Houde D., Sanche L.,** DNA Base Modifications Mediated by Femtosecond Laser-Induced Cold Low-Density Plasma in Aqueous Solutions, J Phys Chem Lett. 10 (11) (2019) 2753–2760.

7. **Osychenko A.A., Zalessky A.D., Bachurin A.V., Martirosyan D.Y., Egorova M.S., Nadtochenko V.A.,** Stain-free enucleation of mouse and human oocytes with a 1033 nm femtosecond laser, J Biomed Opt. 29 (6) (2024) 065002.

THE AUTHORS

ZALESSKY Alexandr D.
aleksandr.zalesskij@phystech.edu

OSYCHENKO Alina A.
alina.osychenko@chph.ras.ru

Nanomaterials based on carbon framework for cells stimulation

U.E. Kurilova [1, 2] ✉, D.T. Murashko [2], V.V. Suchkova [1, 2], I.A. Suetina [3],

M.V. Mezentseva [3], L.I. Russu [3], A.Yu. Gerasimenko [1, 2]

[1] I.M. Sechenov First Moscow State Medical University, Moscow, Russia;

[2] National Research University of Electronic Technology, Zelenograd, Moscow, Russia;

[3] The National Research Center for Epidemiology and Microbiology named
after Honorary Academician N.F. Gamaleya, Moscow, Russia

✉ kurilova_10@mail.ru

Abstract. The work is devoted to the technology of formation and study of physical and chemical characteristics and biocompatibility of nanomaterials based on hybrid structures of carbon nanotubes and reduced graphene oxide, obtained by spray deposition and laser processing with nanosecond pulsed laser of 1064 nm wavelength, for bioelectronics applications. The formation of a connected structure between the components was proved with scanning electron microscopy, the optimal power of laser processing was found as 0.07 W to obtain the largest number of connections between carbon nanotubes and reduced graphene oxide, thanks to which high electrical conductivity was achieved. The experiments on electrical stimulation in vitro were provided with the developed setup based on a culture plate, an impulse generator and electrodes connected to samples. Cells seeded on the obtained structures with electrical stimulation demonstrate better proliferation and monolayer forming compared to the control sample. Thus, the developed structures can be successfully used as part of various bioelectronic devices for improved tissue recovery using electrical stimulation.

Keywords: carbon nanotubes, reduced graphene oxide, bioelectronics, fibroblasts, electrical stimulation

Наноматериалы на основе углеродного каркаса для стимуляции клеток

У.Е. Курилова [1, 2] ✉, Д.Т. Мурашко [2], В.В. Сучкова [1, 2], И.А. Суетина [3],

М.В. Мезенцева [3], Л.И. Руссу [3], А.Ю. Герасименко [1, 2]

[1] Первый Московский государственный медицинский университет
имени И. М. Сеченова, Москва, Россия;

[2] Национальный исследовательский университет «МИЭТ», г. Зеленоград, Москва, Россия;

³ Национальный исследовательский центр эпидемиологии и микробиологии
имени почетного академика Н.Ф. Гамалеи, Москва, Россия

✉ kurilova_10@mail.ru

Аннотация. Работа посвящена технологии формирования и исследованию наноматериалов на основе гибридных структур углеродных нанотрубок и восстановленного оксида графена, полученных методом напыления и лазерной обработки наносекундным импульсным лазером с длиной волны 1064 нм для применения в биоэлектронике. Доказано образование связанной структуры между компонентами, благодаря чему достигается высокая электропроводность. Эксперименты по электростимуляции in vitro показали, что клетки на структурированных лазером участках в совокупности с электростимуляцией демонстрируют лучшую пролиферацию и формирование монослоя по сравнению с контрольным образцом. Таким образом, разработанные структуры могут быть успешно использованы для создания чипов, стимулирующих ионные процессы жизнедеятельности клеток биологических тканей в составе различных биоэлектронных устройств.

Ключевые слова: углеродные нанотрубки, восстановленный оксид графена, биоэлектроника, фибробласты, электростимуляция

Introduction

Currently, such field of science as bioelectronics is actively developing. Bioelectronic devices can read signals and stimulate heart, nerve and other tissue regeneration through improved cell proliferation under the influence of electrical impulses [1, 2]. The electrical stimulation changes the transmembrane resting potential of the cells, which has a significant effect on cell functionality and cellular metabolism [3]. An important component of bioelectronic devices are electrically conductive biocompatible interfaces, which conduct efficiently ionic and electronic currents between soft biological tissues and electronic pulse generators [4].

Carbon nanomaterials are promising for flexible bioelectronics applications because they can conduct electrical signals with high resolution and signal-to-noise ratio [5]. These materials have high mechanical flexibility, stability, and tunable properties depending on their functionalization and treatment [6]. It is important to reveal patterns of structuring carbon nanotube systems to form chips that stimulate ionic processes in living cells and biological tissues. In our work we obtained and studied samples of carbon framework nanomaterials used as materials for stimulating connective tissue cells.

Materials and Methods

The process of forming was as follows. As the first step, homogeneous dispersed media were formed with single-wall carbon nanotubes (SWCNT), reduced graphene oxide (rGO), and combination of them to form hybrid structures. Then, up to 50 layers of these dispersions were applied layer by layer onto the surface of clean silicon wafers using the spray deposition method. After that, samples were irradiated with laser using the developed system shown on Fig. 1, *a*, based on a pulsed ytterbium laser with a wavelength of 1064 nm with moving the laser beam along a predetermined path over a sample; under the action of laser radiation, the liquid component evaporated and the nanotubes were oriented and connected for electrical conductivity increasing.

The obtained samples are shown on Fig. 1, *b*. The micro- and nanoarchitecture of the layers of the samples were evaluated with a scanning electron microscope.

Experiments were carried out on electrical stimulation of connective cells (fibroblasts) on the obtained samples with stimulation device based on a culture plate and electrodes connected to the samples. The cells were cultivated the first 24 hours without electrical stimulation, then stimulation was started and continued for 48 hours, after that the cells were stained with Hoechst 33342 and observed with a fluorescence microscope.
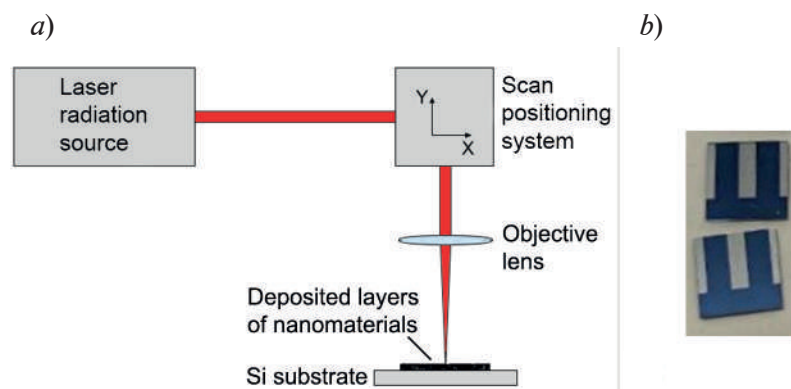

Fig. 1. The scheme of system for laser irradiation of samples (*a*), appearance of obtained samples (*b*)

Results and Discussion

It was found that carbon framework nanomaterials after laser structuring with a power of ≥ 0.07 W are characterized by the formation of bonds between components and branched structure due to photon-phonon interaction (Fig. 2, *a*, *b*). A further increase in the processing power leads to gradual destruction of the structure and the formation of areas with amorphous carbon.

The electrical conductivity of the obtained samples increased with increasing laser processing power, which is associated with the formation of a greater number of bonds between the nanotubes, the highest value obtained was 37.84 ± 1.16 mSm for irradiation power of 0.07 W (the initial value without radiation was 13.07 ± 0.71 mSm). With a further increase in power, the electrical conductivity decreases, which can be explained by the formation of an amorphous phase, which conducts the electrical signal poorly. Thus, by choosing the processing power, materials with different conductivities can be obtained depending on the proposed application.

To test the effectiveness of the developed samples for cell proliferation, electrical stimulation experiments were carried out (Fig. 2, *c−e*). Structured and unstructured areas for experimental sample (Fig. 2, *d*) are marked on Fig. 2, *e*.
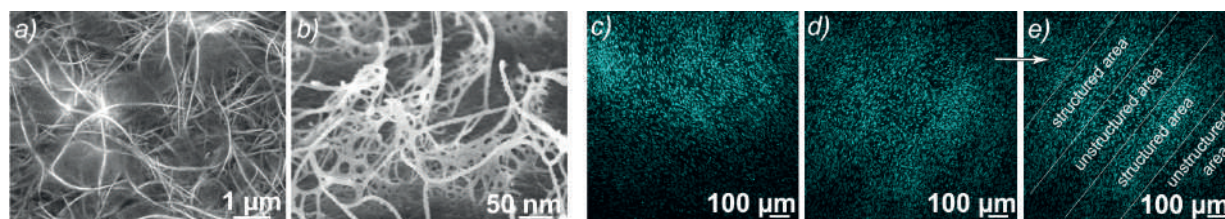
Fig. 2. Results of experiments with obtained samples: SEM images before (*a*) and after (*b*) laser irradiation, fluorescence images of cells on samples: control − cover glass (*c*), experimental sample with structuring and cells stimulation (*d*) and its areas visualization (*e*)

According to microscopy data, connective tissue cells formed a monolayer during cultivation. It is seen that areas structured with laser radiation demonstrate better proliferation of cells on these surfaces compared to unstructured areas. An increase in the cell number was obtained by 4.3 times for cells compared to normal conditions on control samples. The combined effect of the conductive framework and electrical stimulation shows active proliferation associated with electrical conductivity and suitable surface structure for cell adhesion. The morphology of cultured cells does not differ from the control sample, indicating the absence of toxicity.

Conclusion

The method for creating biocompatible nanomaterials from carbon nanomaterial has been developed. The binding of nanotubes together occurs after pulsed laser irradiation in the near-infrared region of the spectrum (1064 nm) with radiation power of 0.07 W. The resulting structures with SWCNT and rGO after laser irradiation were characterized by more than twofold increase in electrical conductivity compared to the original samples. The results of experiments on electrical stimulation of cells showed an increase of cell proliferation on obtained samples. The developed materials can be successfully used for various bioelectronic applications, including electrical stimulation for more effective cultivation for different types of cells, for wearable devices, which record and stimulate cells activity and many others.

REFERENCES

1. **Zhang A., Lieber C.M.,** Nano-bioelectronics, Chemical reviews. 116 (1) (2016) 215–257.

2. **Cho K.W., Sunwoo S.H., Hong Y.J., Koo J.H., Kim J.H., Baik S., Kim D.H.,** Soft bioelectronics based on nanomaterials, Chemical Reviews. 122 (5) (2021) 5068–5143.

3. **Katoh K.,** Effects of electrical stimulation of the cell: wound healing, cell proliferation, apoptosis, and signal transduction, Medical Sciences. 11 (1) (2023) 11.

4. **Deng J., Yuk H., Wu J., Varela C.E., Chen X., Roche E.T., Zhao X.,** Electrical bioadhesive interface for bioelectronics, Nature materials. 20 (2) (2021) 229–236.

5. **Arugula M., Simonian A.,** Nanocarbon-Based Multi-Functional Biointerfaces: Design and Applications, ECS Journal of Solid State Science and Technology. 5 (8) (2016) M3045.

6. **Rastogi S.K., Kalmykov A., Johnson N., Cohen-Karni T.,** Bioelectronics with nanocarbons, Journal of materials chemistry B. 6 (44) (2018) 7159–7178.

THE AUTHORS

KURILOVA Uliana E.
kurilova_10@mail.ru
ORCID: 0000-0002-3388-5146

MEZENTSEVA Marina V.
marmez@mail.ru
ORCID: 0000-0002-8940-7506

MURASHKO Denis T.
skorden@outlook.com
ORCID: 0000-0002-9437-8260

RUSSU Leonid I.
plano77@bk.ru
ORCID: 0000-0001-6353-9917

SUCHKOVA Victoria V.
molodykh1999@gmail.com
ORCID: 0000-0002-3207-7622

GERASIMENKO Alexander Yu.
gerasimenko@bms.zone
ORCID: 0000-0001-6514-2411

SUETINA Irina A.
ikas@inbox.ru
ORCID: 0000-0003-2878-0590

RADIOPHYSICS

Development of an inter-satellite data transmission network for space debris evasion systems

A.A. Popov [1] ✉, V.V. Davydov [1, 2], A.V. Shavshin [1],

D.A. Boldarev [2], D.Yu. Klimenko [1], R.A. Dmitriev [3]

[1] Peter the Great St. Petersburg Polytechnic University, St. Petersburg, Russia;

[2] Bonch-Bruevich Saint-Petersburg State University of Telecommunications, St. Petersburg, Russia;

[3] The Russian Institute of Radionavigation and Time, St. Petersburg, Russia

✉ alexander_popov_work@mail.ru

Abstract. The space debris problem was revealed. Research of space debris situation data from open sources of information such as European Space Agency was carried out. Methods of satellite protection were revealed. Collision avoidance system was proposed. It consists of satellites with a built-in location system and low speed mesh-network. Location satellites are used for long-range precise detection of objects with trajectories which are dangerous for protected spacecrafts, while the data is transmitted with CubeSat chain. The aim of this work is to develop an inter-satellite network for technical information exchange. As a result of the research, LoRa technology is selected because of low power consumption and significant coverage range of a single device. The network operation was simulated using MATLAB software and calculated results confirmed that the proposed method is adequate.

Keywords: inter-satellite network, LoRa, network simulation, mesh network, space debris, collision avoidance

Разработка межспутниковой сети передачи данных для систем уклонения искусственных спутников земли от космического мусора

А.А. Попов [1] ✉, В.В. Давыдов [1, 2], А.В. Шавшин [1],

Д.А. Болдарев [2], Д.Ю. Клименко [1], Р.А. Дмитриев [3]

[1] Санкт-Петербургский политехнический университет Петра Великого, Санкт-Петербург, Россия;

[2] Санкт-Петербургский государственный университет телекоммуникаций им. проф. М.А. Бонч-Бруевича, Санкт-Петербург, Россия;

[3] Российский институт радионавигации и времени, Санкт-Петербург, Россия

✉ alexander_popov_work@mail.ru

Аннотация. Обоснована проблема, связанная с повреждением спутниковых группировок в результате столкновения с неиспользуемыми объектами на орбите Земли.

Предложена система для уклонения искусственных спутников Земли от космического мусора. Она состоит из спутников с бортовыми радиолокационными станциями и кубсатов, объединенных в меш-сеть. Модель сети была разработана в среде MAT-LAB. Оценка качественных параметров сети показала возможность применения такой конфигурации для передачи данных.

Ключевые слова: межспутниковая сеть, mesh-сеть, модель сети, LoRa, космический мусор, уклонение от космического мусора

Introduction

Artificial Earth Satellites (AES) are among the most powerful tools across a wide range of fields, such as science, telecommunications, radio navigation, and many others [1−3]. Satellite systems are extremely important; therefore, all space nations strive to improve their operational reliability and efficiency [4, 5]. However, modern spaceflights must contend with space debris, which poses a threat to both AES and manned spacecraft [6]. Under the conditions of accumulating space debris in low Earth orbit (LEO), the safety of spacecraft is becoming one of the key challenges of modern astronautics. According to the European Space Agency (ESA), there are more than 40000 objects larger than 10 cm in orbit, and the number of small debris fragments amounts to hundreds of millions [7, 8]. A collision with such objects could lead to damage or complete destruction of satellites, which would result in significant economic losses and pose a threat to further space exploration.

A complex solution to the abovementioned problem is required, consisting of specialized AES carrying equipment to detect potentially dangerous trajectories of small space debris and the creation of inter-satellite networks for exchanging operational information needed to adjust the orbital parameters of the threatened spacecraft. This paper examines one variant of such a network. The structural diagram of the network and its operational principle are shown in Figure 1.

Fig. 1. Structural diagram of the network; 1 − AES detecting space debris;
2 − space debris; 3 − AES − participant of the mesh network;
4 − satellite threatened by the detected object; 5 − intersection of the debris trajectory and the orbit of the at-risk satellite

Materials and Methods

Technologies of the Internet of Things (IoT) were considered as the main devices for organizing networks because of their low power consumption which is necessary for implementation on CubeSats.

Among the different ones, LoRa technology was chosen as the primary transmission scheme.

LoRa (Long Range) is a wireless communication technology based on Chirp Spread Spectrum (CSS) modulation, designed for low-power, long-range data transmission in the sub-GHz bands. It is widely used in low-power wide-area networks (LPWANs). In this work, the LoRa physical layer is considered with reference to the SX1276 transceiver chip, which implements the modulation and coding schemes defined by the datasheet [9].

The justification for this choice is in use of CSS modulation, which provides a large processing gain and enables long-range communication compared to other low-power IoT technologies. Moreover, LoRa can reliably decode signals at very low signal-to-noise ratios down to around negative tens dB for high spreading factors with additional robustness provided by forward error correction at the physical layer. These properties make LoRa particularly suitable for long-distance communication in low Earth orbit scenarios, where link budgets are highly constrained.

Simulation in MATLAB software, a time-based discrete event simulator, was used to calculate the main parameters of the network.

The simulations were performed specifically for the LoRa32 platform, which integrates the SX1276 transceiver operating at a carrier frequency of 868 MHz. The modeling included the estimation of maximum communication distance using the Friis free-space propagation model, the achievable data rate as a function of spreading factor and coding rate, and the probability of bit error under various channel conditions.

Detail review of simulation stages:

1. Parameters of the transceiver devices are specified: transmitter power, minimum receiver sensitivity threshold below which the signal cannot be detected, carrier frequency, and the gain of the transmitting and receiving antennas.

2. The orbital altitudes for satellites within one orbital plane are defined, along with the observation time for simulation visualization.

3. Orbital planes are generated for three groups: equatorial, polar, and inclined. It is possible to adjust the inclination, the right ascension of the ascending node, and the number of orbital planes in each group. Satellites are evenly distributed along each orbit within the group, according to the specified number and initial phase. For each satellite, the true anomaly and Cartesian coordinates are calculated. All satellite parameters are stored in a global matrix.

4. After the physical placement of satellites is completed, they are considered as nodes of a data transmission network.

A classic case of CubeSat stabilization in a single plane is considered, where the main lobe of the antenna radiation pattern points toward the Earth. The antenna orientation for each node is defined by the angle relative to the velocity vector in the plane formed by that vector and the orbital plane normal. This angle can also be changed to model the stabilization type.

The deviation of the dipole antenna pattern from the isotropic pattern in the direction of every other node is calculated. A dipole antenna is chosen due to its omnidirectional coverage capability, required under varying satellite orientations, and its low mass.

5. The communication range is calculated, and a connectivity matrix is built according to the Distance-Vector routing protocol model. This stage includes: calculation of free-space path loss as a function of wavelength; 5 dB noise to simulate various network losses reducing communication range; calculation of received power based on transmitter power, antenna gains with anisotropy taken into account, free-space attenuation, and distance losses; application of a function specific to LoRa technology (SX1276 chip), which collects metrics for each inter-satellite channel pair using received power, bandwidth, spreading factor, and coding rate. Signal-to-noise ratio and bit error rate are computed.

For each channel, the maximum communication distance is determined and, along with the SNR (threshold SNR = −20 dB for LoRa in this case), the feasibility of communication is decided and reflected in the connectivity matrix. Radio propagation delay is also calculated for each channel and stored in a separate matrix.

6. Isolated clusters and individual satellites are identified.

7. Nodes with the largest physical separation are identified, and the most efficient route in terms of transmission time is constructed using the Distance-Vector protocol model. Key parameters are evaluated, including packet transmission time, relative bit rate, signal-to-noise ratio at each hop and bit error probability along the route. Arbitrary node pairs may also be selected for analysis.

8. The same procedure is performed for the pair of nodes with the maximum propagation delay in the network. This allows assessment of the same parameters under worst-case conditions, ensuring that performance between arbitrary nodes will be superior to this worst-case baseline.

9. Visualization of all calculations described above is carried out.

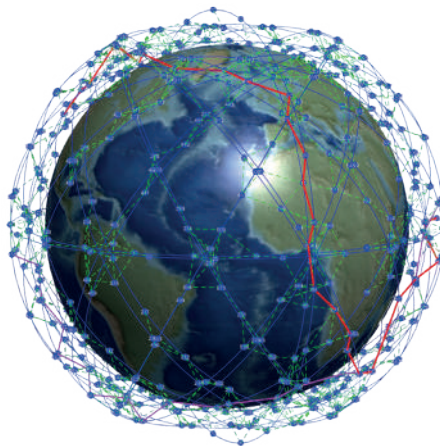Example of such visualization is shown in the Figure 2.

Fig. 2. Model of the network

Results and Discussion

Key results of the simulation are represented in Table 1.

They were calculated as average between twenty simulations with 20 minutes difference in time for 500 satellites.

Table 1

Results of simulation

Transmitter	SX1276
Antenna gain	2 dBi
Calculated max link distance	1945.27 km
Time delay for 30-byte packet (15256 km)	21.7 s (purple)
Time delay for longest link in the network	28.9 s (red)
Mean SNR for purple path	1.82 dB
Mean SNR for red path	1.56 dB
Relative transmission rate	11.07 bps (purple)
Relative transmission rate	8.31 bps (red)

The maximum link distance was determined from the longest successfully established connection, implying that the SNR in that channel remained above −20 dB and the distance did not exceed the value predicted by the Friis propagation model.

End-to-end delays were calculated assuming the highest achievable LoRa coding rate and including routing hopping for a 30-byte packet, which was selected as the minimal payload required for collision avoidance.

The reported mean SNR values account for the entire multi-hop mesh path.

Relative transmission rates were obtained by dividing the packet payload by the corresponding transmission time and are presented to enable comparison with alternative communication systems.

Also, the calculation of bit errors was performed for chosen nodes 1 and 500. The topology is represented in Figure 3.
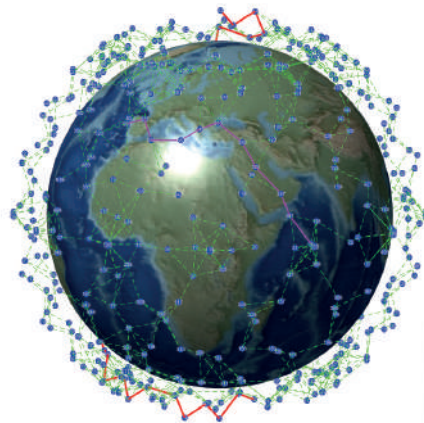

Fig. 3. Model of bit errors calculation

Table 2

Results of bit errors calculation

channel	BER
From 1 to 367	5.5235e-04
From 367 to 387	2.2218e-04
From 387 to 366	6.1843e-04
From 366 to 386	1.0180e-04
From 386 to 365	6.1857e-04
From 365 to 540	3.2315e-05
From 540 to 560	2.2215e-04
From 560 to 346	5.8258e-04
From 346 to 325	6.3956e-04
From 325 to 500	1.3506e-04

Bit errors for intersatellite channels were calculated using the following formula because it is suitable for lora chirp spread spectrum modulation:

$$BER = \frac{erfc\left(10^{\frac{SNR}{10}}\right)}{2}.$$

Errors are not larger than six ten thousandths. They can be lowered using code rate enlargement. Each node recovers errors of previous transmission.

A mesh network meets all the requirements regarding architecture and scalability. It allows many nodes to be integrated, which will connect all satellites around the Earth so each individual device can send and receive data with any other node in the network thanks to signal routing. Therefore, the transmitter and receiver do not require direct radio contact, unlike in peer-to-peer networks. Moreover, this architecture is supported by many modern variants of technologies.

Also, IoT devices and protocols can achieve significant efficiency in space because of low signal path loss, low transmission power and small sizes of the telecommunication devices [10, 11].

Conclusion

The model for intersatellite mesh network was developed. It contains mechanism for different satellite orbits creation including true anomaly calculation, so that model is basically discrete time-event simulator, tx/rx parameters setting, distance vector protocol simulation and delay and snr estimations for chosen links.

It should be noted that a network like this will significantly reduce the threat of collisions with space debris for satellites of various types, as well as make manned space expeditions much safer.

REFERENCES

1. **Zhang A., Tariq A., Quddoos A., Ullah S., Abdullah-Al-Wadud M.,** Spatio-temporal analysis of urban expansion and land use dynamics using google earth engine and predictive modelsb, Scientific Reportsyu. 15 (1) (2025) 6993.

2. **Petrov A.A., Zaletov D.V., Davydov V.V., Shapovalov D.V.,** Peculiarities of Constructing a Scheme for Formation of a Microwave Excitation Signal in a Cesium Atomic Clock, Journal of Communications Technology and Electronics. 66 (3) (2021) 295−299.

3. **Kumar M., Yadav S., Behera P.K.,** Analyzing the position and stability of the Lagrangian points under the gravitational effect of the Sun, Moon and the Earth including its oblateness, Astronomy and Computing. 52 (2025) 100966.

4. **Kocifaj M., Kundracik F., Wallner S.,** Low Earth Orbit satellite fragmentation rates are critically disrupting the natural night sky background, Monthly Notices of the Royal Astronomical Society Letters. 541 (1) (2025) L47−L51.

5. **Lukashev N.A., Moroz A.V.,** Compact microwave frequency standard on Hg-199 ions for navigation systems, Journal of Physics: Conference Series. 1236 (1) (2019) 012068.

6. **Ryan S.,** pyBLOSSUM: An open-source python repository for assessing the ballistic limit of spacecraft structures under space debris impact, International Journal of Impact Engineering. 203 (2025) 105365.

7. **Miyoshi K., Yoshimura Y., Hanada T.,** Identification of two collided objects from in-situ debris measurements, Advances in Space Research. 75 (12) (2025) 8721−8727.

8. **Ledkov A., Aslanov V.,** Hybrid electrostatic ion beam shepherd schemes for active space debris removal from GEO to disposal orbit Astrodynamics. 9 (2) (2025) 273−288.

9. SX1276-7-8-9 Datasheet. URL: https://semtech.my.salesforce.com/sfc/p/#E0000000JelG/a/2R0000001Rbr/6EfVZUorrpoKFfvaF_Fkpgp5kzjiNyiAbqcpqh9qSjE Accessed Sep. 6, 2025.

10. **Petrov A.A., Grebenikova N.M.,** Some Directions of Quantum Frequency Standard Modernization for Telecommunication Systems, Lecture Notes in Computer Science (including subseries Lecture Notes in Artificial Intelligence and Lecture Notes in Bioinformatics). 11118 LNCS. (2018) 641−648.

11. **Wigchert J., Sciancalepore S., Oligeri G.,** Detection of Aerial Spoofing Attacks to LEO Satellite Systems via Deep Learning, Computer Networks. 269 (2025) 111408.

THE AUTHORS

POPOV Alexander A.
alexander_popov_work@mail.ru
ORCID: 0009-0004-8401-0181

DAVYDOV Vadim V.
davydov_vadim66@mail.ru

SHAVSHIN Artyom V.
shavshin2107@gmail.com
ORCID: 0000-0002-3597-8901

BOLDAREV Dmitriy A.
boldarev2001@inbox.ru

KLIMENKO Daria Yu.
dasha.klimenko.01@inbox.ru
ORCID: 0000-0002-1216-2192

DMITRIEV Roman A.
Rusher.official@gmail.com
ORCID: 0000-0002-2964-1165

THEORETICAL PHYSICS

Qubit-qubit entanglement in the Tavis–Cummings model with two independent resonators

A.R. Bagrov ✉[1], E.K. Bashkirov[1]

[1] Samara National Research University, Samara, Russia

✉ alexander.bagrov@mail.ru

Abstract. In this paper, a three-qubit Tavis–Cummings model with two independent lossless single-mode resonators is considered. It is assumed that the initial states of the resonator fields are thermal fields and the qubits are in genuine entangled W- and GHZ-type states. For the model under study and the specified initial states of the resonator fields and qubits, we have exactly solved the quantum Liouville equation for the full density matrix. The full density matrix was used to calculate the entanglement parameters — negativity and fidelity. The computer simulation results showed that in the investigated model, the entanglement for all initial qubit states breaks down rapidly with increasing intensity of the thermal fields of the resonators compared to the previously investigated three-qubit models. Moreover, a sudden death of entanglement is observed even for vacuum resonator fields.

Keywords: independent resonators, fidelity, qubits, negativity, sudden death of entanglement, single-photon transitions, thermal field, entanglement

Кубит-кубитное перепутывание в модели Тависа–Каммингса с двумя независимыми резонаторами

А.Р. Багров ✉[1], Е.К. Башкиров[1]

[1] Самарский национальный исследовательский университет, г. Самара, Россия

✉ alexander.bagrov@mail.ru

Аннотация. В работе рассматривается трехкубитная модель Тависа–Каммингса с двумя независимыми одномодовыми резонаторами без потерь. Предполагается, что начальным состоянием полей резонаторов являются тепловые поля, а кубиты находятся в истинно перепутанных состояниях W- и GHZ-типа. Для исследуемой модели и указанных начальных состояний полей резонаторов и кубитов нами было точно решено квантовое уравнение Лиувилля для полной матрицы плотности. Полная матрица плотности использовалась для вычисления параметров перепутывания — отрицательности и степени совпадения. Результаты компьютерного моделирования показали, что в исследуемой модели перепутанность для всех начальных состояний кубитов быстро разрушается с увеличением интенсивности тепловых полей резонаторов по сравнению с ранее исследуемыми трехкубитными моделями. Более того, даже для вакуумных полей резонаторов наблюдается эффект мгновенной смерти перепутывания.

Introduction

Multiqubit genuine entangled qubit states are the foundation for various areas of quantum technology [1, 2]. In particular, entangled qubit states are used in quantum computers. The elementary cells of any quantum computer are so-called gates, which allow the performance of various operations on qubits, i.e., the building of various quantum algorithms. Descriptions of physical realizations of two- and three-qubit gates can be found, for example, in [3]. The increased interest in three-qubit systems is explained by the fact that they can be used for the creation of universal three-qubit gates of the Toffoli or Fredkin type, which can significantly simplify codes of quantum error corrections and will allow the creation of more complex quantum algorithms for solving various problems. Despite the large number of experimental and theoretical works devoted to the study of entangled states, many aspects of the entanglement, especially in the case of multiqubit systems, need further detailed study. One of the serious problems arising when using entangled states in quantum information processing problems is the inevitable degradation of entangled states and the sudden death of entanglement [4, 5]. These effects have been studied in detail in various two-qubit systems, and much less work is devoted to the study of sudden death of entanglement with respect to multiqubit systems (see refs. in [6]).

In this paper, we study in detail the dynamics of qubit entanglement for a three-qubit model in which three qubits are trapped in two independent resonators and interact with the corresponding mode of the resonator field via single-photon processes. For the model under study we have solved exactly the quantum Liouville equation for the full density matrix describing the "three qubits+two modes of the resonator field". This density matrix was used to calculate the fidelity, the negativity criterion, and to analyze the dynamics of qubit entanglement.

The Tavis−Cummings model and its solution

In this work, the dynamics of entanglement of three identical qubits Q_1, Q_2 and Q_3 are investigated. Qubit Q_1 is trapped in the resonator a, qubits Q_2 and Q_3 are in the resonator b. Qubits resonantly interact with the quantum thermal field mode of their ideal resonator via single-photon processes. The interaction Hamiltonian of the model under study in standard notations and approximations is written in the following form

$$H_{Int} = \hbar\gamma\left(\sigma_{Q_1}^+ \xi + \sigma_{Q_1}^- \xi^+ + \sigma_{Q_2}^+ \eta + \sigma_{Q_2}^- \eta^+ + \sigma_{Q_3}^+ \eta + \sigma_{Q_3}^- \eta^+\right), \tag{1}$$

where $\sigma_l^+ = |+\rangle_{ll}\langle-|$ and $\sigma_l^- = |-\rangle_{ll}\langle+|$ are the transition operators between the excited $|+\rangle_l$ and the ground $|-\rangle_l$ states in the l-th qubit ($l = Q_1$, Q_2, Q_3), $\xi^+(\eta+)$ and $\xi(\eta)$ are the creation and the annihilation operators of the photons in the mode of the resonator $a(b)$, γ is the qubit-photon coupling.

As the initial state of the resonator field, we choose a thermal states with a density matrixes of the form:

$$\wp_{F_a}(0) = \sum_{n_a} p_{n_a} |n_a\rangle\langle n_a|, \quad \wp_{F_b}(0) = \sum_{n_b} p_{n_b} |n_b\rangle\langle n_b|, \tag{2}$$

Here, there are weight coefficients $p_{n_i} = \dfrac{\langle n \rangle_i^{n_i}}{(1 + \langle n \rangle_i)^{n_i+1}}$, $\langle n \rangle_i = \dfrac{1}{e^{\hbar \omega_i / k_B T_i} - 1}$ is the mean number of

photons in the i-th resonator ($i = a, b$), T_i is the cavity temperature. Let the initial states of qubits be the W-states, such as

$$|W_1(0)\rangle_{Q_1 Q_2 Q_3} = \cos\theta \,|+,+,-\rangle + \sin\theta \sin\varphi \,|+,-,+\rangle + \sin\theta \cos\varphi \,|-,+,+\rangle, \tag{3}$$

$$|W_2(0)\rangle_{Q_1 Q_2 Q_3} = \cos\theta \,|-,-,+\rangle + \sin\theta \sin\varphi \,|-,+,-\rangle + \sin\theta \cos\varphi \,|+,-,-\rangle, \tag{4}$$

or GHZ-state

$$|G(0)\rangle = \cos\phi \,|+,+,+\rangle + \sin\phi \,|-,-,-\rangle. \tag{5}$$

Here θ, φ, and ϕ are the parameters that determine the initial degree of qubit entanglement.

We derived the solutions of the quantum Liouville equation for the whole density matrix $\wp_{Q_1 Q_2 Q_3 F_a F_b}$ of the considered system with Hamiltonian (1) and the indicated initial states for the qubits and the resonator field (2)-(5)

$$i\hbar \frac{\partial \wp_{Q_1 Q_2 Q_3 F_a F_b}}{\partial t} = \left[H_{Int}, \wp_{Q_1 Q_2 Q_3 F_a F_b} \right]. \tag{6}$$

Even compact solutions for the quantum Liouville equation (6) look too large and for this reason are not presented in this paper to save room.

In this paper, our focus was on two parameters of entanglement: pairwise negativity $\varepsilon_{Q_i Q_j}(\gamma t)$ and fidelity $F(\gamma t)$. The fidelity is written as follows [7]: $F\left[\wp(0), \wp'(t)\right] = Tr\left[\wp(0)\wp'(t)\right]$, where $\wp(0) \equiv \wp_{Q_1 Q_2 Q_3}(0)$ is the initial three-qubit density matrix, $\wp'(t) \equiv \wp_{Q_1 Q_2 Q_3}(t)$ is the three-qubit density matrix at subsequent time instants t. The three-qubit density matrix can be obtained from the full density matrix by averaging over the field variables of the two resonators $\wp_{Q_1 Q_2 Q_3} = Tr_{F_a} Tr_{F_b} \wp_{Q_1 Q_2 Q_3 F_a F_b}$.

We define the negativity $\varepsilon_{Q_i Q_j}(\gamma t)$ in a standard way [8]: $\varepsilon_{Q_i Q_j} = -2\sum \lambda_{l,ij}^-$, where $\lambda_{l,ij}^-$ are the negative eigenvalues of the two-qubit density matrixes partially transposed in variables of one qubit $\wp_{ij}^{T_1}$. To calculate the negativity of two qubits, we need to compute a partially transposed reduced two-qubit density matrix over the variables of one qubit $\wp_{Q_i Q_j}^{T_1}$, whose elements are defined as follows via the two-qubit density matrix $\left\langle p_i, m_j \left| \wp_{Q_i Q_j} \right| k_i, l_j \right\rangle^{T_1} = \left\langle k_i, m_j \left| \wp_{Q_i Q_j} \right| p_i, l_j \right\rangle$, where $|p\rangle, |m\rangle, |k\rangle, |l\rangle = |+\rangle, |-\rangle$ and two-qubit density matrix $\wp_{Q_i Q_j} = Tr_{Q_x} \wp_{Q_1 Q_2 Q_3}$ $(i, j, x = 1, 2, 3; i \neq j \neq x)$.

Results and Discussion

The results of computer modeling of the pairwise negativities $\varepsilon_{Q_i Q_j}(\gamma t)$ and fidelity $F(\gamma t)$ for initial qubit W-state (3) and thermal field (2) are shown in Fig. 1. Figures represent the behavior of negativities, calculated for various mean photon numbers $\langle n \rangle$ with the initial parameters $\theta = \arccos(1/\sqrt{3})$, $\varphi = \pi/4$. In Fig. 2, we plot the fidelity for the initial qubit GHZ-state (5) and thermal field (2) in the model (1) and model "three qubits in common resonator" with the initial parameters $\phi = \pi/4$.

The following conclusions can be drawn from the presented figures. From Figs. 1 and 2, we can clearly see that the maximum degree of entanglement decreases monotonically with increasing intensity of the thermal fields of the resonators $\langle n \rangle$ for any initial states of qubits (3)-(5). From the comparison of Fig. 1, a and 1, b, we can conclude that the Q_2 and Q_3 qubits are more robust to the thermal noise of the resonator than the Q_1 and Q_2 (or Q_1 and Q_3) qubits. Moreover, the maximum entanglement degree of qubits Q_2 and Q_3 can exceed the initial pairwise entanglement of qubits $\varepsilon_{Q_i Q_j} = (\sqrt{5} - 1)/3$ for the W-states (3)-(4). Moreover, from Fig. 1, a and Fig. 1, b we can clearly see that at some moments of time negativity takes zero values $(\varepsilon_{Q_i Q_j}(\gamma t) = 0)$. This suggests the presence of an sudden death effect of entanglement qubits for the W-state (3) even in the case of low intensities of the thermal fields of the resonators $\langle n_a \rangle = \langle n_b \rangle = 0.001$. The entangled W-type states (3)-(4) behave identically and for this reason the plots for the W-state (4) are not given. An analysis of the behavior of the fidelity (see Fig. 1, c and Fig. 2, a) shows that the initial genuine entangled W-states (3)-(4) or GHZ-state (5) never return to the initial states during the evolution process.
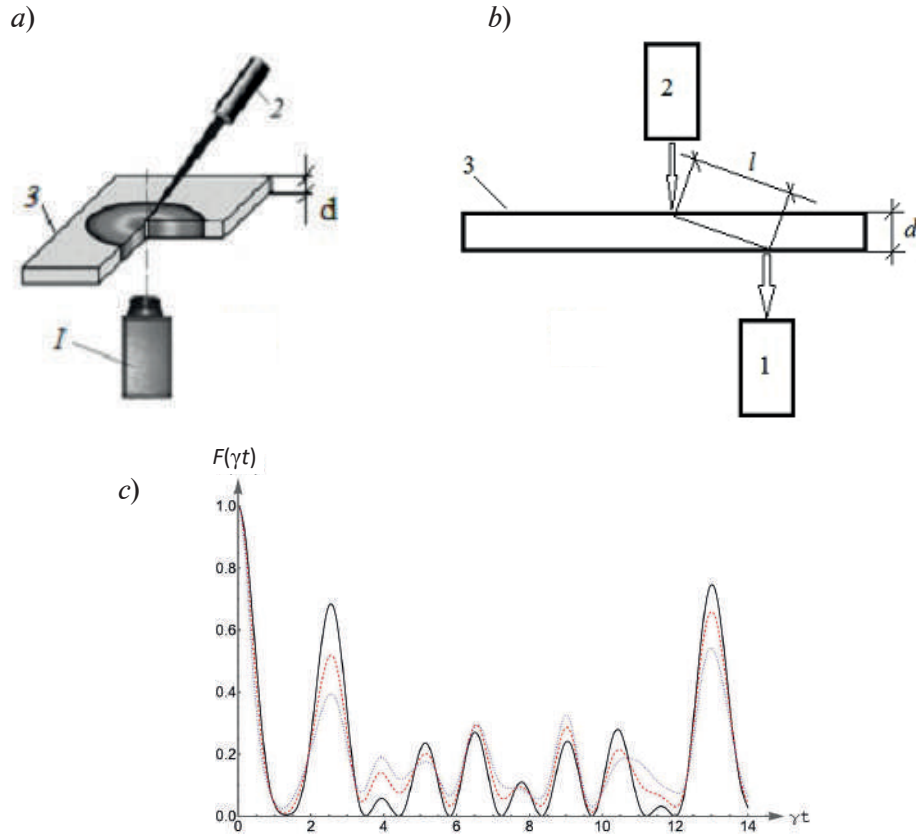
Fig. 1. The negativity $\varepsilon_{Q_iQ_j}(\gamma t)$ (a, b) and fidelity $F(\gamma t)$ (c) as functions of the scaled time γt for the initial W-state of the form (3). The mean number of photons: $\langle n_a \rangle = \langle n_b \rangle = 0.001$ (black solid line), $\langle n_a \rangle = \langle n_b \rangle = 0.2$ (red dashed line), $\langle n_a \rangle = \langle n_b \rangle = 0.5$ (blue dotted line). Initial parameters: $\theta = \arccos(1/\sqrt{3})$, $\varphi = \pi/4$
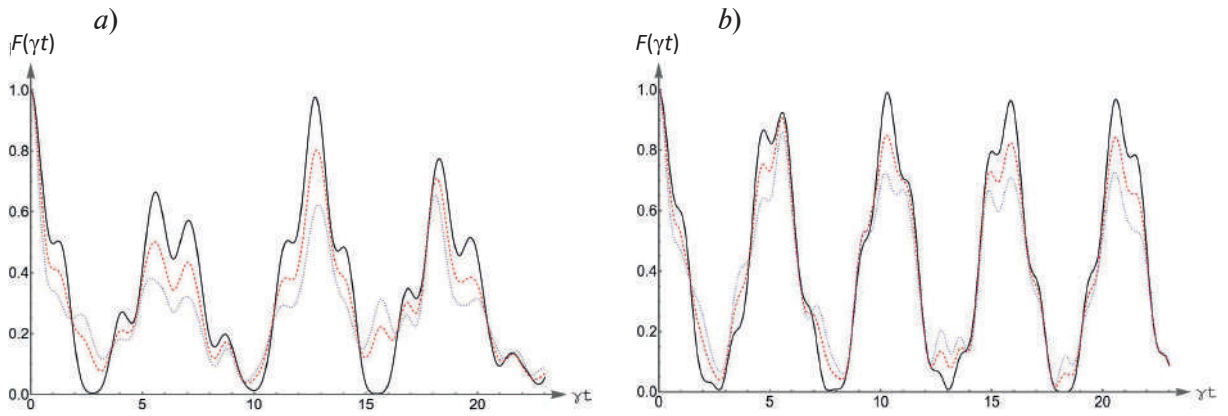

Fig. 2. The fidelity $F(\gamma t)$ as a function of the scaled time γt for the initial GHZ-state of the form (5) in the model (1) (a) and in the model "three qubits in common resonator" (b). The mean number of photons: $\langle n_a \rangle = \langle n_b \rangle = 0.001$ (black solid line), $\langle n_a \rangle = \langle n_b \rangle = 0.2$ (red dashed line), $\langle n_a \rangle = \langle n_b \rangle = 0.5$ (blue dotted line). Initial parameter: $\phi = \pi/4$

Thus, the initial entanglement is completely destroyed even in the case of the vacuum field of the resonator $(\langle n \rangle \to 0)$. From the comparison of Fig. 2, a and Fig. 2, b, it can be seen that the entanglement of qubits in the model with three qubits in a common resonator is more robust to the thermal noise of the resonator than the model studied in this paper. A similar result is obtained for genuine entangled W-type states (3)-(4) (see refs. [9]).

Conclusion

Thus, in this paper we have exactly solved the quantum Liouville equation for the three-qubit Tavis−Cummings model in which one of the qubits Q_1 is in the resonator a, and the two remaining qubits Q_2 and Q_3 are trapped in the second resonator b. It is assumed that all qubits are identical and their coupling to the field is equal. Our focus was on the genuine entangled Werner and Greenberger−Horn−Zeilinger states, and the fields of the resonators are in the thermal state. The computational results show that in the model under study, the genuine entangled states are quite fragile with respect to the thermal noise of the resonators compared to the previously studied three-qubit models [9]. We also show, using the fidelity $F(\gamma t)$, that the W- and GHZ-type states never return to the initial states during evolution, even for vacuum fields of $(\langle n \rangle \to 0)$ resonators. Moreover, the evolution of the negativity criterion shows that the sudden death of pair entanglement occurs for both W-states (3)-(4).

REFERENCES

1. **Tao Y.,** Quantum entanglement: principles and research progress in quantum information processing, Theoretical and Natural Science. 30 (1) (2024) 263−274.

2. **Wang Y., Song X.,** Quantum Science and Quantum Technology, Statistical Science. 35 (1) (2020) 51−74.

3. **Chouikh A. et al.,** Implementation of universal two- and three-qubit quantum gates in a cavity QED, Optical and Quantum Electronics. 48 (10) (2016) 1−15.

4. **Yu T., Eberly J.H.,** Sudden death of entanglement, Science. 323 (2009) 598−601.

5. Almeida M. P. et al., Environment-induced sudden death of entanglement, Science. 316 (2007) 579−582.

6. **Bagrov A.R., Bashkirov E.K.,** Dynamics of entanglement in a model consisting of an isolated atom and two Tavis-Cummings atoms with many-photon transitions, Quantum Information Processing. 24 (2025) 154.

7. **Jozsa R.,** Fidelity for mixed quantum states, Journal of Modern Optics. 41 (12) (1994) 2315−2323.

8. **Peres A.,** Separability Criterion for Density Matrices, Physical Review Letters. 77 (8) (1996) 1413−1415

9. **Bagrov A. R., Bashkirov E. K.,** Sudden death of entanglement in a thermal three-qubit Tavis-Cummings model, IEEE Proceedings of ITNT 2023. (2023) 10139206.

THE AUTHORS

BAGROV Alexander R.
alexander.bagrov@mail.ru
ORCID: 0000-0002-1098-0300

BASHKIROV Eugene K.
bash@ssau.ru
ORCID: 0000-0001-8682-4056

УСЛОВИЯ ПУБЛИКАЦИИ СТАТЕЙ
в журнале «Научно-технические ведомости
Санкт-Петербургского государственного политехнического университета.
Физико-математические науки»

1.ОБЩИЕ ПОЛОЖЕНИЯ

Журнал «Научно-технические ведомости Санкт-Петербургского государственного политехнического университета. Физико-математические науки» является периодическим печатным научным рецензируемым изданием. Зарегистрирован в Федеральной службе по надзору в сфере информационных технологий и массовых коммуникаций (Свидетельство ПИ №ФС77-52144 от 11 декабря 2012 г.) и распространяется по подписке агентства «Роспечать» (индекс издания 71823).

С 2008 года журнал издавался в составе сериального издания "Научно-технические ведомости СПбГПУ". **Сохраняя преемственность и продолжая научные и публикационные традиции сериального издания «Научно-технические ведомости СПбГПУ», журнал издавали под сдвоенными международными стандартными сериальными номерами ISSN 1994-2354 (сериальный) 2304-9782.** В 2012 году он зарегистрирован как самостоятельное периодическое издание **ISSN 2304-9782** (Свидетельство о регистрации ПИ № ФС77-52144 от 11 декабря 2012 г.). С 2012 г. начат выпуск журнала в двуязычном оформлении.

Издание входит в Перечень ведущих научных рецензируемых журналов и изданий (перечень ВАК) и принимает для печати материалы научных исследований, а также статьи для опубликования основных результатов диссертаций на соискание ученой степени доктора наук и кандидата наук по следующим основным научным направлениям: **Физика, Математика, Механика**, включая следующие шифры научных специальностей: 1.1.8., 1.1.9., 1.3.2., 1.3.3., 1.3.4., 1.3.5., 1.3.6., 1.3.7., 1.3.8., 1.3.11., 1.3.19.

Журнал представлен в Реферативном журнале ВИНИТИ РАН и включен в фонд научно-технической литературы (НТЛ) ВИНИТИ РАН, а также в международной системе по периодическим изданиям «Ulrich's Periodicals Directory». Индексирован в базах данных «Российский индекс научного цитирования» (РИНЦ), Web of Science (Emerging Sources Citation Index).

Периодичность выхода журнала – 4 номера в год.

Редакция журнала соблюдает права интеллектуальной собственности и со всеми авторами научных статей заключает издательский лицензионный договор.

2. ТРЕБОВАНИЯ К ПРЕДСТАВЛЯЕМЫМ МАТЕРИАЛАМ
2.1. Оформление материалов

1. Рекомендуемый объем статей – 12-20 страниц формата А-4 с учетом графических вложений. Количество графических вложений (диаграмм, графиков, рисунков, фотографий и т.п.) не должно превышать шести.

2. Число авторов статьи, как правило, не должно превышать пяти человек.

3. Авторы должны придерживаться следующей обобщенной структуры статьи: вводная часть (актуальность, существующие проблемы – объем 0,5 – 1 стр.); основная часть (постановка и описание задачи, методика исследования, изложение и обсуждение основных результатов); заключительная часть (предложения, выводы – объем 0,5 – 1 стр.); список литературы (оформление по ГОСТ 7.0.5-2008).

В списки литературы **рекомендуется** включать ссылки на научные статьи, монографии, сборники статей, сборники конференций, электронные ресурсы с указанием даты обращения, патенты.

Как правило, **нежелательны** ссылки на диссертации и авторефераты диссертаций (такие ссылки допускаются, если результаты исследований еще не опубликованы, или не представлены достаточно подробно).

В списки литературы **не рекомендуется** включать ссылки на учебники, учебно-методические пособия, конспекты лекций, ГОСТы и др. нормативные документы, на законы и постановления, а также на архивные документы (если все же необходимо указать такие источники, то они оформляются в виде сносок).

Рекомендуемый объем списка литературы для обзорных статей – не менее 50 источников, для остальных статей – не менее 10.

Доля источников давностью менее 5 лет должна составлять не менее половины. Допустимый процент самоцитирования – не выше 10 – 20. Объем ссылок на зарубежные источники должен быть не менее 20%.

4. УДК (UDC) оформляется и формируется в соответствии с ГОСТ 7.90-2007.

5. Набор **текста** осуществляется в редакторе **MS Word.**

6. **Формулы** набираются в редакторе MathType (не во встроенном редакторе Word) (мелкие формулы, символы и обозначения набираются без использования редактора формул). **Таблицы** набираются в том же формате, что и основной текст. В тексте буква «ё» заменяется на букву «е» и оставляется только в фамилиях.

7. **Рисунки** (в формате .tiff, .bmp, .jpeg) и **таблицы** оформляются в виде отдельных файлов. Шрифт – **Times New Roman**, размер шрифта основного текста – 14, интервал – 1,5. Таблицы большого размера могут быть набраны кеглем 12. Параметры страницы: поля слева – 3 см, сверху и снизу – 2 см, справа – 1,5 см. Текст размещается без знаков переноса. Абзацный отступ – 1 см.

2.2. Представление материалов

1. Представление всех материалов осуществляется в электронном виде через электронную редакцию (http://journals.spbstu.ru). После регистрации в системе электронной редакции автоматически формируется персональный профиль автора, позволяющий взаимодействовать как с редакцией, так и с рецензентом.

2. Вместе с материалами статьи должно быть представлено экспертное заключение о возможности опубликования материалов в открытой печати.

3. Файл статьи, подаваемый через электронную редакцию, должен содержать только сам текст без названия, списка литературы, аннотации и ключевых слов, фамилий и сведений об авторах. Все эти поля заполняются отдельно через электронную редакцию.

2.3. Рассмотрение материалов

Предоставленные материалы (п. 2.2) первоначально рассматриваются редакционной коллегией и передаются для рецензирования. После одобрения материалов, согласования различных вопросов с автором (при необходимости) редакционная коллегия сообщает автору решение об опубликовании статьи. В случае отказа в публикации статьи редакция направляет автору мотивированный отказ.

При отклонении материалов из-за нарушения сроков подачи, требований по оформлению или как не отвечающих тематике журнала материалы не публикуются и не возвращаются.

Редакционная коллегия не вступает в дискуссию с авторами отклоненных материалов.

При поступлении в редакцию значительного количества статей их прием в очередной номер может закончится **ДОСРОЧНО**.

E-mail: physics@spbstu.ru,
Тел. редакции 8 (812) 552-62-16.
Сайт журнала: https://physmath.spbstu.ru/